Cranfield University

Flow Control and Prediction Group
Cranfield College of Aeronautics
Beds, MK43 0AL
UK.

PhD thesis, Academic year 2000 - 2001

Franck BELLONE

New Models for the Prediction of Attachment-lines Behaviour at Hypersonic Speeds

---

Supervised by Professor D.I.A. Poll

24 January 2002

Abstract

This investigation concentrates on the attachment-line flow behaviour under wind tunnel and flight conditions. A turbulence model for incompressible, equilibrium flow was developed for low Reynolds number down to and including relaminarisation. This was then extended to compressible flow using CFD to analyse experiments in which the heat transfer was measured. The extension is based upon the introduction of two Reynolds numbers to correlate turbulence in the inner and outer regions of the viscous layer. This requires the addition of just one constant, which is determined from the experimental heat transfer data. The turbulence model was then used to calibrate an approximate heating prediction method based upon the reference temperature concept. This method was then used to determine the minimum conditions for sustainable turbulent attachment-line flow in presence of large sources of disturbance, such as trip wires. It has been shown that existing criteria for the minimum conditions provide excessively optimistic predictions. Therefore new, more accurate criteria were proposed.

Acknowledgements

The author would like to express his gratitude to Professor D.I.A Poll for all his guidance and encouragement throughout this research.

No knowledge can be certain, if it is not based upon mathematics or upon some other knowledge which is itself based upon the mathematical sciences. Instrumental, or mechanical, science is the noblest and, above all others, the most useful.

Leonardo da Vinci (1425 - 1519)

There is one more thing ..... It's been emotional.

Vinnie Jones
Lock, Stock and
Two Smoking Barrels.

Contents

Nomenclature

Symbols

a	Speed of sound [m/sec].
A	Coefficient connecting $\bar{R}$ to Re (equations 3.3 and 3.5) or random variable as in equation D.28 for example or station along the model used by Jones (figure G.24) or variable connecting the turbulent incompressible Stanton number to $\bar{R}$ (equation M.10) or damping length constant as defined by equation 4.14.
A'	Function in the reference temperature model (equation 6.13).
$\bar{A}_n$	Coefficient for finite difference equation E.52.
A^+	Damping parameter in the turbulence model (see equation 4.14).
B	Random variable as in equation D.28 for example or station along the model used by Jones (figure G.24) or variable connecting the turbulent incompressible Stanton number to $\bar{R}$ (equation M.10).
B'	Function in the reference temperature model (equation 6.13).
B_1 to B_3	Wall derivative numerical coefficients (equations E.69 to E.71).
$\bar{B}_n$	Coefficient for finite difference equation E.53.
B^+	Constant used in Cebeci [16] turbulence model (equation 4.40).
c	Streamwise velocity ratio as defined by equation E.18.
C	Random variable as in equation D.28 for example or station along the model used by Jones (figure G.24) or additive constant in the logarithmic law of the wall.
C'	Function in the reference temperature model (equation 6.13).
Cf	Skin friction coefficient.
CFL	CFL number as defined by equation D.15.
$\bar{C}_n$	Coefficient for finite difference equation E.54.
Cp	Specific heat coefficient at constant pressure [J/kg.K] or Pressure coefficient.
Cv	Specific heat coefficient at constant volume [J/kg.K].
C^*	Cumpsty and Head criterion (equation 2.5).
d	Distance by which an end plate extend ahead of the cylinder upstream tip (see figure G.20 for example) or depth of a roughness element i.e. cavity.
dS	Area of a cell surface (equation D.1 ; [m]).
dV	Volume of a computational cell [m^3].
D	Cylinder diameter [m] or random variable as in equation D.28 for example or station along the model used by Jones (figure G.24).
$\bar{D}_n$	Coefficient for finite difference equation E.55.
D_1	Coefficient for finite difference derivatives defined by equation E.47.
D_2	Coefficient for finite difference derivatives defined by equation E.48.

$\frac{dUe}{dX}$	Chordwise velocity gradient taken at the edge of the velocity viscous layer $[m^{-1}]$.
e	Internal energy defined by equation D.9.
E	Total energy (equation D.8).
$\vec{F}$	Vector of the primitive variables (equation D.10).
f	Transformed stream function (equation E.13).
f_1	Function in the reference temperature model (equation 6.12).
f'	Crossflow velocity ratio as defined by equation E.17.
F_2	Function in the reference temperature model (equation 6.12).
F_{Kleb}	Klebanoff function (equation 4.11).
F_{wake}	Wake function in Baldwin-Lomax turbulence model (equation 4.44).
g	Total enthalpy ratio as defined by equation E.19.
Grid-B1	Created grid for Beckwith run 15 conditions (section F.1.4 and figures F.17 to F.19).
Grid-H1 to Grid-H3	Created grids for Holden run 36 conditions (section F.1.4 and figures F.14 to F.16).
h	Heat transfer coefficient $h = \frac{q_W}{T_r - T_W}$.
H	Enthalpy [Joule] or Shape factor.
I	Vector co-ordinates as going around the cylinder (figure D.5).
IN	Maximum number of grid points in the I direction.
It	Number of iterations.
J	Vector co-ordinates as moving away from the cylinder surface in a normal direction to the wall (figure D.5).
JN	Maximum number of grid points in the J direction.
k	Roughness height [m or inches as specified] or von Kármán's constant.
k_t	Turbulent thermal conductivity (equation 4.39).
K	Vector co-ordinates as going along the cylinder (figure D.5) or Grid stretching factor used in the boundary layer code (equation E.49 ; $K = 1$ and $K = 1.03$ in laminar and turbulent mode respectively).
KN	Maximum number of grid points in the K direction.
k_t	Thermal conductivity (equation 4.20).
K1	Coefficient contained in the reference temperature T* (equations 6.10 and 6.11).
k_1	Outer eddy viscosity coefficient (see equation 4.9).
K2	Coefficient contained in the reference temperature T* (equation 6.10 and 6.11).
K3, K4	Coefficients contained in the reference temperature T^* (equation 6.11).
l	Density-Viscosity product ratio as defined by equation E.21 or mixing length or length of a roughness element (in spanwise direction) or mixing length scale (equation 4.4) depending on usage.
l1, l2	Mixing length scales (equation 4.3).
l^*	Modified density-viscosity product ratio as defined by equation E.22.
l^{**}	Modified density-viscosity product ratio as defined by equation E.23.

L	Cylinder length [m].
M	Mach number.
$\vec{n}$	Unit vector normal to cell surfaces (equation D.1).
Npoints	Number of grid points within the computational domain.
N_u	Nusselt number as defined by equation G.6.
P	Pressure [N/m^2].
Pt1	Point located in the centre of the computational cell at the wall at the attachment-line itself as shown by figure D.16.
Pt2	Point located in the centre of the computational cell close to the wall at the attachment-line itself as shown by figure D.16.
Pr	Molecular Prandtl number (Pr=0.72 or 0.70).
Pr_t	Turbulent Prandtl number, $Pr_t = 0.9$.
$\dot{q}$	Heat transfer rate [W/m^2.s].
Q	Velocity magnitude ($\sqrt{u^2 + v^2 + w^2}$) [m/sec] or conservative variables in equation D.11.
Q_o	Conservative variables at t=0 (equation D.12).
Q_1	Conservative variables after the first iteration (equation D.12).
r	Recovery factor (equation 2.17) or Radius of curvature [deg].
R	Specific gas constant (R=286.7 J/kg.K for air and 296.79 J/kg.K for nitrogen) or Navier-Stokes equations in equation D.11 or Reynolds number.
$\|\|R\|\|_2$	Residual as defined by equation D.14.
$\bar{R}$, Rbar	Attachment-line Reynolds number (equation 2.1).
$\bar{R}_{mc}$	Attachment-line Reynolds number for minimum conditions at which turbulent flow can occur.
$\bar{R}_{mini}$	Function in the reference temperature model (equation 6.12).
Re	Free-stream Reynolds number.
R_θ	Reynolds number based on the momentum thickness.
s	Sutherland's law constant [K] or distance as defined in equations D.28 and D.42.
St	Stanton number based on recovery temperature i.e. $\frac{q}{\rho V Cp(Tr-Tw)}$.
$\bar{St}$	Stanton number based on stagnation temperature i.e. $\frac{q}{\rho V Cp(To-Tw)}$.
t	Time [sec].
T	Temperature [K].
T_c	Characteristic temperature as defined by equation 5.7.
T^*	Temperature of reference [K] (equation 2.16 for example).
u or u	Velocity component corresponding to the x co-ordinate component i.e. chordwise direction [m/sec].
U_1	Non-dimensional chordwise velocity gradient (equation M.4).
U_{diff}	Velocity magnitude in Baldwin-Lomax turbulence model (equation 4.46).
u_τ	Shear stress velocity $u_\tau = (\tau_W/\rho)^{1/2}$ or $u_\tau = (\tau_w/\rho_w)^{1/2}$.
v or v	Velocity component corresponding to the y co-ordinate component i.e. spanwise direction [m/sec].

w or w	Velocity component corresponding to the z co-ordinate component [m/sec] or width of a roughness element (chordwise direction).
W	Primitive variables in equation D.11 or dependent variable in finite difference (equation E.31) or function in the reference temperature model (equation 6.13).
x or X	Co-ordinate component in the chordwise direction, normal to the attachment-line (figure A.5).
y	Co-ordinate component in the spanwise direction i.e along the attachment-line (figure A.5).
Y	Distance in the normal to the wall direction [m] (see for example equation L.15).
Y^+	Inner layer non-dimensional length scale as defined by equation 4.14.
z	Co-ordinate component normal to the cylinder surface (figure A.5).
Z	Distance from the wall normal to the surface [m] (equation F.2 for example).

Greek Symbols

α_1 to α_4	"Standard form" coefficients for parabolic partial differential equation (equations E.32 to E.43).
β	Inviscid velocity gradient parameter defined by equation E.24.
γ	Specific heat coefficient ($\gamma = 1.4$ for nitrogen and air).
δ	Boundary layer thickness [m].
Δt	Amount of time needed to achieve one iteration (equation D.15).
δ^*	Displacement thickness [m].
δ_k^*	Kinematic displacement thickness as defined by equation 4.10.
δ^+	Reynolds number as defined by equation 4.47.
η	Attachment-line characteristic length (equation 2.2) or Transformed co-ordinates as defined by equation E.12.
$\bar{\eta}$	Input value of the transformed co-ordinates (equation E.59).
θ	Polar angle as going around the cylinder, normal to the attachment-line or Momentum loss thickness [m] or Static temperature ratio defined by equation E.20.
θ_k	kinematic momentum thickness defined by equation 4.54.
λ	Bulk viscosity coefficient, $\lambda = (-2/3)\mu$ or eddy-conductivity (equation 4.19).
Λ	Sweep angle [deg].
μ	Dynamic viscosity [kg/m.sec].
ν	Kinematic viscosity [m^2/sec].
ξ	Transformed co-ordinates defined by equation E.11.
Π	Function in Cebeci's turbulence model (equation 4.51) or Wake strength (figure I.2).

ρ	Density [kg/m^3].
Υ	Damping function in the turbulence model as defined by equation 4.13.
τ	Shear stress.
$\bar{\tau}$	Matrix of the shear stress forces as defined by equations D.4 and D.5.
ϕ	Non-dimensional eddy viscosity [kg/m.sec] (equation 4.7.
ψ	Riemann invariant or non-dimensional stream function (equation E.13).
ω	Local vorticity as defined by equation 4.43.
Ω	Energy equation term as defined by equation E.25 or Difference between the inviscid and viscous value of a variable [%] (figure F.1) or Cebeci's coefficient (equation 4.52).
∇	Rotational.

Subscripts

0.99	Boundary layer edge taken at 99.9% of the inviscid value.
a	Conditions at or along the attachment-line.
adiaW	Adiabatic wall conditions.
c	Variable evaluated via the characteristic temperature T_c (equation 5.7).
D	Variable based on the cylinder diameter.
e	Conditions at the edge of the boundary layer.
Ho	Variable corresponding to the total enthalpy.
HT	Variable obtained for heat transfer i.e. from Stanton number.
i	Inner region of a turbulent boundary layer.
I	Variable evaluated in the I direction or initial profile guessed (equations E.56 to E.58) .
Inf-swept	Variable evaluated from the infinite swept conditions.
J	Variable evaluated in the J direction.
K	Variable evaluated in the K direction.
Local	Local value of the variable.
max	Maximum value of the variable.
model	Variable evaluated using the reference temperature models (e.g. equation 6.11).
N	Normal component of a variable.
o	Outer region of a turbulent boundary layer.
O	Stagnation or total conditions.
perf	Variable matching the incompressible turbulent relations.
r	Recovery conditions.
SF	Variable obtained from the skin friction.

t	Turbulent.
T	Variable corresponding to the temperature or thermal profile.
V	Variable corresponding to the velocity along the attachment-line.
W or w	Wall conditions.
$\Lambda = 0$	Variable evaluated from conditions obtained over a non-swept cylinder.
∞	Free-stream conditions or infinity.

Superscripts

T	Transposed form of a vector.
*	Variable transformed via the reference temperature T^*.
'	Fluctuating quantity or partial derivative with respect to η depending on usage.
-	Average quantity with respect to time.
$\rightarrow$	Vector.

Abbreviations

AL	Attachment-line.
BL	Boundary layer.
CFD	Computational fluid dynamics.
RLV	Reusable launch vehicle.
R.M.S.	Root mean square.
S.I.	System international.
TPS	Thermal protection system.

Note that the co-ordinates system used in the Navier-Stokes code (figure D.5) differs from the system used in the boundary layer code (figure E.1). The co-ordinates system used in the present investigation is as shown by figure A.5 and as reported in the nomenclature.

Chapter 1

Introduction

During their re-entry phase, Reusable Launch Vehicles (RLVs) dissipate their kinetic energy by aerodynamic breaking. Typically this involves angles of attack over 30° (Poll [52]). The large drag forces generated are associated with very high levels of heat transfer at the vehicle's surface. This is most severe near stagnation regions and along the attachment-lines that form on bodies, wings, fins etc. as shown by figure A.1.

In the design process, an accurate prediction of the heat transfer to the vehicles surface is crucial for the specification of the vehicle thermal protection system (TPS). Reduction of uncertainty in the TPS design process will lead to reduced vehicle weight, increases in payload and optimisation of the performance (path) - giving longer missions and cheaper access to space. According to reference [43], for a vehicle in which the ratio of payload mass to maximum take off mass is 10%, 1% saving in structure mass produces a 9% payload increase.

There have been a number of experimental investigations carried out on attachment-line viscous layer characteristics e.g. [5][6][7][25][35][38]. However, Schlieren pictures, static

pressure and heat transfer distributions along the attachment-line have been the main information available from the experimental tests. Moreover, investigators have usually used assumptions such as the infinite swept conditions in the course of their data analysis. Unfortunately, taken at face value, there is a large scatter in the results such as, for example, the attachment-line Reynolds number $\bar{R}$ at which the onset of transition was found to occur (figure A.2). In order to accurately estimate the attachment-line heating levels, researchers assume the worst case which is fully turbulent flow along the body, wing and tail attachment-lines - see publication on the X-34, reference [34]. By adding a "safety" factor to the prediction, the thermal protection system is designed without fear of damaging the vehicle.

Before more experimental work is performed, the reason for the scatter needs to be understood. The aim of the present investigation is to develop a more comprehensive understanding of the different characteristics of the attachment-line viscous layer. By combining accurate, detailed CFD to provide local flow information and experimental data, current knowledge can be reassessed. This approach covers the range of conditions typically encountered by RLVs during re-entry (figure A.3). Since the thermal protection system might become non-smooth in service, tripped boundary layer is considered. Berry et al. [7] have shown that an isolated roughness element can have a dramatic effect on the heat flux, when it is positioned along the local attachment-line structures (figure A.4).

In chapter 2, key definitions will be given and different attachment-line parameters will be defined. Laminar flow will then be investigated and computational results will be validated (chapter 3). In chapter 4, a brief literature review on turbulence models for equilibrium flow will be given and in chapter 5 a new "low Reynolds number" model will

be developed. Using this new model and experimental data, leading edge heating will be studied (chapter 6). In chapter 7, a criterion for minimum conditions at which turbulent attachment-line flow can occur downstream of a source of large disturbances will be developed. Finally conclusions will be given.

Chapter 2

The attachment-line flow

2.1 Definition of the attachment-line

Figure A.5 gives a sketch of the flow near the leading edge of a swept wing. The attachment-line lies along the line AA and separates the flow which passes over the upper surface from the flow passing over the lower surface. Should the wing be unswept and the attachment-line will become the locus of stagnation points. When the wing is swept, there is a flow in the spanwise direction with an associated viscous layer - the so called attachment-line boundary layer. This can be laminar, transitional or turbulent depending on the local conditions.

2.2 The infinite swept assumption

As described by Cumpsty and Head [24], the attachment-line boundary layer is somewhat similar to the asymptotic boundary layer on a flat plate. In the attachment-line case, the rate of the viscous layer growth due to the friction is balanced by the lateral divergence of the flow, just as in the asymptotic suction case where growth is balanced by the with-

drawal of fluid through the surface. This means that the attachment-line boundary layer, provided that it is fully laminar or fully turbulent and that there is no spanwise variation in the outer inviscid flow, will have no property variation in the spanwise direction.

When the normal to leading edge component of the free-stream Mach number is higher than unity, a bow shock is formed in front of the wing leading edge. Depending upon the sweep angle and M_∞, the flow along the attachment-line can be subsonic or supersonic (appendix C shows the calculation of the flow properties along the supersonic, infinite swept, attachment-line).

In data analysis for experiments on swept cylinders, previous authors (e.g. [5][12][37][38]) have assumed that the infinite swept conditions are reached very close to the upstream tip i.e. small L/D. However, it is easily shown that even when the bow shock is parallel to the cylinder, the infinite swept conditions might not be reached until very large values of L/D. Figure A.6 shows a swept cylinder in a supersonic free-stream flow. The bow shock is attached at the tip and eventually becomes parallel to the leading edge at station A. However, a single streamline crossing the bow shock at station A will reach the edge of the attachment-line viscous layer at a station further downstream than station B - station C say. Therefore, spanwise invariance in the boundary layer is achieved further downstream than the location at which the bow shock becomes parallel to the leading edge. In previous studies, data analysis has always involved the use of the infinite swept assumption. However, since this may introduce errors, in this study the local values of the flow properties are used.

In the present report, the notation shown by figure A.5 will be used i.e. the axis X

lies in the chordwise direction, normal to the attachment-line, the axis Y runs along the attachment-line (spanwise direction) and the axis Z complete the orthogonal axis system by being normal to the surface. The velocities U, V and W correspond to the axis X, Y and Z respectively. The variables at the edge of the viscous layer will be denoted by the subscript "e" and the subscript "a" will point out the variables evaluated at the attachment-line location itself.

2.3 The attachment-line viscous layer parameters

Poll [49] explains that the infinite swept, attachment-line flow can be fully described by only 6 variables namely the Reynolds number, edge Mach number, the ratio of the wall to the stagnation temperature, the ratio of the Sutherland's law constant to the stagnation temperature, s/T_o, the specific heat coefficient γ and the Prandtl number. In reference [49] he proposed an attachment-line Reynolds number $\bar{R}$ (equation 2.1) based upon a length scale η (equation 2.2).

$$\bar{R} = \frac{V_{ae} \cdot \eta}{\nu_{ae}} = \left(\frac{{V_{ae}}^2}{\nu_{ae} \cdot \frac{dU_e}{dX}} \right)^{\frac{1}{2}} \tag{2.1}$$

where V_{ae} is the spanwise edge velocity [m/s], ν_{ae} is the edge kinematic viscosity [m^2/sec] and dU_e/dX is the edge chordwise velocity gradient [m^{-1}]. The length scale η is defined as follow

$$\eta = \sqrt{\frac{\nu_{ae}}{\frac{dU_e}{dX}}} \tag{2.2}$$

Other Reynolds numbers have been used to characterise the attachment-line viscous layer such as R_θ as used by Pfenninger [48] (equation 2.3).

$$R_\theta = \frac{V_{ae}.\theta_a}{\nu_{ae}} \tag{2.3}$$

where θ_a is defined as follow

$$\theta_a = 0.4044.\frac{\nu_{ae}}{\sqrt{\frac{dU_e}{dX}}} \tag{2.4}$$

Cumpsty and Head [24] proposed a parameter C^* (suitable for laminar and turbulent flow) to characterise the incompressible turbulent boundary layer flow along the attachment-line of an infinite swept cylinder i.e.

$$C^* = \frac{{V_{ae}}^2}{\nu_{ae}.\frac{dU_e}{dX}} \tag{2.5}$$

where μ_{ae} is the edge dynamic viscosity [kg/m.sec].

Poll explained in reference [49] that for incompressible infinite swept flow there is an exact solution for the laminar attachment-line boundary layer equations (the velocity profile being tabulated in most standard boundary layer texts). Due to this fact, it is possible to directly link the length scale η to others viscous layer parameters i.e.

$$\delta_{0.99} = 3.055\eta \tag{2.6}$$

where $\delta_{0.99}$ [m] represents the boundary layer thickness taken at 99.0% of the inviscid value.

$$\delta^* = 1.026\eta \tag{2.7}$$

where δ^* is the displacement thickness [m].

$$\theta = 0.4044\eta \tag{2.8}$$

in which θ is the momentum thickness. Finally it follows

$$R_\theta = 0.4044.(C^*)^{\frac{1}{2}} = 0.4044\bar{R} \tag{2.9}$$

In reference [49] Poll also explained that when the spanwise boundary layer flow is investigated under the effect of circular trip wires set normal to the attachment-line flow (figure A.5), two more independent variables must be introduced i.e. k the trip wire diameter and s the spanwise separation between the trip and the turbulence detector. The corresponding non-dimensional groups are as follow

$$\frac{k}{\eta} \qquad and \qquad \frac{s}{\eta}$$

Poll and Paisley [53] later added that for tapered wings, the two following variables also ought to be considered:

$$\frac{dr}{dY} \qquad or \qquad \frac{d\eta}{dY}$$

with r being the local leading edge radius.

Poll in references [49] [50] noted that, for a Prandtl number of unity, there is a simple relationship between the edge skin friction Cf_{ae} and the edge Stanton number St_{ae} (equation 2.10).

$$St_{ae} = \frac{Cf_{ae}}{2} \tag{2.10}$$

He proposed that, by analogy to the flat plate flow, small variations in the Prandtl number could be taken into account by introducing an empirical correction i.e.

$$St_{ae} = Pr^{-\frac{2}{3}}.\frac{Cf_{ae}}{2} \tag{2.11}$$

In the absence of evidence to the contrary this was assumed to hold for both laminar and turbulent flows.

Using the exact solution of the equations governing the incompressible laminar attachment-line flow the variation of Cf_{ae} with the attachment-line Reynolds number was obtained i.e.

$$Cf_{ae} = \frac{1.141}{\bar{R}} \tag{2.12}$$

Hence, the variation of the Stanton number with attachment-line Reynolds number for incompressible laminar flows over a wide range of Prandtl number follows i.e.

$$St_{ae} = \frac{1.141}{2.Pr^{\frac{2}{3}}.\bar{R}} \tag{2.13}$$

Also in references [49] [50] Poll used the turbulent experimental skin friction measurements obtained by Cumpsty and Head [24] on incompressible attachment-line flow over swept cylinders. Using the same model, he increased the amount of data and obtained a relation between the skin friction and the attachment-line Reynolds number $\bar{R}$ for incompressible turbulent flow i.e.

$$Cf_{ae} = \frac{0.0592}{\bar{R}^{0.4}} \tag{2.14}$$

From equations 2.11 and 2.14 the variation of the Stanton number with $\bar{R}$ for incompressible turbulent flow follows i.e.

$$St_{ae} = \frac{0.0592}{2.Pr^{\frac{2}{3}}.\bar{R}^{0.4}} \tag{2.15}$$

To extent this to compressible flow, Poll [49] used the well known reference temperature concept.

Reference Temperature

The reference temperature concept was originally derived to correlate exact solutions of the laminar boundary layer equations for flat plate flows with zero pressure gradient (see reference [66] and [30] for more information). It is based on the idea that, within a compressible boundary layer, there is a local temperature which can be used to evaluate reference values for the temperature dependent transport properties i.e. ρ and μ. When these are substituted into the incompressible relations for Reynolds number with edge Stanton number and edge skin friction, the appropriate compressible values are obtained. Thus, the problem is reduced to finding the value of the reference temperature in terms of the independent variables i.e. Mach number, wall-to-stagnation temperature ratio, s/T_o and, if necessary, Reynolds number.

Poll [49] proposed that following Eckert [30] the reference temperature method was appropriate for attachment-line problems in the infinite swept conditions and that it could be represented by this simple relation

$$T^* = T_{ae} + K1\,(T_W - T_{ae}) + K2\,(T_r - T_{ae}) \tag{2.16}$$

where K1 and K2 are constant. Poll [49], using data available at the time, estimated these to be 0.10 and 0.60 respectively. T_r in equation 2.16 represents the recovery temperature which is the wall temperature when there is no heat transfer. The value of T_r is determined by use of the recovery factor r when

$$r = \frac{T_r - T_{ae}}{T_o - T_{ae}} \tag{2.17}$$

or

$$\frac{T_r}{T_{ae}} = 1 + r.\left(\frac{\gamma - 1}{2}\right).M_{ae} \tag{2.18}$$

For turbulent, flat plate zero pressure gradient flow it is well known that the recovery factor can be approximated by

$$r = (Pr)^{\frac{1}{3}} \tag{2.19}$$

whereas for laminar flat plate flow with zero pressure gradient the approximation of r becomes

$$r = \sqrt{Pr} \tag{2.20}$$

Although it has been assumed by some others (e.g. [6][12][25][35][38][40]) that these relations apply to the attachment-line flow, this has never been demonstrated.

The transformed attachment-line Reynolds number for compressible flow $\bar{R}^*$ was then introduced i.e.

$$\bar{R}^* = \left(\frac{{V_{ae}}^2}{{\nu_{ae}}^* . \frac{dUe}{dX}}\right)^{\frac{1}{2}} = \frac{\bar{R}}{\left(\frac{\mu^*}{\mu_{ae}} . \frac{T^*}{T_{ae}}\right)^{\frac{1}{2}}} \tag{2.21}$$

For compressible turbulent flow, the transformed Stanton number along the attachment-line becomes

$$St^*_{ae} = \frac{\dot{q}_w}{\rho^* . V_{ae} . Cp . (T_r - T_w)} = St_{ae} . \left(\frac{T^*}{T_{ae}}\right) \tag{2.22}$$

hence

$$St_{ae} = St^*_{ae} . \bar{R*}^2 . \left(\frac{\mu^*}{\mu_{ae}}\right) . \frac{1}{\bar{R}^2} \tag{2.23}$$

In the present investigation, it was decided to use the local values of the flow properties instead of the infinite swept assumption. CFD will therefore be used to supply the missing local flow information (see appendices D and E for the description of the numerical codes). Moreover the attachment-line Reynolds numbers $\bar{R}$ and $\bar{R}^*$ will be used to characterise the attachment-line features instead of R_θ or even C^*.

Chapter 3

Laminar Flow

3.1 Introduction

In order to study the attachment-line viscous layer, the flow properties taken at the edge of the boundary layer must be evaluated since the Stanton number, St_{ae} and attachment-line Reynolds number $\bar{R}$ for example depend on them.

$$\bar{R} = \sqrt{\frac{V_{ae}^2}{\nu_{ae} \cdot \frac{dUe}{dX}}} \tag{3.1}$$

$$St_{ae} = \frac{-\dot{q}_w}{\rho_{ae} V_{ae} C_P T_{ae} \left(\frac{Tr}{T_{ae}} - \frac{T_W}{T_{ae}}\right)} \tag{3.2}$$

Navier-Stokes calculations (appendix D) were undertaken to supply the local flow information. Full description of how the edge of the thermal and velocity viscous layers was accurately located is given in appendix F. However, results are presented below and generalities of the laminar attachment-line boundary layer are given.

3.2 Variation of the edge flow properties along the attachment-line

The spanwise distributions of flow properties taken at the edge of their respective layers and non-dimensionalised with the infinite swept values are found to collapse to single curves when $M_\infty.cos\Lambda$ exceeds approximately 2.5. This is shown for cylinders swept at 60^o in figures A.7 to A.9 and for 70^o in figures A.10 to A.12. Note that computational runs had to be created in order to complete the range of $M_\infty.cos\Lambda$ (the details of these runs are given in table B.2).

The collapse is the result of the so called "Mach number independence" principle. At high speeds and for perfect gas, certain aerothermodynamic quantities such as the pressure, temperature, velocity etc. and flowfield structure (e.g. shock wave shapes) become essentially independent of Mach number. The hypersonic Mach number independence principle has a mathematical foundation. This is shown in reference [3] section 4.3.

Figure A.13 shows that, for a given Mach number, the spanwise velocity distribution is independent of the sweep angle for L/D values higher than 8. However, this contrasts other flow properties such as the static temperature and pressure which do exhibit clear sweep dependence for given Mach numbers (figures A.14 and A.15).

The high Mach number independence of properties along the attachment-line could be exploited in future investigations. To this end, the values corresponding to the velocity and temperature distributions of Poitiers run19 at $\Lambda = 60^o$ and Holden run25 at $\Lambda = 70^o$ (two runs that represent the average distributions) are given in tables B.14, B.15 and

shown in figures A.7 to A.11. For the static pressure distribution at 60° of sweep, Poitiers run19 was also though to represent the average distributions (figure A.9). However, for 70° of sweep, created run2 seems best to represent the static pressure distribution when $M_\infty.cos\Lambda$ exceeds approximately 2.5 (figure A.12).

3.2.1 Validation of the results

The accuracy of the results obtained depends on the computational results and on the way the edges of the velocity and thermal profiles have been found. Some of the validation of the computational results such as the grid and solution convergence are given in appendix F. However, some validation of the results are also presented below.

Heat transfer

A comparison of the heat transfer rates (Stanton numbers) from the Navier-Stokes calculations, the laminar boundary layer code and the experiments is shown in figure A.16 for Poitiers Run19 ($M_\infty = 7.14$, $\Lambda = 60°$, $T_w/T_o = 0.38$). It should be noted that when determining the Stanton number, the local flow properties obtained from the laminar Navier-Stokes calculations were used. It can be seen from figure A.16 that heat transfer rates from both codes agree. Moreover, agreement between experiments and computation is well within experimental uncertainty, which in this case is approximately ±10%.

Local profiles

Total enthalpy, velocity and temperature profiles from the Navier-Stokes code (MGNS3D, appendix D) have been compared with those obtained from the boundary layer code (appendix E), using the local edge values from the Navier-Stokes calculations. These results are presented in figures A.17 to A.19 and show that the Navier-Stokes profiles and the boundary layer profiles are almost identical.

Flow property changes across the bow shock

The jumps in velocity and temperature across the bow shock predicted by the Navier-Stokes code have been compared with those obtained from the 2D oblique shock relations. Figures A.20 and A.21 show that the two methods give identical results. Moreover, within the shock layer (plateau on figure A.20), the local values agree with the infinite swept values. This confirms the high Mach number independence feature described above since, for this particular case, (Poitiers Run19, $\Lambda = 60°$), $M_\infty.cos\Lambda$ is approximately 3.6. Both figures (A.20 and A.7) show that the infinite swept conditions are reached at about 15 diameters from the tip.

Surface pressure coefficient of the attachment-line

Pressure coefficients, Cp, normalised with Cp at the attachment-line, obtained from the Navier-Stokes code and estimated by the modified Newtonian theory are compared for Holden Run36 at a station L/D of 13.9 in figure A.22. The results are in very good agreement for θ up to 30°. It is also useful to note that Beckwith and Gallagher (reference

[5]) found that their experimental surface static pressure data agreed with the modified Newtonian theory for θ up to approximately 20^o.

3.3 Local attachment-line Reynolds number

3.3.1 Attachment-line chordwise velocity gradient

Appendix F, section F.2 shows how the attachment-line chordwise velocity gradient and attachment-line Reynolds number have been extracted from the Navier-Stokes calculations.

The variation of the chordwise velocity gradient along the attachment-line for 60^o of sweep is shown in figure A.23. This shows that the results obtained from Holden Run 34 and Jones Run 2 seem very poor (scattered results) for $\frac{L}{D}$ less than 4. Some oscillations are also visible for Poitiers Run 19 at high values of $\frac{L}{D}$. These imperfections are believed to be due to the method used to estimate the location of the edge of the velocity boundary layer. Indeed, in appendix F, section F.1.2 it is shown that the edge of the velocity boundary layer must be treated with great care if oscillations in the spanwise distribution of variables are to be prevented (see figures F.2 and F.3). Navier-Stokes errors are not thought to be the cause of such problems, since these have been shown to be accurate - see section F.1.4. Nonetheless, although the oscillations are unsatisfactory, the error involved in the estimation of the chordwise velocity gradient is 10% at most. However, for Jones Run2, the data considered in the present investigation are located at stations $\frac{L}{D}$ of 3.8 and 4.7 where the results for the chordwise velocity gradient are satisfactory. It should also be noted that 90% of the distributions of the chordwise velocity gradient

obtained in the present study are of a much higher accuracy, as shown for example in figure A.24: Holden Run12. However, the results are included to demonstrate that investigations of swept cylinders are not as straight forward as has been assumed in the past.

Despite the fact that the chordwise velocity gradient distributions are not as smooth as the velocity or temperature distributions, figure A.23 still shows some important features. The infinite swept values are achieved from an $\frac{L}{D}$ value between 3 and 4, irrespective of the Mach number. Previously it has been shown that the local value of any flow properties only reached the infinite swept levels at much greater spanwise distances (figures A.7 to A.11 for example).

Figures A.23 (60° of sweep) and A.25 (70° of sweep) show that the value of L/D at which the infinite swept value is reached is not strongly dependent upon $M_\infty.cos\Lambda$. This contrasts the velocity, temperature and pressure as described previously in section 3.2. The value of L/D at which the infinite swept condition is reached was also found to be independent of the sweep angle for a given Mach number (figure A.26). Again this contrasts the temperature and pressure but agrees with the velocity (see section 3.2, figures A.13 to A.15).

Figure A.25 contains a very wavy distribution for Holden run25 at L/D greater than 8 . This feature does have an impact on the results for this particular case, since the cylinder was approximately eleven diameters long (see appendix G and references [37] [38]). Since they were very different from the rest, these results were judged to be in error and the infinite swept value was used to normalise the results.

For both 60° and 70° of sweep angle, it has been found that the infinite swept values are achieved for $\frac{L}{D} \geq 4$, independent of the normal to leading edge Mach number. As for $\frac{L}{D} \leq 4$, it was believed that the most accurate local distributions were given by Poitiers Run 19 for $\Lambda = 60°$ and the created run2 for $\Lambda = 70°$ (see figures A.23 and A.25). Tables B.14 and B.15 give these local values that can be used by future investigators to estimate gradients.

3.3.2 Attachment-line Reynolds number

The $\bar{R}$ distributions along the attachment-line of 60° and 70° swept cylinders were obtained for a range of values of $M_\infty.cos\Lambda$. Figure A.27 shows that for 60° of sweep, the poor distributions of the chordwise velocity gradient (figure A.23) have only a small impact. In fact, the difference between Holden Run 34 (oscillating distribution) and Poitiers Run 19 (smooth distribution) is at the most 6.0%. A comparison between these two runs is legitimate since they both involve values of $M_\infty.cos\Lambda$ higher than 2.5. The $\bar{R}$ distributions along a 70° swept cylinder is shown in figure A.28.

The most important feature revealed by figures A.27 and A.28 is the convergence of the local $\bar{R}$ values towards the infinite swept conditions with increasing L/D. Indeed, the infinite swept values are not reached before an $\frac{L}{D}$ of 12 for 60° of sweep and an $\frac{L}{D}$ of 18 for 70°. This is one of the important findings from the present study. It means that in previous investigations large errors were introduced, in the data analysis, when the infinite swept assumption was applied to situations close to the cylinder upstream tip. For example Holden et al. [37] [38] made measurements at stations L/D as low as 0.3 over cylinders swept at 66.5°. In subsequent data reduction, they used the infinite swept

assumption giving errors in $\bar{R}$ of up to 60%!

In the present investigation, a single Navier-Stokes solution was obtained for each combination of sweep angle, cylinder diameter and free-stream Mach number used in the various experiments. From this, the local value of the attachment-line Reynolds number was extracted. Since the flow was laminar it is known that the solutions scale with Reynolds number i.e.

$$\bar{R} = A.\sqrt{R_D} \tag{3.3}$$

Hence, provided that A remains constant, the values of the local Reynolds number can be obtained at any desired free-stream Reynolds number without the need to run the Navier-Stokes code again. Note that equation 3.3 is equivalent to

$$\left(\frac{(V_{ae})^2}{\nu_{ae}.\frac{dU_e}{dX}}\right)^{\frac{1}{2}} = A.\left(\frac{Q_\infty.D}{\nu_\infty}\right)^{\frac{1}{2}} \tag{3.4}$$

leading to

$$A^2 = \frac{\nu_\infty}{\nu_{ae}}.\left(\frac{V_{ae}}{Q_\infty}\right)^2.\frac{d\left(\frac{X}{D}\right)}{d\left(\frac{U_e}{U_\infty}\right)}.\frac{1}{cos\Lambda} \tag{3.5}$$

All four ratios present in this expression are functions of the free-stream Mach number, sweep angle, cylinder diameter and s/T_o only. The local coefficient A was calculated for the Navier-Stokes run since both the free-stream Reynolds number based on the diameter R_D and the local $\bar{R}$ were known. Knowing $R_{\infty D}$ for the experimental runs conducted at the same free-stream Mach number, sweep angle and cylinder diameter, the local values of $\bar{R}$ were obtained.

It must be noted that the Navier-Stokes solutions were obtained on smooth surface cylinders. The results extracted from these solutions were also used with experimental runs involving 2D trip wires, end plates etc. If a roughness element is introduced into a supersonic flow field a shock wave will appear from it. Hence, the spanwise flow properties will vary as the shock is crossed and therefore CFD results may not be accurate. However, it was found that, to the present level of accuracy, the roughness elements had no impact onto the spanwise edge flow properties used in the present study (see appendix M).

3.4 Local Stanton number

The local Stanton number St_{ae} is given by

$$St_{ae} = \frac{-\dot{q}_W}{\rho_{ae}.V_{ae}.Cp.T_{ae}.\left(\frac{T_r}{T_{ae}} - \frac{T_W}{T_{ae}}\right)} \tag{3.6}$$

The heat transfer rate $\dot{q}_W$ is measured directly and reported in the experiments described in appendix G (excepted for Beckwith et al. who supply the Stanton number itself. see section G.4.4 for more information.). The flow properties at the edge of the boundary layer come from the Navier-Stokes computations and this makes St_{ae} a mix of experimental and computational data.

3.4.1 Recovery factor

The recovery temperature is calculated using the boundary layer code. For a particular run and L/D, the local values of $\bar{R}$, M_{ae} and T_o are input into the boundary layer

code. The wall-to-stagnation temperature ratio is then varied until the predicted Stanton number is zero (adiabatic conditions). In this case, the wall temperature is equal to the recovery temperature.

It was found that, for a fixed Prandtl number (0.72), the recovery factor increased with M_{ae} and varied with s/T_o as shown in figure A.29. This figure also reveals that r increases by only 1.7% for M_{ae} ranging from 1 to 10 and for stagnation temperatures between 500K to 1200K. In the case of zero pressure gradient flat plate flow, the recovery factor variation is a decreasing function of the Mach number (see figure A.30 taken from reference [3]) and that the frequently used approximation that r equals $\sqrt{Pr}$ involves only 2.4% error over a wide range of Mach number. Due to the small variation of the recovery factor with Mach number in the attachment-line case, a simple approximation can be used without much error i.e.

$$r = (Pr)^{0.45} \tag{3.7}$$

This result agrees with those of reference [59] which provides power law relations between the recovery factor and Prandtl numbers for a wider range of conditions than presented herein. However, in certain cases notably Bushnell, Jones, Holden and Poitiers (appendix G) the values of the recovery factor obtained from the boundary layer code were used for the data reduction in the present investigation. These are shown in figure A.29.

Having extracted the local heat transfer rates from the experiments, calculated the local flow properties at the edge of the attachment-line boundary layer and obtained the local recovery temperature, the local Stanton number can be calculated. For all the other

experimental runs, equation 3.8 was used.

$$St_{ae} = \frac{-\dot{q}_W}{\frac{\rho_{ae}}{\rho_\infty}.\frac{V_{ae}}{Q_\infty}.Cp.\frac{T_{ae}}{T_\infty}.\left(\frac{T_r}{T_{ae}} - \frac{T_W}{T_{ae}}\right).\rho_\infty.Q_\infty.T_\infty} \tag{3.8}$$

The ratios $\frac{\rho_{ae}}{\rho_\infty}$, $\frac{V_{ae}}{Q_\infty}$, $\frac{T_{ae}}{T_\infty}$ and $\frac{T_r}{T_o}$ (which leads to $\frac{T_r}{T_{ae}}$) come directly from the computation (MGNS3D and boundary layer code, appendices D and E respectively). They depend only on sweep angle, free-stream Mach number and s/T_o. The heat transfer rate, wall temperature, free-stream density, velocity and temperature correspond directly to the experimental run being considered.

Strictly speaking, although the sweep angle and cylinder diameter are fixed, in a given wind tunnel, the free-stream Mach number always vary slightly with the free-stream Reynolds number (see figures G.3, G.14 and G.23). Therefore, correction factors may need to be applied. This investigation is reported in appendix F, section F.3. However, it was concluded that the local values of $\frac{T_{ae}}{T_\infty}$, $\frac{P_{ae}}{P_\infty}$ and $\frac{V_{ae}}{Q_\infty}$ given by the Navier-Stokes solution can be assumed to be independent of Reynolds number for the purpose of the data reduction.

3.5 Laminar theory

As explained in chapter 2, in 1978 Poll [49] proposed an approximate relation between the Stanton number and $\bar{R}$ for laminar flow i.e.

$$St_{ae} = \frac{1.141}{2.Pr^{\frac{2}{3}}.\bar{R}} \tag{3.9}$$

He found that this was in good agreement with exact numerical solutions and available experimental data covering sweep angles from 0^o to 70^o, $\frac{T_W}{T_o}$ from nearly zero to adiabatic conditions, M_{ae} from 0 to 8 and T_∞ higher than 50K (lower limit for perfect gas).

Using the boundary layer code, a data set that covers flight conditions (with no real gas effects) to wind tunnel testing conditions was created for air. This involved $\bar{R}$ values up to 3000, edge Mach numbers between 0 and 8, $\frac{T_W}{T_o}$ between 0.1 and unity and s/T_o from 0.03 to 0.37 (T_o from 300K to 4000K). This data set was used with four values of the molecular Prandtl number i.e. 0.7, 0.8, 0.9 and unity.

It should be noted that, although dissociation of O_2 begins at 2000 K (beyond this limit the gas is not perfect anymore ; see reference [3]), for the high Mach number, cold wall conditions, the maximum temperature encountered in the attachment-line viscous layer, T_{max}, is much less than T_o. Using the boundary layer code for a wide range of conditions (i.e. wind tunnel and flight conditions), it was found that T_{max}/T_o is never likely to exceed 0.5 in situations of practical importance. Therefore, it was chosen to have a maximum T_o value of 4000 K.

For altitudes between sea level and 70 kms, the free-stream temperature is approximately constant at 245 ± 30K. Considering, the extreme case of a vehicle flying at sea level ($T_\infty \approx 275$K), with wings swept at 90^o, the stagnation temperature encountered is 3800 K for an edge Mach number of 8 (equation 3.10). In the generated data set, the edge Mach number was limited to 8 since, at higher Mach numbers, T_o exceeds 4000 K and

therefore the gas is not perfect anymore.

$$\frac{T_o}{T_\infty} = 1 + \left(\frac{\gamma - 1}{2}\right).{M_\infty}^2 = \frac{T_o}{T_{ae}} = 1 + \left(\frac{\gamma - 1}{2}\right).{M_{ae}}^2 \tag{3.10}$$

Considering the incompressible part of the generated data set, it was found that the skin friction could be simply related to $\bar{R}$ independently of the Prandtl number i.e.

$$Cf_{ae} = \frac{1.141}{\bar{R}} \tag{3.11}$$

However, the relation linking the Stanton number with attachment-line Reynolds number was found to be Prandtl number dependent i.e.

$$St_{ae} = \frac{1.141}{2.Pr^{0.605}.\bar{R}} \tag{3.12}$$

Note that the correction for Prandtl number shown in equation 3.12 is slightly different that as assumed by Poll (equation 3.9).

Considering the whole data set (incompressible and compressible data), equation 3.12 was found to become as follow

$$St_{ae} = \frac{1.315}{2.Pr^{0.605}.\bar{R}} \tag{3.13}$$

Equation 3.13 was found to predict the Stanton number within $\pm 13\%$ as shown by figures A.31 and A.32 ($Pr = 1$ and $Pr = 0.7$ respectively). Note that for clarity only the extreme values of the edge Stanton number for a given $\bar{R}$ are shown in figures A.31 and A.32.

In order to improve agreement with the laminar theory, a correction for T_r/T_{ae}, T_w/T_{ae} and s/T_o was sought. Figure A.33 shows the variation of the product $St_{ae}.\bar{R}$ with $(T_r/T_{ae})-1$ for different values of T_w/T_{ae}. It can be seen that the wall temperature has very little effect. However $St_{ae}.\bar{R}$ varies almost linearly with $(T_r/T_{ae})-1$. Moreover, the slope of this line (called Θ) was found to be almost directly proportional to s/T_o, as shown by figure A.34. Therefore the improved relation can be written as

$$St_{ae}.\bar{R} = \left[1 + \frac{0.13.\left(\frac{S}{T_o}\right).\left(\frac{T_r}{T_{ae}}-1\right).Pr^{0.605}}{0.5705}\right].\frac{1.141}{2.Pr^{0.605}} \tag{3.14}$$

Using equation 3.14, predictions of the laminar Stanton number are within ±5% for flight conditions and wind tunnel testing conditions as shown by figure A.35 where predictions from the model (equation 3.14) are compared with the exact laminar solution.

The result expressed in equation 3.14 may also be written in the reference temperature (T^*) form (this concept is described in chapter 2, section 2.3). Recalling the relationship between the Stanton number and $\bar{R}$ for incompressible flow once transformed via the reference temperature i.e.

$$St_{ae}{}^* = \frac{A}{\bar{R}^*} \tag{3.15}$$

where A is defined as follow

$$A = \frac{1.141}{2.Pr^{0.605}} \tag{3.16}$$

From equations 2.21, 2.22 and 3.15 it follows

$$St_{ae}{}^{*}.\bar{R}^{*} = St_{ae}.\bar{R}.\left(\frac{\mu_{ae}}{\mu^{*}}\frac{T^{*}}{T_{ae}}\right)^{\frac{1}{2}} \tag{3.17}$$

For laminar flow it is known that

$$St_{ae}.\bar{R} = A.f\left(M_{ae}, T_w/T_{ae}, T_r/T_{ae}, s/T_o\right) \tag{3.18}$$

then

$$\frac{St_{ae}.\bar{R}}{A} = \left(\frac{\mu^{*}}{\mu_{ae}}\frac{T_{ae}}{T^{*}}\right)^{\frac{1}{2}} = f\left(M_{ae}, T_w/T_{ae}, T_r/T_{ae}, S/T_o\right) \tag{3.19}$$

where the function f is obtained from equation 3.14 i.e.

$$f = 1 + \frac{0.13.\left(\frac{S}{T_o}\right).\left(\frac{T_r}{T_{ae}} - 1\right).Pr^{0.605}}{0.5705} \tag{3.20}$$

3.6 Link between $\bar{R}$ and R_θ

As explained previously (chapter 2, section 2.3), for laminar incompressible flow, with a wall to stagnation temperature ratio of unity, the ratio of the momentum thickness Reynolds number to the attachment-line Reynolds number is constant at 0.4044 (equation 2.9).

By considering a wide range of conditions i.e. M_{ae} from 0 to 8, T_w/T_o between 0.2 and unity and s/T_o of 0.028 and 0.276, it was found that the ratio $R_\theta/\bar{R}$ deviated considerably

from the incompressible value (0.4044) as shown by figure A.36. The data presented in this figure can be fitted within ±8.5% by

$$\frac{R_\theta}{\bar{R}} = \frac{3.51.10^{-4}{M_{ae}}^3 - 2.69.10^{-3}.{M_{ae}}^2 - 3.10^{-2}M_{ae}}{f\left(s/T_o\right)} + 0.4044 + D \tag{3.21}$$

where D is defined as follows

$$D = \frac{0.0667\left(1 - \frac{T_w}{T_o}\right)^2 + 0.0671\left(1 - \frac{T_w}{T_o}\right)}{f\left(s/T_o\right)} \tag{3.22}$$

with the function $f\left(s/T_o\right)$ defined as follows

$$f\left(s/T_o\right) = 32\left(\frac{s}{T_o}\right)^2 - 1.74\left(\frac{s}{T_o}\right) + 1.025 \tag{3.23}$$

Figure A.37 shows the comparison between the exact value of $R_\theta/\bar{R}$ and the predictions given by equations 3.21 to 3.23.

3.7 Experimental data

The state of the flow is determined by comparing the experimental data (described in appendix G) with estimation from equation 3.14. An example is given in figure A.38, which shows that, in this case, the experimental data are estimated to within ±15%. This level corresponds to the experimental accuracy of the heat transfer measurements (±10%) combined with the accuracy of equation 3.14 (±5%).

By considering all the cases available listed in tables B.4, B.6, B.8, B.10, B.11 and B.13, it was found that laminar flow existed along the entire attachment-line for Holden runs

34, 4, 7, 10, 18, 19, 21, Poitiers runs 19, 70, Bushnell runs 2, 3, 4, 5, 6, 7a, 7b, 12, 13, Beckwith runs 39 to 44, 54 to 65 and Jones runs 1, 2 (figure A.39).

3.7.1 Discarded data points

In the course of the investigation, some data points were found to lie below the 15% uncertainty band. For Holden et al. [37][38], every measurement taken from heat transfer gauge HT128 was significantly different from those of the other heat transfer gages. This gauge also gave heat transfer measurements below the 15% error band as shown for example in figure A.40. Consequently, data from this gauge were discarded.

Bushnell Run1 (figure A.41) was also found to lie below the 15% uncertainty band. Of the 149 runs considered, Bushnell run 1 is the only complete run which involves a heating level below the minimum laminar prediction. Since run 1 contributes less than 1% of the total data set, it was assumed that an experimental fault must have occurred when the measurements were taken. Consequently this run was disregarded.

Finally in reference [40] Jones explains that "*the plate shock wave, which is relatively weak compared to the fin shock wave, appears to pass undisturbed through the fin shock and to intersect the fin. [...] The two shock waves intersect nearest station B.*" (see figure G.24). From figure A.42 which shows Jones run 2, it can be seen that the flow at station A, closest station to the cylinder upstream tip, is disturbed by either the shock interaction phenomenon or the nature of the plate boundary layer (e.g. turbulent boundary layer or even separated region at the plate/wedge junction). In any case, measurements taken at stations A and B cannot be considered for the purpose of the present investiga-

tion since the local flow properties obtained from the Navier-Stokes solution do not take into consideration such effects. Moreover, although station C is located downstream the shock/shock interaction, it is believed that the data taken at this station are subjected to the same effects as at station B (i.e. shock interaction). The results are identical at these two locations (figure A.42). Therefore, only experimental measurements obtained at stations D and E were considered.

3.8 Conclusions

It has been shown that the assumption of infinite swept conditions for data reduction and analysis can lead to major errors for both the local attachment-line Reynolds number and Stanton number. This is particularly true for experiments conducted on short models i.e. when L/D may be less than 10.

The spanwise variation of the local flow properties at the edge of the viscous layer was found to be Mach number independent for a given sweep angle when the normal to leading edge Mach number exceeded approximately 2.5. Tables of the local flow properties were derived for 60^o and 70^o of sweep and $M_\infty.cos\Lambda$ higher than 2.5.

The flat plate relationship giving the recovery factor as a function of the Prandtl number was found to be inaccurate in the case of the attachment-line. A simple relation suitable for attachment-line flow over a wide range of conditions was found to be

$$r = (Pr)^{0.45}$$

Edge flow properties extracted from the CFD solutions obtained on smooth cylinder surfaces were coupled with experimental measurements for non-smooth conditions (e.g. trip wires, endplates etc.). It was found that the roughness elements did not change the flow field and therefore edge flow properties could be used directly (appendix M).

For compressible, wind tunnel and flight conditions, a simple relation predicting the Stanton number variation within ±13% was obtained i.e.

$$St_{ae} = \frac{1.315}{2.Pr^{0.605}.\bar{R}}$$

The maximum error was decreased to ±5% by correcting for s/T_o and T_r/T_{ae} i.e.

$$St_{ae}.\bar{R} = \left[1 + \frac{0.13.\left(\frac{S}{T_o}\right).\left(\frac{T_r}{T_{ae}} - 1\right).Pr^{0.605}}{0.5705}\right].\frac{1.141}{2.Pr^{0.605}}$$

It was shown that the above relation could be related to a reference temperature i.e.

$$St_{ae}.\bar{R} = \left(\frac{\mu_{ae}}{\mu^*}\frac{T^*}{T_{ae}}\right)^{\frac{1}{2}}.\left(\frac{1.141}{2.Pr^{0.605}.\bar{R}}\right)$$

Finally a model for the variation of the ratio of the momentum thickness Reynolds number to the attachment-line Reynolds number with edge Mach number, wall-to-stagnation temperature ratio and s/T_o was proposed. Predictions were found to be within ±8.5% of the exact laminar solution.

Chapter 4

Brief review on turbulence models

4.1 Introduction

When the instantaneous Navier-Stokes equations are time-averaged, for turbulent flow, several new terms appear. They are known as Reynolds stresses. In the attachment-line boundary layer, the Reynolds stresses present in the X and Z momentum equations (equations E.2 and E.4) are $-\bar{\rho}\bar{u'v'}$ and $-\bar{\rho}\bar{v'w'}$. This produces a situation in which there are more unknowns than equations. To overcome this problem the Reynolds stresses are modelled in terms of other quantities. Over the years, several approaches have been proposed. However, for equilibrium flow, Boussinesq's eddy-diffusivity and Prandtl's mixing length concepts are the simplest and the best known.

4.2 Mixing length

Strictly Boussinesq's eddy-diffusivity and Prandtl's mixing length concepts are only applicable to equilibrium flows where the free-stream velocity distribution is characterised

by a constant value of the parameter

$$\beta = (\delta^*/\tau_w) \cdot (dP/dX)$$

which represents the ratio of pressure forces to shear forces in the boundary layer.

In 1877, by drawing an analogy with molecular viscosity, Boussinesq [10] was the first to suggest the modelling of the Reynolds stresses by introducing the concept of the eddy viscosity i.e.

$$-\bar{\rho}\bar{u'v'} = \bar{\rho}\varepsilon\left(\frac{\partial u}{\partial Y}\right) \qquad and \qquad -\bar{\rho}\bar{v'w'} = \bar{\rho}\varepsilon\left(\frac{\partial v}{\partial Z}\right) \tag{4.1}$$

where ε represents the eddy viscosity which has dimensions of the product of a velocity and a length. The difficulty rests on finding proper velocity and length scales.

Alternatively, in 1925 Prandtl proposed that each Reynolds stress could be related to a local length scale and velocity gradient such that

$$-\bar{\rho}\bar{u'v'} \approx \bar{\rho}(const)u'_{rms}v'_{rms} \approx \bar{\rho}(const)\left(l1\frac{\partial u}{\partial Y}\right)\left(l2\frac{\partial u}{\partial Y}\right) \tag{4.2}$$

and

$$-\bar{\rho}\bar{v'w'} \approx \bar{\rho}(const)v'_{rms}w'_{rms} \approx \bar{\rho}(const)\left(l1\frac{\partial v}{\partial Z}\right)\left(l2\frac{\partial v}{\partial Z}\right) \tag{4.3}$$

where l1 and l2 are called "mixing" lengths. They represent a mean eddy size much larger than the fluid's molecular mean free path. It is convenient to introduce a single scale, l^2,

since the Reynolds stresses can be written as

$$-\bar{\rho}\overline{u'v'} = \bar{\rho}l^2\left(\frac{\partial u}{\partial Y}\right)\left|\frac{\partial u}{\partial Y}\right| \qquad -\bar{\rho}\overline{v'w'} = \bar{\rho}l^2\left(\frac{\partial v}{\partial Z}\right)\left|\frac{\partial v}{\partial Z}\right| \tag{4.4}$$

where the modulus ensures that the Reynolds stresses change sign when the shear stress changes sign (i.e. within separation region). Prandtl's mixing length, l^2, can be related to Boussinesq's eddy viscosity, ϵ, i.e.

$$\epsilon = l^2\left|\frac{\partial u}{\partial Y}\right| \qquad \epsilon = l^2\left|\frac{\partial v}{\partial Z}\right| \tag{4.5}$$

However, it should be noted that, although there may be an exact numerical solution of the equations for a given turbulence model, there is no sound theoretical basis for any turbulence model. Indeed, after over 70 years, the physical validity of all models is still questionable. In the case of mixing length, l cannot be directly measured. It can only be inferred from experimental measurements of the turbulent shear stress and velocity gradient.

The turbulent boundary layer may be considered to consist of two main regions. These are the inner region which is dominated by viscous shear and strongly influenced by the wall and the outer region which is mainly determined by the turbulent Reynolds stresses and is governed largely by conditions at the edge of the boundary layer.

Information upon the distribution of l and ϵ across the boundary layer comes from experimental data. The distribution of l is conveniently described by two separate empirical functions. In the inner region, but away from the wall (i.e. $Y^+ \geq 50$ where Y^+ is defined

in the next section) l is proportional to Y i.e.

$$l_i = kY \tag{4.6}$$

where k is von Kármán's constant. In the outer region, the mixing length is found to be approximately proportional to the boundary layer thickness, i.e.

$$\frac{l_o}{\delta} = constant = \phi \tag{4.7}$$

Note that the two equations above are correct for incompressible as well as compressible flows subject to the condition of Morkovin's hypothesis [45] which suggests that the turbulence structure is virtually the same at low speeds as at $M_{ae} < 5-7$ (see appendix J).

Cebeci and Smith [21] have suggested that, for zero pressure gradient boundary layers, at high Reynolds number ϕ lies between 0.075 and 0.09 (see sections 4.6 and 4.7 for more information).

Considering Boussinesq's eddy viscosity ε and its relation to Prandtl's mixing length, l^2, (equation 4.5), it follows in the inner region

$$(\varepsilon)_i = (l_i)^2 \left|\frac{\partial u}{\partial Y}\right| \tag{4.8}$$

In the outer region, Cebeci and Smith [21] assumed the eddy viscosity to be defined by

$$(\varepsilon)_o = k_1 . u_e . \delta_k^* . F_{Kleb} \tag{4.9}$$

where δ_k^* is the kinematic displacement thickness i.e.

$$\delta_k^* = \int_0^\infty \left[1 - \left(\frac{u}{u_e}\right)\right] .dY \tag{4.10}$$

In equation 4.9, F_{Kleb} represents the Klebanoff intermittency function (defined below) which brings the eddy viscosity to zero at the edge of the boundary layer.

$$F_{Kleb} = \left[1 + 5.5\left(0.3.\frac{Y}{Y_{max}}\right)^6\right]^{-1} \tag{4.11}$$

Although the universality of the parameter k_1 has been the subject of many discussions (see sections 4.6 and 4.7), it is generally taken as a constant for high Reynolds number flows with a value between 0.016 and 0.017.

4.3 Van Driest's model

The effects of viscosity are such that the mixing length model is unsatisfactory in regions very close to the wall. Although Prandtl's model gives zero Reynolds stress at the wall, it does not exhibit the appropriate non-linear decay of the Reynolds stresses as the surface is approached. To correct this defect, Van Driest [62] proposed an improvement to Prandtl's model by introducing a damping function, Υ, such that

$$l_i = kY\Upsilon \tag{4.12}$$

where Υ is defined as follows

$$\Upsilon = 1 - exp\left(-\frac{Y^+}{A^+}\right) \tag{4.13}$$

with

$$A^+ = \frac{A.U_\tau}{\nu} \qquad and \qquad Y^+ = \frac{Y.U_\tau}{\nu} \tag{4.14}$$

where A^+ is the damping parameter empirically determined by Van Driest to be 26 for high Reynolds number flows with zero pressure gradient. The variable U_τ is the friction velocity i.e.

$$U_\tau = \left(\frac{\tau_w}{\rho_w}\right)^{\frac{1}{2}} \tag{4.15}$$

where τ_w is the wall shear stress and ρ_w is the wall density.

The eddy viscosity for the inner region becomes

$$(\varepsilon)_i = (kY)^2.\left[1 - exp^{-\left(\frac{Y^+}{A^+}\right)}\right]^2.\left(\frac{\partial v}{\partial Z}\right) \tag{4.16}$$

4.4 Turbulent Prandtl number

In addition to the modelling of the Reynolds stresses, solutions of the turbulent boundary layer equations, for flows with heat transfer, also require the Reynolds heating term $-\bar{\rho}v'\bar{H}'_o$. This is usually modelled via the eddy-conductivity concept i.e.

$$-v'\bar{H}'_o = \lambda_t \frac{\partial H_o}{\partial Y} \tag{4.17}$$

where λ_t is the eddy conductivity and H_o is the total enthalpy related to the static enthalpy, H, i.e.

$$\bar{H}_0 = \bar{H} + \frac{\bar{u}^2 + \bar{w}^2}{2} \tag{4.18}$$

Equation 4.19 can also be written as

$$-v'\bar{H}'_o = \frac{Cp.\varepsilon}{Pr_t}.\frac{\partial \bar{H}_o}{\partial Y} \tag{4.19}$$

Introducing the definition of the turbulent Prandtl number i.e.

$$Pr_t = \frac{Cp.\varepsilon}{\lambda_t} \tag{4.20}$$

Pr_t is usually taken to be constant at 0.9.

4.5 Summary

To solve the turbulent Navier-Stokes equations or the boundary layer equations, the Reynolds stresses must be modelled. Boussinesq's eddy viscosity concept gives

$$-\bar{\rho}\bar{u'v'} = \bar{\rho}\varepsilon\left(\frac{\partial u}{\partial Y}\right) \tag{4.21}$$

whereas Prandtl's mixing length concept gives

$$-\bar{\rho}\bar{u'v'} = \bar{\rho}l^2\left(\frac{\partial u}{\partial Y}\right)\left|\frac{\partial u}{\partial Y}\right| \tag{4.22}$$

The mixing length, l, and eddy viscosity, ε, are related as follows

$$\varepsilon = l^2.\left|\frac{\partial u}{\partial Y}\right| \tag{4.23}$$

In the inner region, but away from the wall (i.e. $Y^+ \geq 50$), the mixing length (with Van Driest's model) and eddy viscosity yields

$$l_i = k.Y.\left(1 - e^{-\frac{Y^+}{A^+}}\right) \qquad or \qquad \varepsilon_i = l_i^2.\left|\frac{\partial u}{\partial Y}\right| \tag{4.24}$$

In the outer region, with the Klebanoff function for the eddy viscosity, the following expressions apply

$$\frac{l_o}{\delta} = \phi \qquad or \qquad \varepsilon_o = k_1.u_e.\delta_c^*.F_{Kleb} \tag{4.25}$$

The Reynolds stresses for the inner and outer regions can hence be evaluated:

$$-\bar{\rho}\bar{u'v'} = \bar{\rho}(k.Y)^2.\left(1-e^{-\frac{Y+}{A+}}\right)^2.\left(\frac{\partial u}{\partial Y}\right).\left|\frac{\partial u}{\partial Y}\right| \tag{4.26}$$

$$-\bar{\rho}\bar{u'v'} = \bar{\rho}(\phi.\delta)^2.\left(\frac{\partial u}{\partial Y}\right).\left|\frac{\partial u}{\partial Y}\right| \qquad or$$

$$-\bar{\rho}\bar{u'v'} = \bar{\rho}.k_1.u_e.\int_0^\infty \left[1-\left(\frac{u}{u_e}\right)\right]dY.\left[1+5.5\left(0.3.\frac{Y}{Y_{max}}\right)^6\right]^{-1}.\left(\frac{\partial u}{\partial Y}\right) \tag{4.27}$$

Evaluation of the Reynolds heating term $-\bar{\rho}\bar{v'H_o'}$ is achieved using

$$-\bar{v'H_o'} = \frac{Cp.\varepsilon}{Pr_t}.\frac{\partial \bar{H}_o}{\partial Y} \tag{4.28}$$

It can be seen that, in order to achieve the closure of the turbulent boundary layer equations, the von Kármán's constant, k, the damping parameter, A^+, the outer mixing length, l_o/δ, and the turbulent Prandtl number, Pr_t, must be known. These parameters are deduced from examination of experimental data and have been subject to many investigations (see sections 4.6 and 4.7).

4.6 Extensions to Van Driest's model

Patankar and Spalding, in reference [47], suggest that the damping of turbulent fluctuations is more likely to be influenced by the local value of the shear stress than by the wall value. In which case, equation 4.14 becomes

$$A^+ = \frac{A}{\nu}.\left(\frac{\tau}{\rho}\right)^{\frac{1}{2}} \qquad and \qquad Y^+ = \frac{Y}{\nu}.\left(\frac{\tau}{\rho}\right)^{\frac{1}{2}} \tag{4.29}$$

Kays et al. [42] have considered Van Driest's model for incompressible flow. They also used the local value of the shear stress and, in addition, applied the damping function Υ right across the viscous layer. This leads to the following equations for the mixing length.

For $Y < (\phi\delta/k)$

$$l = kY\Upsilon \tag{4.30}$$

For $Y > (\phi\delta/k)$

$$l = \phi.\delta.\Upsilon \tag{4.31}$$

with Υ as defined by equation 4.13 and ϕ as defined below

$$\phi = \frac{l_o}{\delta} = 0.25.R_\theta^{-\frac{1}{8}} \tag{4.32}$$

In their model, the damping parameter, A^+, and von Kármán's constant, k, are constant at 26 and 0.44 respectively. However the turbulent Prandtl number was varied i.e.

$$Pr_t = \frac{1}{Pr}.\left[1 - 0.1.\sqrt{\frac{\mu_t}{\mu}}\right] \tag{4.33}$$

with the condition that Pr_t can never be lower than 0.86. The variable μ_t is the turbulent molecular viscosity i.e.

$$\mu_t = \bar{\rho}.\varepsilon \tag{4.34}$$

In 1970, Cebeci [16] developed a model for two-dimensional and axisymmetric flows, free-stream Mach numbers between 0 and 6.7 and momentum Reynolds numbers from 2000 to 16000. This model was based on the eddy viscosity concept with a k_1 value of 0.0168 and a von Kármán's constant of 0.40. The ratio Y^+/A^+ was defined i.e.

$$-\frac{Y^+}{A^+} = -\frac{Y}{\nu_w}.\left(\frac{\tau_w}{\rho}\right)^{\frac{1}{2}}.\frac{1}{A^+} \tag{4.35}$$

with the damping parameter, A^+, being

$$A^+ = 26.\left(\frac{\rho_w}{\bar{\rho}}\right)^{\frac{1}{2}}.\left(\frac{\bar{\mu}}{\mu_w}\right) \tag{4.36}$$

where $\bar{\rho}$ and $\bar{\mu}$ are the local averaged values of the density and dynamic viscosity respectively. In the outer region, Cebeci used the Klebanoff intermittency function (equation 4.11) with the following modification

$$F_{Kleb} = \left[1 + 5.5\left(\frac{Y}{\delta}\right)^6\right]^{-1} \tag{4.37}$$

To solve the energy equation, the turbulent Prandtl number was varied i.e.

$$Pr_t = \frac{k.\left[1 - exp\left(-Y^+/A^+\right)\right]}{k_t.\left[1 - exp\left(-Y^+\sqrt{Pr}/B^+\right)\right]} \tag{4.38}$$

where k_t is the turbulent thermal conductivity defined as follows

$$k_t = \frac{\mu_t.Cp}{Pr_t} = 0.44 \tag{4.39}$$

and B^+ is a constant i.e.

$$B^+ = 34.\left(\frac{\rho_w}{\bar{\rho}}\right)^{\frac{1}{2}}.\left(\frac{\bar{\mu}}{\mu_w}\right) \tag{4.40}$$

Cebeci [16] concluded that for incompressible flow, the model was quite accurate, except near separation where the predictions were poor. For compressible flow, good predictions were obtained for high Reynolds numbers ($R_\theta \geq 3500$), wall temperature close to the adiabatic condition and Mach numbers up to 6. However, the computed results were found to deviate from the experimental data as the heat transfer increased.

One of the most popular models for use in CFD is that due to Baldwin and Lomax [4]. This was found suitable for two and three-dimensional separated, high Reynolds number, adiabatic, subsonic and supersonic flows. The model is patterned after that of Cebeci [16] (see above) with modifications that avoid the necessity for finding the edge of the boundary layer. For the inner region, the following eddy viscosity model was used

$$\varepsilon_i = \bar{\rho}.l^2.|\omega| \tag{4.41}$$

where the mixing length, l, is defined according to equation 4.24. The damping parameter, A^+, (equation 4.42) and von Kármán's constant, k, are kept at 26 and 0.4 respectively.

$$A^+ = \frac{A}{\nu_w}.\left(\frac{\tau_w}{\rho_w}\right)^{\frac{1}{2}} \qquad and \qquad Y^+ = -\frac{Y}{\nu_w}.\left(\frac{\tau_w}{\rho_w}\right)^{\frac{1}{2}} \tag{4.42}$$

In equation 4.41, the variable ω represents the magnitude of the local vorticity, defined for a three-dimensional flow as

$$\omega = \sqrt{\left(\frac{\partial u}{\partial Y} - \frac{\partial v}{\partial X}\right)^2 + \left(\frac{\partial v}{\partial Z} - \frac{\partial w}{\partial Y}\right)^2 + \left(\frac{\partial w}{\partial X} - \frac{\partial u}{\partial Z}\right)^2} \tag{4.43}$$

For the outer region:

$$\varepsilon_o = 1.6.k_1.F_{wake}.F_{Kleb} \tag{4.44}$$

where F_{Kleb} is the Klebanoff intermittency function (equation 4.11) and k_1 is taken to be 0.0168. The two variables F_{wake} and F_{Kleb} are related to the function

$$F(Y) = Y.|\omega|\left[1 - exp\left(\frac{-Y^+}{A^+}\right)\right] \tag{4.45}$$

where ω is the local vorticity (equation 4.43). Equation 4.45 has a maximum value along the normal distance Y. This maximum value and the location where it occurs are denoted by F_{max} and Y_{max} respectively. In equation 4.44, F_{wake} is taken to be either $Y_{max}.F_{max}$ or $0.25.Y_{max}.U^2{}_{diff}/F_{max}$, whichever is smaller where U_{diff} is defined i.e.

$$U_{diff} = \sqrt{u^2 + v^2 + w^2} \tag{4.46}$$

4.7 Low Reynolds number effects

There have been numerous authors who suggested that there are low Reynolds number effects in fully turbulent flows (e.g. [14][15][18][20][33][39][57][65]). Moreover, there have been a wide varieties of ways of including these effects into turbulence models.

In 1971, Huffman and Bradshaw [39] concentrated on the log law of the wall to determine whether k and A^+ (hence C ; equation I.6 of appendix I) are variables or universal constants. They argued that "the boundary layer data currently available is not accurate enough to check the validity of the logarithmic law at low Reynolds numbers" and decided to analyse experimental data obtained in duct flows (e.g. channel, pipe and annular flows). The authors believed that, in duct flows, the Reynolds number effects on the inner layer are stronger than in the zero pressure gradient flat plate boundary layer and thus effects should be easier to detect. They then analysed experimental data obtained on axisymmetric wall jet flow, axisymmetric and 2D boundary layer flows.

They concluded that the logarithmic law of the wall with constant coefficients i.e. A^+ of 26, C of 5.0 and k of 0.41 was valid over a wide range of Reynolds numbers, provided the dimensionless shear-stress gradient in the inner layer, $\partial\tau^+/\partial Y^+$, was not much greater than 10^{-3}. However, for larger values, the damping parameter A^+ increases rapidly, as shown by figure A.43, whilst the von Kármán's constant k remains at 0.41. These conclusions contradict Simpson's work [57] who suggested that k and C (hence A^+) varied with Reynolds number even when $\partial\tau^+/\partial Y^+$ was less than 10^{-3}.

In 1971, Bushnell and Morris [14] analysed a large amount of published experimental velocity, pressure and density profiles measured on the walls of wind tunnels. Edge Mach numbers ranging from 4.67 to 20.8 and wall-to-stagnation temperature ratios from 0.26 to unity were considered. The authors argued that nozzle wall boundary layers have the advantage of being thick, readily accessible and can be fully turbulent at Reynolds number much lower than for flat plate or cone zero-pressure gradient boundary layers. In

order to conduct their analysis, they assumed local similarity of the flow i.e. u/u_e, P/P_e and ρ/ρ_e are only functions of Y/δ (δ being here the thickness of the density viscous layer).

Using an A^+ value of 26 to start with, the comparison between the experimental measurements and prediction was found to be poor. However they suggested that "because of possible inaccuracies in the present analysis procedure (such as the similarity assumption) and the incompleteness of some of the data, considerable scatter exists". Nevertheless, a general trend was suggested in which the eddy viscosity (coefficient k_1 in equation 4.9), the von Kármán's constant, k, and the maximum value of the mixing length increases with decreasing Reynolds number (figures A.44 to A.46). This results is in agreement with previous investigation (see for example Simpson [57]). Bushnell and Morris [14] also specified that, in low speed flows, the increasing trend of k_1, k and $\left(\frac{l}{\delta}\right)_{max}$ with decreasing Reynolds number is commonly correlated against R_θ (based on the edge conditions). However, in hypersonic (where generally $\rho_w \ll \rho_e$ and $\mu_w \gg \mu_e$), they proposed that the wall conditions and a wall-friction velocity were more appropriate. Hence, they introduced the Reynolds number $\delta^+{}_{ww}$ where

$$\delta^+{}_{ww} = \frac{\rho_w.\delta.u_\tau}{\mu_w} \tag{4.47}$$

Note that for consistency, the damping parameter must be calculated at the wall along with the shear stress velocity

$$u_\tau = (\frac{\tau_W}{\rho_w})^{1/2} \tag{4.48}$$

$$A^+ = \frac{\rho_w.A.u_\tau}{\mu_w} = 26 \tag{4.49}$$

In 1973, Cebeci [18] investigated the universality of von Kármán's constant, k, and outer eddy viscosity coefficient, k_1 (equation 4.9). Using the wall shear stress and a fixed A^+ value at 26, he concluded that good agreement with the incompressible flat plate experimental data (skin friction and shape factor) was obtained for k_1 of 0.0168 and k of 0.40. However, agreement was found to be even better when the outer eddy viscosity coefficient, k_1, was varied with Reynolds number (for $R_\theta \geq 425$) i.e.

$$k_1 = k_{1HR}\left(\frac{1+\Pi_{HR}}{1+\Pi}\right) \tag{4.50}$$

where the values of the variables at high Reynolds number are denoted by the subscript HR i.e. k_{1HR} is 0.0168 and Π_{HR} is 0.55. The variable Π is calculated as follow

$$\Pi = 0.55\left[1 - exp\left(-0.243\sqrt{\Omega} - 0.298\Omega\right)\right] \tag{4.51}$$

where Ω is

$$\Omega = \frac{R_\theta}{425} - 1 \tag{4.52}$$

Cebeci [18] then extended equation 4.50 to compressible flows by replacing R_θ by the kinematic quantity $R_{\theta k}$ defined as follows

$$R_{\theta k} = \frac{u_e.\theta_k}{\nu_w} \tag{4.53}$$

in which ν_w is the wall kinematic viscosity and θ_k is the kinematic momentum thickness defined by

$$\theta_k = \int_0^\infty \frac{u}{u_e}\left(1 - \frac{u}{u_e}\right) dY \tag{4.54}$$

However, in reference [18], Cebeci does not justify the use of "kinematic" rather than the actual momentum thickness.

In 1975, Bushnell and Carry [15] investigated the variation of the maximum value, across the viscous layer, of the mixing length parameter, l/δ, for compressible, low Reynolds number boundary layers. They concentrated on the determination of whether low Reynolds number amplification of shear stress was a result of the proximity of the transition. Experimental measurements of the mean velocity profiles and skin friction with an A^+ value of 26 were used to calculate $(l/\delta)_{max}$. Considering data obtained on wall-nozzle walls (measurements achieved far downstream the transition point hence, involving the viscous layer outer and inner regions to be turbulent), it was found that the maximum value of l/δ decreased with decreasing δ_w^+ (figure A.47). However, when using experimental data obtained downstream of natural transition (occuring on plates, cones and cylinders), $(l/\delta)_{max}$ was found to increase with decreasing δ_{ww}^+ (figure A.48). Hence they concluded that the amplification of $(l/\delta)_{max}$, at low Reynolds number, was a function of proximity to transition and therefore of residue present in the transition process.

In 1980, Fernholz and Finley [33] conducted a comprehensive review of the existing methods for the prediction of the temperature-velocity relationship in compressible, steady, turbulent boundary layer with and without heat transfer but with no wall transpiration. Collecting a very large amount of experimental data, mainly obtained from flat plates and wall-nozzle boundary layers (see reference [32]), and using the log-law of the wall with Van Driest transformed velocities $\bar{u}^*/u_\tau$ (see reference [33]) they found that the wake strength was better correlated when the Reynolds number $R_{\theta ew}$ was used rather than $R_{\theta ee}$ (figure

A.49).

$$R_{\theta ew} = \frac{\rho_e.\theta.V_e}{\mu_w} = R_\theta.\frac{\mu_e}{\mu_w} \tag{4.55}$$

The distinctions between the two Reynolds numbers was especially important at low Reynolds numbers i.e. less than 1000. The authors also added that the decay of the wake component to zero at Reynolds number of approximately 500 (Coles's [22] expression equation I.8, figure I.2 in appendix I) would not be captured if the velocities were not transformed.

The authors explain the significance of $R_{\theta ew}$ by noting that "the physical explanation of the Reynolds number as the ratio of momentum flux to shear stress, might be interpreted as the ratio of the maximum values, which are, to a first approximation, the momentum flux at the outer edge of the boundary layer $\rho_e V_e^2$ and the shear stress at the wall τ_w." Hence, substituted τ_w by $\mu_w\left(\partial\bar{V}/\partial Y\right)_w$ and the gradient by V_e/θ led to the following

$$\frac{\rho_e.V^2}{\tau_w} = \frac{\rho_e.V_e^2}{\mu_w\left(\partial\bar{V}/\partial Y\right)_w} = \frac{\rho_e.V_e^2}{\mu_w\left(V_e/\theta\right)} = \frac{\rho_e.\theta.V_e}{\mu_w} \tag{4.56}$$

In 1995, Yardley [65] developed a low Reynolds number turbulence model for incompressible, equilibrium flow. The investigation was based upon experimental measurements of velocity profiles obtained on axisymmetric pipe flow and 2D channel flow. In addition, Yardley used data obtained by Danks [26] on the brass cylinder originally tested by Cumpsty and Head [24] and on a "suction" cylinder originally designed to accommodate mass transfer.

The damping parameter, A^+, (equation 4.16) and the outer mixing length parameter, ϕ, (equation 4.7) were varied until the computed velocity profile matched the experiment data (k was kept equal to 0.41). Excellent fits were obtained in all cases.

Yardley's approach is similar to the technique used by Huffman and Bradshaw [39]. Once a fit to the profile was obtained, Yardley [65] checked the consistency of all the calculated quantities e.g. R_θ, H and Cf. It should be noted that this approach does not rely on a single point measurement and makes no a priori assumption about the law of the wall. The only assumption made was that von Kármán's constant was fixed at 0.41. The author specifies that this was justified "a posterior" by the fact that experimental data could be reproduced to a very high level of accuracy. The following functions for the damping parameter and outer mixing length were obtained (see also figures A.50 to A.53).

for $\delta^+_{ww} \leq 200$

$$A^+ = \frac{2561.8}{\delta^+_{ww} - 26.3} + 17.75 \tag{4.57}$$

For $\delta^+_{ww} > 200$, the damping parameter can be evaluated using:

$$A^+ = 26\left[1 + 0.75.exp\left(-0.0055\delta^+_{ww}\right)\right] \tag{4.58}$$

The outer mixing length expression for external flows was found to be

$$\frac{l_o}{\delta} = 0.11 - 0.028tanh\left(\frac{\delta^+_{ww} - 500}{130}\right) \tag{4.59}$$

However, it was noted by Surah [59] that solution of the boundary layer equations was obtained more efficiently if the outer mixing length was replaced by the following relations.

$$\frac{l_o}{\delta} = 0.138 - 0.2\left(\frac{{\delta_{ww}^+}^3}{1.10^9}\right) \tag{4.60}$$

which holds for $\delta_{ww}^+ \leq 600$. For $\delta_{ww}^+ > 600$, the following expression is used

$$\frac{l_o}{\delta} = 0.082\left[1 + 2.47exp\left(-0.0046\delta_{ww}^+\right)\right] \tag{4.61}$$

Figure A.52 shows that the two above relations of the outer mixing length are in very good agreement with Yardley's expression (equation 4.59). For internal flows (e.g. pipe and channel flows), the outer mixing length (figure A.53) is

$$\frac{l_o}{\delta} = 0.115\left[1 + 1.2exp\left(-0.012\delta_{ww}^+\right)\right] \tag{4.62}$$

Figure A.54 shows the variation of the additive constant, C, present in the log-law of the wall (equation I.6) with Reynolds number δ_{ww}^+ as obtained by Yardley for incompressible flow with zero pressure gradient and no mass transfer.

Yardley [65] was able to calculate all the characteristics (i.e. the velocity profiles, skin friction coefficient, shape factor, wake strength etc.) of the incompressible equilibrium flow at the attachment-line with and without mass transfer using a constant k value of 0.41 but varying A^+ and l_o/δ with Reynolds number. Note that the damping of the turbulent fluctuations was calculated via equation 4.14 in which the shear stress is evaluated at the wall.

4.8 Conclusions

Before the mid-seventies, a large number of investigations were aimed at modelling the Reynolds stresses in incompressible, equilibrium, turbulent boundary layers with no mass and heat transfer. At the time, the variables used for the closure methods (A^+, k, k_1, l_o/δ and Pr_t) were subject to great uncertainties. Kays et al. [42], Cebeci [17][18] and Huffman and Bradshaw [39] concluded that von Kármán's constant k was a universal constant ($k = 0.40 - 0.44$) whereas Simpson [57] and Cebeci and Mosinskis [20] claimed it varied with Reynolds number. In addition, amongst all the investigations described in the present chapter, only Kays et al. [42] suggested that the turbulent Prandtl number, Pr_t, was a function of the viscosity ratio ϵ/μ. Similar comments could be made about the universality of the other "constant" used for closure. However, one must bear in mind that none of these investigators was ever able to calculate all the flow characteristics (skin friction, velocity profiles, shape factor etc.) accurately. It is believed that the lack of accurate experimental data is the cause of much of the uncertainty. However, on balance, the turbulent Prandtl number and von Kármán's constant, k, are subject to least uncertainty and hence are most probably universal constants.

Yardley [65] using accurate experimental measurements of velocity profiles obtained on pipe flow and channel flow (where Reynolds number effects on the inner layer are stronger than in a boundary layer and thus easier to detect) was able to match all the incompressible flow characteristics. He came to the conclusion that k was effectively constant. However, this being the case, the damping parameter, A^+, and outer mixing length parameter, ϕ, must be functions of Reynolds number. This supports the conclusions of Huffman and Bradshaw [39].

Of all the investigations dedicated to turbulence modelling, only a small number of studies tried to tackle compressible flows. Hence, the present investigation concentrates on calculating the Reynolds stresses for equilibrium, compressible flow without mass transfer. The present work will be based on Yardley's approach since he is the only investigator able to match all the incompressible velocity profiles and properties. The von Kármán's constant, k, and the turbulent Prandtl number will be kept constant (k=0.41 and $Pr_t = 0.90$). Consequently, the damping parameter, A^+, and the outer mixing length will be allowed to vary with Reynolds number.

Chapter 5

Turbulence model for compressible flows

5.1 Introduction

It is well known that in high Reynolds number ($\delta^+_{ww} \geq 800$) incompressible flow, the von Kármán's parameter, k, the Van Driest damping parameter, A^+, and non-dimensional outer mixing length, l_o/δ, are constant (e.g. [4][65]). For high speed flows in which Morkovin's hypothesis [45] applies ($M_{ae} < 5-7$) the turbulence structure is virtually the same as that at low speeds (see appendix J) i.e. for high Reynolds number compressible flow, k, A^+ and l_o/δ are constant and have the same values as in low speed flow.

Yardley [65] has shown that for low Reynolds number, incompressible flows without mass and heat transfer, good fits to velocity profiles can be obtained with k being constant and A^+ and l_o/δ varying with Reynolds number. It is assumed that, by the choice of a suitable definition of Reynolds number, the low Reynolds number variation can be extended to high speed. However, the definition of the Reynolds number which takes into account the flow compressibility and heating effects is unknown.

It has been shown in the previous chapter that Yardley's [65] low Reynolds number turbulence model accurately predicts the incompressible characteristics of the attachment-line flow including the velocity profiles. In high speed flows, there are no velocity profiles available at present. This is mainly due to the fact that, at tunnel scale, supersonic and hypersonic attachment-line flows involve very thin viscous layers. However, accurate values of the heat transfer rate at the wall can be obtained (see chapter G). Using the lessons learned from Yardley's investigation, together with accurate surface heat-transfer measurements, the turbulence model can be extended to compressible, low Reynolds number, equilibrium flow.

5.2 First Hypothesis

5.2.1 Introduction

In the first instance, it was assumed that, for compressible flow, the variations of A^+ and l_o/δ were functions of the same Reynolds number - irrespective of its definition. Hence, A^+ can be expressed as a function of l_o/δ only.

For closure, equations 4.26 and 4.27 were used to estimate the Reynolds stresses, with the assumption that von Kármán's constant is 0.41 and that the turbulent Prandtl number is 0.90. Three alternative definitions of damping length constant, A, (thus of the ratio $-Y^+/A^+$) were also considered i.e.

Definition A.

$$-\frac{Y^+}{A^+} = -\frac{Y}{\nu_w}.\left(\frac{\tau_w}{\rho_w}\right)^{\frac{1}{2}}.\frac{1}{A^+} \qquad and \qquad A = A^+.\nu_W.\left(\frac{\tau_W}{\rho_W}\right)^{-\frac{1}{2}} \tag{5.1}$$

Definition B.

$$-\frac{Y^+}{A^+} = -\frac{Y}{\nu}.\left(\frac{\tau_w}{\rho}\right)^{\frac{1}{2}}.\frac{1}{A^+} \qquad and \qquad A = A^+.\nu.\left(\frac{\tau_W}{\rho}\right)^{-\frac{1}{2}} \tag{5.2}$$

Definition C.

$$-\frac{Y^+}{A^+} = -\frac{Y}{\nu}.\left(\frac{\tau}{\rho}\right)^{\frac{1}{2}}.\frac{1}{A^+} \qquad and \qquad A = A^+.\nu.\left(\frac{\tau}{\rho}\right)^{-\frac{1}{2}} \tag{5.3}$$

Definitions A, B and C differ in that the shear stress, kinematic viscosity and density are either evaluated from the wall conditions, the local conditions or a mixture of the two. Definition A was proposed by Cebeci [18] and Baldwin and Lomax [4]. Definition B was originally suggested by Van Driest [62] and has been widely used [17][20][65] (see chapter 4). Definition C, which appears to be the most logical of the three, was suggested by Patankar and Spalding [47] and also used by Kays et al. [42].

For the development of the turbulence model, accurate local heat transfer rate measurements data are required. Only the results of Holden et al. [37][38], Bushnell et al. [12][13] Poitiers University [35][6] and Jones [40] present sufficient information for the present analysis (see appendix G).

Two sets of fully turbulent data points were selected for study. The first consisted of measurements taken along the attachment-line for a given set of test conditions i.e. fixed

free-stream conditions, T_w/T_o and sweep angle ; a typical example is given in figure A.55. For the second, data were recorded at a fixed spanwise location, L/D, on the model for a range of free-stream Reynolds numbers. In this latter set, only the local Reynolds number $\bar{R}$ varied as shown for example in figure A.56 and table B.7. However, it should be noted that M_∞, hence M_{ae} does vary slightly with free-stream Reynolds number (3% increase maximum for a Reynolds number per meter varying from $2.3.10^6$ to $3.4.10^7$; see for example Bushnell et al. conditions). In the present work, the subscript s denotes runs from the second kind.

In order to evaluate the turbulent Stanton number, the recovery factor r is needed (see equation 3.8). Therefore, as a first step, the recovery factor was calculated using the boundary layer code with Yardley's incompressible turbulence model (equations 4.57 to 4.62). Figure A.57 shows that values of r calculated in this way can be approximated by

$$r = Pr^{0.41}$$

Using Yardley's turbulence model (equations 4.57 to 4.61) to link A^+ to l_o/δ (figure A.58), the damping parameter was varied until the computed heat transfer rate matched the experimental value.

5.2.2 Effects of the different definitions of Y^+/A^+

Figures A.59 and A.60 show the effects of the different definitions of the ratio Y^+/A^+ for Poitiers Run60s (fixed location L/D, varying local Reynolds number). It can be seen that the choice of methods has a major impact on A^+, but only a small impact on l_o/δ. Definition A yields A^+ values that are much higher than those from definitions B and

C. Since, at high Reynolds numbers i.e. $\delta^+_{ww} > 800 - 1000$, A^+ must approach 26 to be consistent with high Reynolds numbers turbulence models such as Kays et al. and Baldwin-Lomax (see chapter 4), definition A cannot be physically correct.

Figure A.59 also shows that, at high Reynolds numbers, definitions B and C give almost the same results. However, as the Reynolds number decreases, the difference between the two increases. This is due to the fact that, as the Reynolds number decreases, the inner region occupies a greater proportion of the total viscous layer thickness. Therefore, as the Reynolds number decreases, the local shear stress, in the inner region, cannot be approximated by the wall shear stress, as shown by figure A.61. Therefore, definition B of the ratio Y^+/A^+ is not suitable for low Reynolds number flows. Hence, definition C is the only one that exhibits the correct behaviour.

5.2.3 Definition of the Reynolds numbers

It was found that, whatever the definition of the Reynolds number and damping function $-Y^+/A^+$, the damping parameter, A^+, and non-dimensional outer mixing length, l_o/δ, could not be correlated by a single Reynolds number. Reynolds numbers based on momentum thickness and friction velocity δ^+ (see equations below) were tried with the viscosity and density (ratio in brackets in equations 5.4 and 5.5) evaluated either at the wall temperature, the temperature at the edge of the viscous layer, the maximum temperature within the boundary layer and the recovery temperature or any combination of these.

$$R_\theta = V_{ae}.\theta.\left(\frac{\rho}{\mu}\right) \tag{5.4}$$

$$\delta^+ = \left(\frac{\rho}{\mu}\right) .\delta. \sqrt{\frac{\tau_w}{\rho_w}} \tag{5.5}$$

where $(\tau_w/\rho_w)^{\frac{1}{2}}$ is the friction velocity.

In total, 32 Reynolds number definitions were considered (see table B.1), including the momentum Reynolds number $R_{\theta ew}$ (edge density, wall viscosity in equation 5.4) suggested by Fernolz and Finley [33] and $\delta^+{}_{ww}$ (wall density and viscosity in equation 5.5) proposed by Bushnell et al. [14].

Figures A.62 to A.69 show some of the results obtained using equation 5.3 (definition C). Clearly no single line fits the data. Hence, it can be concluded that, in compressible flow, the inner and outer regions depend on different Reynolds numbers.

It should be noted that for clarity, an average of the data obtained per run was done but only for the first kind of runs used. In other words, although the value of A^+ and l_o/δ were obtained for every turbulent data points along the attachment-line (see figure A.55) the average of these two parameters and Reynolds number was plotted on figures A.62 to A.69. However, the conclusions drawn from the average values are the same as would be drawn if the local values of A^+, l_o/δ and Reynolds number had been used.

5.2.4 Conclusions

It was found that definition A (equation 5.1) of the damping function could not be physically correct since A^+ would not approach the high Reynolds number value i.e. 26. Moreover, it was shown that at low Reynolds number (typical of the attachment-line

flow), the local shear stress cannot be approximated by its wall value anymore. Therefore, definition B can be disregarded and definition C is the one to use.

It has be seen that no single Reynolds number can correlate the variation of both, the damping parameter, A^+, and non-dimensionalised outer mixing length, l_o/δ. Hence, the first hypothesis was proved wrong.

5.3 Second Hypothesis

5.3.1 Introduction

In this case, it was then assumed that in each of the two layers, the turbulence characteristics were functions of Reynolds numbers defined in different ways. This is possible, since, in compressible flow, Reynolds numbers can be defined in many different ways.

The extensive investigation carried out by Fernholz and Finley [33] (see chapter 4), suggested that, for zero pressure gradient flat plate flow, the outer mixing length varies with $R_{\theta ew}$ (edge density and wall viscosity in equation 5.4 or see equation 4.56). Bushnell et al. [14] suggested that the damping parameter, A^+, varies with δ^+_{ww} (equation 4.47).

The variation of l_o/δ with $R_{\theta ew}$ was initially designated as "Guess 1" on figure A.70. In addition, it was noticed that Yardley's turbulence model (equations 4.57 to 4.62) was in better agreement with the "suction" cylinder data than the brass cylinder data (figure A.71). Hence, "target" points were created, as indicated in figure A.72. These were chosen so that as Reynolds number increases, they diverge from the laminar value at an

$\bar{R}$ of 245. This was done since Poll [49] demonstrated that, for incompressible flow, in the presence of gross disturbances, laminar flow could not be sustained beyond an $\bar{R}$ of 245.

With the guessed variation of l_o/δ with $R_{\theta ew}$ and using definition C of the damping function (equation 5.3), A^+ was varied until the incompressible target points were matched. This is shown in figure A.73 along with the compressible data points from Holden et al. [37][38], Bushnell et al. [12][13] Poitiers University [35][6] and Jones [40]. It is clear that, although the incompressible target points are matched, a large deviation appears within the compressible data.

5.3.2 Characteristic temperature

In order to manipulate the compressible data points, a characteristic temperature, T_c, that brings the compressible data onto the incompressible line was evaluated. This allows the compressible data to be shifted from right to left in figure A.73 i.e.

$$\delta_c^+ = \frac{\rho_c}{\mu_c}.\delta.\left(\frac{\tau_w}{\rho_w}\right)^{\frac{1}{2}} \qquad (5.6)$$

where T_c is evaluated via the simple trial function

$$\frac{T_c}{T_e} = 1 + C_1\left(\frac{T_w}{T_e} - 1\right) + C_2\left(\frac{T_r}{T_e} - 1\right) \qquad (5.7)$$

where C_1 and C_2 are two empirical coefficients. It should be noted that T_c must always lie within the thermal profile. In addition, for physical consistency, T_c must always correspond to a temperature within the thermal profile in the inner region, since it is used

to calculate the Reynolds number that correlates the damping parameter. For adiabatic wall conditions, the temperature in the wall region is constant at T_r. Hence, the sum of the coefficients C_1 and C_2 must be unity. Therefore, there is only one free constant to be determined.

The coefficient C_1 (and hence C_2) could be determined from figure A.73. However it was found that, with the initial guess of the outer mixing length variation with $R_{\theta ew}$ (figure A.70), the characteristic temperature did not lie within the thermal profile i.e. physically unrealistic. Although many other Reynolds numbers were considered, none gave a good data collapse with T_c inside the thermal profile. Thus the outer mixing length variation with $R_{\theta ew}$ was changed to allow the compressible data to collapse onto the incompressible line with T_c lying inside the thermal profile. This was possible since, for a given Reynolds number, an increase in l_o/δ translates into a decrease in A^+. By applying T_c, the compressible data can be shifted from right to left until they matched the incompressible line.

The converged variation of l_o/δ with $R_{\theta ew}$ is shown in figure A.74 along with the incompressible model of Kays et al. [42] (see chapter 4) and data from Holden et al. [37][38], Bushnell et al. [12][13] Poitiers University [35][6] (description in appendix G).

Figure A.74 shows that the Kays model agrees with the current study for the range of $R_{\theta ew}$ tackled by Kays et al. i.e. $R_{\theta ew}$ between 467 and 1270 (see reference [42]). It can also be seen that, at values of $R_{\theta ew}$ lower than approximately 170, the outer mixing length decreases suddenly with decreasing Reynolds number. This is due to the use of the local shear stress since it causes the variation of the mixing length across the viscous layer to

exhibit a "bell shape" (figure A.75). When the wall shear stress is used, the mixing length keeps on increasing across the inner region until it reaches the value determined by the outer mixing length value l_o. When the local shear stress is used, the maximum value of the mixing length may never reach the constant outer value. To overcome this problem, it was decided to create a plateau from the location were the mixing length reaches its peak (figure A.76). Therefore, the outer mixing length variation with Reynolds number, as shown by figure A.74, is as follows

For $R_{\theta ew} \leq 168$

$$\frac{l_o}{\delta} = 6.10^{-8}.(R_{\theta ew})^{2.85} \tag{5.8}$$

For $R_{\theta ew} > 168$

$$\frac{l_o}{\delta} = 0.08 + 0.064exp\,[-0.00135R_{\theta ew}] \tag{5.9}$$

The converged variation of the damping parameter, A^+, with Reynolds number δ_c^+ (equation 5.6) is shown in figure A.77. The coefficients C_1 and C_2 were found to be easily determined without much ambiguity. The values obtained were

$$C_1 = 0.75 \pm 0.03 \qquad\qquad C_2 = 1 - C_1$$

The data fairing shown in figure A.77 can be represented by the following relations

For $\delta_c^+ \leq 225$

$$A^+ = \left[\frac{77.9\delta_c^+ - 2571.4}{2.69.10^{-4}\delta_c^{+3} + 0.069\delta_c^+ - 16.6}\right] + 23.8 \tag{5.10}$$

For $\delta_c^+ > 225$

$$A^+ = 26.0 + 15.0exp\left(-0.0077\delta_c^+\right) \tag{5.11}$$

It is important to note that the characteristic temperature, T_c, could be used to form many different Reynolds numbers (equations 5.4 and 5.5). However, it was found that only δ_c^+ (equation 5.6) gave a value of T_c that lay within the thermal profile. With C_1 and C_2 fixed at 0.75 and 0.25, it was found that the characteristic temperature, T_c, was approximately ($\pm$10%) equal to the maximum temperature within the thermal profile, T_{max}. The effects of C_1 and C_2 on the prediction of the compressible results are investigated in section 5.6.3.

5.4 Recovery factor

Now that A^+ and l_o/δ have been correlated and C_1 and C_2 have been determined, the boundary layer code can be re-run in order to obtain the correct variation of the recovery factor with edge Mach number, Reynolds number etc. Figure A.78 shows that r is best approximated by the following equation rather than when the Prandtl number is powered to 0.41 as obtained previously using Yardley's turbulence model.

$$r = (Pr)^{0.46} \tag{5.12}$$

Using the revised relation for the recovery factor, the recovery temperature, T_r, was calculated for each data point. It was found that this new approximation did not change the characteristic temperature by much. Therefore the values of C_1 and C_2 were kept at 0.75 and 0.25 respectively. For example, considering the run undertaken at Poitiers University

by Bernard [6] over a cylinder swept at 80° (Run 73, M_{ae} of 5.9, T_w/T_o of 0.39, 2D trip wire), with r approximated by $Pr^{0.41}$, T_c is 362.6 K and δ_c^+ is 88.2 whereas with $Pr^{0.46}$, T_c 361.1 K and δ_c^+ becomes 88.8. This corresponds to a variation in T_c of less than half a percent and only 0.7% in δ_c^+.

Nevertheless, a third iteration of the recovery factor variation with M_{ae} was conducted. No changes in r were obtained and the solution was effectively fully converged. Therefore, for compressible attachment-line flow, the turbulent recovery factor can be approximated by equation 5.12.

Note that the approximation of the laminar recovery factor (Pr powered to 0.45 ; equation 3.7 of chapter 3) is almost identical to the approximation of the turbulent recovery factor (Pr powered to 0.46 ; equation 5.12). Since at very low Reynolds numbers (typical of relaminarisation) the turbulent and laminar Stanton numbers must approach one another, the laminar and turbulent recovery factors must be similar. Therefore, since the attachment-line flow is typically a low Reynolds numbers flow, it is not surprising to observe similarities in the approximations of the laminar and turbulent recovery factors (equations 3.7 and 5.12). The variation of r with decreasing Reynolds number and varying edge Mach number is investigated in chapter 7.

Beckwith and Gallagher [5] obtained an estimate of the recovery factor by measuring the variation of the heat transfer rate at the wall with wall temperature. Their results are shown in figure A.79 along with the approximations for attachment-line and flat plate flows. It can be seen that the approximation of r for attachment-line flow (equation 5.12) is more satisfactory than the flat plate approximation. The maximum difference between

Beckwith et al. data and the attachment-line approximation is 1.8% whereas the flat plate approximation yields 2.7%. The recovery to stagnation temperature ratio was calculated from

$$\frac{T_r}{T_o} = \frac{1 + r\left(\frac{\gamma-1}{2}\right).M_{ae}{}^2}{1 + \left(\frac{\gamma-1}{2}\right).M_{ae}{}^2} \tag{5.13}$$

5.5 Prediction of incompressible flow characteristics

5.5.1 Shape factor

The shape factor variation with momentum thickness Reynolds number, R_θ, for subsonic equilibrium flow is shown in figure A.80. This figure shows good agreement between the prediction made from the current turbulence model (equations 5.8 to 5.11) and experimental data (taken from reference [29]) over the complete range of Reynolds number. Figure A.80 also shows that the shape factor variation with R_θ is identical (within the experimental uncertainty) for attachment-line and flat plate flows. This is due to the fact that both flows obey the law of the wall (see for example reference [65]).

Note that the turbulence model developed in the present investigation (equations 5.8 to 5.11) is referred to as the "current model".

For a given turbulence model, the difference in shape factor given by the boundary layer equations for flat plate and attachment-line is approximately 1% as shown by figure A.81. Note that Cebeci's model [18] (equations 4.50 to 4.52, k_1 varying) was used since shape factor data from this model are given for flat plate in reference [21]. The difference be-

tween the two sets of equations (flat plate and attachment-line boundary layer equations) is well below the scatter involves in the experimental data (up to ±8% ; figure A.81).

Prediction of the shape factor variation with R_θ using the high Reynolds number turbulence model developed by Kays et al. [42] (equations 4.30 to 4.34) is shown in figure A.82. Prediction from the current turbulence model (equations 5.8 to 5.11) with the high Reynolds number values of A^+ (26) and l_o/δ (0.08) is also shown. It can be seen that these two models are unsatisfactory at Reynolds numbers R_θ less than 2000. Figure A.82 also shows that by applying the damping factor across the whole viscous layer and varying the turbulent Prandtl number with viscosity ratio as suggested by Kays et al. [42] (see previous chapter) does not improve the prediction of H since Kays et al model gives similar prediction as the current model with A^+ and l_o/δ of 26 and 0.08 respectively.

Figure A.83 shows the predictions obtained from Cebeci's [18] turbulence models with k_1 constant and varying (equations 4.50 and 4.52). At high Reynolds numbers ($R_\theta \geq 10^4$) the effects of varying k_1 are insignificant. Moreover, Cebeci's prediction is slightly lower than the experimental data. At Reynolds number R_θ less than 3000, the effects of varying k_1 becomes significant and the prediction is improved compared to that with fixed k_1 (0.0168). However, although the shape factor is well predicted at low Reynolds number when k_1 is varied, there is a singularity in Cebeci's model (see equations 4.51 and 4.52) which means that predictions cannot be made when R_θ is lower than 425.

Predictions made from Yardley's [65] turbulence model (equations 4.57 to 4.61) are shown in figure A.84 along with predictions from the current model (equations 5.8 to 5.11). It can be seen that Yardley's model produces a kink at an R_θ of approximately 2000. This

feature is due to the "roller caster" present in the variation of l_o/δ with δ^+_{ww} (equations 4.60 and 4.61). Nevertheless Yardley's model stays well within the scatter of the experimental data.

The best predictions of the shape factor are obtained from the current model and Cebeci's turbulence model with k_1 varying (equations 4.50 and 4.52) down to an R_θ of 425.

5.5.2 Skin friction

The skin friction variation with momentum thickness Reynolds number, R_θ, for incompressible flow is shown in figure A.85 (experimental data taken from reference [29]). It can be seen that the current turbulence model gives a prediction that is well within the scatter of the experimental data (±15% at the most) over the complete range of R_θ. Moreover, figure A.85 shows that at very low Reynolds numbers (i.e. $R_\theta \approx 200$) the skin friction reaches a maximum. It must be stressed that this is not associated with laminar turbulent intermittency that occurs during transition since this occurs at lower Reynolds number (see Poll [49]). Rather the flow is fully turbulent but exhibits low Reynolds number effects (see Yardley [65]).

Figure A.86 shows that models developed by Kays et al [42] (equations 4.30 to 4.34) and Cebeci [18] (equations 4.50 and 4.52) do not predict the roll over. Only the model developed in the present study and Yardley's model capture this feature (figure A.87). These are the only models in which A^+ increases with decreasing Reynolds number. As noted earlier (figure A.71) Yardley's model predicts the "suction" cylinder results better than those from the brass cylinder. This feature can also be seen in figure A.87. However,

the model developed in the present study predicts both data sets with the same accuracy.

Prediction of the velocity profile at very low Reynolds number ($\bar{R}$ value of 450, R_θ is approximately 450) is shown by figure A.88. Predictions of the same velocity profile by Kays et al [42] (equations 4.30 to 4.34) and Cebeci with constant k_1 [18] (equations 4.50 and 4.52) were found to be poor in comparison - see figure A.89. However, predictions from Cebeci's model with k_1 varying are in good agreement with the experimental data.

5.5.3 Wake strength

The variation of the incompressible wake strength, $\Delta w/w_\tau$, with momentum thickness Reynolds number, R_θ, is shown in figures A.90 and A.91 along with predictions from the current model. The experimental data are taken from reference [29] with the most recent (most accurate) shown in figure A.91. It can be seen that the present model predicts the trend of the data well and that the wake strength becomes zero at an R_θ value of approximately 170.

Figure A.91 also shows that, although at high Reynolds numbers (i.e. $R_\theta \geq 800$) the current model gives identical results to Coles's [22], it does not agree at low Reynolds numbers. This is partly due to the fact that Coles based his work on flat plate flows, whereas the present study concentrates upon attachment-line flows. Nevertheless, it was also found that this difference was very sensitive to the variation of the outer mixing length, l_o/δ, with $R_{\theta ew}$. For example, figure A.74 shows that for an $R_{\theta ew}$ of approximately 600, the experimental data for l_o/δ scatter from approximately 0.10 to 0.12. These two extreme values correspond to a wake strength variation from 0.74 to 1.13 as shown in

figure A.91. Nevertheless, both predictions stay within the scatter of the experimental data.

Predictions of the wake strength variation with Reynolds number given by turbulence models from Cebeci [18], Kays et al. [42] and Yardley [65] are given in figures A.92 and A.93. Both Cebeci's models, (constant and varying k_1) give identical, poor, predictions at high Reynolds numbers (i.e. $R_\theta \geq 2000$). However at lower R_θ, the prediction of the wake strength is much improved by varying k_1. The Kays model gives more accurate prediction than Cebeci's models at high Reynolds numbers (i.e. $R_\theta \geq 4000$) but is very poor at the lower Reynolds numbers. Finally, of all the models presented in figures A.92 and A.93, Yardley's gives the best prediction. However, at R_θ values of approximately 1000, Yardley's model leads to a small kink. This feature was found to be caused by the "roller caster" in the outer mixing length variation (see figure A.52).

It can be concluded that the turbulence model developed in the present study is the only model giving smooth, accurate, predictions of all the incompressible flow characteristics (e.g. Cf_e, H, velocity profile and wake strength) at high Reynolds numbers as well as at very low Reynolds numbers.

5.6 Prediction of compressible flow characteristics

5.6.1 Heat transfer

Figures A.94 and A.95 show typical examples of the comparison between the predicted and the experimental heat transfer rates.

Every experimental data point obtained by Holden et al. [37][38], Bushnell et al. [12][13], Poitiers University [35][6], Beckwith and Gallagher [5] and Jones [40] (appendix G) were also considered. Points agreeing within ±10% of the prediction given by the new turbulence model were said to be fully turbulent. Note that the approximation of the turbulent recovery factor r with Prandtl number (equation 5.12) was used to achieved the data analysis, except for Beckwith and Gallagher's experiments where r was calculated exactly for every data points from the boundary layer code using the new turbulence model. This is because Beckwith and Gallagher [5] measured the heat transfer in near adiabatic conditions where T_w is close to T_r. Therefore, a small error in the estimation of T_r could lead to major errors in the evaluation of the Stanton number (see equation 3.6).

Four experimental data points were found to lie at least 28% higher than the prediction given by the new turbulence model. These data points were discarded as they represent only 1.5% of the total number of the 262 data points classified as fully turbulent. In addition, tests performed by Beckwith et al. [5] at 60° of sweep angle were found to give heating rates that are much lower than the prediction. This series of test is the only one not fitting the current prediction. Therefore, data points obtained by Beckwith et al. [5] at 60° of sweep angle were discarded (see appendix K).

5.6.2 Overshoot data points

In chapter 3, it was seen that data points agreeing within ±15% with the laminar model (equation 3.14) were laminar. In the present chapter, the data points agreeing within ±10% with predictions from the current turbulence model are said to be fully turbulent.

Therefore, the data points not classified as laminar or fully turbulent are said to be transitional.

However, it should be noted that some of the transitional data points still lie within ±10% of the fully turbulent heating level (figures A.40 and A.96). Consequently, only data points downstream of the maximum local Stanton number were designated as "fully turbulent". Points ahead of the maximum were taken to be transitional.

Figure A.97 shows the error distribution of the turbulent data points with the overshoot phenomenon and the Gaussian distribution included. The variable ΔSt_{ae}, on the X axis, is the difference in per cent between the experimental and the computed Stanton number for a given $\bar{R}$. On the Y axis, the Gaussian function f for the experimental data points is calculated as follow

$$f(X) = \frac{F}{slice\ \Delta St_{ae}} \tag{5.14}$$

where the variable "*slice* ΔSt_{ae}" represents the steps in ΔSt_{ae} used on the X axis (here *slice* ΔSt_{ae} is 2). The function F is

$$F(X) = \frac{Npts}{Ntotal} \tag{5.15}$$

where *Npts* is the number of data points fitting in a given value of *slice* ΔSt_{ae}. The variable *Ntotal* is the total number of data points considered. The theoretical Gaussian function [60] also shown in figure A.97 is

$$f(X) = \frac{1}{\sigma\sqrt{2\pi}}.exp\left[-\frac{1}{2}.\left(\frac{X}{\sigma}\right)^2\right] \tag{5.16}$$

where σ is the deviation in per cent i.e.

$$\sigma = \sum_{N=0}^{Ntotal} \frac{X^2}{Ntotal} \qquad and \qquad X^2 = \left(\frac{Stae_{expt} - Stae_{code}}{Stae_{code}}\right)^2 \tag{5.17}$$

and N is the number of points.

Figure A.97 suggests that overshoot data points could be exhibiting behaviour that is different from the fully turbulent boundary layer, since they appear to create a distribution on their own i.e. small bell shape for ΔSt_{ae} from 15%. Figure A.98 shows the same distribution but this time without the overshoot data points together with the Gaussian distribution for comparison. The number of fully turbulent data points is decreased from 262 to 253.

In addition, from figure A.98, it can be concluded that there is a probability of 98% that experimental measurements agree within 15% with the predicted heat transfer (see reference [60] page 114 for more information). This is comparable with the stated maximum uncertainty of the experimental measurements themselves (appendix G).

Finally, figures A.97 and A.98 indicate that the distribution of the differences agree closely with the theoretical Gaussian form. This suggets that all differences are random errors only (i.e. experimental measurements errors) and not a systematic difference. The error distribution does not match the theoretical Gaussian distribution perfectly since the number of data available (253 data points) is still relatively small.

5.6.3 Effects of C_1 and C_2

The coefficients C_1 and C_2 used in the estimation of the characteristic temperature (equation 5.7) were estimated to be 0.75 and 0.25 (± 0.03) respectively. It was found that an increase in C_1 of 0.03 units, or 4%, and a corresponding decrease in C_2 of the same amount produced a maximum increase in the Stanton number of 2.4% as shown by figure A.99. This variation is well within the experimental uncertainty which is $10 - 15\%$. Hence, it can be concluded that the predicted heating rate is insensitive to the values of C_1 and C_2.

5.7 Problem encountered

It was noticed that, in some cases, the turbulent boundary layer code could not converge at conditions near relaminarisation i.e. at high A^+ values. It was found that the boundary layer code was written in such a way that the initial value of δ_c^+ always approximated 30. At this particular value there is no corresponding A^+ (see figure A.77). Therefore, the code has convergence difficulties at low Reynolds numbers and sometimes cannot find a solution. In some cases e.g. high Mach number, adiabatic wall, convergence was achieved at A^+ values in excess of 100. However, for cold wall cases, numerical difficulties were encountered for values of A^+ greater than 60. Other numerical schemes might not be subject to the same problem.

5.8 Equations of the new turbulence model

The new turbulence model is based upon Prandtl's mixing length concept. The Prandtl number, Pr_t, and von Kármán's parameter, k, are constant at 0.90 and 0.41 respectively.

As suggested by Patankar and Spalding [47], the local shear stress was used so that the damping parameter A^+ and ratio Y^+/A^+ are defined as follow

$$A^+ = \frac{A}{\nu}.\left(\frac{\tau}{\rho}\right)^{\frac{1}{2}} \qquad and \qquad Y^+ = -\frac{Y}{\nu}.\left(\frac{\tau}{\rho}\right)^{\frac{1}{2}} \tag{5.18}$$

The damping parameter, A^+, was found to be a function of the Reynolds number δ_c^+ such that

For $\delta_c^+ \leq 225$

$$A^+ = \left[\frac{77.9\delta_c^+ - 2571.4}{2.69.10^{-4}\delta_c^{+3} + 0.069\delta_c^+ - 16.6}\right] + 23.77 \tag{5.19}$$

For $\delta_c^+ > 225$

$$A^+ = 26.0 + 15.0exp\left(-0.0077\delta_c^+\right) \tag{5.20}$$

where the Reynolds number δ_c^+ is defined as

$$\delta_c^+ = \frac{\rho_c}{\mu_c}.\delta.\left(\frac{\tau_w}{\rho_w}\right)^{\frac{1}{2}} \tag{5.21}$$

The density, ρ, and viscosity, μ, are evaluated at a characteristic temperature, T_c, where

$$\frac{T_c}{T_e} = 1 + 0.75\left(\frac{T_w}{T_e} - 1\right) + 0.25\left(\frac{T_r}{T_e} - 1\right) \tag{5.22}$$

The outer mixing length, l_o/δ, was found to be a function of the Reynolds number $R_{\theta ew}$ such that

For $R_{\theta ew} \leq 168$

$$\frac{l_o}{\delta} = 6.10^{-8}.(R_{\theta ew})^{2.85} \tag{5.23}$$

For $R_{\theta ew} > 168$

$$\frac{l_o}{\delta} = 0.08 + 0.064 exp\left[-0.00135 R_{\theta ew}\right] \tag{5.24}$$

where $R_{\theta ew}$ is

$$R_{\theta ew} = V_{ae}.\theta.\left(\frac{\rho_e}{\mu_w}\right) \tag{5.25}$$

5.9 Conclusions

A turbulence model for equilibrium flows (i.e. pipe, channel, attachment-line and flat plate flows) has been developed for a wide range of Reynolds numbers. The model was based upon Prandtl's mixing length concept and Van Driest's model. The local shear stress was used and von Kármán's constant, k, and turbulent Prandtl number were fixed at 0.41 and 0.90 respectively. The damping parameter, A^+, was found to vary with Reynolds number, δ_c^+, based on the friction velocity and a characteristic temperature T_c. However, the outer mixing length, l_o/δ, was found to vary with the momentum Reynolds number, $R_{\theta ew}$, in which the edge and wall conditions were used for the density and viscosity respectively.

The two coefficients C_1 and C_2 present in the definition of the characteristic temperature were found to be 0.75 and 0.25 respectively. In all cases, it was found that T_c was within $\pm 10\%$ of the maximum temperature inside the thermal profile. It was noted that of the 32 different definitions of Reynolds number considered, only δ_c^+ with C_1 of 0.75 and C_2 of 0.25 produced a characteristic temperature that lay within the thermal profile.

Predictions were obtained that were well within the experiments uncertainty of all incompressible flow properties (i.e. skin friction, shape factor, wake strength and velocity profiles) as well as high speed heat transfer rates.

Others turbulence models such that from Kays et al. [42] and Cebeci [18] have been shown to be unsatisfactory in predicting incompressible flow properties especially at the very low Reynolds numbers typical of attachment-line flows. In addition, although Yardley's turbulence model [65] could accurately predict the incompressible flow properties over a wide range of Reynolds numbers, it was found to involve a kink due to the "roller caster" present in the variation of l_o/δ with Reynolds number. Only the turbulence model developed in the present study yields smooth predictions with uncertainties comparable with those from experimental data i.e. typically $10 - 15\%$.

Finally, it was found that the approximation of the turbulent recovery factor was very close to the laminar approximation (Prandtl number powered to 0.45 and to 0.46 for laminar and turbulent flow respectively). Since the attachment-line flow is known for being a low Reynolds number flow, it was not surprising to find similar approximations of the recovery factors for this type of flow.

Chapter 6

An improved model for leading edges heating

6.1 Introduction

In this chapter, a model for estimating leading edge heating under a wide range of conditions is developed. The turbulence model described in the previous chapter is used to generate a data set that covers both flight conditions and wind tunnel conditions. This involves attachment-line Reynolds numbers ranging from 350 to 2500, edge Mach numbers between 0.3 and 8, wall-to-stagnation temperature ratios between 0.1 and unity and stagnation temperatures of 300, 800 and 4000 K. As explained in chapter 3, section 3.5, for high speed, cold wall condition, the maximum temperature encountered within the attachment-line viscous flow is T_{max} and not T_o. Results from the boundary layer code (with the new turbulence model ; see previous chapter) showed that, for the high Mach number, cold wall conditions, T_{max} never exceeds $T_o/2$. Therefore, the maximum T_o value of 4000 K, corresponds to a T_{max} of 2000 K, which is the temperature at which significant O_2 dissociation begins i.e. the upper limit of a perfect gas (reference [3]).

A generated data set was used since it does not involve measurements uncertainty and therefore scatter in the generated data can only be due to numerical inaccuracy. Hence, the accuracy of the leading edge heating model is only due to how well the flow physics can be modelled.

6.2 Incompressible turbulent relation

Using the boundary layer code with the new turbulence model, the variation of the incompressible turbulent Stanton number with attachment-line Reynolds number was obtained as shown by figure A.100. It was found that, for such a wide range of $\bar{R}$, a single correlation was not accurate enough. Therefore, seven relations were extracted (figure A.101) i.e.

For $245 < \bar{R} \leq 262.08$

$$St_{ae} = \frac{1.7443.10^{-9}}{\bar{R}^{-2.6}} \tag{6.1}$$

For $262.08 < \bar{R} \leq 320$

$$St_{ae} = \frac{1.715.10^{-3}}{\bar{R}^{0.1221}} \tag{6.2}$$

For $320 < \bar{R} \leq 410$

$$St_{ae} = \frac{0.0109}{\bar{R}^{0.1989}} \tag{6.3}$$

For $410 < \bar{R} \leq 610$

$$St_{ae} = \frac{0.0362}{\bar{R}^{0.3981}} \tag{6.4}$$

For $610 < \bar{R} \leq 900$

$$St_{ae} = \frac{0.0479}{\bar{R}^{0.4423}} \tag{6.5}$$

For $900 < \bar{R} \leq 1400$

$$St_{ae} = \frac{0.0392}{\bar{R}^{0.4133}} \tag{6.6}$$

For $1400 < \bar{R} \leq 3000$

$$St_{ae} = \frac{0.0208}{\bar{R}^{0.3261}} \tag{6.7}$$

6.3 The "perfect" conditions

Using the boundary layer code with the new turbulence model, the Stanton number for every data points of the generated data set was obtained. The reference temperature (concept introduced in chapter 2) that brings $\bar{R}$ and St_{ae} onto the incompressible turbulent relations (equations 6.1 to 6.7) was calculated via the following equation (see appendix L for the derivation of this equation)

$$\left(\frac{T^*}{T_{ae}}\right) \cdot \left(\frac{1+\frac{s}{T^*}}{1+\frac{s}{T_{ae}}}\right)^{\frac{2B}{4-3B}} = \left(\frac{A}{St_{ae}.\bar{R}^B}\right)^{\frac{4}{4-3B}} \tag{6.8}$$

where s is the constant of the Sutherland's law (110.4 K for air) and A and B are the coefficients in the incompressible power laws (equations 6.1 to 6.7) such that

$$St_{ae}{}^* = \frac{A}{\bar{R*}^B} \tag{6.9}$$

The reference temperature, T*, evaluated via equation 6.8 will be referred to as "perfect" i.e. T^*_{perf}. The Stanton number and $\bar{R}^*$ evaluated from T^*_{perf} will be referred to as ${St_{ae}}^*_{perf}$ and $\bar{R}^*_{perf}$ respectively. Note that since A and B are only functions of $\bar{R}^*$, iterations are needed in order to solve equation 6.8. It was found that four iterations at the most were needed if the values of A and B were found to be dependent of $\bar{R}$ at first (initial guessed values).

Figures A.102 and A.103 show that the simple reference temperature model of the type proposed by Eckert [30] and with constant coefficients (see equation 6.10) cannot accurately predict the trend of the generated data for the wide range of conditions considered herein.

$$\frac{T^*}{T_{ae}} - 1 = K1\left(\frac{T_W}{T_{ae}} - 1\right) + K2\left(\frac{T_r}{T_{ae}} - 1\right) \tag{6.10}$$

Therefore, a more complicated model is needed.

6.4 Leading edge heating model

It was found that a model of the following form could be fitted to the generated data set within ±5% as shown by figures A.104 and A.105.

$$\frac{T^*}{T_{ae}} - 1 = K1\left[K3\left(\left(\frac{T_r}{T_{ae}} - 1\right) - K2\right) + K4\left(\left(\frac{T_r}{T_{ae}} - 1\right) - K2\right)^2\right] \tag{6.11}$$

with

$$\frac{K1 - 1}{\frac{T_w}{T_{ae}} - 1} = f_1 - F_2\left[1 - 2\left(\frac{\bar{R}}{\bar{R}_{mini}}\right) + \left(\frac{\bar{R}}{\bar{R}_{mini}}\right)^2\right] \tag{6.12}$$

$$f_1 = -0.107 - 1.38exp\left(-0.869.\frac{T_w}{T_{ae}}\right)$$

$$F_2 = 0.1426\left(\frac{T_w}{T_{ae}}\right)^2 - 0.8153\left(\frac{T_w}{T_{ae}}\right) + 0.8702$$

$$\bar{R}_{mini} = 106.67\left(\frac{T_w}{T_{ae}}\right)^2 - 480.0\left(\frac{T_w}{T_{ae}}\right) + 1713.3$$

$$K2 = W\left[A' + B'exp\left(C'\bar{R}\right)\right] \tag{6.13}$$

$$W = \left[-0.87 - 0.77exp\left(-14\frac{s}{T_o}\right)\right]\left[\frac{T_w}{T_{ae}} - 1.13879\right]$$

$$A' = -2.64.10^{-2}\left(\frac{T_w}{T_{ae}}\right)^2 + 6.61.10^{-2}\left(\frac{T_w}{T_{ae}}\right) + 1.1$$

$$B' = -3.81.10^{-1}\left(\frac{T_w}{T_{ae}}\right)^2 + 2.29\left(\frac{T_w}{T_{ae}}\right) - 2.25$$

$$C' = 2.86.10^{-4}\left(\frac{T_w}{T_{ae}}\right)^2 - 1.71.10^{-3}\left(\frac{T_w}{T_{ae}}\right) - 7.14.10^{-4}$$

$$K3 = \left[0.22exp\left(-3.1.10^{-3}\bar{R}\right) + 0.137\right]\left[1 + 0.4\frac{s}{T_o}\right] \tag{6.14}$$

$$K4 = \left[5.10^{-2}exp\left(-6.5.10^{-4}\bar{R}\right) - 4.10^{-3}\right]\left[1 + 3\frac{s}{T_o}\right] \tag{6.15}$$

Comparisons with experimental data from Holden et al. [37][38], Bushnell et al. [12][13], Poitiers University [35][6], Beckwith et al. [5] and Jones [40] (see appendix G for more information) show a data collapse to within $\pm 17\%$ as shown by figure A.106. This uncertainty corresponds to the model's uncertainty i.e. $\pm 5\%$ combined with the uncertainty of the experimental heat transfer measurements i.e. typically $\pm 10 - 15\%$.

The transformed experimental data sets (via the T^* model) were then plotted under

the form of an error distribution (figure A.107). The variable $\Delta St_{ae}{}^{*}$ and function $f(X)$ are described in chapter 5, section 5.6.2. Figure A.107 shows good agreement between the experimental data and the theoretical Gaussian distribution. This suggests that all differences within the experimental data are due to random errors only (i.e. experimental measurements) and not systematic errors. This agreement allows the estimation of the true extent of the maximum uncertainty brought by the T^{*} model since the Gaussian distribution considers an infinity of data points rather than just 253 from the experiments.

The estimated deviation, σ, of the Gaussian distribution was found to be approximately 7.0% which means that the maximum uncertainty brought by the T^{*} model (equation 6.11) is 21% (3 deviations). Note that the experimental data gave a similar estimation of the maximum uncertainty i.e. $\pm$17%.

Finally, the variation of the ratio $\bar{R}^{*}/\bar{R}$ with edge Mach number and T_w/T_o is shown in figures A.108 and A.109 for wind tunnel and flight conditions respectively. Those figures were obtained using equation 6.11 with an $\bar{R}$ value constant at 1000. However, it was found that the effect of $\bar{R}$ upon $\bar{R}^{*}/\bar{R}$ is weak ($\pm$5% in the worst case i.e. high Mach number).

6.5 Eckert's model

On the basis of Eckert's [30] definition of the reference temperature (equation 6.10), the values of K1 and K2 were optimised for the generated data set. This was done by plotting the "perfect" reference temperature against the reference temperature from the model, $T^{*}{}_{model}$ (here equation 6.10). The best fit was found to be $\pm$22% (figure A.110) with

$$K1 = 0.09 \qquad \text{and} \qquad K2 = 0.28$$

Having obtained the best "theoretical" values of K1 and K2, the data from Holden et al. [37][38], Bushnell et al. [12][13], Poitiers University [35][6], Beckwith and Gallagher [5] and finally Jones [40] were then considered (appendix G). Figure A.111 shows the collapse onto the incompressible variation to be within 28% uncertainty.

These results were then plotted as an error distribution (figure A.112). In this case, the deviation σ was found to be 9.0% therefore the maximum uncertainty is 27.0% (compared to 21.0% with equation 6.11). Note in passing that most of the data shown by figure A.112 lie on the right hand side which means that using Eckert's model (even with the optimum K1 and K2 values) tends to overestimate the transformed Stanton number.

Figure A.113 shows the effects upon the present experimental data set of the K1 and K2 values as obtained by Poll [49] ($K1 = 0.10$, $K2 = 0.60$ with equation 6.10). It can be seen that, although Beckwith and Gallagher [5] data set fits the incompressible relation within $\pm 20\%$ uncertainty, a large scatter is encountered amongst the other experimental data that were not available at the time. It can therefore be concluded that, even by using Eckert's model with $K1$ of 0.09 and $K2$ of 0.28, a major improvement to the application of the reference temperature to attachment-line boundary layer flow was made.

6.6 Location of T^* within the thermal profile

The reference temperature, T^*, given by equation 6.11 was found to always lie within the thermal profile and thus corresponds to a physically realisable temperature. However, the

location within the layer was found to vary with Reynolds number, edge Mach number, wall-to-stagnation temperature ratio and s/T_o.

Using Eckert's model (equation 6.10), with the optimum constant K1 and K2 values, T^* was found to move towards T_{max} within the thermal profile. The extreme location was found to be for conditions reached by Holden run 27 ($\bar{R}$ of approximately 800, M_{ae} of 3.4, T_w/T_o ratio of 0.26 and s/T_o of 0.09) as shown by figure A.114. For this particular case, T^* is 5.4% higher than T_{max} which, although outside the predicted thermal layer, is well within the experimental measurement uncertainty. However, when equation 6.11 is used, T^*/T_{ae} equals 1.40, which brings the reference temperature inside the profile. Moreover, amongst all the data points considered in the present study (generated and experimental data sets), only Holden run 27 involves a value of T^* that is higher than T_{max} when Eckert's model is used.

6.7 Model for the skin friction

The aim of the present section is to determine whether the new T^* models are directly applicable to the prediction of the skin friction. Recalling the definitions of the Stanton number and skin friction, it may be written i.e.

$$St_{ae}{}^* = St_{ae}.\left(\frac{T^*}{T_{ae}}\right)_{HT} \tag{6.16}$$

$$Cf_{ae}{}^* = Cf_{ae}.\left(\frac{T^*}{T_{ae}}\right)_{SF} \tag{6.17}$$

where the subscripts HT and SF denotes the temperature ratios for heat transfer and skin friction respectively. It follows that

$$\frac{St_{ae}{}^*}{Cf_{ae}{}^*} = \frac{St_{ae}}{Cf_{ae}} \cdot \left(\frac{T^*}{T_{ae}}\right)_{HT} \cdot \left(\frac{T_{ae}}{T^*}\right)_{SF} \tag{6.18}$$

It is well known that, in zero pressure gradient flow, there is a simple relationship between heat transfer and skin friction known as the Reynolds analogy. Cebeci and Bradshaw [19] suggested that for air and a Prandtl number of 0.7 this is given by

$$\frac{St_{ae}}{Cf_{ae}/2} \approx \frac{1.11}{1 - 1.2\sqrt{Cf_{ae}/2}} \tag{6.19}$$

See page 177 of reference [19] for the derivation of equation 6.19.

Using the boundary layer code (turbulence model from the previous chapter) for a wide range of incompressible conditions ($245 < \bar{R} < 3000$, $M_{ae} = 0$, $T_w/T_o = 1$, $T_o = 400$K and $Pr = 0.72$), it was found that the ratio $St_{ae}{}^*/Cf_{ae}{}^*$ is constant at $0.595 \pm 3\%$ as shown by figure A.115 and this closely matches equation 6.19.

The generated data set previously described in section 6.1 was then considered. For every data point the skin friction was plotted against the Stanton number. Figure A.116 shows that the generated compressible data set agrees with the incompressible relations as the ratio $St_{ae}{}^*/Cf_{ae}{}^*$ is now $0.62 \pm 8\%$. This suggests that compressibility has only a very small effect. Hence, it can be concluded from equation 6.18 and figure A.116 that

$$\frac{St_{ae}{}^*}{Cf_{ae}{}^*} = \frac{St_{ae}}{Cf_{ae}} \approx 0.62 \pm 8\% \tag{6.20}$$

Therefore it follows that

$$\left(\frac{T^*}{T_{ae}}\right)_{HT} = \left(\frac{T^*}{T_{ae}}\right)_{SF} \tag{6.21}$$

Hence, there is only one reference temperature and Eckert's model (equation 6.10) and equation 6.11 can be used for the estimation of the skin friction.

6.8 Conclusions

It the present chapter, it was found that Eckert's form of the reference temperature [30] could not fit the variation of T^* with T_w/T_{ae} and T_r/T_{ae} for a wide range of conditions to an uncertainty less than $\pm 28\%$. In this case, the optimum constant value of K1 and K2 were found to be 0.09 and 0.28 respectively.

It was found that Poll's estimated values of the two coefficients K1 and K2 present in the model were only suitable for a limited range of conditions.

A more complicated model was developed to increase accuracy of the predictions. This was found to have only $\pm 7\%$ uncertainty on average and $\pm 21\%$ at the most for a very wide range of conditions, covering flight conditions (no real gas effects) and wind tunnel conditions.

It was also found that whatever model is used, the reference temperature always lies within the thermal profile.

Finally, it was shown that the reference temperatures used to estimate the Stanton number were directly applicable to the skin friction estimation. The ratio St_{ae}/Cfe was found to be $0.62 \pm 8\%$ and independent of compressibility, of the Reynolds number, edge Mach number, wall temperature and s/T_o.

Chapter 7

Minimum conditions for turbulent flow

7.1 Introduction

The models for the variation of the laminar and turbulent Stanton numbers with attachment-line Reynolds number lead to curves of the kind sketched in figure A.117. In all cases, the laminar and turbulent lines cross and the point of intersection gives the minimum conditions for which turbulent flow can occur. For a smooth surface, the minimum conditions will corresponds to a certain value of $\bar{R}$. This is a function of the free-stream conditions, wall temperature, edge Mach number, leading edge geometry etc. When a roughness element is introduced (e.g. trip wire), the attachment-line Reynolds number for transition onset is reduced. In general, $\bar{R}$ is also function of the size of the source of disturbance. However, there will come to a point where, no matter how big the source of disturbance, $\bar{R}$ will not decrease further. This is the $\bar{R}$ that corresponds to the minimum conditions for turbulence.

In 1983, Poll [51] proposed an empirical criterion for determining the minimum conditions

for which compressible turbulent flow can occur when in presence of large disturbances i.e.

$$\bar{R}^*_{mc} = 245 \pm 15\% \tag{7.1}$$

In the present chapter, Poll's criterion is revised using the latest "tools" developed in the previous chapters i.e. the reference temperature model, the laminar model etc. A "data" set that embraced wind tunnel conditions as well as flight conditions (no real gas effects) was generated for M_{ae} from 0.3 to 8.0, T_w/T_o between 0.1 and unity and T_o of 450 K, 800 K and 4000 K (see chapter 6 for the justification of this generated data set).

7.2 Minimum conditions

The full reference temperature method (equation 6.11) was used to evaluate the Stanton number for given conditions. The value of $\bar{R}$ was then reduced until the turbulent Stanton number, St_{aeT}, was equal to the laminar Stanton number, St_{aeL}, under the same conditions. In this case, St_{aeL} was obtained from the exact laminar solution. This particular attachment-line Reynolds number is denoted $\bar{R}_{mc}$ (see figure A.118).

7.3 Criterion for minimum conditions

Recalling the variation of the transformed Stanton number with the transformed attachment-line Reynolds number i.e.

$$St_{ae}{}^* = \frac{A}{\bar{R}^{*B}} \tag{7.2}$$

Using equations 2.21 and 2.22, it follows

$$St_{ae}.\frac{\rho_{ae}}{\rho^*} = \frac{A}{\left[\bar{R}.\left(\frac{\mu_{ae}}{\mu^*}.\frac{\rho^*}{\rho_{ae}}\right)^{\frac{1}{2}}\right]^B} \tag{7.3}$$

$$St_{ae}.\bar{R}^B = A.\left(\frac{\mu^*}{\mu_{ae}}.\frac{\rho^*}{\rho_{ae}}\right)^{\frac{B}{2}}.\left(\frac{\rho^*}{\rho_{ae}}\right)^{1-B} \tag{7.4}$$

For laminar flow, $B = 1$ hence

$$St_{ae}.\bar{R} = A_L.\left(\frac{\mu_L{}^*}{\mu_{ae}}.\frac{\rho_L{}^*}{\rho_{ae}}\right)^{\frac{1}{2}} \tag{7.5}$$

where the subscript L refers to the laminar conditions. For turbulent flow, $B = B$ therefore

$$St_{ae}.\bar{R}^B = A_T.\left(\frac{\mu_T{}^*}{\mu_{ae}}.\frac{\rho_T{}^*}{\rho_{ae}}\right)^{\frac{1}{2}}.\left(\frac{\mu_T{}^*}{\mu_{ae}}.\frac{\rho_T{}^*}{\rho_{ae}}\right)^{\frac{B-1}{2}}.\left(\frac{\rho_T{}^*}{\rho_{ae}}\right)^{1-B} \tag{7.6}$$

where the subscript T refers to the turbulent conditions. At the minimum conditions, the laminar and turbulent Stanton numbers are equal. Therefore, from equations 7.5 and 7.6, it follows that

$$\left(\bar{R}_{mc}\right)^{B-1} = \frac{A_T}{A_L}.\left(\frac{\mu_T{}^*}{\mu_L{}^*}.\frac{\rho_T{}^*}{\rho_L{}^*}\right)^{\frac{1}{2}}.\left(\frac{\mu_T{}^*}{\mu_{ae}}.\frac{\rho_T{}^*}{\rho_{ae}}\right)^{\frac{B-1}{2}}.\left(\frac{\rho_T{}^*}{\rho_{ae}}\right)^{1-B} \tag{7.7}$$

where the subscript mc denotes the minimum conditions. Recalling that

$$\bar{R}^*_{mc} = \bar{R}_{mc}.\left(\frac{\mu_{ae}}{\mu_T{}^*}.\frac{\rho_T{}^*}{\rho_{ae}}\right)^{\frac{1}{2}} \tag{7.8}$$

$$\bar{R}_{mc} = \bar{R}^*_{mc}.\left(\frac{\mu_T{}^*}{\mu_{ae}}.\frac{\rho_T{}^*}{\rho_{ae}}\right)^{\frac{1}{2}}.\left(\frac{\rho_{ae}}{\rho_T{}^*}\right) \tag{7.9}$$

With equation 7.9, equation 7.7 becomes

$$\left(\bar{R}_{mc}\right)^{B-1} = \left(\bar{R}^*_{mc}\right)^{B-1} . \left(\frac{\mu_T{}^*}{\mu_{ae}} . \frac{\rho_T{}^*}{\rho_{ae}}\right)^{\frac{B-1}{2}} . \left(\frac{\rho_{ae}}{\rho_T{}^*}\right)^{B-1} \tag{7.10}$$

$$\left(\bar{R}_{mc}\right)^{B-1} = \frac{A_T}{A_L} . \left(\frac{\mu_T{}^*}{\mu_L{}^*} . \frac{\rho_T{}^*}{\rho_L{}^*}\right)^{\frac{1}{2}} . \left(\frac{\mu_T{}^*}{\mu_{ae}} . \frac{\rho_T{}^*}{\rho_{ae}}\right)^{\frac{B-1}{2}} . \left(\frac{\rho_T{}^*}{\rho_{ae}}\right)^{1-B} \tag{7.11}$$

or from equations 7.10 and 7.11

$$\bar{R}^*_{mc} = \left(\frac{A_T}{A_L}\right)^{\frac{1}{B-1}} . \left(\frac{\mu_T{}^*}{\mu_L{}^*} . \frac{\rho_T{}^*}{\rho_L{}^*}\right)^{\frac{1}{2(B-1)}} \tag{7.12}$$

Results for the generated data set are presented in figure A.119. The best data fairing was obtained with the following characteristics.

$$\left(\frac{A_T}{A_L}\right)^{\frac{1}{B-1}} = 245 \qquad \text{and} \qquad B = -1.9$$

Therefore, the criterion for minimum conditions is

$$\bar{R}^*_{mc} = 245 . \left(\frac{\mu_L{}^*}{\mu_T{}^*} . \frac{\rho_L{}^*}{\rho_T{}^*}\right)^{\frac{1}{5.8}} \tag{7.13}$$

This is shown in figure A.119. Although the turbulence model developed in chapter 5 would have produced a more accurate $\bar{R}^*_{mc}$ value than the T^* model, it could not be used due to convergence difficulties occurring near relaminarisation (see chapter 5, section 5.7). The $\bar{R}^*_{mc}$ results presented in figure A.119 corresponds to the best results achievable. No scatter is present in the data since only smooth mathematical functions were involved.

However, a ±5% error band is shown in figure A.119 to account for the uncertainty of the T^* model itself (equation 6.11).

It must be noted that for practical purposes, the laminar model (equation 3.14) could be used instead of the exact laminar solution. Figure A.120 shows that if the laminar model is used the results obtained still collapse within ±5%. This uncertainty is due to the uncertainty of the laminar model alone since $\bar{R}^*_{mc}$ was obtained from the "best method" (i.e. exact laminar solution and T^* model) whereas the ratio $\left(\frac{\mu_L^*}{\mu_T^*}.\frac{\rho_L^*}{\rho_T^*}\right)$ was obtained using the laminar model. However, the maximum uncertainty of $\bar{R}^*_{mc}$ is ±10% since it arises from the laminar model uncertainty (±5%) coupled with the T^* model uncertainty (±5%).

Experimental data obtained at Poitiers University (runs 81s, 82s, 84s and 85s) and by Bushnell (runs 12 to 19 at L/D of 5.3) were then considered (tables B.7 and B.8 respectively). Figures A.121 to A.125 show very good agreement between the experiments and predictions of the heating intensity and transition location made from the laminar and T^* models (equations 3.14 and 6.11). Laminar and turbulent heating levels are predicted, at the most, within ±12% and ±15% respectively which is well within the uncertainty of the models (±5%) combined with experimental errors (typically ±10 – 15%). The attachment-line Reynolds number corresponding to the location of the transition onset was then transformed into $\bar{R}^*_{mc}$. Figure A.126 show that experimental data agree within ±16% at the most (depending on where transition onset is estimated to be ; figures A.121 to A.125) with the model for minimum conditions (equation 7.13). This result is quite remarkable since the location of the transition onset is predicted within the same order of magnitude as the laminar and turbulent heating intensity. Note that Poll's [49] incompressible experimental data was also added to figure A.126 (equation 7.1).

7.4 Standard NASA criterion

In many references written by NASA researchers (i.e. [7][34]), the ratio of the laminar Reynolds number based on the momentum thickness, R_θ, to the edge Mach number, M_{ae}, is used to characterise the conditions for the onset of transition. Figure A.127 shows that for M_{ae} less than 1.5, the onset of transition can be correlated (approximately) with a constant value of $R_{\theta mc}$. For edge Mach numbers higher than 3, the transition onset can be correlated with a constant value of the ratio $R_{\theta mc}/M_{ae}$. However although these criteria ($R_{\theta mc}$ and $R_{\theta mc}/M_{ae}$) are wind tunnel correlation, they cannot be justified on any known physical grounds.

Berry et al. [7] used experiments results from a 0.013-scale model of the X-33 at Mach 6 to obtained the variation of $R_{\theta mc}/M_{ae}$ characterising the minimum conditions with the size of the disturbances, k/δ (roughness elements ; see figure A.128). At high values of k/δ i.e. very large disturbances, the ratio $R_{\theta mc}/M_{ae}$ at transition onset is approximately 50. This is very close to the minimum conditions obtained from the generated data set (see figure A.129). The stagnation temperature for the data presented in this figure is 450 K which is close to that used by Berry et al. [7].

In addition, it was found that over the range of edge Mach number considered, the wall to edge temperature ratio had only a small effect upon the critical momentum thickness Reynolds number as shown by figure A.129.

Using the generated data set for a wide range of conditions (wind tunnel and flight conditions), it was found that $R_{\theta mc}$ was a function of s/T_o as shown by figure A.130. Moreover,

for a given edge Mach number, $R_{\theta mc}$ decreases with increasing T_o (hence, decreasing s/T_o). This suggests that wind tunnel results cannot be applied directly to flight conditions since these results are too optimistic. Figure A.130 shows that for edge Mach number higher than 3, $R_{\theta mc}/M_{ae}$ is approximately 50 for wind tunnel conditions but around 33 for flight conditions (51% difference as shown by figure A.130).

The data presented in figure A.130 can be fitted within ±10% by

$$R_{\theta mc} = \left[1.11 + 25.7\left(\frac{s}{T_o}\right) - 20.1\left(\frac{s}{T_o}\right)^2\right].{M_{ae}}^2 + \\ + \left[7.03 - 39.6\left(\frac{s}{T_o}\right)\right].M_{ae} + 99.04 \qquad (7.14)$$

Estimates from equation 7.14 are shown in figure A.131.

7.5 Attachment-line Reynolds number for minimum conditions

In chapter 6, section 6.4 the ratio $\bar{R}^*/\bar{R}$ was obtained for fully turbulent flow under a wide range of conditions (see, for example, figure A.108). The variation of $\bar{R}^*_{mc}$ characterising the minimum conditions at which transition can occur under a large source of disturbance was also obtained for a wide range of conditions (equation 7.13, figure A.126). By combining the two results, the attachment-line Reynolds number for the minimum conditions, $\bar{R}_{mc}$, was obtained and is shown in figures A.132 and A.133 for wind tunnel and flight conditions respectively. Uncertainty of the Reynolds number $\bar{R}_{mc}$ is due to the uncertainty of $\bar{R}^*/\bar{R}$ and $\bar{R}^*_{mc}$ which is ±5% due to the uncertainty involved by the T^* model combined with uncertainty of the laminar model (i.e.±5%). This leads to a maximum uncertainty of

the Reynolds number $\bar{R}_{mc}$ of ±10%. Using the exact laminar solution would decrease this maximum uncertainty to ±5% only. However, it was found that the use of the laminar model gives more "conservative" predictions of $\bar{R}_{mc}$ than when the exact solution is used (figure A.134 ; flight conditions) and the difference between the two predictions (exact and model for the laminar part) is in reality less than ±5%.

Similarly, $\bar{R}_{mc}$ can be obtained from the ratio $R_\theta/\bar{R}$ for laminar flow (see chapter 3, equation 3.21 and figure A.36) combined with equation 7.14. In this case, the maximum uncertainty of $\bar{R}_{mc}$ is ±18.5% since $R_\theta/\bar{R}$ and $R_{\theta mc}$ have an uncertainty of ±8.5% and ±10% respectively. If good accuracy is required, the exact laminar solution should be used to calculate $R_\theta/\bar{R}$. This will lead to an overall uncertainty of $\bar{R}_{mc}$ of ±10%.

Comparison of the Reynolds number $\bar{R}_{mc}$ obtained from $\bar{R}^*/\bar{R}$ and $\bar{R}^*_{mc}$ (laminar model used) and from $R_\theta/\bar{R}$ and $R_{\theta mc}$ is shown in figure A.135 for flight conditions. The variable $\Delta\bar{R}_{mc}$ was evaluated from

$$\Delta\bar{R}_{mc} = \frac{2\left[\bar{R}_{T^*} - \bar{R}_{R_\theta}\right]}{\bar{R}_{T^*} + \bar{R}_{R_\theta}} \tag{7.15}$$

where the subscript T^* denotes the use of $\bar{R}^*/\bar{R}$ and $\bar{R}^*_{mc}$ and the subscript R_θ points out the use of $R_\theta/\bar{R}$ and $R_{\theta mc}$.

The maximum difference between the two methods (using the laminar model to estimate $\bar{R}^*_{mc}$) is approximately 22% as shown by figure A.136. This is well inside the resulting uncertainty from both methods i.e. ±10% due to $\bar{R}^*/\bar{R}$ and $\bar{R}^*_{mc}$ (when the laminar model is used) coupled with ±18.5% from $R_\theta/\bar{R}$ and $R_{\theta mc}$ which results in an possible

maximum difference of ±28.5%. When the exact laminar solution is used to estimate $\bar{R}^*_{mc}$ the uncertainty on the data stays at 22%. However, the possible maximum difference is decreased from ±28.5% to ±22.5%.

Which ever method is used, the trend of $\bar{R}_{mc}$ with edge Mach number is identical i.e. $\bar{R}_{mc}$ is an increasing function of Mach number. For given conditions, cooling the wall decreases $\bar{R}_{mc}$. This means that at a given station L/D along the cylinder, the attachment-line flow goes from being originally laminar to turbulent as the wall is cooled. Finally, the effects of the wall temperature are emphasised at high edge Mach number.

The experimental data shown in figures A.121 to A.125 were then considered i.e. runs 81s, 82s, 84s and 85s carried out at Poitiers University and runs 12 to 19 undertaken by Bushnell at an L/D of 5.3 (see also tables B.7 and B.8). Figure A.132 could be used to estimate $\bar{R}_{mc}$ since all the runs considered were undertaken at an s/T_o value of approximately 0.138. The difference in $\bar{R}_{mc}$ from the experiments and the calculation (or figure A.132) is within ±23% which corresponds to the experimental uncertainty of $\pm 10 - 15\%$ combined with the uncertainty of the model (using $\bar{R}^*/\bar{R}$ and $\bar{R}^*_{mc}$) which is ±10% at the most.

7.6 Variation of the recovery factor

In previous chapters, it was seen that the approximations of the laminar and turbulent recovery factor were almost identical (see equations 3.7 and 5.12). This result is not surprising since, as the Reynolds number is decreased, the turbulent Stanton number must approach its laminar value. At the minimum conditions for turbulence, the laminar

and turbulent Stanton numbers are equal. Therefore, the laminar and turbulent recovery factors must be identical. It is well known that the attachment-line flow is a low Reynolds number flow. Due to this fact, it is not surprising to observe similar values for the laminar and turbulent recovery factors. However, the major question is how does the turbulent recovery factor approach its laminar value when the edge Mach number and Reynolds number are decreased ?

7.6.1 Decreasing edge Mach number

Using the turbulence model, for $\bar{R}$ values of 500 and 1000 and an s/T_o ratio of 0.138 ($Pr = 0.72$), the variation of the laminar and turbulent recovery factors was obtained (figure A.137). At low edge Mach number, the turbulent recovery factor is higher than its laminar value. As the Mach number increases, the turbulent recovery factor decreases rapidly and the laminar value increases slowly. For an $\bar{R}$ value of 1000, for example, the laminar and turbulent recovery factors match each other at an edge Mach number of approximately 2.2 (for $\bar{R}$ of 500, this arisen at an edge Mach number of approximately 1.9). However, this does not correspond to the minimum conditions at which turbulence can occur since for $M_{ae} \approx 2.2$, $\bar{R}_{mc}$ is less than approximately 300 (see figure A.137). Further increasing the Mach number results in the laminar recovery factor being higher than the turbulent value. As M_{ae} is further increased, the turbulent recovery factor reaches its minimum and then starts increasing again. For $\bar{R}$ of 1000, the undershoot of the turbulent recovery factor is less than 2% of the laminar value. The variation of r with edge Mach number could not be predicted for M_{ae} values beyond 5 since the code could not converge. Nevertheless, using figure A.132 for an $\bar{R}$ value of 1000 and cold wall conditions, the minimum conditions are reached for an edge Mach number value between

approximately 6 and 7 (for $\bar{R}$ of 500, minimum conditions occur at M_{ae} between 4 and 5 approximately). Therefore, an extrapolation between the value of r from which the code stopped converging and the value corresponding to the minimum conditions was done (dash line in figure A.137).

It was found that the variation of the laminar recovery factor with edge Mach number was function of s/T_o only. However, for turbulent flow, the variation of r with M_{ae} was found to depend upon $\bar{R}$ but to be independent of s/T_o.

7.6.2 Decreasing Reynolds number

Figure A.138 shows the variation of the laminar and turbulent recovery factors with attachment-line Reynolds number for an edge Mach number of 2. It can be seen that as $\bar{R}$ is decreased, the turbulent recovery factor approaches its laminar value from above. For a M_{ae} value of 2, relaminarisation occur at an $\bar{R}$ value of approximately 280. This results is confirmed by figure A.132.

Considering an edge Mach number of 5, the variation of the turbulent recovery factor with $\bar{R}$ differs from the variation obtained for a M_{ae} value of 2 (figures A.139 and A.138 respectively). For M_{ae} of 5, at high Reynolds number (i.e. $\bar{R}$ more than 1800), the turbulent recovery factor is higher than the correspondent laminar value. However, at $\bar{R}$ values less than 1800, the laminar recovery factor becomes higher than its turbulent value. A minimum in the turbulent recovery factor is reached at an $\bar{R}$ of approximately 1100. The undershoot of the turbulent recovery factor is less than 2% of the laminar value. Further decreasing the Reynolds number results in an increase in r. Predictions of r from the code

stop at an $\bar{R}$ value of 700 but, using the results shown in figure A.132, an interpolation was made. For edge Mach number of 5 and cold wall conditions (i.e. T_w/T_o less than 0.6), relaminarisation occurs at $\bar{R}$ values between 500 and 600 (see figure A.132) leading to the interpolation of r shown in figure A.139 (dash line).

It was shown that the variation of r with edge Mach number and Reynolds number is complex. In addition, it was shown that the variation of r predicted by the turbulence model is consistent with predictions of r at the minimum conditions given by the laminar and T^* models and the model for minimum conditions.

7.7 Conclusions

A criterion $\bar{R}^*_{mc}$ characterising the minimum conditions for which turbulent flow can occur under a large source of disturbances (e.g. end plates, large trip wires etc.) was obtained. This was found to be accurate to within $\pm 10\%$ for wind tunnel conditions as well as flight conditions (no real gas effects) when compared with a generated data set. With the consideration of few wind tunnel experimental cases, the model uncertainty was shown to be $\pm 16\%$ at the most.

To characterise the minimum conditions, the NASA standard method is to use the ratio $R_{\theta mc}/M_{ae}$ extracted from wind tunnel tests and is valid of edge Mach numbers higher than 3. However, it was found that this ratio was a strong function of s/T_o, suggesting that wind tunnel results cannot be applied directly to flight conditions. Therefore, a model to estimate $R_{\theta mc}$ was proposed. This embraces effects of s/T_o and is valid for a wide range of edge Mach number. Its maximum uncertainty was found to be $\pm 10\%$.

The attachment-line Reynolds number characterising the transition onset in presence of large disturbances, $\bar{R}_{mc}$, was obtained from $\bar{R}^*/\bar{R}$ and $\bar{R}^*_{mc}$. Its maximum uncertainty was estimated to be $\pm 10\%$ due to the uncertainty of the reference temperature model ($\pm 5\%$) and of the laminar model ($\pm 5\%$). By considering a limited number of experimental data, predictions of $\bar{R}_{mc}$ characterising the transition onset was shown to be $\pm 23\%$ in the worst case. This corresponds to the uncertainty of the $\bar{R}_{mc}$ model ($\pm 10\%$) coupled with experimental uncertainty ($\pm 10 - 15\%$). When the exact laminar solution is used the maximum uncertainty of the $\bar{R}_{mc}$ model decreases from $\pm 10\%$ to $\pm 5\%$.

The variation of the laminar and turbulent recovery factors with edge Mach number and Reynolds number was shown to be complex. Predictions made from the turbulence model (chapter 5) were shown to be consistent with predictions from the $\bar{R}_{mc}$ model at relaminarisation.

Chapter 8

Conclusions

This investigation concentrated on the study of the attachment-line flow behaviour under wind tunnel and flight conditions but with no real gas effects. It is based upon the use of accurate computational results coupled with available experimental data.

8.1 Laminar flow

A model for the laminar Stanton number was developed. This included the effects of Reynolds number, edge Mach number, Prandtl number and Sutherland law constant to stagnation temperature ratio. The maximum uncertainty of the model was estimated to be ±15% corresponding to the combination of the model's uncertainty of ±5% and the experimental measurements uncertainty i.e. typically ±10%.

A model for the variation of the ratio of the momentum thickness Reynolds number to the attachment-line Reynolds number, $R_\theta/\bar{R}$, with edge Mach number, wall-to-stagnation temperature ratio and s/T_o was also proposed. Predictions were found to be within ±8.5% of the exact solution.

One of the novel aspects of the present work is the use of CFD to provide estimates of the local flow properties. A large number of previous investigations have based data reduction upon the infinite swept conditions. However, it was found that this can lead to very large errors. This is particularly true for experiments conducted on short models where L/D may be less than 10, and sweep angles may be 60^o or more.

It was found that the spanwise variation of the local edge flow properties was Mach number independent for a given sweep angle when the normal to leading edge Mach number exceeded approximately 2.5.

The attachment-line recovery factor was considered for a wide range of conditions. It was found that the recovery factor was approximately $Pr^{0.45}$.

8.2 Turbulent flow

A turbulence model based upon the mixing length and damping function concept was developed. Local values of flow properties were used and both von Kármán's constant, k, and turbulent Prandtl number were fixed at 0.41 and 0.90 respectively. The Van Driest damping parameter, A^+, and the non-dimensional outer mixing length, l_o/δ, were found to increase with decreasing Reynolds number. The damping parameter was found to vary with a characteristic inner region Reynolds number, δ_c^+, based upon the viscous layer thickness, the friction velocity and a kinematic viscosity based upon a characteristic temperature T_c. However, the outer mixing length l_o/δ was shown to vary with the compound momentum thickness Reynolds number, $R_{\theta ew}$, based upon momentum thickness,

edge velocity, edge density and wall viscosity.

Incompressible velocity profiles and flow properties such as the skin friction, shape factor and wake strength were predicted to within the scatter of the experimental data (typically ±15%). For compressible flow, heating intensity was predicted to within the experimental data uncertainty (10 – 15%) for a wide range of conditions. The turbulence models proposed by Cebeci [18] and Kays et al. [42] were shown to be unsatisfactory for attachment-line flows at Reynolds numbers typical of flight.

Using the new turbulence model, it was found that, for a wide range of edge Mach number, the turbulent recover factor could be approximated by the Prandtl number raised to the power 0.46. This is almost identical to the laminar approximation (Prandtl number raised to the power 0.45). This is due to the fact that, as the Reynolds number is decreased the turbulent Stanton number eventually approaches the laminar value. Hence, the difference between the turbulent and laminar recovery factor must decreases with Reynolds number. Since the attachment-line flow is a low Reynolds number flow, even at flight conditions, it is not surprising to find similar recovery factors for both laminar and turbulent flow.

A new model of the reference temperature was developed in order to predict the turbulent Stanton number. Its uncertainty was estimated to be ±7% on average and ±21% at the most.

Eckert's form of the reference temperature [30] was also considered due to its simplicity. It was found that Poll's [49] estimated values of the two coefficients K1 and K2 present in the model were only suitable for a limited range of conditions. For wind tunnel

and flight conditions, the best values for K1 and K2 were found to be 0.09 and 0.28 respectively. This produced a maximum uncertainty of ±22%. When considering experimental measurements, the uncertainty of the model was estimated to be ±9% on average and ±27% at the most.

The two reference temperature models used to estimate the Stanton number were shown to be directly applicable to the skin friction estimation since, the ratio of these two parameters was found to be constant at approximately $0.62 \pm 8\%$ and independent of compressibility, Reynolds number, edge Mach number, wall temperature and s/T_o.

8.3 Minimum conditions for turbulence

A criterion, $\bar{R}^*_{mc}$, based on the reference temperature and characterising the minimum conditions for which turbulent flow can occur downstream of a large source of disturbances (e.g. end plates, large trip wires etc.) was obtained. The model uncertainty was shown to be ±10%. By considering a limited number of experimental cases, prediction of the Reynolds number at which turbulence can occur was found to be accurate to within ±16%. This was due to experimental uncertainty.

To characterise the minimum conditions for turbulence, NASA uses the ratio $R_{\theta mc}/M_{ae}$ which is extracted from wind tunnel testing and is valid of edge Mach numbers higher than 3. However, it was shown that this ratio is a strong function of s/T_o, suggesting that wind tunnel results cannot be applied directly to flight conditions. Therefore, a model was proposed to estimate $R_{\theta mc}$. This embraces effects of s/T_o and is valid for a wide range of edge Mach number. The uncertainty was found to be ±10% at the most.

The attachment-line Reynolds number characterising the transition onset in presence of large disturbances, $\bar{R}_{mc}$, was obtained from $\bar{R}^*/\bar{R}$ and $\bar{R}^*_{mc}$. Its uncertainty was estimated to be $\pm 10\%$ and this was due to the uncertainty of the reference temperature model ($\pm 5\%$) and of the laminar model ($\pm 5\%$). By considering a limited number of experimental data, predictions of $\bar{R}_{mc}$ characterising the transition onset was shown to be $\pm 23\%$ in the worst case. This corresponds to the uncertainty of the $\bar{R}_{mc}$ model ($\pm 10\%$) coupled with experimental uncertainty ($\pm 10 - 15\%$). When the exact laminar solution is used the maximum uncertainty of the $\bar{R}_{mc}$ model decreases from $\pm 10\%$ to $\pm 5\%$ only.

The variation of the laminar and turbulent recovery factors with edge Mach number and Reynolds number was proved to be complex. Predictions made from the turbulence model were shown to be consistent with predictions from the $\bar{R}_{mc}$ model at relaminarisation.

References

[1] ADAMS, J.C. et al. (Feb 1973). Hypersonic lifting body windward surface flowfield analysis for high angles of incidence. *(Arnold Engineering Development Center, Arnold Air Force Station, Tennessee, AD 75-64-99).*

[2] AMES RESEARCH STAFF. (1953). Equations, tables, and charts for compressible flow. *(NACA Report 1135).*

[3] ANDERSON, J.D (1989). Hypersonic and high temperature gas dynamics. *(Mc Graw Hill Series in aeronautical and aerospace).*

[4] BALDWIN, B.S. and LOMAX, H. (January 1978). Thin layer approximation and algebraic model for separated turbulent flows. *(AIAA 78-257).*

[5] BECKWITH, I.E. and GALLAGHER, J.J. (April 1959). Local heat transfer and recovery temperatures on a yawed cylinder at a Mach number of 4.15 and high Reynolds numbers. *(NASA MEMO 2-27-59L).*

[6] BENARD, E. (1998). Contribution a l'etude de la transition de couche limite sur un cylindre en fleche en ecoulement hypersonique. *(These de Doctorat, Universite de Poitiers France).*

[7] BERRY, S.A., HORVATH, T.J., HOLLIS, B.R., THOMPSON, R.A. and HAMILTON II, H.H. (1999). X-33 Hypersonic boundary layer transition. *(AIAA 99-3560).*

[8] BLOTTNER, F.G. (Feb 1970). Finite difference methods of solution of the boundary layer equations. *(AIAA Jounal, Vol. 8, No. 2, pp193 - 205).*

[9] BOROWSKI, E.J. and BORWEIN, J.M. (1989). Dictionary of mathematics. *(Harper Collins Publishers, pp 174).*

[10] BOUSSINESQ, J. (1877). Theorie de l'ecoulement tourbillant. *(Mem. Press. Acad. Sci. XXIII 46 Paris).*

[11] BRADSHAW, P. (1994). Turbulence: the chief outstanding difficulty of our subject. *(Experiments in Fluids, Vol. 16, pp203 - 216).*

[12] BUSHNELL, D.M (Dec 1965). Interference heating on a swept cylinder in region of intersection with a wedge at Mach number 8. *(NASA TN D-3094).*

[13] BUSHNELL, D.M. and HUFFMAN, J.K. (Aug 1967). Investigation of heat transfer to leading edge of a 76° swept fin with and without chordwise slots and correlations of swept leading edge transition data. *(NASA TM-X-1475).*

[14] BUSHNELL, D.M. and MORRIS, D.J. (Aug 1971). Shear-stress, eddy-viscosity and mixing-length distributions in hypersonic turbulent boundary layer. *(NASA TM-X-2310).*

[15] BUSHNELL, D.M., CARRY, A.M. and HOLLEY, B.B. (Aug 1975). Mixing length in low Reynolds number compressible turbulent boundary layers. *(AIAA Journal, Vol. 13, No 8, pp1119 - 1121).*

[16] CEBECI, T. (1970). Calculation of compressible turbulent boundary layers with heat and mass transfer. *(AIAA Paper, No 70-741).*

[17] CEBECI, T. (1973). Variation of the Van Driest damping parameter with mass transfer. *(AIAA Journal, Vol. 11, pp237).*

[18] CEBECI, T. (1973). Kinematic eddy viscosity at low Reynolds numbers. *(AIAA Journal, Vol. 11, pp102).*

[19] CEBECI, T. and BRADSHAW, P. (1984). Physical and computational aspects of convective heat transfer. *(Springer-Verlag New York inc).*

[20] CEBECI, T. and MOSINSKIS G.J. (1971). Computation of incompressible turbulent boundary layers at low Reynolds numbers. *(AIAA Journal, Vol. 9, No 8, pp1632 - 1634).*

[21] CEBECI, T. and SMITH, A.M.O. (1974). Analysis of turbulent boundary layers. *(Applied mathematics and mechanics, 15. Academic Press).*

[22] COLES, D. (1955). The law of the wall in turbulent shear flow. *(50 jahre grenzschicht-forschung, ed. H.Görtler & W.Tollmein, pp153 - 163).*

[23] CONTE, S.D. (1965). Elementary numerical analysis. *(McGraw-Hill, Inc., New York).*

[24] CUMPSTY, N.A. and HEAD, M.R. (May 1967). The calculation of three-dimensional turbulent boundary layers. *(Aeronautical Quarterly, Vol. 18, pp150 - 164).*

[25] DA COSTA, J.L. (March 1990). Contribution a l'etude de la transition de bord d'attaque par contamination en ecoulement hypersonique. *(These de Doctorat, Universite de Poitiers, France).*

[26] DANKS, M. (1995). Issues relating to laminar flow control on the leading edge of swept wings. *(PhD thesis, University of Manchester, School of engineering).*

[27] DAVIS, R.T. (May 1970). Numerical solution of the hypersonic viscous shock layer equations. *(AIAA Jounal, Vol. 8, No. 5, pp843 - 851).*

[28] DORRANCE, W.H. (1962). Viscous hypersonic flow. *(McGraw-Hill, Inc., New York).*

[29] DUSSAUGE, J.P. et al. (July 1996). Turbulent boundary layers in subsonic and supersonic flow. *(AGARD-AG-335).*

[30] ECKERT, E.R.G. (March 1955). Engineering relations for friction and heat transfer to surfaces in high velocity flow. *(Journal of Aeronautical Sciences, Vol. 22, pp585 - 587).*

[31] FERNHOLZ, H.H. (1969). Geschwindigkeitsprofile, temperaturprofile und halbempirische gesetze in kompressiblen turbulenten grenzschichten bei kontantem druck. *(Ing. Arch. 38, pp311 - 328).*

[32] FERNHOLZ, H.H. and FINLEY, P.J. (June 1977). A critical compilation of compressible turbulent boundary layer data. *(AGARD-AG-223).*

[33] FERNHOLZ, H.H. and FINLEY, P.J. (May 1980). A critical commentary on mean flow data for two-dimensional compressible turbulent boundary layers. *(AGARD-AG-253).*

[34] FUHRMANN, H.D., HILDEBRAND, J. and LALICATA, T. (April 1999). Aerothermodynamic Overview, X-34 *(Journal of Spacecraft and Rockets, Vol. 36, No. 2).*

[35] GAILLARD, L. (Dec 1993). Etude de la transition de bord d'attaque sur un cylindre en fleche en ecoulement hypersonique. *(These de Doctorat, Universite de Poitiers France).*

[36] HIRSCH, C. (1990). Numerical computation of internal and external flows. *(Publisher John Wiley and Sons (Chichester) Vol 2, pp495 - 498).*

[37] HOLDEN, M.S., KOLLY, J.M. and BOWER, D.R. (July 1994). Attachment line transition studies on swept cylindrical leading edges at Mach numbers from 10 to 12. *(Calspan-UB Research Center, Report Number 2610-6).*

[38] HOLDEN, M. and KOLLY, J. (June 1995). Attachment line transition studies on swept cylindrical leading edges at Mach numbers from 10 to 12. *(AIAA 95-2279).*

[39] HUFFMAN, G.D. and BRADSHAW, P. (1971). A note on von Kármán's constant in low Reynolds number turbulent flows. *(J. Fluid Mech., Vol 53, part 1, pp45 - 60).*

[40] JONES, R.A. (July 1964). Heat transfer and pressure investigation of a fin plate interference model at a Mach number of 6. *(NASA TN D-2028).*

[41] JONES, R.A. and GALLAGHER, J.J. (May 1961). Heat transfer and pressure distributions of a 60° swept delta wing with dihedral at a Mach number of 6 and angles

of attack from 0° to 52°. *(NASA TM X-544).*

[42] KAYS, W.B., MOFFAT, R.J and THIELBAHR, W.H. (1970). Heat transfer to the highly accelerated turbulent boundary layer with and without mass addition. *(J. Heat Transfer, Vol. 92, pp499).*

[43] KIMMEL, R. and WALKER, S.H. (March 1999). Research directions in hypersonic boundary layer transition. *(White paper, meeting held at Wright-Patterson AFB on 4 November 1998).*

[44] LIOU, M.S. (1995). Progress towards an improved CFD method: AUSM+. *(AIAA Paper 95-1701).*

[45] MORKOVIN, M.V. (1961). Effects of compressibility on turbulent flows. *(Mechanics of turbulence: international symposium, Marseille (France), Gordon and Breach Publ. 1964, New York).*

[46] OSHER, S. and SOLOMON, F. (1982). Upwind difference schemes for hyperbolic conservation laws. *(Math Comp 38:339-374).*

[47] PATANKAR, S.V. and SPALDING, D.B. (1967). Heat and mass transfer in boundary layers. *(Morgan-Grampiar Press, London).*

[48] PFENNINGER, W. (May 1965). Recent developments in boundary layer research PART IV. *(AGARDograph 97).*

[49] POLL, D.I.A. (1978). Some aspects of the flow near a swept attachment line with particular reference to boundary layer transition. *(PhD thesis, Cranfield University, College of Aeronautics).*

[50] POLL, D.I.A. (1981). Skin friction and heat transfer at an infinite swept attachment line. *(Aeronautical Quarterly, Vol. 32, pp299 - 318).*

[51] POLL, D.I.A. (1983). The development of intermittent turbulence on a swept attachment line including the effects of compressibility. *(Aeronautical Quarterly, Vol. 34, pp1 - 23).*

[52] POLL, D.I.A. (June 1984). Transition description and prediction in three-dimensional flows. *(AGARD-R-709).*

[53] POLL, D.I.A. and PAISLEY, D.J. (March 1985). On the effect of wing taper and sweep direction on leading edge transition. *(Aeronautical Journal, Paper 1202, pp109 - 117).*

[54] QIN, N. and LUDLOW, D.K. (July 1999). A cure for anomalies of Osher and AUSM+ schemes for hypersonic viscous flows around swept cylinders. *(22nd International Symposium on Shock Waves, Imperial College, London, UK).*

[55] RICHTMYER, R.D. and MORTON, K.W. (1967). Difference methods for initial value problems. *(Interscience Publishers, New York, second edition).*

[56] SCHLICHTING, H. (1968). Boundary layer theory. *(McGraw-Hill, New York, 6th edition).*

[57] SIMPSON, R.L. (1970). Characteristics of turbulent boundary layers at low Reynolds number with and without transpiration. *(Journal of Fluid Mechanics, Vol. 42, pp769 - 802).*

[58] STAINBACK, P.C. (1964). Heat transfer measurements at a Mach number of 8 in the vicinity of a 90° interior corner aligned with the free stream velocity. *(NASA TN D-2417).*

[59] SURAH, D. (March 2000). Investigation of attachment line characteristics in hypersonic flows. *(PhD thesis, Cranfield University, College of Aeronautics).*

[60] TAYLOR, J.R. (1982). An introduction to error analysis. The study of uncertainties in physical measurements. *(University Science Books, Mill Valley, California).*

[61] VAN DRIEST, E.R. (1951). Turbulent boundary layer in compressible fluids. *(Journal of Aeronautical Sciences, Vol. 18, pp145 - 160).*

[62] VAN DRIEST, E.R. (1956). On turbulent flow near the wall. *(Journal of Aeronautical Sciences, Vol. 23, p1007).*

[63] WALZ, A. (1966). Stromungs- und temperaturgrenzschichten. *(Verlag G. Braun Karlsruhe).*

[64] WEATHERILL, N.P. (1990). Structured grid generation. *(Lecture series. von Karman. Institute for fluid dynamics).*

[65] YARDLEY, M.R. (Nov. 1995). An investigation into the mechanisms of turbulent boundary layer relaminarisation on swept wing leading edges. *(PhD thesis, Manchester School of Engineering, Aerospace Engineering Division).*

[66] YOUNG, A.B.W. and JANSSEN, E. (1952). The compressible boundary layer. *(Journal of the Aeronautical Sciences, Vol. 19, pp229 - 236 and 288).*

Appendix A

Figures

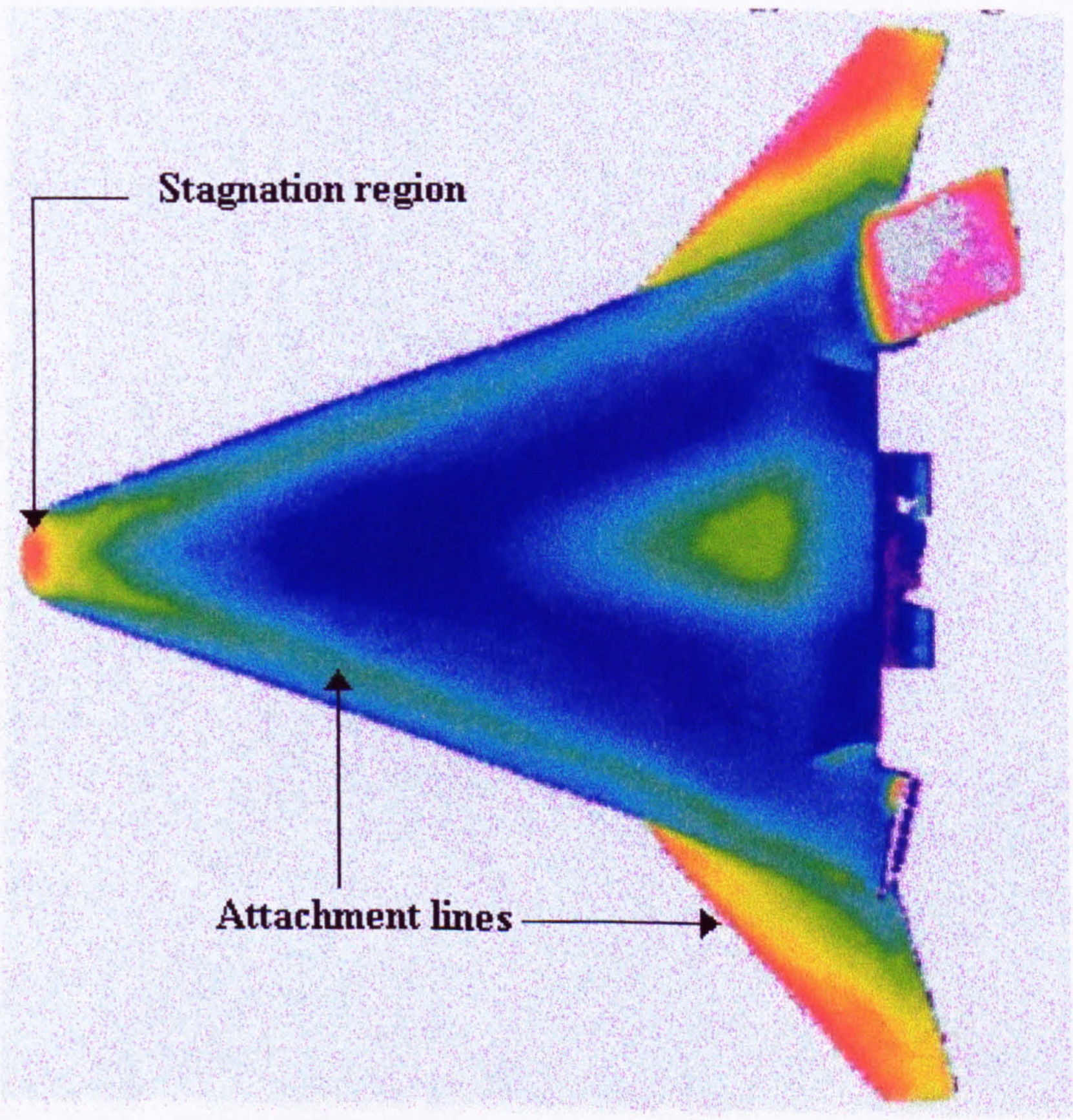

Figure A.1: Global surface heating image on the X-33 windward face after Berry et al. [7]. ($M_\infty = 6$, $R_\infty = 7.9.10^6$ per foot, incidence of 40^o and body flap deflection of 20^o).

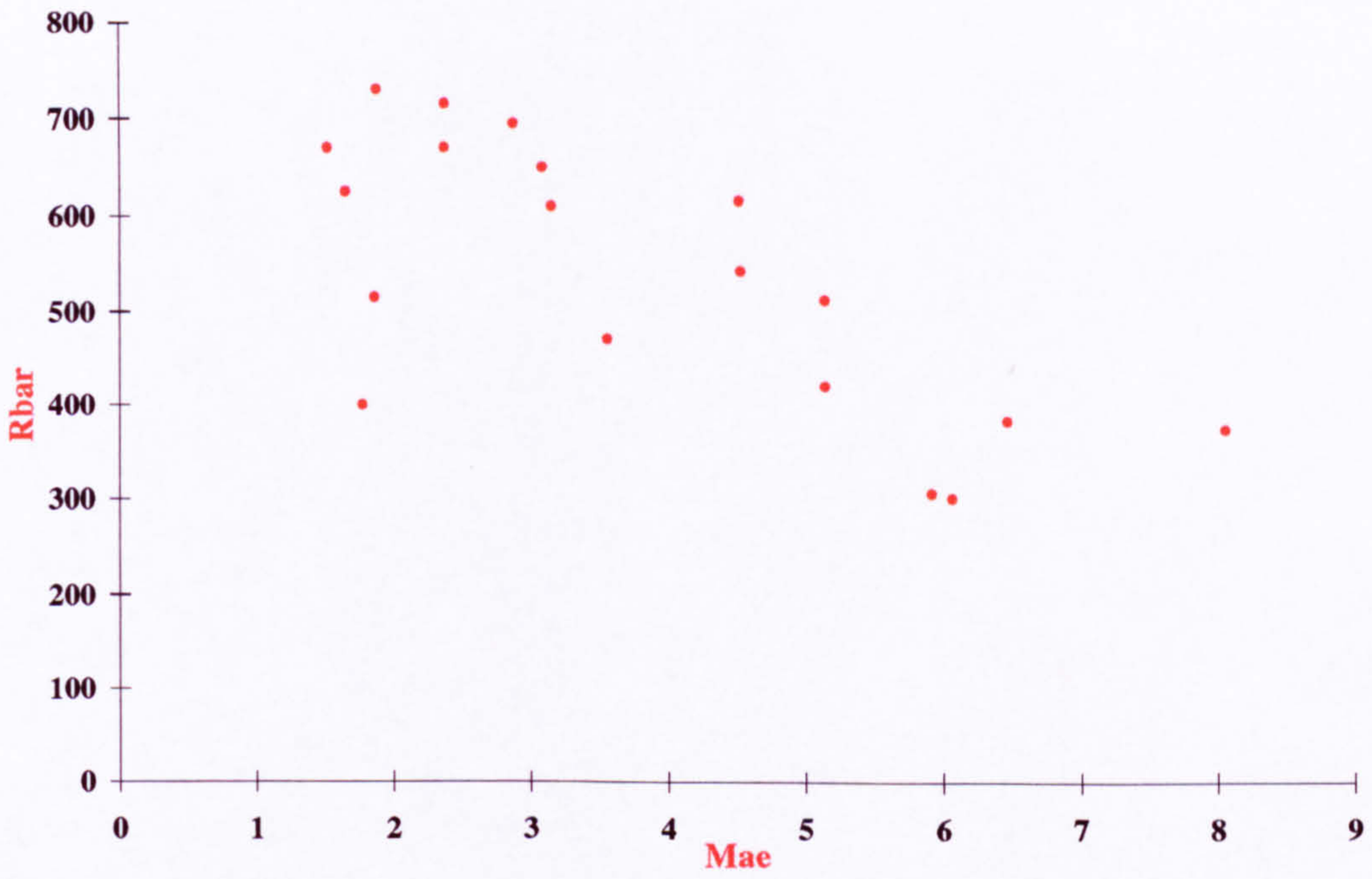

Figure A.2: Attachment-line Reynolds number at which transition occurs vs Edge Mach number along the attachment-line (part of the available data: 10 different investigators).

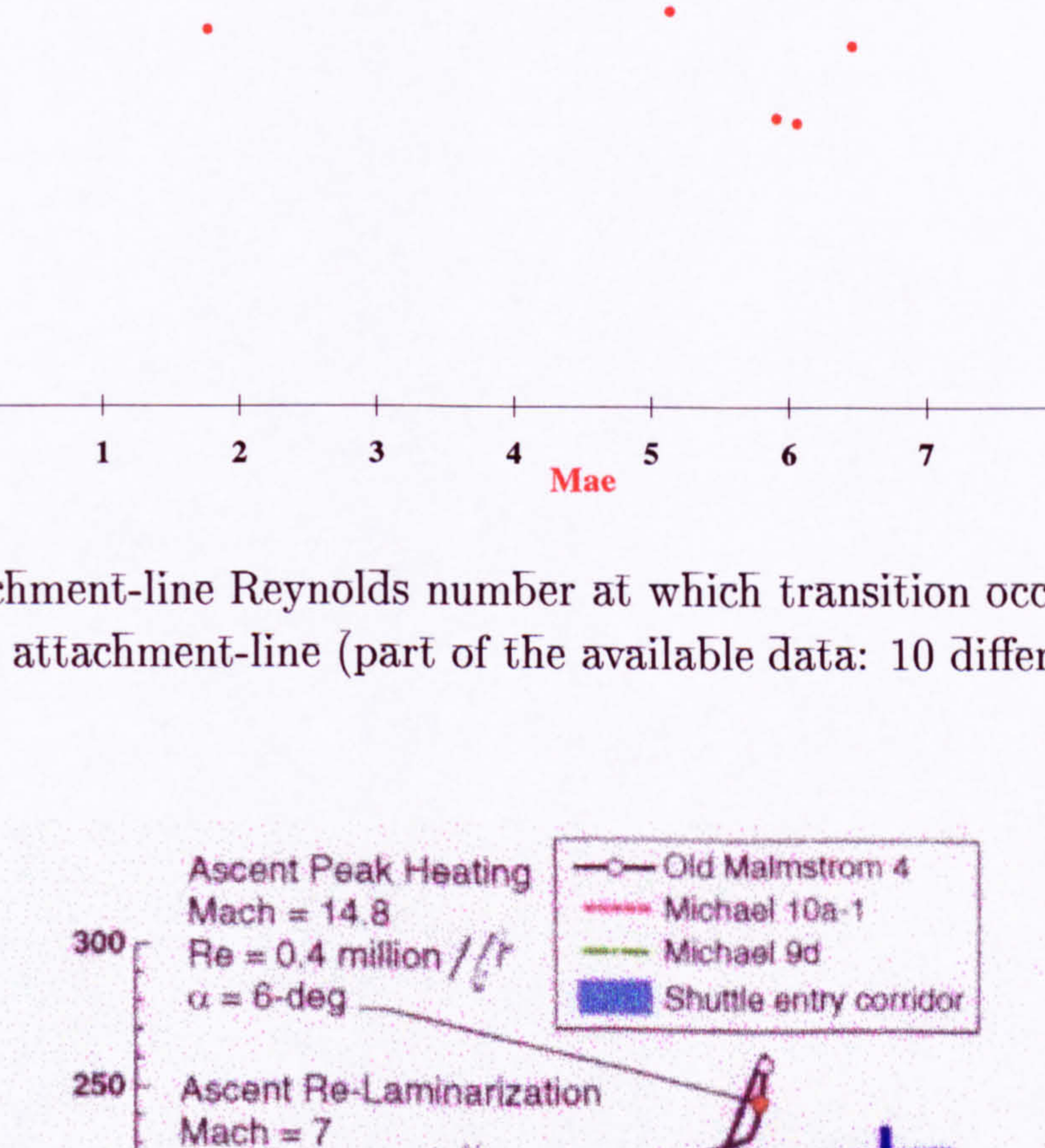

Figure A.3: Typical trajectory of Reusable Launch Vehicles after Berry et al. [7].

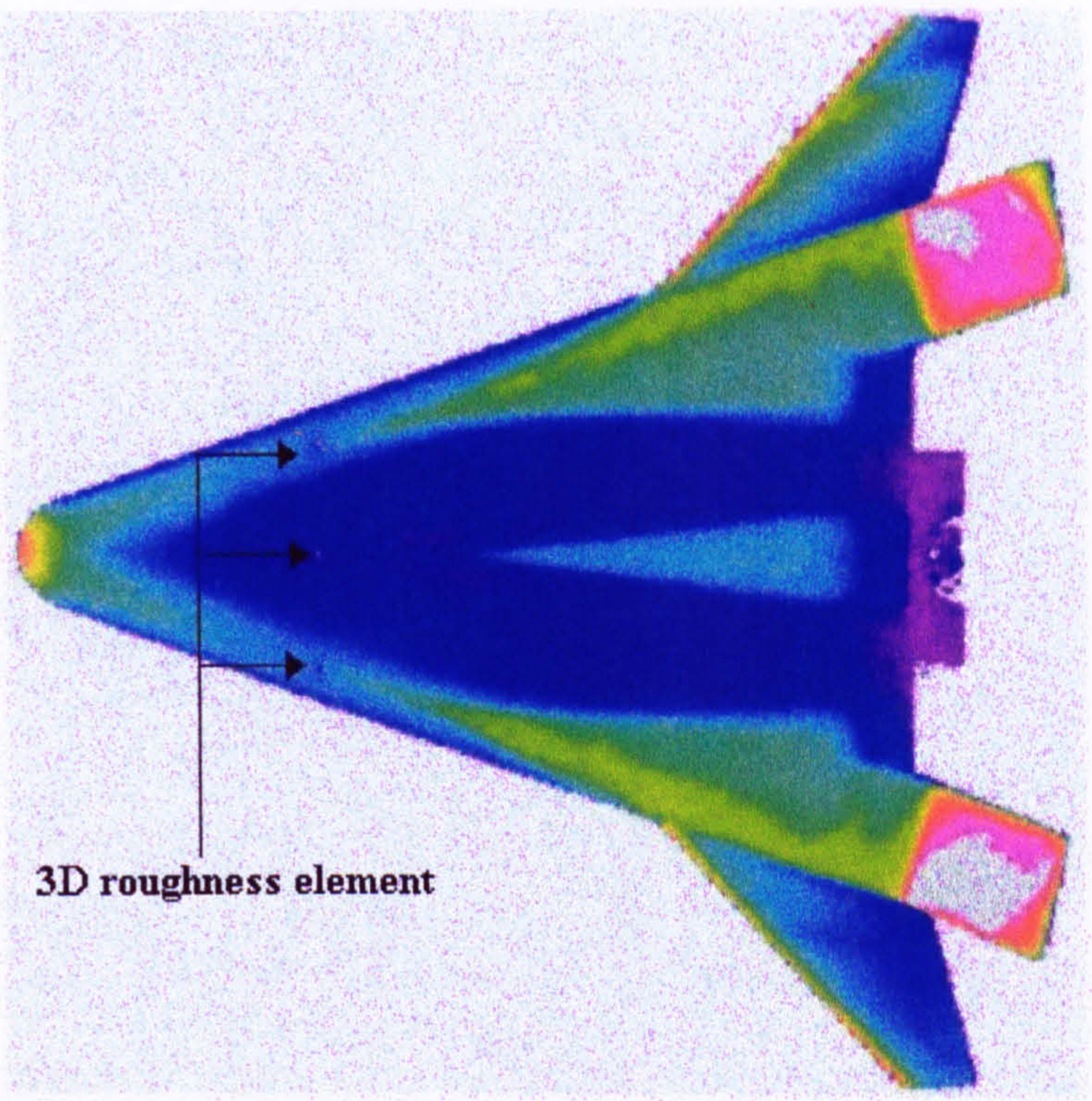

Figure A.4: Effects of a single 3D roughness element upon transition along the centre line and attachment-lines of the X-33 windward face after Berry et al. [7] ($M_\infty = 6$, $R_\infty = 3.1.10^6$ per foot, incidence of 30^o and body flap deflection of 20^o).

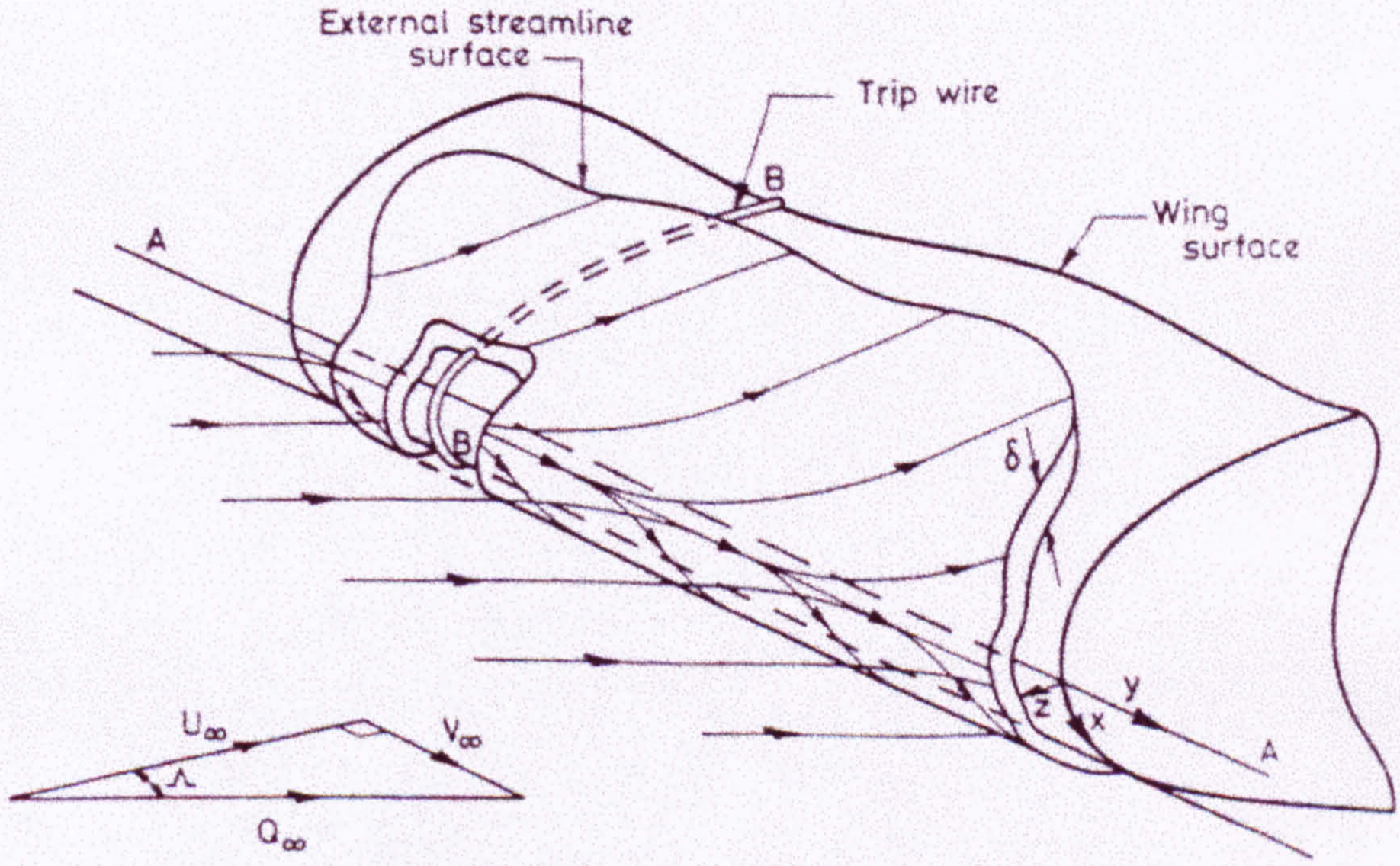

Figure A.5: Flow near the leading edge of a swept wing / cylinder after Poll and Paisley [53].

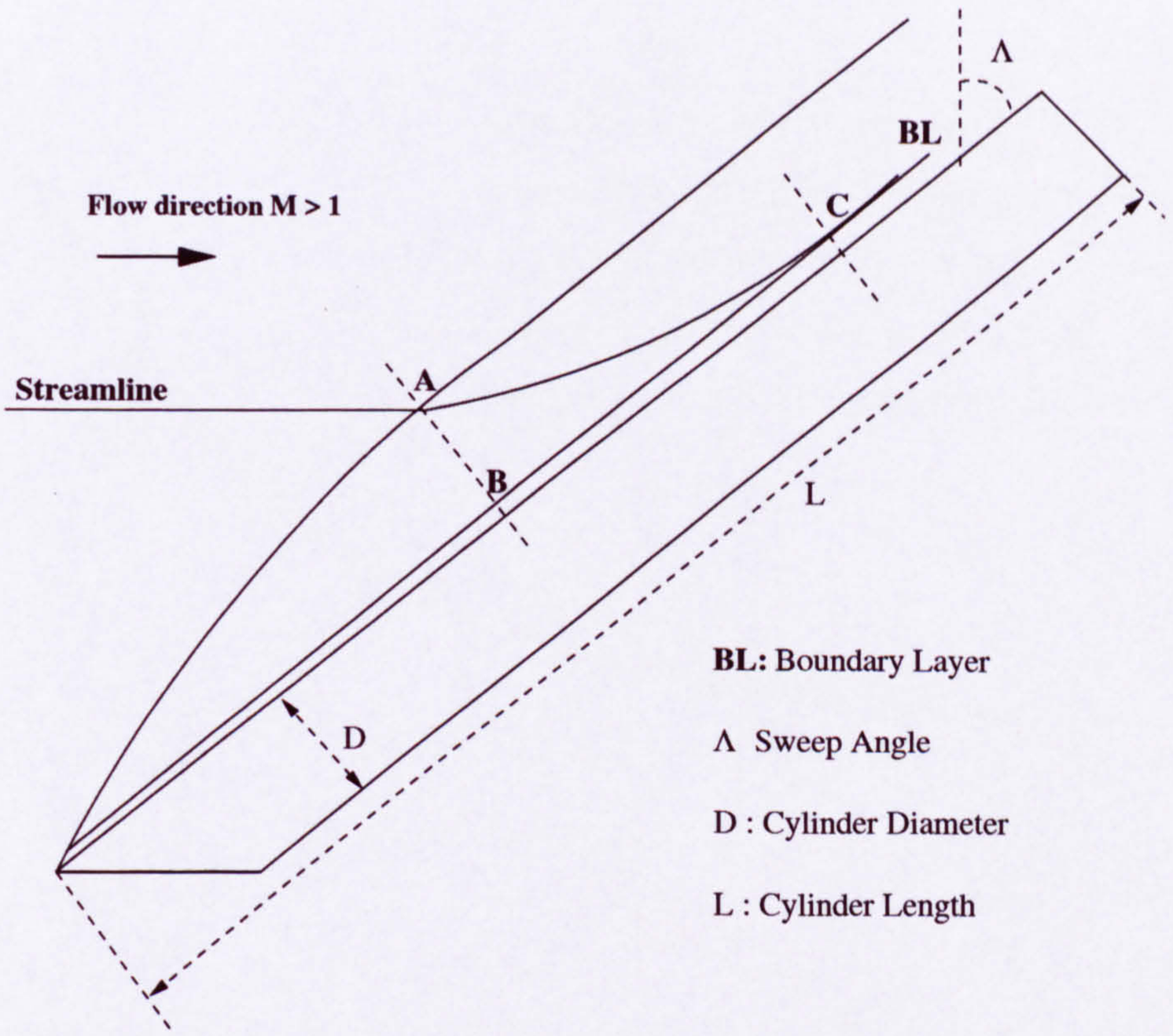

Figure A.6: Schematic of the path of a single stream line when crossing a bow shock.

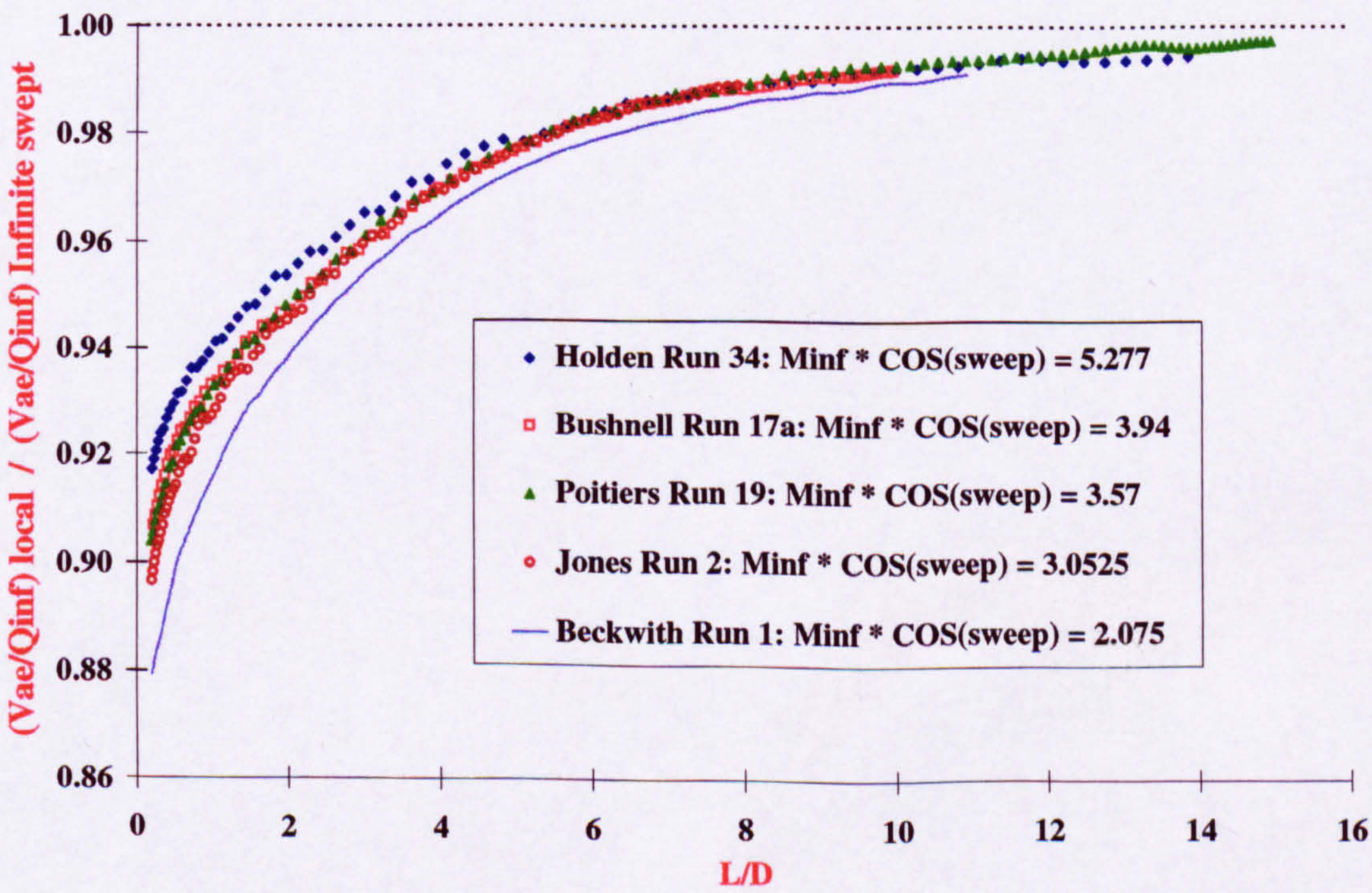

Figure A.7: Edge velocity distribution along the attachment-line of a cylinder swept at 60^o.

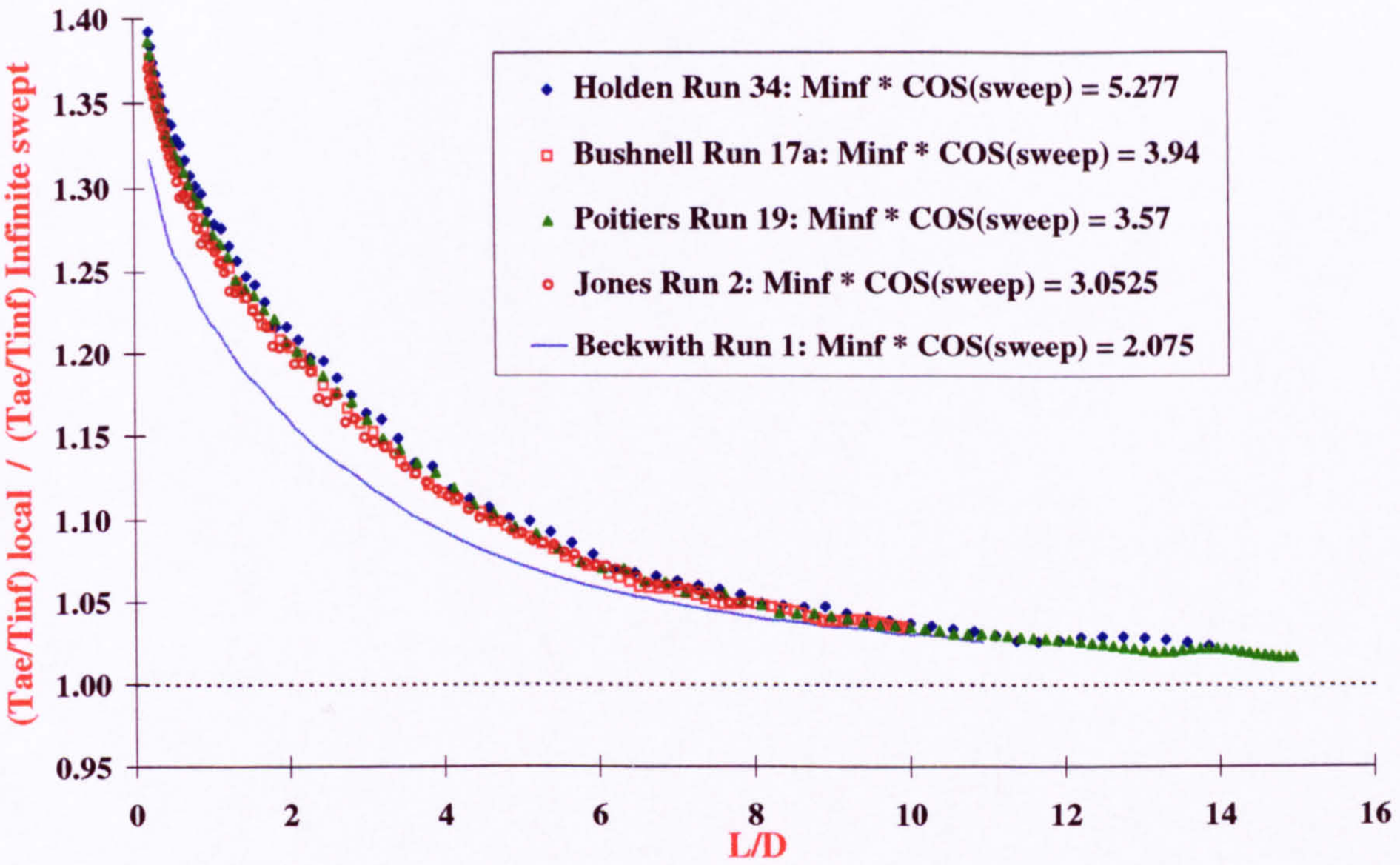

Figure A.8: Edge Static temperature distribution along the attachment-line of a cylinder swept at 60^o.

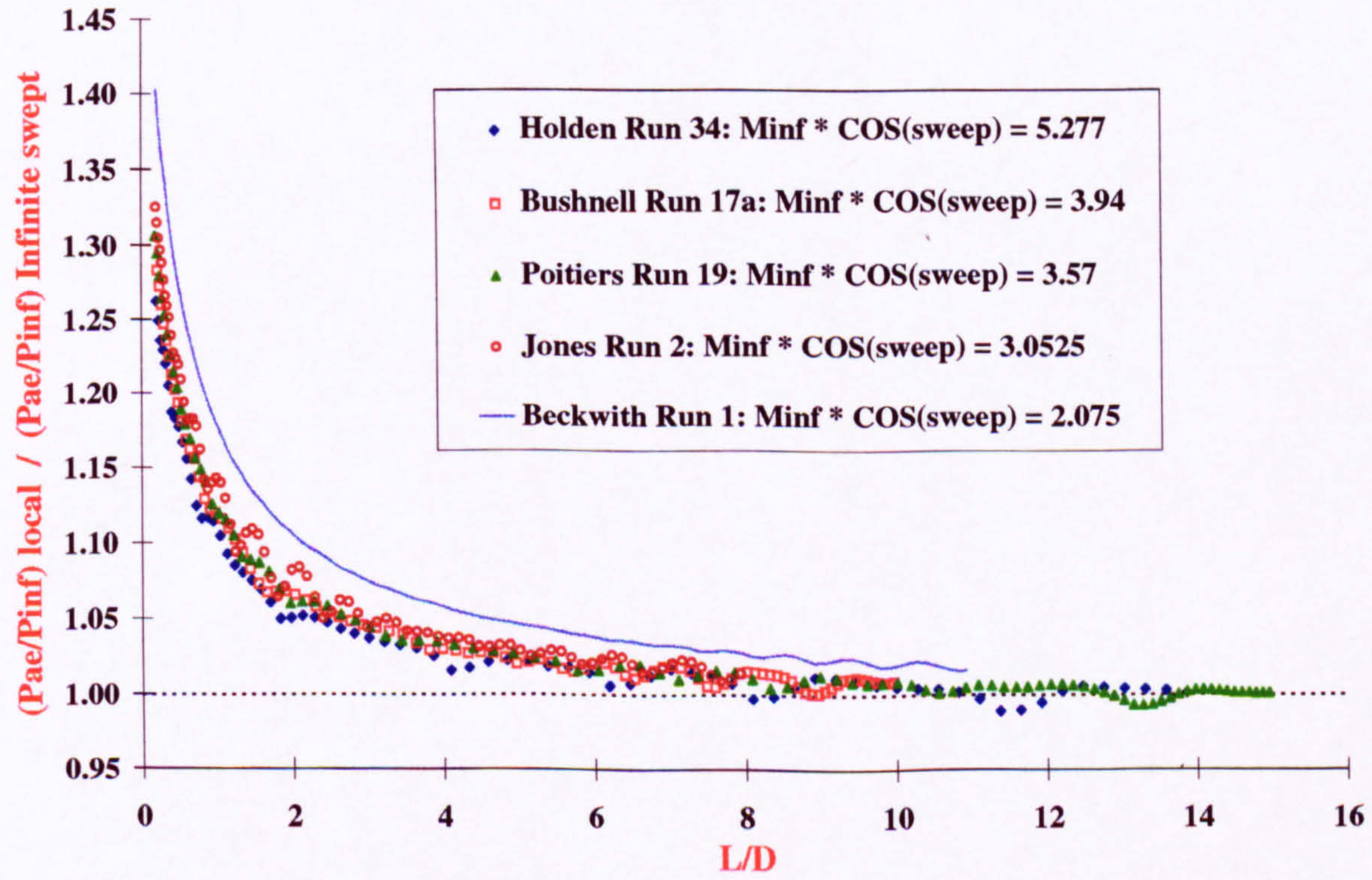

Figure A.9: Surface static pressure distribution along the attachment-line of a cylinder swept at 60^o.

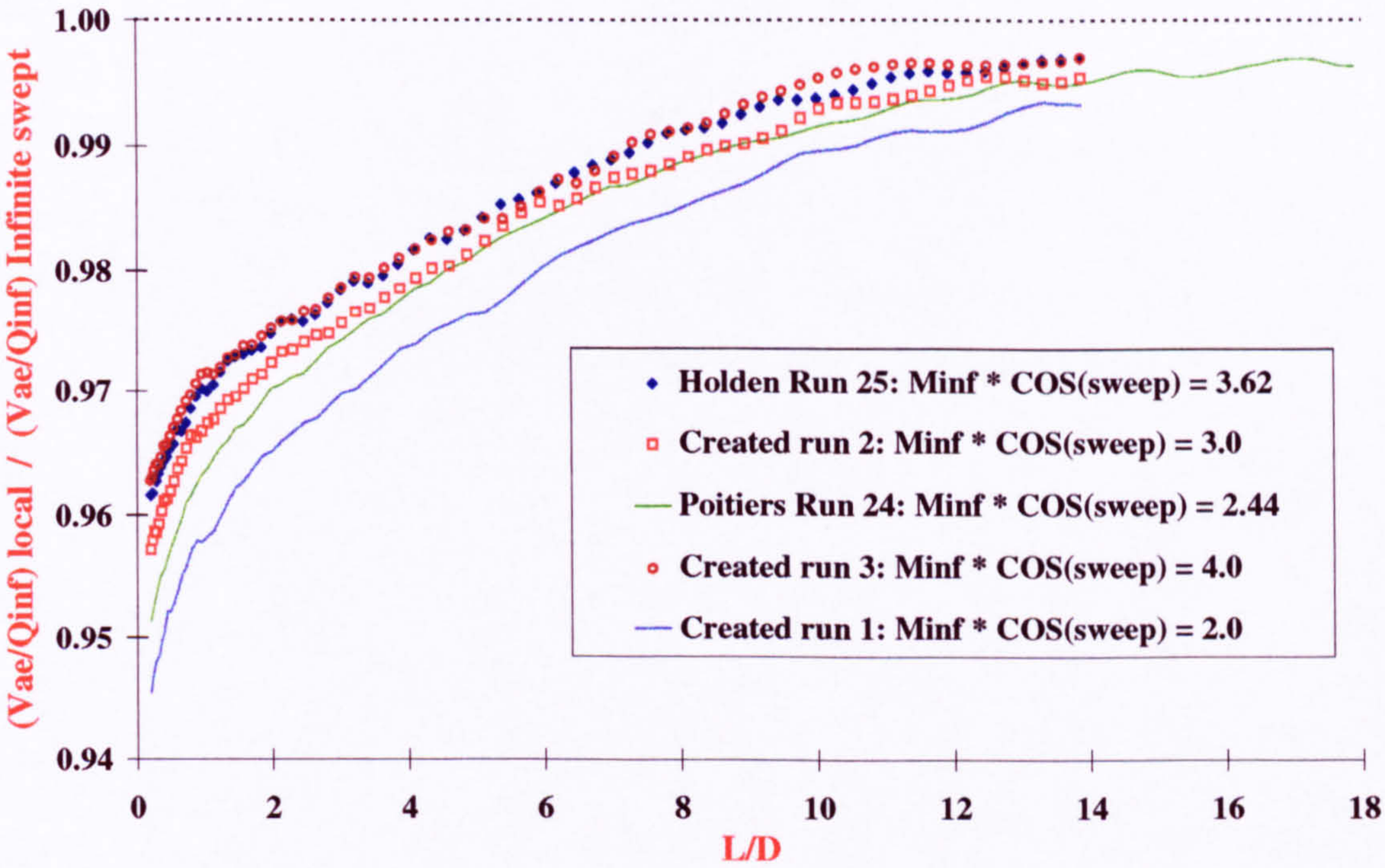

Figure A.10: Edge velocity distribution along the attachment-line of a cylinder swept at 70°.

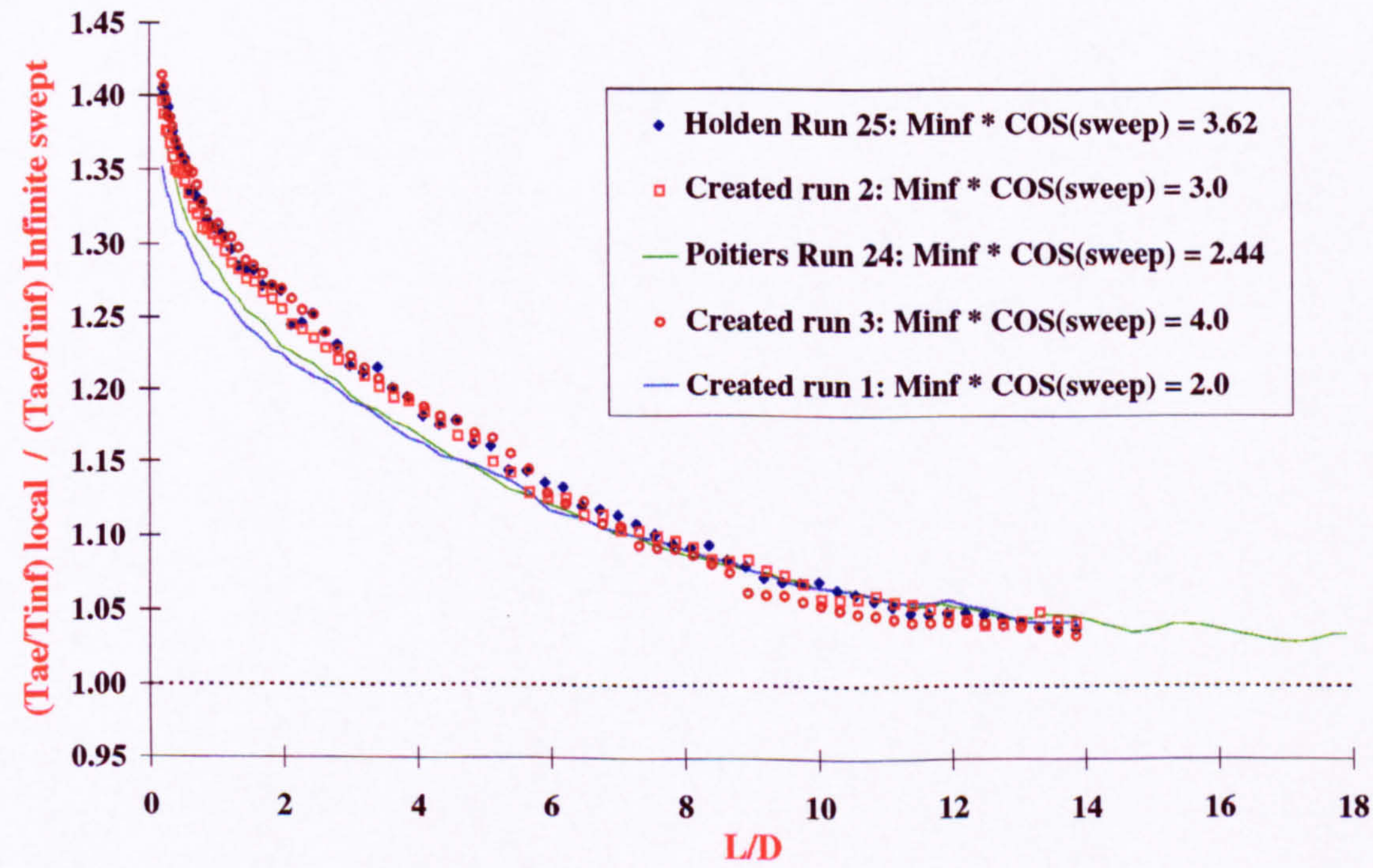

Figure A.11: Edge static temperature distribution along the attachment-line of a cylinder swept at 70°.

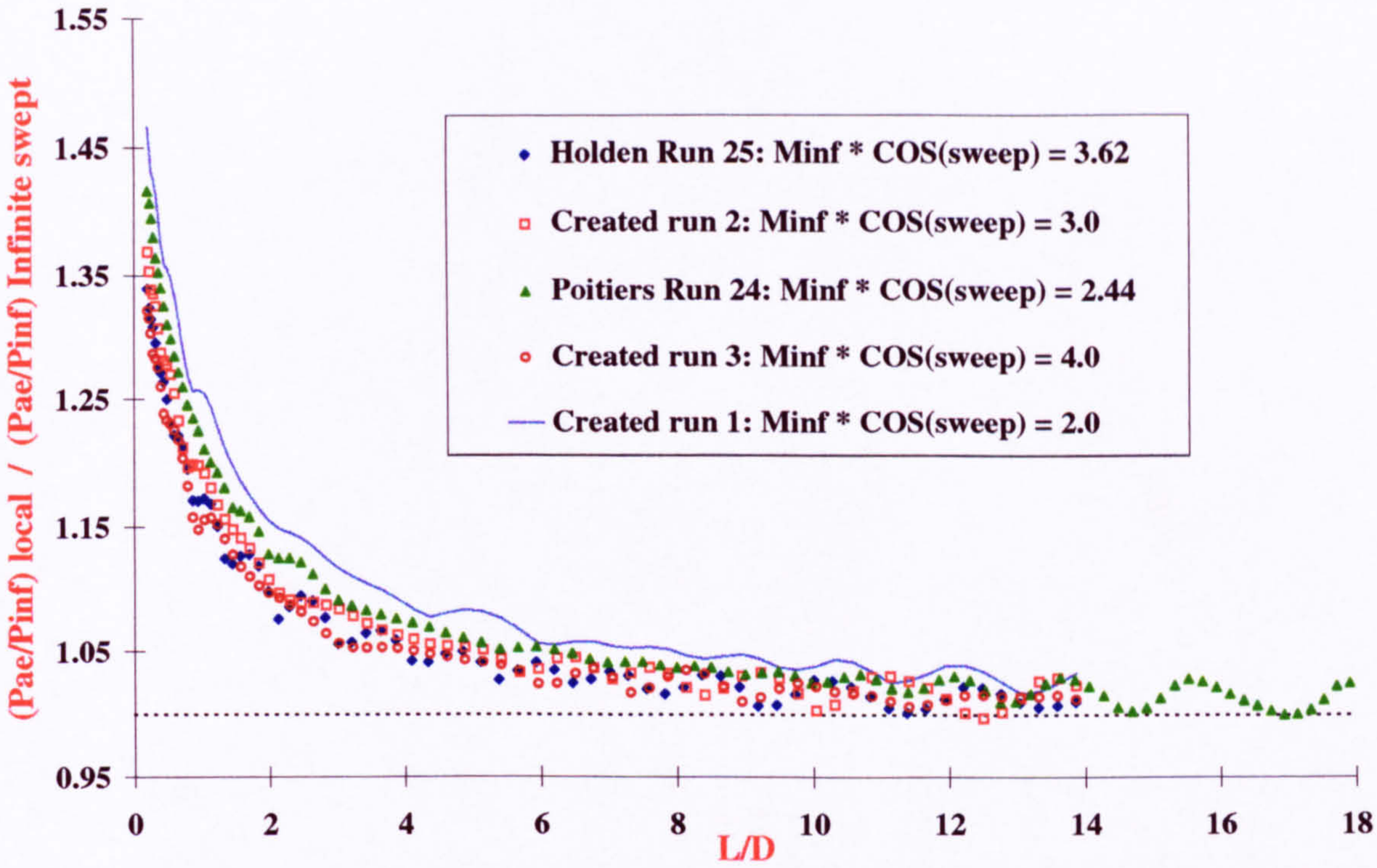

Figure A.12: Surface static pressure distribution along the attachment-line of a cylinder swept at 70°.

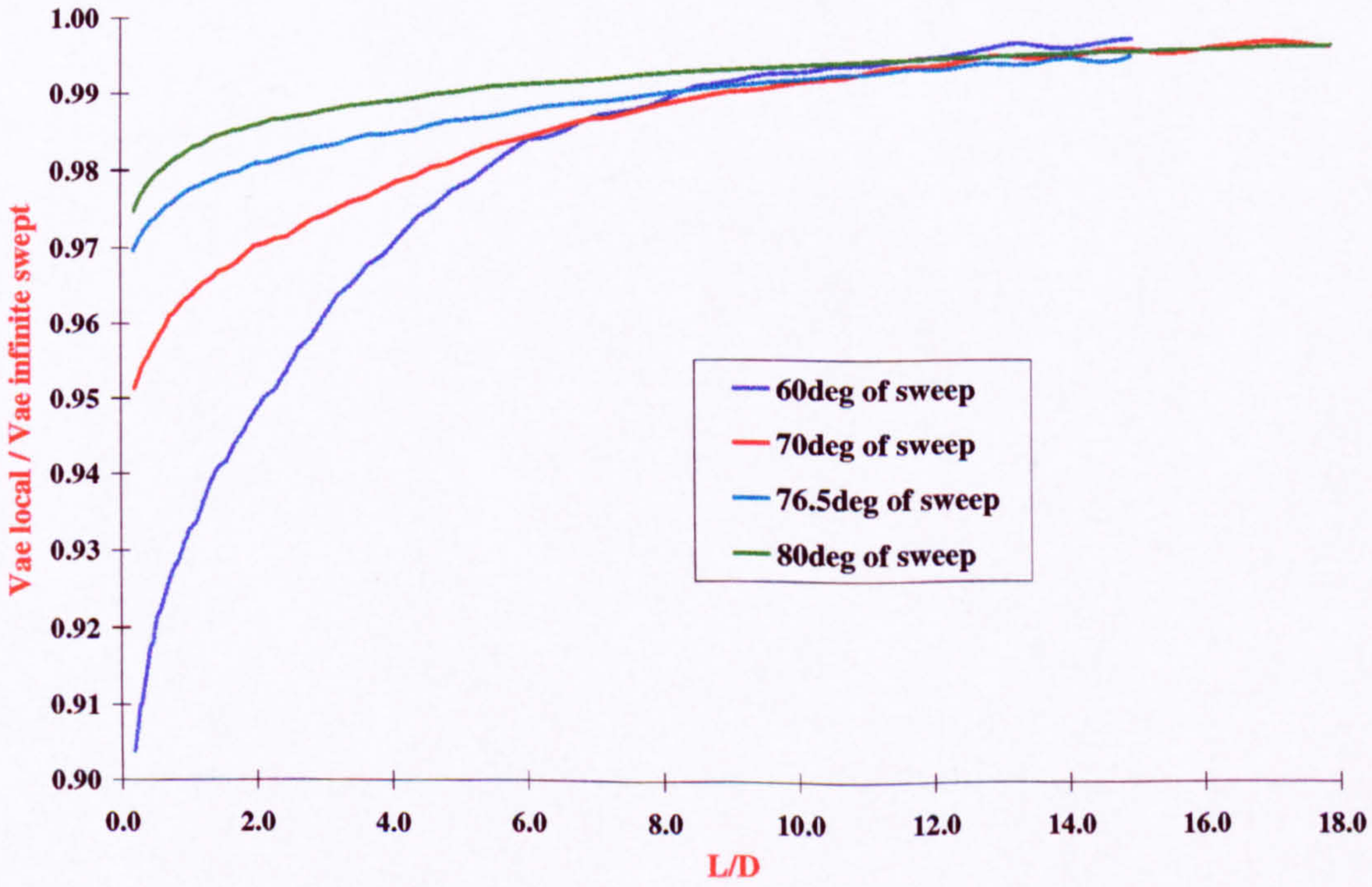

Figure A.13: Variation of the spanwise edge velocity with sweep angle for a given Mach number (Poitiers [6][35], $M_\infty = 7.14$, Runs 19, 24, 9 and 70).

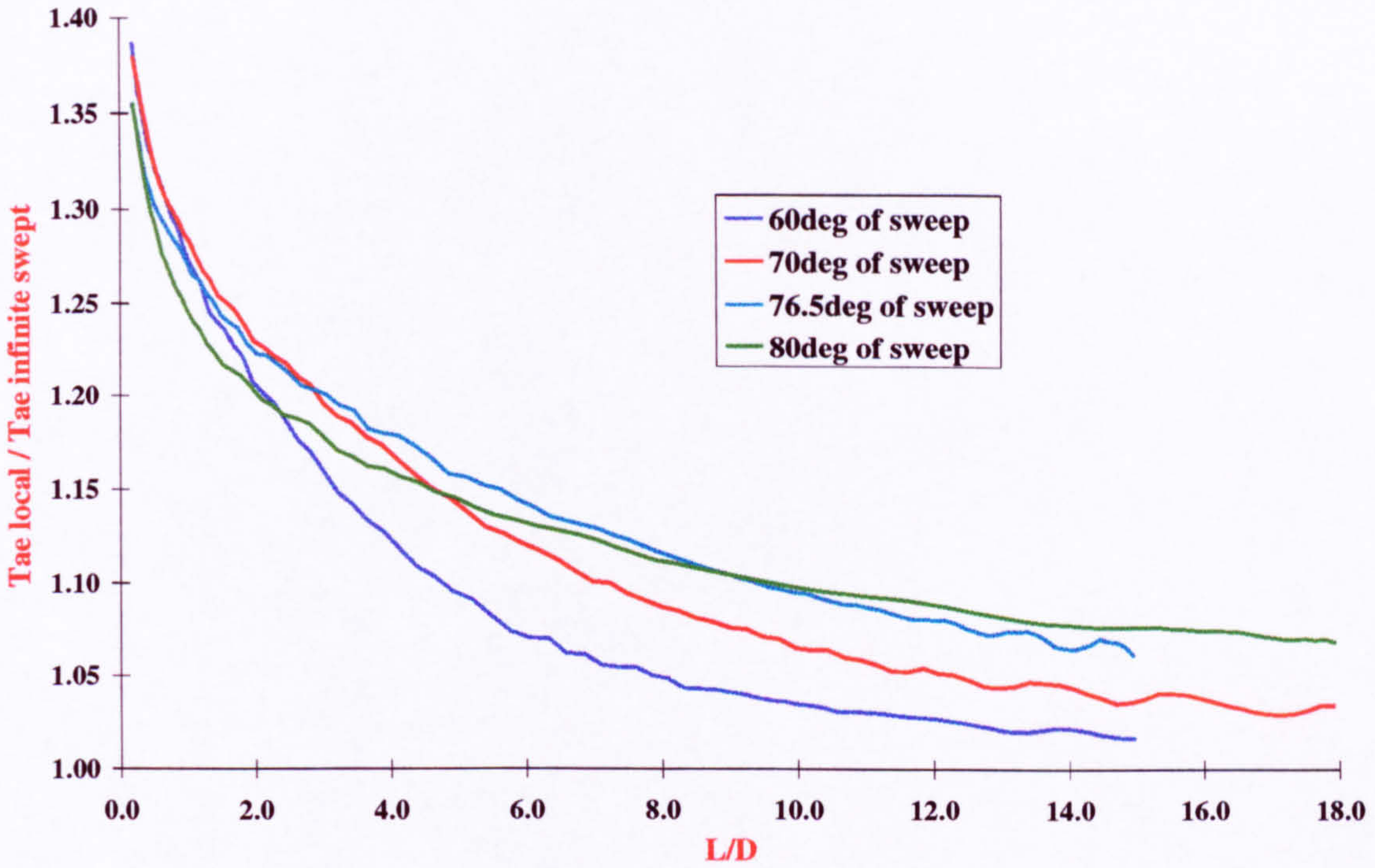

Figure A.14: Variation of the spanwise edge static temperature with sweep angle for a given Mach number (Poitiers [6][35], $M_\infty = 7.14$, Runs 19, 24, 9 and 70).

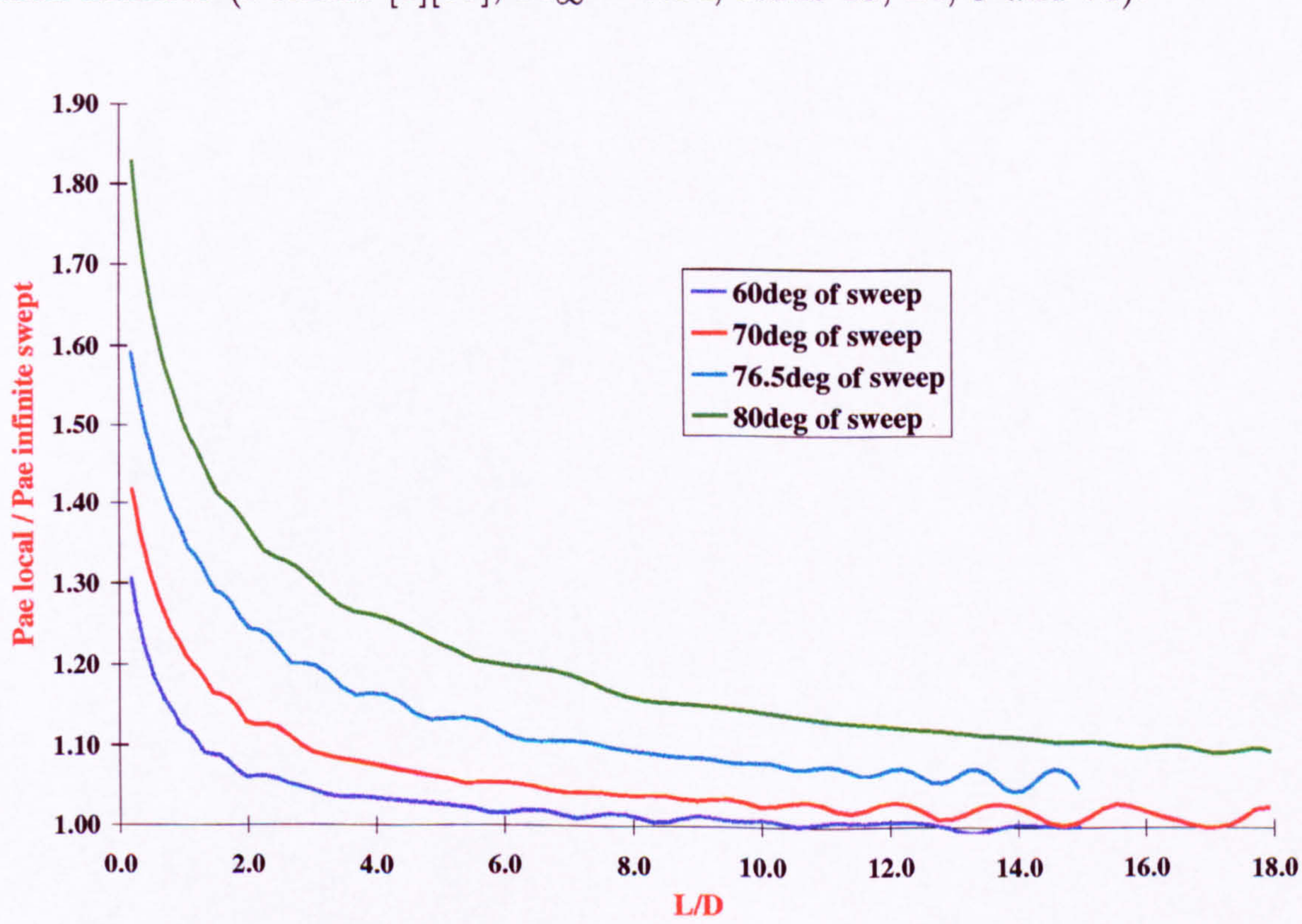

Figure A.15: Variation of the spanwise edge static pressure with sweep angle for a given Mach number (Poitiers [6][35], $M_\infty = 7.14$, Runs 19, 24, 9 and 70).

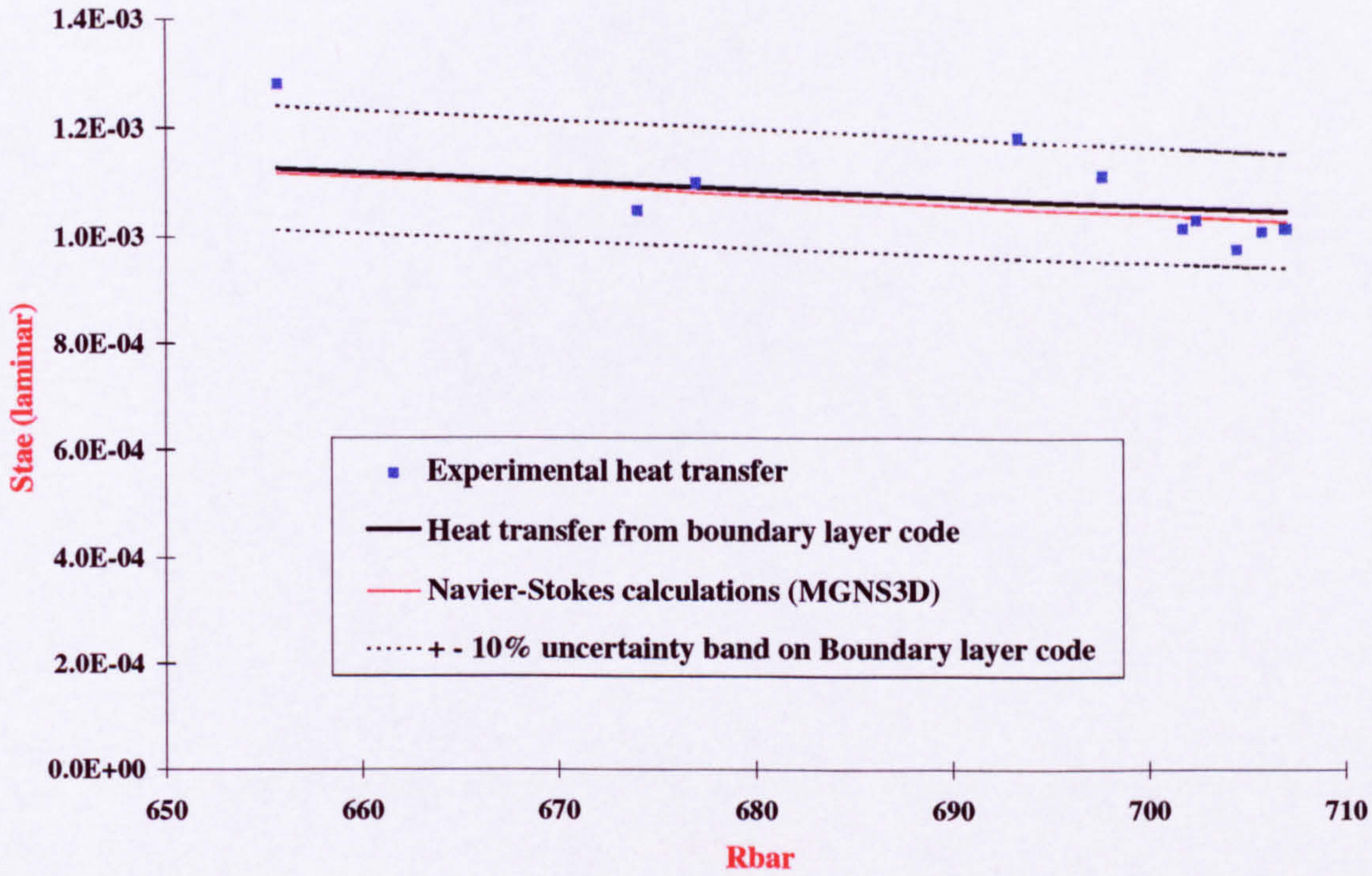

Figure A.16: Comparison of the laminar heat transfer from experimental measurements, Navier-Stokes calculations and boundary layer calculations. (Poitiers run19, $M_\infty = 7.14$, $\Lambda = 60^o$, $T_w/T_o = 0.38$).

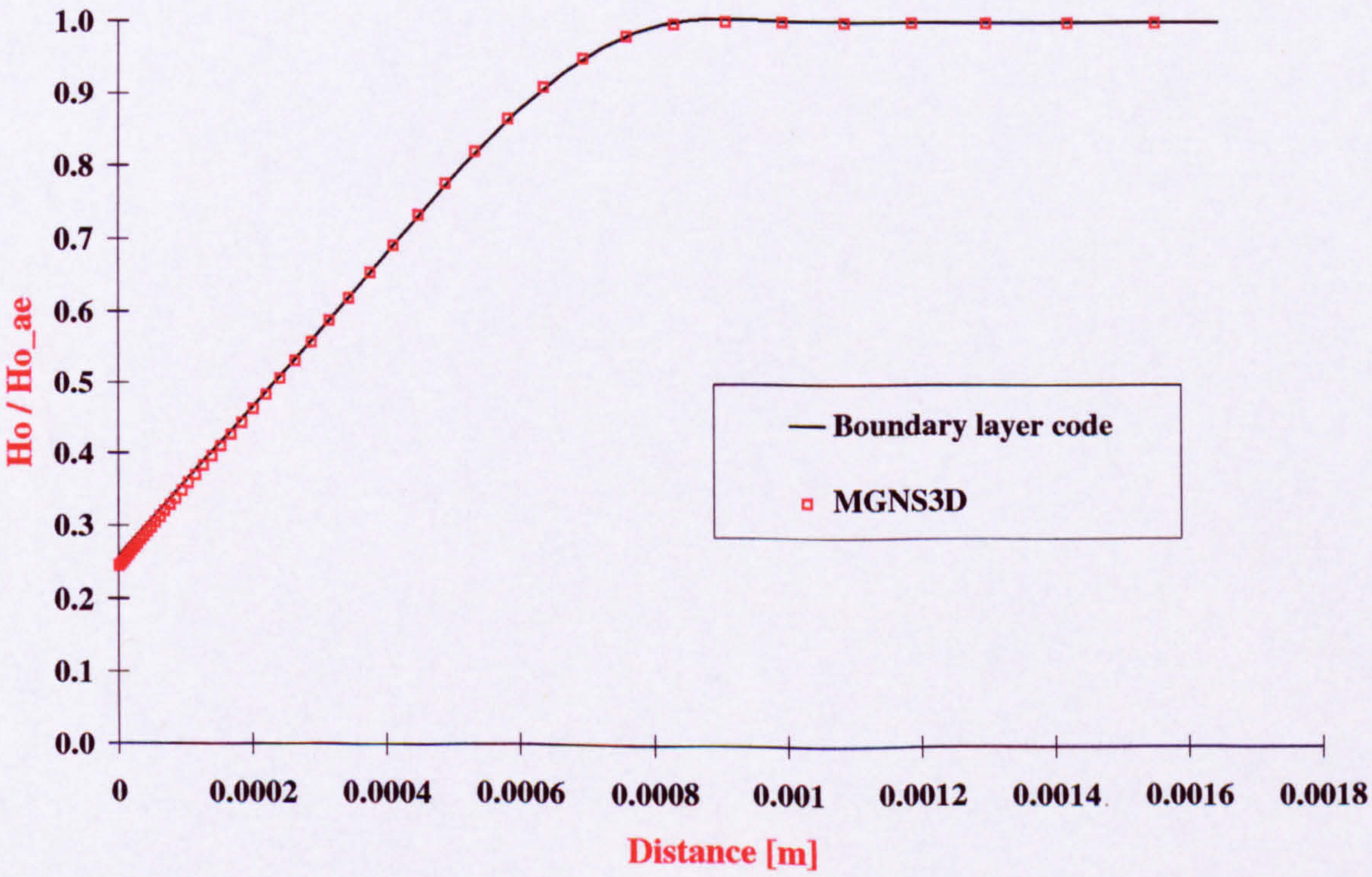

Figure A.17: Comparison of the total enthalpy profiles obtained from the Navier-Stokes code MGNS3D and the boundary layer code. (Holden Run36, $M_\infty = 10.6$, $\Lambda = 80^o$, $R_{D\infty} \approx 9.5.10^5$).

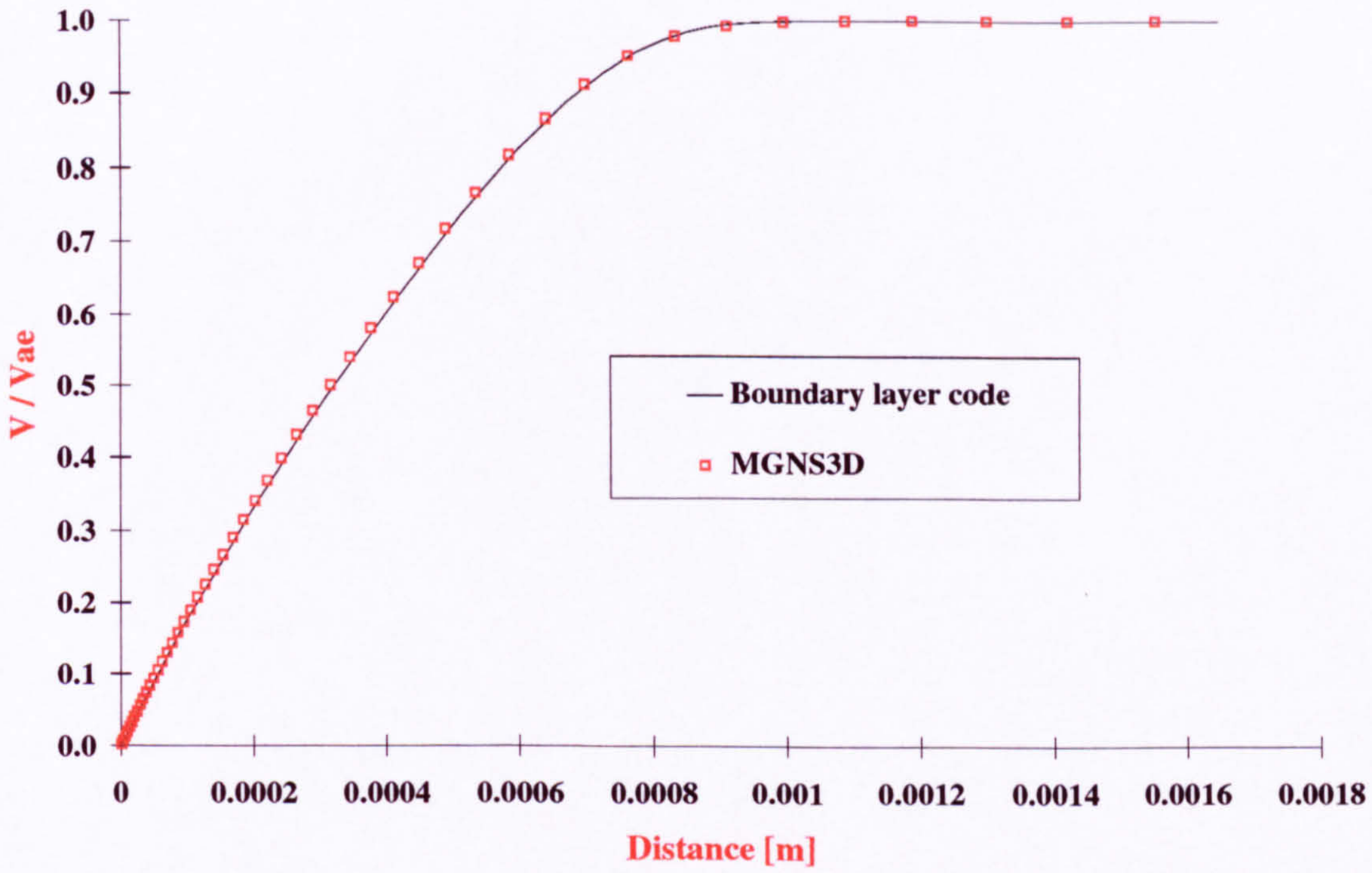

Figure A.18: Comparison of the velocity profiles obtained from the Navier-Stokes code MGNS3D and the boundary layer code. (Holden Run36, $M_\infty = 10.6$, $\Lambda = 80^o$, $R_{D\infty} \approx 9.5.10^5$).

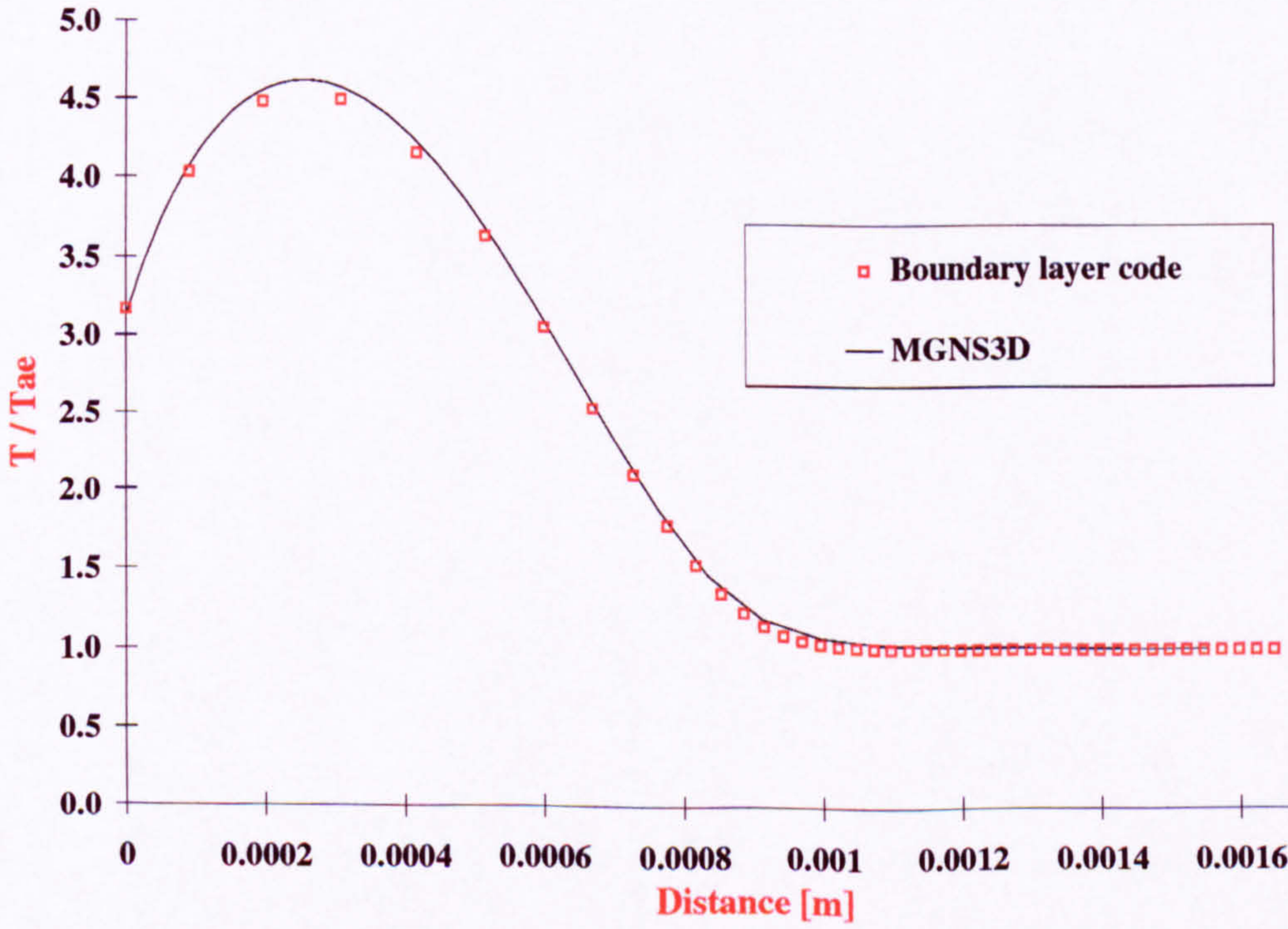

Figure A.19: Comparison of the temperature profiles obtained from the Navier-Stokes code MGNS3D and the boundary layer code. (Holden Run36, $M_\infty = 10.6$, $\Lambda = 80^o$, $R_{D\infty} \approx 9.5.10^5$).

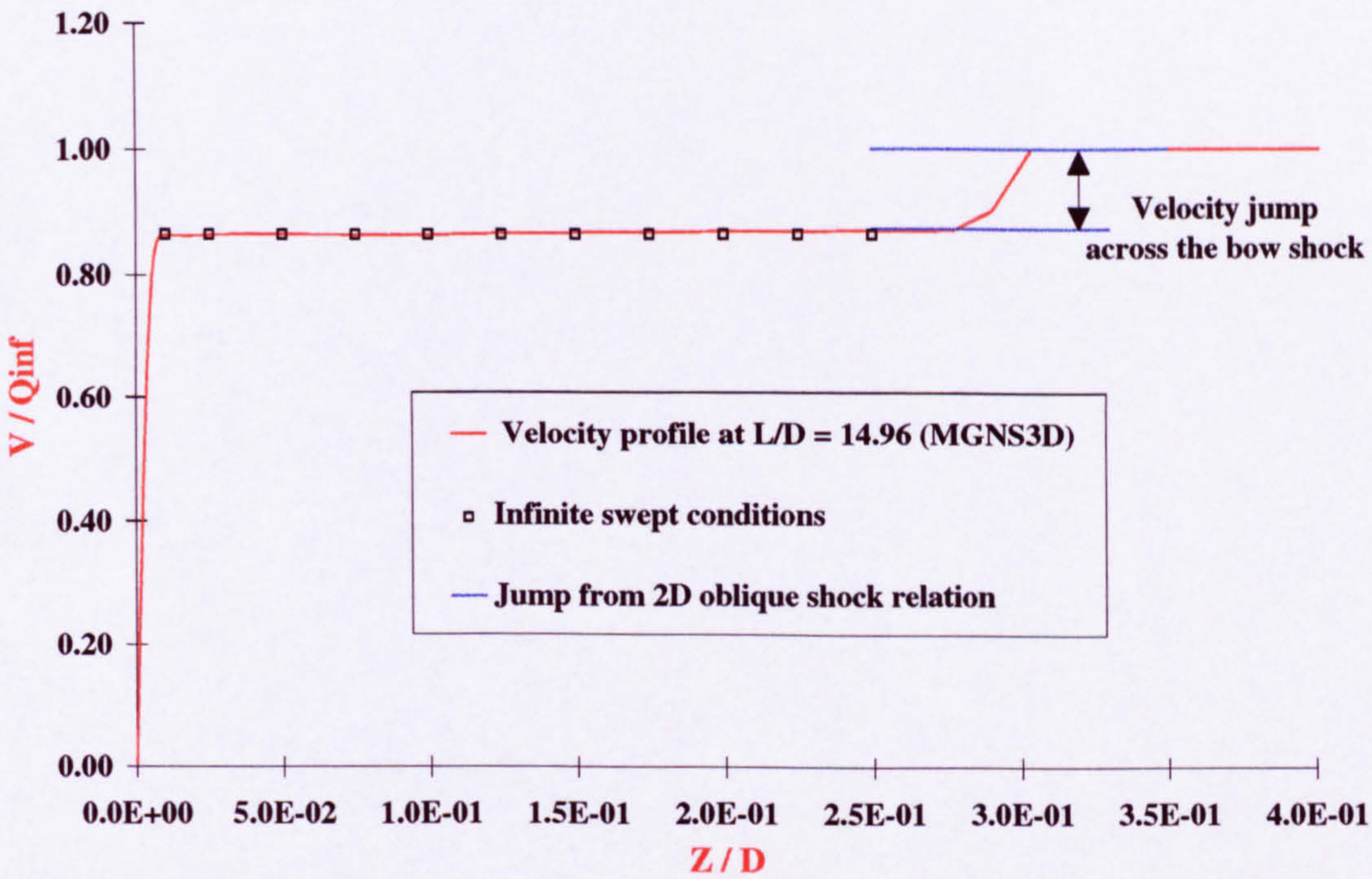

Figure A.20: Comparison of the velocity jump across the bow shock as predicted by MGNS3D and the 2D oblique shock relations. (Poitiers Run19, $M_\infty = 7.14$, $\Lambda = 60^o$, $\frac{L}{D} = 15$, $R_{D\infty} \approx 3.0.10^5$).

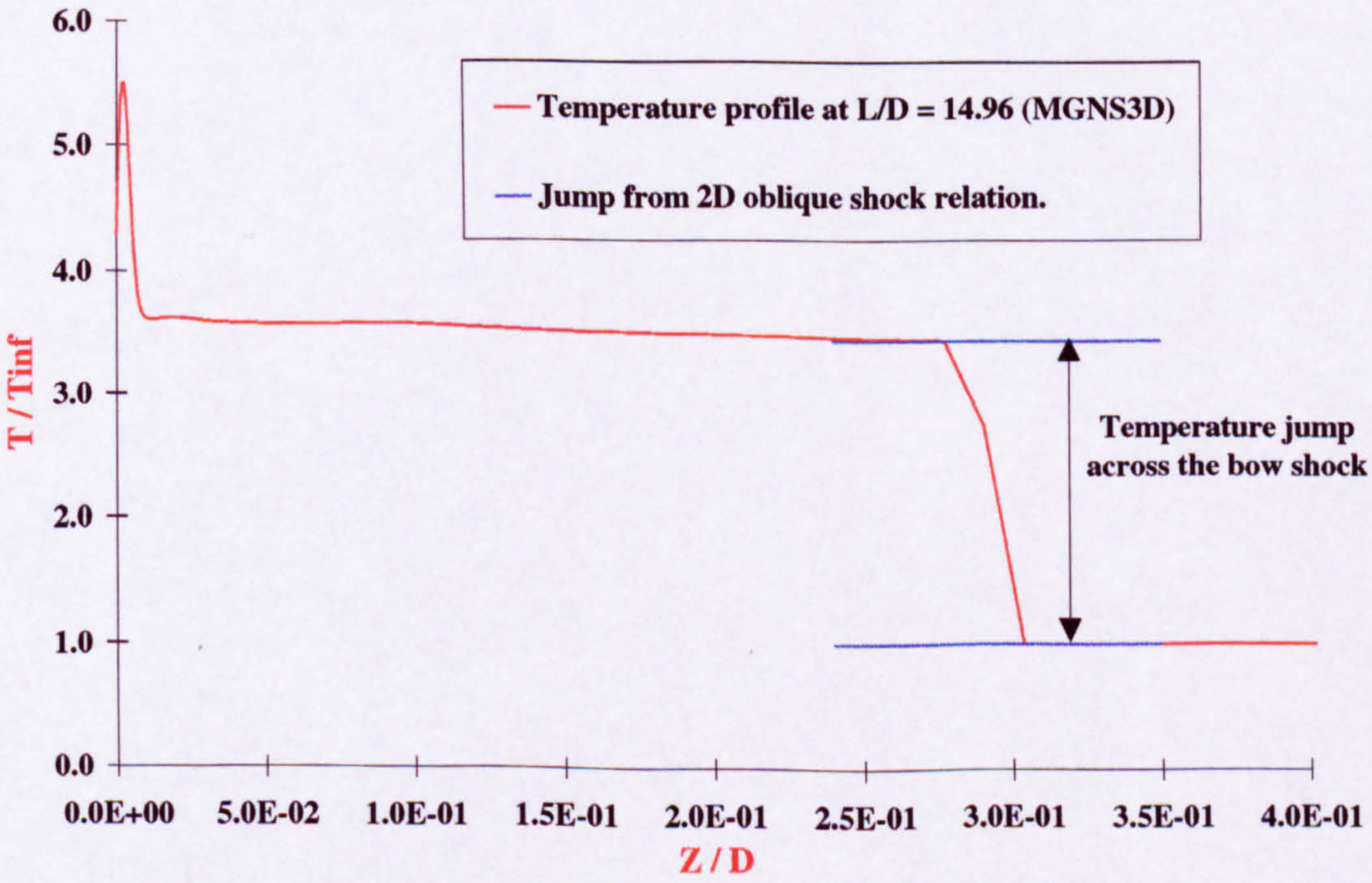

Figure A.21: Comparison of the temperature jump across the bow shock as predicted by MGNS3D and the 2D oblique shock relations. (Poitiers Run19, $M_\infty = 7.14$, $\Lambda = 60^o$, $\frac{L}{D} = 15$, $R_{D\infty} \approx 3.0.10^5$).

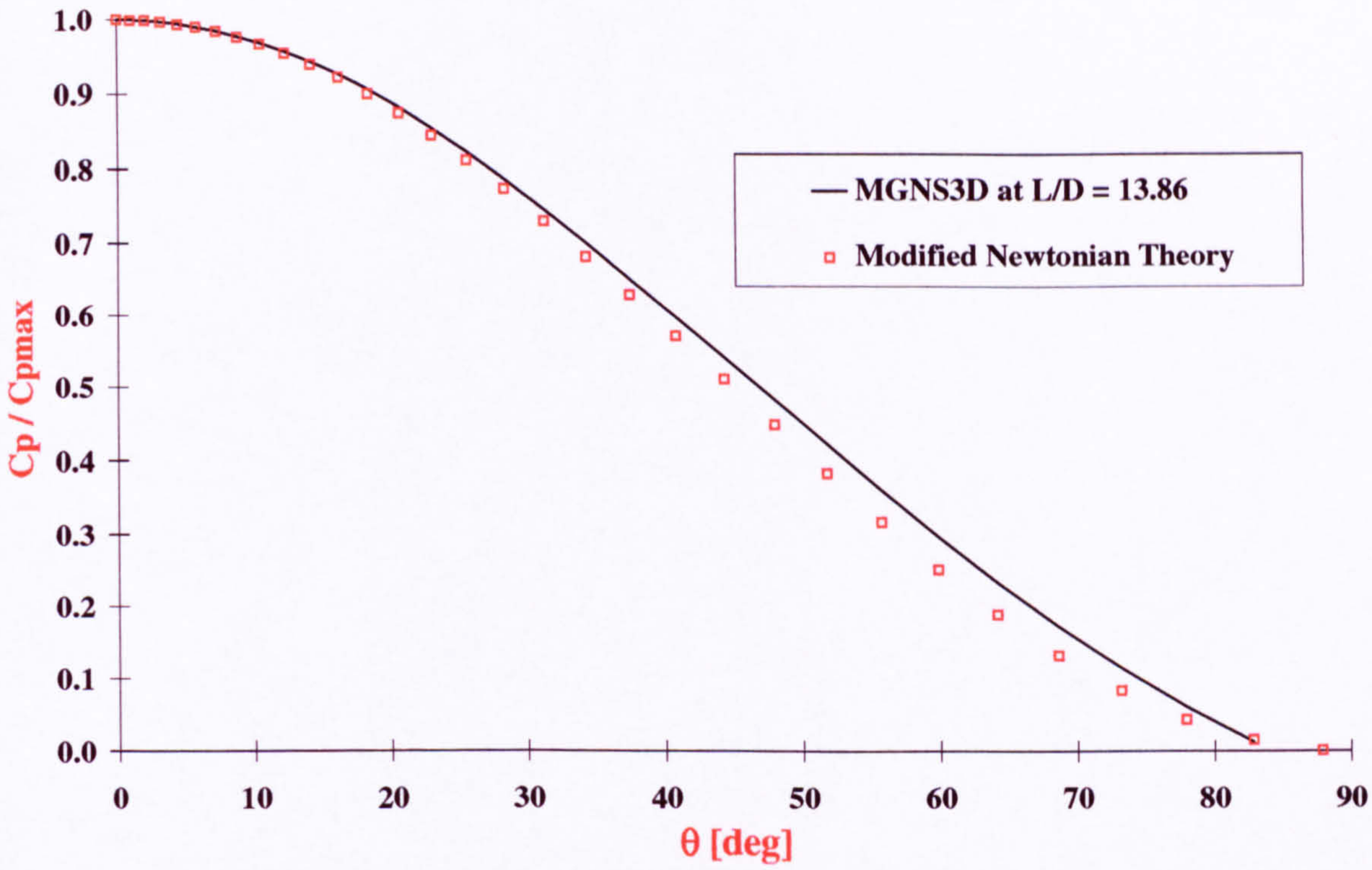

Figure A.22: Normalised coefficients obtained from MGNS3D and from modified Newtonian theory (Holden Run36, $M_\infty = 10.6$, $\Lambda = 80^o$, $\frac{L}{D} = 13.9$).

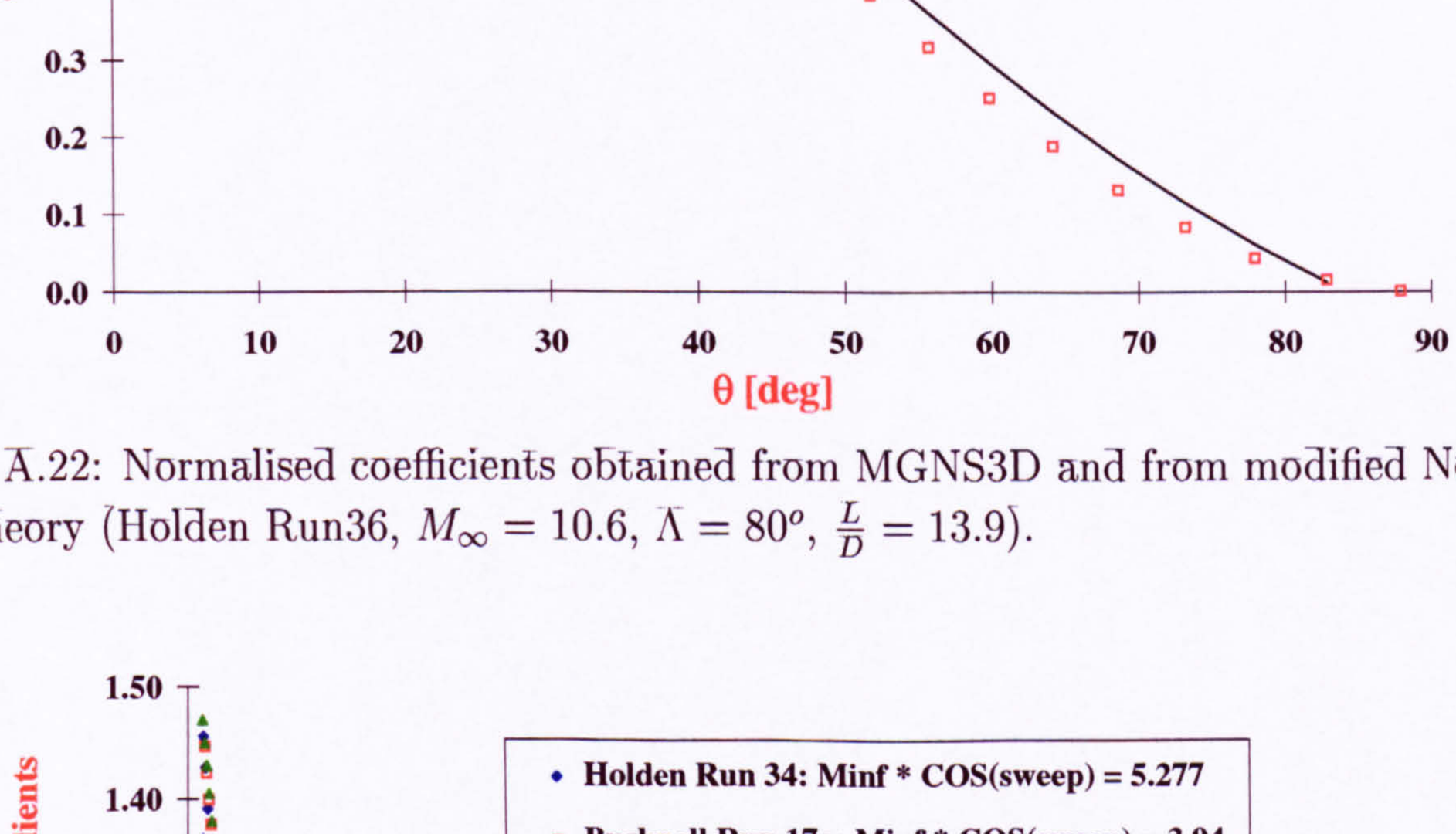

Figure A.23: Distribution of the local chordwise velocity gradient (non-dimensionalised by its infinite swept value) along the attachment-line of a 60^o swept cylinder.

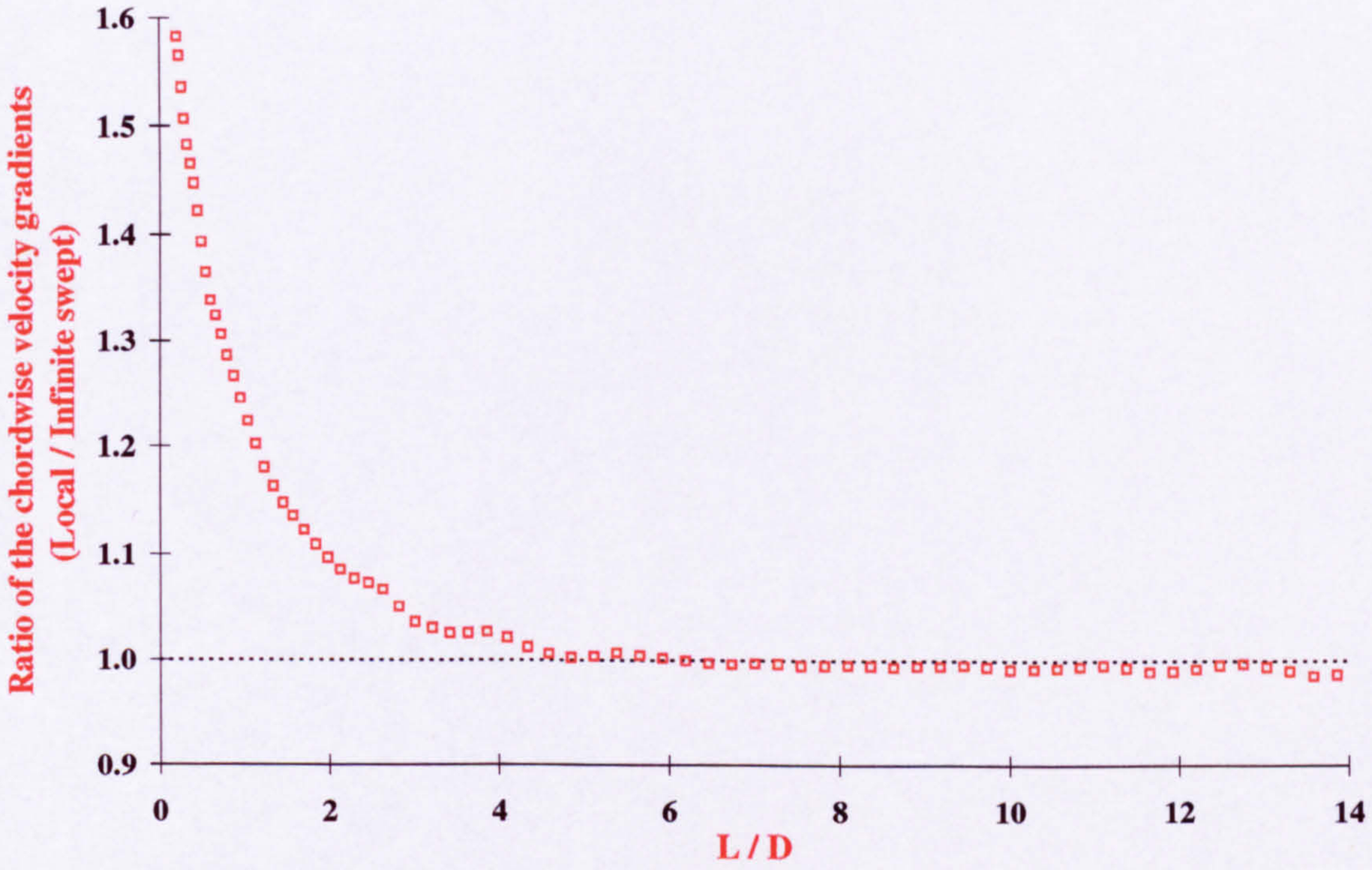

Figure A.24: Distribution of the local chordwise velocity gradient (non-dimensionalised by its infinite swept value) along the attachment-line of a 76.5^o swept cylinder (Holden Run12, $M_\infty = 10.6$).

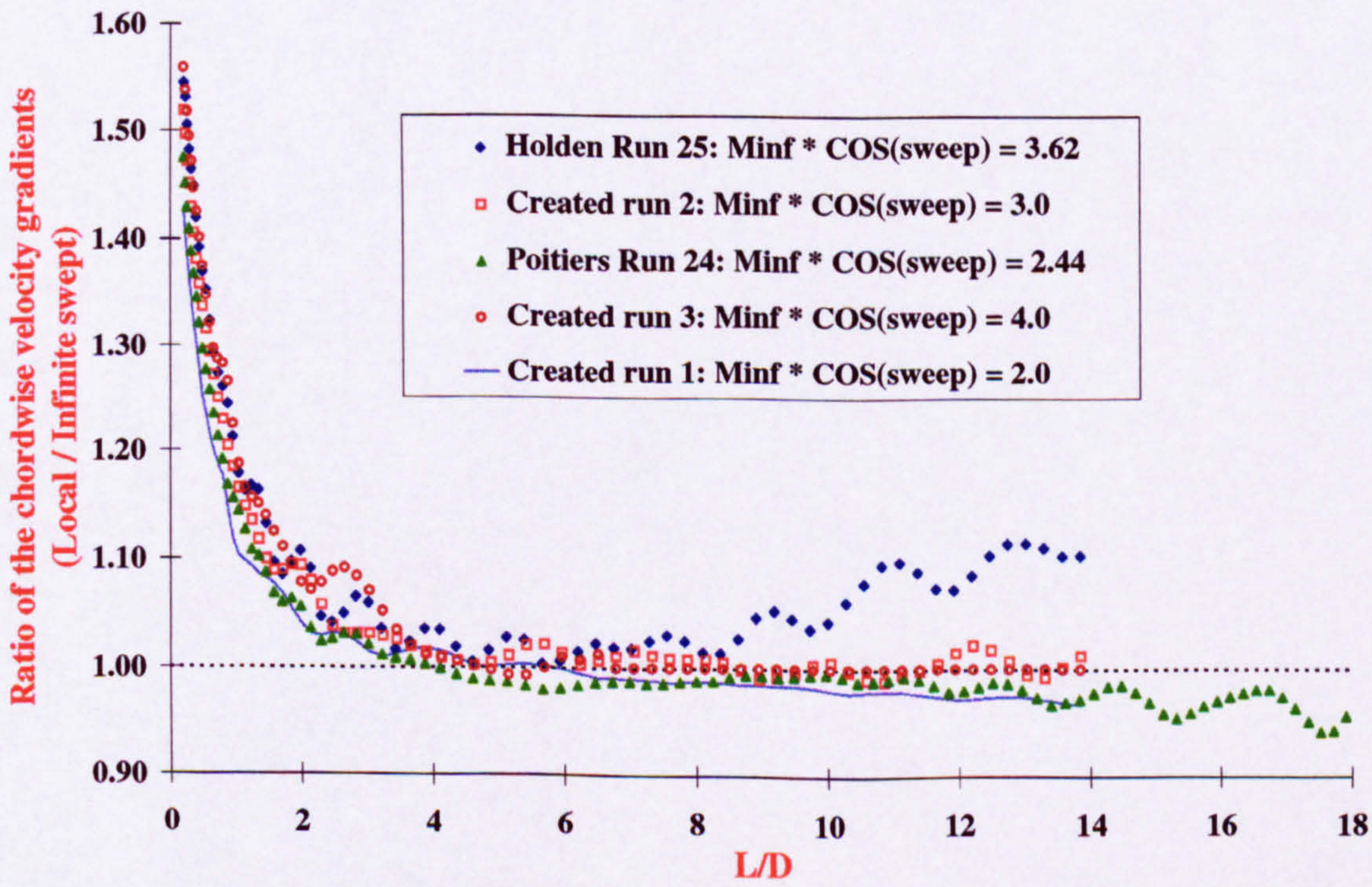

Figure A.25: Distribution of the local chordwise velocity gradient (non-dimensionalised by its infinite swept value) along the attachment-line of a 70^o swept cylinder.

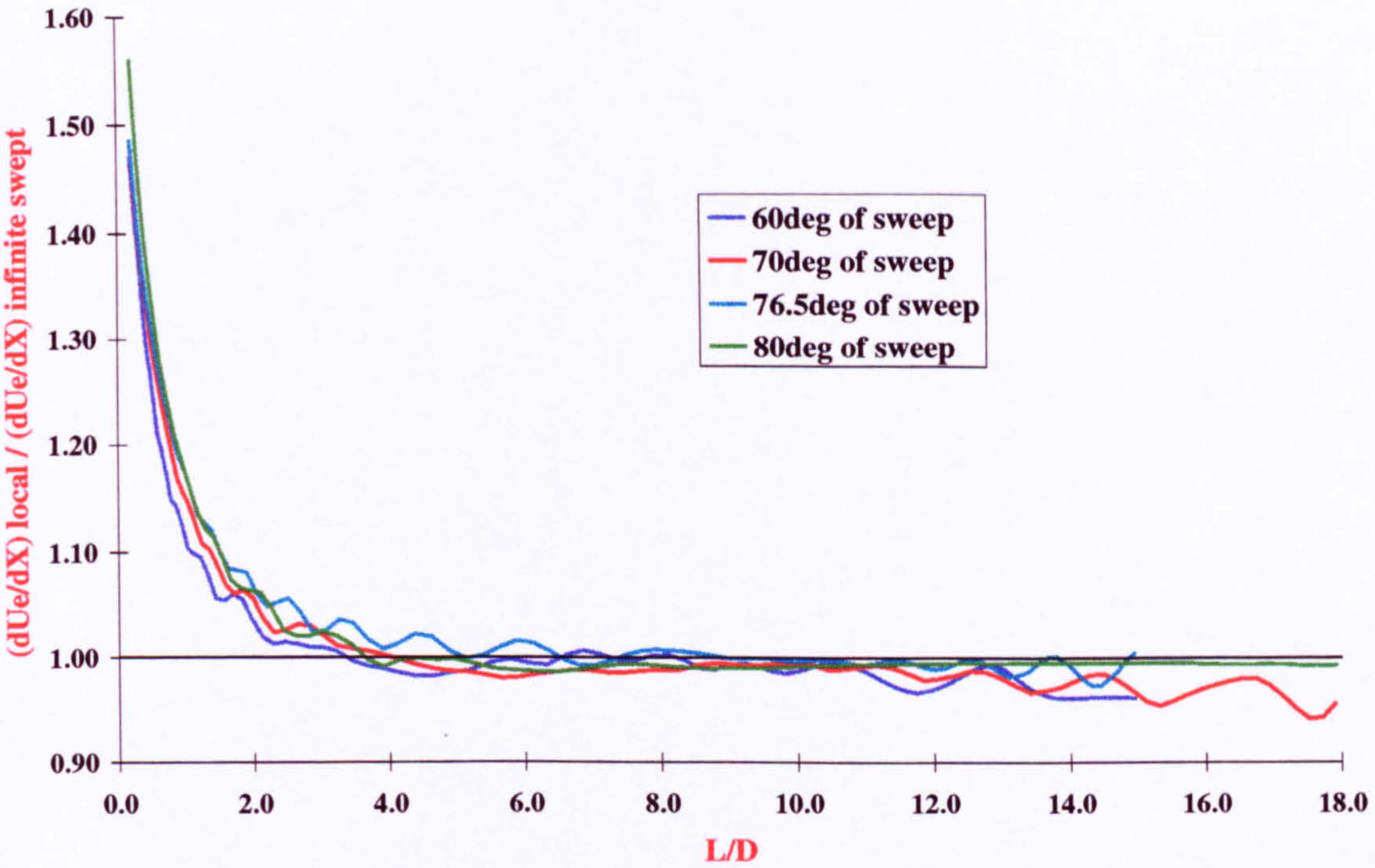

Figure A.26: Variation of the attachment-line chordwise velocity gradient with sweep angle for a given Mach number (Poitiers [6][35], $M_\infty = 7.14$, Runs 19, 24, 9 and 70).

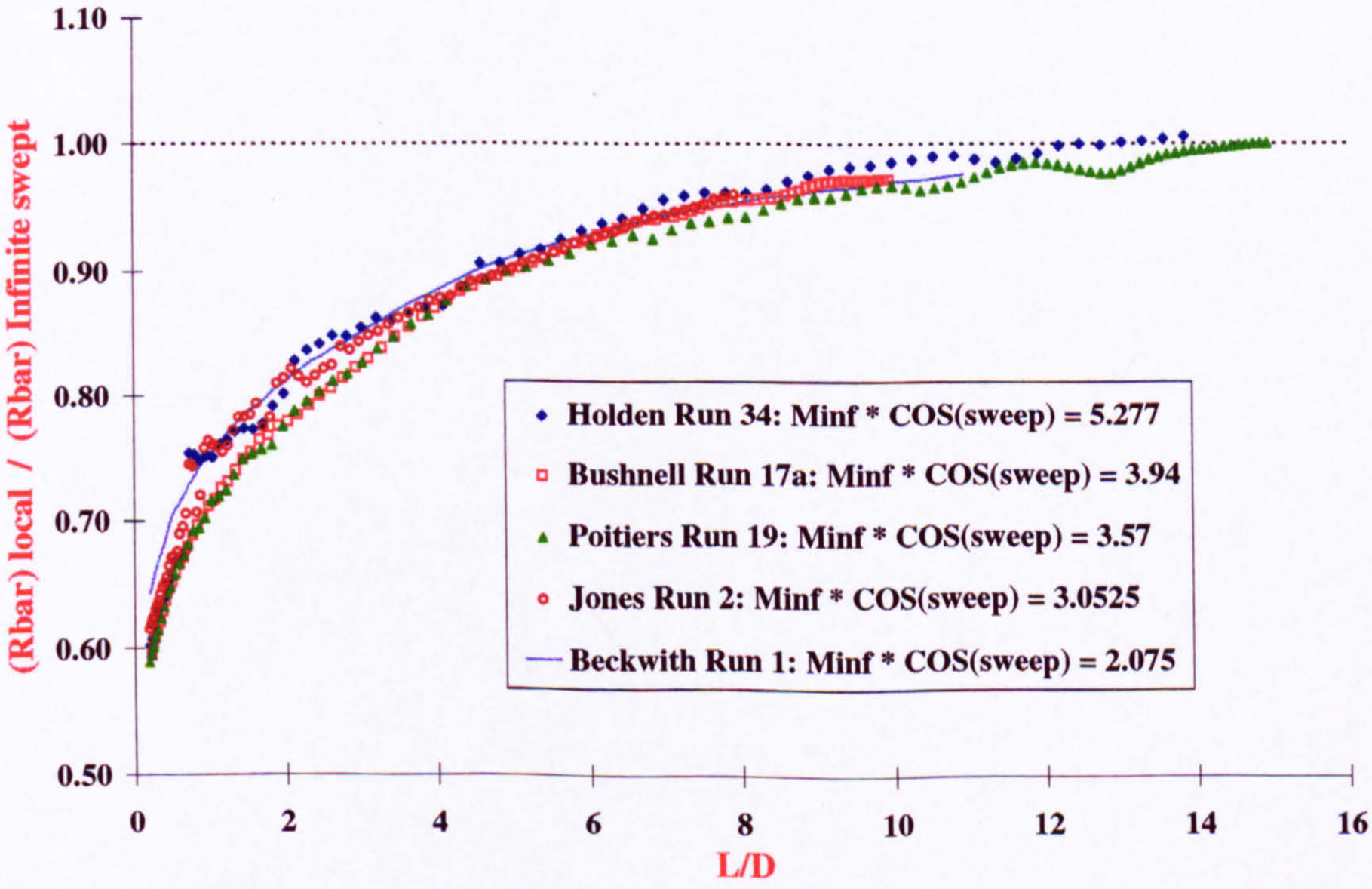

Figure A.27: Distribution of the local $\bar{R}$ (non-dimensionalised by the infinite swept $\bar{R}$) along the attachment-line of a 60° swept cylinder.

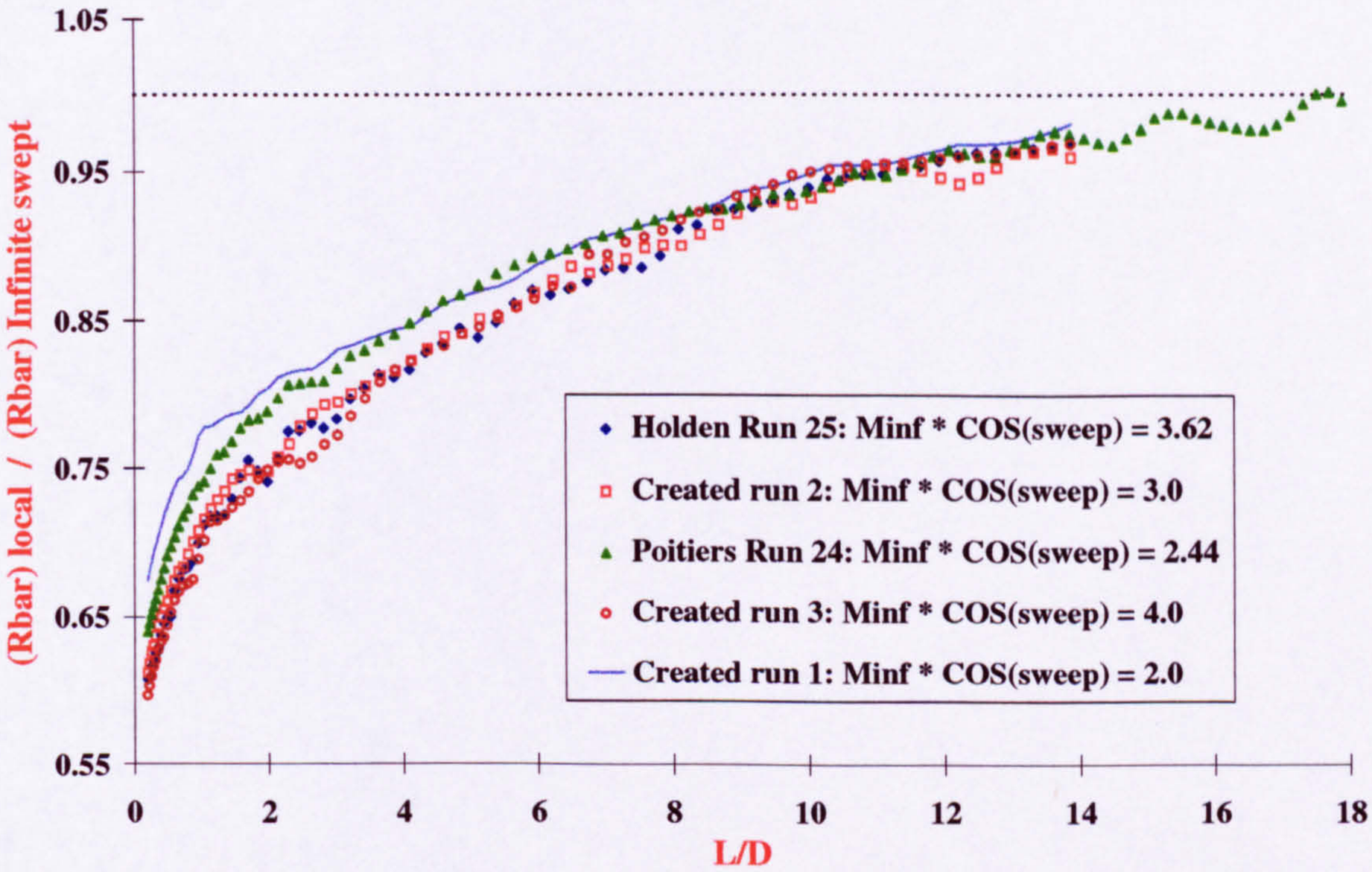

Figure A.28: Distribution of the local $\bar{R}$ (non-dimensionalised by the infinite swept $\bar{R}$) along the attachment-line of a 70^o swept cylinder.

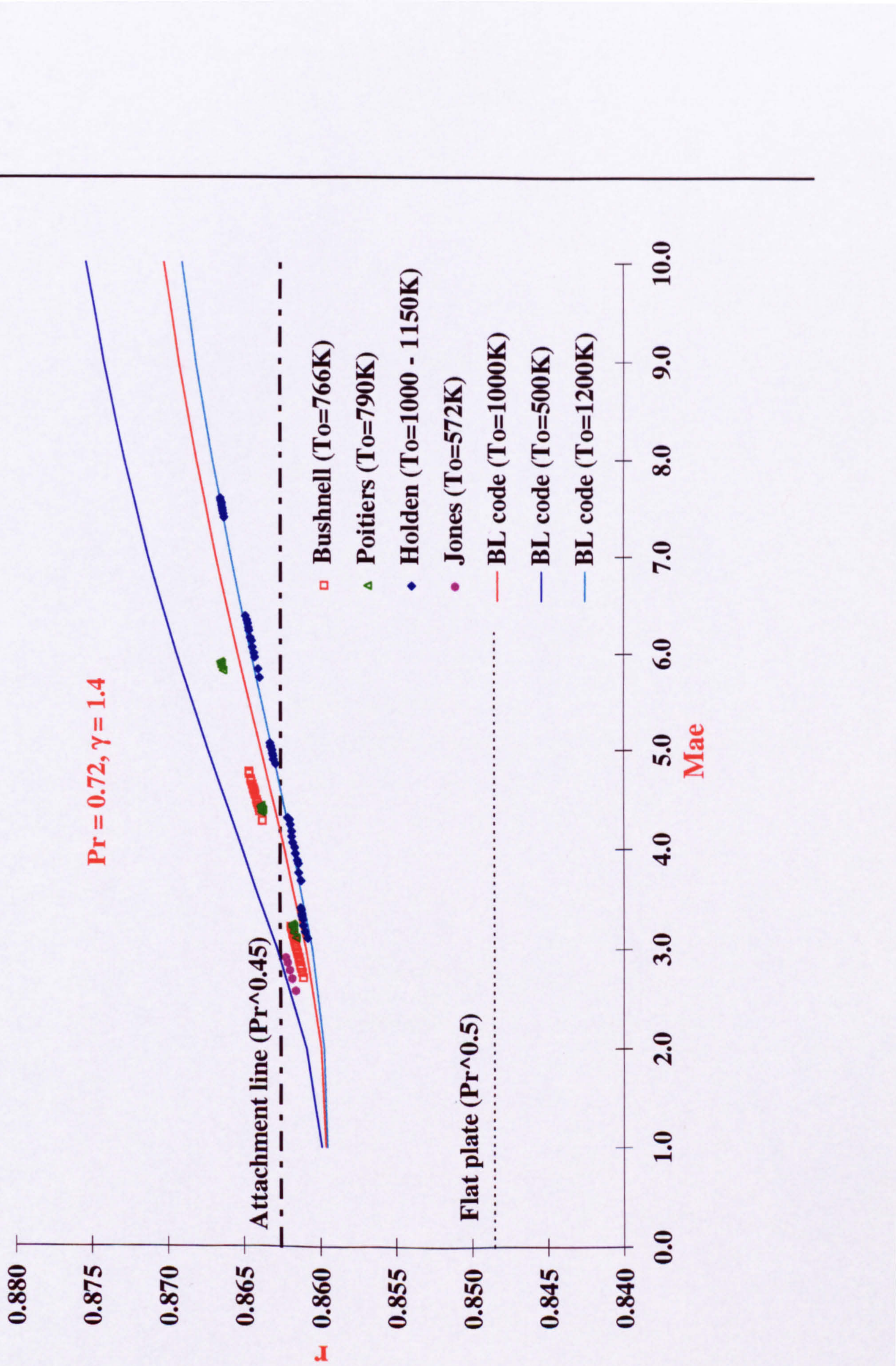

Figure A.29: Variation of the laminar recovery factor with M_{ae} as obtained from the boundary layer code for $Pr = 0.72$, $\gamma = 1.4$ and $500 \leq T_o \leq 1200K$.

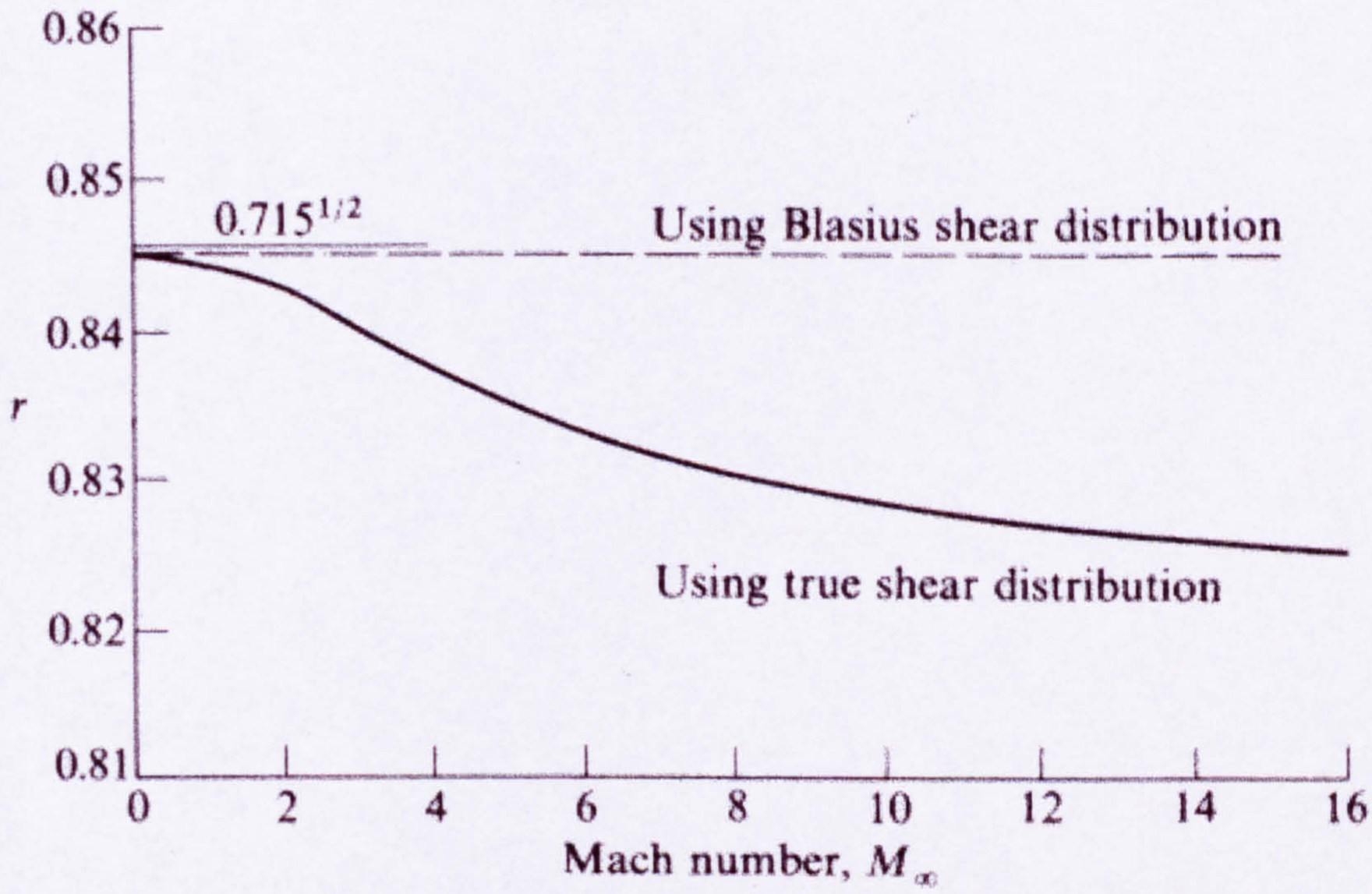

Figure A.30: Variation of the recovery factor r with Mach number for laminar flat plate flow.

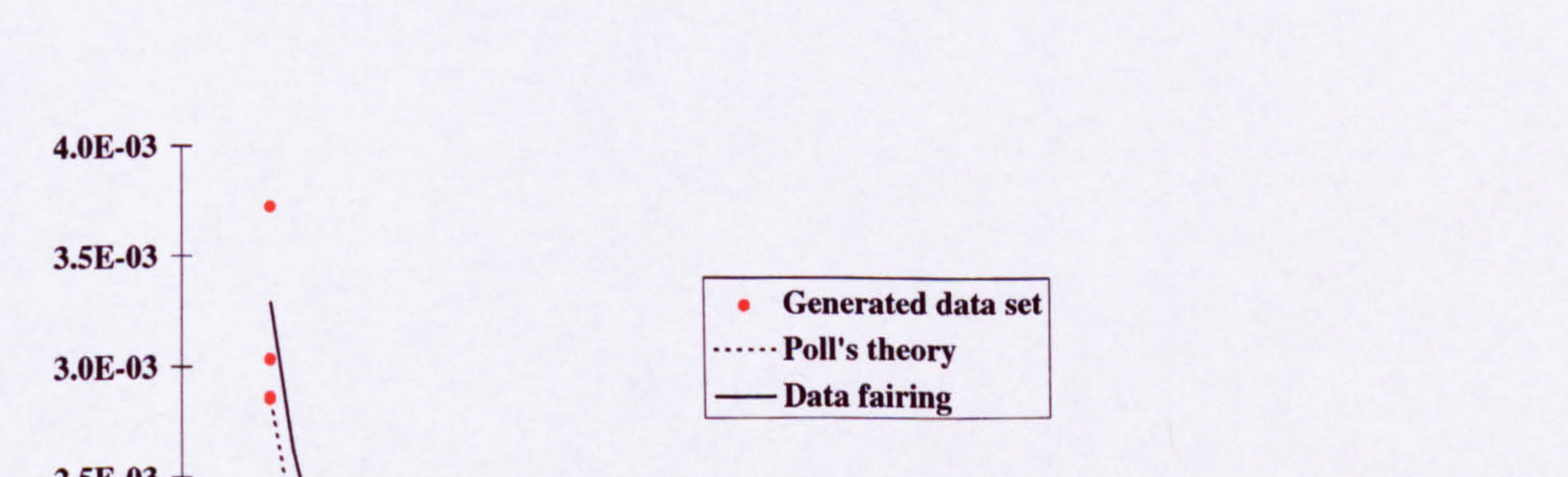

Figure A.31: Variation of the Stanton number with $\bar{R}$ as obtained by the boundary layer code (equation 3.13) and compared with Poll's theory [49]. Pr of unity.

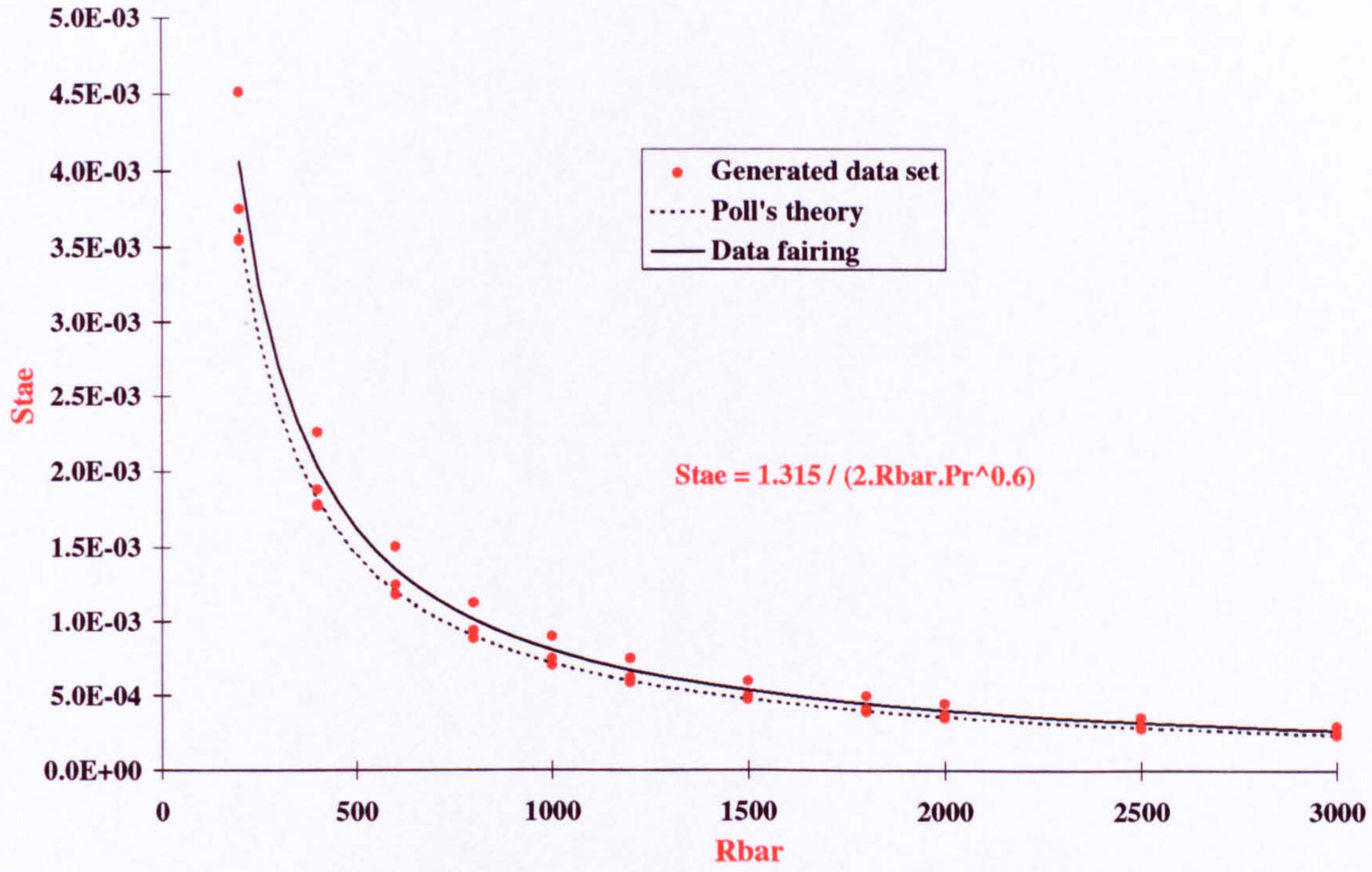

Figure A.32: Variation of the Stanton number with $\bar{R}$ as obtained by the boundary layer code (equation 3.13) and compared with Poll's theory [49] $Pr = 0.7$.

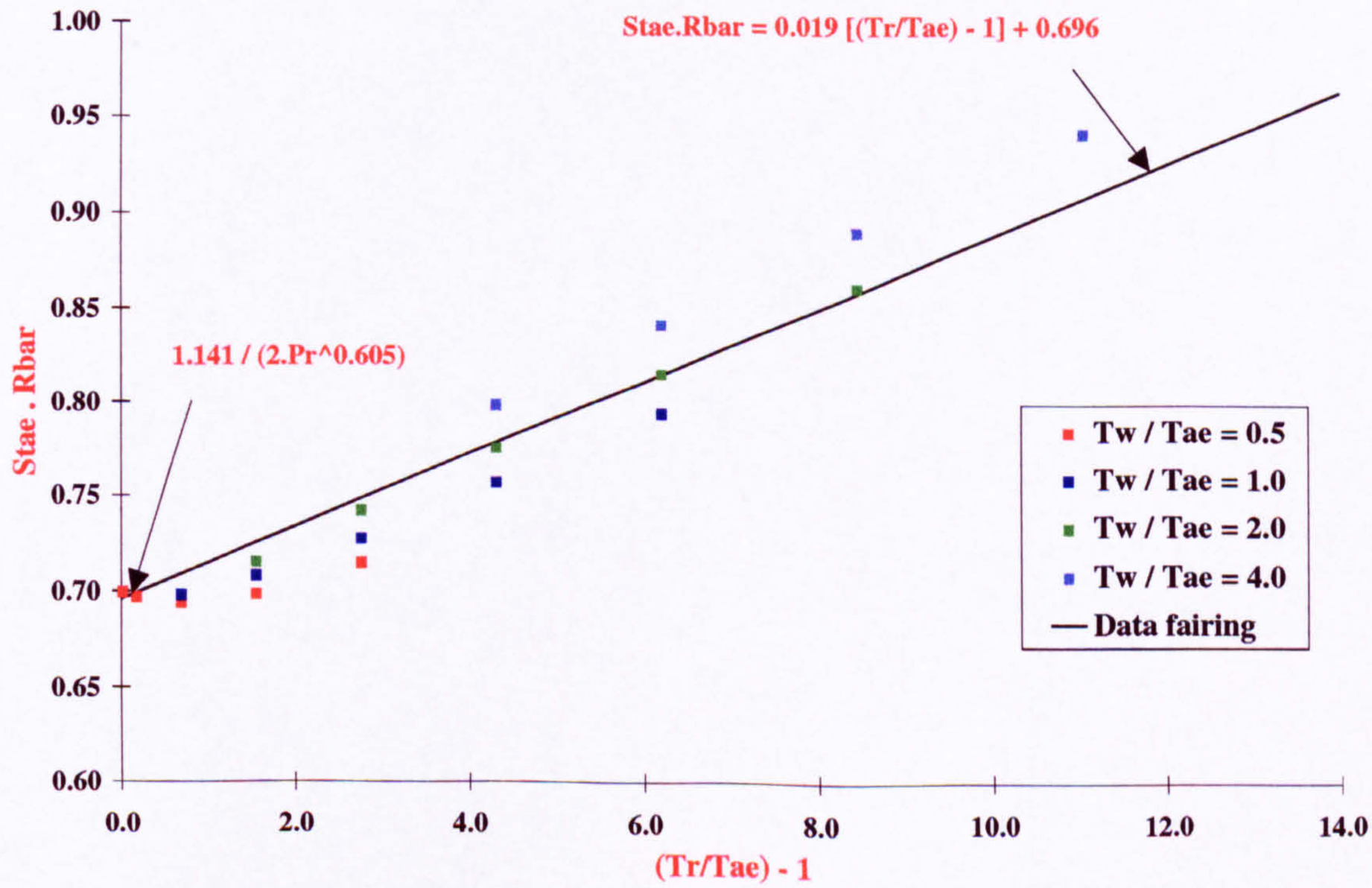

Figure A.33: Variation of the product $St_{ae}.\bar{R}$ with $(T_r/T_{ae}) - 1$ for different values of T_w/T_{ae}. Laminar attachment-line flow ; Air, $T_o = 800$ K, $s/T_o = 0.138$ and $Pr = 0.72$.

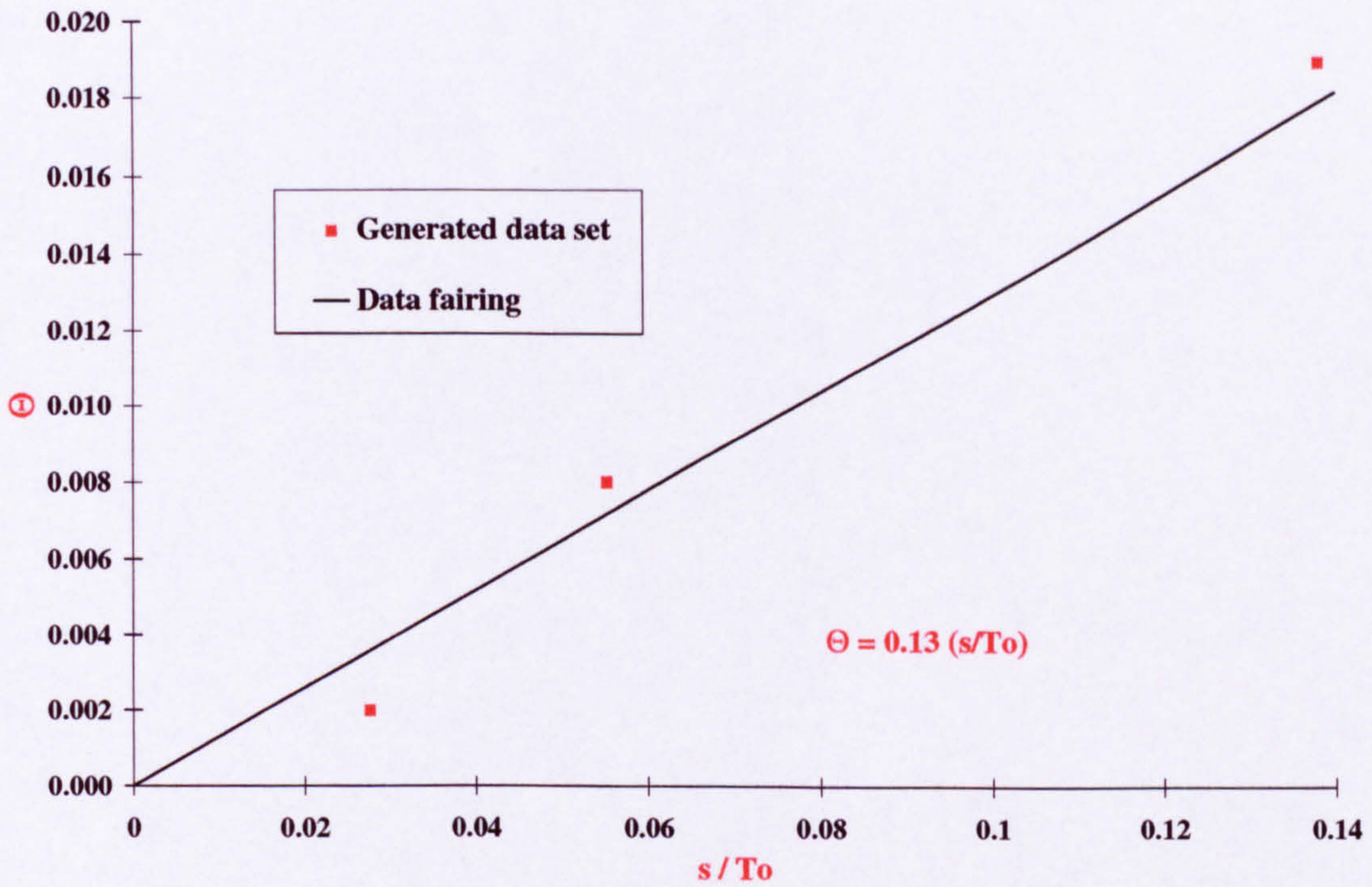

Figure A.34: Variation of the slope with s/To in equation $St_{ae}.\bar{R} = slope.(S/T_o).(T_r/T_{ae} - 1) + 0.696$. Laminar attachment-line flow ; Air, $s = 110.4$ K and $Pr = 0.72$.

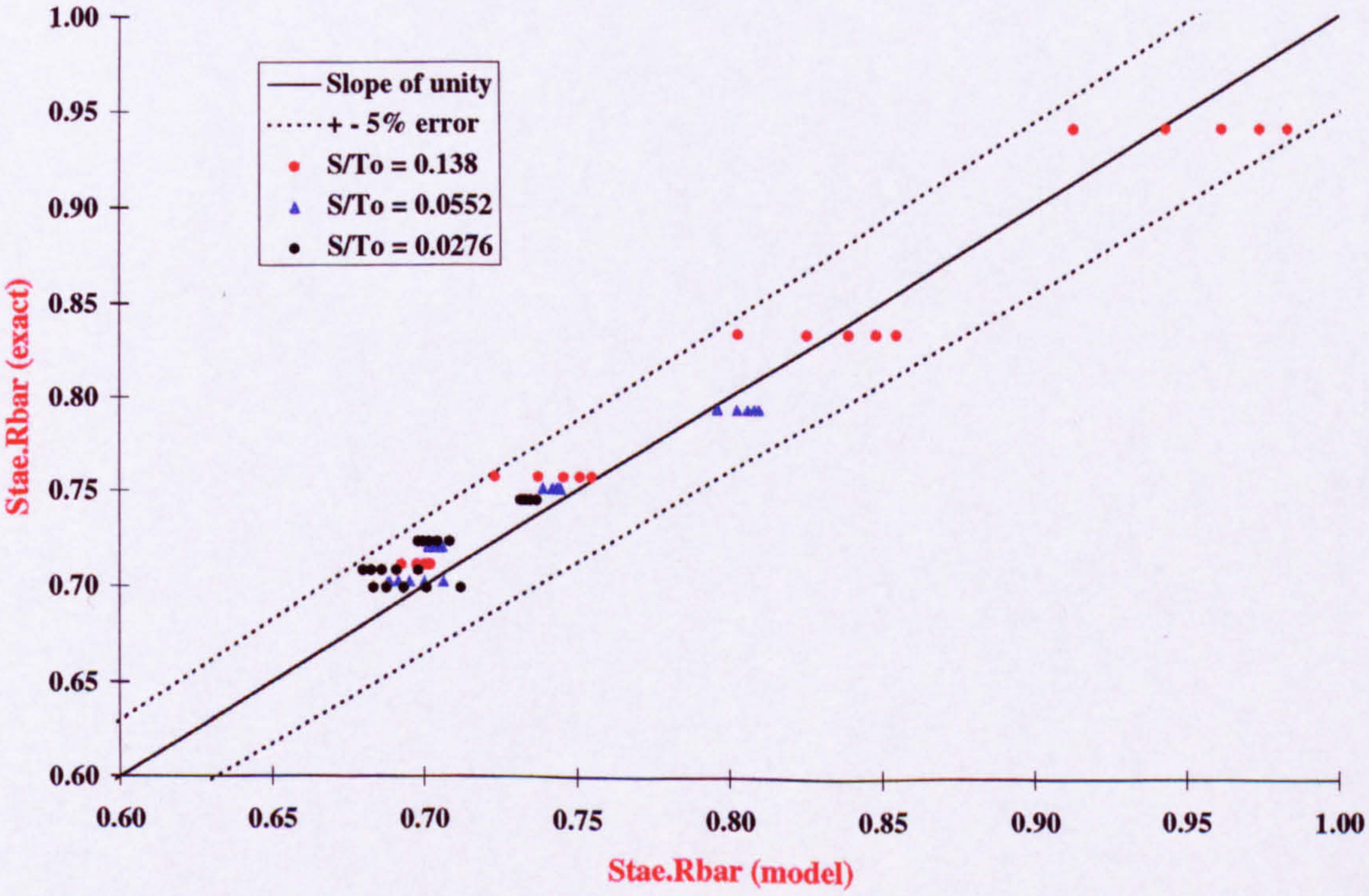

Figure A.35: Comparison of the exact $St_{ae}.\bar{R}$ and from the model (equation 3.14) for Air, $M_{ae} \leq 8$, T_w/T_o between 0.1 and unity, $T_o \leq 4000$ K, Pr between 0.7 and unity.

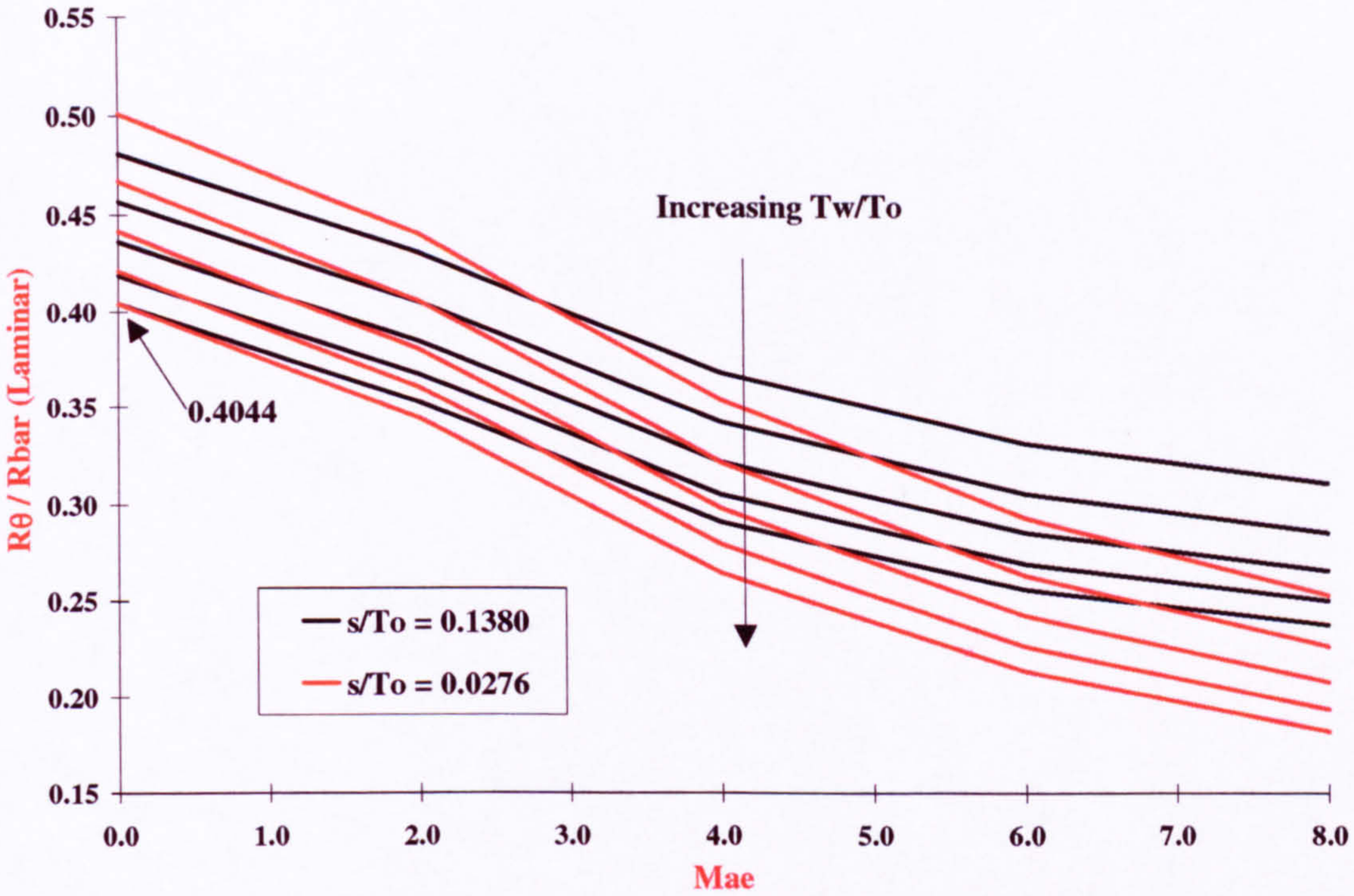

Figure A.36: Variation of the Reynolds number ratio $R_\theta/\bar{R}$ with edge Mach number, wall to stagnation temperature ratio and s/T_o for laminar flow. (T_w/T_o of 0.2, 0.4, 0.6, 0.8 and 1).

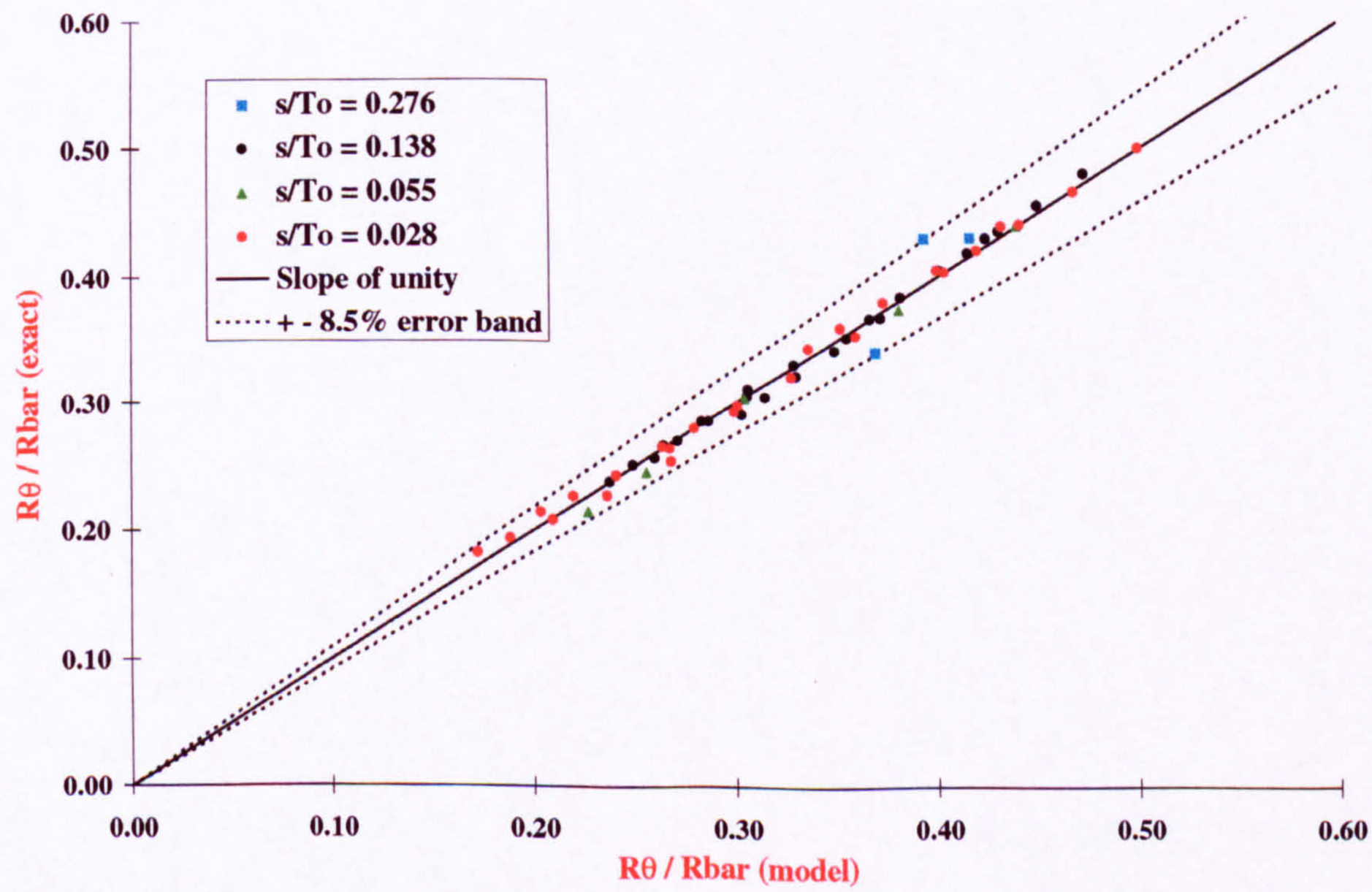

Figure A.37: Comparison between the exact value of $R_\theta/\bar{R}$ and predictions from the model (equations 3.21 to 3.23).

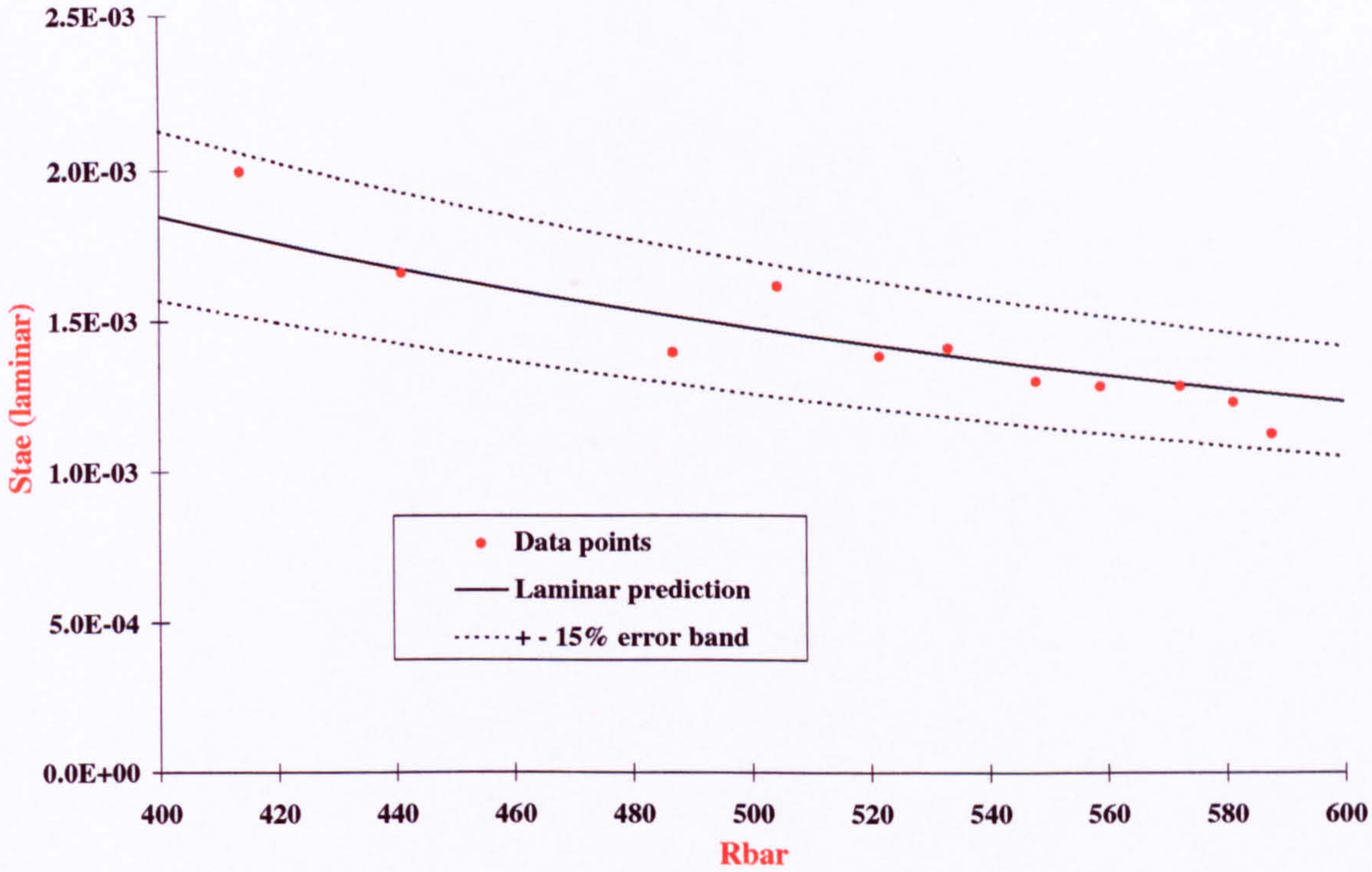

Figure A.38: Comparison between the laminar prediction (equation 3.14)and data from Holden et al. [37] [38] Run7 ($M_\infty = 10.45$, $\Lambda = 66.5^o$, $T_W/T_o = 0.27$, 2D trip wire).

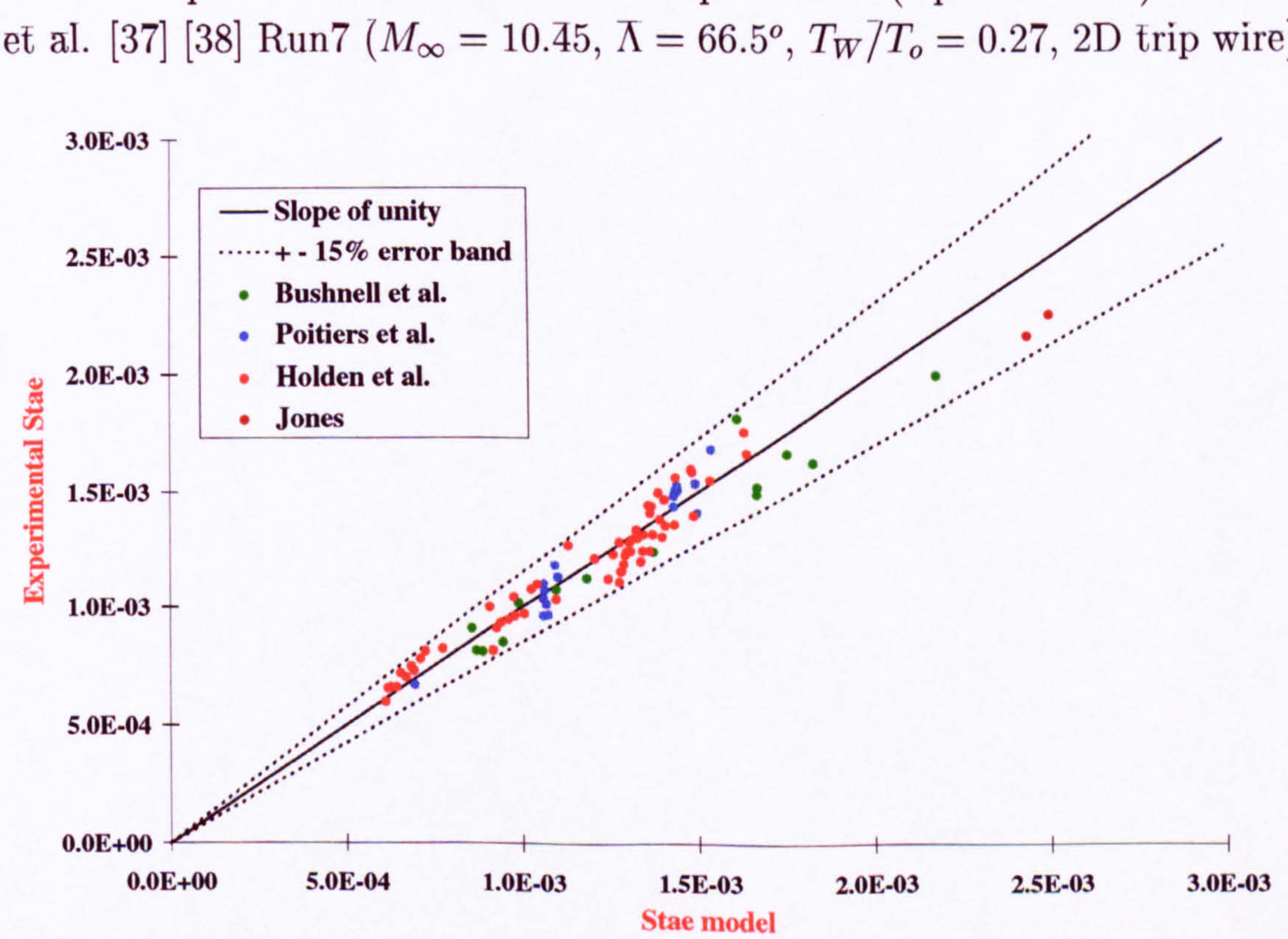

Figure A.39: Comparison between the laminar prediction (equation 3.14) and experimental data from Holden et al. [37][38], Bushnell et al. [12][13], Poitiers University [35][6], Beckwith et al. [5] and Jones [40] ($4.15 \leq M_\infty \leq 10.6$, $0^o \leq \Lambda \leq 80^o$, $0.25 \leq \frac{T_W}{T_o} \leq 0.92$).

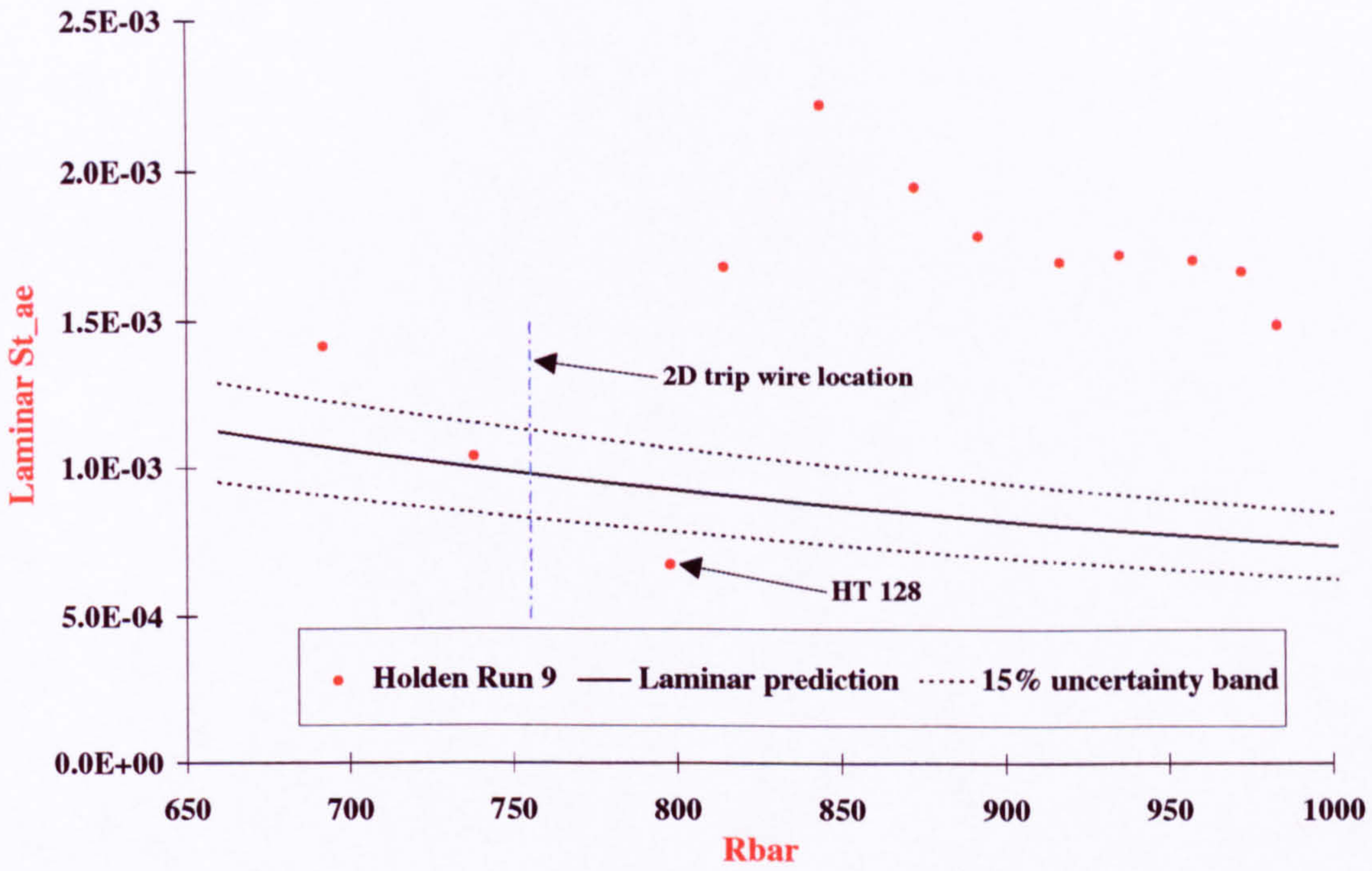

Figure A.40: Variation of the laminar Stanton number along the attachment-line with $\bar{R}$. Holden run 9 (2D trip wire: k=0.015 inches, $M_\infty = 10.5$, $\Lambda = 66.5^o$, $R_{D\infty} = 6.1.10^5$).

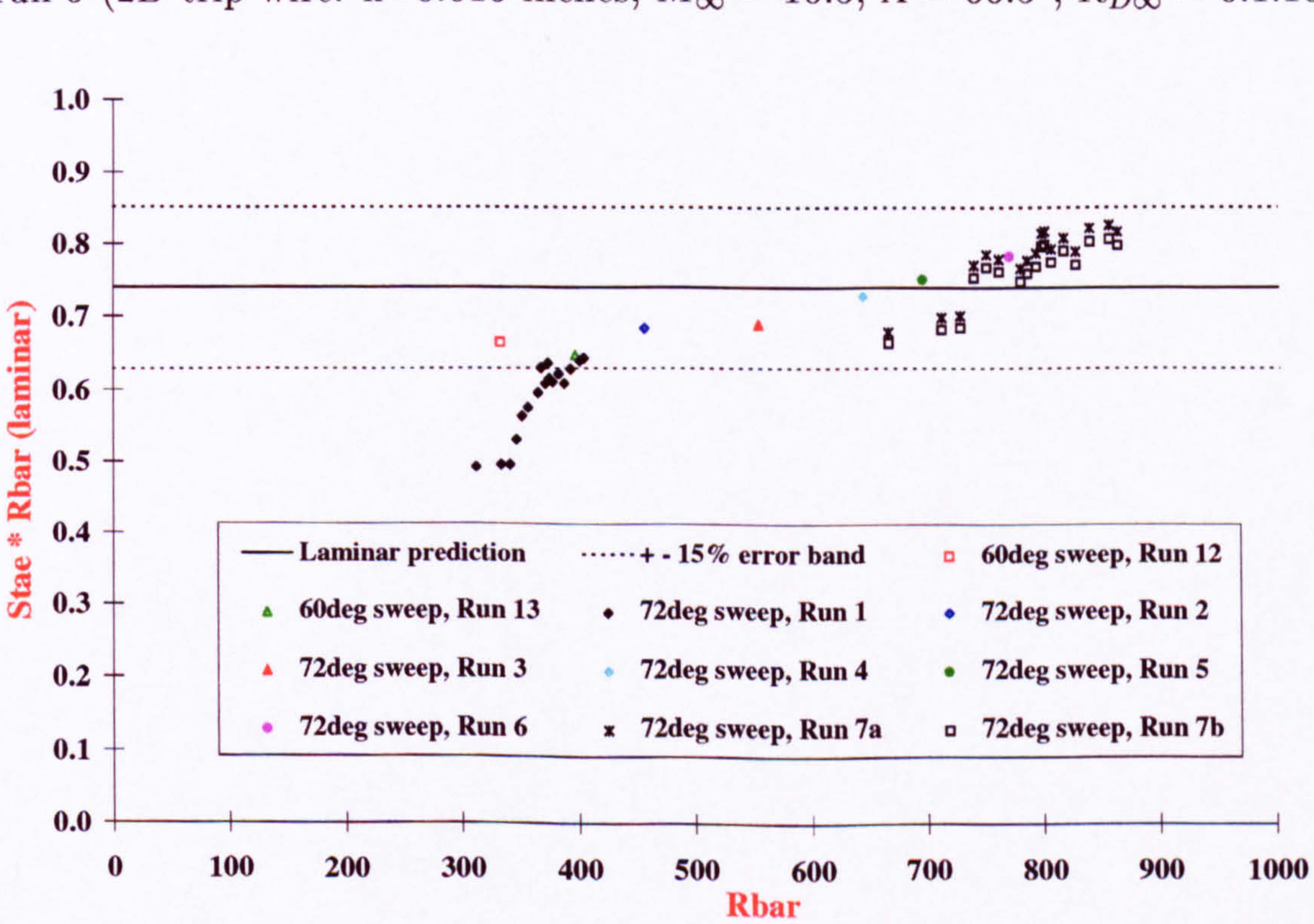

Figure A.41: Data from Bushnell et al. [12] [13] for laminar attachment-line flow. $M_\infty \approx 7.9$, $\Lambda = 60^o$ and 72^o, $T_W/T_o \approx 0.39$. Prediction ; equation 3.14.

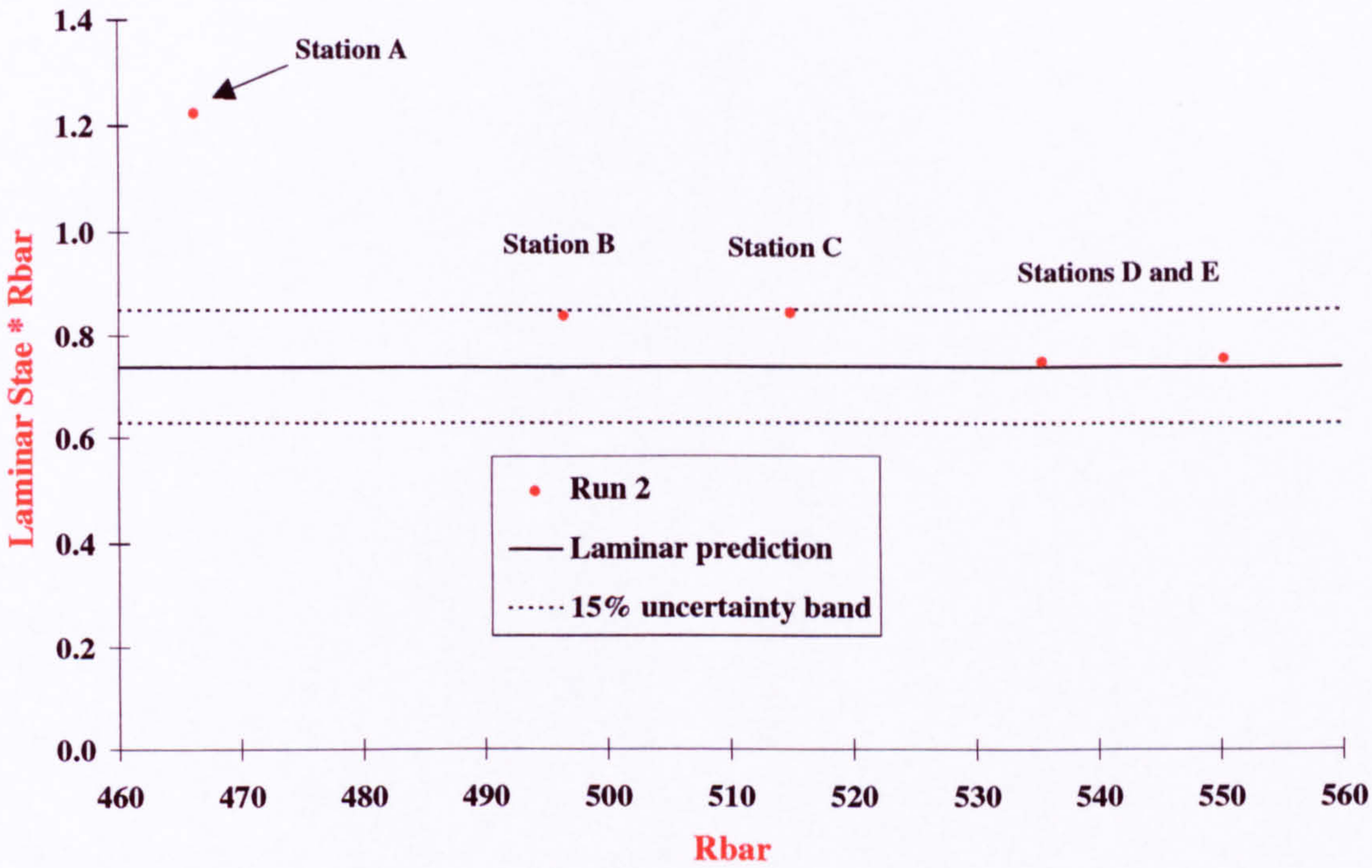

Figure A.42: Comparison of the Stanton number and $\bar{R}$ from Jones run 2 with the laminar prediction. ($M_\infty = 6.1$, $\bar{\Lambda} = 60^o$, $T_W/T_o = 0.52$ and $R_{D\infty} = 2.1.10^5$ per meter).

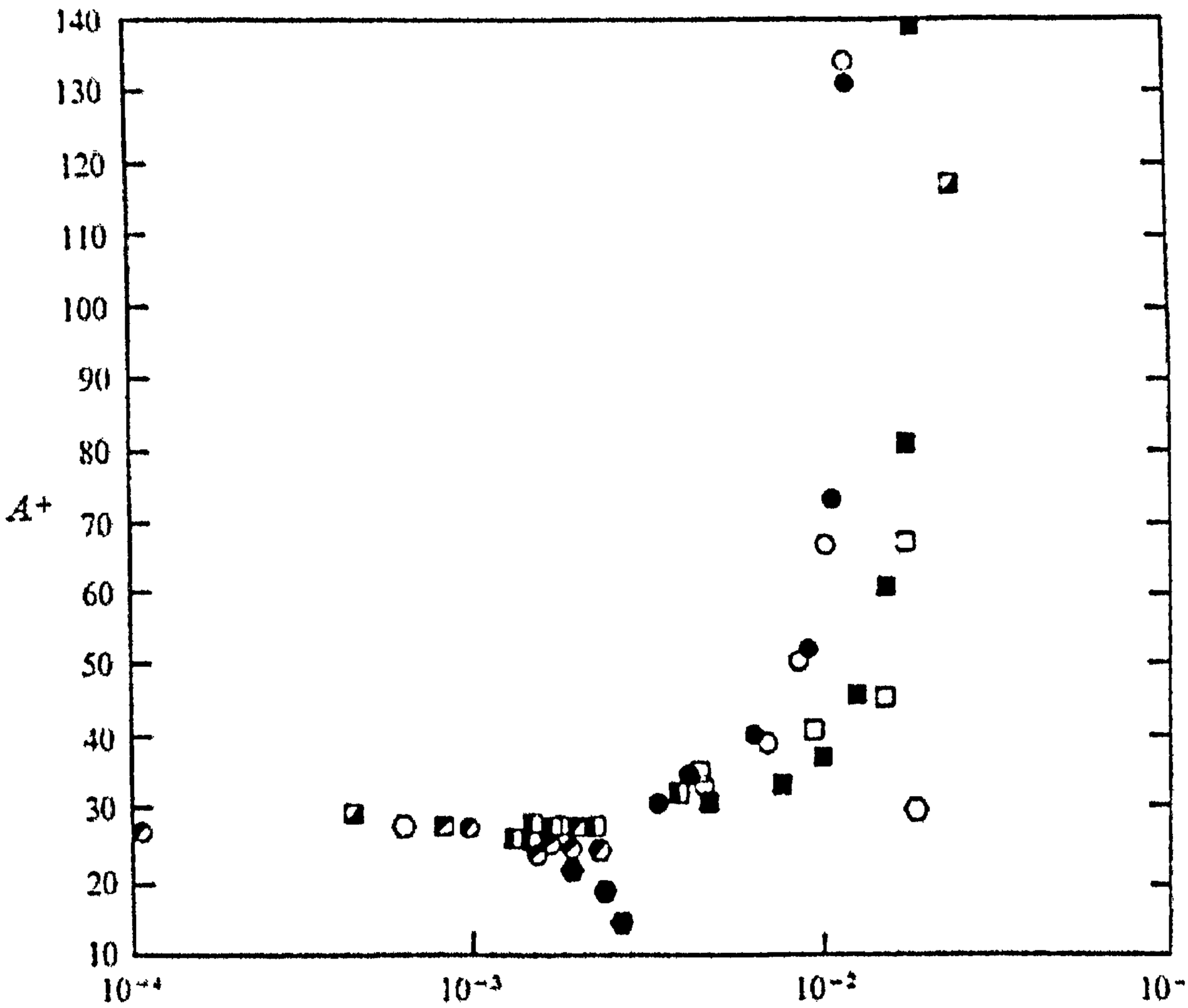

Figure A.43: Variation of the damping parameter A^+ for two-dimensional and axisymmetric flows with dimensionless shear-stress gradient in the inner layer, $\partial\tau^+/\partial Y^+$ as found by Huffman and Bradshaw [39].

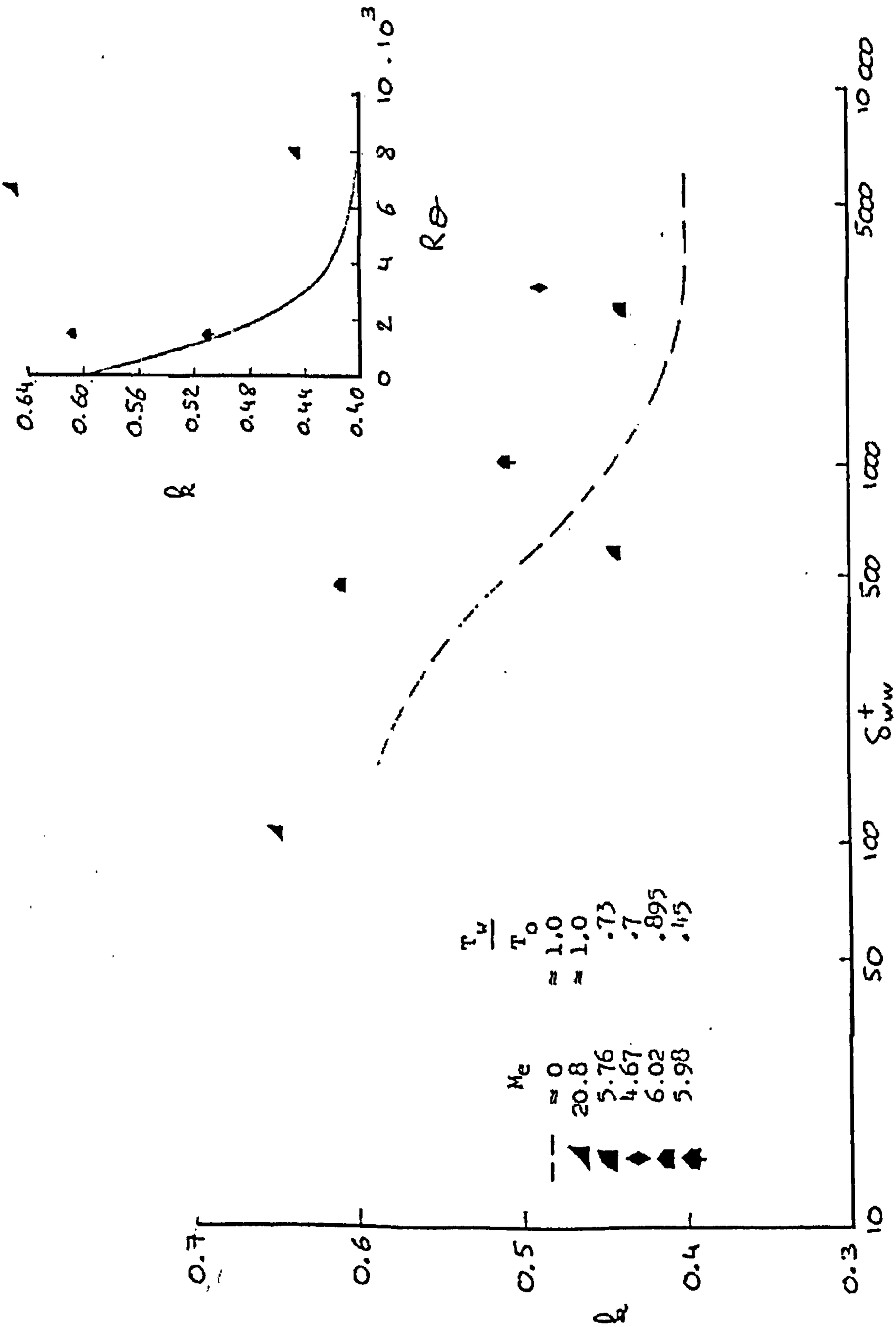

Figure A.44: Variation of von Kármán's constant with Reynolds number δ^+_{ww} (equation 4.47) as found by Bushnell and Morris [14].

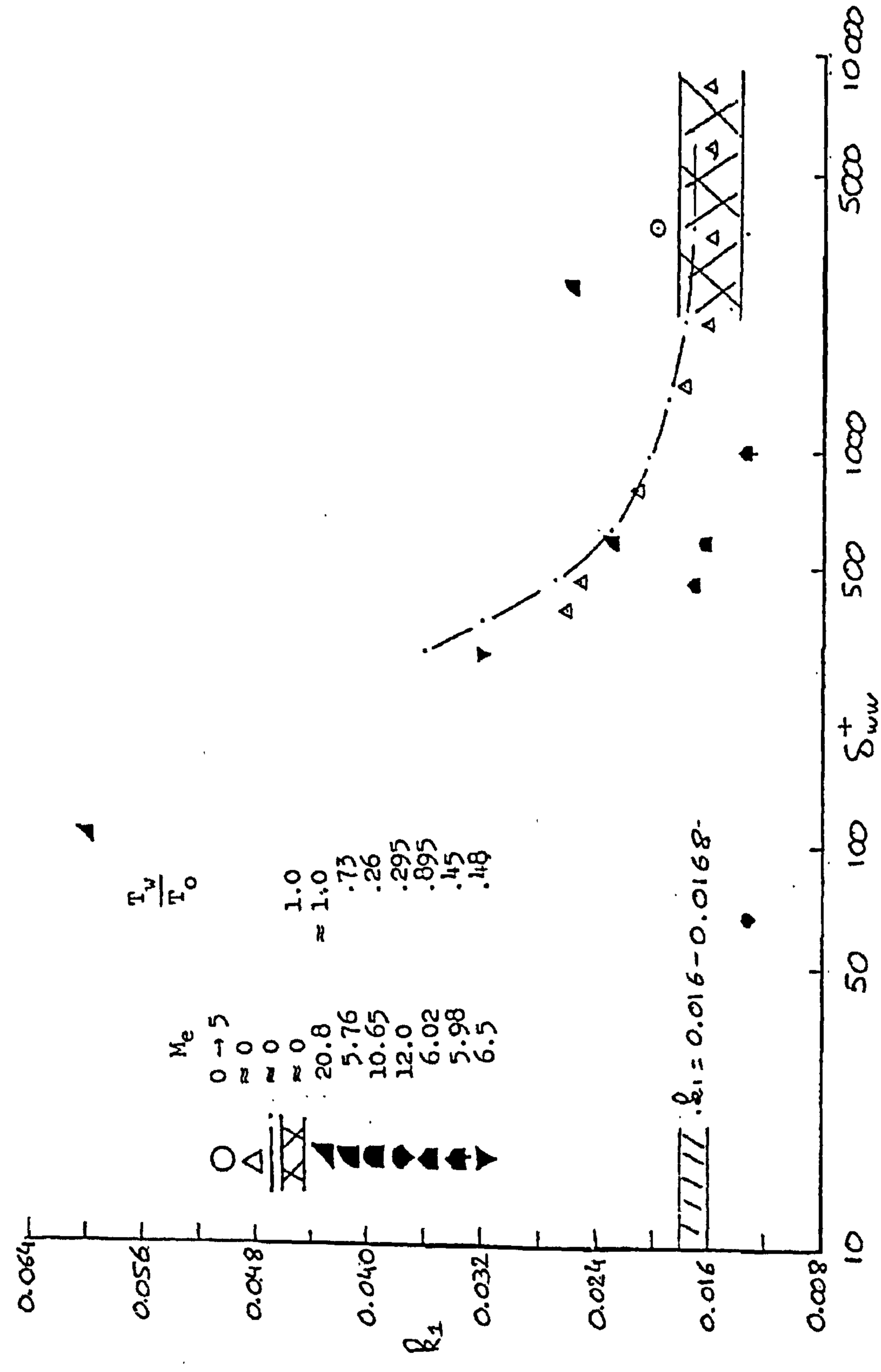

Figure A.45: Variation of the coefficient k_1 (or eddy viscosity in equation 4.9) with Reynolds number δ^+_{ww} (equation 4.47) as found by Bushnell and Morris [14].

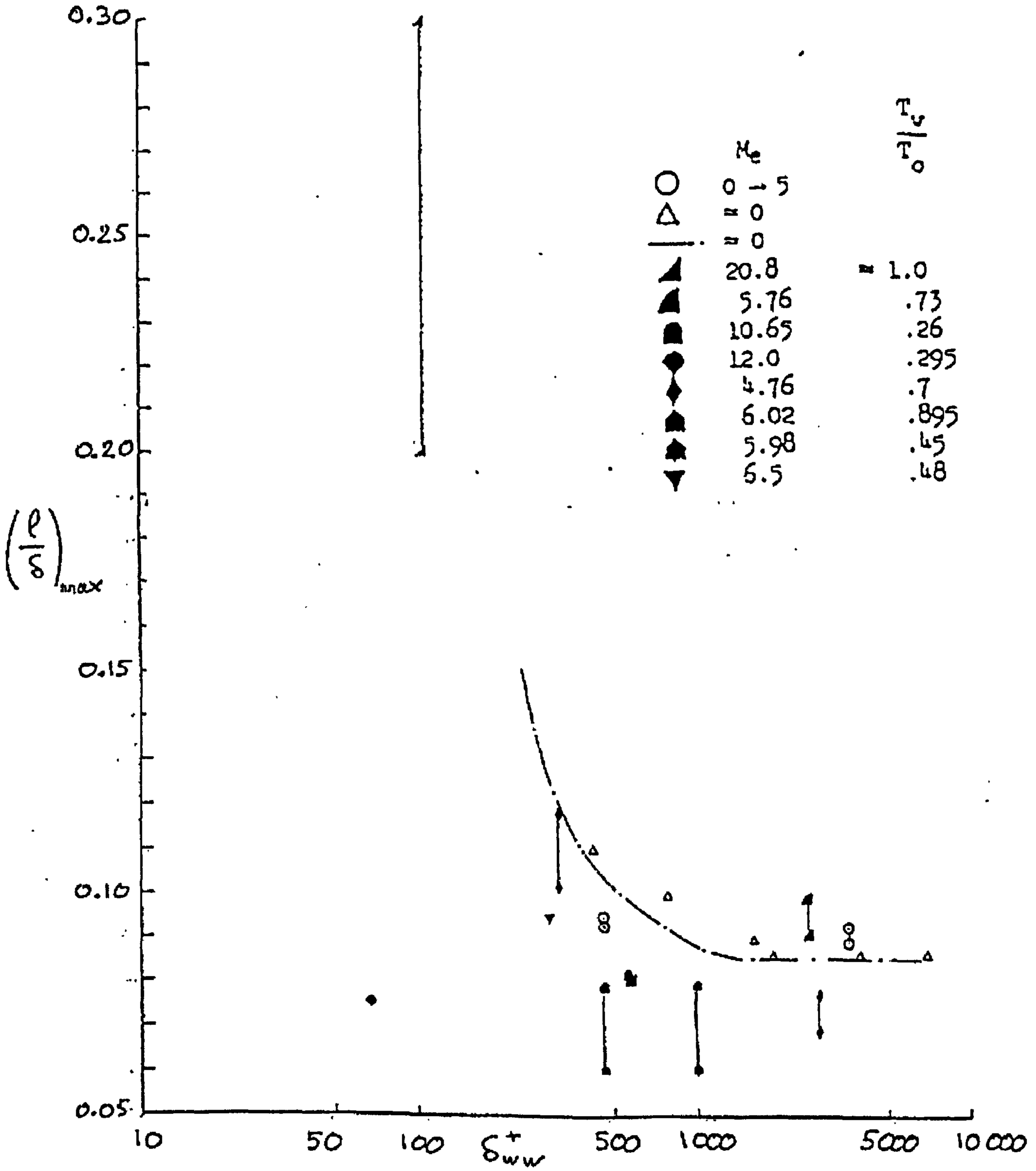

Figure A.46: Variation of the maximum value of the mixing length with Reynolds number δ^+_{ww} (equation 4.47) as found by Bushnell and Morris [14].

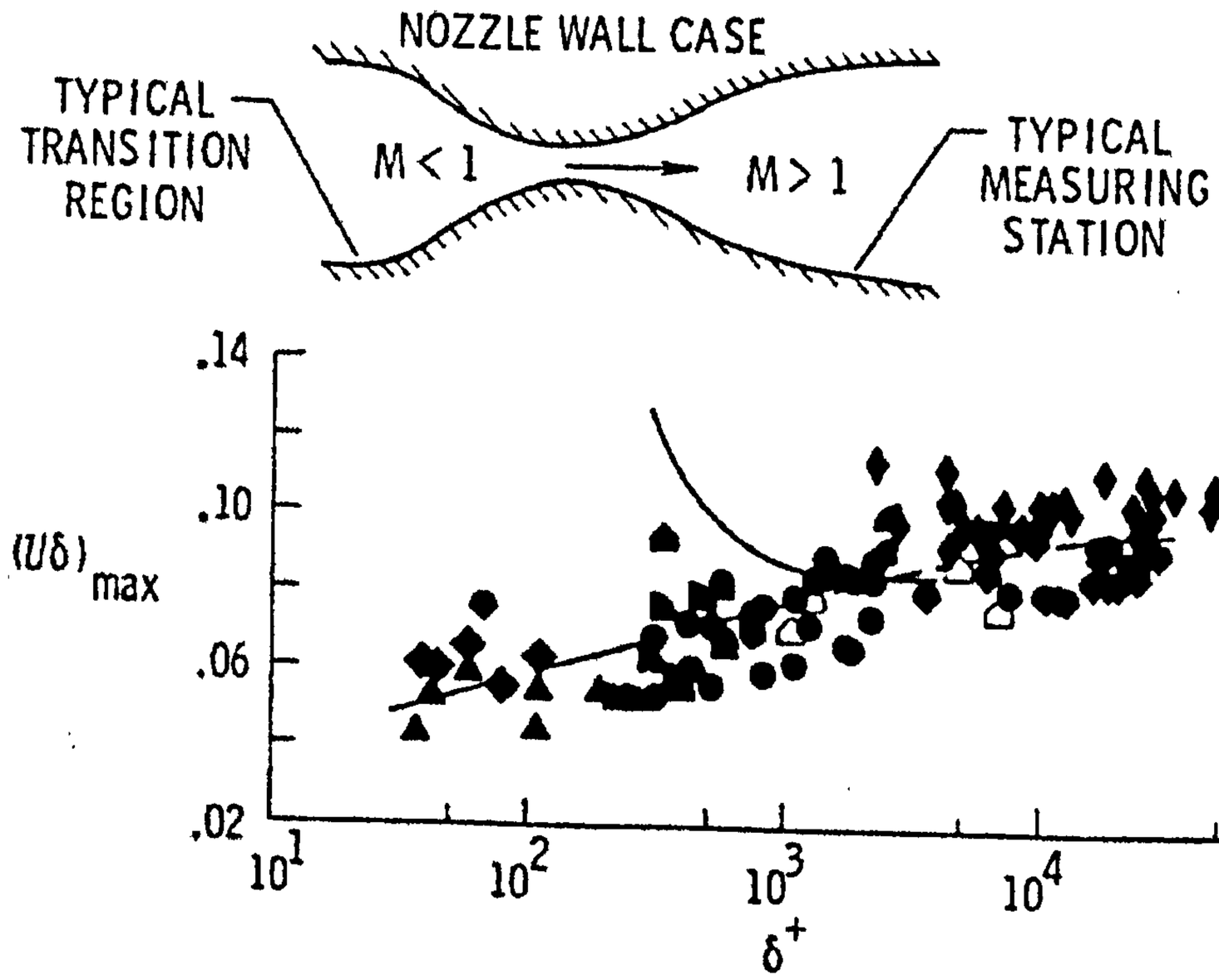

Figure A.47: Variation of $(l/\delta)_{max}$ with Reynolds number δ^+_{ww} for compressible nozzle wall flow after Bushnell et al. [15].

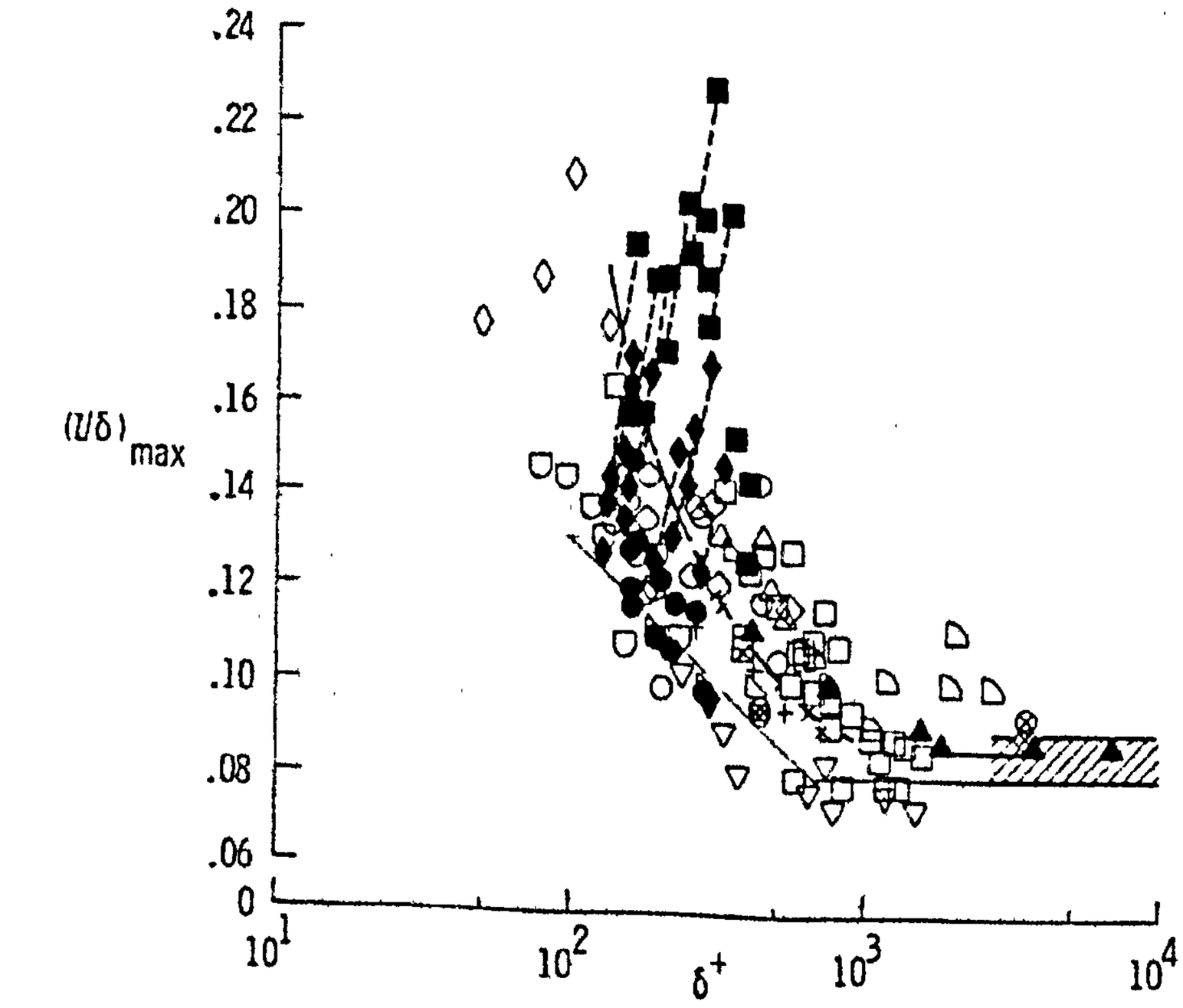

Figure A.48: Variation of $(l/\delta)_{max}$ with Reynolds number δ^+_{ww} for compressible flow over plates, cones and cylinders after Bushnell et al. [15].

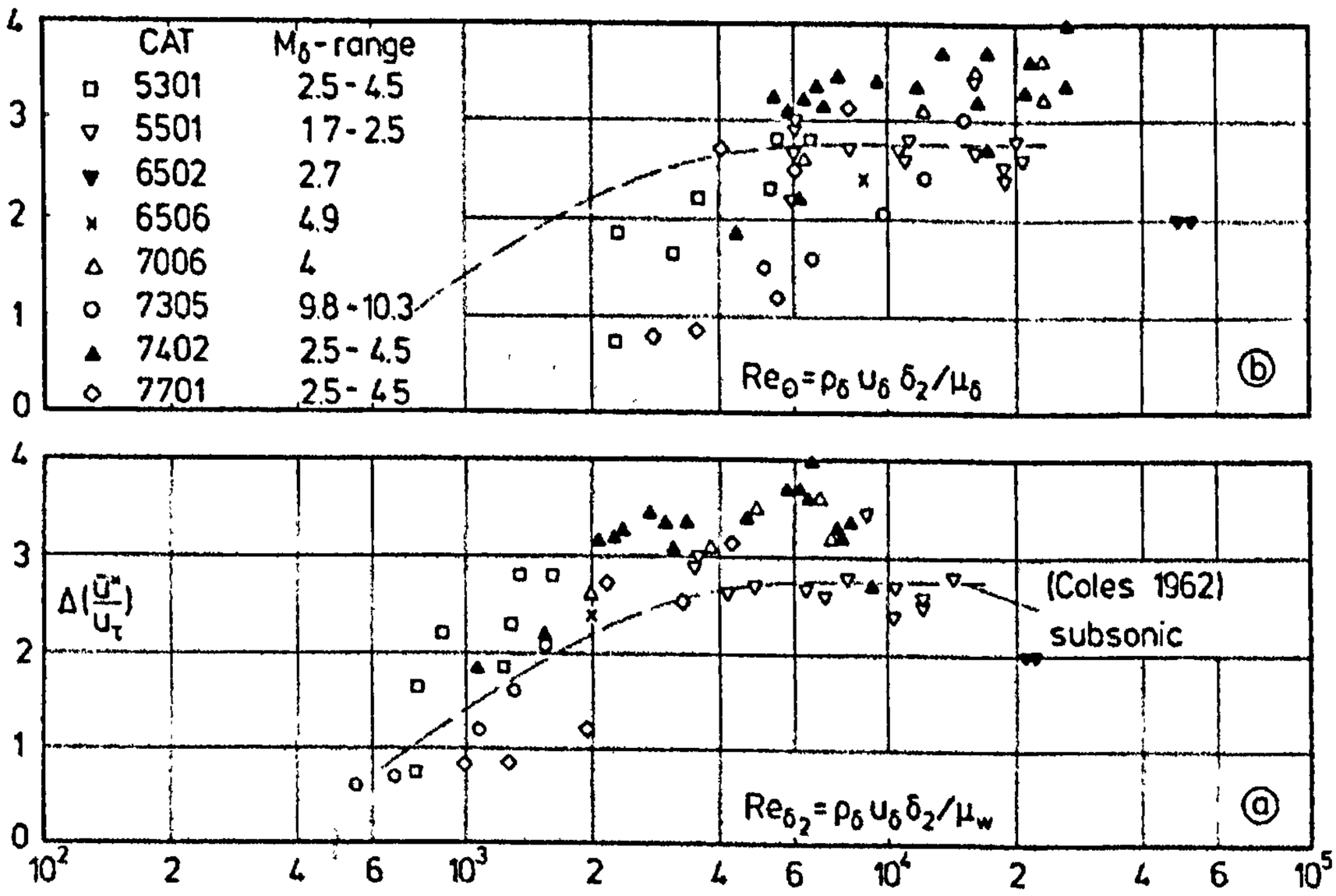

Figure A.49: Variation of the wake strength in a compressible equilibrium turbulent boundary layer (zero pressure gradient, adiabatic wall, no mass transfer) after Fernholz and Finley [33].

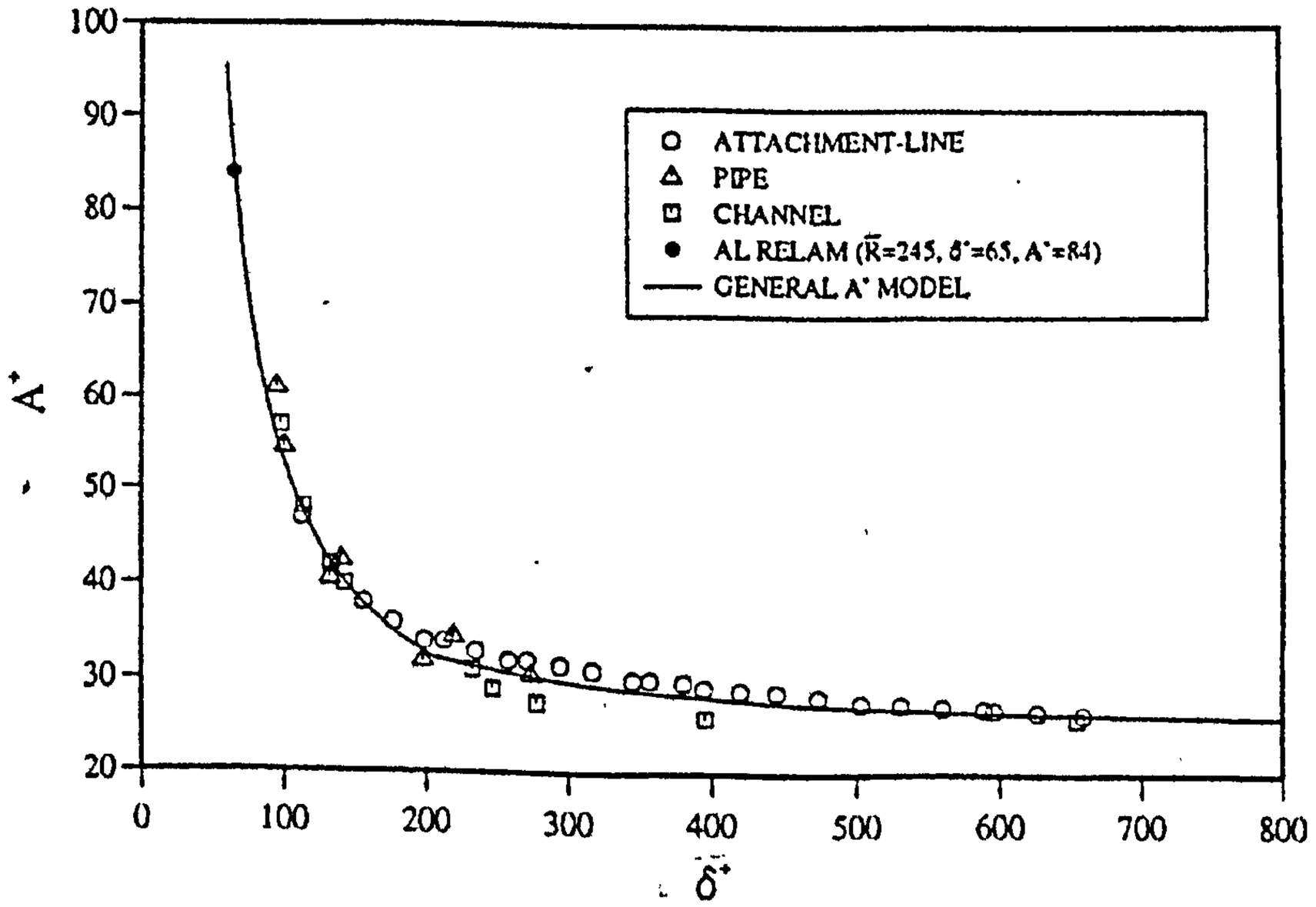

Figure A.50: Variation of the damping parameter A^+ with Reynolds number δ^+_{ww} for incompressible attachment-line, pipe and channel flow after Yardley [65]; equations 4.57 and 4.58.

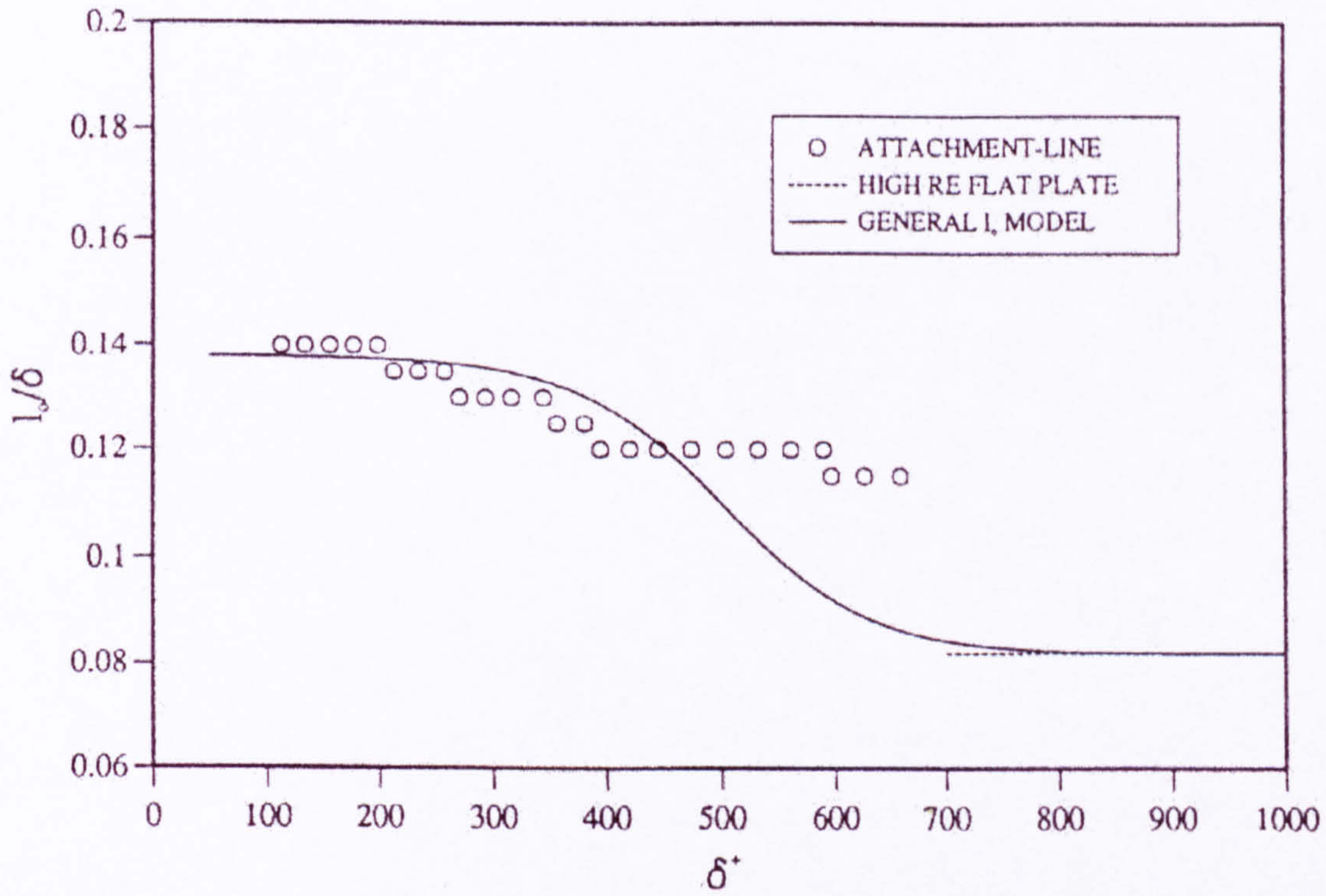

Figure A.51: Variation of the outer mixing length with Reynolds number δ^+_{ww} for incompressible external flows after Yardley [65]; equation 4.59.

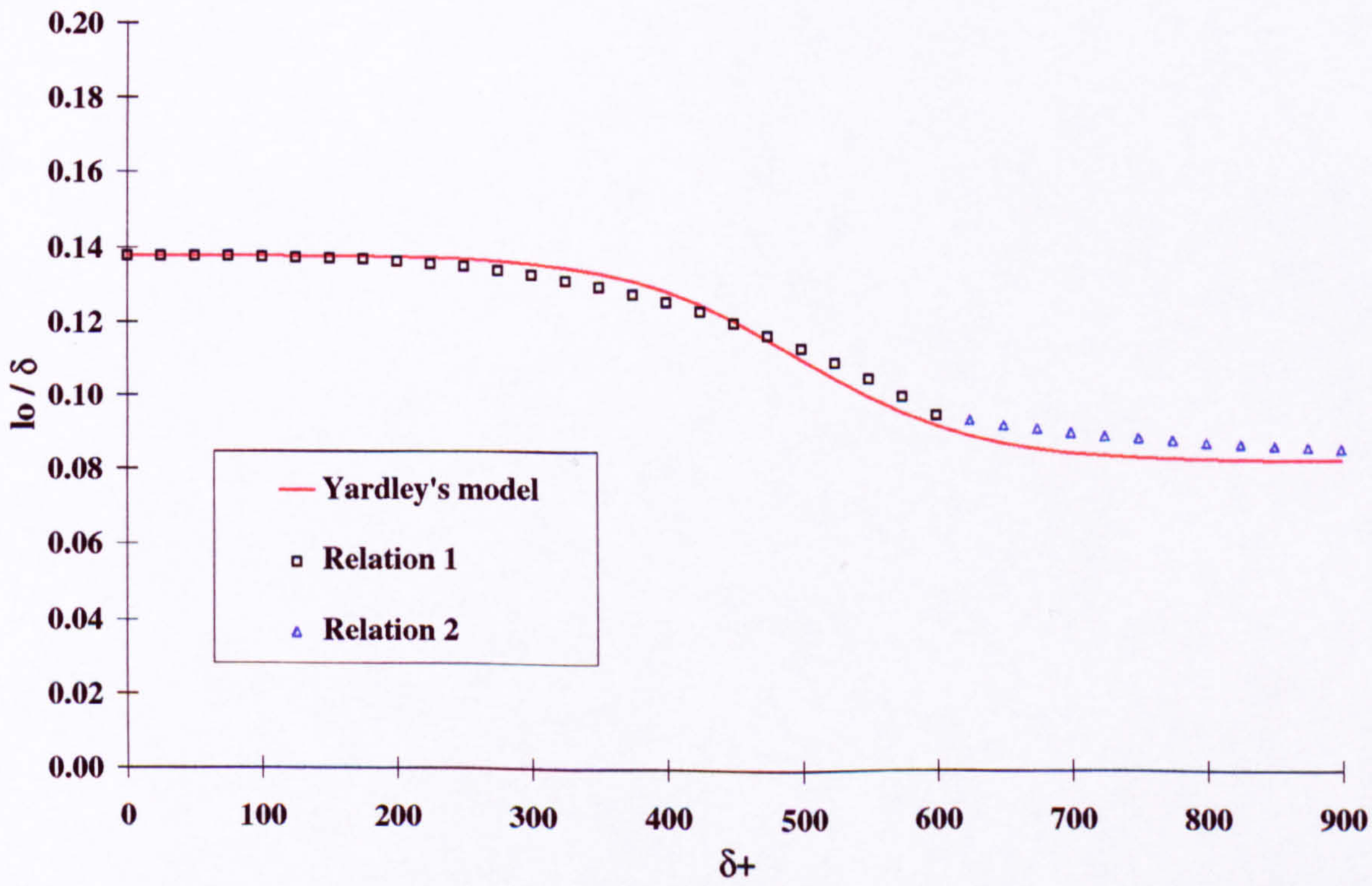

Figure A.52: Comparison of the outer mixing length expressions. Yardley's model: equation 4.59; relations 1 and 2: equations 4.60 and 4.61 respectively.

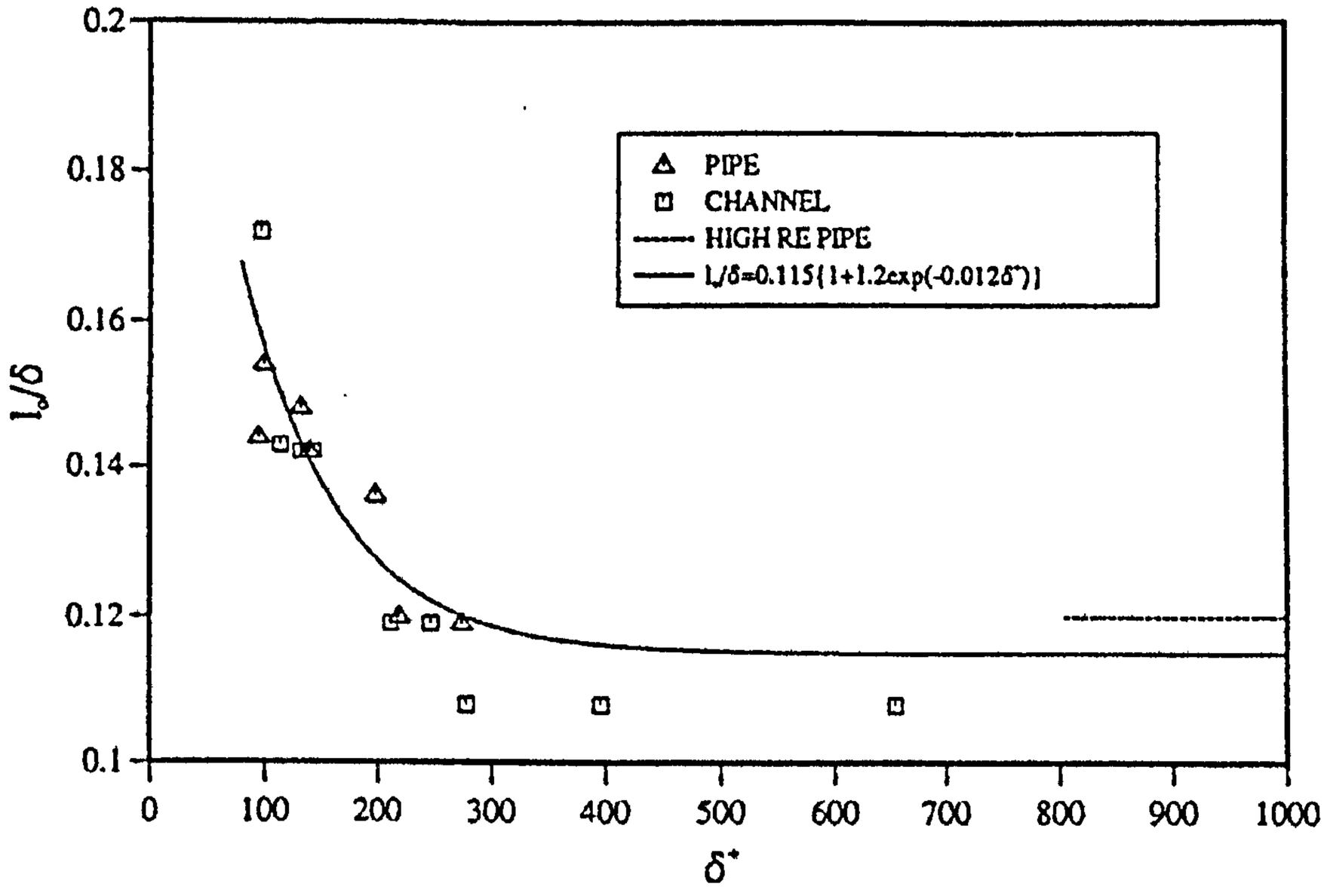

Figure A.53: Variation of the outer mixing length with Reynolds number δ^+_{ww} for incompressible internal flows after Yardley [65]; equation 4.62.

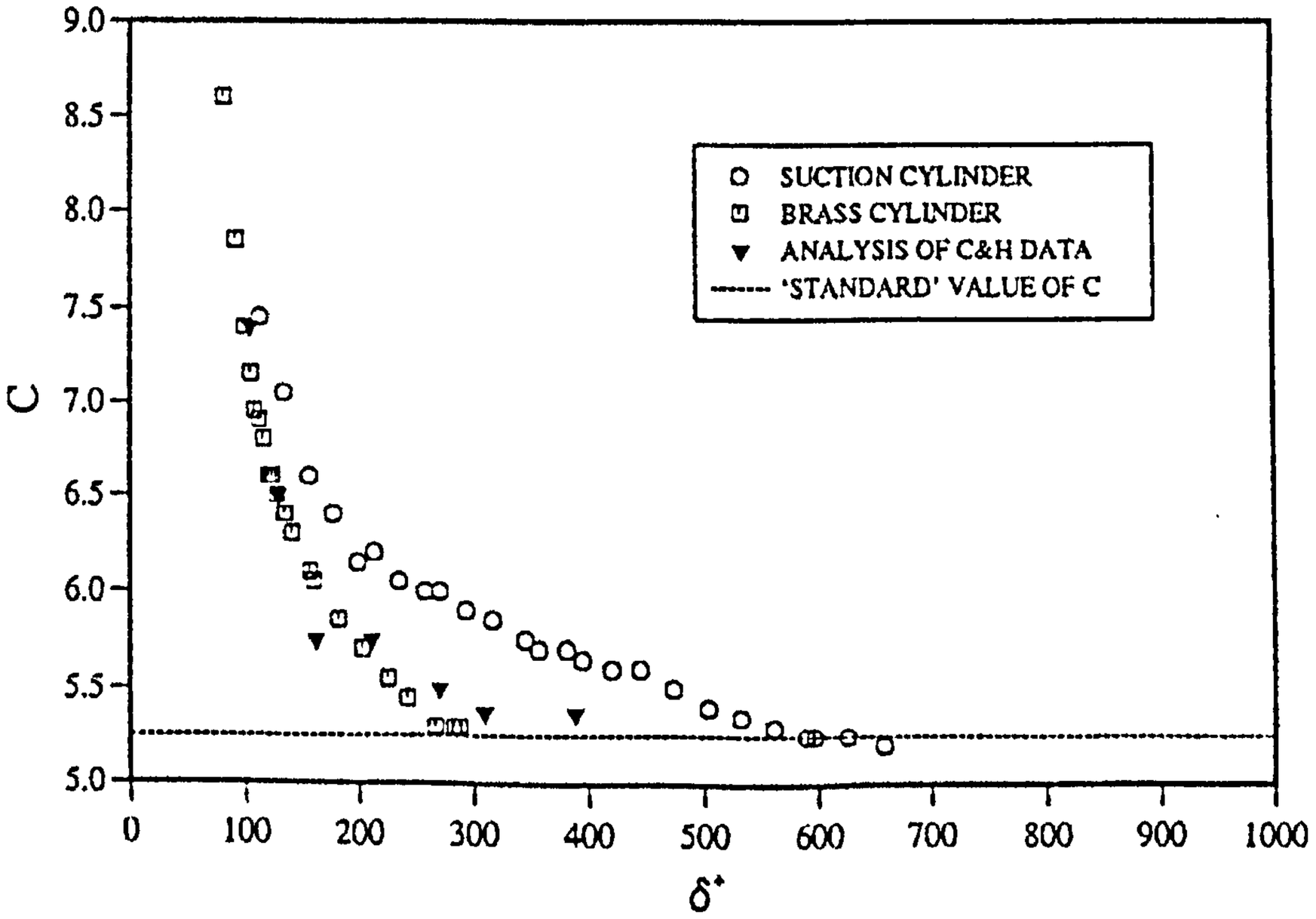

Figure A.54: Variation of the logarithmic law additive constant C with Reynolds number δ^+_{ww} for incompressible flow with zero pressure gradient and no mass transfer after Yardley [65].

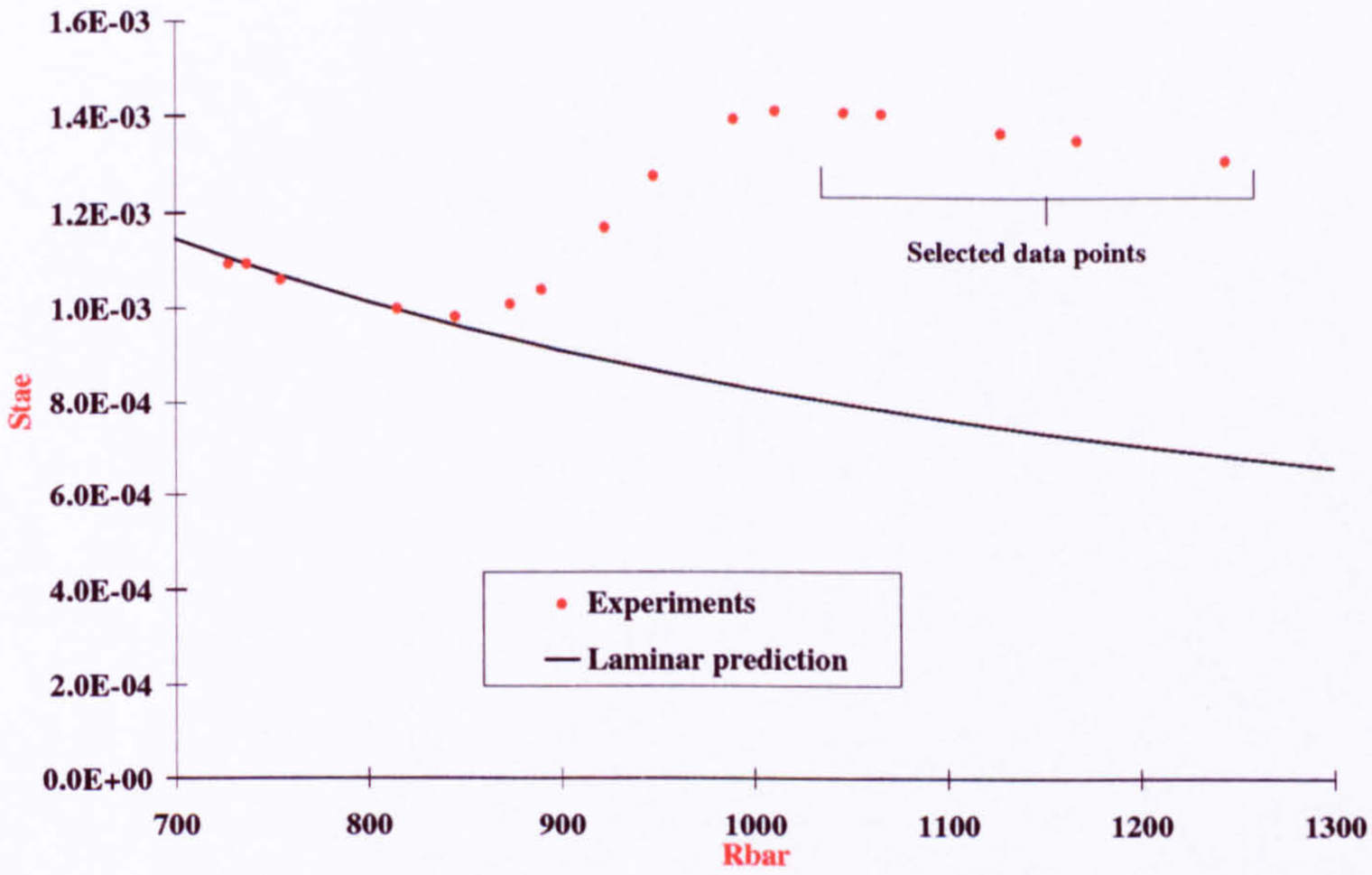

Figure A.55: Typical selected run for the development of the turbulence model. Fixed Free-stream conditions but varying local flow properties. (Poitiers University [35], End plate, $M_\infty = 7.14$, $T_w/T_o = 0.38$).

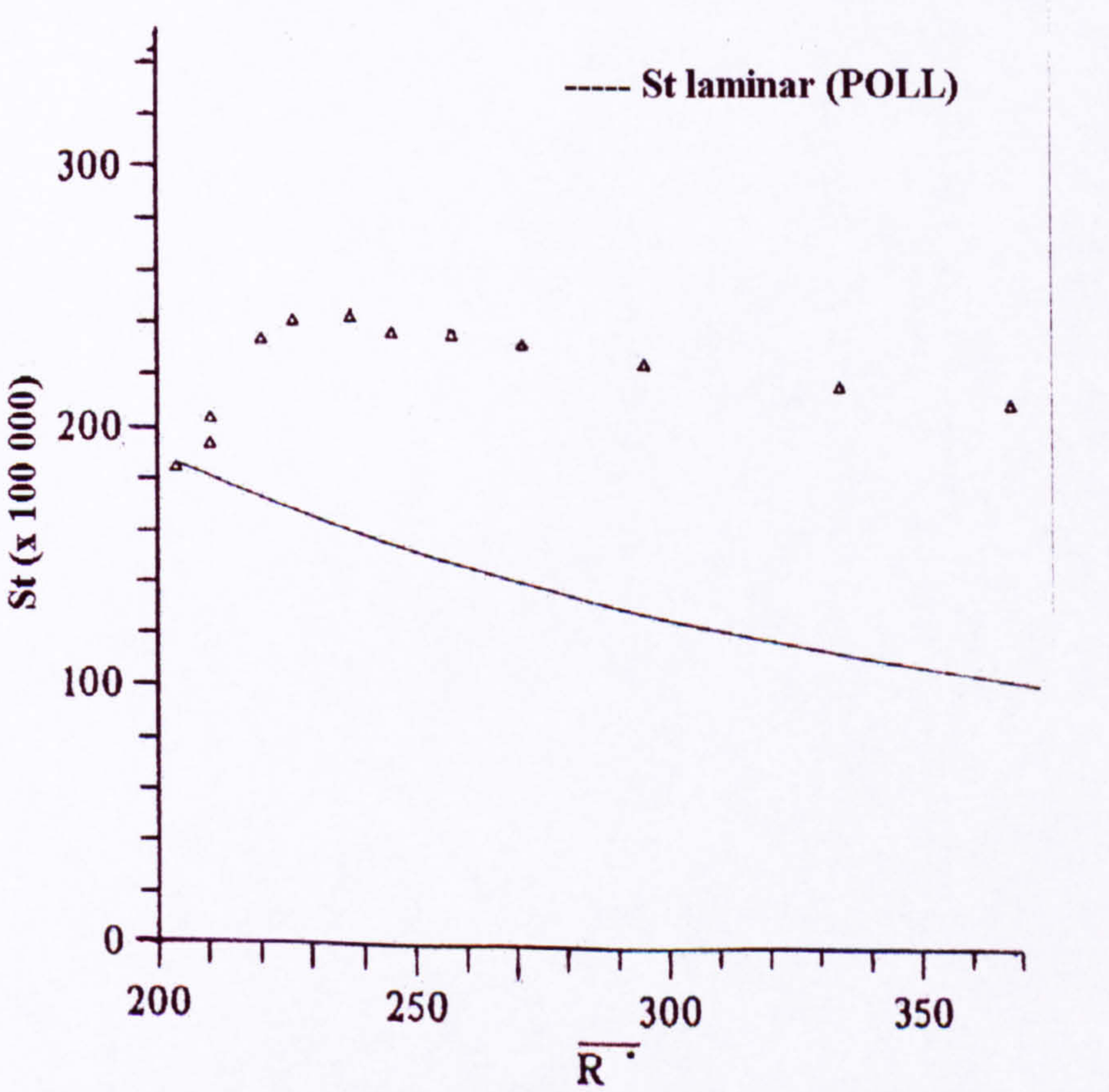

Figure A.56: Typical selected run for the development of the turbulence model. Fixed local flow properties but varying local and free-stream Reynolds number. (Poitiers University [6], End plate, $M_\infty = 7.14$, $\Lambda = 60^o$, $T_w/T_o = 0.41$, $L/D = 12.80$).

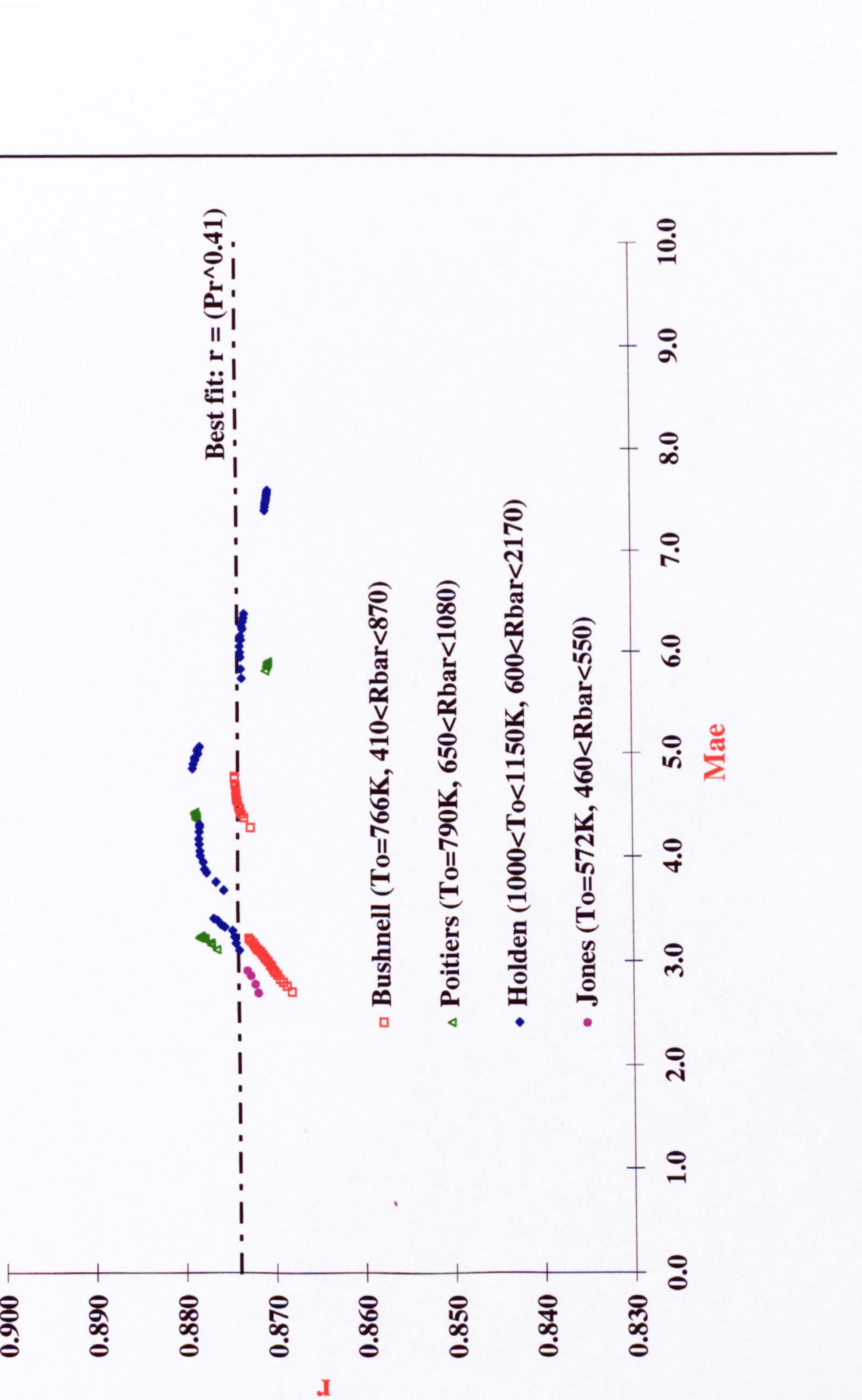

Figure A.57: Variation of the turbulent recovery factor with edge Mach number for compressible flow covering a wide range of $\bar{R}$ and stagnation temperatures as predicted by Yardley's incompressible turbulence model [65]. (Air, $Pr = 0.72$, $Pr_t = 0.9$, $\gamma = 1.4$).

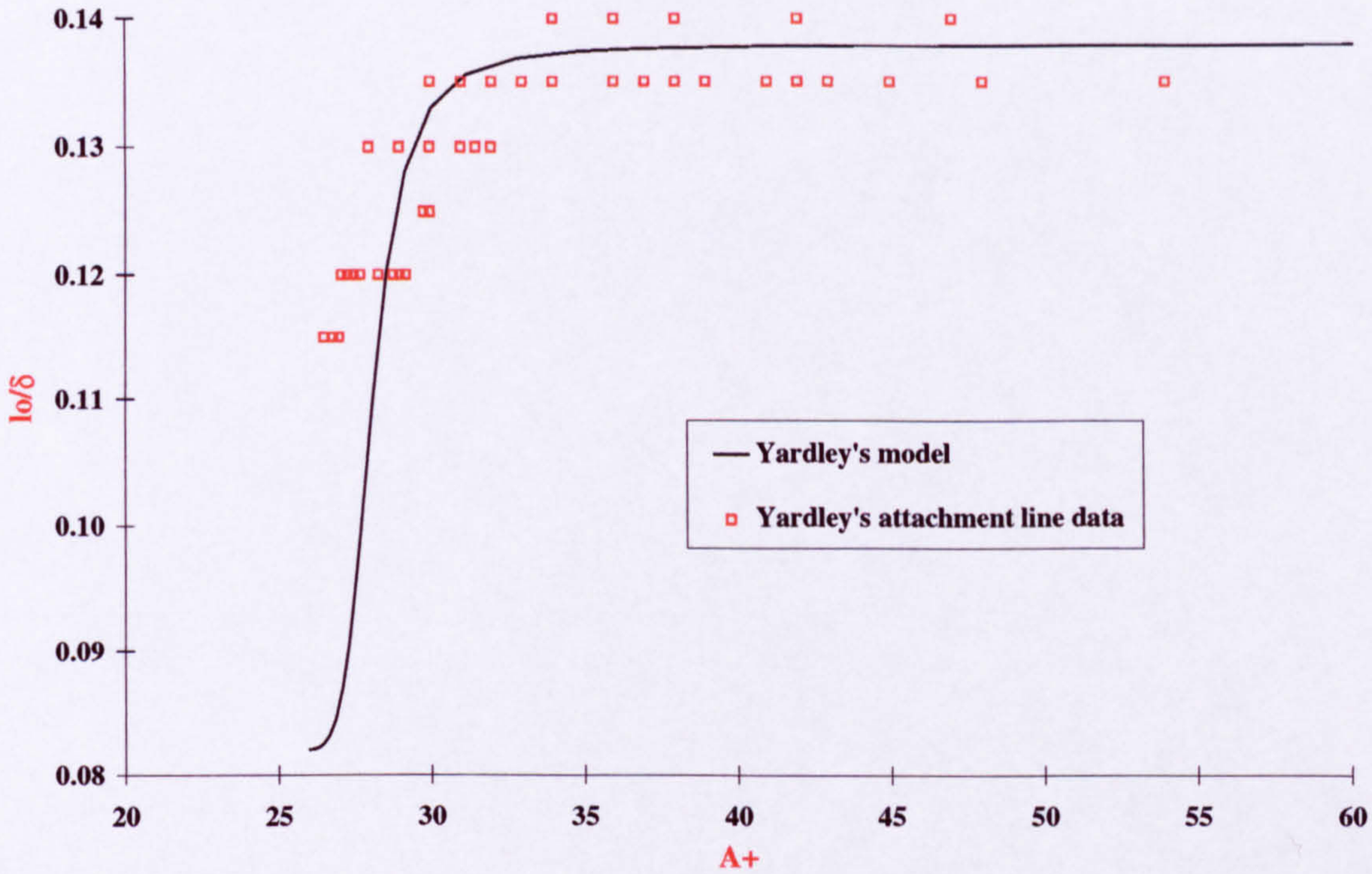

Figure A.58: Variation of the damping factor $\bar{A}^+$ with outer mixing length l_o/δ as obtained by Yardley [65].

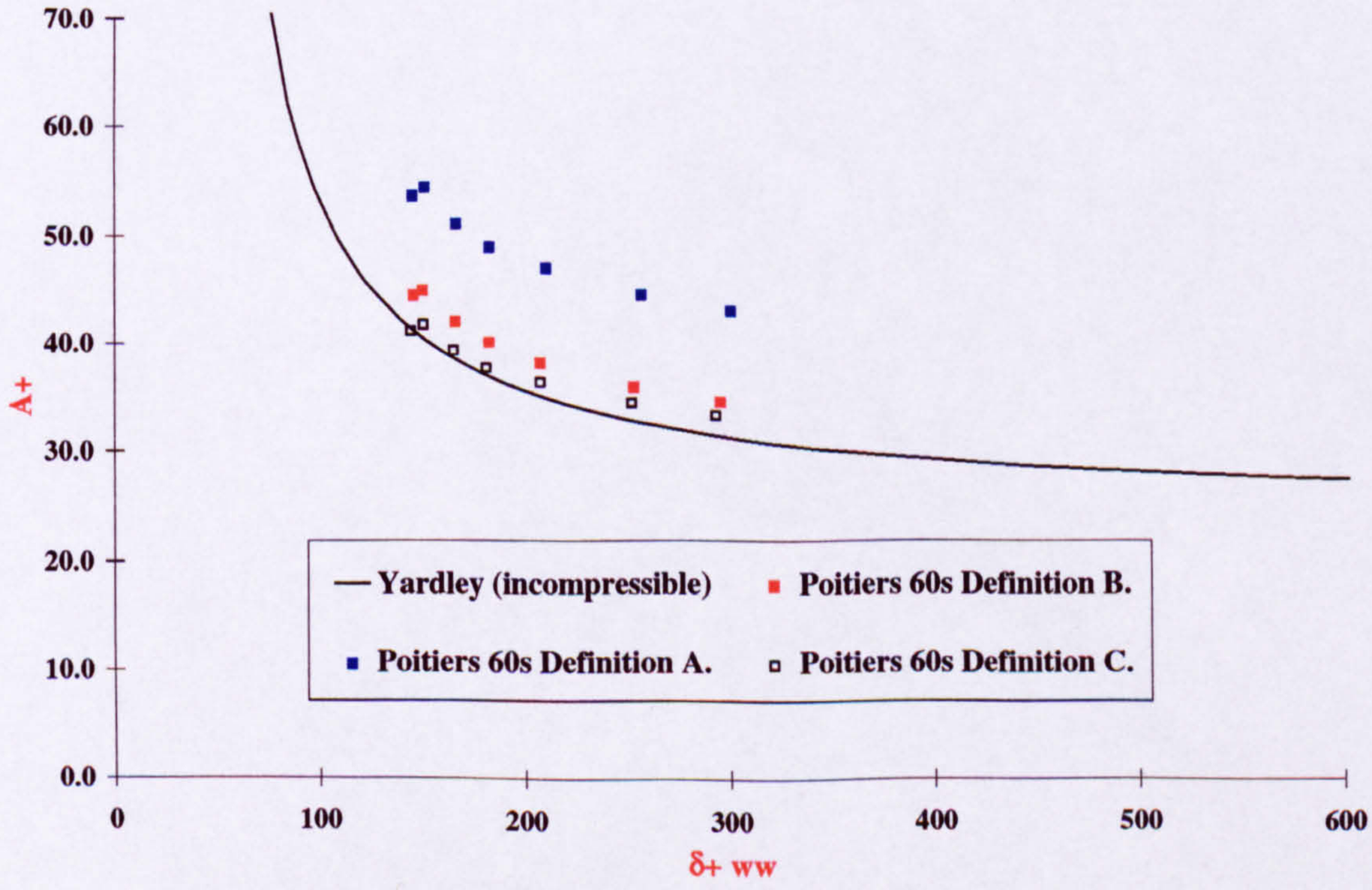

Figure A.59: Effect of the different definitions of $-\frac{Y^+}{A^+}$ upon the damping parameter $\bar{A}^+$ for Poitiers Run60s, $\bar{\Lambda} = 60^o$, $M_{ae} = 3.2$.

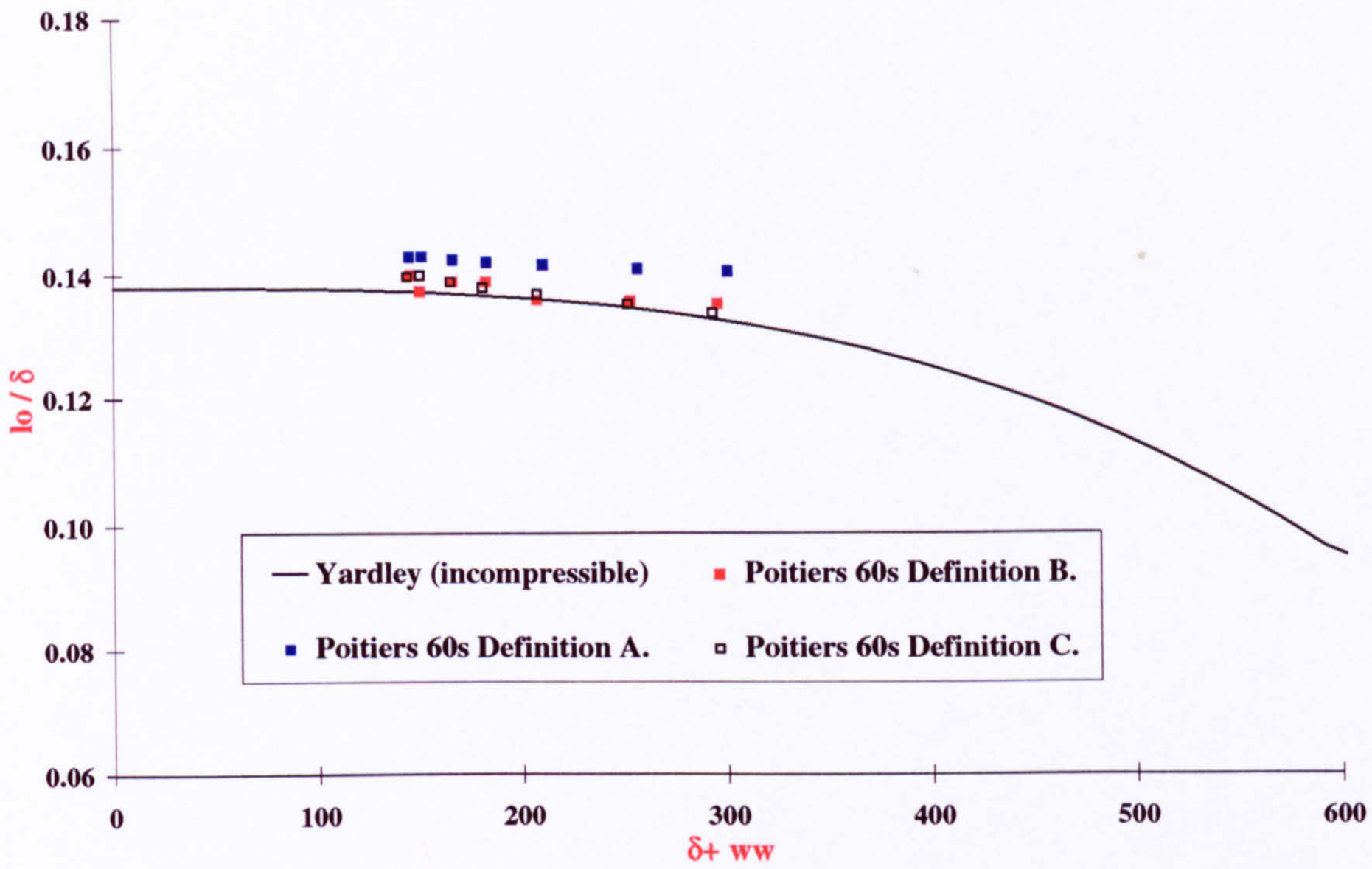

Figure A.60: Effect of the different definitions of $-\frac{Y^+}{A^+}$ upon the outer mixing length l_o/δ for Poitiers Run60s, $\bar{\Lambda} = 60^o$, $M_{ae} = 3.2$.

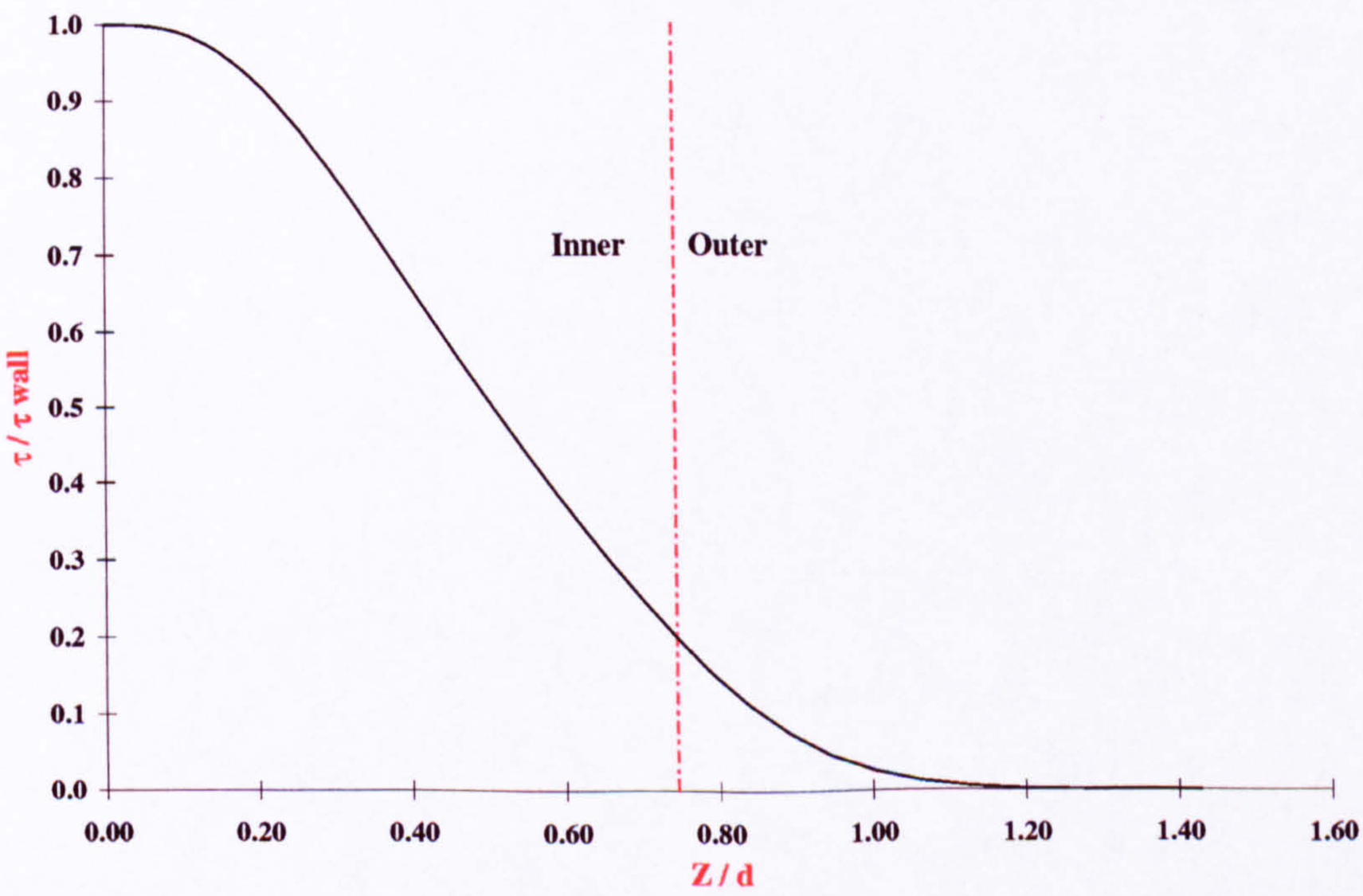

Figure A.61: Variation of the shear stress τ across the viscous layer at low Reynolds number. Incompressible flow, Yardley's [65] turbulence model (equations 4.57 to 4.61. ($\bar{R} = 250$, $M_{ae} = 0.0$, $T_w/T_o = 1.0$, $T_o = 800K$).

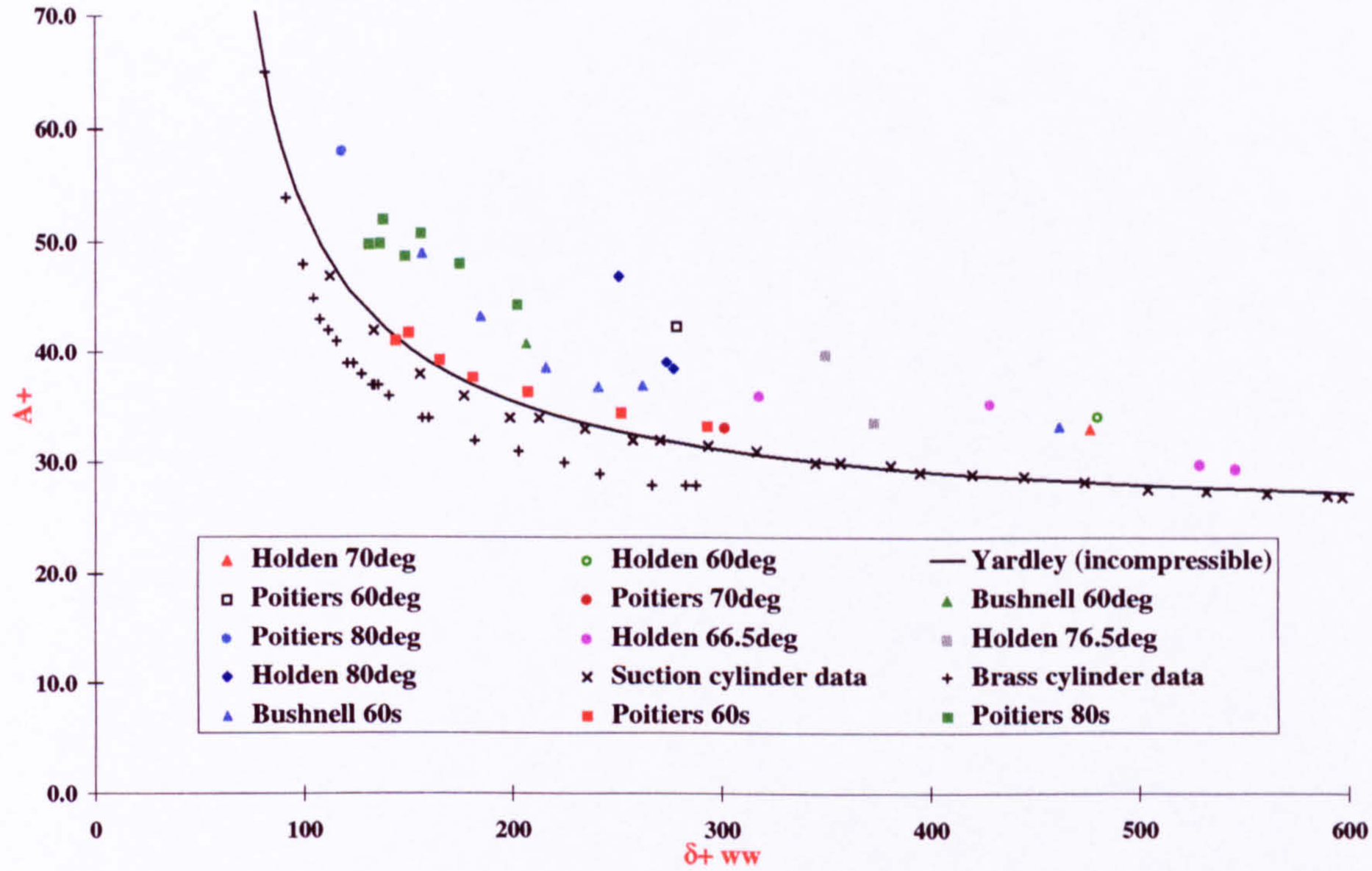

Figure A.62: Variation of the damping parameter A^+ with Reynolds number δ^+_{ww} (see table B.1).

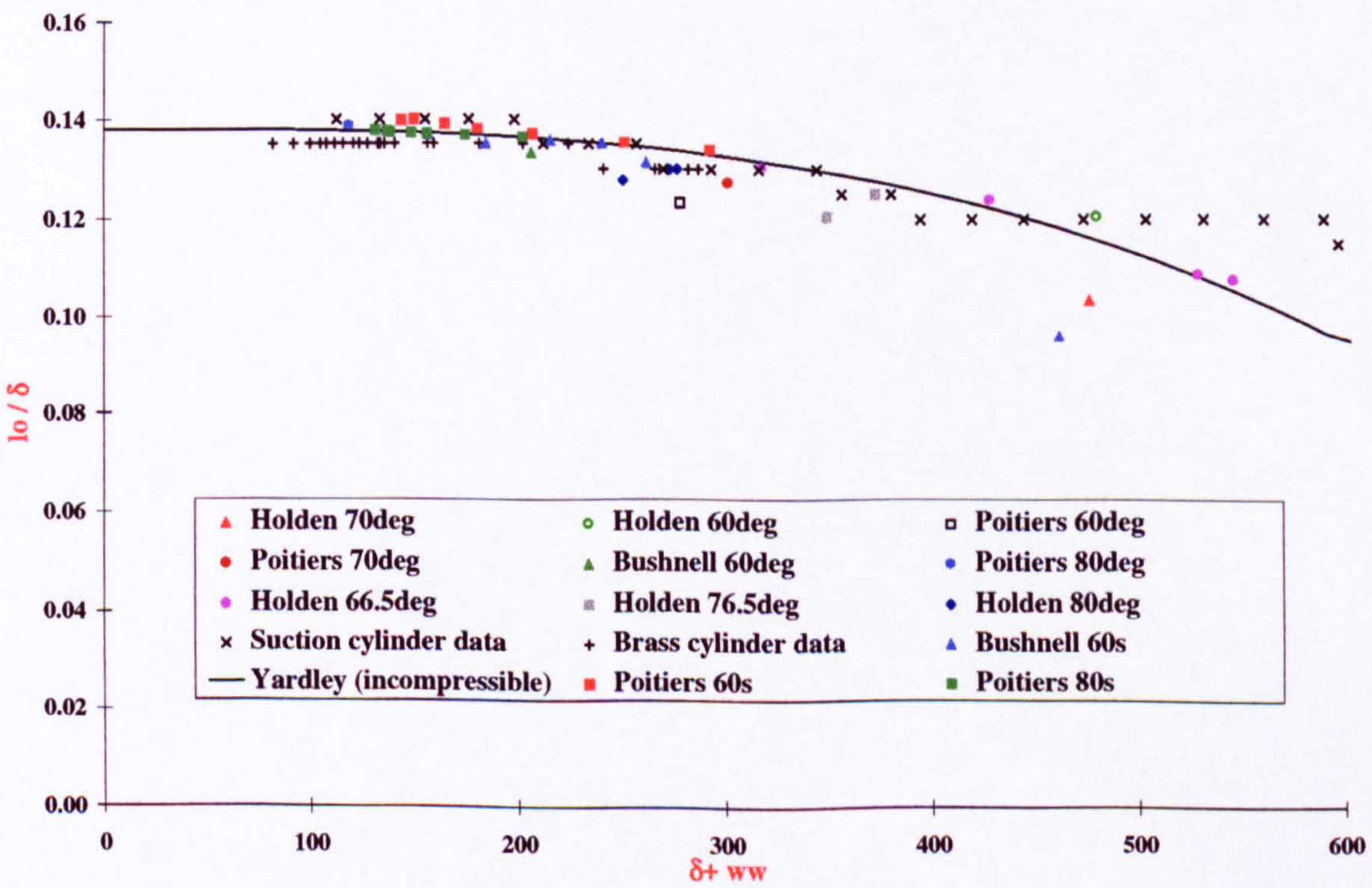

Figure A.63: Variation of the outer mixing length l_o/δ with Reynolds number δ^+_{ww} (see table B.1).

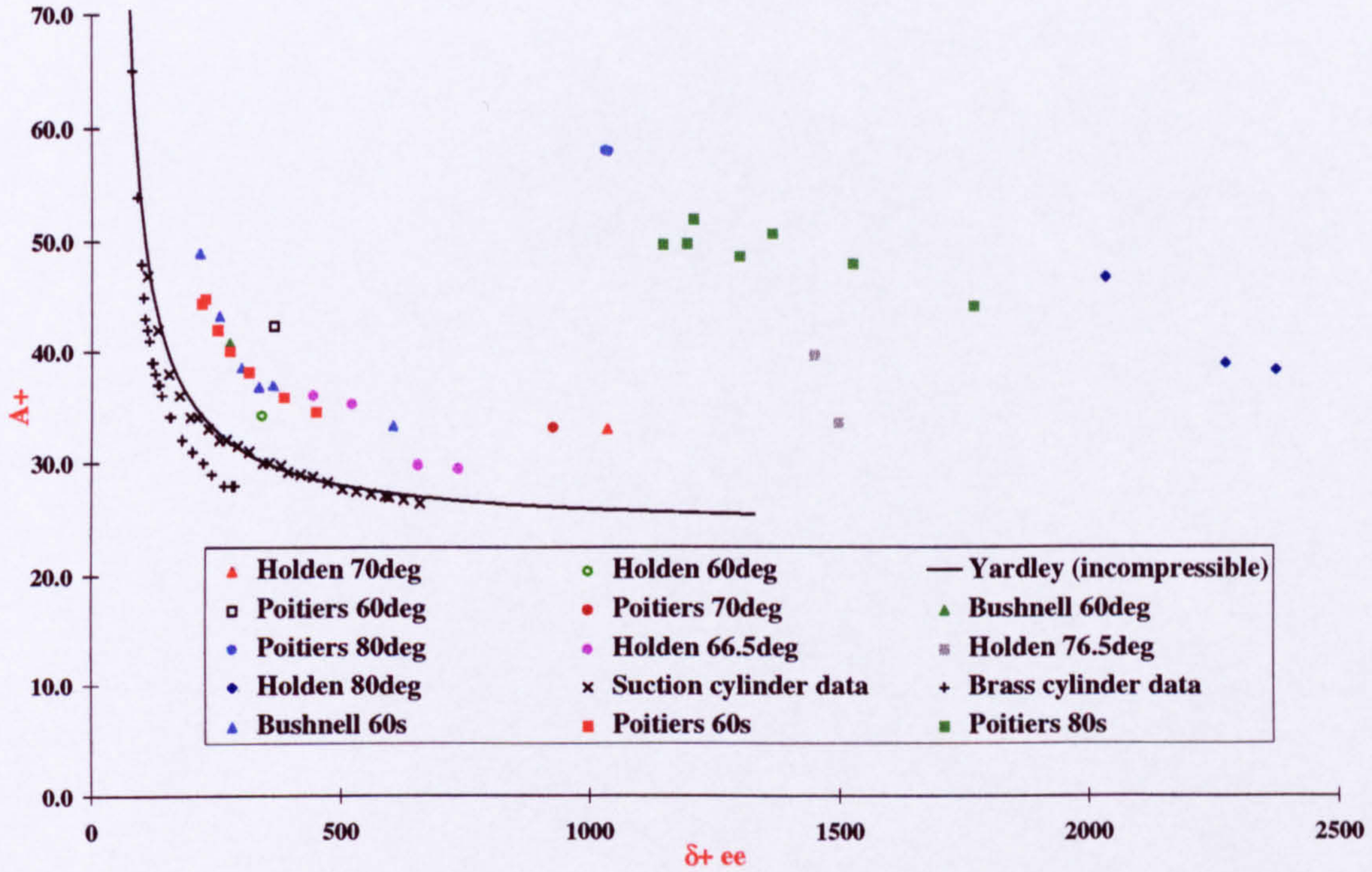

Figure A.64: Variation of the damping parameter A^+ with Reynolds number δ^+_{ee} (see table B.1).

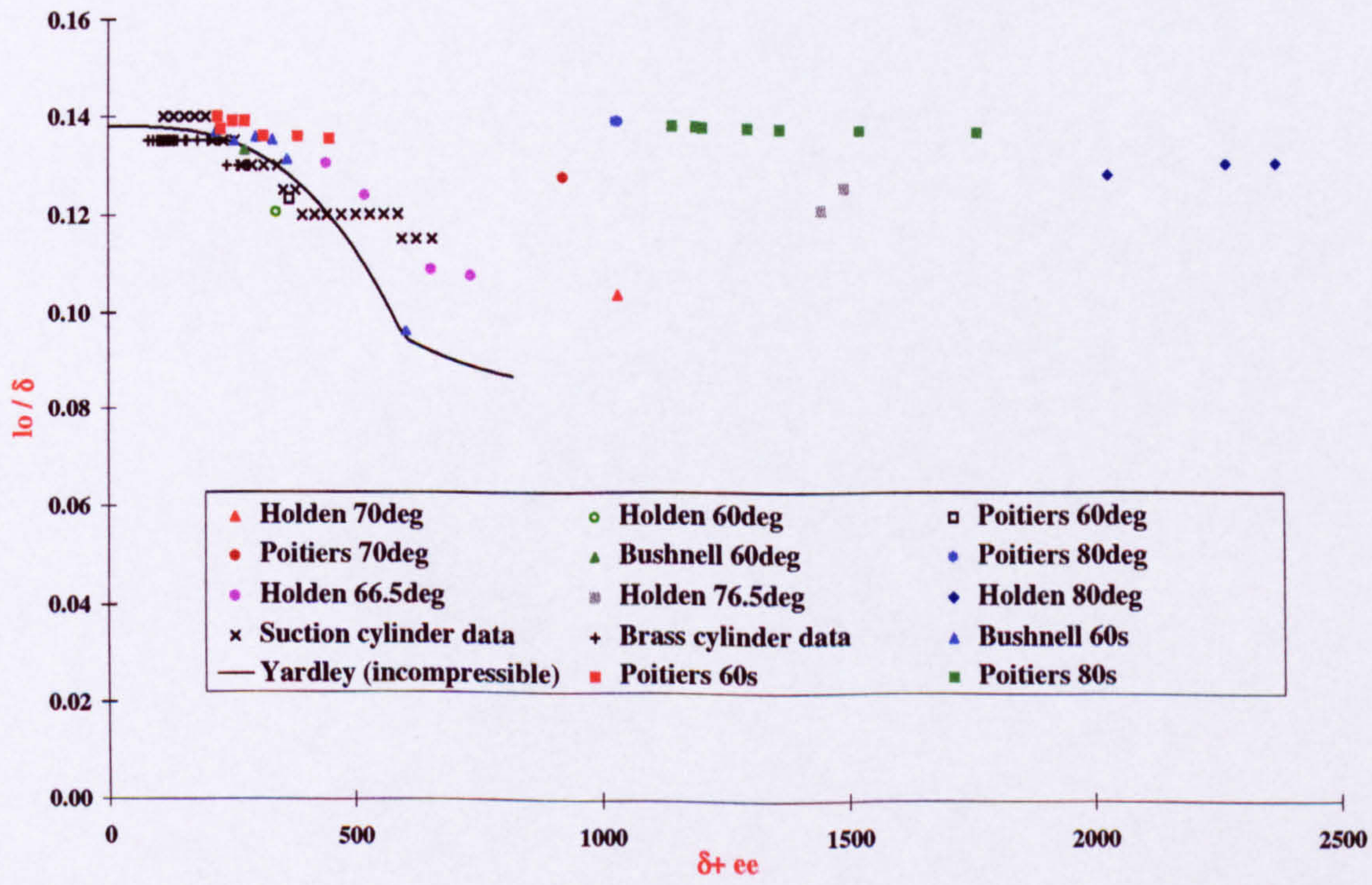

Figure A.65: Variation of the outer mixing length l_o/δ with Reynolds number δ^+_{ee} (see table B.1).

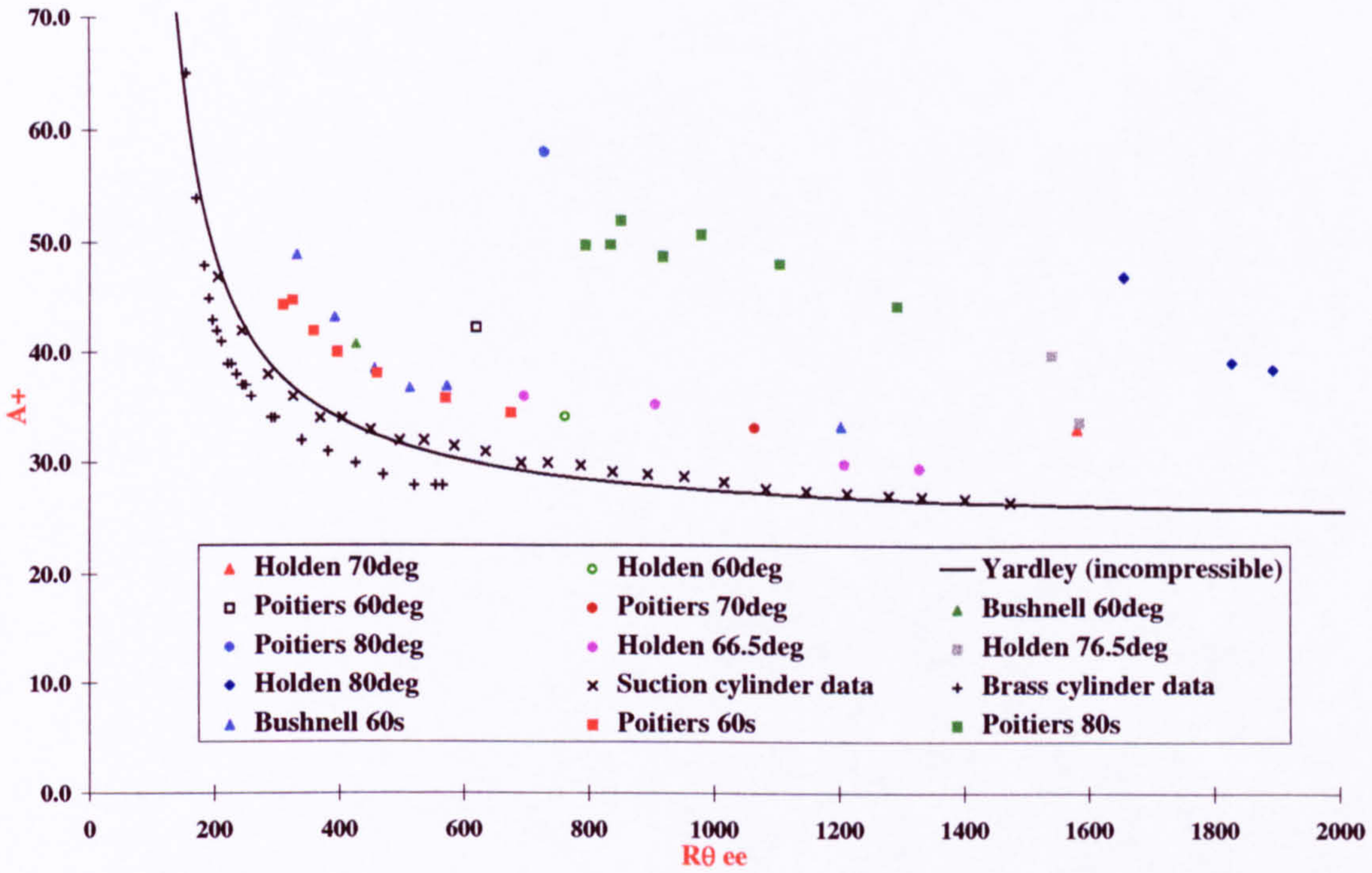

Figure A.66: Variation of the damping parameter A^+ with Reynolds number $R_{\theta ee}$ (see table B.1).

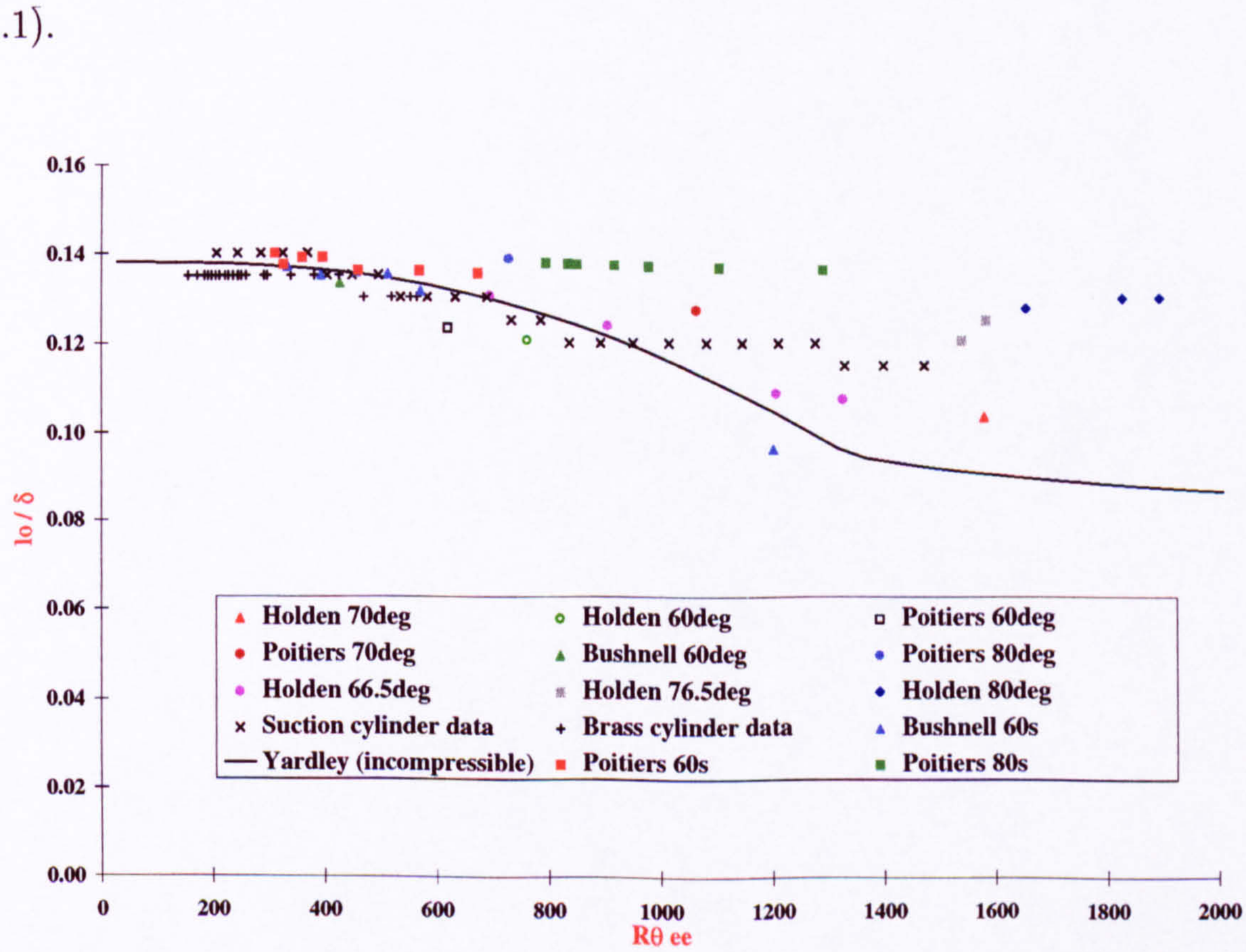

Figure A.67: Variation of the outer mixing length l_o/δ with Reynolds number $R_{\theta ee}$ (see table B.1).

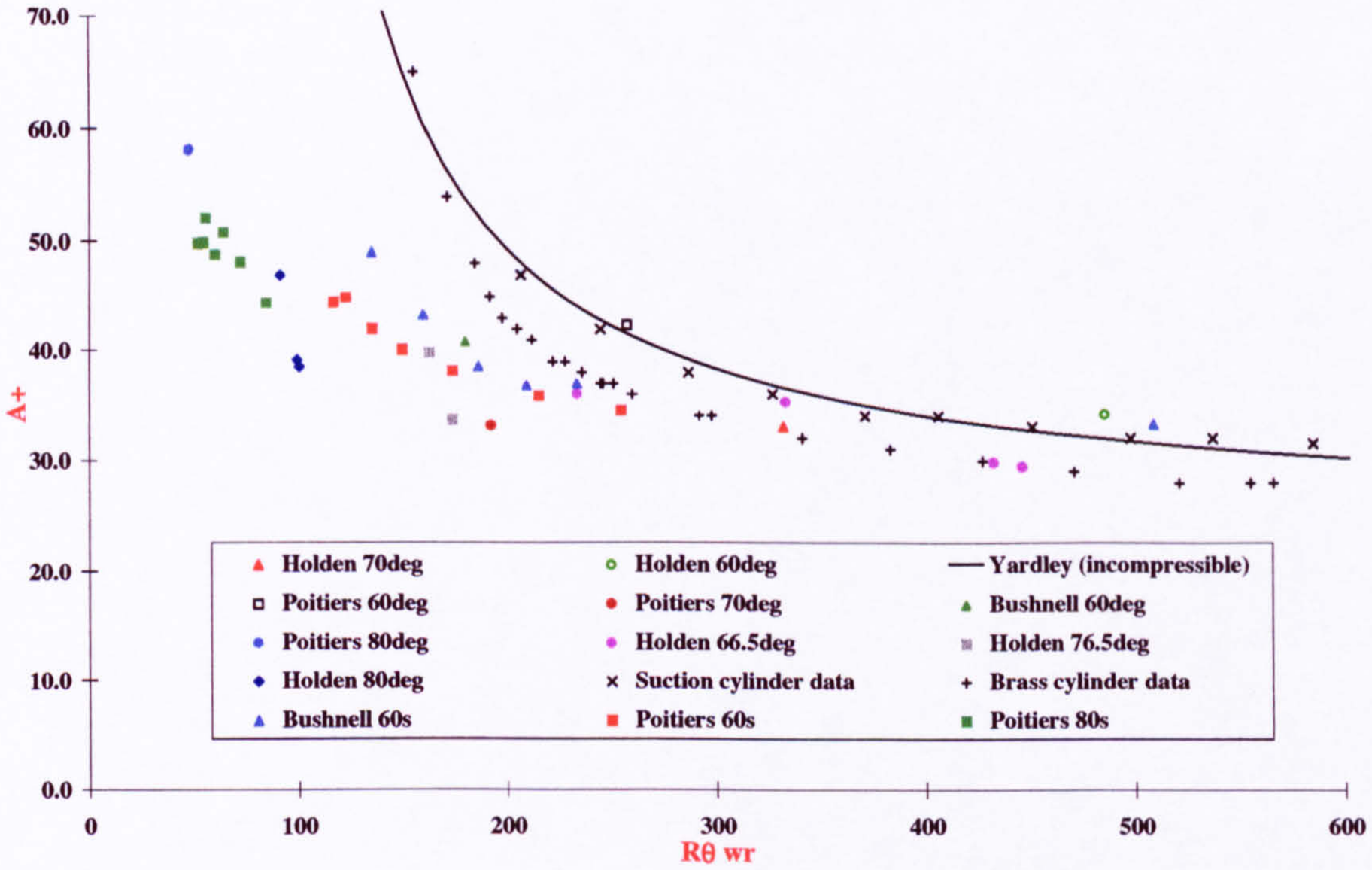

Figure A.68: Variation of the damping parameter A^+ with Reynolds number $R_{\theta wr}$ (see table B.1).

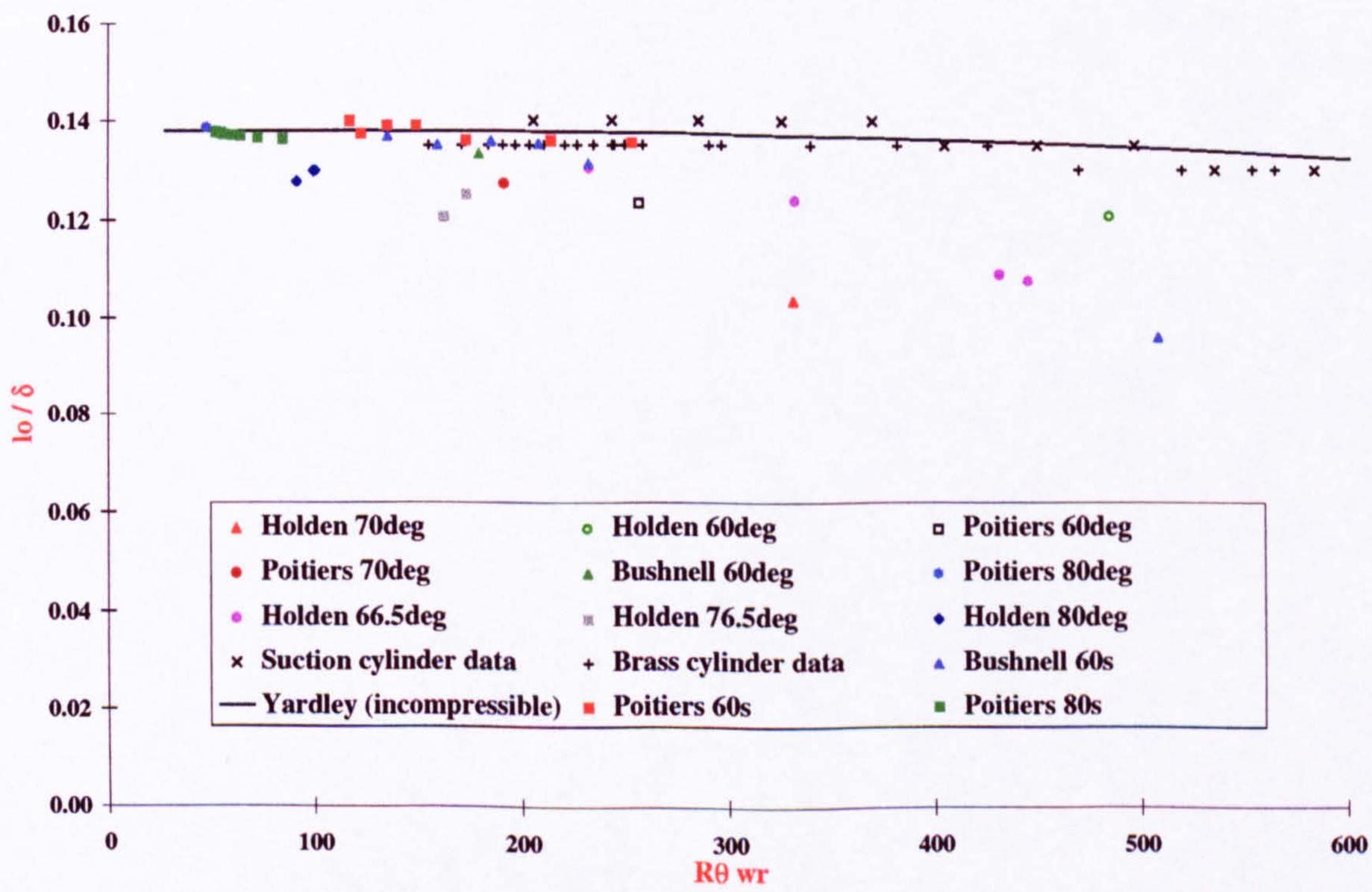

Figure A.69: Variation of the outer mixing length l_o/δ with Reynolds number $R_{\theta wr}$ (see table B.1).

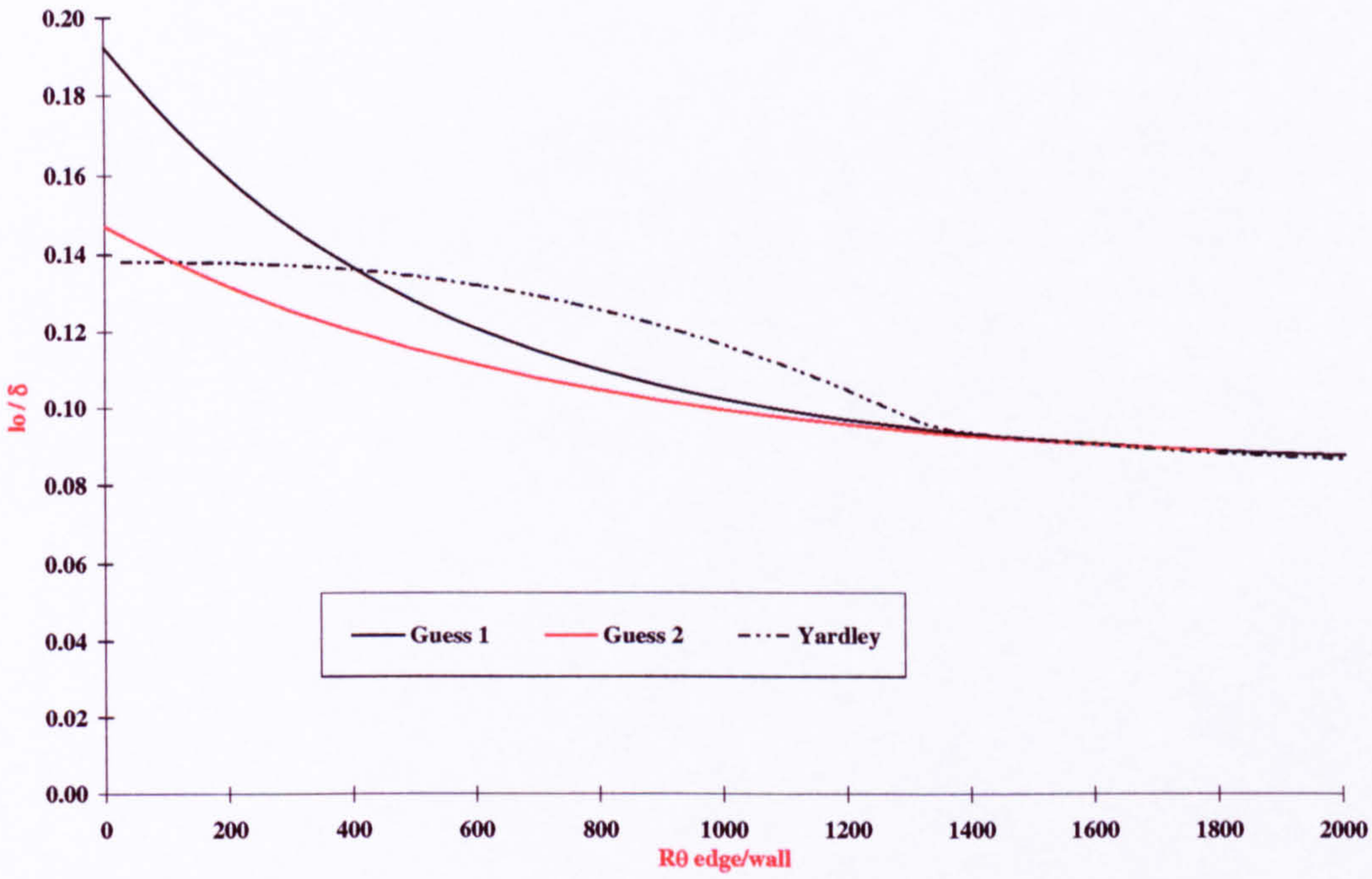

Figure A.70: Guessed variations of the outer mixing length with Reynolds number $R_{\theta ew}$ for incompressible equilibrium boundary layers.

Figure A.71: Typical velocity profile in an incompressible low Reynolds number boundary layer. Yardley's model [65] ; equations 4.57 to 4.61. ($\bar{R} = 300$, $M_{ae} = 0.0$, $T_w/T_o = 1.0$, $T_o = 350K$).

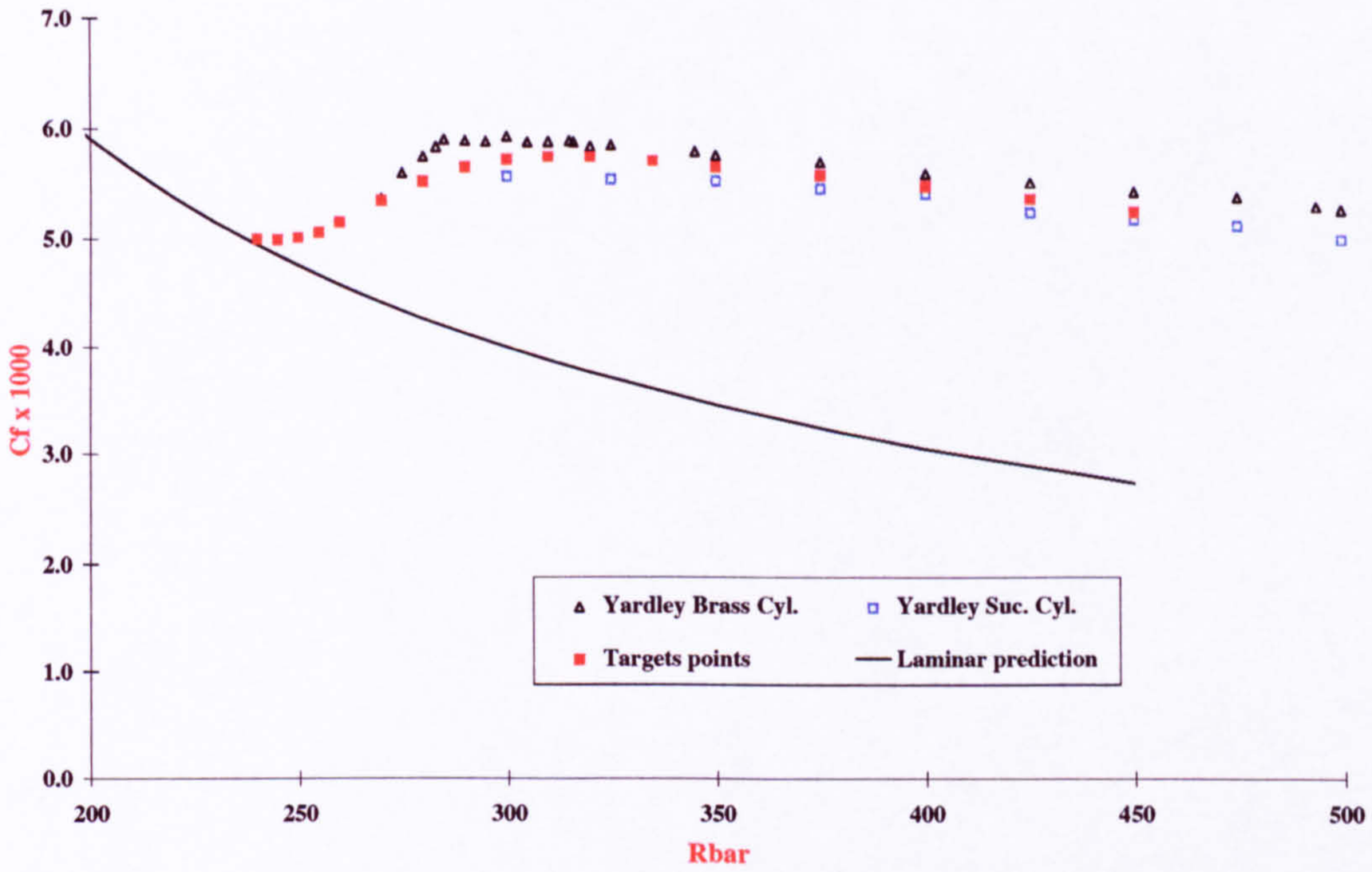

Figure A.72: Incompressible skin friction target points vs attachment-line Reynolds number $\bar{R}$.

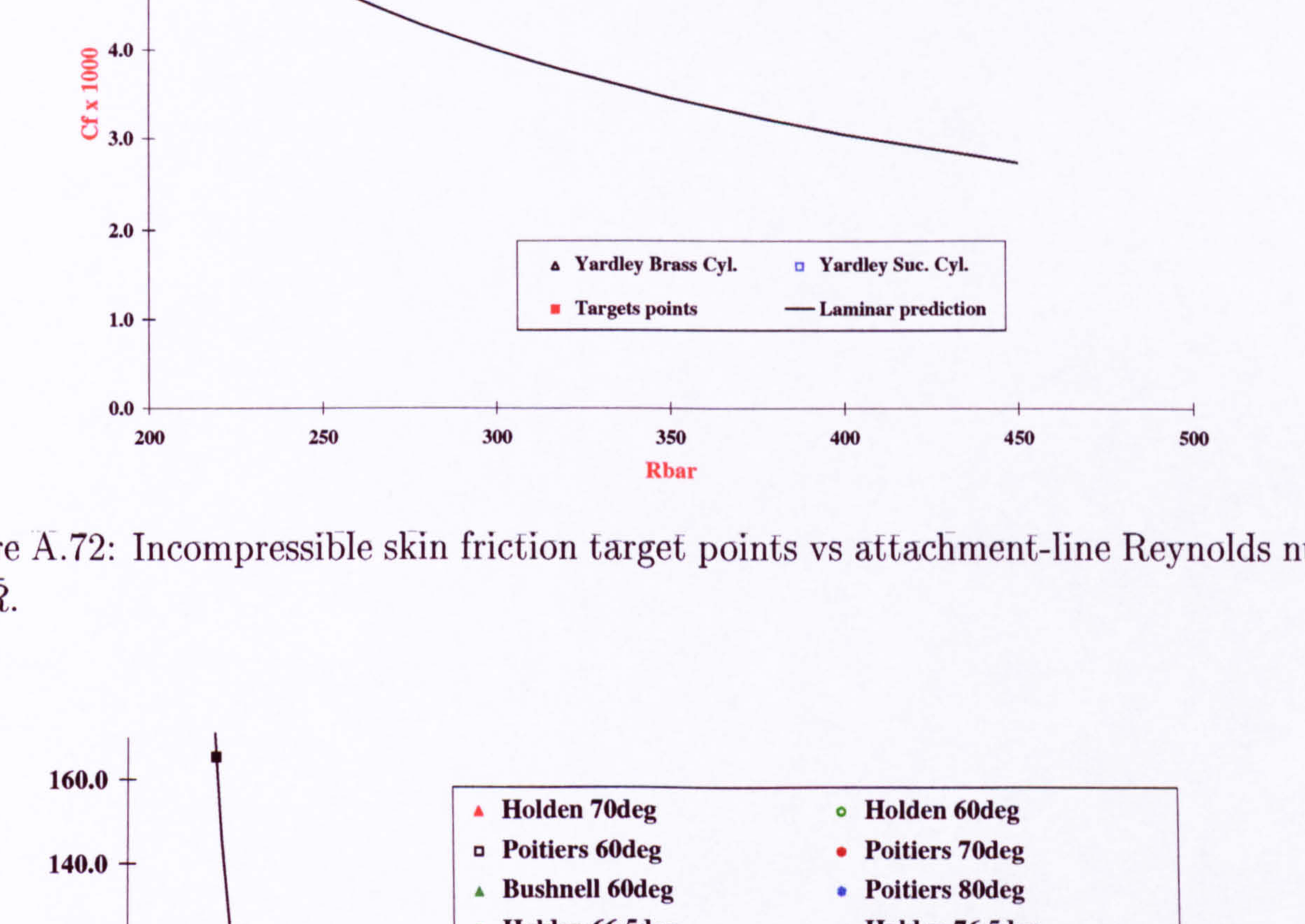

Figure A.73: Variation of the Damping parameter with Reynolds number δ^+_{ww}.

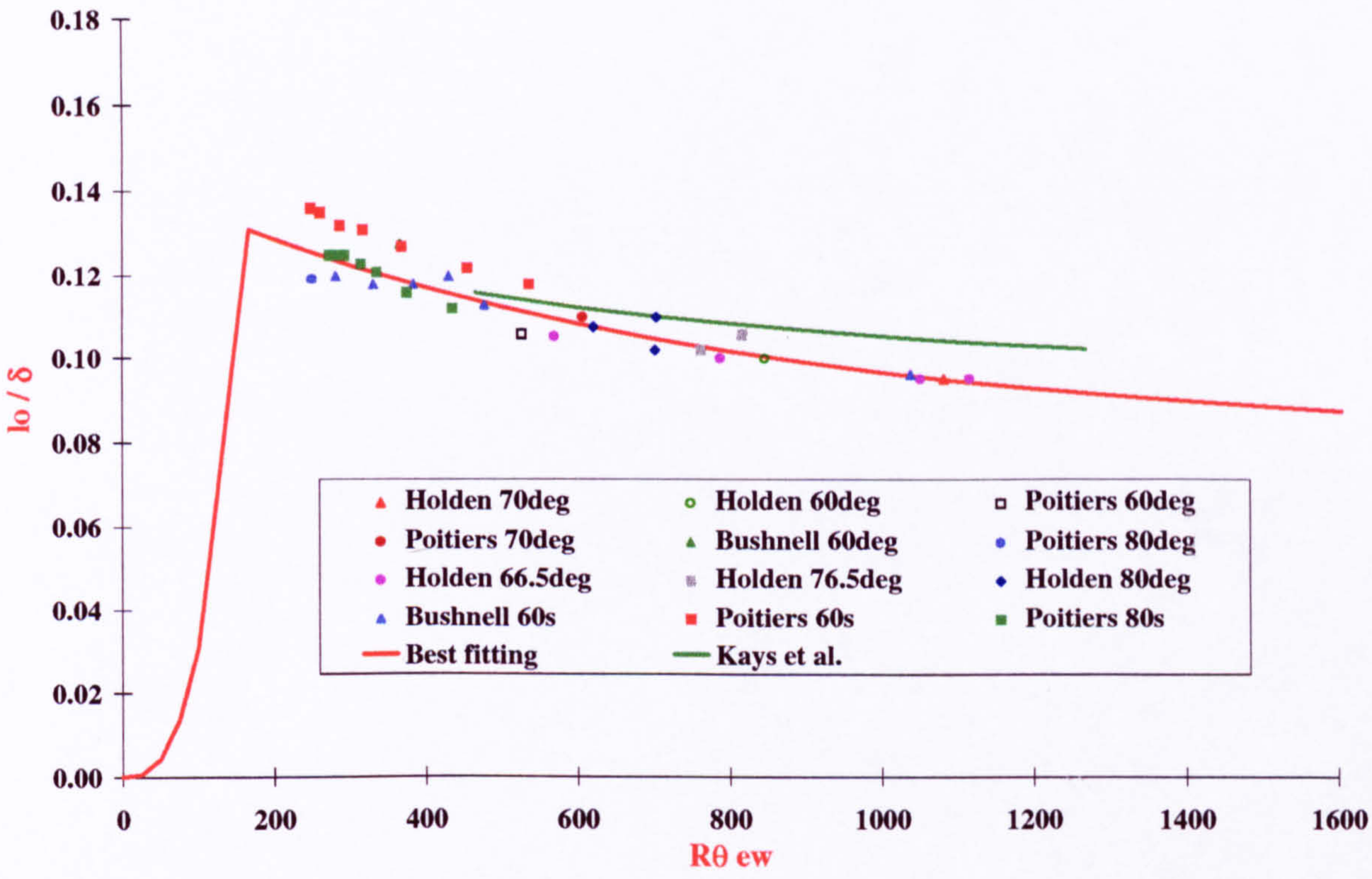

Figure A.74: Variation of the outer mixing length l_o/δ with Reynolds number $R_{\theta ew}$.

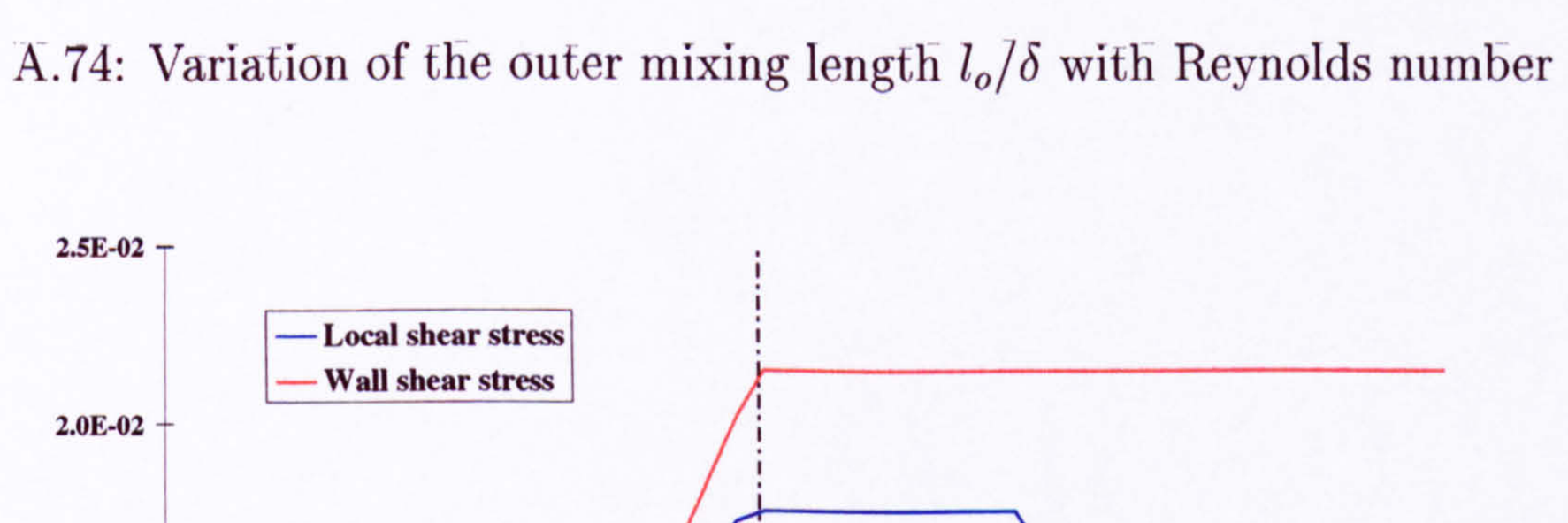

Figure A.75: Variation of the mixing length across the viscous layer using the wall shear stress and the local shear stress. $A^+ = 26$, $l_o/\delta = 0.08$ ($\bar{R} = 415$, $M_{ae} = 3.0$, $T_w/T_o = 0.5$, $T_o = 800K$).

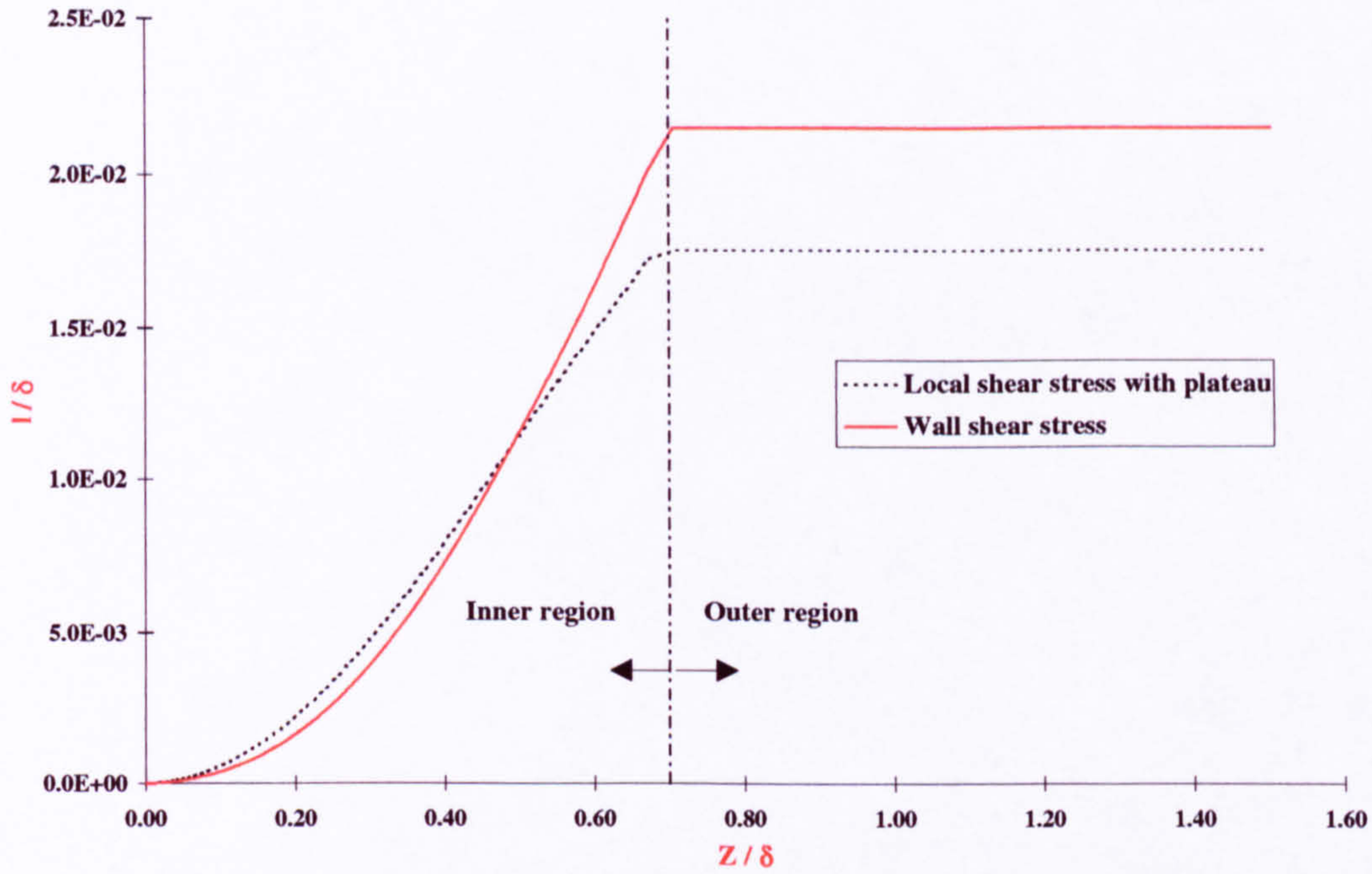

Figure A.76: Variation of the mixing length across the viscous layer using the wall shear stress and the local shear stress by creating a plateau from the maximum value of the outer mixing length. $A^+ = 26$, $l_o/\delta = 0.08$ ($\bar{R} = 415$, $M_{ae} = 3.0$, $T_w/T_o = 0.5$, $T_o = 800K$).

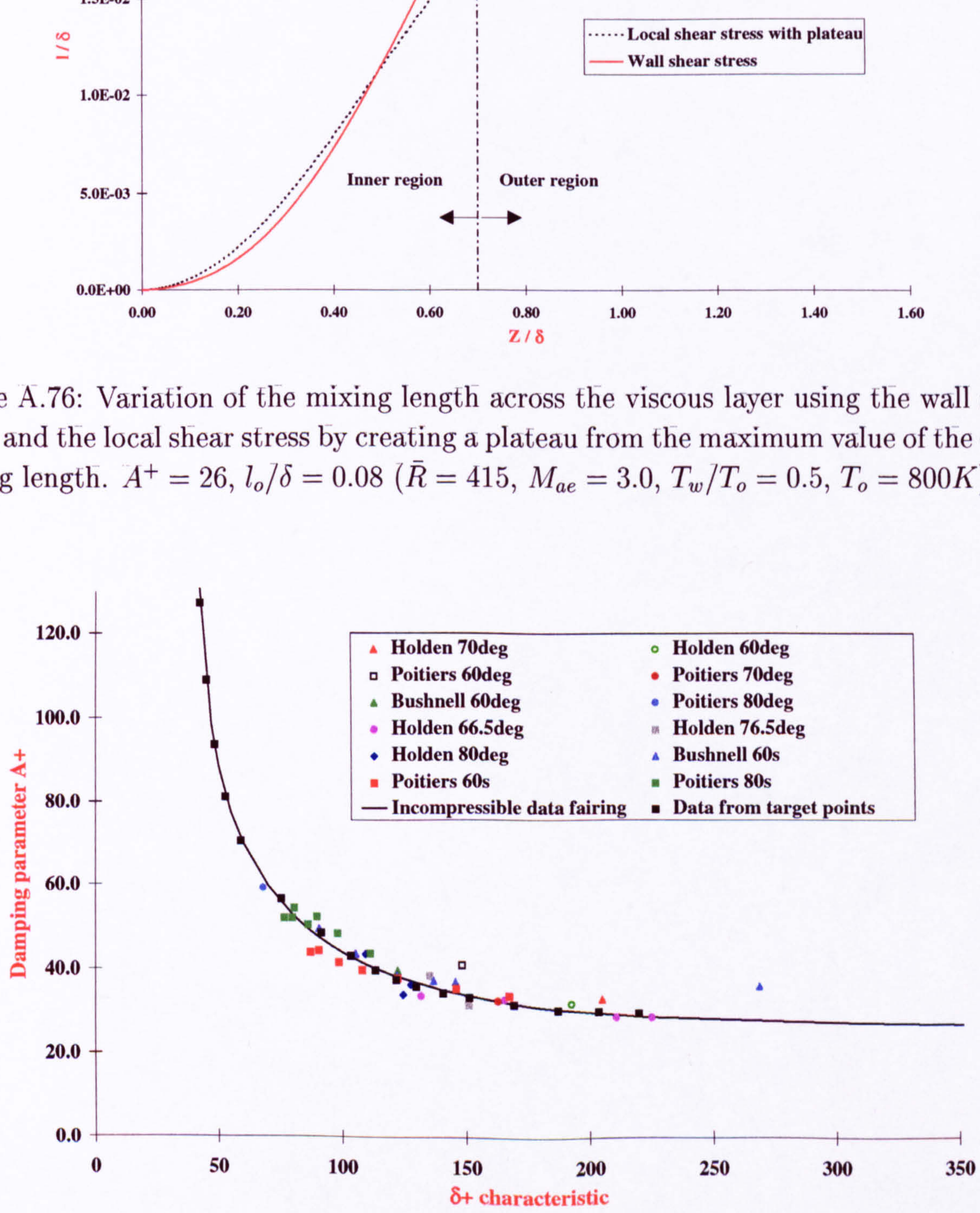

Figure A.77: Variation of the damping parameter A^+ (equation 5.3) with Reynolds number δ_c^+ for equilibrium flow.

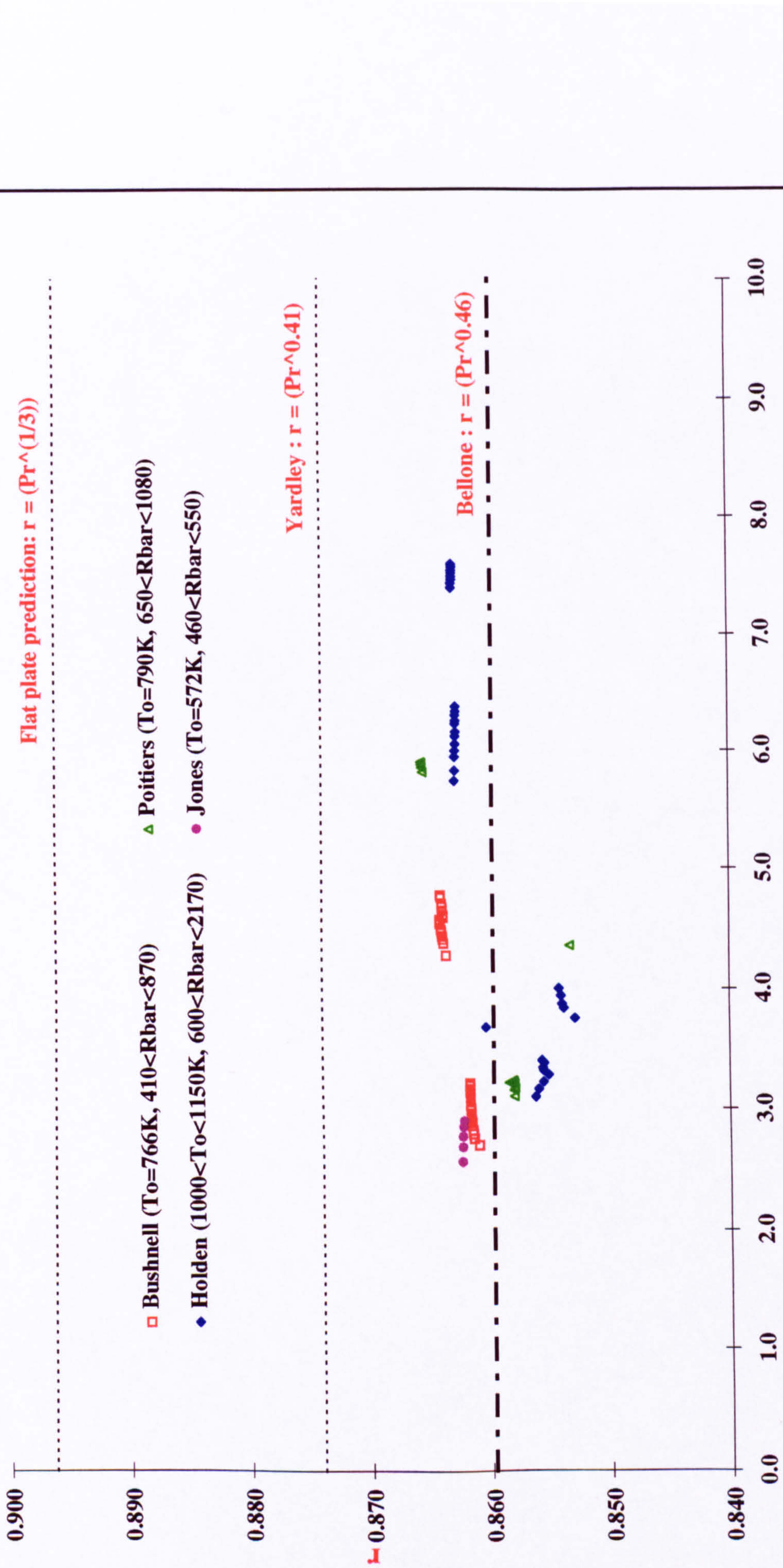

Figure A.78: Variation of the turbulent recovery factor with edge Mach number for a wide range of $\bar{R}$ and stagnation temperatures as predicted by the present turbulence model. (Air, $Pr = 0.72$, $Pr_t = 0.9$, $\gamma = 1.4$).

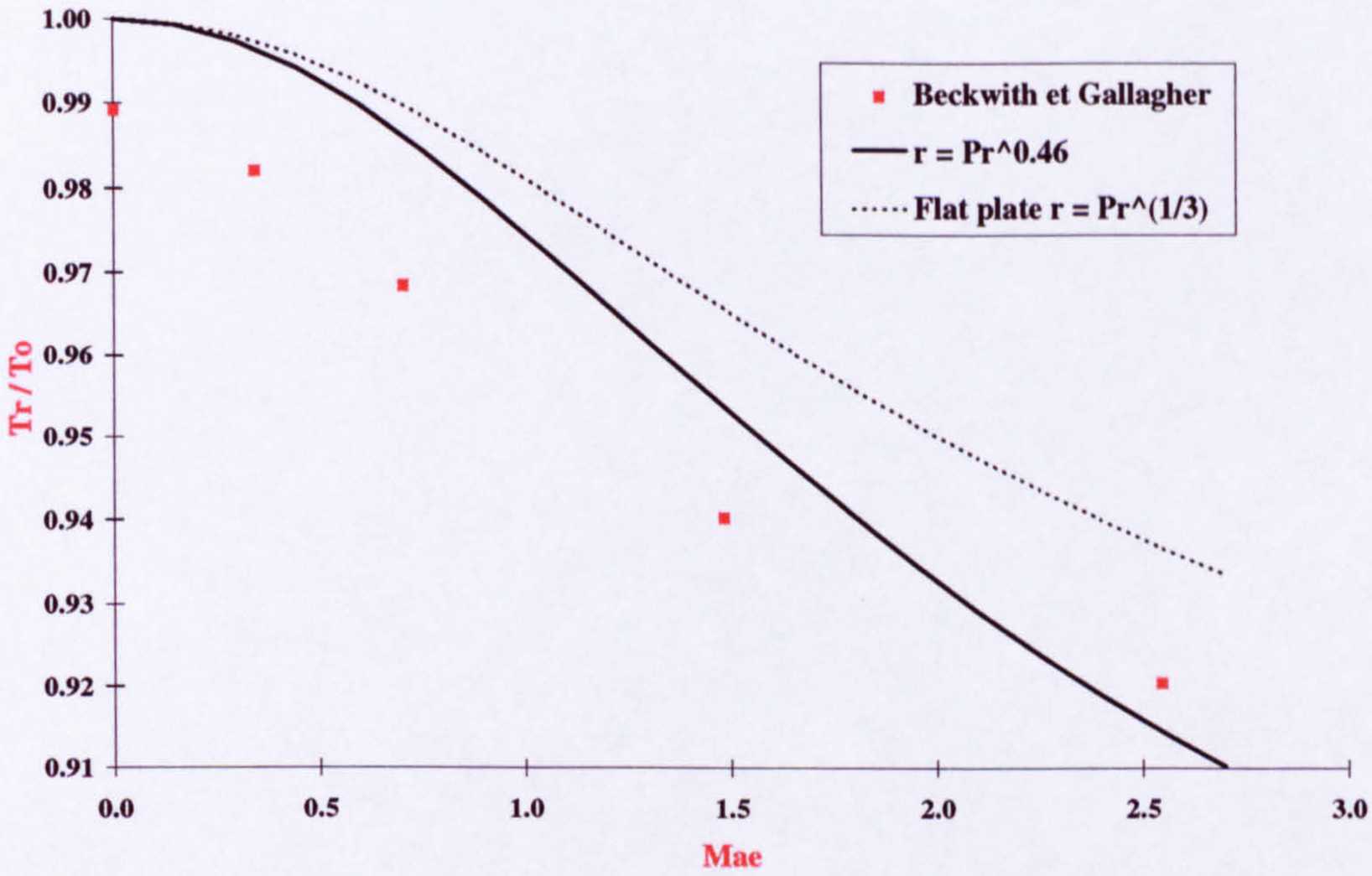

Figure A.79: Variation of the recovery to stagnation temperature ratio with edge Mach number as estimated by Beckwith and Gallagher [5].

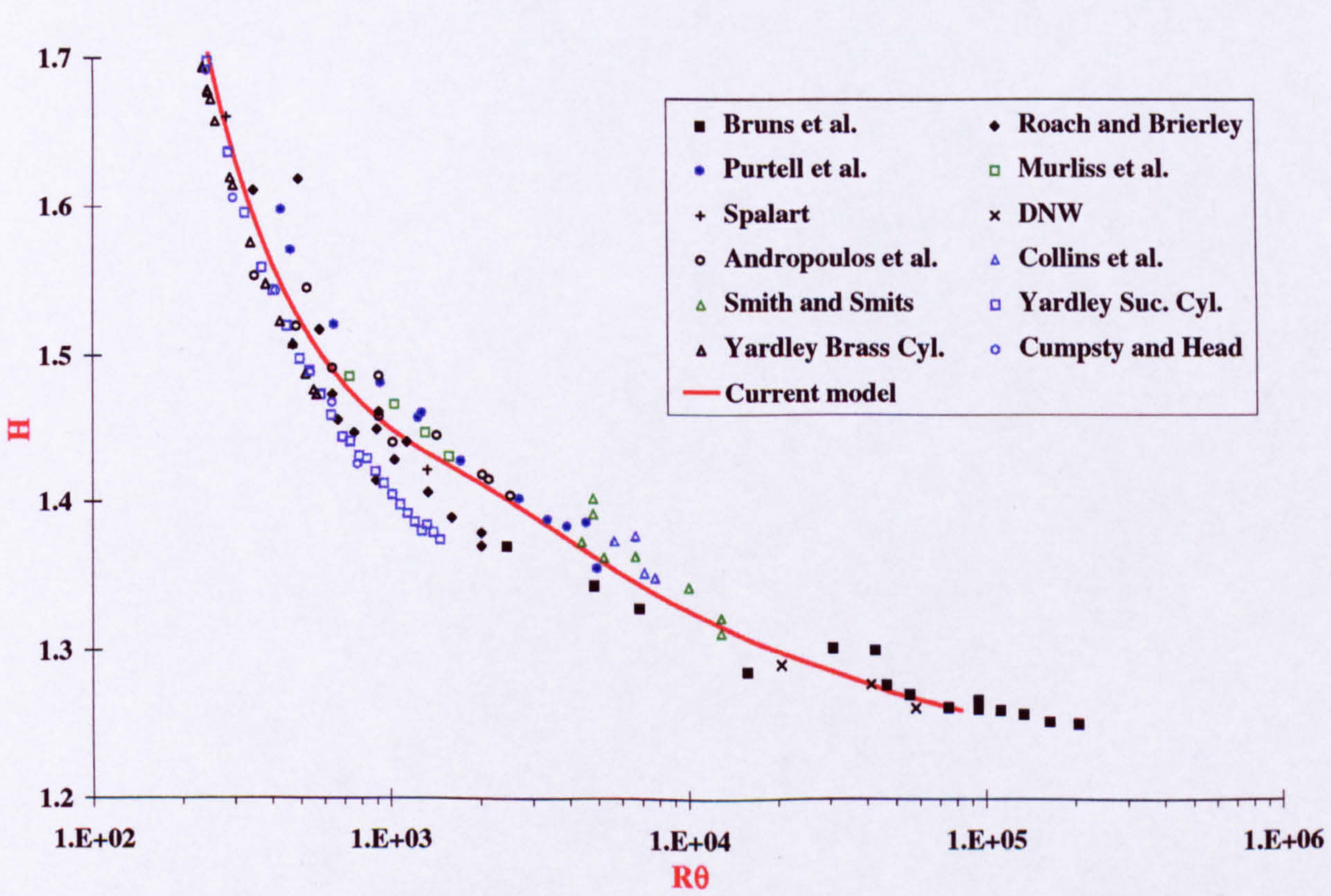

Figure A.80: Variation of the shape factor for incompressible flows. Experimental data from reference [29].

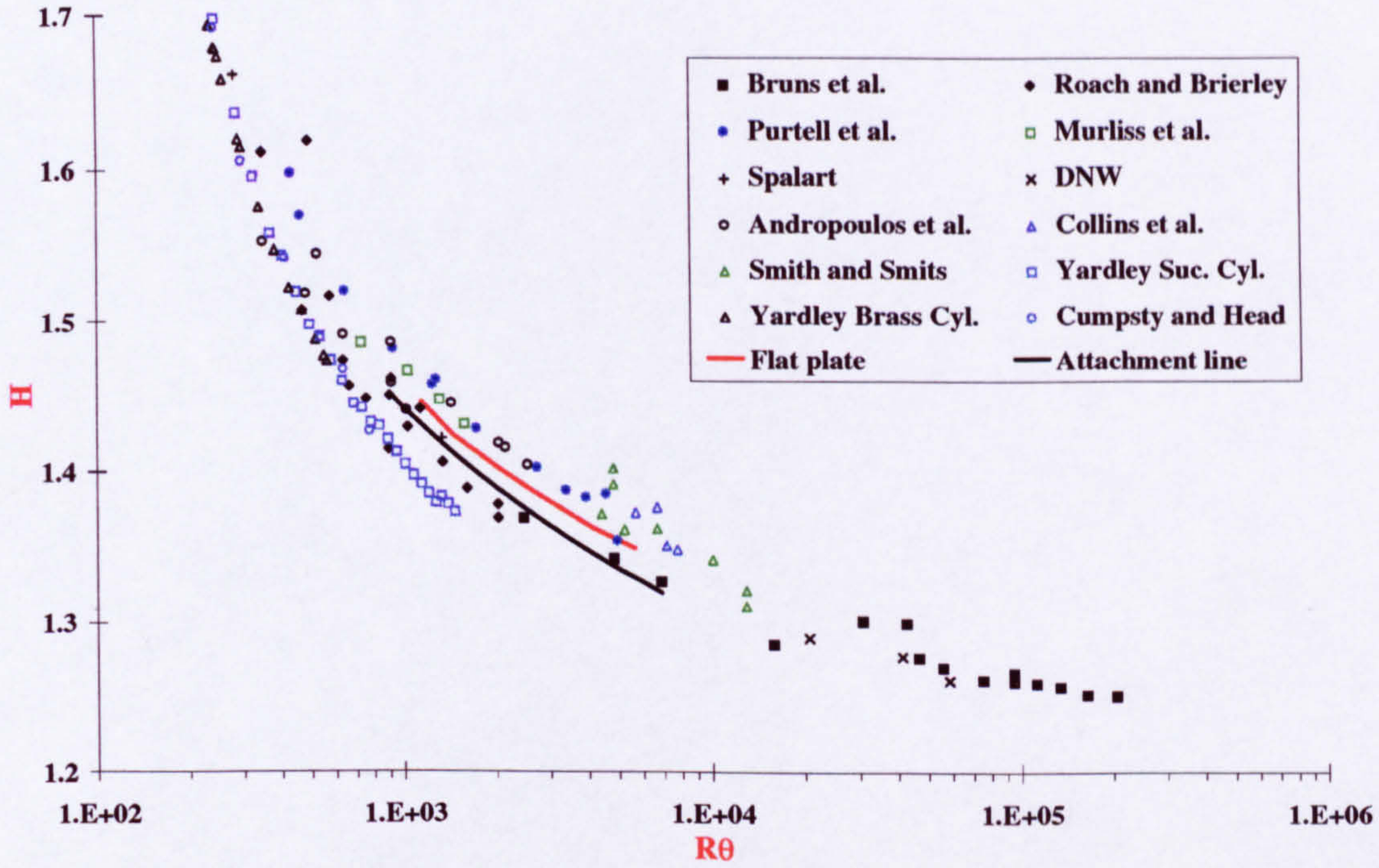

Figure A.81: Variation of the shape factor for incompressible flows. Predictions from Cebeci's turbulence model [18] (equations 4.50 to 4.52, k_1 varying) used for flat plate and attachment- line flows. Experimental data from reference [29].

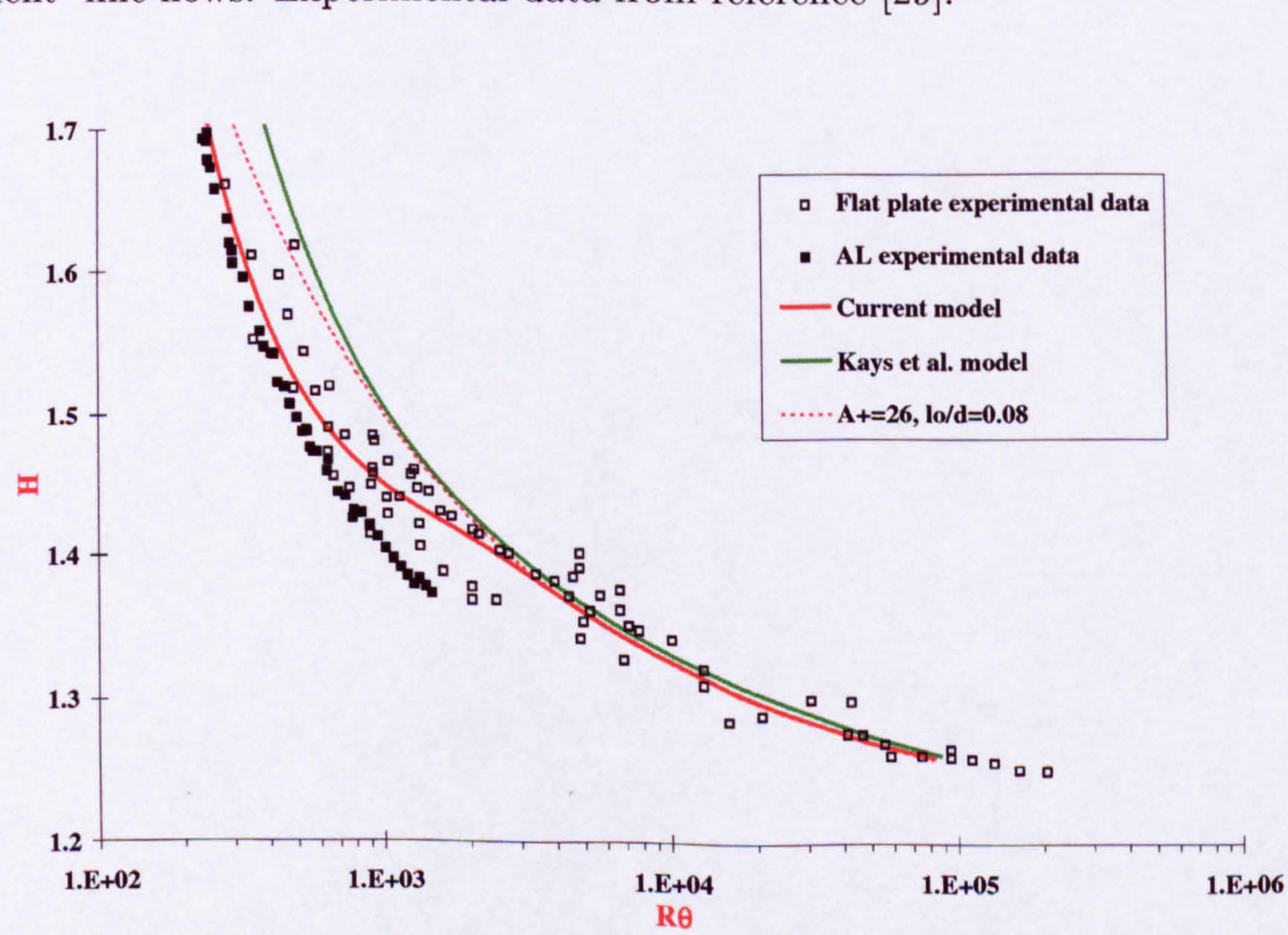

Figure A.82: Variation of the shape factor for incompressible flows. Predictions from Kays et al. turbulence model [42] (equations 4.30 to 4.34) and high Reynolds number model ($A^+ = 26$ and $l_o/\delta = 0.08$). Experimental data from reference [29].

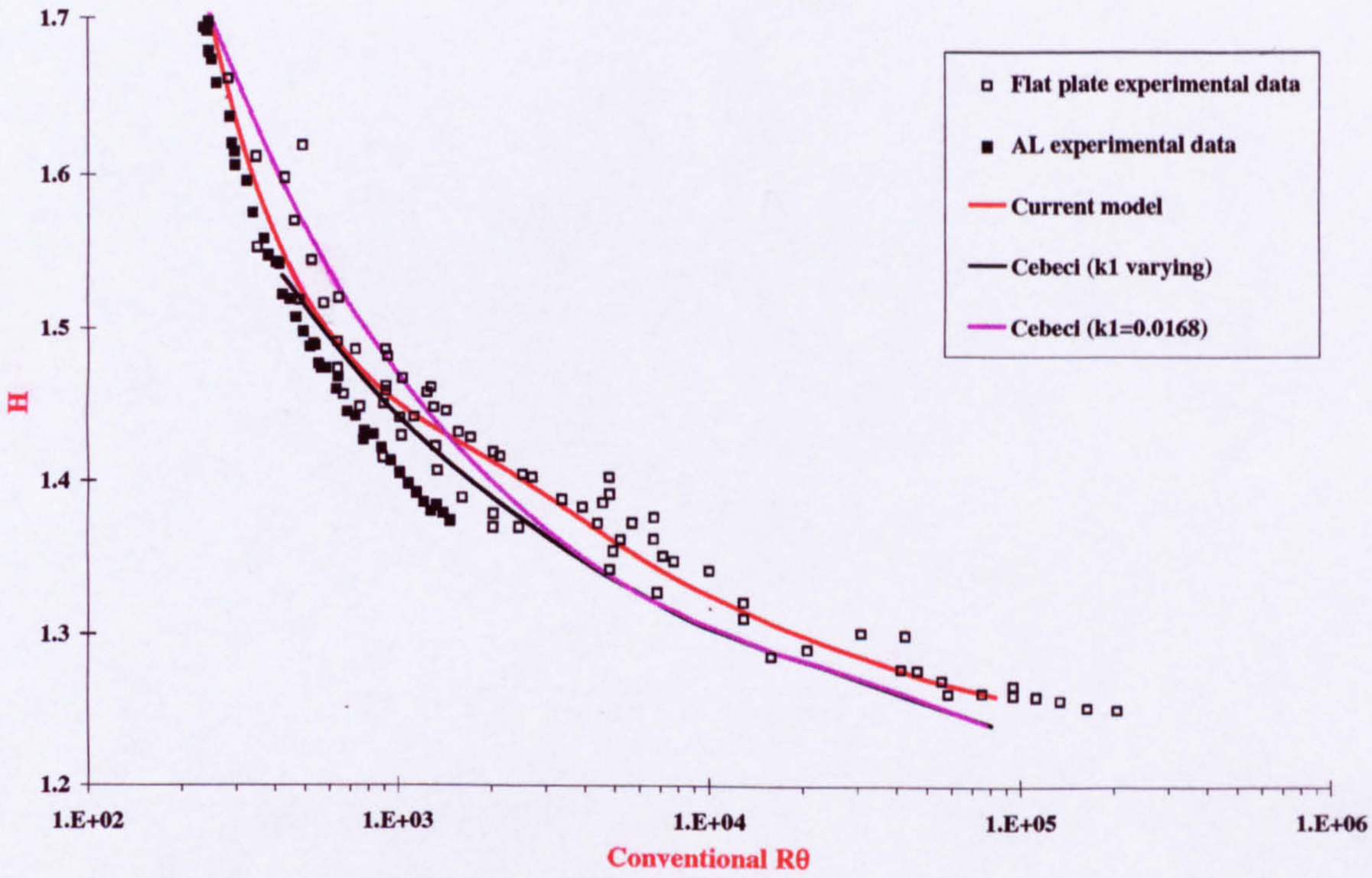

Figure A.83: Variation of the shape factor for incompressible flows. Predictions from Cebeci's turbulence model [18] (equations 4.50 to 4.52) k_1 fixed and varying. Experimental data from reference [29].

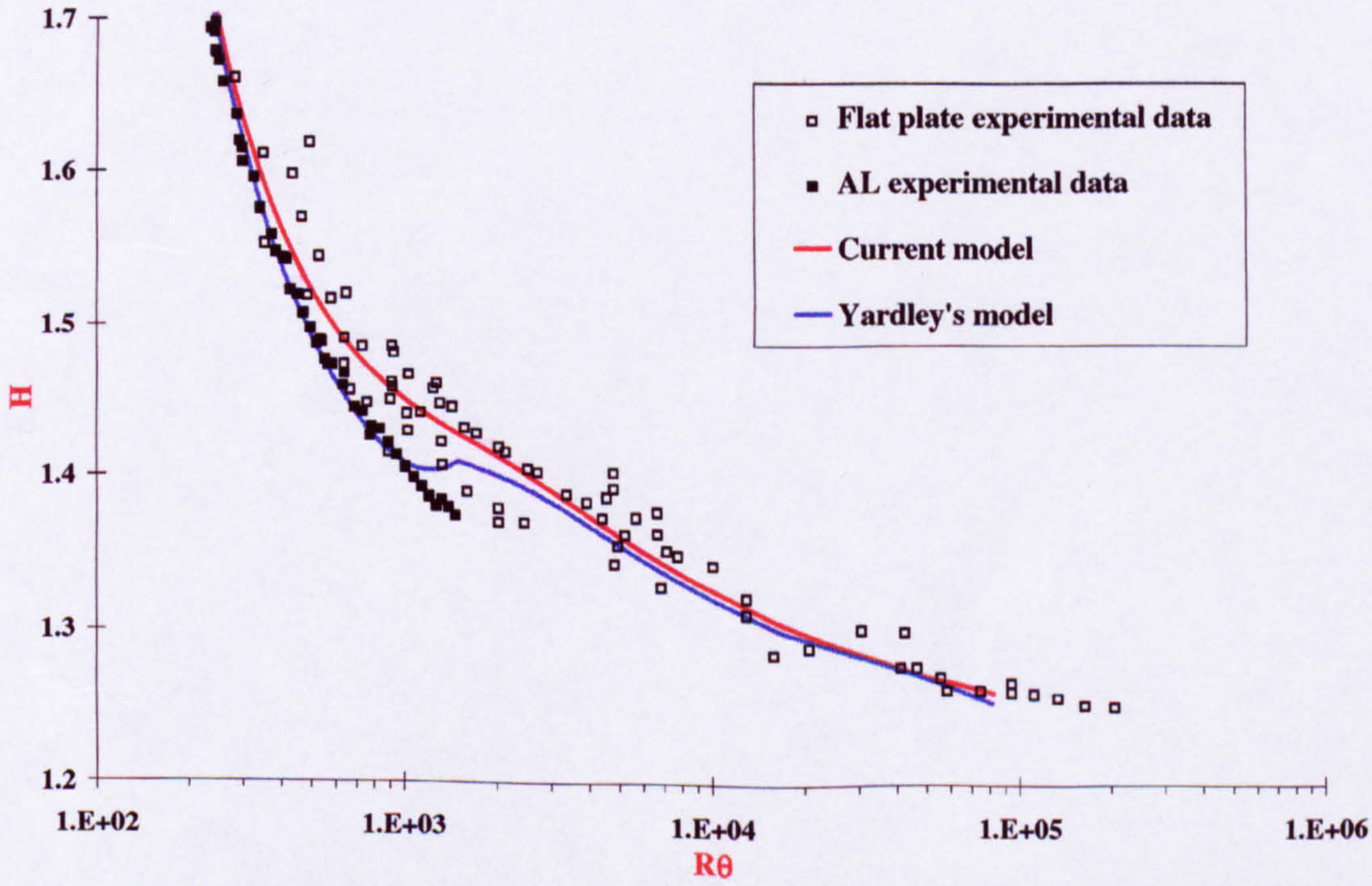

Figure A.84: Variation of the shape factor for incompressible flows. Predictions from Yardley's turbulence model [65] (equations 4.57 to 4.61) and from the current model (equations 5.8 to 5.11). Experimental data from reference [29].

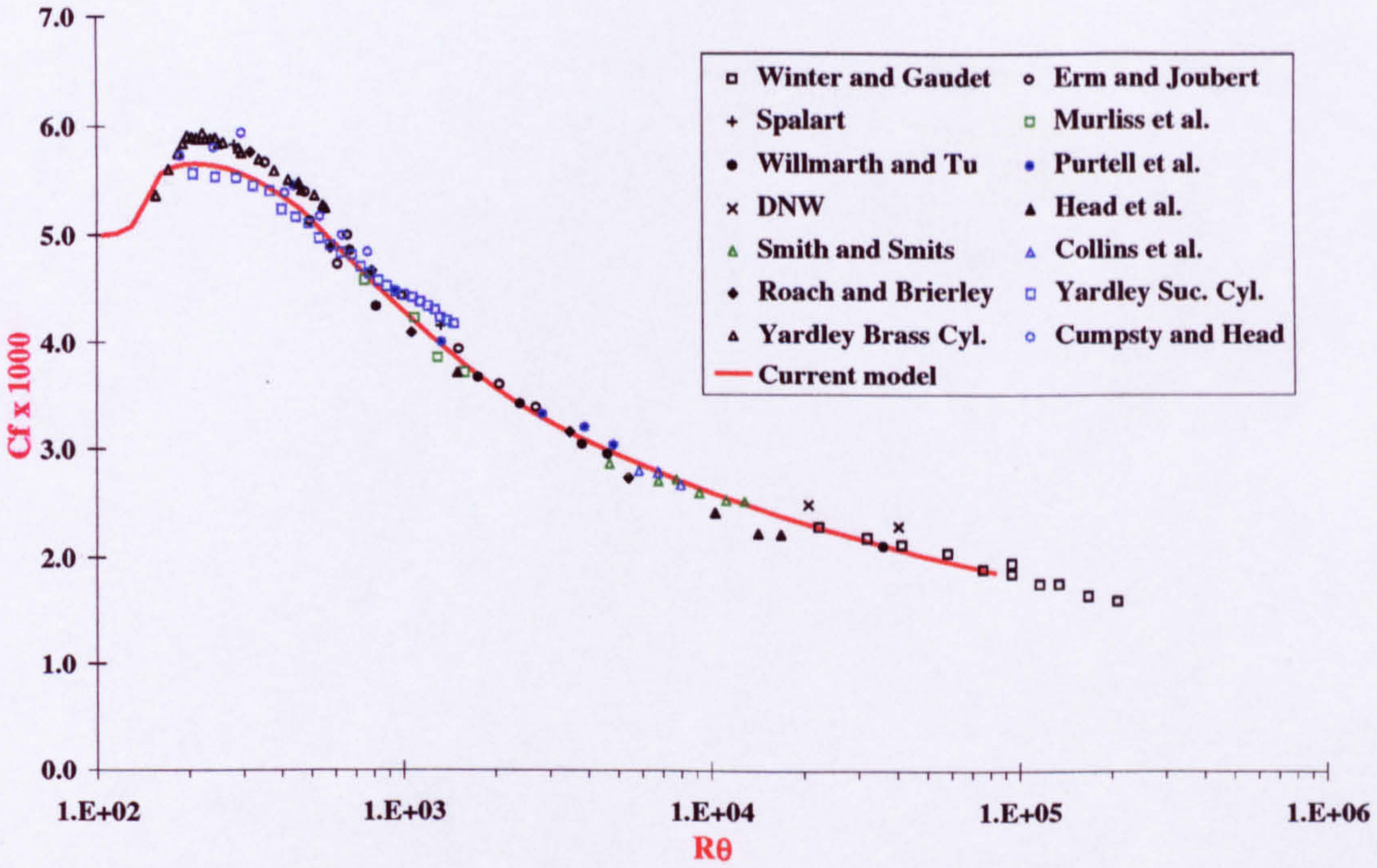

Figure A.85: Variation of the skin friction for incompressible flows. Prediction from the current model, equations 5.8 to 5.11. Experimental data from reference [29].

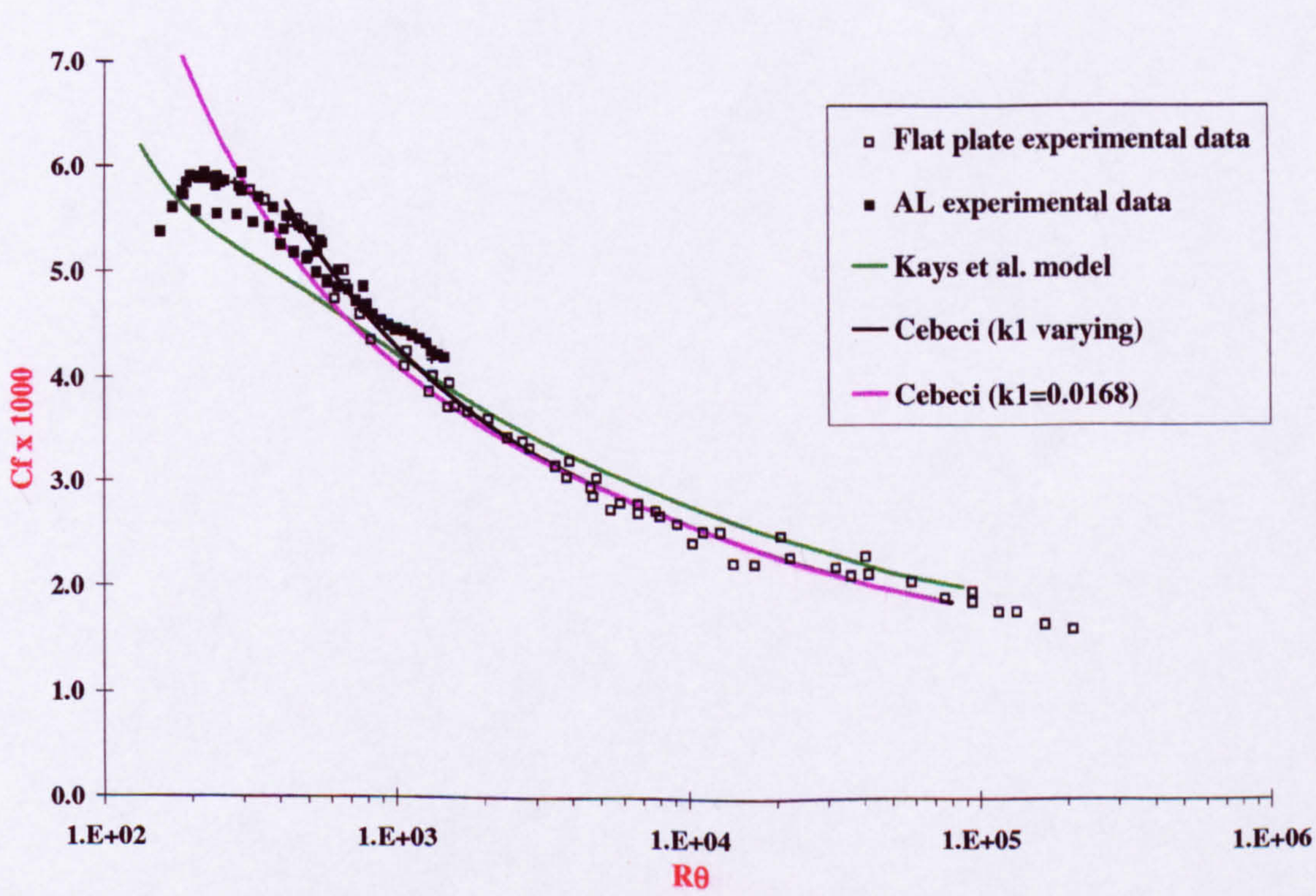

Figure A.86: Variation of the skin friction for incompressible flows. Turbulence models from Kays et al. [42] (equations 4.30 4.34) and Cebeci [18] (equations 4.50 to 4.52). Experimental data from reference [29].

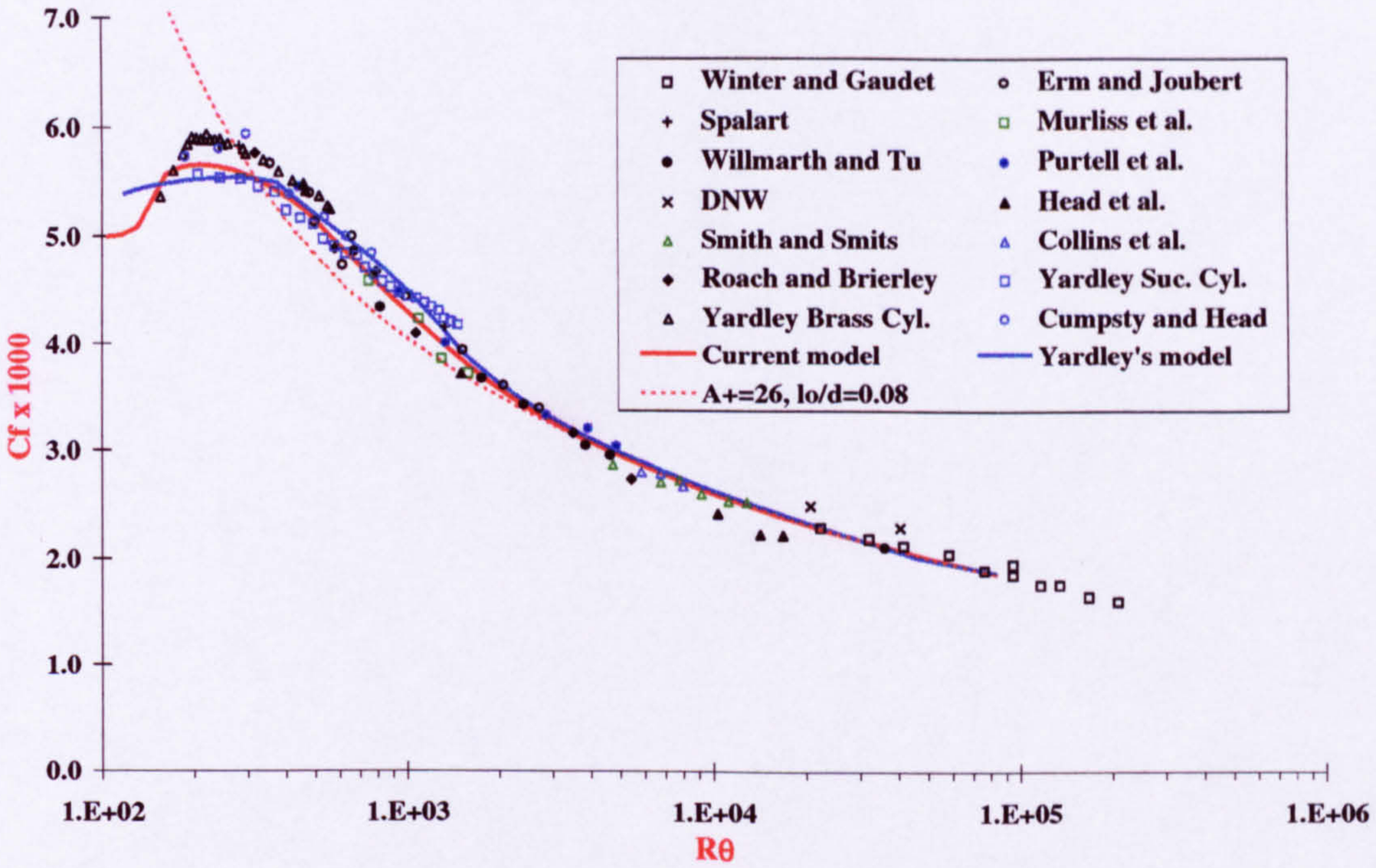

Figure A.87: Variation of the skin friction for incompressible flows. Turbulence models from Yardley [65] (equations 4.57 to 4.61) and from the current model (equations 5.8 to 5.11). Experimental data from reference [29].

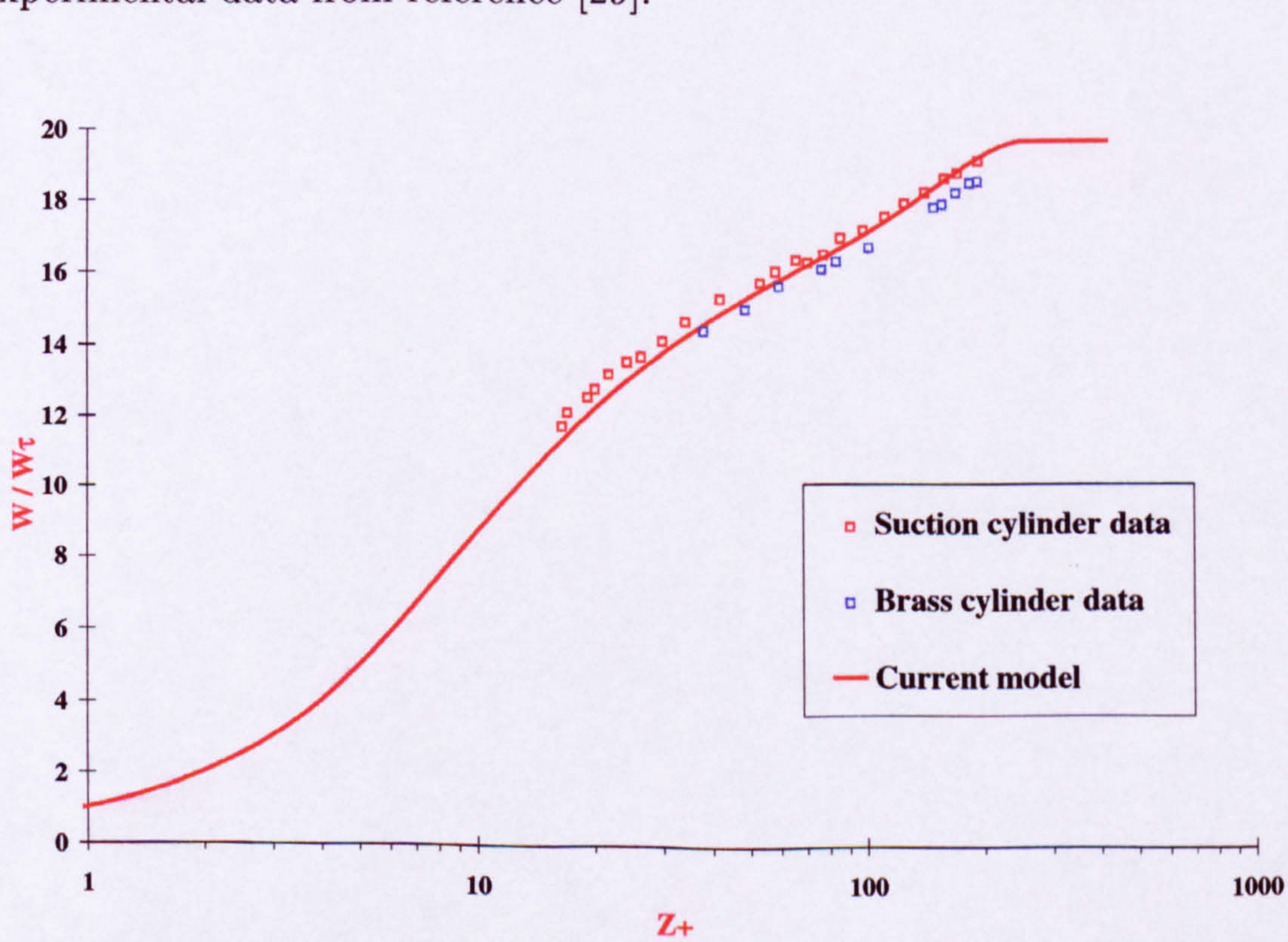

Figure A.88: Velocity profile in an equilibrium, incompressible flow at very low Reynolds number ($\bar{R} = 450$, $R_\theta \approx 450$, $M_{ae} = 0$, T_w/T_o of unity, $T_o = 350K$). Prediction from current model (equations 5.8 to 5.11). Experimental data from reference Yardley [65].

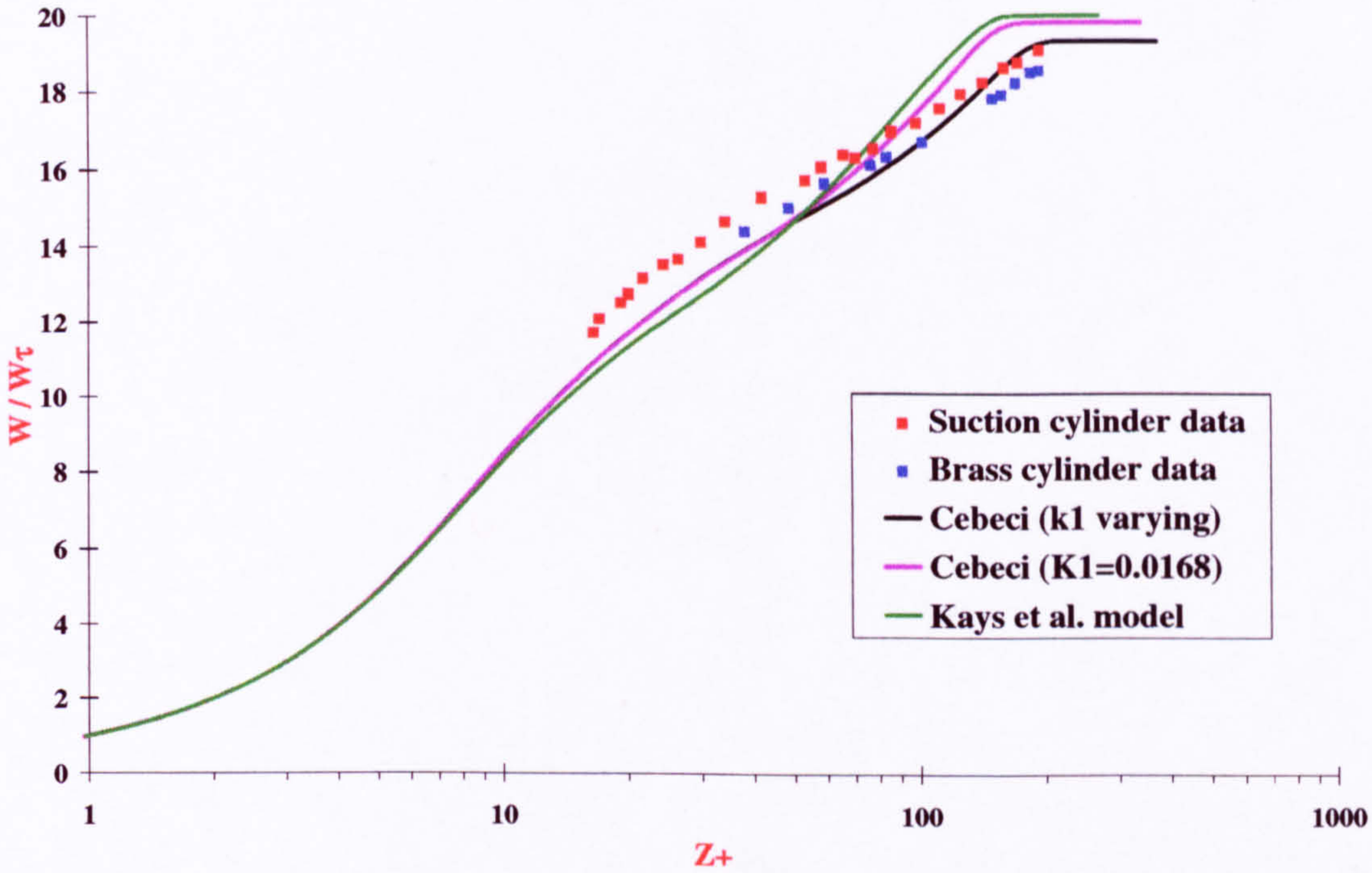

Figure A.89: Velocity profile in an equilibrium, incompressible flow at very low Reynolds number ($\bar{R} = 450$, $R_\theta \approx 450$, $M_{ae} = 0$, T_w/T_o of unity, $T_o = 350K$). Turbulence models from Kays et al. [42] and Cebeci [18]. Experimental data from reference Yardley [65].

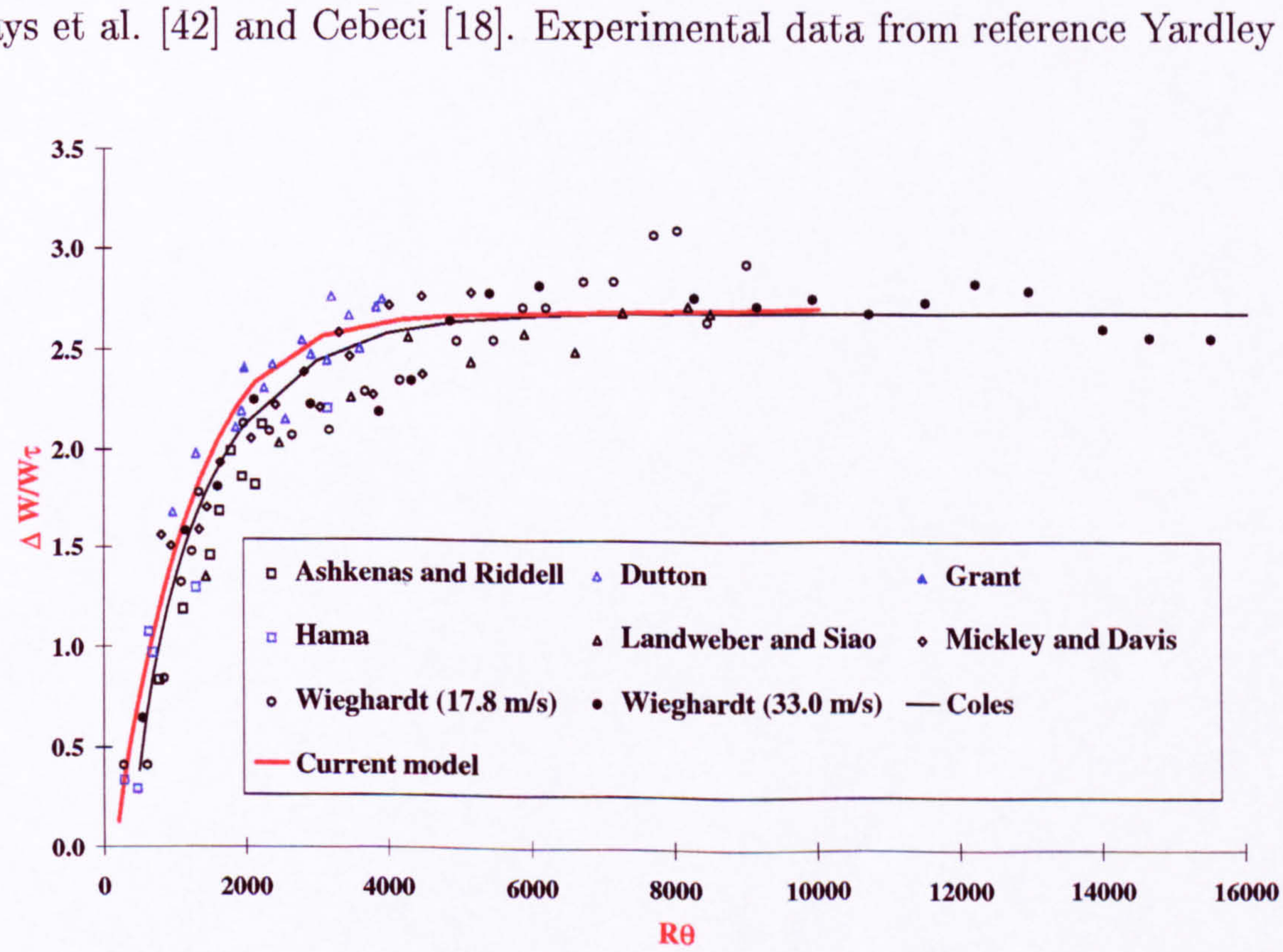

Figure A.90: Variation of the wake strength with Reynolds number for incompressible flow. Prediction from current turbulence model (equations 5.8 to 5.11). Experimental data from reference [29].

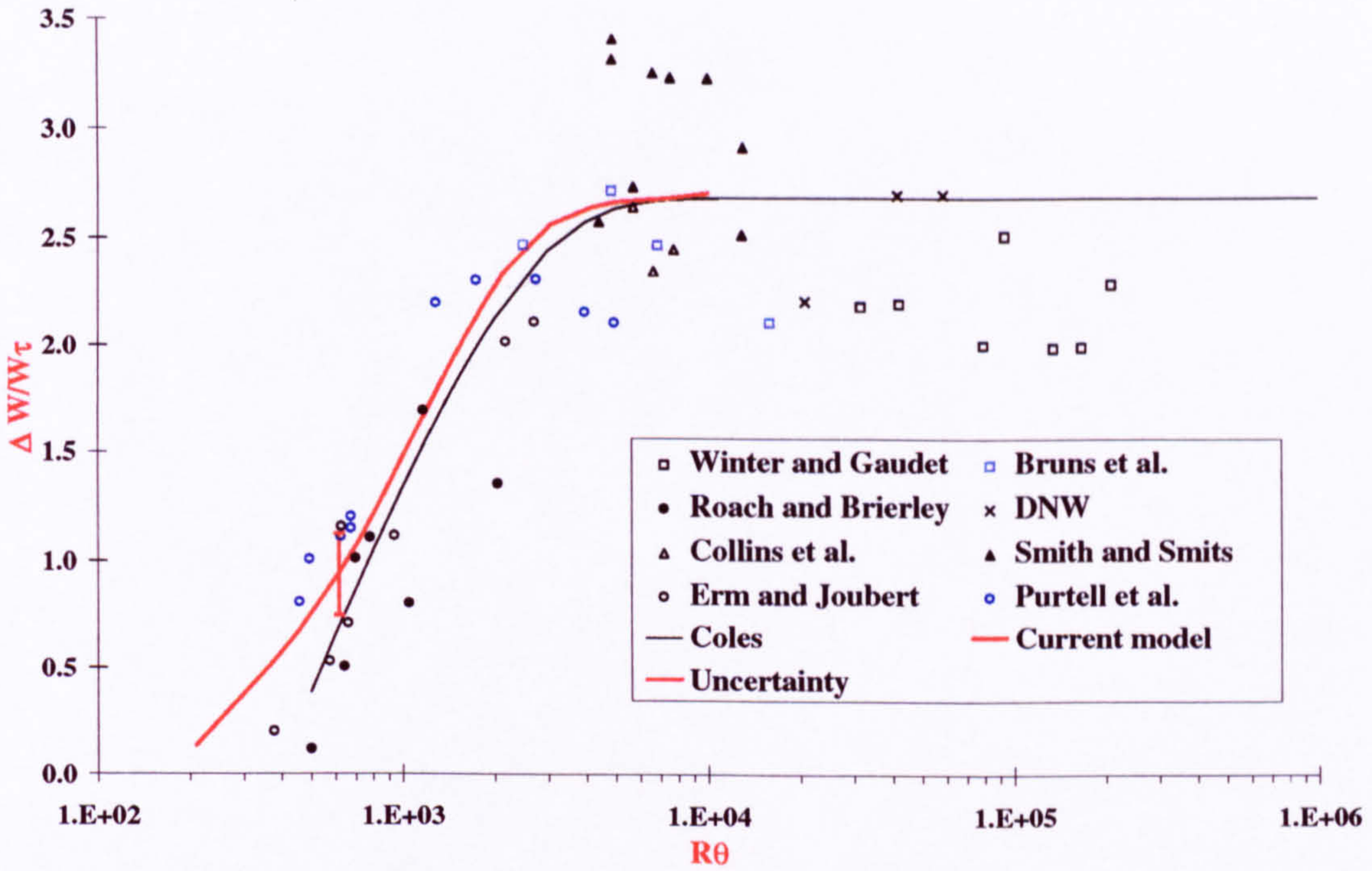

Figure A.91: Variation of the wake strength with Reynolds number for incompressible flow. Prediction from current turbulence model (equations 5.8 to 5.11). More recent experimental data from reference [29].

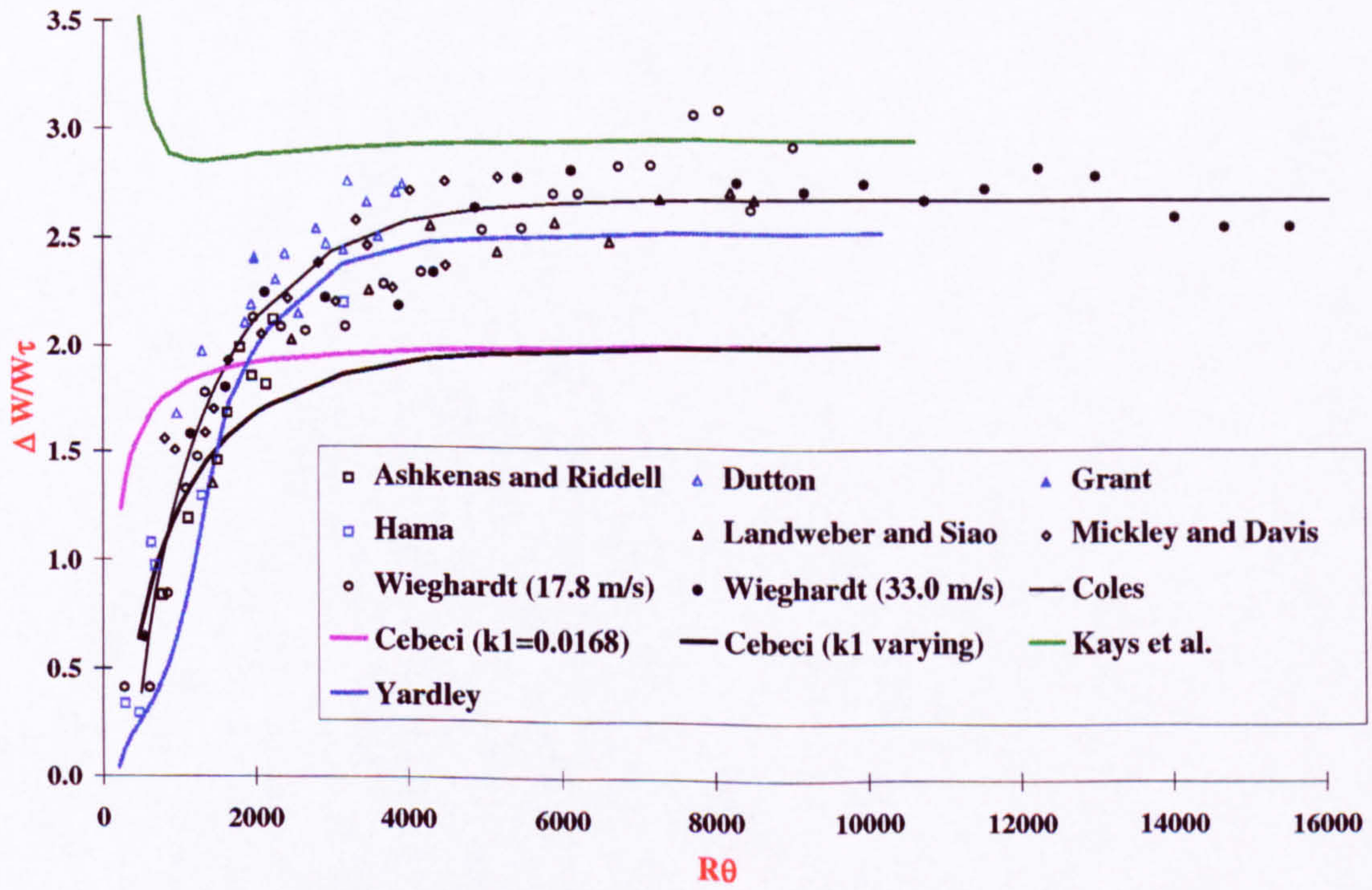

Figure A.92: Variation of the wake strength with Reynolds number for incompressible flow. Turbulence models from Kays et al. [42], Cebeci [18] and Yardley [65]. Experimental data from reference [29].

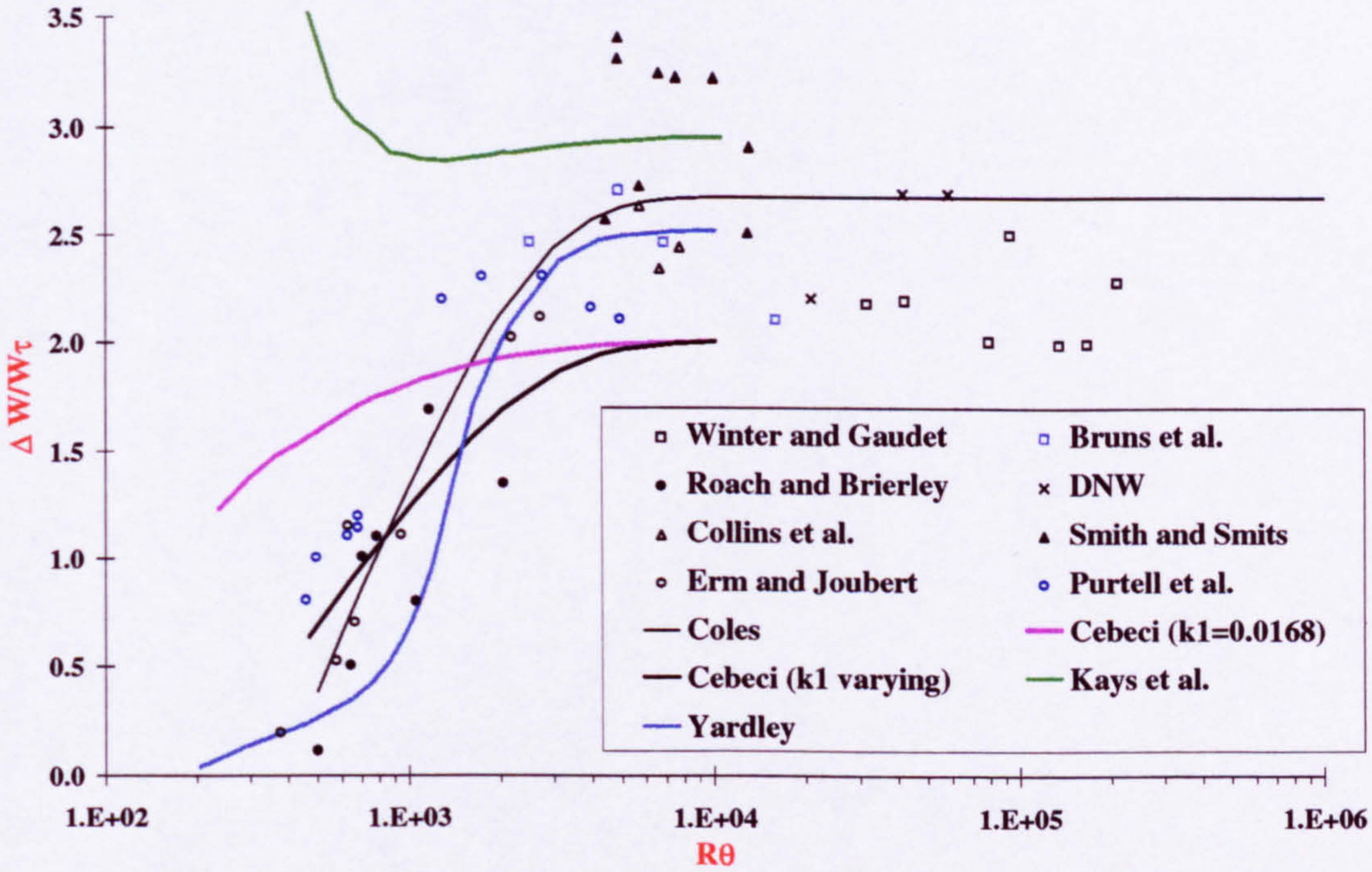

Figure A.93: Variation of the wake strength with Reynolds number for incompressible flow. Turbulence models from Kays et al. [42], Cebeci [18] and Yardley [65]. More recent experimental data from reference [29].

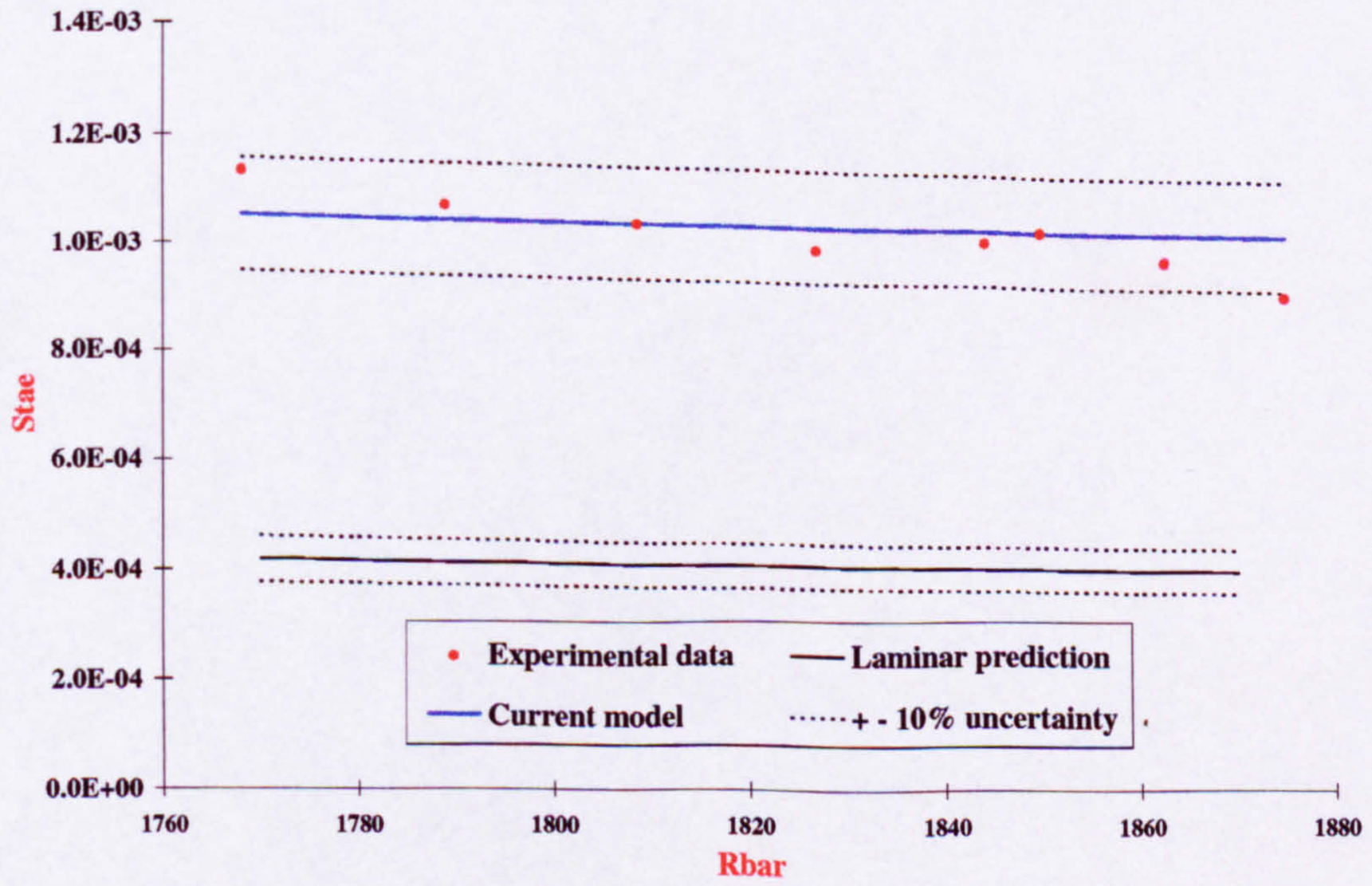

Figure A.94: Comparison of the heat transfer rate from prediction and experiments. (Holden et al. [37][38], $M_\infty = 10.6$, $\Lambda = 75^o$, $T_w/T_o = 0.26$, 2D trip wire of k=0.03").

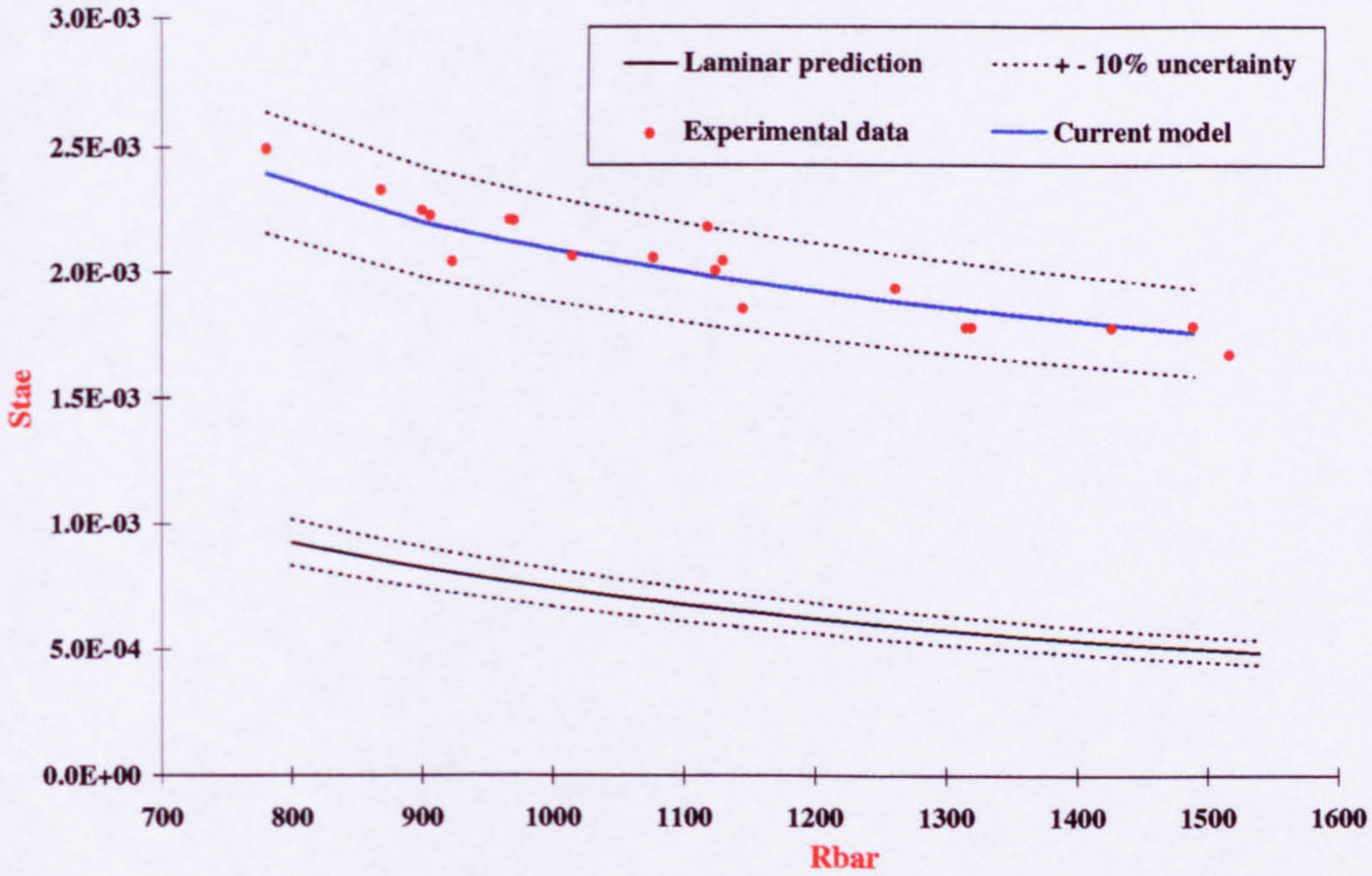

Figure A.95: Comparison of the heat transfer rate from prediction and experiments. (Beckwith et al. [5], $M_\infty = 4.15$, $\Lambda = 40^o$, $T_w/T_o = 0.92$, endplate).

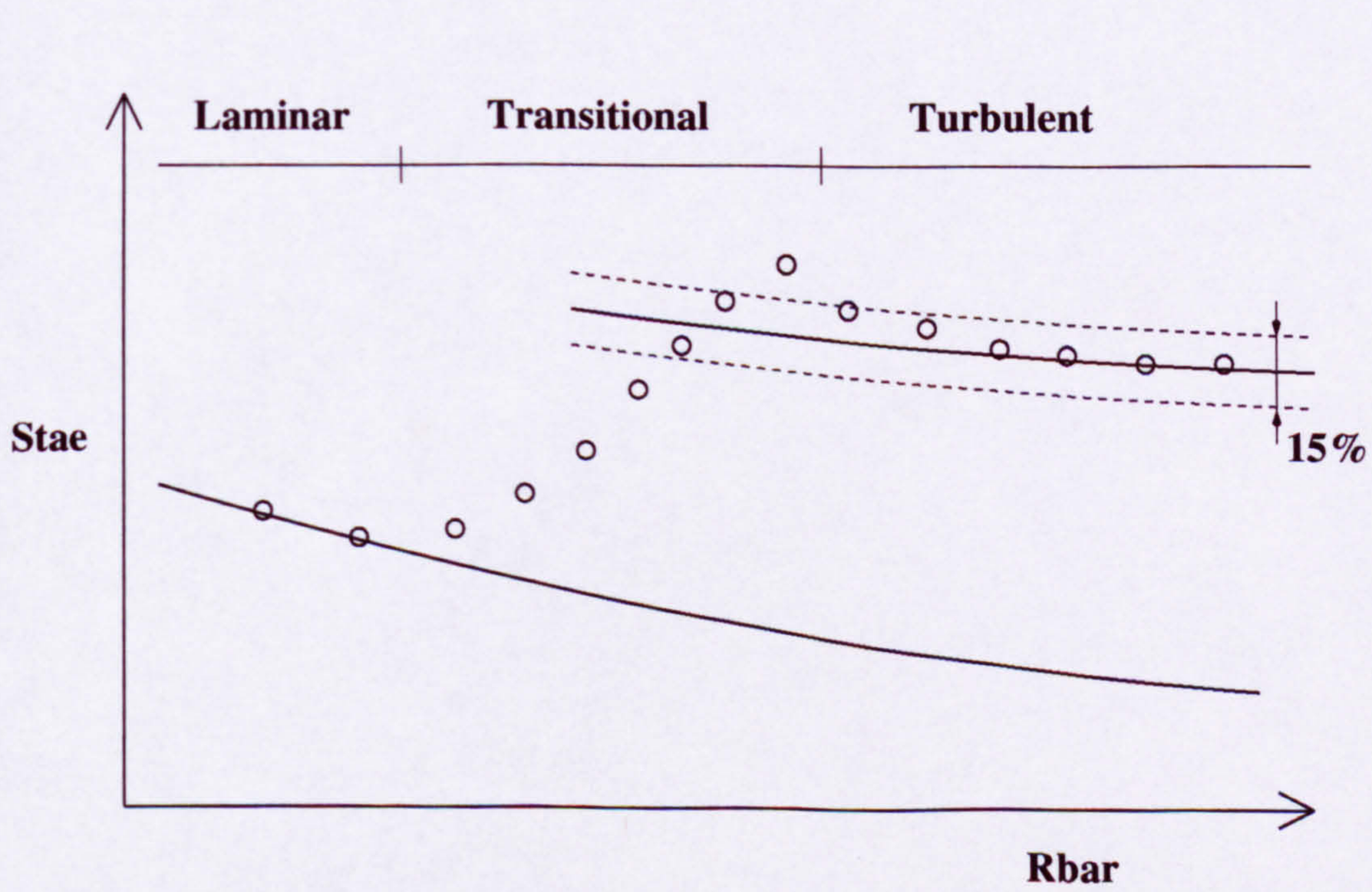

Figure A.96: Schematic of the typical variation of the heating level as the viscous layer changes from fully laminar to transitional to fully turbulent.

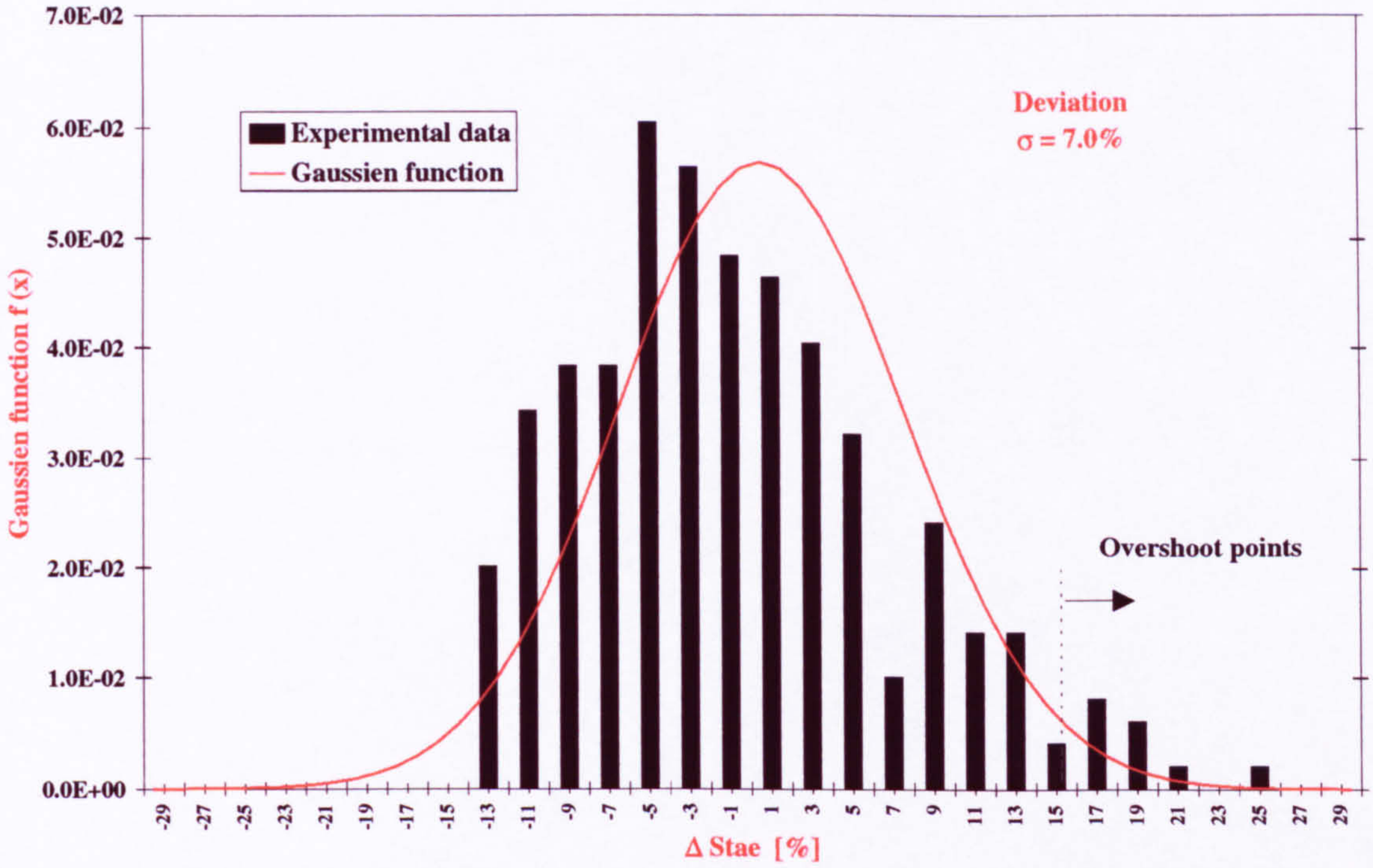

Figure A.97: Gaussian distribution of the fully turbulent experimental data points with data points corresponding to the overshoot phenomenon.

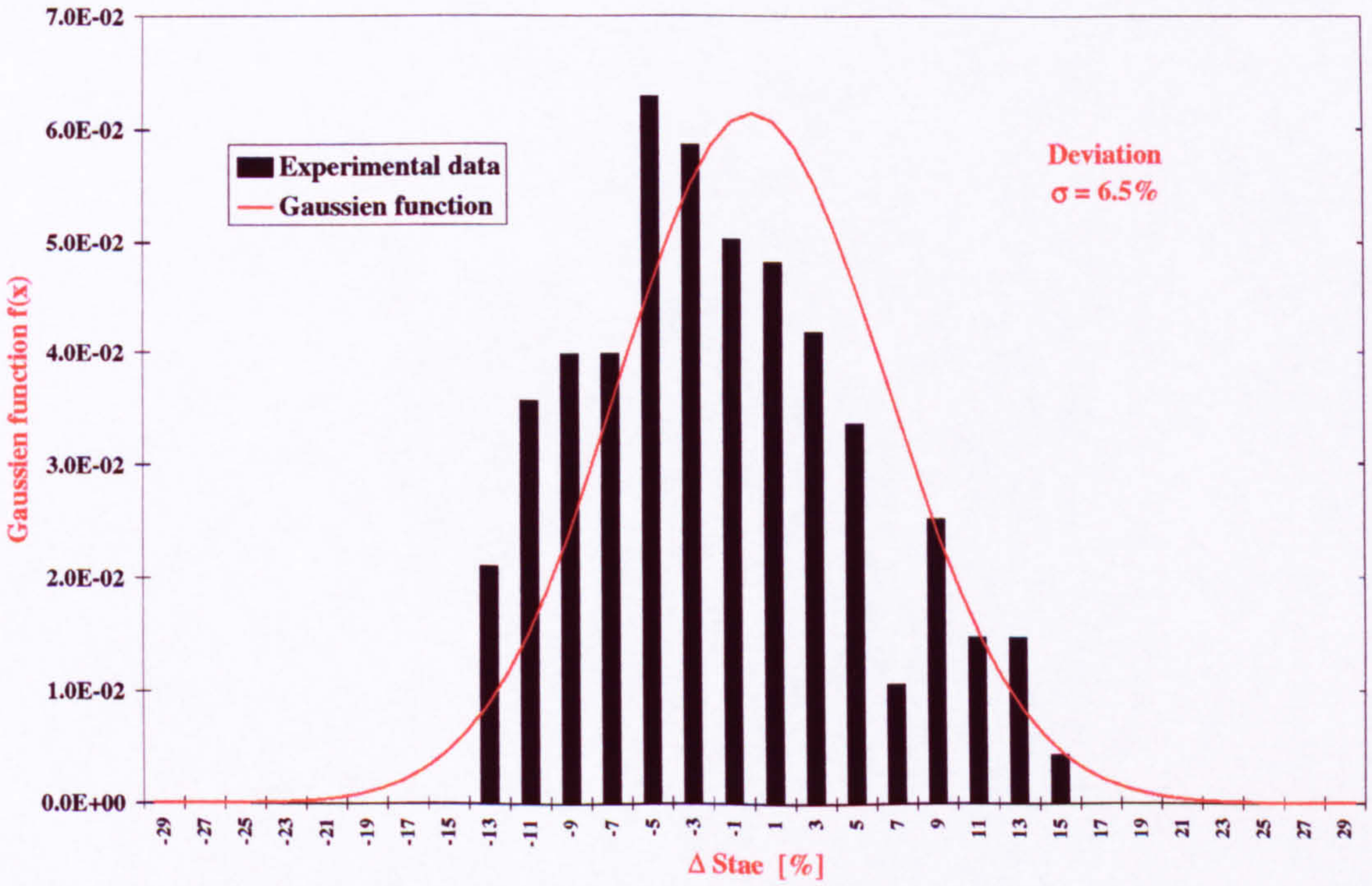

Figure A.98: Gaussian distribution of the fully turbulent experimental data points only (No overshoot data points). Experiments from Holden et al. [37][38], Bushnell et al. [12][13], Poitiers University [35][6], Beckwith and Gallagher [5] and Jones [40].

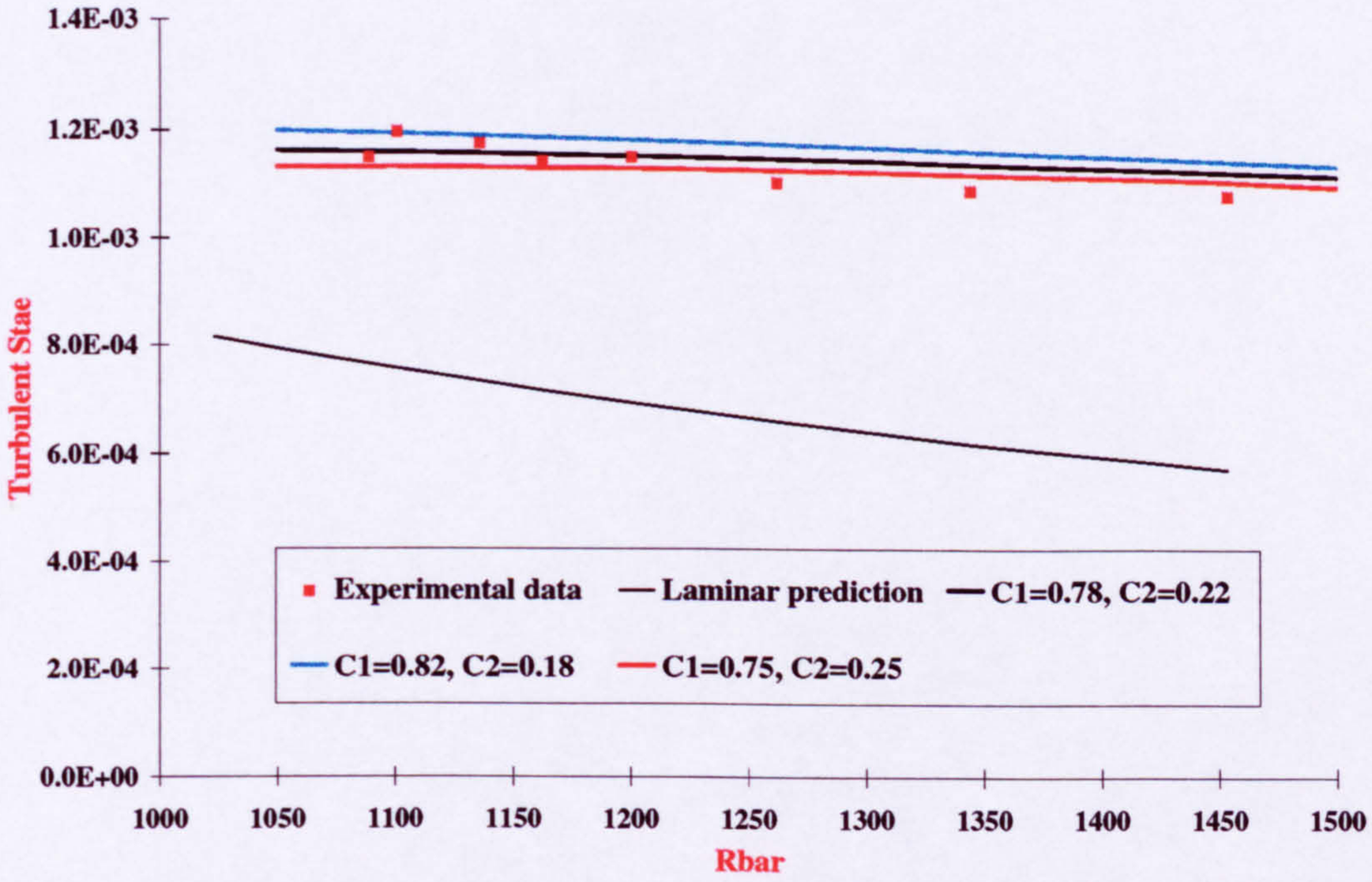

Figure A.99: Variation of the heat transfer intensity with the coefficients C_1 and C_2 of the characteristic temperature (equation 5.7). Poitiers University [35][6] ; Run 82s $M_{ae} = 5.9$, $T_w/T_o = 0.39$, $\Lambda = 80^o$.

Figure A.100: Variation of the fully turbulent Stanton number with attachment-line Reynolds number for incompressible flow. Bellone's turbulence model (see section 5.8), $Pr = 0.72$, $\gamma = 1.4$ and $Pr_t = 0.9$).

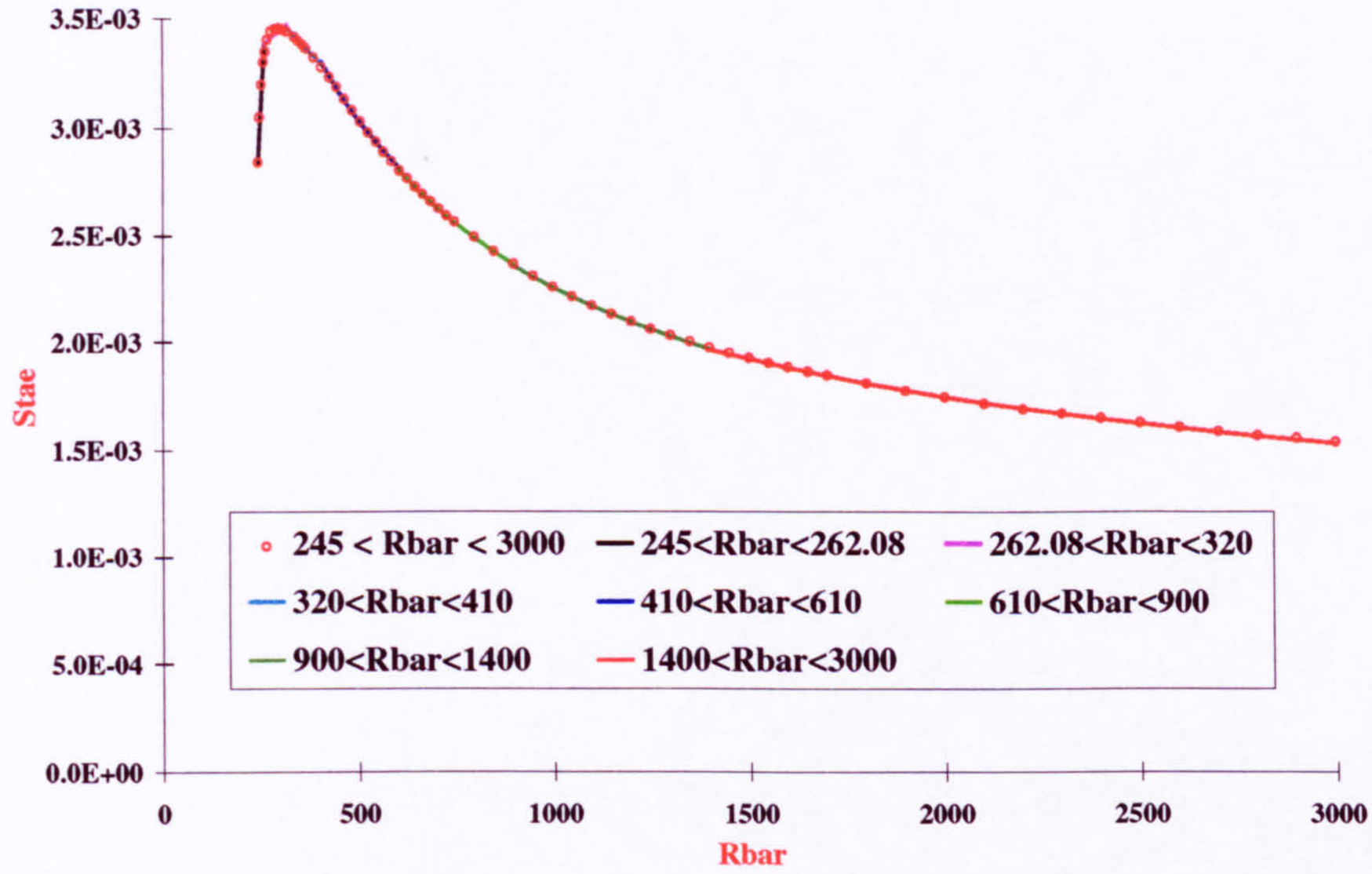

Figure A.101: Relations connecting the fully turbulent Stanton number with attachment-line Reynolds number for incompressible flow (equations 6.1 to 6.7).

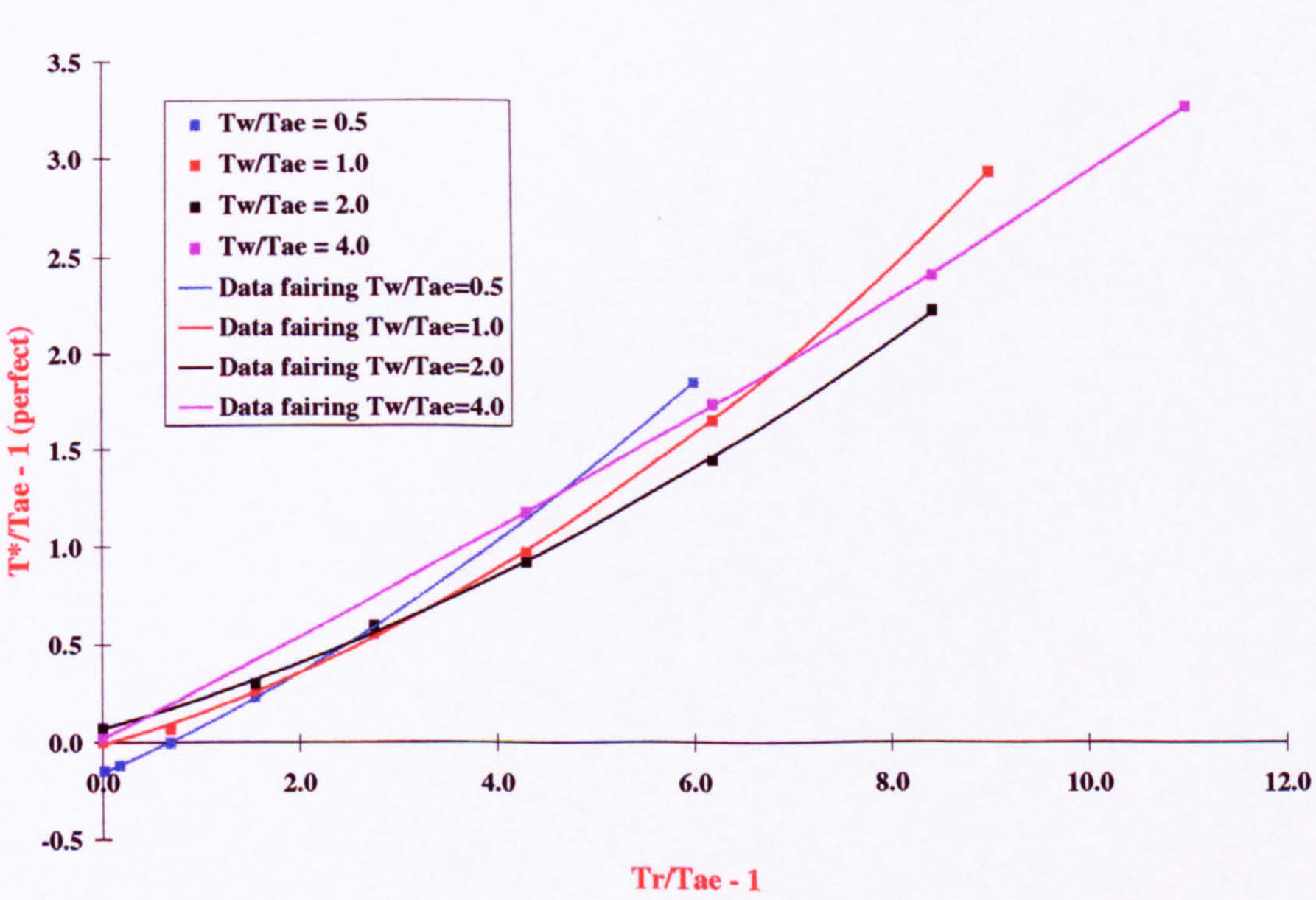

Figure A.102: Variation of the "perfect" reference temperature with T_r/T_{ae} for different values of T_w/T_{ae} (Air, $Pr = 0.72$, $\bar{R} = 1500$, $T_o = 800$K).

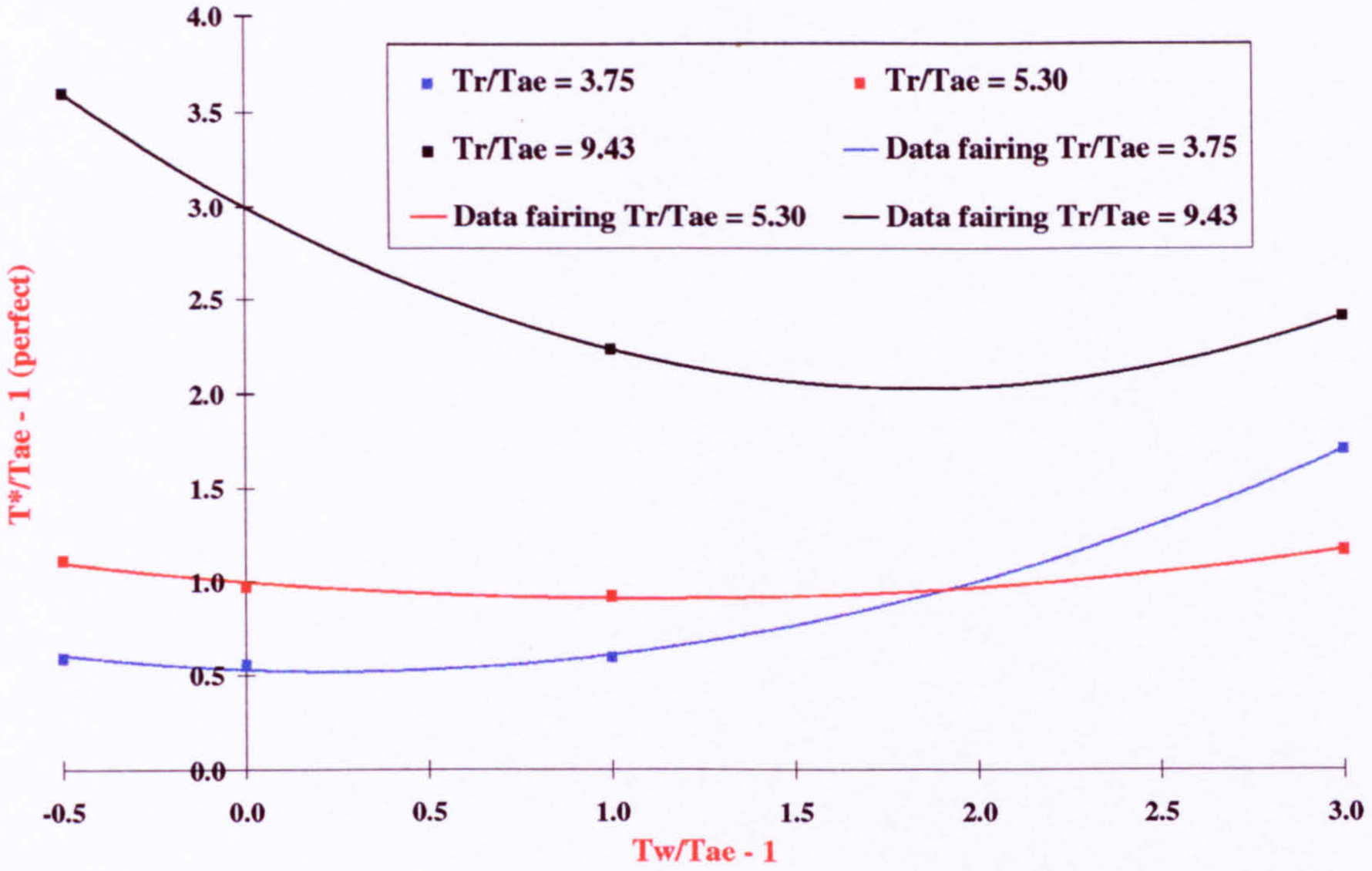

Figure A.103: Variation of the "perfect" reference temperature with T_w/T_{ae} for different values of T_r/T_{ae} (Air, $Pr = 0.72$, $\bar{R} = 1500$, $T_o = 800$K).

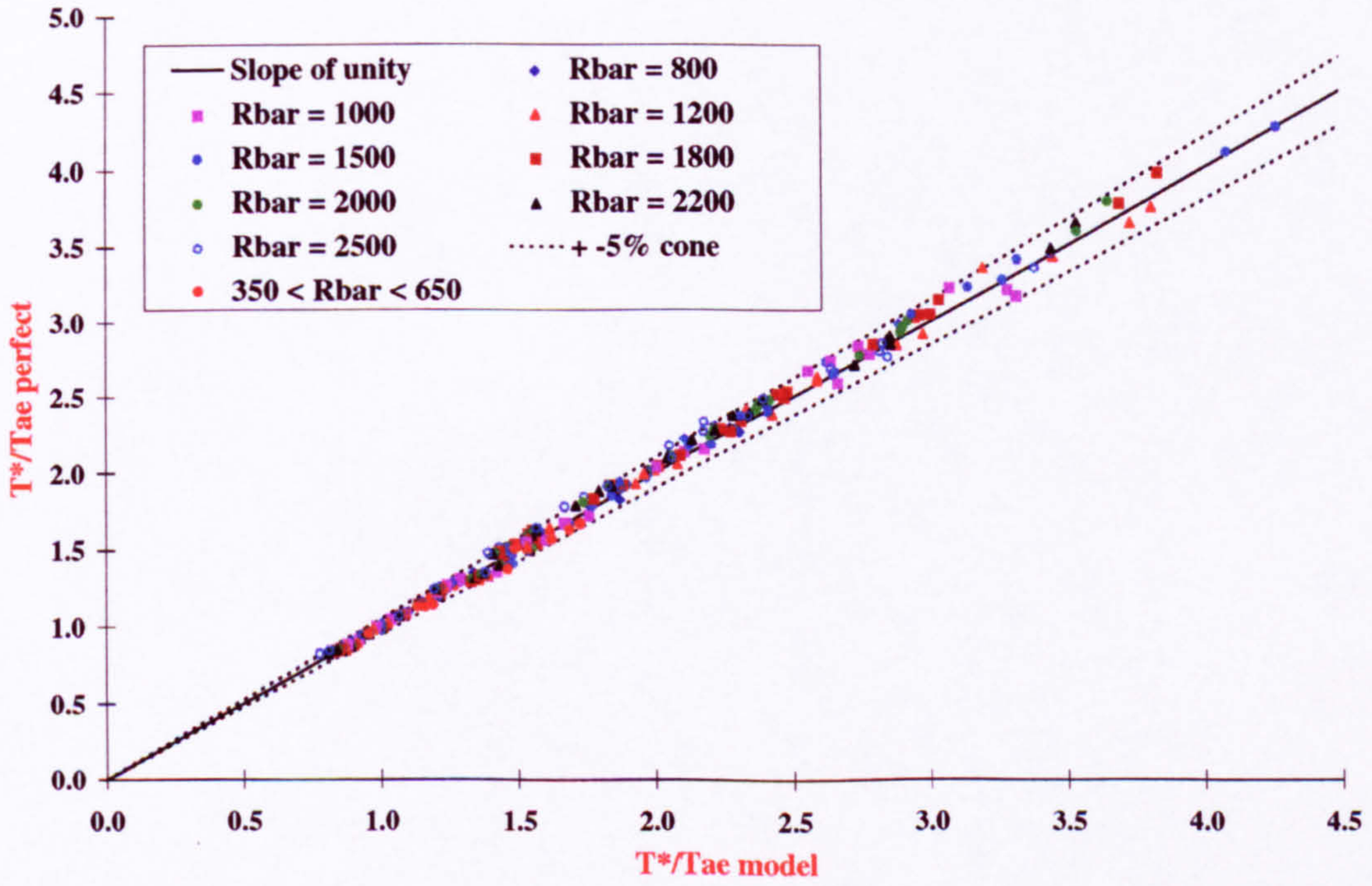

Figure A.104: Comparison of the perfect reference temperature with the model (equation 6.11). $Pr = 0.72$, $\gamma = 1.4$, $s = 110.4$K.

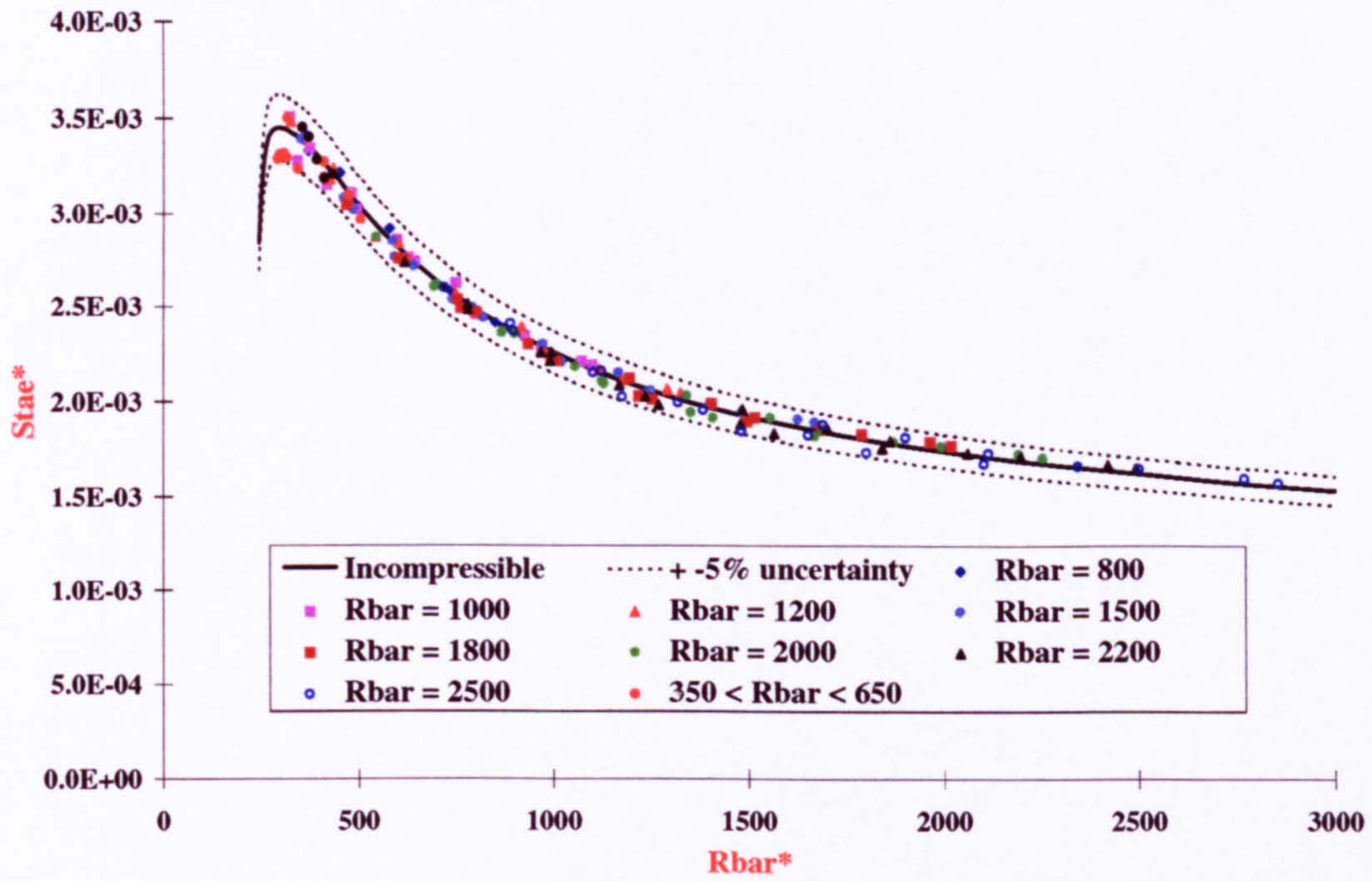

Figure A.105: Variation of transformed Stanton number with transformed Reynolds number $\bar{R}^*$ ($\bar{R} \leq 2500$, $M_{ae} \leq 8$, $0.1 \leq T_w/T_o \leq 1.0$ and $300 \leq T_o \leq 4000$K).

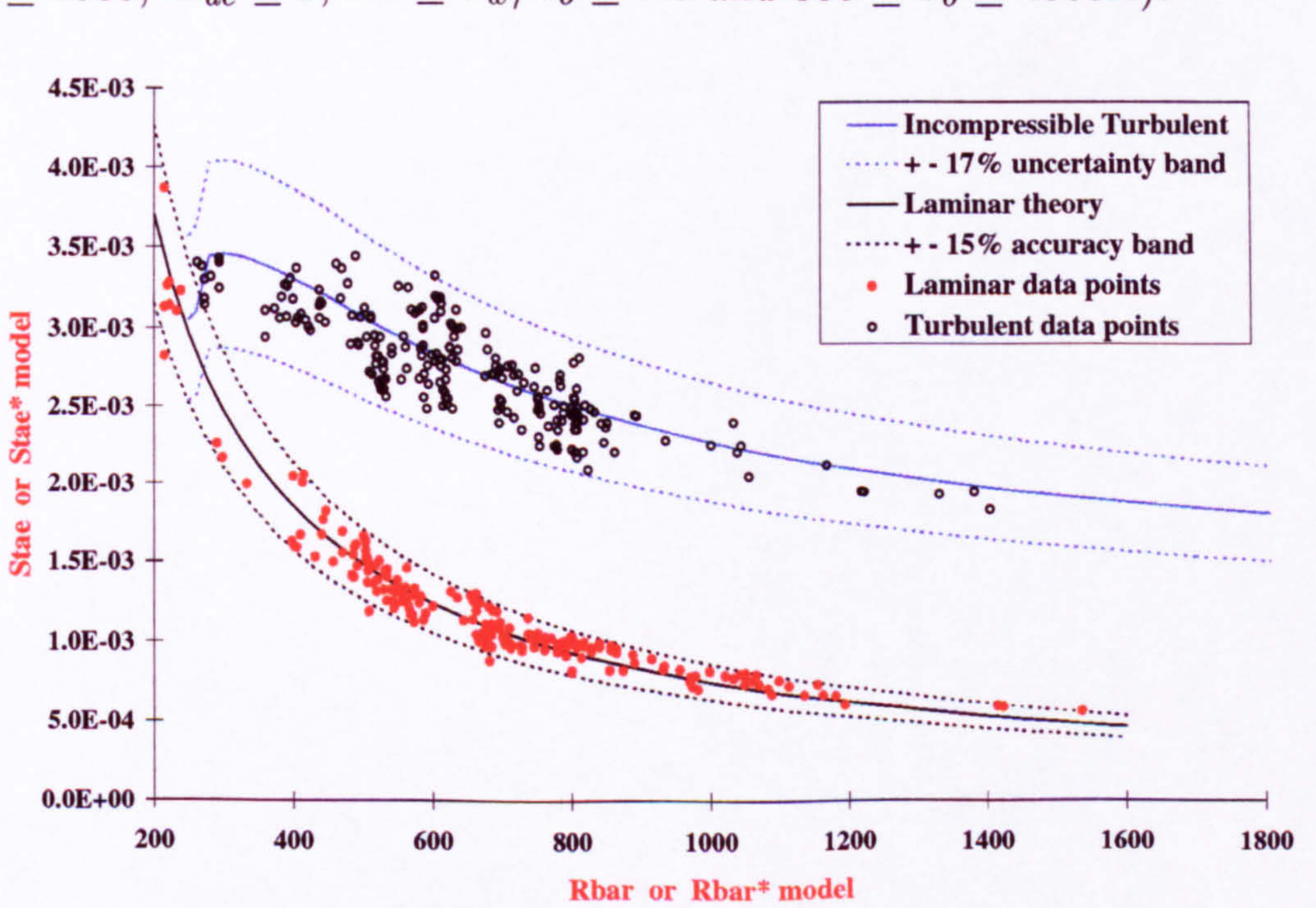

Figure A.106: Laminar and turbulent attachment-line heating rates. Reference temperature model (equation 6.11) used for turbulent data points. Laminar model (equation 3.14). Experimental data from Holden et al. [37][38], Bushnell et al. [12][13], Poitiers University [35][6], Beckwith and Gallagher [5] and Jones [40].

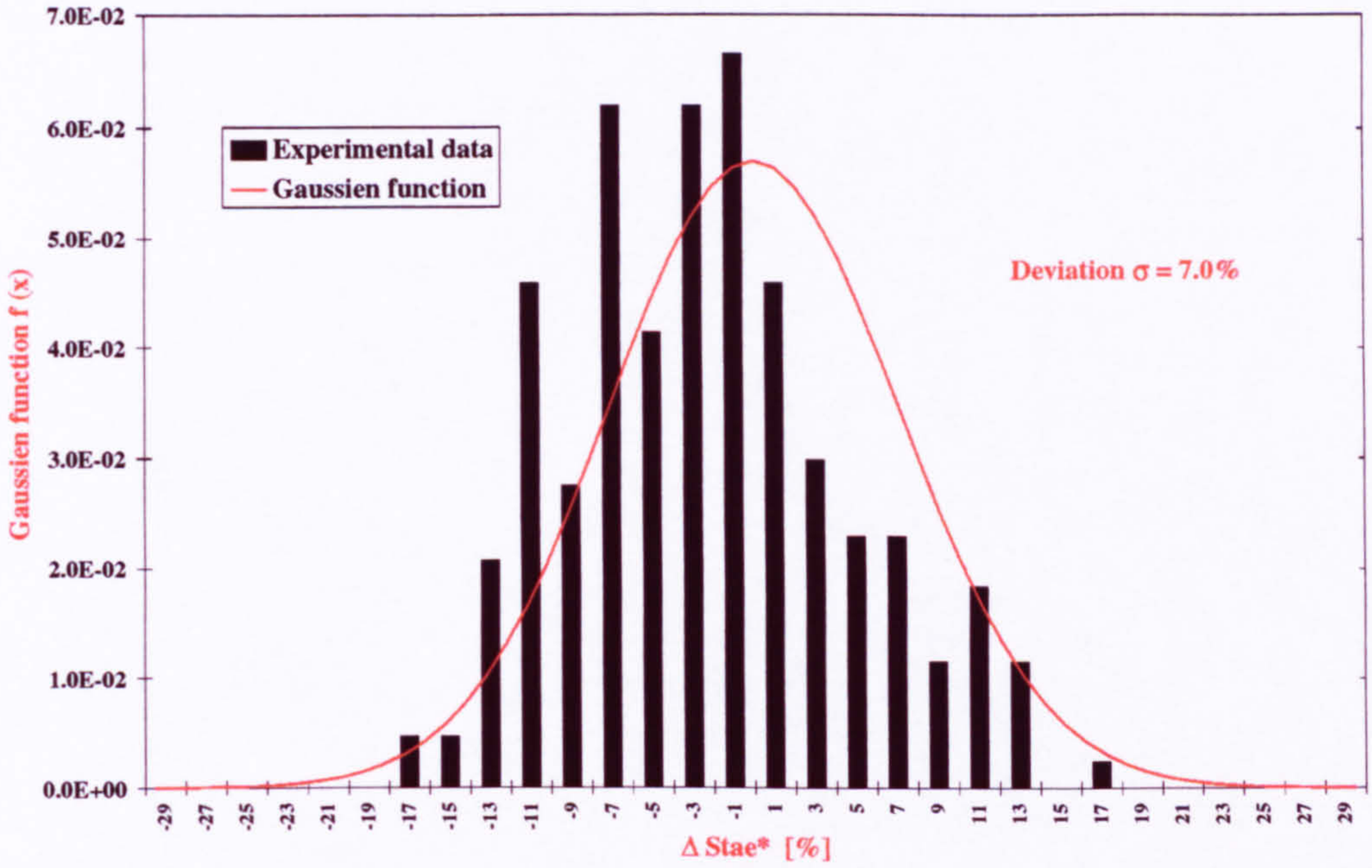

Figure A.107: Error distribution of the fully turbulent experimental data points when reduced via the reference temperature (equation 6.11). Experimental data from Holden et al. [37][38], Bushnell et al. [12][13], Poitiers University [35][6], Beckwith and Gallagher [5] and Jones [40].

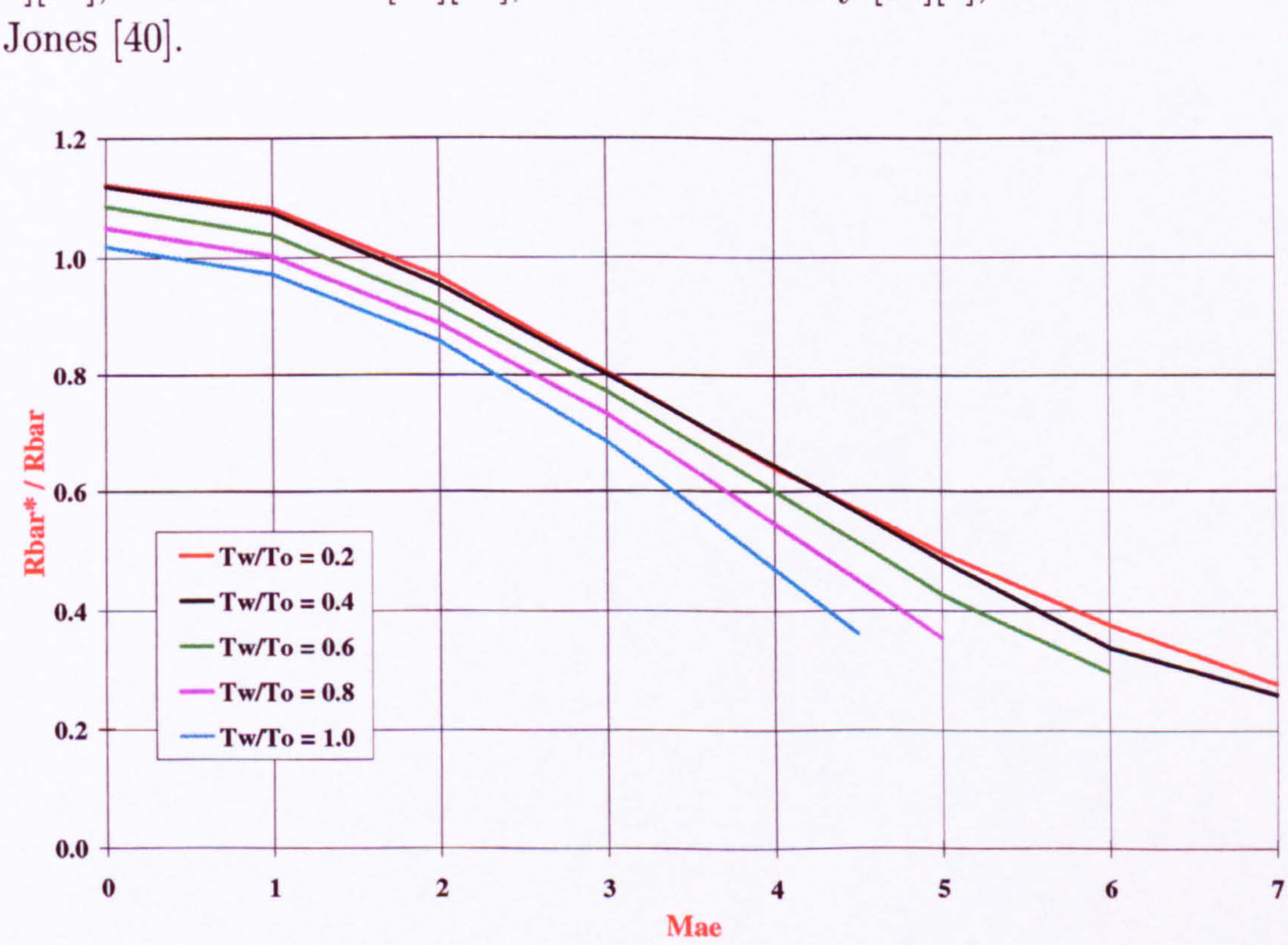

Figure A.108: Variation of the ratio $\bar{R}^*/\bar{R}$ with edge Mach number and T_w/T_o ($\bar{R} = 1000$). Reference temperature from equation 6.11. Wind tunnel conditions, $s/T_o = 0.138$.

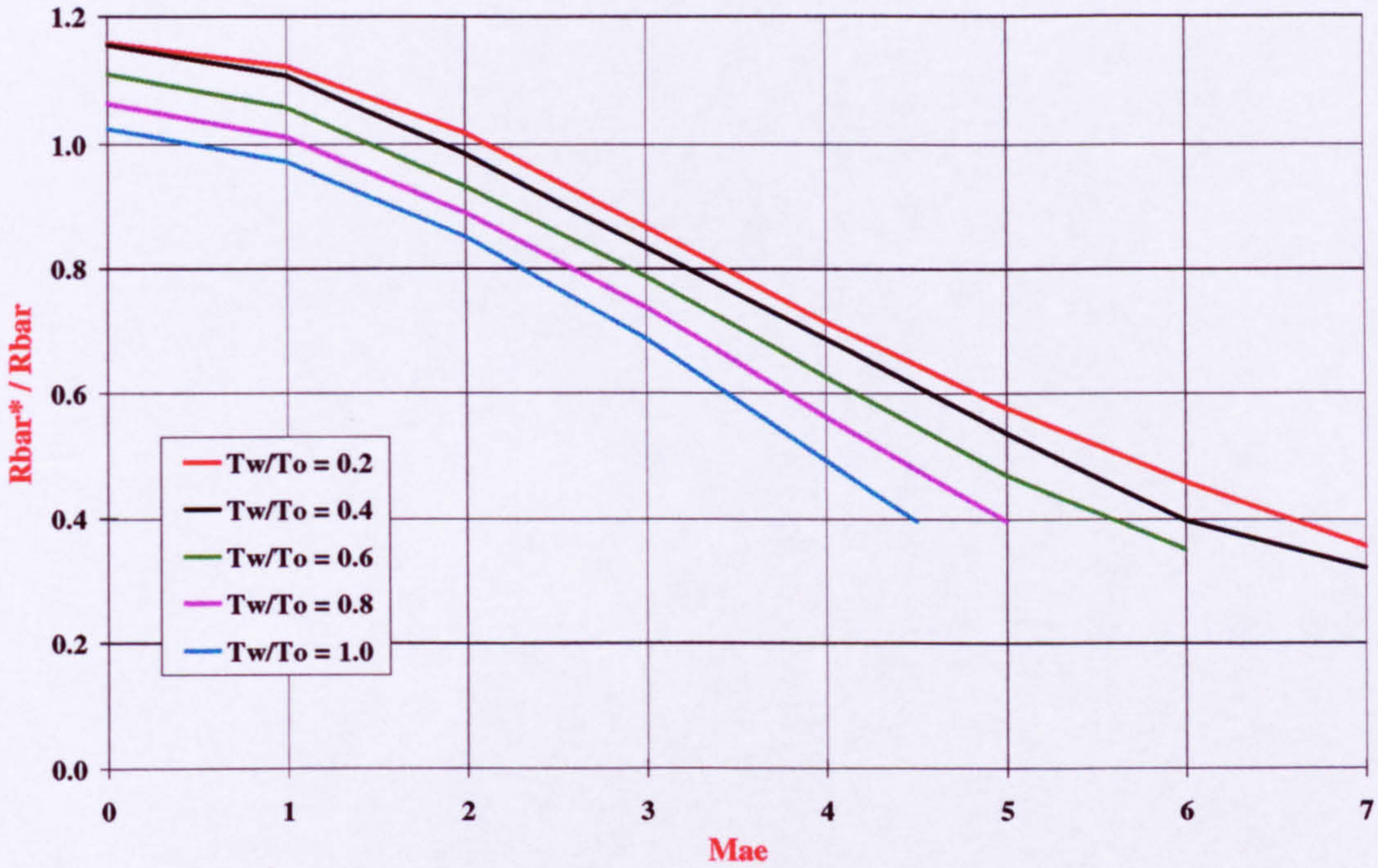

Figure A.109: Variation of the ratio $\bar{R}^*/\bar{R}$ with edge Mach number and T_w/T_o ($\bar{R} = 1000$). Reference temperature from equation 6.11. Flight conditions, $s/T_o = 0.028$.

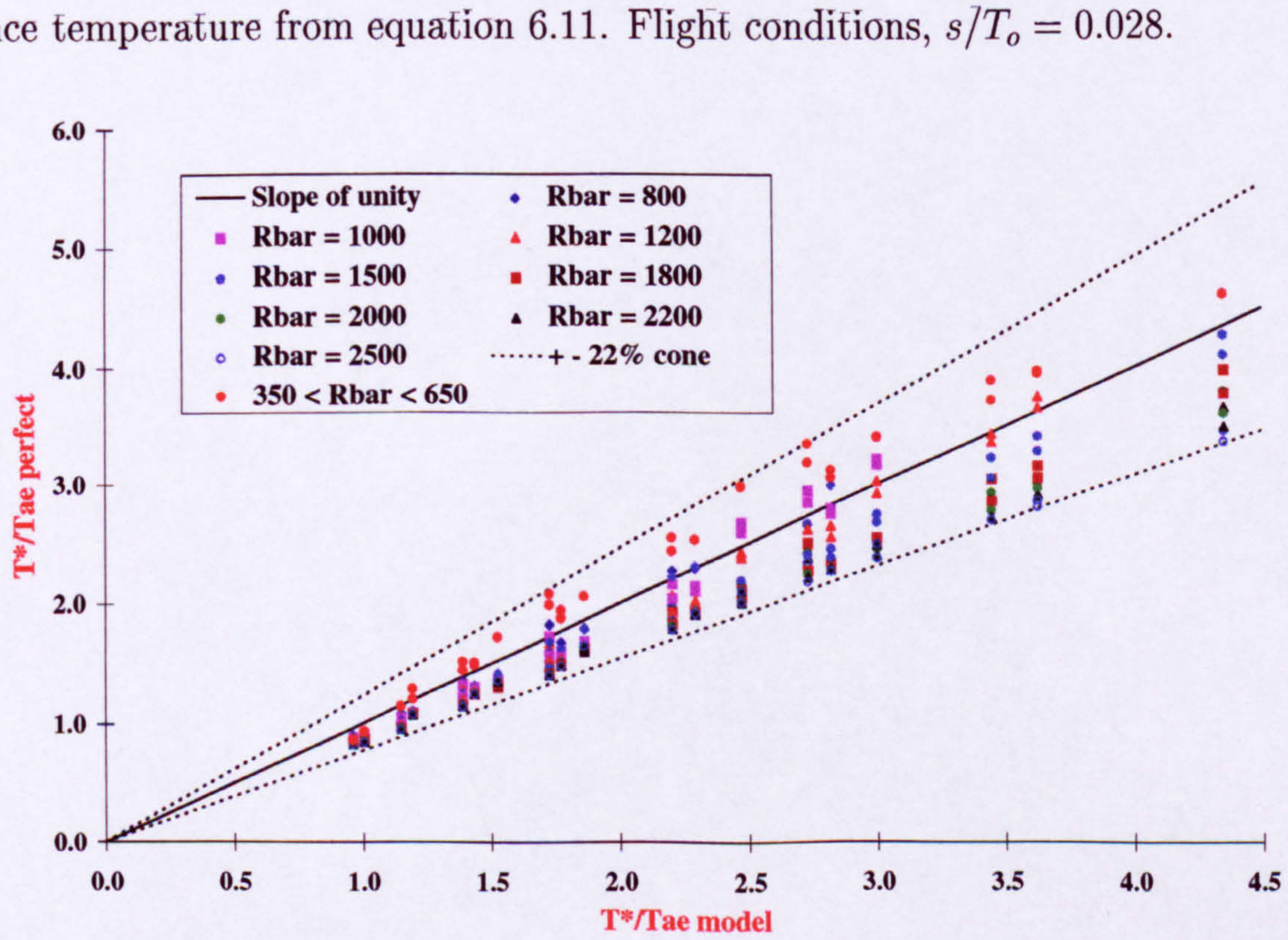

Figure A.110: Comparison between the perfect reference temperature and the estimation from Eckert's model [30] (equation 6.10) with $K1 = 0.09$ and $K2 = 0.28$.

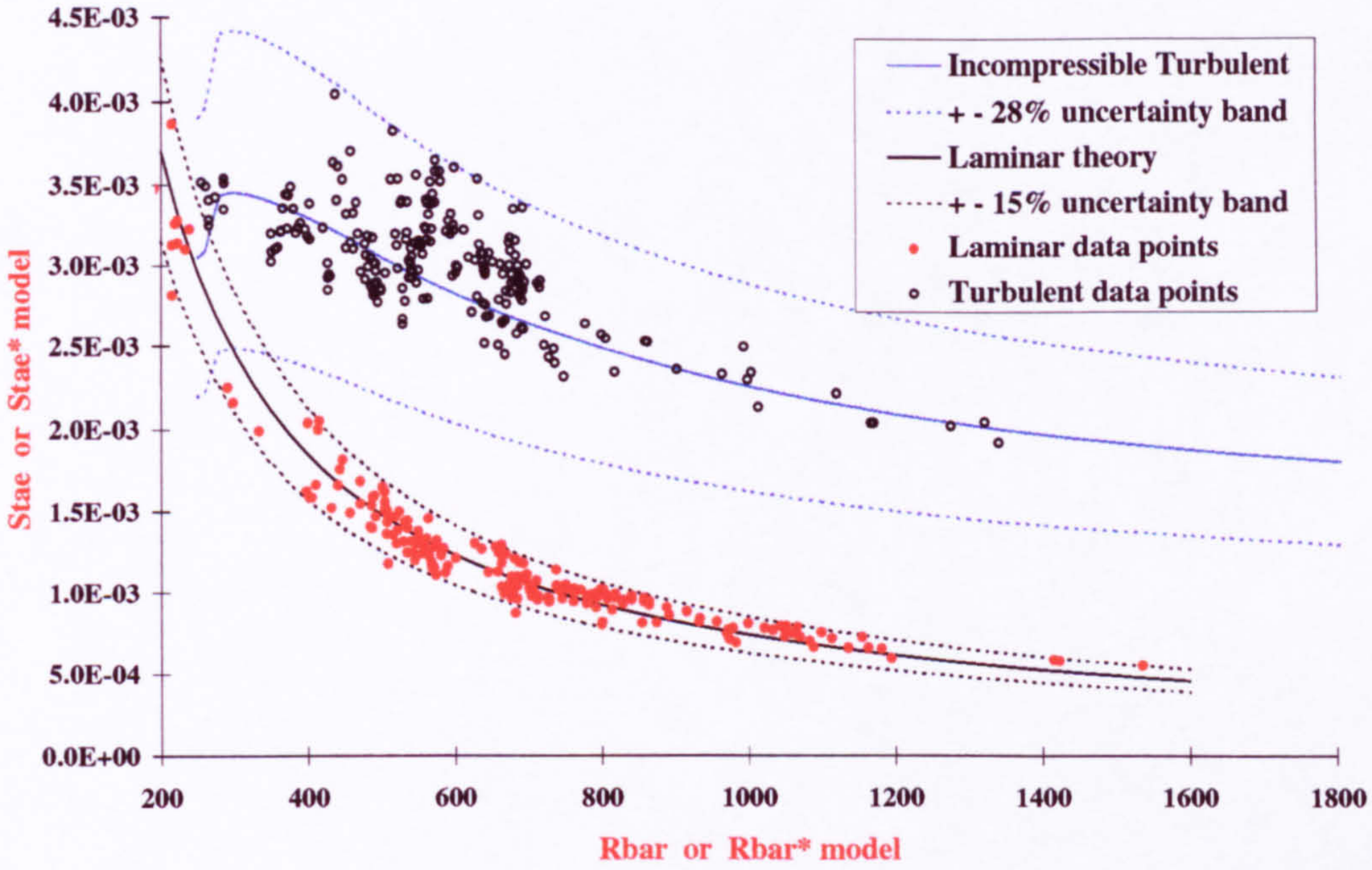

Figure A.111: Laminar and turbulent attachment-line heating rate. Eckert's model [30] used for turbulent data points with $K1 = 0.09$ and $K2 = 0.28$. Laminar model (equation 3.14). Experimental data from Holden et al. [37][38], Bushnell et al. [12][13], Poitiers University [35][6], Beckwith and Gallagher [5] and Jones [40].

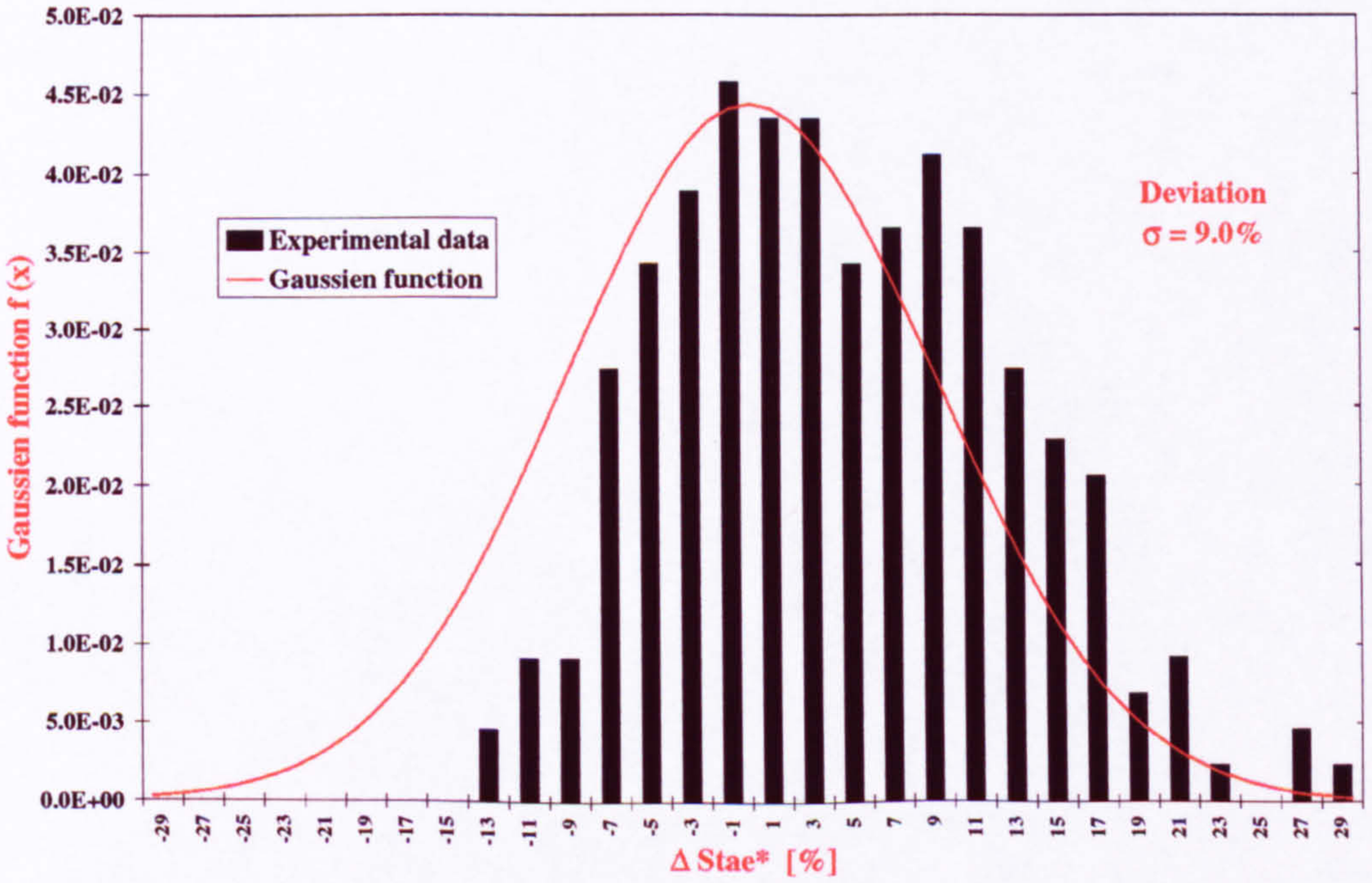

Figure A.112: Error distribution of the fully turbulent experimental data points when reduced via the reference temperature from Eckert's model [30] with $K1 = 0.09$ and $K2 = 0.28$. Experimental data from Holden et al. [37][38], Bushnell et al. [12][13], Poitiers University [35][6], Beckwith and Gallagher [5] and Jones [40].

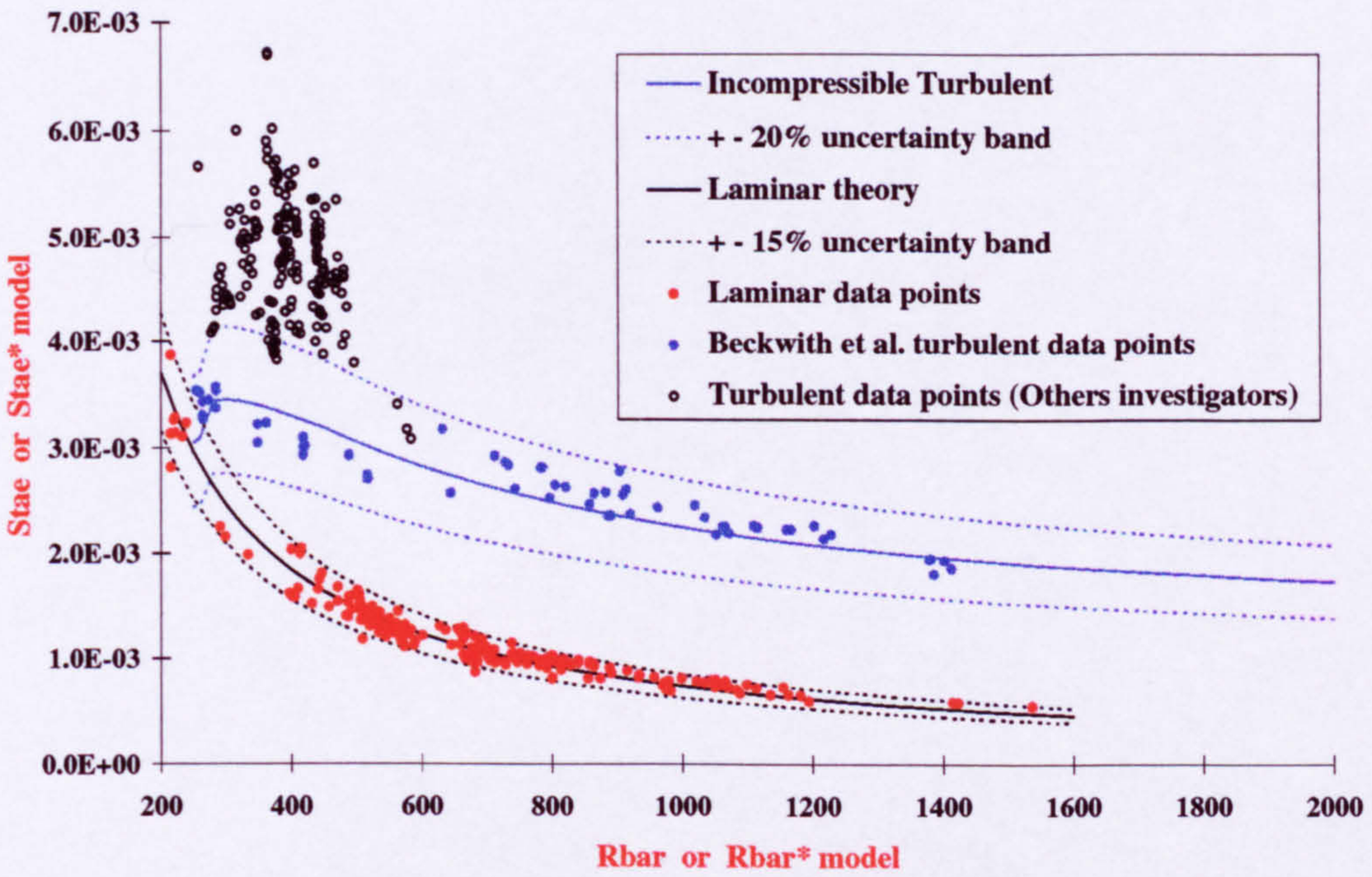

Figure A.113: Calculation of the fully turbulent attachment-line boundary layer using Eckert's model [30] and Poll's [49] constant values of K1 and K2 ($K1 = 0.10$ and $K2 = 0.60$). Experimental data from Holden et al. [37][38], Bushnell et al. [12][13], Poitiers University [35][6], Beckwith and Gallagher [5] and Jones [40].

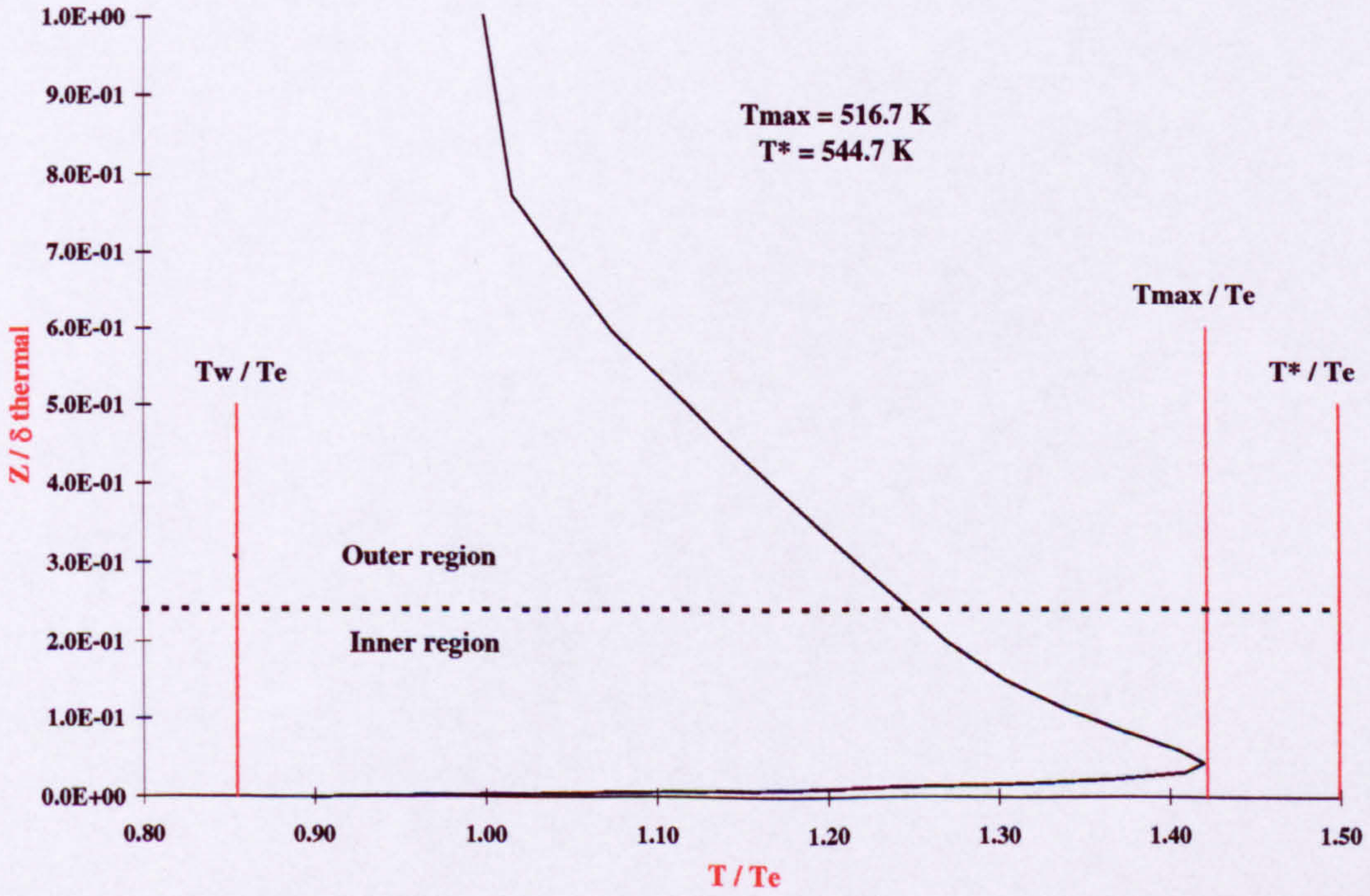

Figure A.114: Location of the reference temperature within the thermal profile with $K1 = 0.09$ and $K2 = 0.28$. Run 27 achieved by Holden et al. [37][38], $M_{ae} = 3.4$, $\Lambda = 60^o$, $L/D = 6.13$.

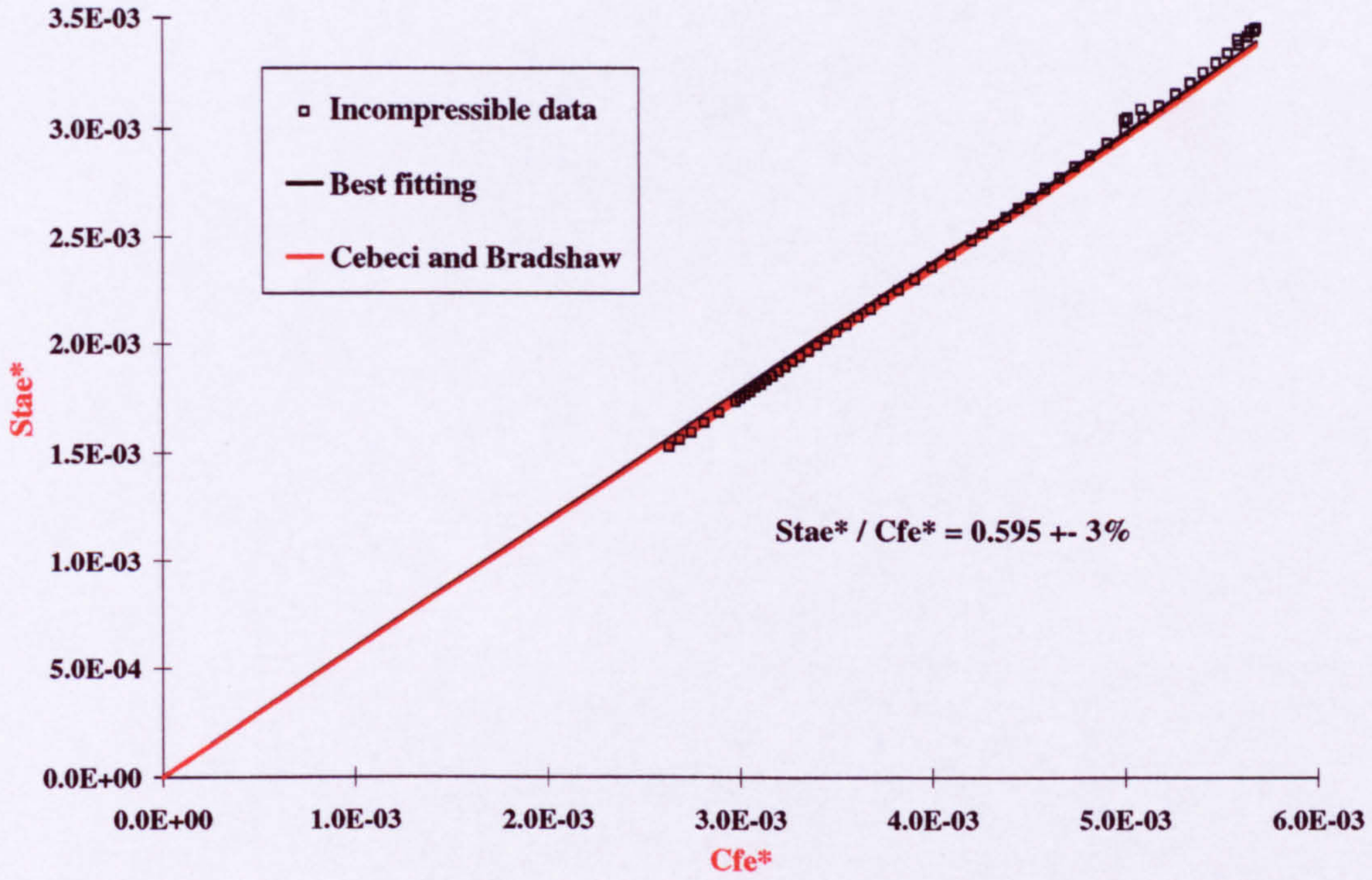

Figure A.115: Relationship between the Stanton number and skin friction for incompressible flow.

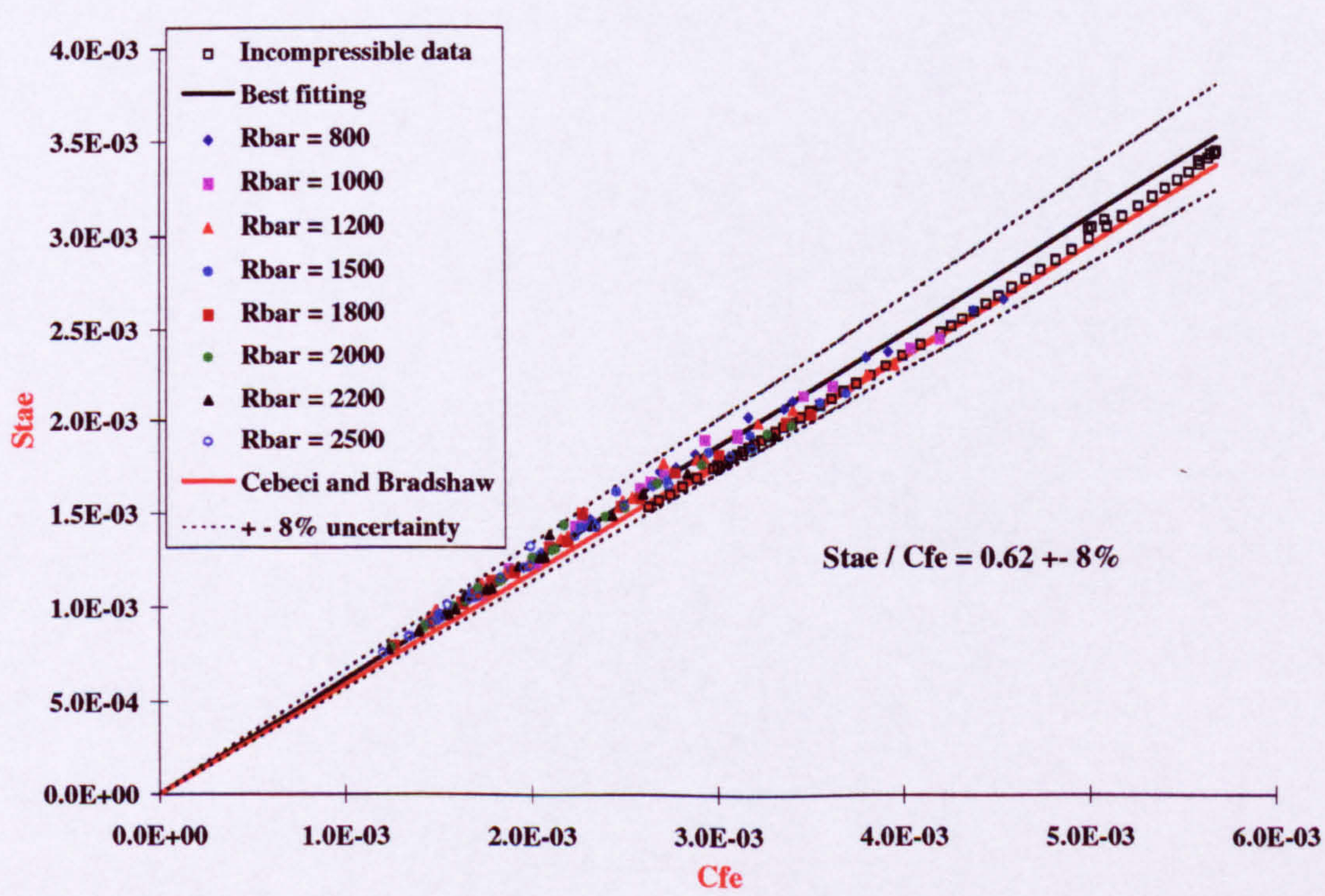

Figure A.116: Relationship between the Stanton number and skin friction (wind tunnel and flight conditions).

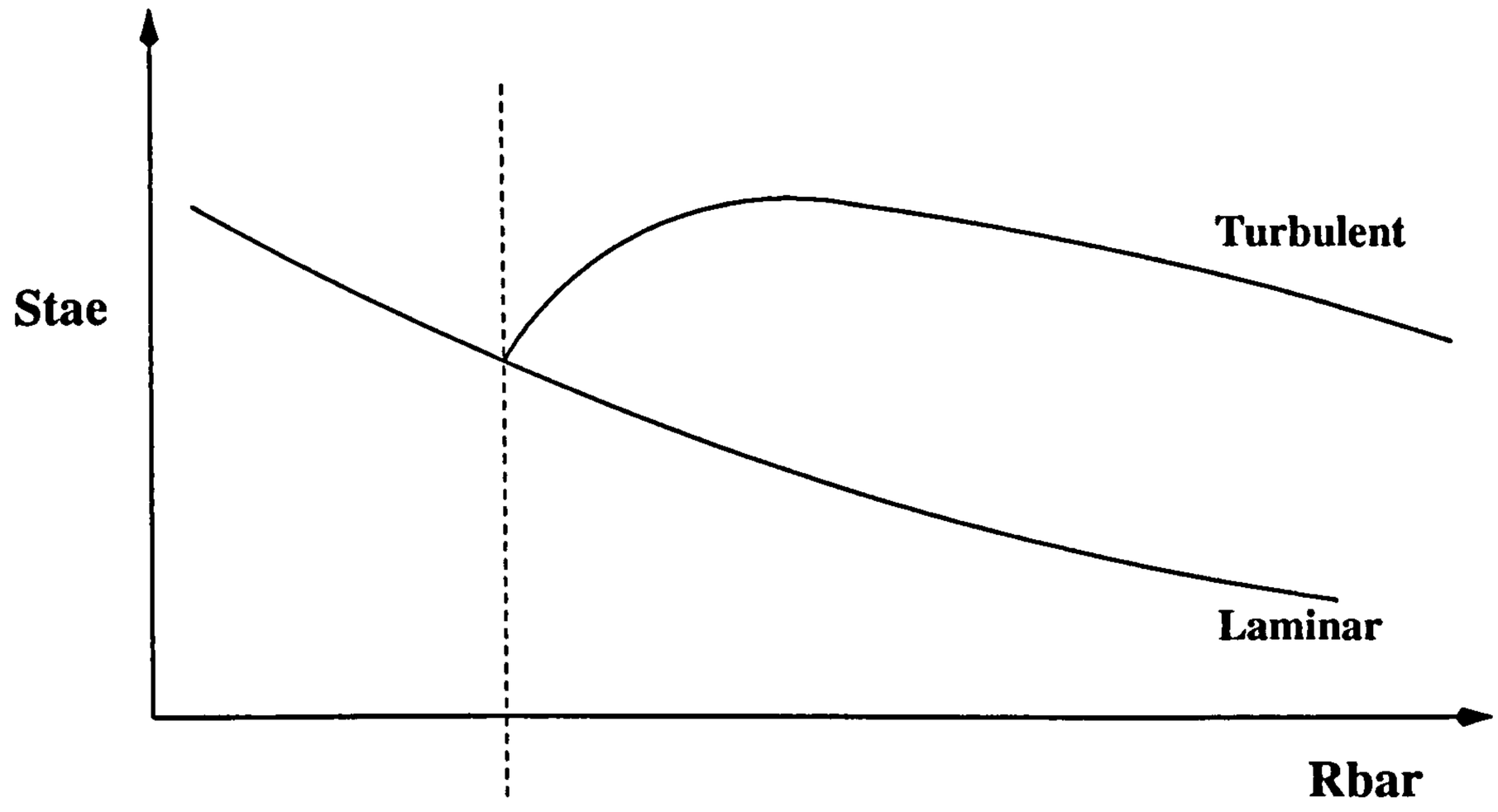

Figure A.117: Typical variation of the laminar and turbulent Stanton numbers with attachment-line Reynolds number.

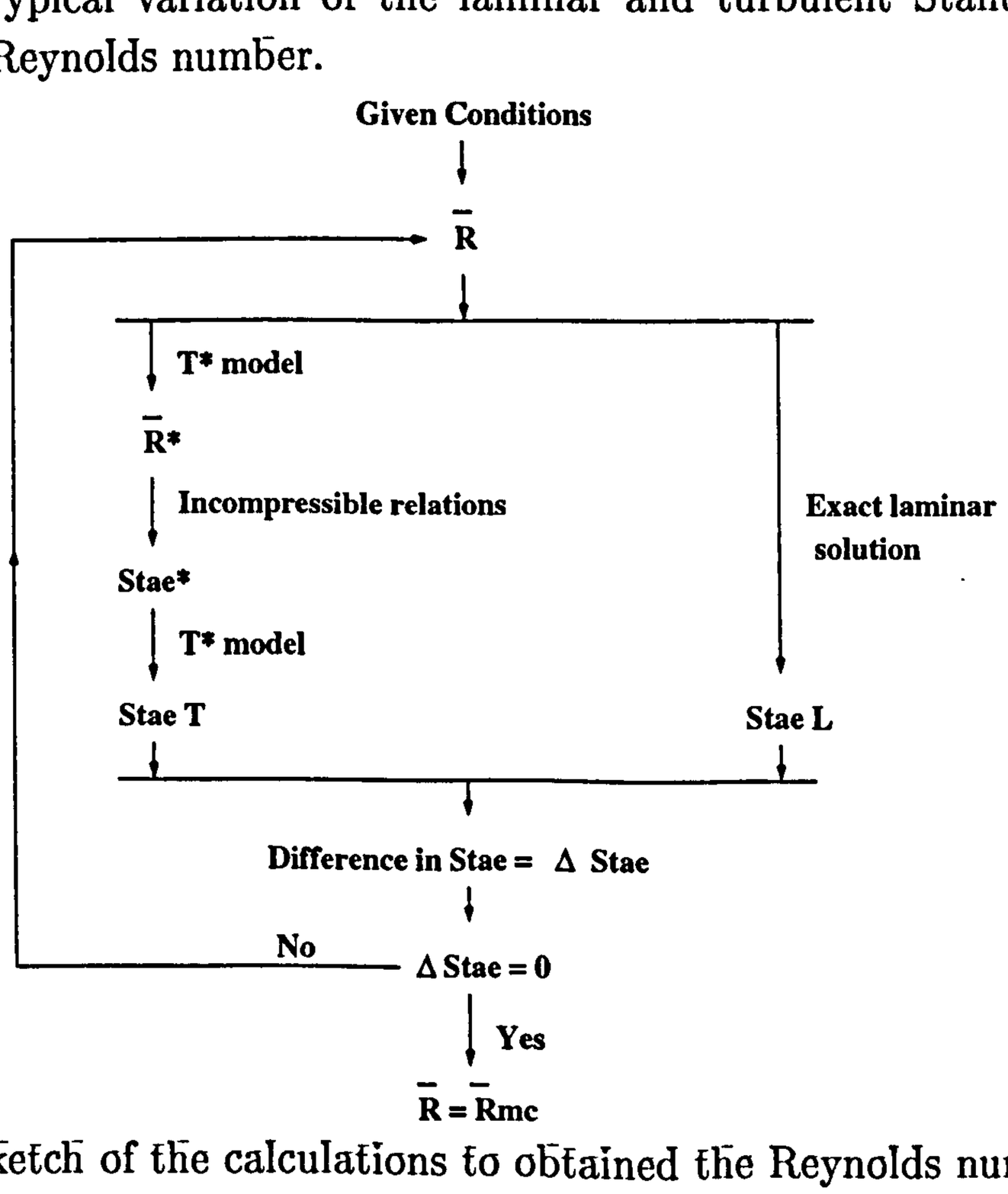

Figure A.118: Sketch of the calculations to obtained the Reynolds number for minimum conditions $\bar{R}_{mc}$ under large disturbances. Incompressible relations : equations 6.1 to 6.7.

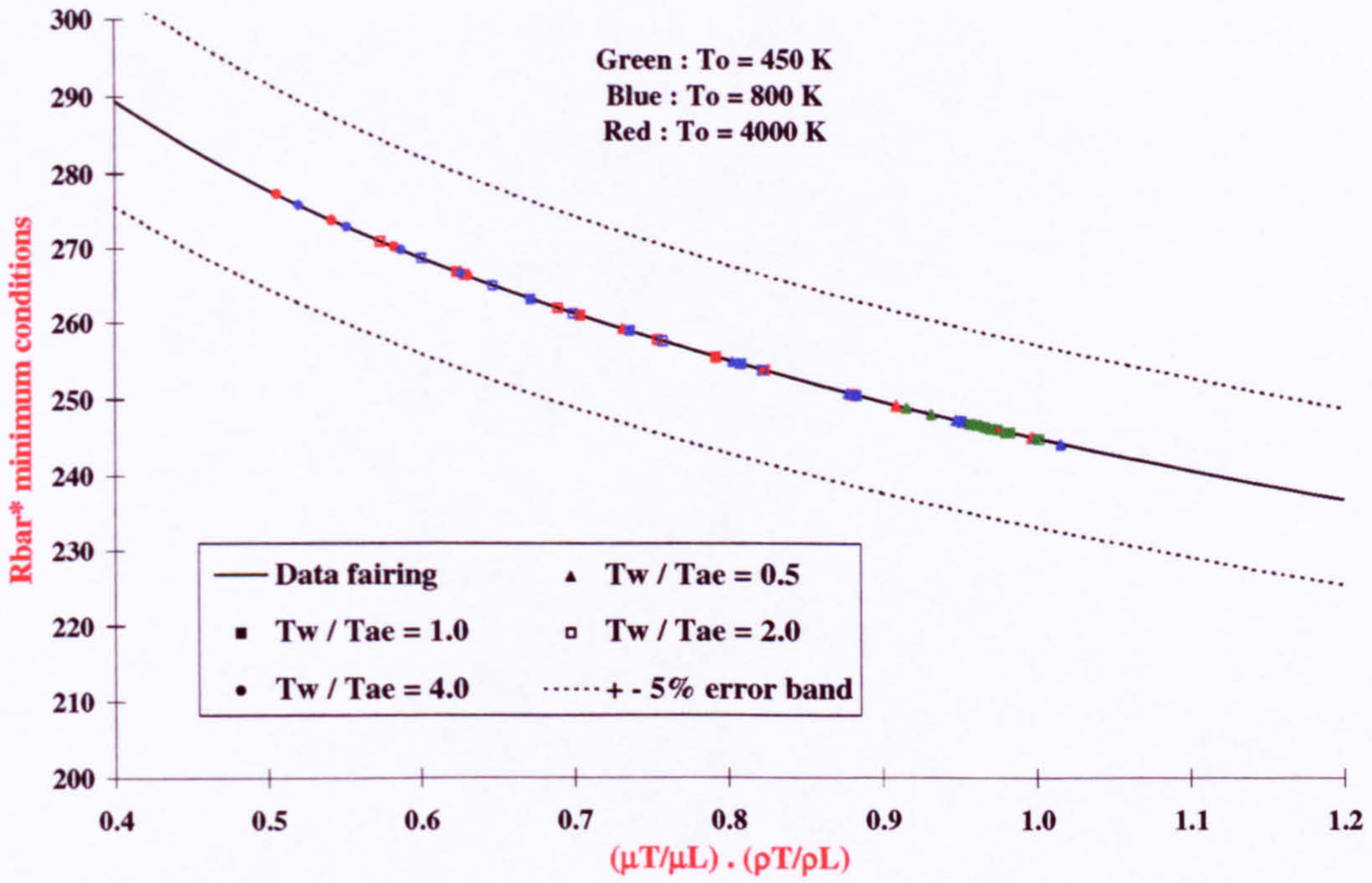

Figure A.119: Variation of $\bar{R}^*$ for the minimum conditions at which turbulent flow can occur.

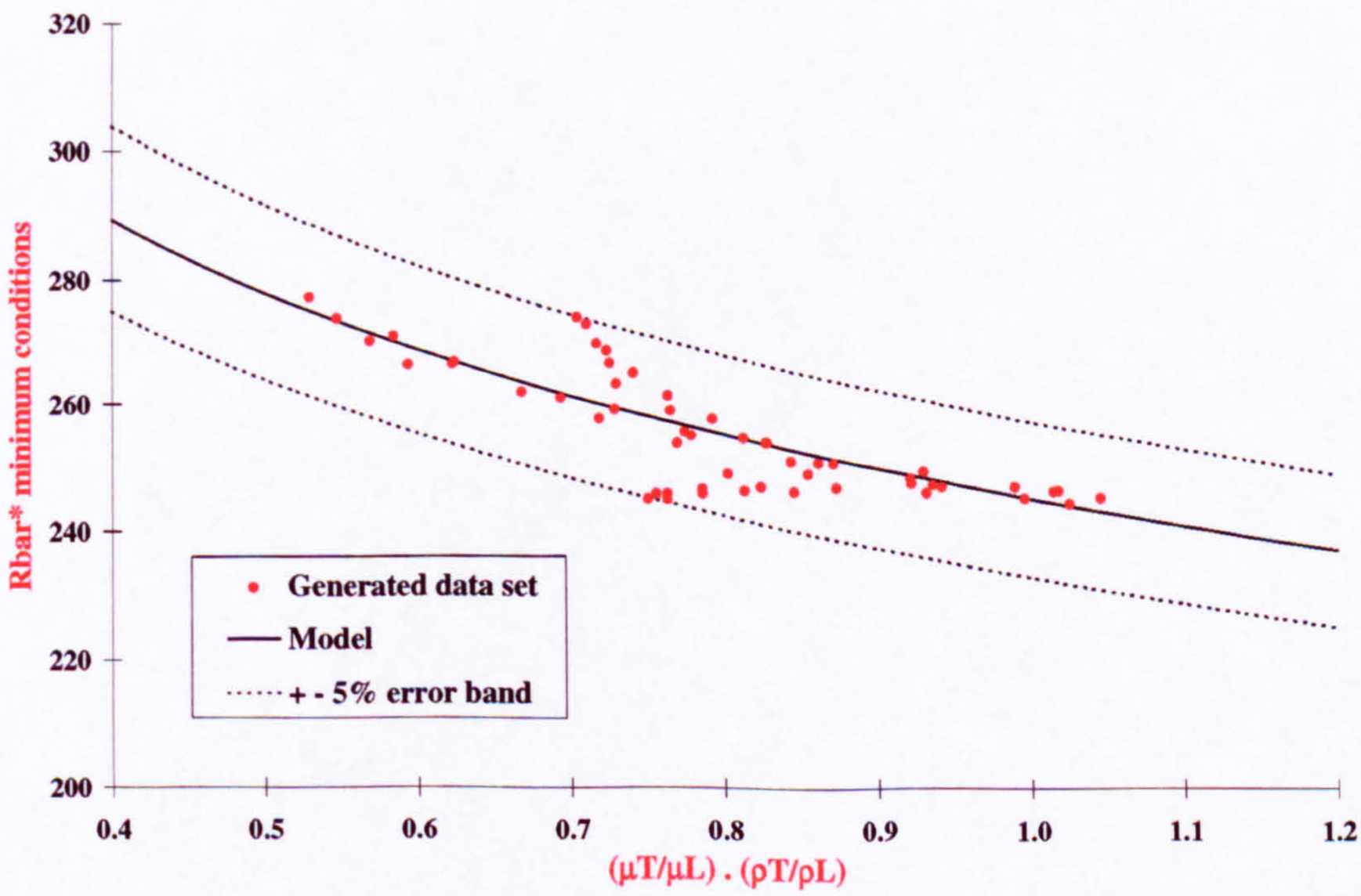

Figure A.120: Criterion characterising the minimum conditions at which turbulent flow occurs under large disturbances. Model from equation 7.13.

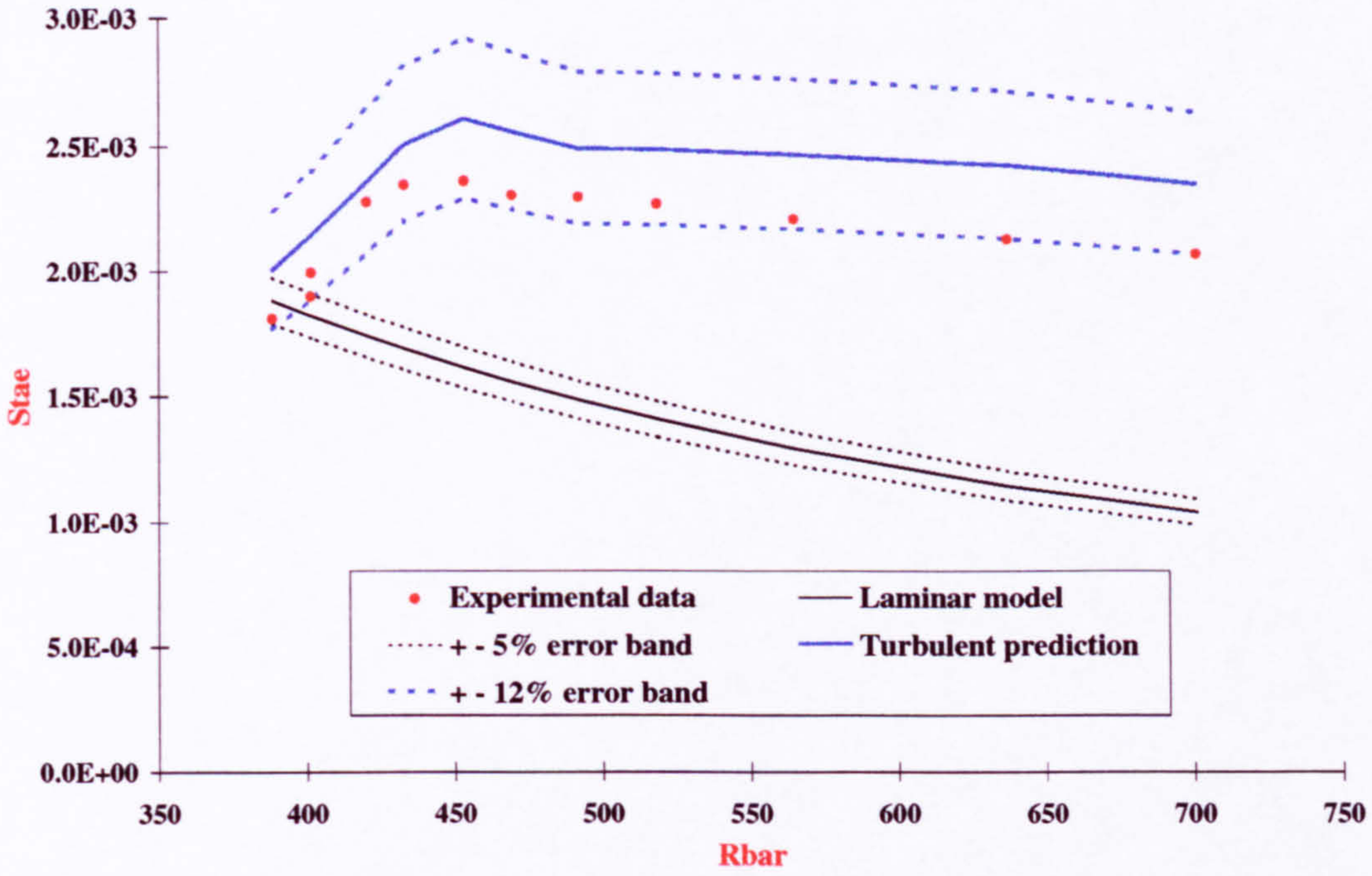

Figure A.121: Comparison between experimental data and predictions from the laminar and T^* models (equations 3.14 and 6.11 respectively). Poitiers Run81s, $M_\infty = 7.14$, $\Lambda = 60^o$, $T_w/T_o = 0.41$, $9.4.10^4 \leq R_{D\infty} \leq 3.10^5$.

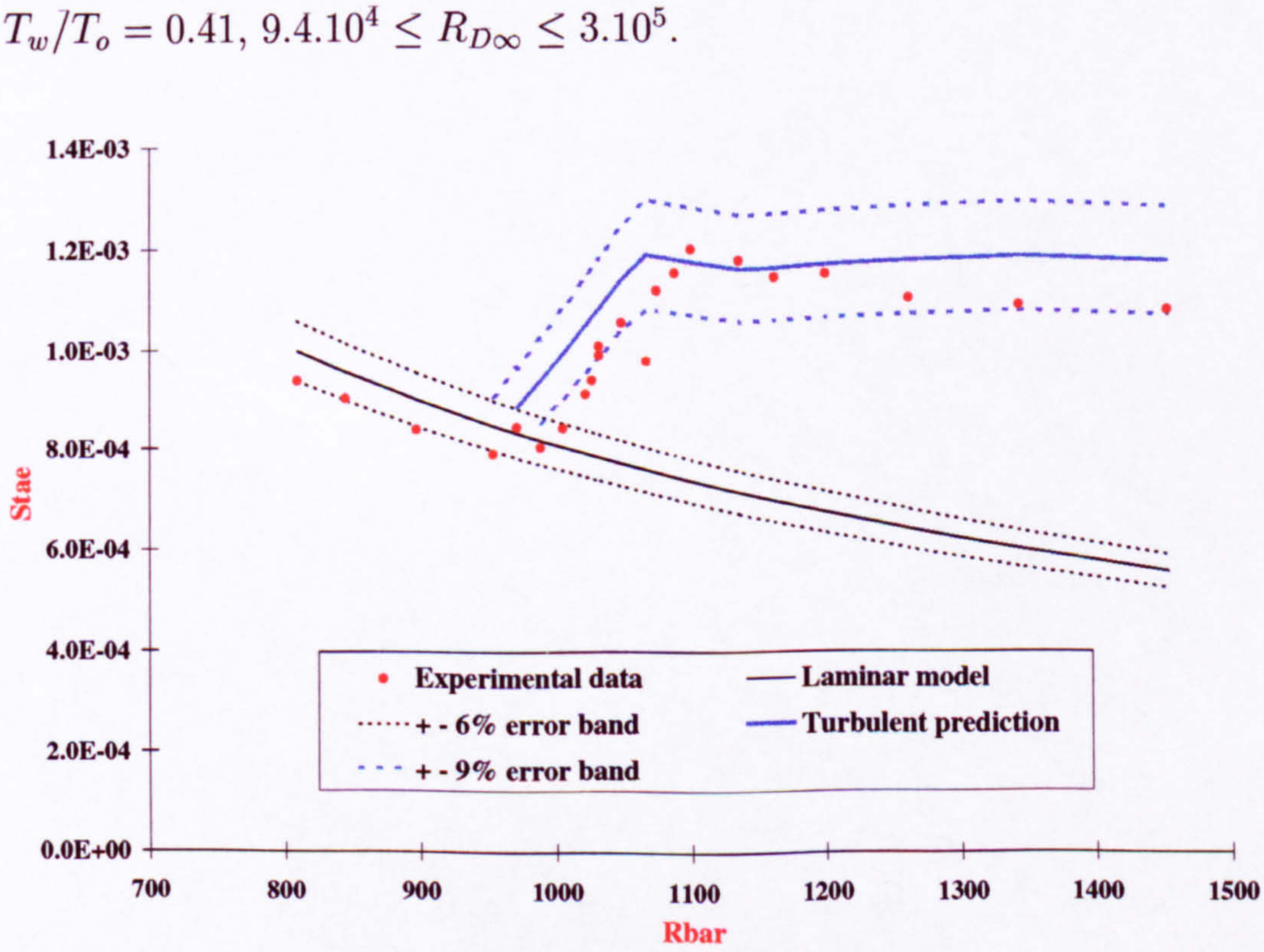

Figure A.122: Comparison between experimental data and predictions from the laminar and T^* models (equations 3.14 and 6.11 respectively). Poitiers Run82s, $M_\infty = 7.14$, $\Lambda = 80^o$, $T_w/T_o = 0.39$, $1.5.10^5 \leq R_{D\infty} \leq 4.9.10^5$.

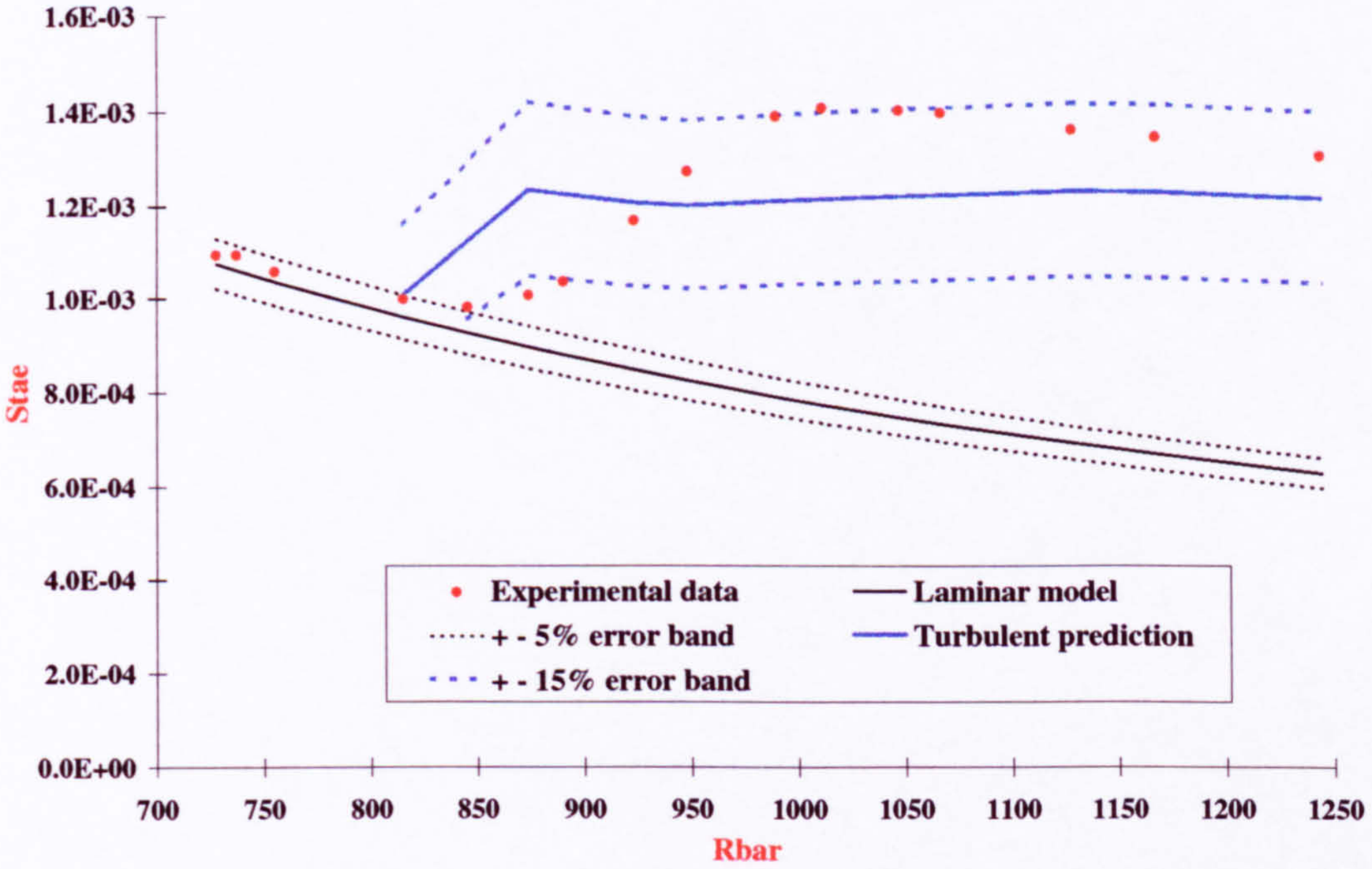

Figure A.123: Comparison between experimental data and predictions from the laminar and T^* models (equations 3.14 and 6.11 respectively). Poitiers Run84s, $M_\infty = 7.14$, $\Lambda = 76^o$, $T_w/T_o = 0.38$, $1.4.10^5 \leq R_{D\infty} \leq 4.2.10^5$.

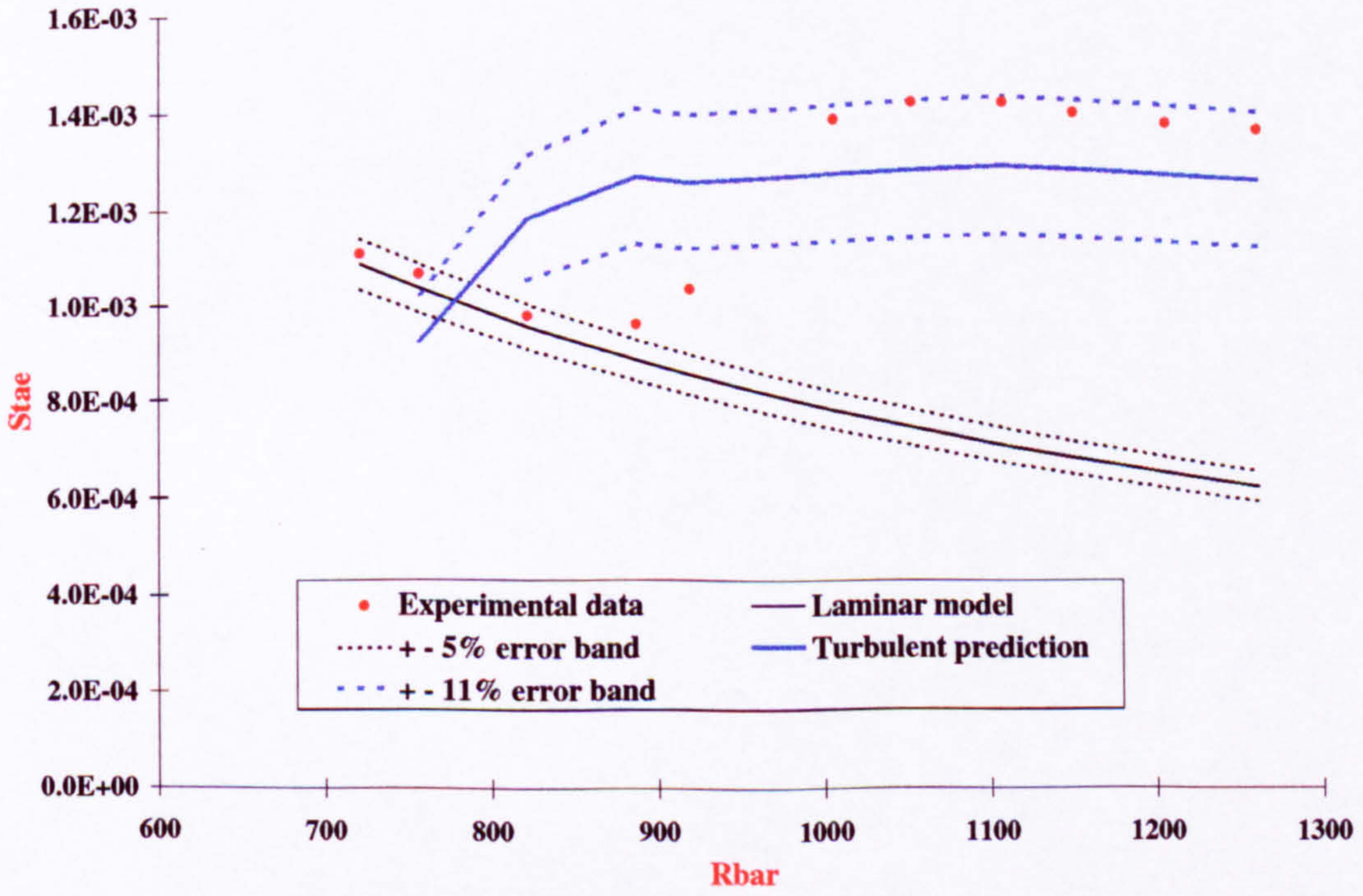

Figure A.124: Comparison between experimental data and predictions from the laminar and T^* models (equations 3.14 and 6.11 respectively). Poitiers Run85s, $M_\infty = 7.14$, $\Lambda = 76^o$, $T_w/T_o = 0.38$, $1.4.10^5 \leq R_{D\infty} \leq 4.4.10^5$.

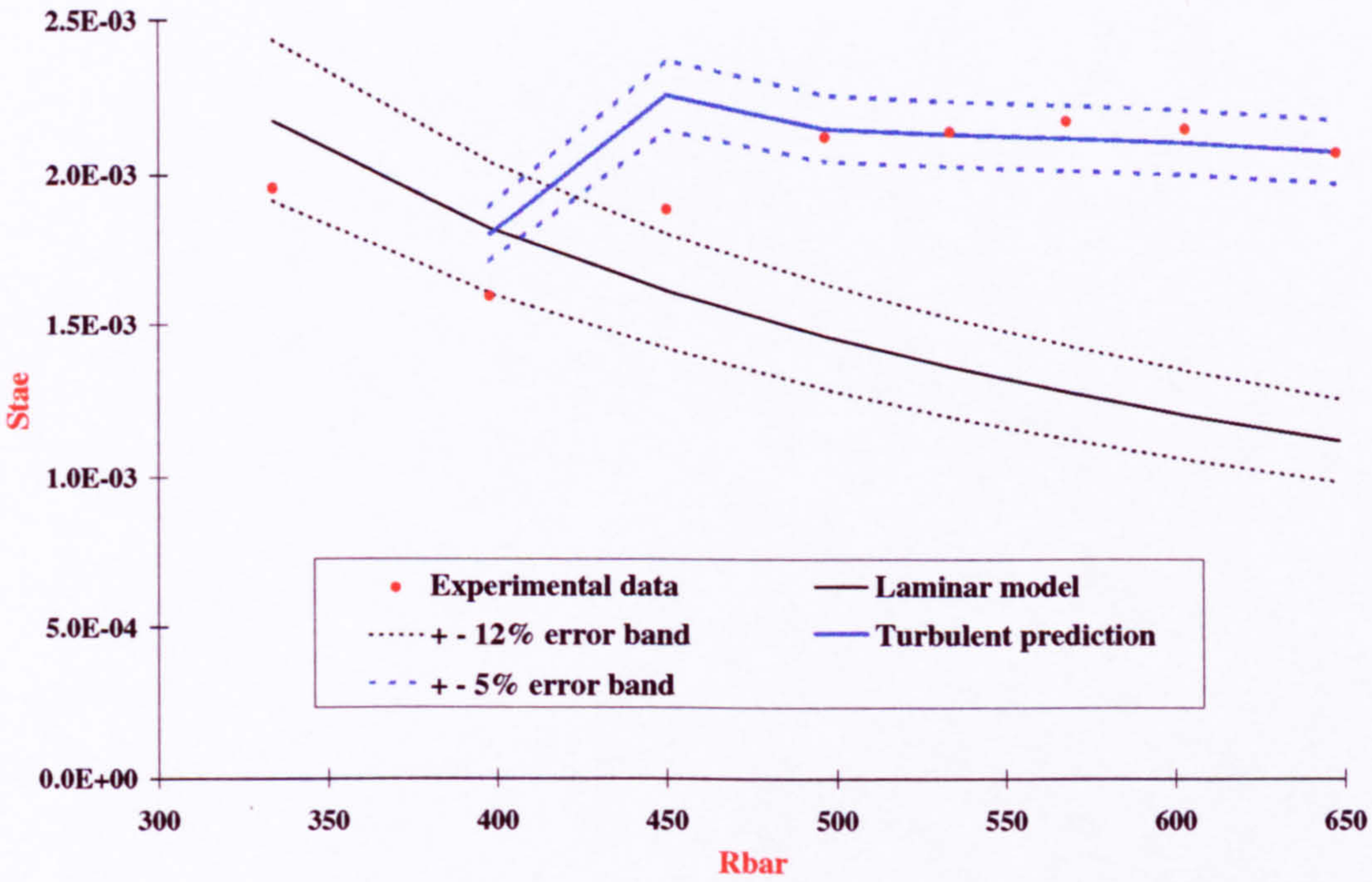

Figure A.125: Comparison between experimental data and predictions from the laminar and T^* models (equations 3.14 and 6.11 respectively). Bushnell Runs 12 to 19, $L/D = 5.3$, $M_\infty = 7.81$, $\Lambda = 60^o$, $T_w/T_o \approx 0.40$, $8.8.10^4 \leq R_{D\infty} \leq 3.3.10^5$.

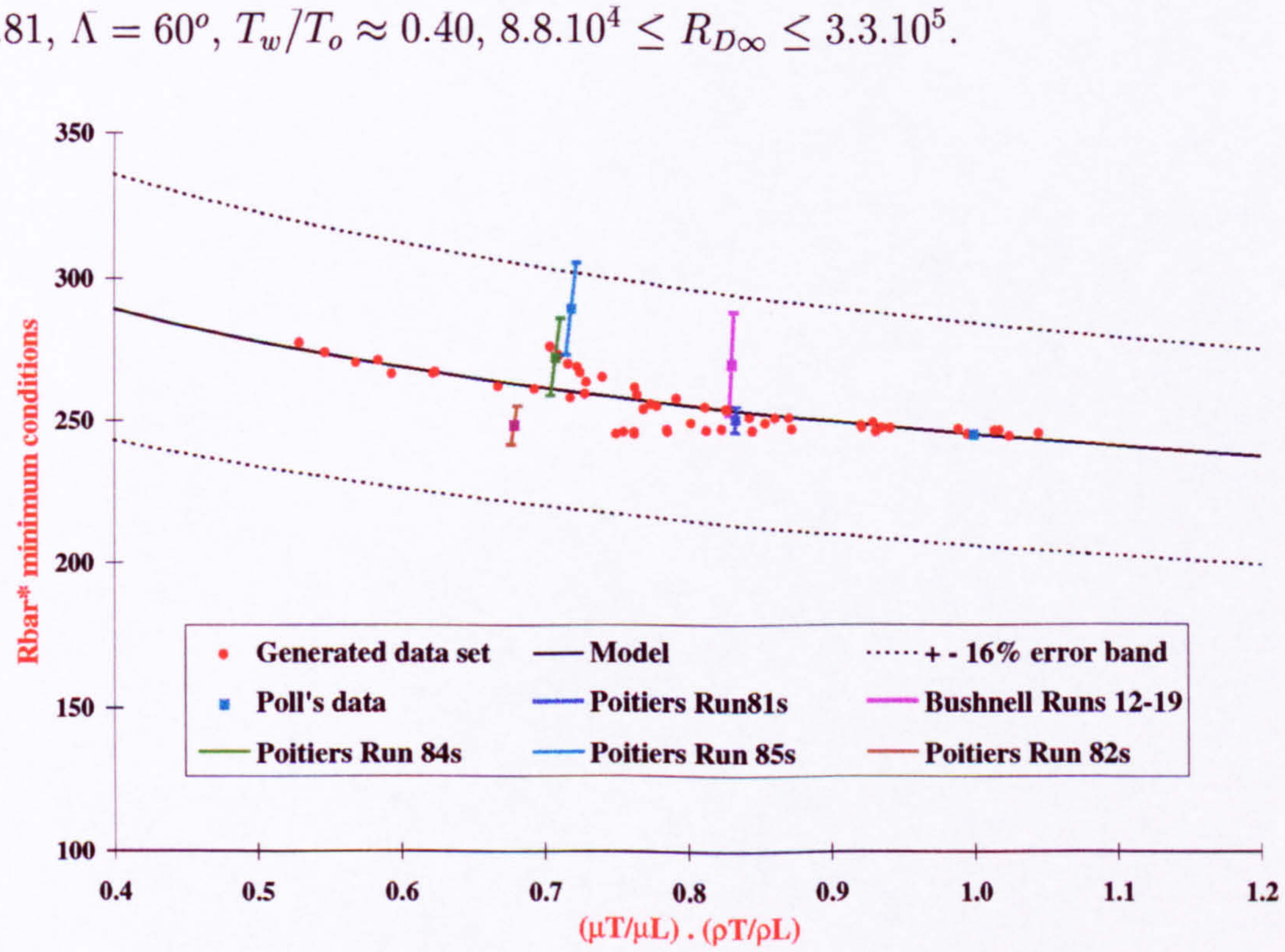

Figure A.126: Criterion characterising the minimum conditions at which turbulent flow occurs under large disturbances. Model from equation 7.13. Experiments from Poitiers runs 81s, 82s, 84s and 85s and Bushnell runs 12 to 19 at L/D of 5.3.

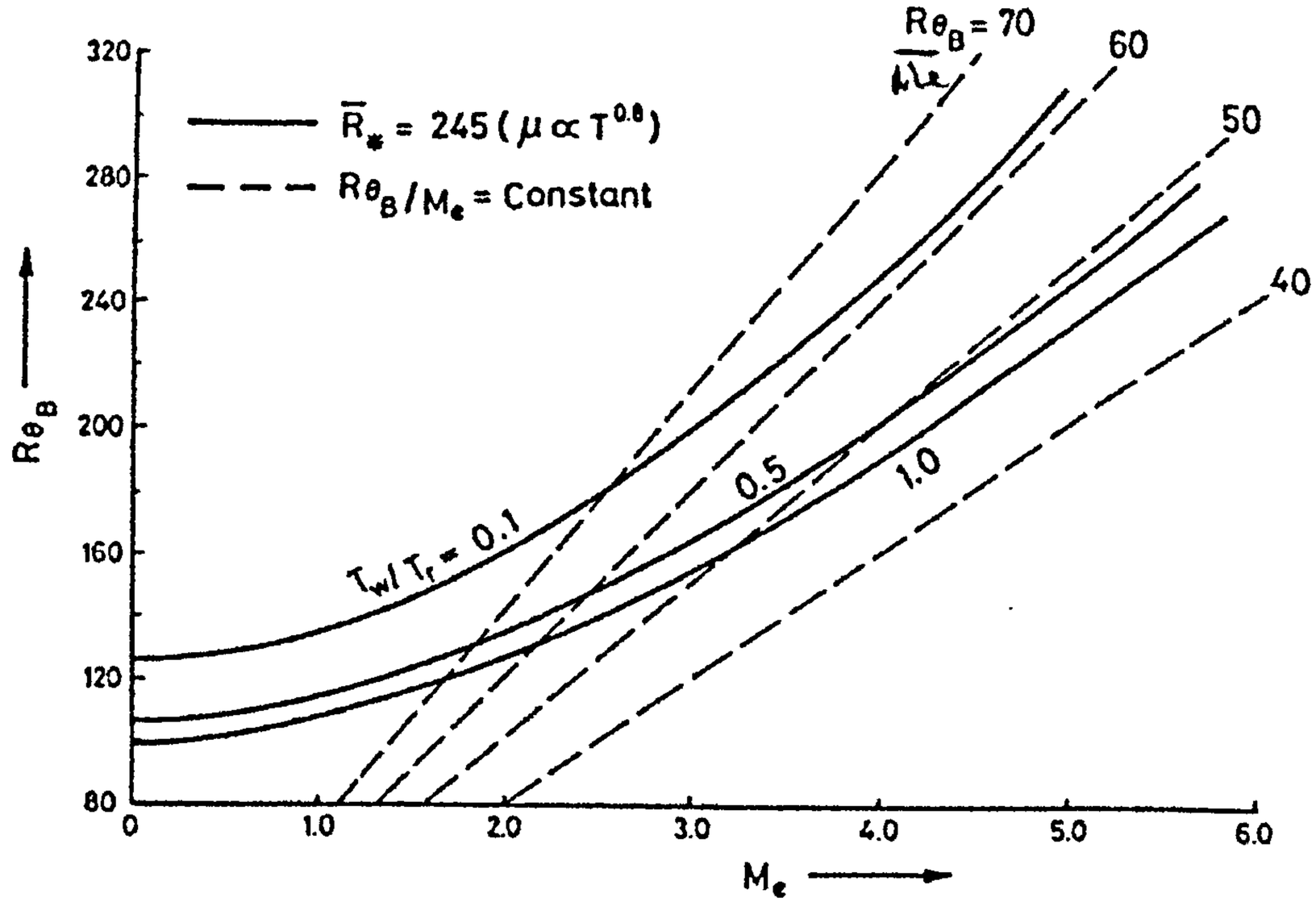

Figure A.127: Necessary conditions for the onset of transition in terms of R_θ, edge Mach number and wall to recovery temperature ratio after Poll [51].

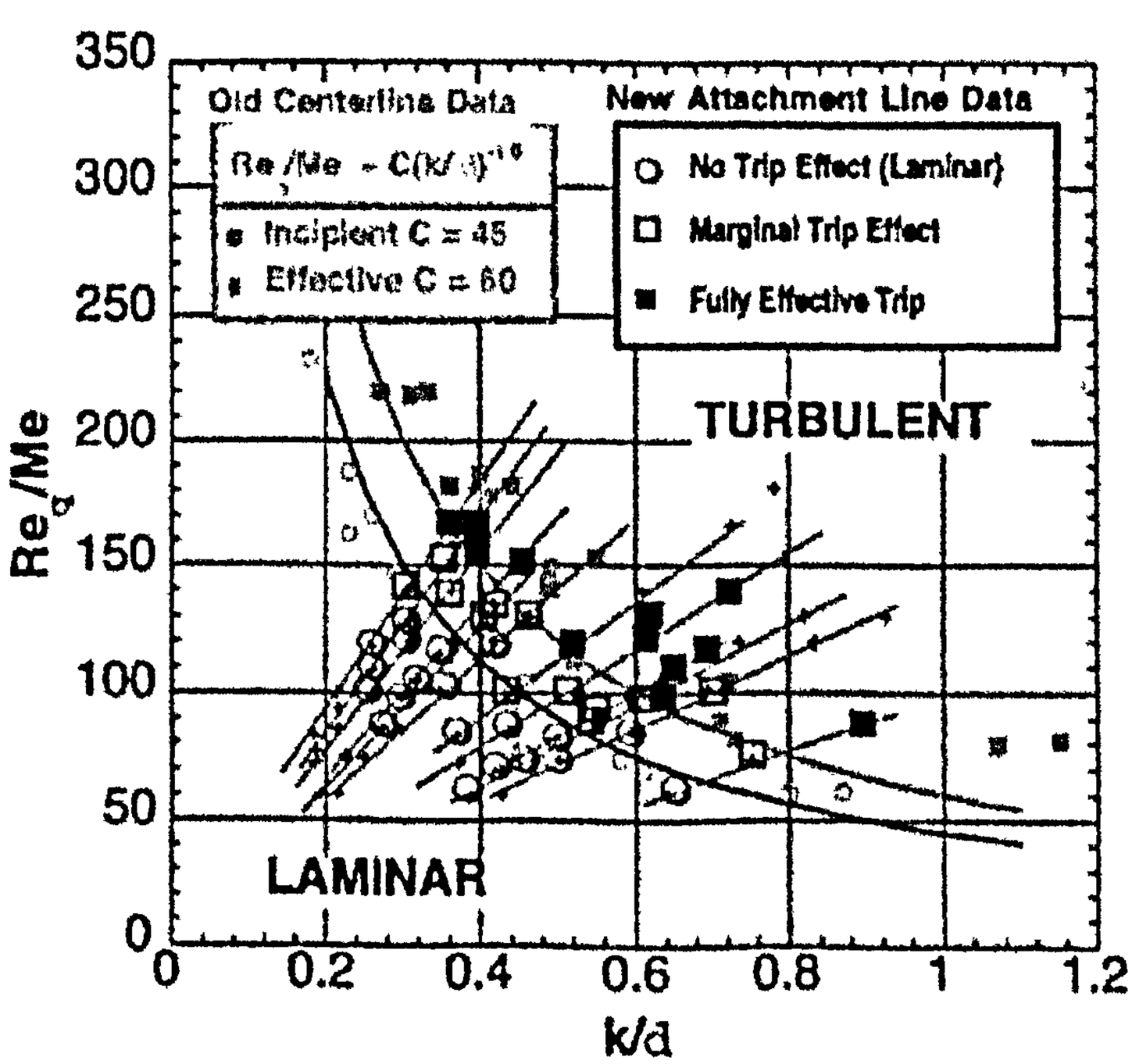

Figure A.128: Wind tunnel results of the X-33 windward attachment-line transition correlation after Berry et al. [7]. k/d : ratio of the roughness element height to the boundary layer thickness.

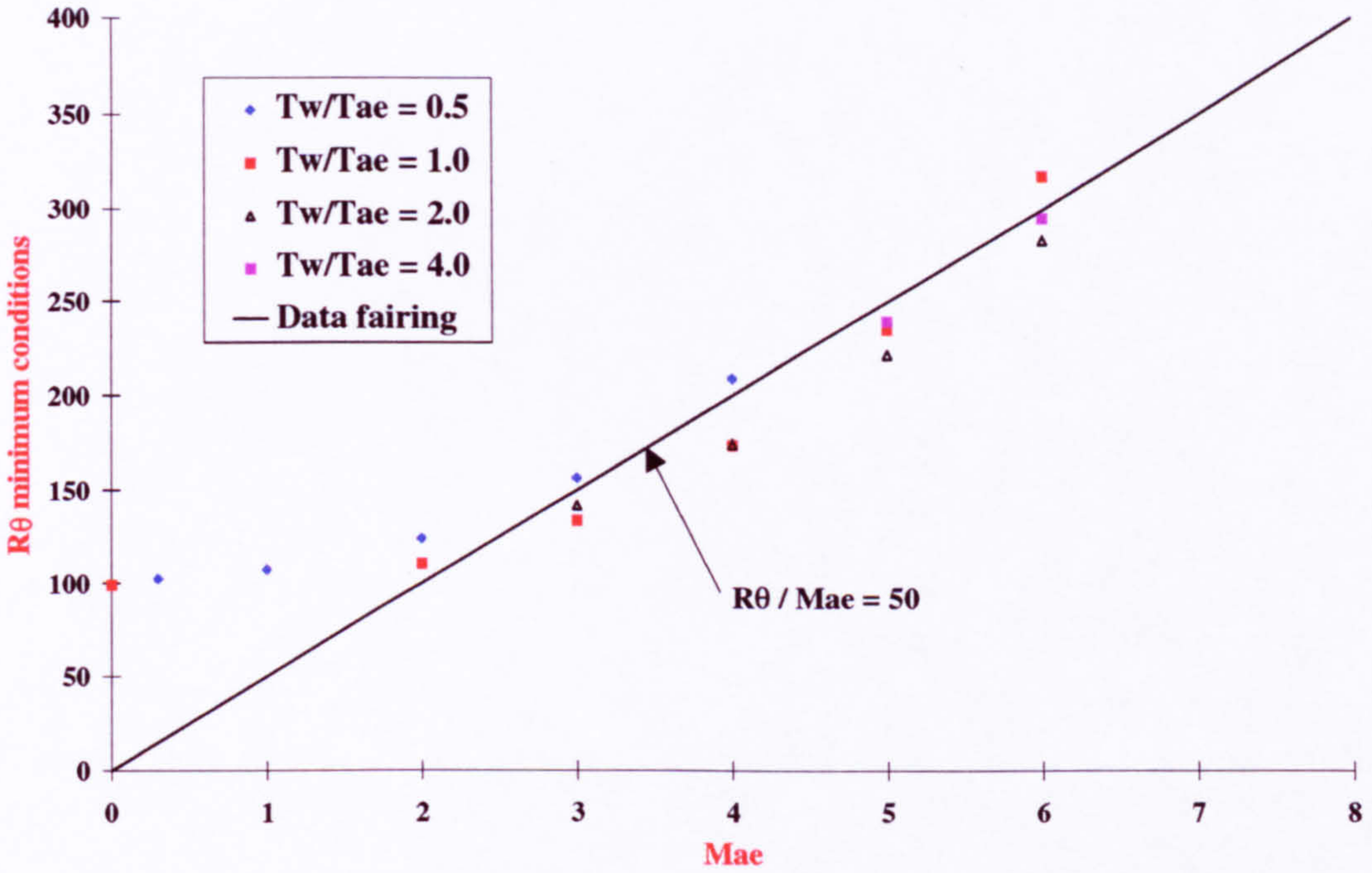

Figure A.129: Variation of R_θ with M_{ae} for the minimum conditions for transition onset under large source of disturbances. Wind tunnel conditions, $T_o = 450$K.

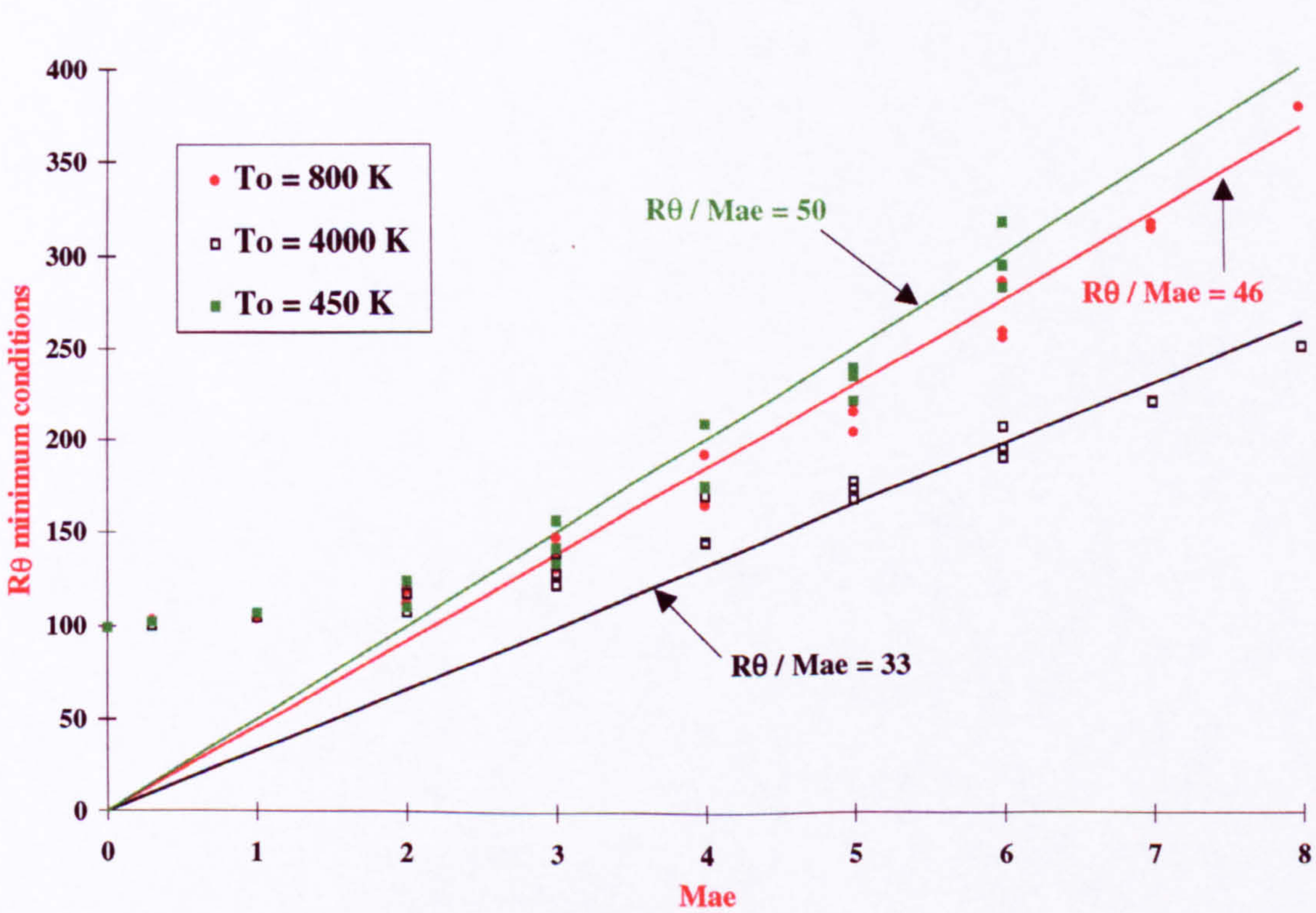

Figure A.130: Variation of the laminar R_θ with M_{ae} for the minimum conditions for transition onset under large source of disturbances. Wind tunnel and flight conditions.

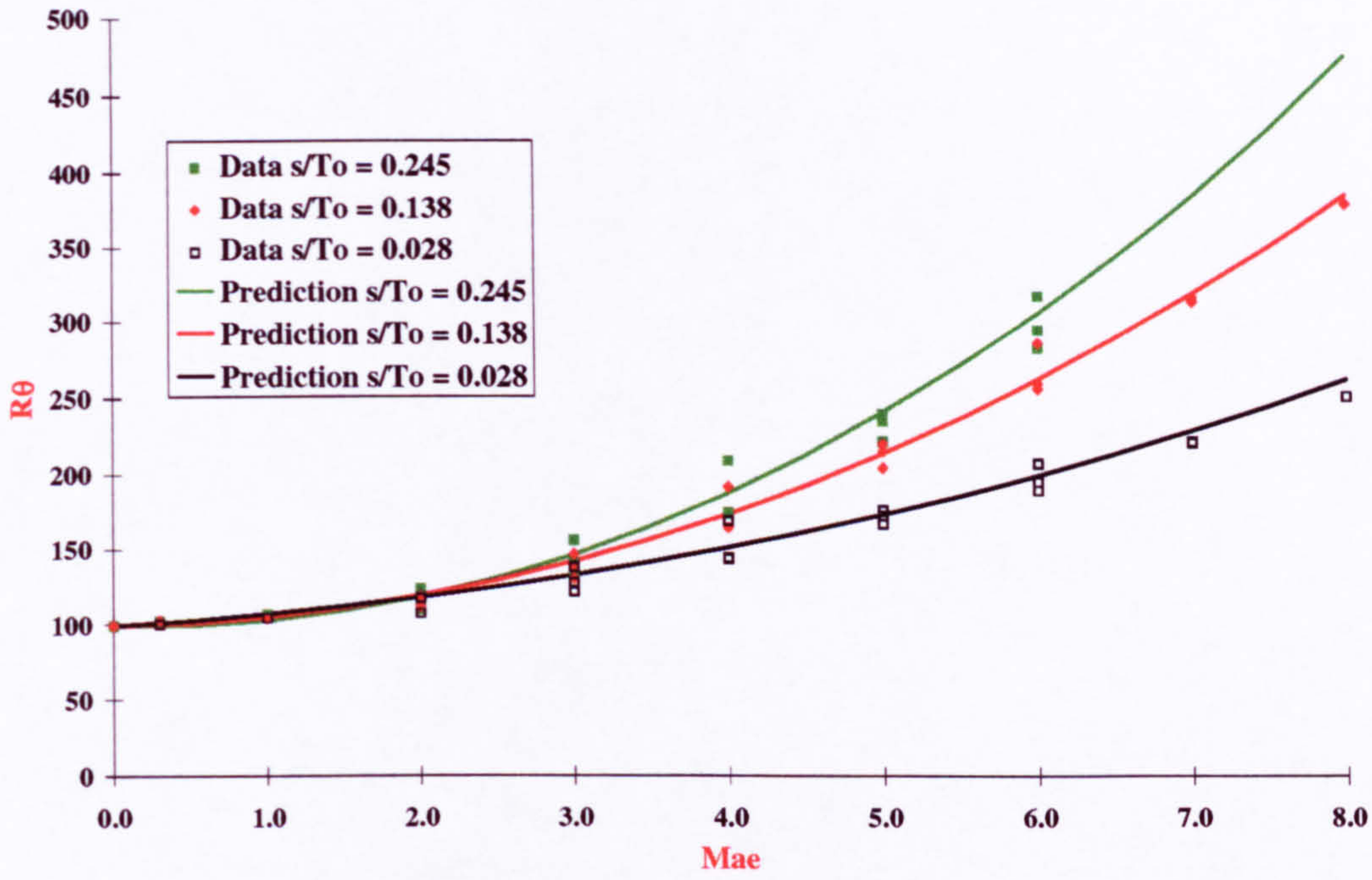

Figure A.131: Variation of the Reynolds number R_θ for the minimum conditions at which turbulent flow can occur under large sources of disturbances. Wind tunnel and flight conditions. Predictions from equation 7.14.

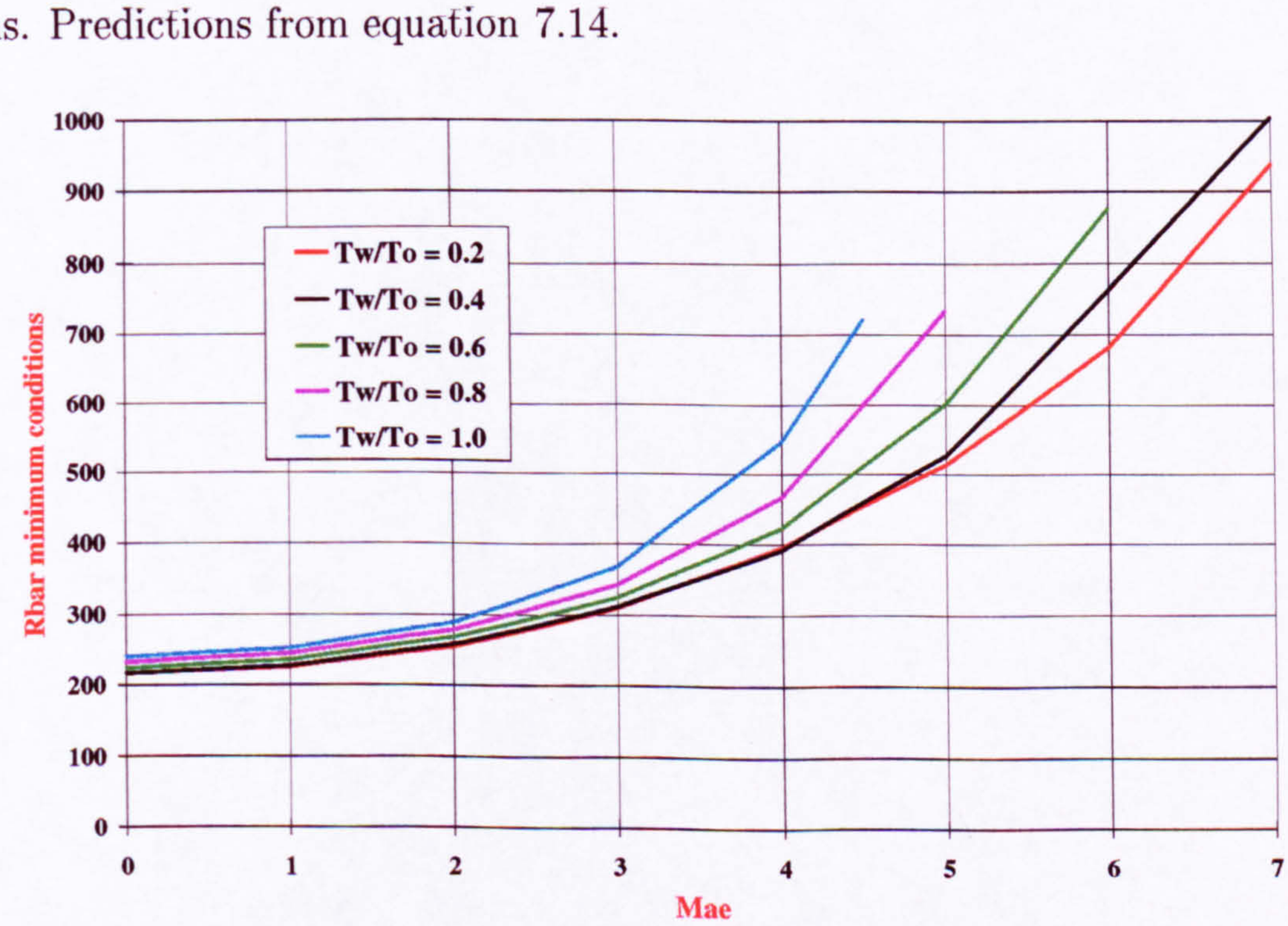

Figure A.132: Variation of the Reynolds number $\bar{R}_{mc}$ for the minimum conditions at which turbulent flow can occur under large sources of disturbances. T^* and laminar models ; wind tunnel conditions, $s/T_o = 0.138$.

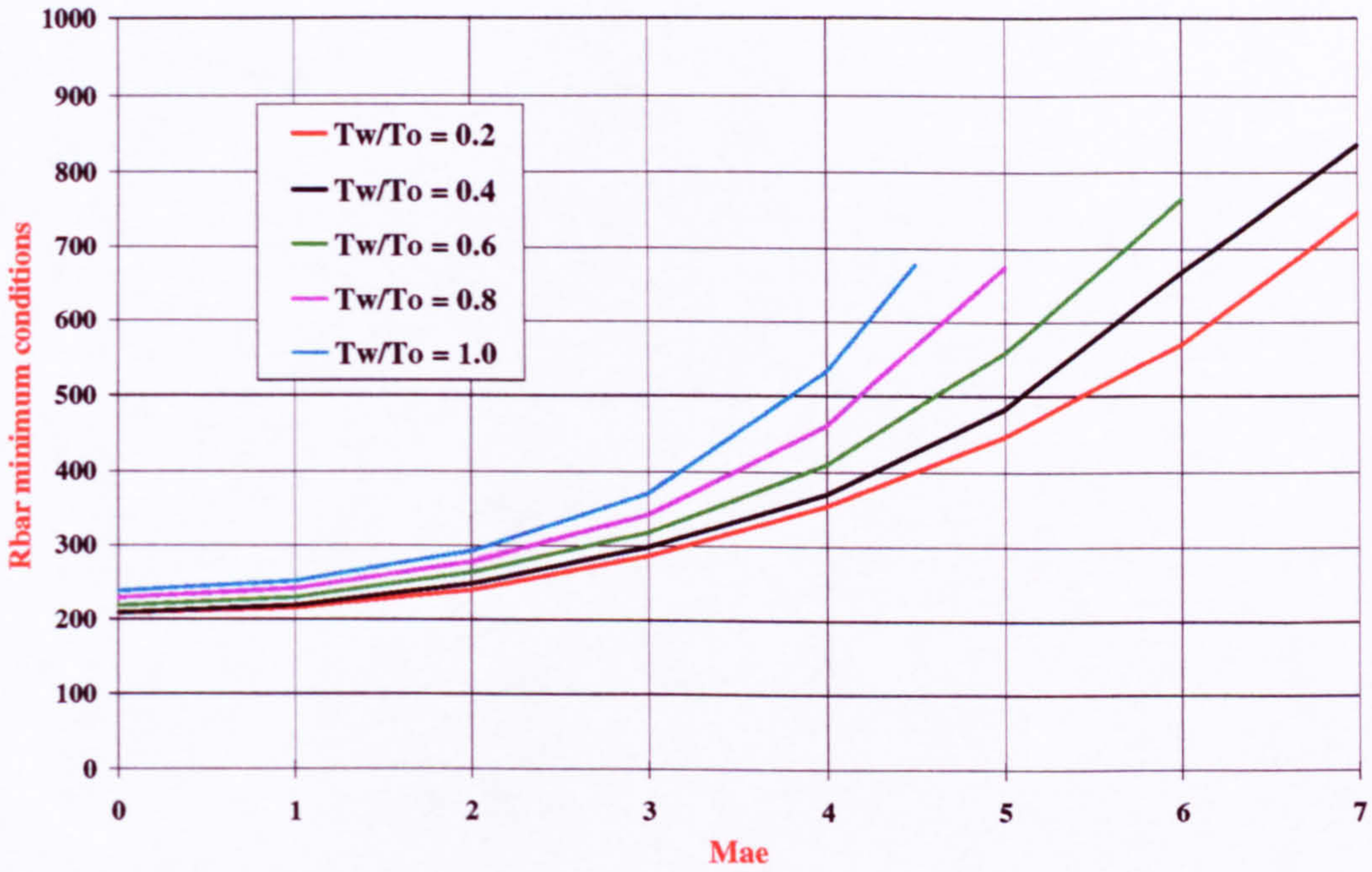

Figure A.133: Variation of the Reynolds number $\bar{R}_{mc}$ for the minimum conditions at which turbulent flow can occur under large sources of disturbances. T^* and laminar models ; flight conditions, $s/T_o = 0.028$.

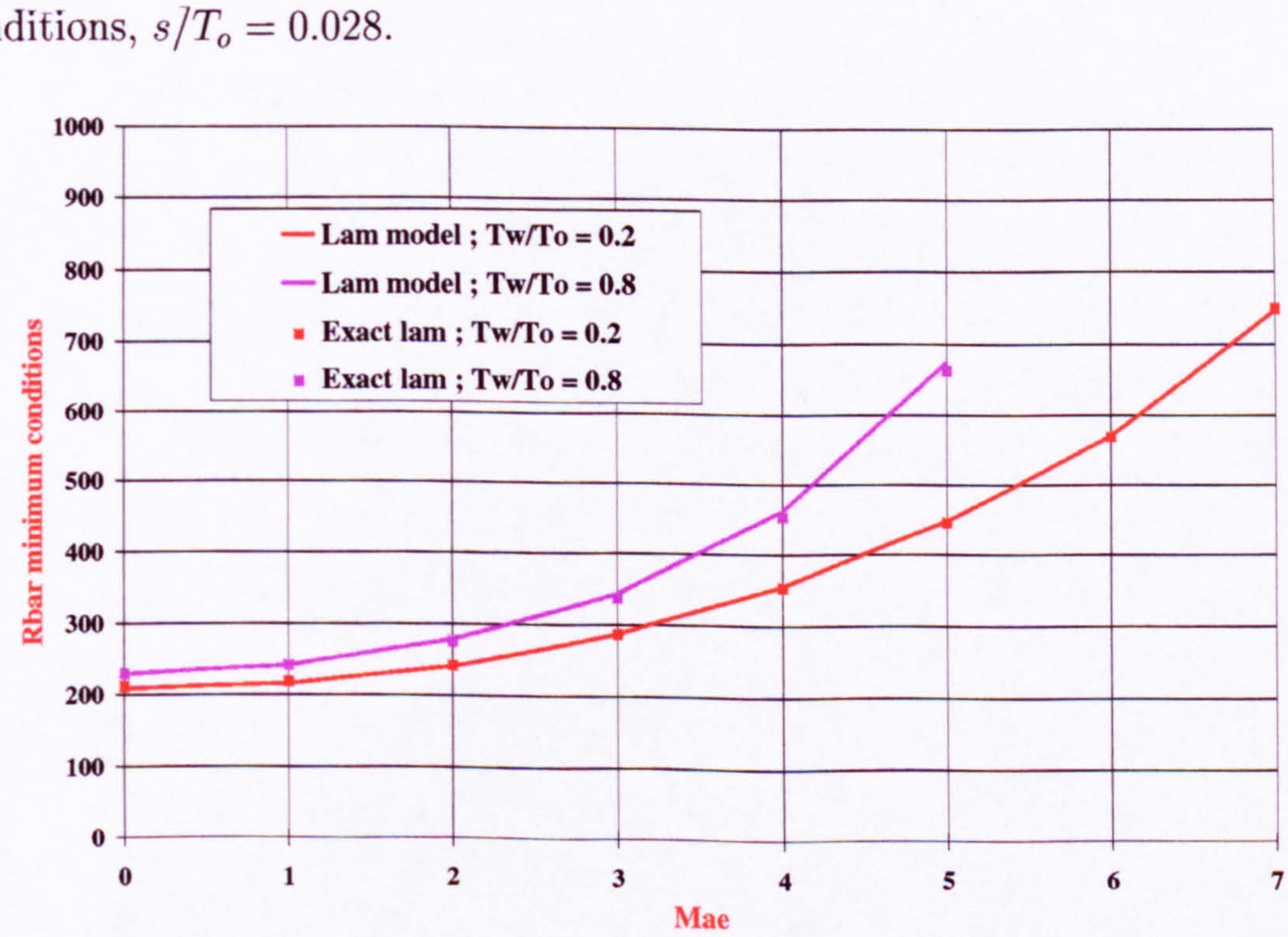

Figure A.134: Variation of the Reynolds number $\bar{R}_{mc}$ for the minimum conditions at which turbulent flow can occur under large sources of disturbances. T^* model and exact laminar solution or laminar model ; flight conditions, $s/T_o = 0.028$.

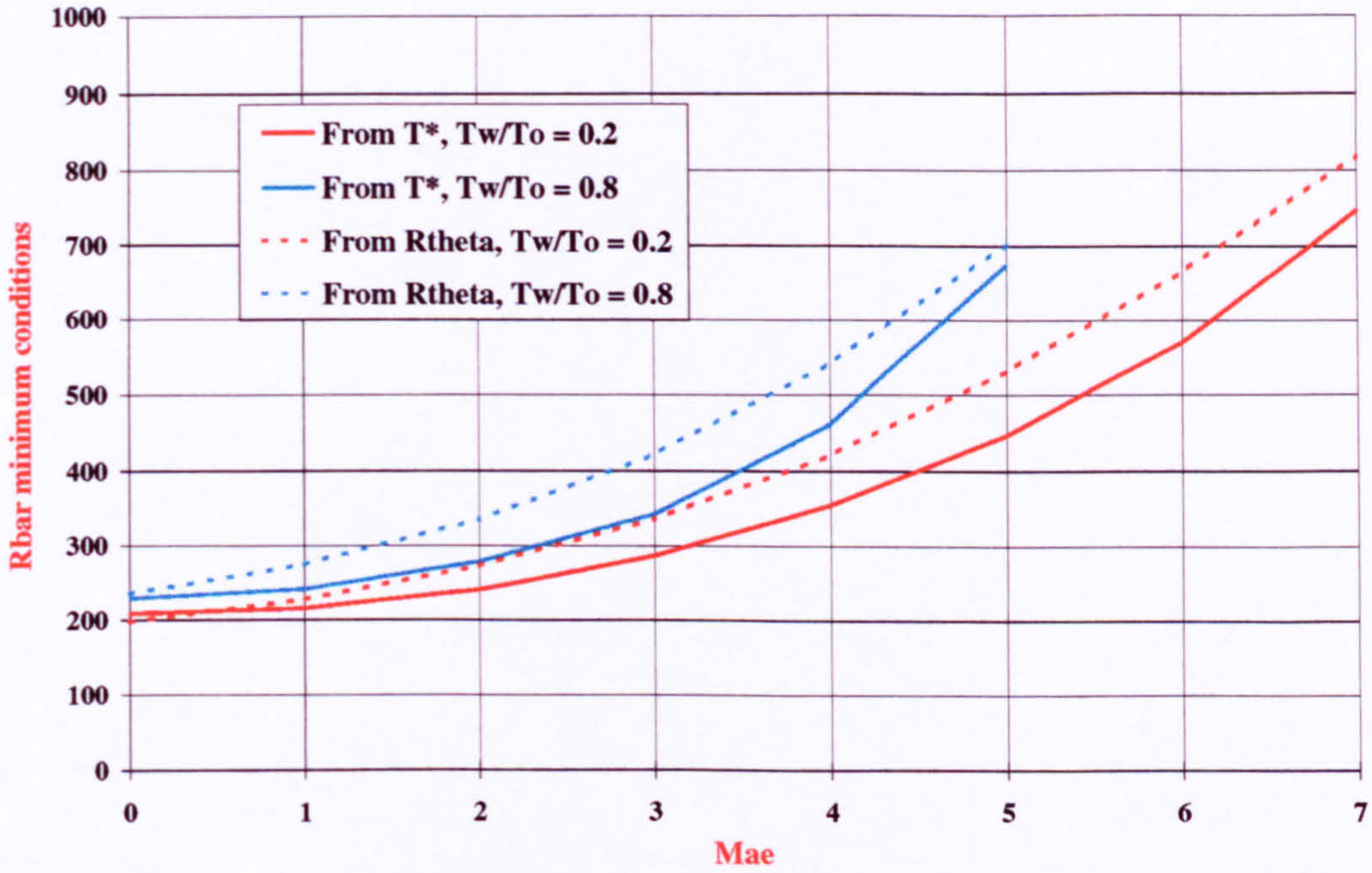

Figure A.135: Comparison of the Reynolds number $\bar{R}_{mc}$ for the minimum conditions obtained from the reference temperature model and the R_θ model ; Flight conditions, $s/T_o = 0.028$.

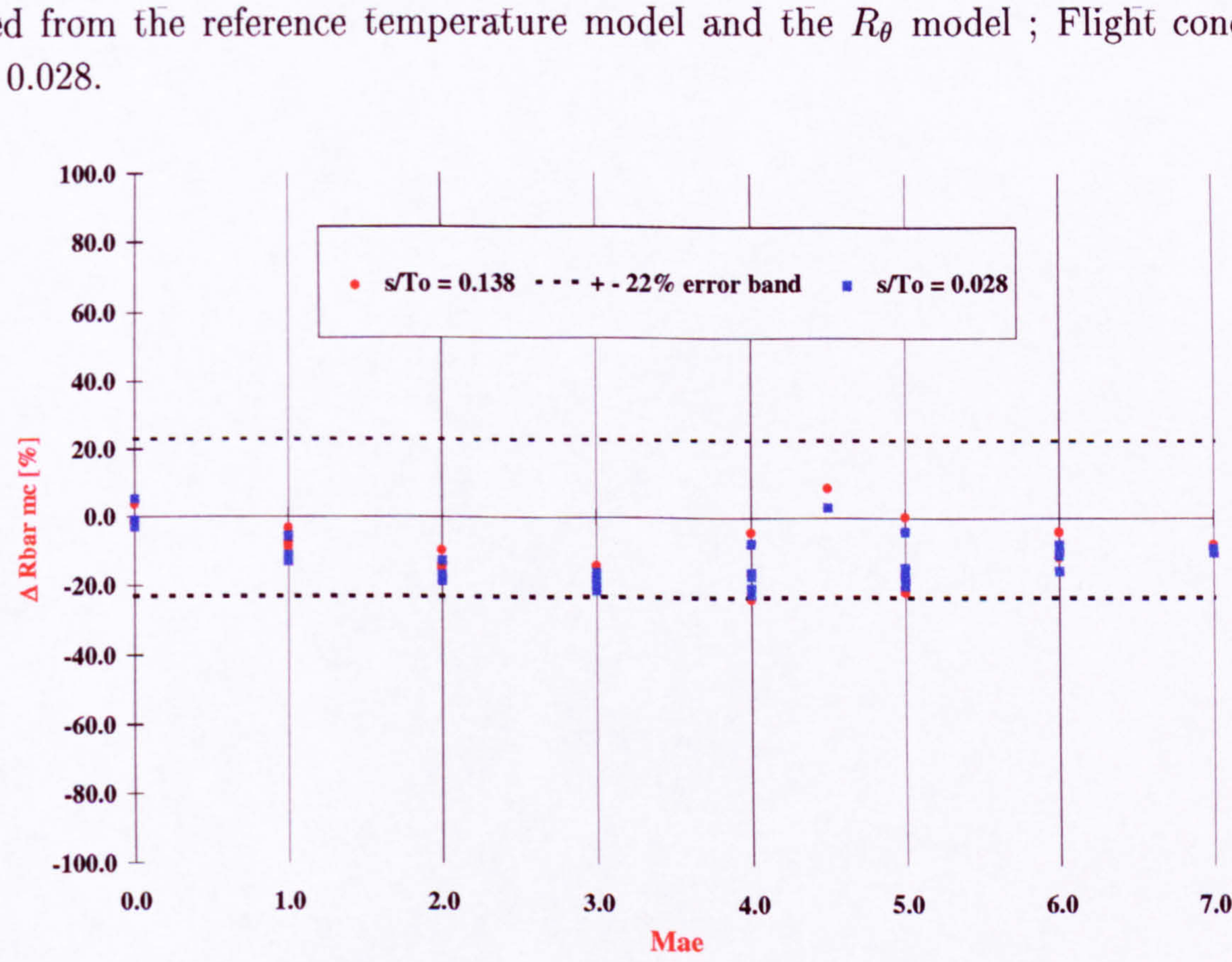

Figure A.136: Variation of the difference in $\bar{R}_{mc}$ when $\bar{R}^*/\bar{R}$ and $\bar{R}^*_{mc}$ (with the laminar model) are used and when $R_\theta/\bar{R}$ and $R_{\theta mc}$ are used.

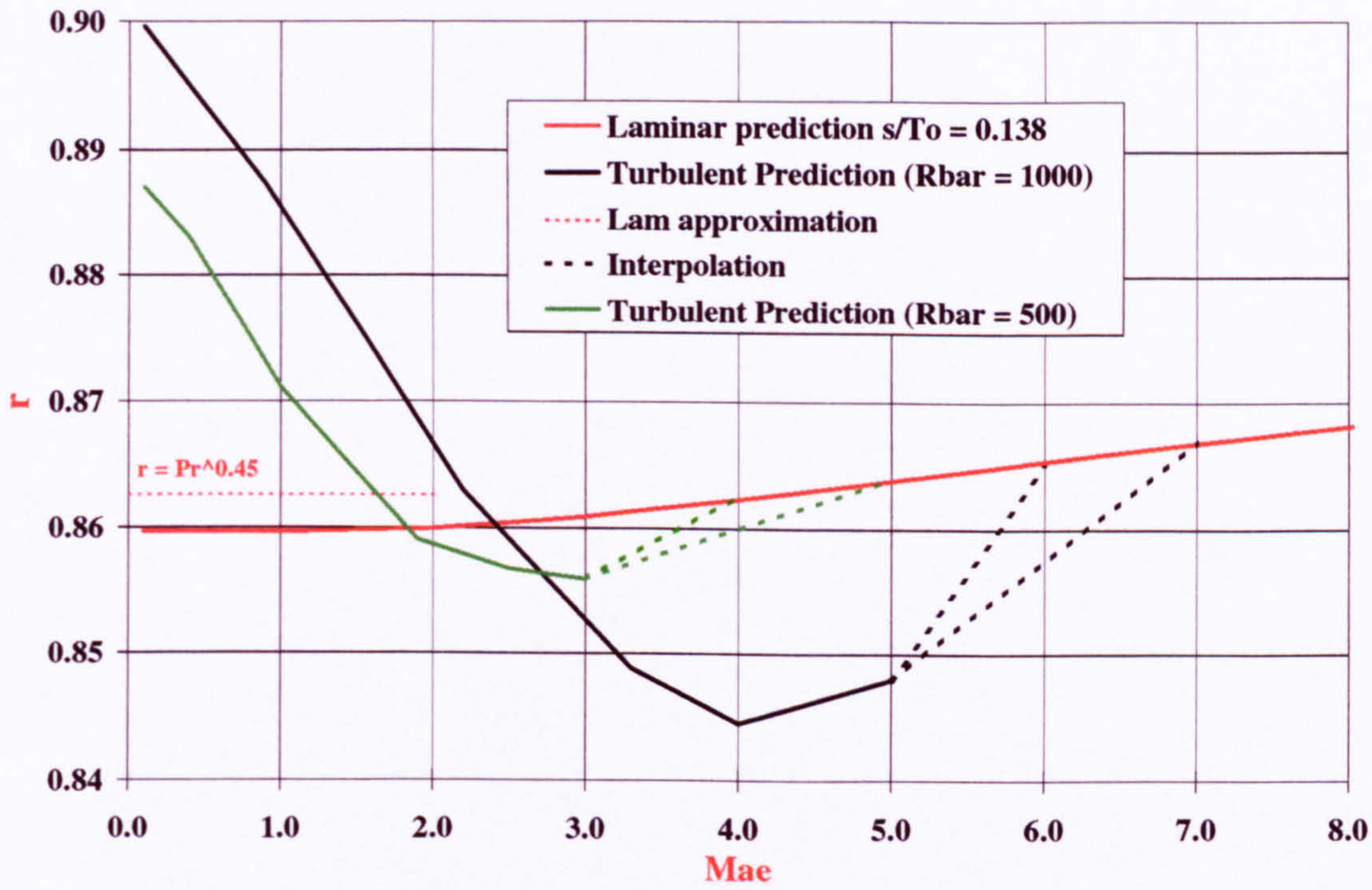

Figure A.137: Variation of the laminar and turbulent recovery factors with edge Mach number and $\bar{R}$. $Pr = 0.72$, $s/T_o = 0.138$.

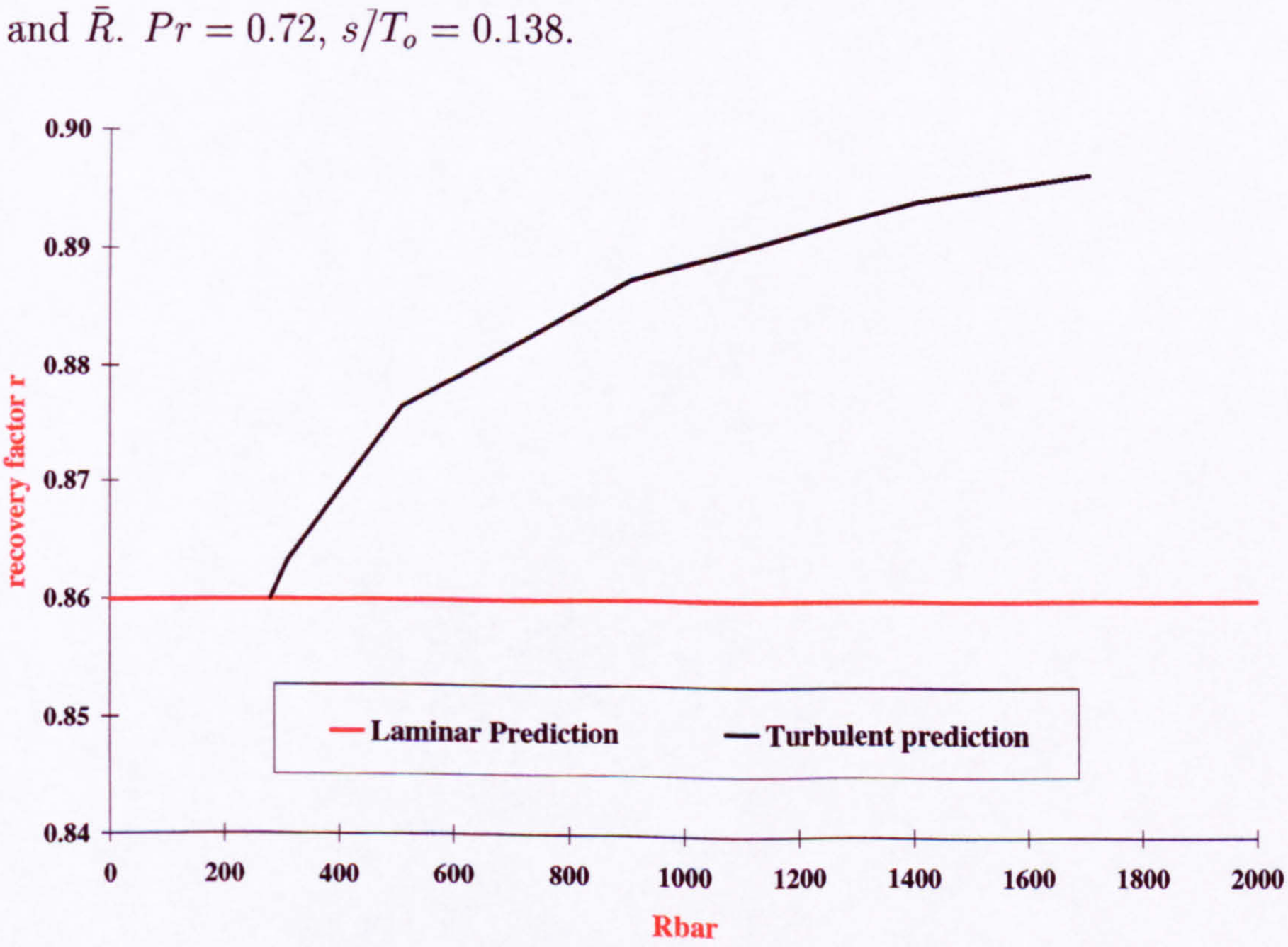

Figure A.138: Variation of the laminar and turbulent recovery factors with attachment-line Reynolds number for an edge Mach number value of 2. $(Pr = 0.72,\ s/T_o = 0.138)$.

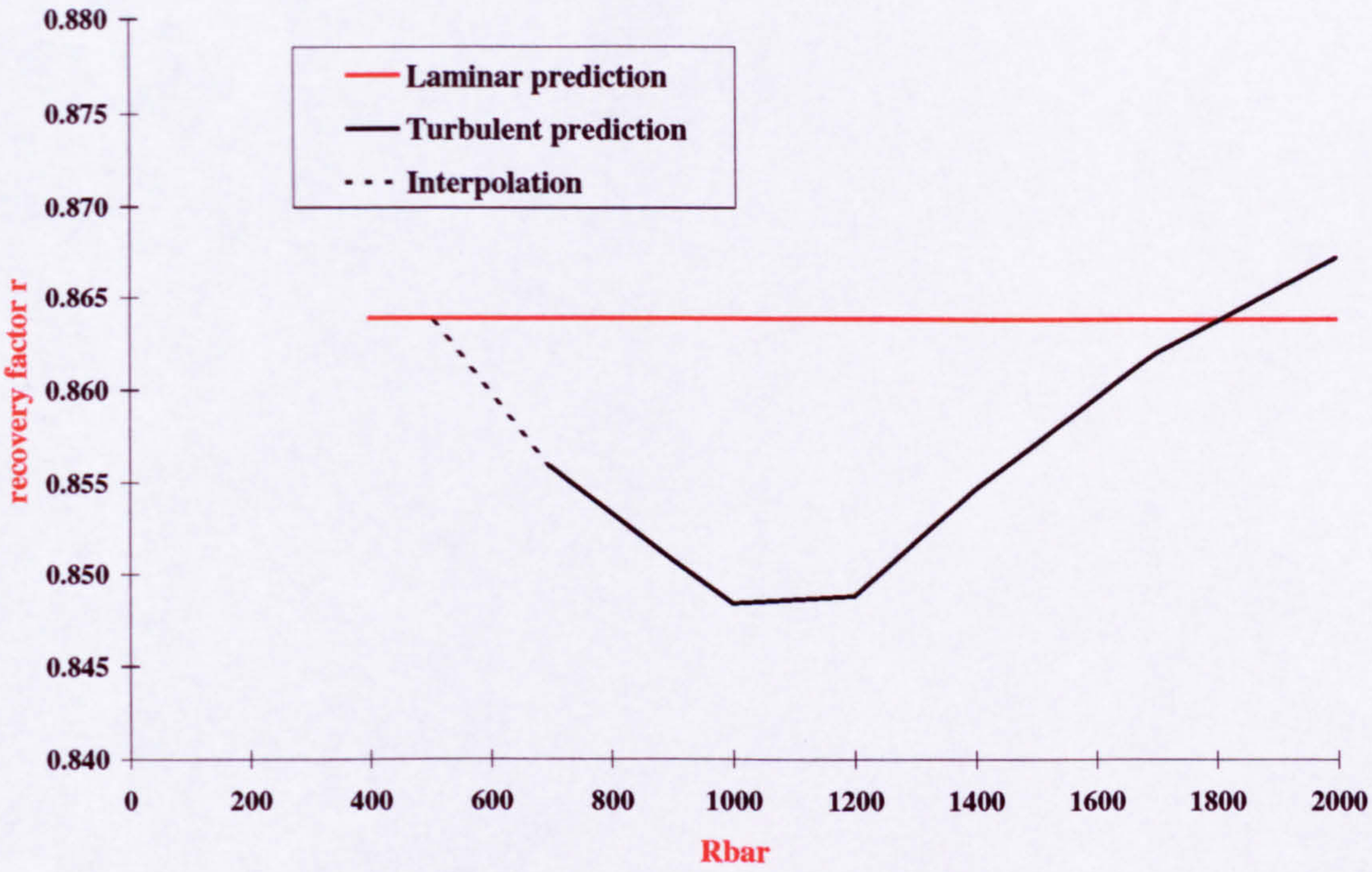

Figure A.139: Variation of the laminar and turbulent recovery factors with attachment-line Reynolds number for an edge Mach number value of 5. ($Pr = 0.72$, $s/T_o = 0.138$).

Appendix B

Tables

$R_{\theta ee} = V_{ae}.\theta.\left(\frac{\rho_e}{\mu_e}\right)$	$R_{\theta we} = V_{ae}.\theta.\left(\frac{\rho_w}{\mu_e}\right)$	$R_{\theta maxe} = V_{ae}.\theta.\left(\frac{\rho_{max}}{\mu_e}\right)$
$R_{\theta ew} = V_{ae}.\theta.\left(\frac{\rho_e}{\mu_w}\right)$	$R_{\theta ww} = V_{ae}.\theta.\left(\frac{\rho_w}{\mu_w}\right)$	$R_{\theta maxw} = V_{ae}.\theta.\left(\frac{\rho_{max}}{\mu_w}\right)$
$R_{\theta emax} = V_{ae}.\theta.\left(\frac{\rho_e}{\mu_{max}}\right)$	$R_{\theta wmax} = V_{ae}.\theta.\left(\frac{\rho_w}{\mu_{max}}\right)$	$R_{\theta maxmax} = V_{ae}.\theta.\left(\frac{\rho_{max}}{\mu_{max}}\right)$
$R_{\theta er} = V_{ae}.\theta.\left(\frac{\rho_e}{\mu_r}\right)$	$R_{\theta wr} = V_{ae}.\theta.\left(\frac{\rho_w}{\mu_r}\right)$	$R_{\theta maxr} = V_{ae}.\theta.\left(\frac{\rho_{max}}{\mu_r}\right)$
$R_{\theta re} = V_{ae}.\theta.\left(\frac{\rho_r}{\mu_e}\right)$	$R_{\theta rw} = V_{ae}.\theta.\left(\frac{\rho_r}{\mu_w}\right)$	$R_{\theta rmax} = V_{ae}.\theta.\left(\frac{\rho_r}{\mu_{max}}\right)$
$R_{\theta rr} = V_{ae}.\theta.\left(\frac{\rho_r}{\mu_r}\right)$		$\delta^+{}_{rr} = \left(\frac{\rho_r}{\mu_r}\right).\delta.\sqrt{\frac{\tau_w}{\rho_w}}$
$\delta^+{}_{ee} = \left(\frac{\rho_e}{\mu_e}\right).\delta.\sqrt{\frac{\tau_w}{\rho_w}}$	$\delta^+{}_{we} = \left(\frac{\rho_w}{\mu_e}\right).\delta.\sqrt{\frac{\tau_w}{\rho_w}}$	$\delta^+{}_{maxe} = \left(\frac{\rho_{max}}{\mu_e}\right).\delta.\sqrt{\frac{\tau_w}{\rho_w}}$
$\delta^+{}_{ew} = \left(\frac{\rho_e}{\mu_w}\right).\delta.\sqrt{\frac{\tau_w}{\rho_w}}$	$\delta^+{}_{ww} = \left(\frac{\rho_w}{\mu_w}\right).\delta.\sqrt{\frac{\tau_w}{\rho_w}}$	$\delta^+{}_{maxw} = \left(\frac{\rho_{max}}{\mu_w}\right).\delta.\sqrt{\frac{\tau_w}{\rho_w}}$
$\delta^+{}_{emax} = \left(\frac{\rho_e}{\mu_{max}}\right).\delta.\sqrt{\frac{\tau_w}{\rho_w}}$	$\delta^+{}_{wmax} = \left(\frac{\rho_w}{\mu_{max}}\right).\delta.\sqrt{\frac{\tau_w}{\rho_w}}$	$\delta^+{}_{maxmax} = \left(\frac{\rho_{max}}{\mu_{max}}\right).\delta.\sqrt{\frac{\tau_w}{\rho_w}}$
$\delta^+{}_{er} = \left(\frac{\rho_e}{\mu_r}\right).\delta.\sqrt{\frac{\tau_w}{\rho_w}}$	$\delta^+{}_{wr} = \left(\frac{\rho_w}{\mu_r}\right).\delta.\sqrt{\frac{\tau_w}{\rho_w}}$	$\delta^+{}_{maxr} = \left(\frac{\rho_{max}}{\mu_r}\right).\delta.\sqrt{\frac{\tau_w}{\rho_w}}$
$\delta^+{}_{re} = \left(\frac{\rho_r}{\mu_e}\right).\delta.\sqrt{\frac{\tau_w}{\rho_w}}$	$\delta^+{}_{rw} = \left(\frac{\rho_r}{\mu_w}\right).\delta.\sqrt{\frac{\tau_w}{\rho_w}}$	$\delta^+{}_{rmax} = \left(\frac{\rho_r}{\mu_{max}}\right).\delta.\sqrt{\frac{\tau_w}{\rho_w}}$

Table B.1: List of the 32 Reynolds number definitions tried to correlate the variation of A^+ and $l_o\delta$.

Author	Run	M_∞	Λ [deg]	Tw/To	To [K]	Diameter [mm]	Reynolds per metre
Holden	34	10.554	60.0	0.289	1020.333	76.2	6.161E+06
	5	10.539	66.5	0.253	1164.333	76.2	7.976E+06
	25	10.591	70.0	0.263	1121.333	76.2	1.271E+07
	31	10.544	75.0	0.258	1143.333	76.2	7.871E+06
	12	10.554	76.5	0.248	1187.333	76.2	1.040E+07
	36	10.582	80.0	0.257	1144.333	76.2	1.240E+07
Poitiers	19	7.14	60.0	0.380	789.474	13.5	2.203E+07
	24	7.14	70.0	0.380	789.474	19	1.977E+07
	9	7.14	76.5	0.380	789.474	33	2.106E+07
	70	7.14	80.0	0.387	785.000	19	1.155E+07
Bushnell	17a	7.880	60.0	0.450	766.483	25.4	1.004E+07
	7a	7.950	72.0	0.450	766.483	25.4	1.039E+07
Beckwith	15	4.15	40.0	0.920	400.670	28.321	3.399E+07
	1	4.15	60.0	0.920	394.261	28.321	4.943E+07
Jones	2	6.105	60.0	0.524	572.317	26.924	7.800E+06
Created	1	5.85	70.0	0.400	750.000	70	1.000E+07
	2	8.77	70.0	0.400	750.000	70	1.500E+07
	3	11.695	70.0	0.226	1417.730	70	1.500E+07

Table B.2: Table of the runs carried out using the Navier-Stokes code MGNS3D.

Gauge label	Position $\frac{L}{D}$ Runs 3, 4, 5, 6, 7, 9, 10 13, 12, 14, 15, 27 and 34	Position $\frac{L}{D}$ Runs 17, 18, 19, 20, 21 and 24	Position $\frac{L}{D}$ Runs 25, 26, 28, 29, 30, 31, 35, 36 and 37
HT125	0.287		
HT126	0.583		
HT128	1.163		
HT129	1.457		
HT109	2.133	2.733	6.243
HT110	2.800	3.400	6.910
HT111	3.467	4.067	7.577
HT112	4.133	4.733	8.243
HT113	4.800	5.400	8.910
HT114	5.467	6.067	9.577
HT115	6.133	6.733	10.243
HT116	6.800	7.400	10.910

Table B.3: Heat transfer gauges locations used in **Holden's** investigation [37] [38].

RUN	M_∞	Λ [deg]	Tw/To	To [K]	D [m]	Re per metre	Surface Feature
27	10.551	60.0	0.258	1139.33	0.0762	8.36942E+06	Smooth
34	10.554	60.0	0.289	1020.33	0.0762	6.16142E+06	Smooth
3	10.559	66.5	0.250	1177.33	0.0762	1.04724E+07	Smooth
4	10.434	66.5	0.260	1134.33	0.0762	2.67159E+06	Smooth
5	10.539	66.5	0.253	1164.33	0.0762	7.97572E+06	Smooth
6	10.566	66.5	0.254	1157.33	0.0762	1.07546E+07	k = 0.015”
7	10.451	66.5	0.268	1097.33	0.0762	2.85203E+06	k = 0.015”
9	10.541	66.5	0.254	1158.33	0.0762	7.98228E+06	k = 0.015”
10	10.537	66.5	0.287	1026.33	0.0762	5.29856E+06	k = 0.015”
13	10.538	66.5	0.277	1063.33	0.0762	5.81693E+06	k = 0.030”
15	10.459	66.5	0.275	1069.33	0.0762	2.87959E+06	k = 0.030”
17	10.559	66.5	0.250	1177.33	0.0762	1.06398E+07	Smooth
18	10.571	66.5	0.253	1165.33	0.0762	1.17815E+07	Smooth
19	10.441	66.5	0.265	1110.33	0.0762	2.69587E+06	Smooth
20	10.587	66.5	0.267	1134.33	0.0762	1.26739E+07	Smooth
21	10.443	66.5	0.266	1106.33	0.0762	2.71785E+06	Endplate
24	10.581	66.5	0.257	1144.33	0.0762	1.22835E+07	Endplate
25	10.591	70.0	0.263	1121.33	0.0762	1.27067E+07	Smooth
26	10.589	70.0	0.262	1125.33	0.0762	1.25459E+07	k = 0.030”
28	10.596	75.0	0.264	1113.33	0.0762	1.30577E+07	k = 0.030”
29	10.596	75.0	0.265	1111.33	0.0762	1.29626E+07	Smooth
30	10.569	75.0	0.255	1156.33	0.0762	1.10171E+07	Smooth
31	10.544	75.0	0.258	1143.33	0.0762	7.87073E+06	Smooth
12	10.554	76.5	0.248	1187.33	0.0762	1.04003E+07	k = 0.015”
14	10.550	76.5	0.246	1196.33	0.0762	1.02953E+07	k = 0.030”
35	10.567	80.0	0.254	1159.33	0.0762	1.09613E+07	Smooth
36	10.582	80.0	0.257	1144.33	0.0762	1.24049E+07	Smooth
37	10.572	80.0	0.253	1163.33	0.0762	1.18701E+07	Smooth

Table B.4: Part of the runs achieved by **Holden et al.** [37] [38] and considered for the purpose of the present study.

RUN	M_∞	Λ [deg]	Tw/To	To [K]	D [mm]	Re per metre	Surface Feature [mm]
19	7.14	60.0	0.38	789.474	13.5	2.203E+07	2D trip wire k=0.14
20	7.14	60.0	0.38	789.474	13.5	2.262E+07	2D trip wire k=0.20
21a	7.14	60.0	0.38	789.474	13.5	2.227E+07	2D trip wire k=0.30
21b	7.14	60.0	0.38	789.474	13.5	1.142E+07	2D trip wire k=0.30
22	7.14	60.0	0.38	789.474	13.5	2.262E+07	2D trip wire k=0.50
23	7.14	60.0	0.38	789.474	13.5	2.262E+07	2D trip wire k=0.60
56	7.14	60.0	0.41	731.707	13.5	2.585E+07	2D trip wire k=0.19
57	7.14	60.0	0.40	750.000	13.5	2.681E+07	2D trip wire k=0.28
59	7.14	60.0	0.41	731.707	13.5	2.045E+07	3D trip wire k=0.16
60	7.14	60.0	0.41	731.707	13.5	2.222E+07	3D plate 0.18*0.5*1.5
61	7.14	60.0	0.39	769.231	13.5	1.815E+07	3D plate 0.07*0.8*2.5
62	7.14	60.0	0.39	784.000	13.5	1.815E+07	3D Ribbon 0.07*0.8
73	7.14	60.0	0.41	731.707	13.5	9.232E+06	3D plate 0.18*0.5*1.5
74	7.14	60.0	0.41	731.707	13.5	9.903E+06	3D plate 0.18*0.5*1.5
75	7.14	60.0	0.41	731.707	13.5	1.087E+07	3D plate 0.18*0.5*1.5
76	7.14	60.0	0.41	731.707	13.5	1.207E+07	3D plate 0.18*0.5*1.5
77	7.14	60.0	0.41	731.707	13.5	1.432E+07	3D plate 0.18*0.5*1.5
78	7.14	60.0	0.41	731.707	13.5	1.819E+07	3D plate 0.18*0.5*1.5
79	7.14	60.0	0.41	731.707	13.5	2.203E+07	3D plate 0.18*0.5*1.5
24	7.14	70.0	0.38	789.474	19.0	1.977E+07	Smooth
27	7.14	70.0	0.38	789.474	19.0	1.896E+07	Groove 2(l)*1(d)
28	7.14	70.0	0.38	789.474	19.0	2.049E+07	Groove 1(l)*2(d)
29	7.14	70.0	0.38	789.474	19.0	1.998E+07	Cavity 1(l)*2(d)*4(w)
30	7.14	70.0	0.38	789.474	19.0	2.091E+07	Groove 5(l)*1(d)
31	7.14	70.0	0.38	789.474	19.0	2.049E+07	Groove 5(l)*2(d)
9	7.14	76.5	0.38	789.474	33.0	2.106E+07	Smooth
12	7.14	76.5	0.24	800.000	33.0	1.919E+07	Smooth
46	7.14	76.5	0.38	788.000	33.0	2.086E+07	Smooth

Table B.5: Part of the runs achieved at **Poitiers university** [6] [35] and considered in the present investigation. l: length in spanwise direction, D: depth and W: width in chordwise direction. Table 1/2.

RUN	M_∞	Λ [deg]	Tw/To	To [K]	D [mm]	Re per metre	Surface Feature [mm]
70	7.14	80.0	0.39	785.000	19.0	1.155E+07	3D plate 0.8*2.5*0.15
63	7.14	80.0	0.40	764.000	19.0	2.613E+07	Smooth
64	7.14	80.0	0.40	766.000	19.0	2.626E+07	2D trip wire k=0.47
65	7.14	80.0	0.39	774.000	19.0	2.689E+07	2D trip wire k=0.60
66	7.14	80.0	0.39	774.000	19.0	2.596E+07	2D trip wire k=0.70
67	7.14	80.0	0.39	774.000	19.0	2.340E+07	2D trip wire k=0.80
68	7.14	80.0	0.39	785.000	19.0	2.575E+07	3D plate 0.07*0.8*2.3
69	7.14	80.0	0.39	773.000	19.0	2.567E+07	3D plate 0.11*0.8*2.6
71	7.14	80.0	0.39	773.000	19.0	1.484E+07	3D plate 0.23*0.8*2.65
72	7.14	80.0	0.40	771.000	19.0	2.101E+07	3D plate 0.35*0.8*2.5

Table B.6: Part of the runs achieved at **Poitiers university** [6] [35] and considered in the present investigation. l: length in spanwise direction, D: depth and W: width in chordwise direction. Table 2/2.

RUN	Λ [deg]	Tw/To	To [K]	D [mm]	L/D considered	Re per metre	Surface Feature [mm]
80s	60.0	0.38	789.474	13.5	10.6	8.058E+06 to 2.416E+07	2D trip wire k=0.60
81s	60.0	0.41	731.707	13.5	12.8	6.770E+06 to 2.203E+07	3D plate 0.18*0.5*1.5
82s	80.0	0.39	773.000	19.0	15.2	8.027E+06 to 2.588E+07	3D plate 0.23*0.8*2.65
84s	76.0	0.38	789.474	19.0	10.6	7.587E+06 to 2.219E+07	End plate l/D=2.79
85s	76.0	0.38	789.474	19.0	9.4	7.608E+06 to 2.326E+07	End plate l/D=1.58

Table B.7: Part of the runs achieved at **Poitiers university** [6] [35] and considered in the present investigation. $M_\infty = 7.14$.

RUN	M_∞	Λ [deg]	Tw/To	To [K]	D [mm]	Re per metre	Surface Feature
1	7.734	72	0.403	767.039	25.4	2.283E+06	End plate
2	7.799	72	0.400	774.428	25.4	3.254E+06	End plate
3	7.867	72	0.399	776.650	25.4	4.790E+06	End plate
4	7.910	72	0.399	777.594	25.4	6.470E+06	End plate
5	7.926	72	0.399	777.594	25.4	7.538E+06	End plate
6	7.941	72	0.398	778.706	25.4	9.237E+06	End plate
7a	7.950	72	0.450	766.483	25.4	1.039E+07	End plate
7b	7.947	72	0.398	779.150	25.4	1.039E+07	End plate
8	7.953	72	0.398	779.706	25.4	1.178E+07	End plate
9	7.953	72	0.397	780.650	25.4	1.307E+07	End plate
10	7.960	72	0.397	727.594	25.4	1.496E+07	End plate
11	8.000	72	0.398	779.594	25.4	3.372E+07	End plate
12	7.810	60	0.400	775.150	25.4	3.465E+06	End plate
13	7.870	60	0.399	777.039	25.4	4.921E+06	End plate
14	7.906	60	0.399	777.261	25.4	6.299E+06	End plate
15	7.928	60	0.399	777.872	25.4	7.677E+06	End plate
16	7.938	60	0.398	778.428	25.4	8.858E+06	End plate
17a	7.880	60	0.450	766.483	25.4	1.004E+07	End plate
17b	7.945	60	0.398	779.039	25.4	1.004E+07	End plate
18	7.951	60	0.398	779.539	25.4	1.132E+07	End plate
19	7.954	60	0.397	780.594	25.4	1.307E+07	End plate
20	8.000	60	0.384	817.317	25.4	3.425E+07	End plate

Table B.8: Part of the runs undertaken by **Bushnell et al.** [12] [13] and considered in the present investigation.

Λ [deg]		Station 3	P2	Station 2	P1	Station 1
60	$\frac{L}{D} =$	6.278	7.175	8.072	8.969	9.865
40	$\frac{L}{D} =$	3.475	4.372	5.268	6.165	7.062
20	$\frac{L}{D} =$	2.501	3.398	4.295	5.192	6.089
10	$\frac{L}{D} =$	2.304	3.201	4.098	4.995	5.892
0	$\frac{L}{D} =$	2.242	3.139	4.036	4.933	5.830

Table B.9: Location of the heat transfer meters (stations 1, 2 and 3) and pressure orifices (P1 and P2) on the model used by **Beckwith et al.** [5] (figure G.20). Distance taken from end plate.

RUN	M_∞	Λ [deg]	Tw/To	To [K]	D [mm]	Re per metre
1	4.15	60	0.92	394.261	28.321	4.943E+07
2	4.15	60	0.92	397.412	28.321	4.042E+07
3	4.15	60	0.92	395.348	28.321	4.590E+07
4	4.15	60	0.92	394.395	28.321	4.897E+07
5	4.15	60	0.92	392.217	28.321	5.777E+07
6	4.15	60	0.92	390.571	28.321	6.683E+07
7	4.15	60	0.92	390.008	28.321	7.062E+07
8	4.15	60	0.92	389.189	28.321	7.695E+07
9	4.15	60	0.92	389.104	28.321	7.768E+07
10	4.15	60	0.92	388.422	28.321	8.401E+07
11	4.15	60	0.92	387.513	28.321	9.424E+07
12	4.15	60	0.92	385.931	28.321	1.195E+08
13	4.15	60	0.92	385.905	28.321	1.201E+08
14	4.15	60	0.92	385.737	28.321	1.236E+08
15	4.15	40	0.92	400.670	28.321	3.399E+07
16	4.15	40	0.92	395.567	28.321	4.525E+07
17	4.15	40	0.92	395.348	28.321	4.590E+07
18	4.15	40	0.92	393.487	28.321	5.229E+07
19	4.15	40	0.92	393.406	28.321	5.261E+07
20	4.15	40	0.92	392.256	28.321	5.759E+07
21	4.15	40	0.92	390.114	28.321	6.988E+07
22	4.15	40	0.92	390.008	28.321	7.062E+07
23	4.15	40	0.92	389.910	28.321	7.133E+07
24	4.15	40	0.92	387.968	28.321	8.882E+07
25	4.15	40	0.92	387.342	28.321	9.644E+07
26	4.15	40	0.92	387.292	28.321	9.710E+07
27	4.15	40	0.92	385.737	28.321	1.236E+08
28	4.15	20	0.92	395.348	28.321	4.590E+07
29	4.15	20	0.92	395.232	28.321	4.626E+07
30	4.15	20	0.92	395.144	28.321	4.653E+07
31	4.15	20	0.92	391.236	28.321	6.285E+07
32	4.15	20	0.92	391.225	28.321	6.291E+07
33	4.15	20	0.92	390.008	28.321	7.062E+07

Table B.10: Runs undertaken by **Beckwith et al.** [5] and considered in the present study (Part 1/2).

RUN	M_∞	Λ [deg]	Tw/To	To [K]	D [mm]	Re per metre
34	4.15	20	0.92	389.550	28.321	7.403E+07
35	4.15	20	0.92	387.603	28.321	9.311E+07
36	4.15	20	0.92	386.441	28.321	1.100E+08
37	4.15	20	0.92	386.432	28.321	1.102E+08
38	4.15	20	0.92	385.737	28.321	1.236E+08
39	4.15	10	0.92	395.348	28.321	4.590E+07
40	4.15	10	0.92	394.703	28.321	4.794E+07
41	4.15	10	0.92	394.362	28.321	4.908E+07
42	4.15	10	0.92	394.344	28.321	4.914E+07
43	4.15	10	0.92	393.072	28.321	5.396E+07
44	4.15	10	0.92	392.427	28.321	5.679E+07
45	4.15	10	0.92	390.804	28.321	6.538E+07
46	4.15	10	0.92	390.331	28.321	6.840E+07
47	4.15	10	0.92	390.008	28.321	7.062E+07
48	4.15	10	0.92	389.375	28.321	7.542E+07
49	4.15	10	0.92	388.608	28.321	8.218E+07
50	4.15	10	0.92	388.608	28.321	8.218E+07
51	4.15	10	0.92	388.598	28.321	8.227E+07
52	4.15	10	0.92	385.737	28.321	1.236E+08
53	4.15	10	0.92	385.328	28.321	1.331E+08
54	4.15	0	0.92	395.586	28.321	4.520E+07
55	4.15	0	0.92	395.503	28.321	4.544E+07
56	4.15	0	0.92	395.348	28.321	4.590E+07
57	4.15	0	0.92	392.739	28.321	5.539E+07
58	4.15	0	0.92	390.008	28.321	7.062E+07
59	4.15	0	0.92	389.861	28.321	7.168E+07
60	4.15	0	0.92	389.826	28.321	7.193E+07
61	4.15	0	0.92	387.319	28.321	9.675E+07
62	4.15	0	0.92	387.288	28.321	9.716E+07
63	4.15	0	0.92	385.737	28.321	1.236E+08
64	4.15	0	0.92	385.245	28.321	1.352E+08
65	4.15	0	0.92	385.229	28.321	1.357E+08

Table B.11: Runs undertaken by **Beckwith et al.** [5] and considered in the present study (Part 2/2).

Station	$\frac{L}{D}$ location
A	0.9434
B	1.8868
C	2.8302
D	3.7736
E	4.7170

Table B.12: Table of the heat transfer and pressure instrumentation location on the model used by **Jones** [40] (figure G.24)

RUN	M_∞	Λ [deg]	D [mm]	Tw/To	To [K]	Po [N/m2]	Re per metre	Surface Feature
1	6.016	60	26.924	0.492	606.261	2.759E+05	2.303E+06	Smooth
2	6.105	60	26.924	0.524	572.317	1.104E+06	7.800E+06	Smooth
3	6.196	60	26.924	0.525	567.983	4.414E+06	2.860E+07	Smooth

Table B.13: Table of the tests conditions for the runs undertaken by **Jones** [40] and considered in the present investigation.

$\frac{L}{D}$	$\frac{\left(\frac{Vae}{Q\infty}\right)_{Local}}{\left(\frac{Vae}{Q\infty}\right)_{Infswept}}$	$\frac{\left(\frac{Tae}{T\infty}\right)_{Local}}{\left(\frac{Tae}{T\infty}\right)_{Infswept}}$	$\frac{\left(\frac{Pae}{P\infty}\right)_{Local}}{\left(\frac{Pae}{P\infty}\right)_{Infswept}}$	$\frac{\left(\frac{dUe}{dX}\right)_{Local}}{\left(\frac{dUe}{dX}\right)_{Infswept}}$	$\frac{\bar{R}_{Local}}{\bar{R}_{Infswept}}$
0.190	0.9038	1.3862	1.3063	1.4702	0.5892
0.307	0.9104	1.3564	1.2529	1.3805	0.6146
0.525	0.9214	1.3203	1.1888	1.2435	0.6580
0.777	0.9277	1.2953	1.1487	1.1488	0.6923
1.021	0.9328	1.2723	1.1197	1.1037	0.7154
1.558	0.9416	1.2357	1.0874	1.0540	0.7528
1.969	0.9481	1.2074	1.0606	1.0364	0.7750
2.455	0.9538	1.1865	1.0585	1.0148	0.8028
3.019	0.9610	1.1597	1.0445	1.0095	0.8268
3.666	0.9677	1.1339	1.0357	0.9919	0.8581
4.142	0.9714	1.1186	1.0328	0.9853	0.8766
5.200	0.9785	1.0916	1.0243	0.9875	0.9032
6.051	0.9839	1.0707	1.0156	0.9942	0.9214
7.114	0.9873	1.0563	1.0095	1.0030	0.9321
8.091	0.9893	1.0488	1.0102	1.0025	0.9423
8.988	0.9915	1.0416	1.0124	0.9926	0.9577
10.007	0.9928	1.0349	1.0080	0.9872	0.9667
11.095	0.9938	1.0304	1.0061	0.9835	0.9733
12.053	0.9948	1.0271	1.0066	0.9710	0.9844
13.026	0.9964	1.0209	0.9961	0.9889	0.9788
14.083	0.9961	1.0217	1.0033	0.9613	0.9950
14.956	0.9973	1.0170	1.0010	0.9613	1.0004

Table B.14: Distribution of the flow properties, chordwise velocity gradient and $\bar{R}$ along the attachment line of a 60^o swept cylinder when $M_\infty.cos\Lambda \geq 2.5$. (Data extrapolated from the CFD run carried out on Poitiers Run 19).

$\frac{L}{D}$	$\frac{\left(\frac{V_{ae}}{Q_\infty}\right)_{Local}}{\left(\frac{V_{ae}}{Q_\infty}\right)_{Inf_swept}}$ Holden Run25	$\frac{\left(\frac{T_{ae}}{T_\infty}\right)_{Local}}{\left(\frac{T_{ae}}{T_\infty}\right)_{Inf_swept}}$ Holden Run25	$\frac{L}{D}$	$\frac{\left(\frac{P_{ae}}{P_\infty}\right)_{Local}}{\left(\frac{P_{ae}}{P_\infty}\right)_{Inf_swept}}$ Created run2	$\frac{\left(\frac{dU_e}{dX}\right)_{Local}}{\left(\frac{dU_e}{dX}\right)_{Inf_swept}}$ Created run2	$\frac{\bar{R}_{Local}}{\bar{R}_{Inf_swept}}$ Created run2
0.201	0.9616	1.4048	0.202	1.3693	1.5187	0.6117
0.320	0.9633	1.3850	0.322	1.3250	1.4293	0.6372
0.490	0.9654	1.3595	0.546	1.2704	1.3152	0.6678
0.724	0.9674	1.3311	0.800	1.1969	1.2287	0.6922
1.040	0.9700	1.3090	1.047	1.1927	1.1651	0.7159
1.573	0.9731	1.2822	1.584	1.1418	1.0895	0.7459
2.130	0.9758	1.2445	2.144	1.0972	1.0798	0.7575
2.631	0.9764	1.2398	2.650	1.0895	1.0312	0.7859
3.008	0.9784	1.2163	3.029	1.0842	1.0313	0.7938
3.636	0.9796	1.2008	3.661	1.0679	1.0197	0.8124
4.097	0.9817	1.1815	4.125	1.0600	1.0094	0.8229
5.114	0.9842	1.1602	5.150	1.0512	1.0109	0.8517
6.195	0.9870	1.1325	6.237	1.0446	1.0034	0.8773
7.008	0.9888	1.1138	7.052	1.0280	1.0163	0.8872
8.095	0.9912	1.0920	8.140	1.0212	1.0090	0.9006
9.186	0.9930	1.0719	9.229	1.0120	0.9927	0.9309
10.006	0.9936	1.0697	10.046	1.0034	1.0070	0.9330
11.103	0.9953	1.0529	11.136	1.0305	0.9951	0.9539
12.204	0.9957	1.0487	12.226	1.0010	1.0223	0.9416
13.031	0.9965	1.0425	13.045	1.0131	0.9944	0.9621
13.861	0.9969	1.0378	13.863	1.0231	1.0129	0.9590

Table B.15: Distribution of the flow properties, chordwise velocity gradient and $\bar{R}$ along the attachment line of a 70^o swept cylinder when $M_\infty.cos\Lambda \geq 2.5$. (Data extrapolated from the created run 2 offering $M_\infty.cos\Lambda = 3.0$ and the CFD run carried out on Holden Run 25).

Appendix C

The Infinite Swept Conditions

C.1 Introduction

In the case of a infinite swept cylinder the following assumptions are made:

- The bow shock is parallel to the cylinder attachment-line (bow shock sweep angle equals cylinder sweep angle). The flow properties are constant along the attachment-line.
- the flow is homenergic, T_o is constant throughout the flow field.
- The flow is isentropic everywhere except across the bow shock.
- The gas is thermally perfect i.e. γ, C_p and R are constant.
- $M_\infty.cos\Lambda > 1$

The notation used in this appendix is as showed by the following figure:

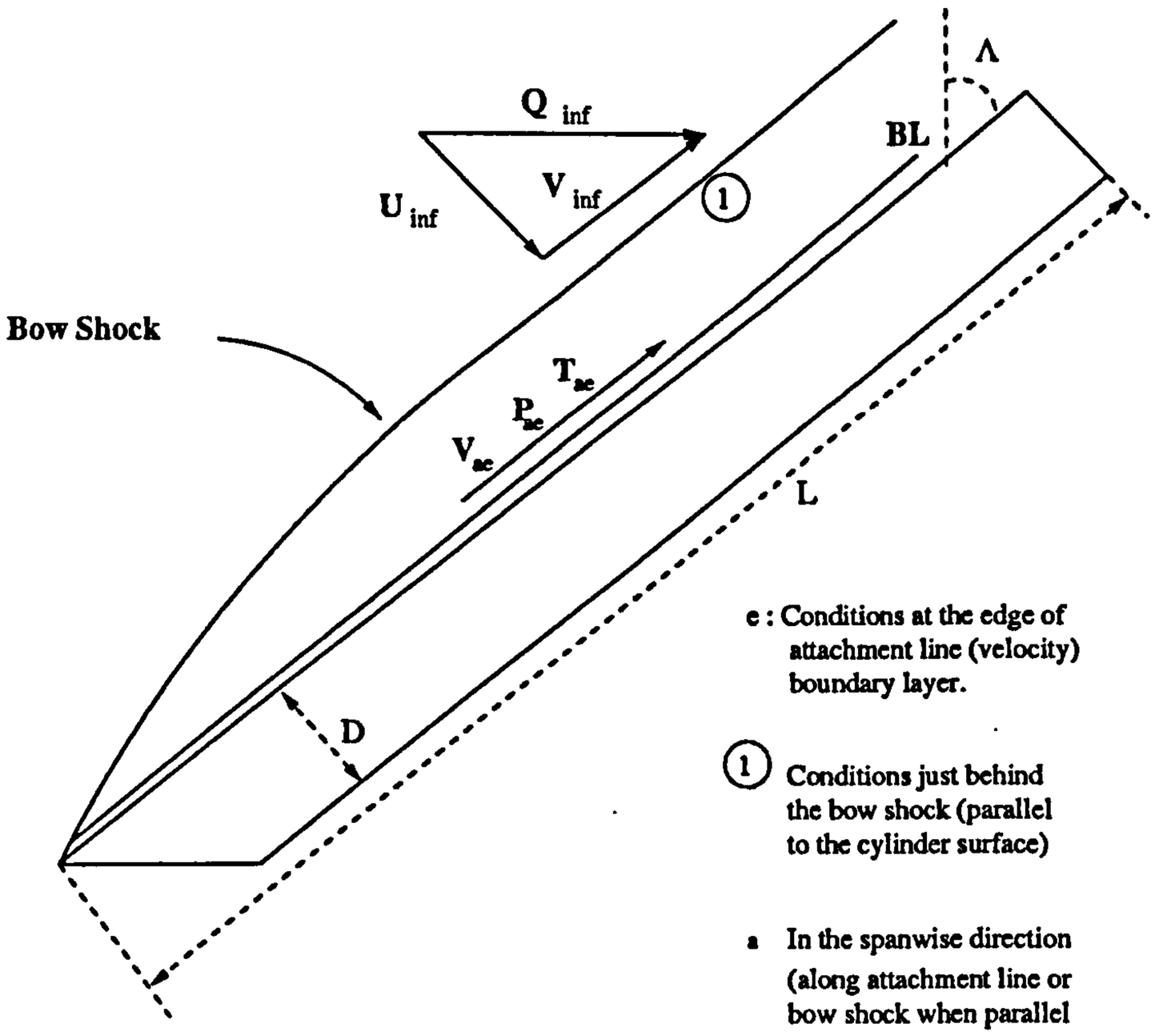

Figure C.1: Schematic diagram showing the notation.

Here the subscript "inf" or ∞ denotes the undisturbed free-stream whereas "e" indicates the conditions taken at the edge of the velocity boundary layer. The subscript "a" points out variables evaluated in the spanwise direction, either along the attachment-line or along the bow shock.

C.2 Evaluation of the attachment-line edge temperature

$$\frac{T_{ae}}{T_\infty} = \frac{T_{ae}}{T_o} . \frac{T_o}{T_\infty} \tag{C.1}$$

$$\Rightarrow \frac{T_{ae}}{T_\infty} = \frac{1 + \left(\frac{\gamma-1}{2}\right) . {M_\infty}^2}{1 + \left(\frac{\gamma-1}{2}\right) . {M_{ae}}^2} \tag{C.2}$$

using equation C.14

$$\frac{T_{ae}}{T_\infty} = \frac{1 + \left(\frac{\gamma-1}{2}\right).{M_\infty}^2}{1 + \left(\frac{\gamma-1}{2}\right).{M_\infty}^2.sin^2\Lambda.\left(\frac{T_\infty}{T_{ae}}\right)} \tag{C.3}$$

$$\frac{T_{ae}}{T_\infty} = \frac{1 + \left(\frac{\gamma-1}{2}\right).{M_\infty}^2}{\frac{T_\infty}{T_{ae}}.\left(\frac{T_{ae}}{T_\infty} + \left(\frac{\gamma-1}{2}\right).{M_\infty}^2.sin^2\Lambda\right)} \tag{C.4}$$

$$\Rightarrow 1 = \frac{1 + \left(\frac{\gamma-1}{2}\right).{M_\infty}^2}{\frac{T_{ae}}{T_\infty} + \left(\frac{\gamma-1}{2}\right).{M_\infty}^2.sin^2\Lambda} \tag{C.5}$$

$$\Rightarrow \frac{T_{ae}}{T_\infty} = 1 + \left(\frac{\gamma-1}{2}\right).{M_\infty}^2 - \left(\frac{\gamma-1}{2}\right).{M_\infty}^2.sin^2\Lambda \tag{C.6}$$

$$\Rightarrow \frac{T_{ae}}{T_\infty} = 1 + \left(\frac{\gamma-1}{2}\right).{M_\infty}^2.\left(1 - sin^2\Lambda\right) \tag{C.7}$$

Hence, it follows

$$\boxed{\Rightarrow \frac{T_{ae}}{T_\infty} = 1 + \left(\frac{\gamma-1}{2}\right).{M_\infty}^2 cos^2\Lambda} \tag{C.8}$$

C.3 Evaluation of the Mach number ratio

$$V_\infty = V_{a1} = V_{ae} = Q_\infty \sin\Lambda \tag{C.9}$$

$$\Rightarrow M_{\infty a}.(\gamma.R.T_{\infty a})^{\frac{1}{2}} = M_{ae}.(\gamma.R.T_{ae})^{\frac{1}{2}} \tag{C.10}$$

with

$$M_{\infty a} = M_\infty.sin\Lambda \tag{C.11}$$

and

$$T_{\infty a} = T_\infty \tag{C.12}$$

$$\Rightarrow M_{ae}.(T_{ae})^{\frac{1}{2}} = M_\infty.sin\Lambda.(T_\infty)^{\frac{1}{2}} \tag{C.13}$$

Hence

$$\boxed{\Rightarrow \frac{M_{ae}}{M_\infty} = sin\Lambda.\left(\frac{T_\infty}{T_{ae}}\right)^{\frac{1}{2}}} \tag{C.14}$$

C.4 Evaluation of the attachment-line static pressure in the presence of a bow shock (i.e. $M_\infty cos\Lambda > 1$)

$$\frac{P_{ae}}{P_\infty} = \frac{P_{ae}}{P_{o\infty}}.\frac{P_{o\infty}}{P_\infty} \tag{C.15}$$

since

$$\frac{T_o}{T_{ae}} = 1 + \left(\frac{\gamma-1}{2}\right).{M_{ae}}^2 = \frac{T_o}{T_\infty}.\frac{T_\infty}{T_{ae}} \tag{C.16}$$

$$\frac{T_o}{T_{ae}} = \frac{1 + \left(\frac{\gamma-1}{2}\right).{M_\infty}^2}{1 + \left(\frac{\gamma-1}{2}\right).{M_\infty}^2 cos^2\Lambda} = 1 + \left(\frac{\gamma-1}{2}\right).{M_{ae}}^2 \tag{C.17}$$

Then

$$\frac{P_{ae}}{P_{o1}} = \left[1 + \left(\frac{\gamma-1}{2}\right).{M_{ae}}^2\right]^{-\frac{\gamma}{\gamma-1}} \tag{C.18}$$

where P_{o1} is the stagnation pressure behind the bow shock (see figure C.1)

$$\Rightarrow \frac{P_{ae}}{P_{o1}} = \left[\frac{1+\left(\frac{\gamma-1}{2}\right).M_\infty{}^2 cos^2\Lambda}{1+\left(\frac{\gamma-1}{2}\right).M_\infty{}^2}\right]^{\frac{\gamma}{\gamma-1}} \tag{C.19}$$

From oblique shock relations (p 10 of reference [2]):

$$\frac{P_{o1}}{P_\infty} = \left[\frac{\gamma+1}{2\gamma M_\infty{}^2 cos^2\Lambda-(\gamma-1)}\right]^{\frac{1}{\gamma-1}} \times \left[\frac{(\gamma+1)\,M_\infty{}^2 cos^2\Lambda.\left((\gamma-1)\,M_\infty{}^2+2\right)}{2\left((\gamma-1)\,M_\infty{}^2 cos^2\Lambda+2\right)}\right]^{\frac{\gamma}{\gamma-1}} \tag{C.20}$$

From equations C.15, C.19 and C.20 it follows

$$\boxed{\frac{P_{ae}}{P_\infty} = \left[\left(\frac{\gamma+1}{2}\right)M_\infty{}^2 cos^2\Lambda\right]^{\frac{\gamma}{\gamma-1}} \times \left[\frac{\gamma+1}{2\gamma M_\infty{}^2 cos^2\Lambda-(\gamma-1)}\right]^{\frac{1}{\gamma-1}}} \tag{C.21}$$

C.5 Evaluation of the chordwise velocity gradient

It is well known that, if $M_\infty cos\lambda$ is greater than 2.5, the pressure distribution in the vicinity of the attachment-line is in good agreement with Modified Newtonian theory i.e.

$$\frac{C_P}{C_{Pmax}} = cos^2\left(\frac{2X}{D}\right) = \frac{P-P_\infty}{P_{ae}-P_\infty} \tag{C.22}$$

which is

$$\frac{P}{P_{ae}} = \left(1-\frac{P_\infty}{P_{ae}}\right)cos^2\left(\frac{2X}{D}\right)+\frac{P_\infty}{P_{ae}} \tag{C.23}$$

At the attachment-line itself, the Mach number normal to the leading edge M_N is zero. Therefore, in the vicinity of the attachment-line, M_N will be very small. In addition, since

the chordwise and spanwise components of the inviscid flow are independent

$$P_{ae} = P_e + \frac{1}{2}\rho_e {U_e}^2 \tag{C.24}$$

$$\Rightarrow {U_e}^2 = \frac{2\left(P_{ae} - P_e\right)}{\rho_{ae}} \tag{C.25}$$

$$\Rightarrow {U_e}^2 = \frac{2P_{ae}}{\rho_e}\left(1 - \frac{P_e}{P_{ae}}\right) \tag{C.26}$$

Hence

$$U_e = \left[\frac{2P_{ae}}{\rho_{ae}}\left(1 - \frac{P_e}{P_{ae}}\right)\right]^{\frac{1}{2}} \tag{C.27}$$

Using equations C.23 and C.27 as well as the perfect gas equation of state it follows that

$$-\frac{P_e}{P_{ae}} = -\left(1 - \frac{P_\infty}{P_{ae}}\right) cos^2\left(\frac{2X}{D}\right) - \frac{P_\infty}{P_{ae}} \tag{C.28}$$

Insert equation C.28 into equation C.27 leads to

$$\frac{U_e}{U_\infty} = \frac{sin\left(\frac{2X}{D}\right)}{M_\infty cos\Lambda}\left[\frac{2}{\gamma}\frac{T_{ae}}{T_\infty}\left(1 - \frac{P_\infty}{P_{ae}}\right)\right]^{\frac{1}{2}} \tag{C.29}$$

and hence by differentiation

$$\frac{dU_e}{dX} = \frac{U_\infty}{D}\frac{2}{M_\infty cos\Lambda}\left[\frac{2}{\gamma}\frac{T_{ae}}{T_\infty}\left(1 - \frac{P_\infty}{P_{ae}}\right)\right]^{\frac{1}{2}} \times cos\left(\frac{2X}{D}\right) \tag{C.30}$$

Therefore the chordwise velocity gradient at the attachment-line itself (X = 0) is given by equation C.31

$$\left(\frac{dU_e}{dX}\right)_{X=0}\frac{D}{U_\infty} = \frac{2}{M_\infty cos\Lambda}\left[\frac{2}{\gamma}\frac{T_{ae}}{T_\infty}\left(1 - \frac{P_\infty}{P_{ae}}\right)\right]^{\frac{1}{2}} \tag{C.31}$$

C.6 Viscosity

The dynamic viscosity, μ, was calculated from Sutherland's law i.e.

$$\frac{\mu_{ae}}{\mu_{ref}} = \left(\frac{T_{ae}}{T_{ref}}\right)^{\frac{3}{2}} \cdot \left(\frac{T_{ref} + s}{T_{ae} + s}\right) \tag{C.32}$$

where for air, μ_{ref} and T_{ref} are $1.79.10^{-5}$ kg/m.s and 288.2 K respectively. For nitrogen, they become $1.75.10^{-5}$ kg/m.s and 293.2 K. Finally the kinematic viscosity ν was obtained i.e.

$$\nu_{ae} = \frac{\mu_{ae}}{\rho_{ae}} \tag{C.33}$$

Appendix D

Navier-Stokes computation for laminar flow

D.1 Governing equations

A Navier-Stokes code (MGNS3D) developed at Cranfield University [54] was used for the present investigation. This solves the Navier-Stokes equations in their integral form for steady laminar flow. It was assumed that the gas was perfect i.e. R, Cp and γ were constant. Body forces (gravity, electromagnetic forces, or any other forces which "act at a distance") were also assumed to be negligible. By defining the surface vector $d\vec{S}$ as follow:

$$d\vec{S} = \vec{n}dS \tag{D.1}$$

with $\vec{n}$ being the unit vector normal to the surface and dS the surface area. Using the co-ordinate system shown in figure D.5 the equations are:

CONTINUITY EQUATION:

$$\oint_s \overbrace{\underbrace{\rho\left(\vec{V}.\vec{n}\right)}_{Inviscid\ Flux}}^{Mass\ Flux} dS = 0 \tag{D.2}$$

MOMENTUM EQUATION:

$$\oint_s \overbrace{\left(\underbrace{\vec{V}\left(\rho\vec{V}.\vec{n}\right) + P\vec{n}}_{Inviscid\ Flux} - \underbrace{\bar{\tau}\vec{n}}_{Viscous\ Flux}\right)}^{Momentum\ Flux} dS = 0 \tag{D.3}$$

where $\bar{\tau}$ is the matrix of the shear stress forces defined by:

$$\bar{\tau} = \begin{bmatrix} \tau_{XX} & \tau_{XY} & \tau_{XZ} \\ \tau_{YX} & \tau_{YY} & \tau_{YZ} \\ \tau_{ZX} & \tau_{ZY} & \tau_{ZZ} \end{bmatrix} \tag{D.4}$$

$$\bar{\tau} = \begin{bmatrix} \lambda\left(\vec{\nabla}.\vec{V}\right) + 2\mu\frac{\partial u}{\partial X} & \mu\left(\frac{\partial v}{\partial X} + \frac{\partial u}{\partial Y}\right) & \mu\left(\frac{\partial u}{\partial Z} + \frac{\partial w}{\partial X}\right) \\ \mu\left(\frac{\partial v}{\partial X} + \frac{\partial u}{\partial Y}\right) & \lambda\left(\vec{\nabla}.\vec{V}\right) + 2\mu\frac{\partial v}{\partial Y} & \mu\left(\frac{\partial w}{\partial Y} + \frac{\partial v}{\partial Z}\right) \\ \mu\left(\frac{\partial u}{\partial Z} + \frac{\partial w}{\partial X}\right) & \mu\left(\frac{\partial w}{\partial Y} + \frac{\partial v}{\partial Z}\right) & \lambda\left(\vec{\nabla}.\vec{V}\right) + 2\mu\frac{\partial w}{\partial Z} \end{bmatrix} \tag{D.5}$$

with λ being the bulk viscosity coefficient defined as $\lambda = -\frac{2}{3}\mu$.

ENERGY EQUATION:

$$\oint_s \overbrace{\left[\underbrace{\left(\rho\vec{V}H_0.\vec{n}\right)}_{Inviscid\ Flux} - \underbrace{\left(k\vec{\nabla}T.\vec{n}\right)}_{} - \underbrace{\left(\vec{V}^T\bar{\tau}\vec{n}\right)}_{Viscous\ Flux}\right]}^{Energy\ Flux} dS = 0 \tag{D.6}$$

where $\vec{V}^T$ is the transposed form of the vector V and H_0 the stagnation enthalpy as defined by equations D.7 to D.9.

$$H_0 = E + \frac{P}{\rho} \tag{D.7}$$

with E being the total energy defined as:

$$E = e + \frac{\vec{V}^2}{2} \tag{D.8}$$

where e is the internal energy per unit mass defined as:

$$e = \frac{P}{(\gamma - 1)\,\rho} \tag{D.9}$$

Solutions were obtained from the evaluation of the primitive variables ρ, u, v, w and P at the centres of every cell in the computational domain. The surface vectors $d\vec{S}$ (equation D.1) and cells volume were evaluated at the start and then stored for every cell. The inviscid and viscous fluxes were then separately evaluated.

D.2 Inviscid Fluxes

Although the primitive variables are obtained through the iteration process at the cells centre (see section D.4), the inviscid fluxes must be calculated at the surfaces centre of every cell in the domain. Therefore the primitive variables ought to be evaluated at these specific locations. Hence a third order MUSCL scheme is used to achieve the interpolation of ρ, u, v, w and P originally obtained at the cell centres onto the surface centres.

Considering 4 cells in only one direction as shown by figure D.1, the primitive variables at the cells centre (points 1, 2, 3 and 4) are known via the iteration process (section D.4). Using the MUSCL scheme (as written in reference [36]), ρ, u, v, w and P are interpolated to point A from the value of the primitive variables at points 1, 2 and 3. Note that point A is located at the centre of the surface between cells 2 and 3. In the same

manner, the primitive variables are calculated at point B (merging with point A) but by considering this time the value of ρ, u, v, w and P at points 2, 3 and 4. A Hybrid scheme [54] (composed of the AUSM+ scheme [44] in the wall tangential directions and of the Osher scheme [46] in the wall normal direction) is then used to evaluate the inviscid fluxes through the surface between cells 2 and 3 via an approximate Riemann solution using data on either sides (A and B) of the interface. This process is applied to every cell surfaces in the computational domain.

The interpolation of the primitive variables as described above cannot be applied successfully everywhere in the flow field. Hence, a limiter is used to prevent spurious oscillations from occurring near the shock wave as shown by figure D.2 (see reference [54] for more information).

D.3 Viscous Fluxes

Consider a single cell in the computational domain (figure D.3), point C is located at the cell centre where the primitive variables are evaluated from the iteration process (see section D.4). Points A, B, D, E, F and G are positioned on each surface centre. From the evaluation of ρ, u, v, w and P at point C, the matrix $\bar{\tau}$ of the shear stress forces (equations D.4 and D.5) and thus the viscous fluxes must be calculated at every surface centres. Hence, an imaginary cell is created around every surface centre. Figure D.4 shows the imaginary cell created around point B only. Although point B is located at the centre of the surface on the right-hand side of the "original cell" it is also positioned at the imaginary cell centre. To calculate at point B the derivatives present in every matrix components (e.g. τ_{YX} etc), the primitive variables are evaluated at every surface centre

of the imaginary cell. A linear interpolation of ρ, v, u, w and P taken at the centre of the two original cells surrounding point B is carried out. This is achieved with respect to the computational "axis" defined by the vector co-ordinates I, J and K for ease (see section D.6). From the evaluation of the primitive variables at the surfaces centre of the imaginary cell, the derivatives in the matrix $\bar{\tau}$ are obtained at the imaginary cell centre (point B) using the Gauss divergence theorem (equation D.10).

$$\int_V \vec{\nabla}.\vec{F}dV = \int_S \vec{F}.d\vec{S} \tag{D.10}$$

where $\vec{F}$ is the vector of the primitive variables, dV the cell volume and $d\vec{S}$ is the surface vector defined by equation D.1 (see reference [9] for more information).

Since imaginary cells are also created around points A, D, E, F and G shown by figure D.4, the derivatives in the matrix $\bar{\tau}$ are known at every surfaces centre of the "original cell". The static temperature, T, is then evaluated directly at point C from the primitive variables at this location by the iteration process. A linear interpolation of T at the surface centre of the original cell (points A, B, D, E, F and G) is carried out using the values of T calculated at point C but also at the centre of the surrounding cells. Using Sutherland's law, the dynamic viscosity, μ, is calculated at the surfaces centre of the original cell. Since μ and the derivatives of the shear stresses are now known, $\bar{\tau}$, and thus the viscous fluxes, can be obtained at the surface centres. The process is applied to every cell in the computation domain.

D.4 Primitive Variables

As already described, the primitive variables ρ, u, v, w and P are obtained by performing iterations. This is achieved using the equation:

$$\int_V \frac{\partial Q}{\partial t} dV + R(W) = 0 \tag{D.11}$$

where W represents the primitive variables, R the Navier-Stokes equations, Q the conservative variables (ρ, ρu, ρv, ρw and ρE), t the time and dV the cell volume. If Q_0 corresponds to the conservative variables at t=0 (the code takes the free-stream values) and Q_1 to the conservative variables after one iteration, equation D.11 becomes:

$$\left(\frac{Q_1 - Q_0}{\Delta t}\right) dV + R\left(W_0\right) = 0 \tag{D.12}$$

hence

$$Q_{n+1} = Q_n - \left(\frac{R_{Wn}.\Delta t}{dV}\right) \tag{D.13}$$

By taking Q_0 as being the free-stream values of the conservatives variables, the primitive variables are obtained directly leading to the evaluation of the inviscid and viscous fluxes at iteration 0. Giving Δt and calculating the volume of every cell, the conservative variables after 1 iteration can be obtained. More iterations are performed until $||R||_2$ becomes very small (see equation below). In other words when the Navier-Stokes equations are satisfied i.e. $R\left(W_t\right) = 0$.

$$||R||_2 = \frac{\sum_{n=1}^{ngrid} R\left(W_{(t)}\right)^2}{\sum_{n=1}^{ngrid} R\left(W_{(0)}\right)^2} \tag{D.14}$$

where *ngrid* is the total number of grid points and "0" corresponds to the first value.

In the code, Δt is set via the CFL number (equation D.15) to the value which makes the solution converge. Since the steady state solution is required, Δt can be different for different cells (a feature called "local time stepping"). Indeed, the optimum Δt value can vary from one cell to another (depending on the size of the cells). Moreover, Δt, for a given cell, can vary as the iterations proceed.

$$Coef1 = |\frac{\vec{u}}{Q_\infty}.d\vec{S}_I| + |\frac{\vec{u}}{Q_\infty}.d\vec{S}_J| + |\frac{\vec{u}}{Q_\infty}.d\vec{S}_K|$$

$$Coef2 = \frac{a}{Q_\infty}\left(|d\vec{S}_I| + |d\vec{S}_J| + |d\vec{S}_K|\right)$$

$$Coef3 = \frac{2.\gamma.\mu.\rho_\infty\left(|d\vec{S}_I|^2 + |d\vec{S}_J|^2 + |d\vec{S}_K|^2\right)}{\mu_\infty.Re.Pr.\rho.dV}$$

$$\frac{\Delta t}{dV} = \frac{CFL}{[Coef1 + Coef2 + Coef3]} \tag{D.15}$$

where $a = \sqrt{\left(\frac{\gamma.P}{\rho}\right)}$ is the speed of sound and $\vec{u}$ is the velocity component vector.

D.5 Input and output parameters

The primitive variables at t=0 (Q_0) are calculated from the physical input parameters. These are the free-stream Mach number, the free-stream unit Reynolds number (per metre), the free-stream static temperature, the wall temperature, the angle of incidence (zero in the case of the present investigation) and the side slip angle (kept to zero in every cases). The computational input data include the CFL number, the choice of scheme (Roe,

Osher, AUSM+, AUSM+W or Hybrid scheme) and the choice of the boundary conditions.

The output file contains the number of iterations performed and the residuals. A solution file in which the values of the primitives variables at every cell centre appear is also generated by the code. By using a post-processor (see section D.7) other relevant information is obtained i.e. the spanwise distribution of the static pressure, velocity and static temperature profiles, total enthalpy plus the heat transfer rate at the wall and the chordwise velocity u taken at the boundary layer edge.

D.6 Grid description

Structured single block grids were generated by the code SWEPTCYL developed at Cranfield University (no publication available describing SWEPTCYL). From the specification of parameters such as the sweep angle, the cylinder diameter and length, the number of grid points in the I, J and K directions, the stretching factor etc. and using a transfinite interpolation grids were generated (see reference [64] section 4 for more information on transfinite interpolation methods). For refined grids (450 000 cells minimum), only a quarter of the circular cylinder was represented in order to reduce memory requirements. The orientation of the cylinder axis (right hand co-ordinates) as well as the direction of the vector co-ordinates I, J and K were as shown by figure D.5.

D.6.1 General shape

Care was taken to ensure that the outer edges of the computational domain closely followed the bow shock development. Thus, the grid was generated in two parts. The first

contained the upstream part of the cylinder and was parabolic in shape. The second formed the downstream part of the cylinder and was cylindrical (figure D.6). In addition, the grid was required to be orthogonal close to the model surface.

D.6.2 Stretching

Stretching was applied between the cylinder surface and the outer edge of the computational domain (J direction), between the upstream tip and the back end (K direction) and between the attachment-line and the edge of the domain at the back of the cylinder in the I direction (figures D.7 to D.9). This produced (within the laminar viscous layer) a minimum of 45 cells in the normal to the wall direction and 96 cells in the spanwise direction.

The fact that the attachment-line runs along one edge of the computational domain (I = 1 plane) allows more cells to be located at the attachment-line as it is easier to create a stretching towards a defined surface such as a wall or the edge of the computational domain.

D.6.3 Boundary conditions

At I = 1 (attachment-line plane), a symmetry boundary condition was specified. To calculate the inviscid and viscous fluxes through the surface Sa (figure D.10), the primitive variables at points C1, C2 but also C3 and C4 must be known. However, C1, C2, C3 and C4 are located at the centre of their respective cells and since cells 3 and 4 are not part of the grid, they have been created. Using the symmetry boundary condition at the plane

I = 1, means that the primitive variables at points C3 and C4 must be the reflection of the primitive variables values of points C1 and C2 respectively. In other words,

$$\rho_{C2} = \rho_{C4} \qquad \rho_{C1} = \rho_{C3}$$

Velocity in I direction at C1 = - Velocity in I direction at C3 etc.

At the computational plane I = IN (figure D.10), a zero-order extrapolation was used. Primitive variables at points C5, C6, C7 and C8 must be known in order to calculate the inviscid and viscous fluxes through surface Sb for example. Values of ρ, u, v, w and P at point C5 are directly copied to points C7 and C8 (zero order extrapolation). Although a linear interpolation for example from points C5 and C6 would seem more appropriate, a zero order extrapolation has the advantage of making the solution process more robust. Moreover, since the investigation is concentrated at the attachment- line, the accuracy of the results (primitive variables) at the plane I = IN (far away from the attachment-line plane) is not a priority.

The symmetry boundary condition was also used at the plane of the cylinder upstream tip (K = 1) as shown by figure D.11. Ghost cells, C3 and C4, were created in order to supply the primitive variables at these locations and to calculate the fluxes through the surface ST (see figure D.11). The primitive variables at points C3 and C4 are the reflected values calculated via the iteration process at points C1 and C2 respectively.

At the wall (J = 0), the non-slip condition is applied hence:

$$u_W = v_W = w_W = 0 \tag{D.16}$$

The pressure gradient in the wall normal direction is set to zero i.e. the pressure at the wall P_W equals the pressure at the centre of the cell next to the wall P_1 (figure D.12 and equation D.17):

$$P_1 = P_W \tag{D.17}$$

Since the temperature at the wall (T_W) is input, it follows:

$$\rho_W = \frac{P_W}{R.T_W} \tag{D.18}$$

Hence the primitive variables are all known at the wall (equations D.16, D.17 and D.18). The inviscid and viscous fluxes at this location are evaluated directly from the primitive variables ρ_W, u_W, v_W, w_W and P_W. However, to calculate the fluxes through surface SC (figure D.12), a ghost cell in the wall was created (point 0 being its centre). The primitive variables at point 0 are obtained by linear interpolation from the primitive variables at points 1 and W (equations D.19 to D.22).

$$P_0 = P_1 = P_W \tag{D.19}$$

$$\rho_0 = 2\rho_W - \rho_1 \tag{D.20}$$

$$T_0 = \frac{P_0}{R.\rho_0} \tag{D.21}$$

$$u_0 = 2u_W - u_1$$

$$v_0 = 2v_W - v_1$$

$$w_0 = 2w_W - w_1 \tag{D.22}$$

At the outer edge of the computational domain (J = JN), the boundary conditions depends on the Mach number normal to the edge, M_{Ne}. Indeed, to calculate the fluxes through surface SF for example (figure D.13), the primitive variables need to be evaluated at centre of the ghost cell 3 (point 3 on figure D.13). The way the primitive variables are interpolated to this point depends on whether the inflow is supersonic or subsonic.

The Navier-Stokes equations link five independent variables. Hence five eigenvalues exist. If all five eigenvalues have the same sign, the flow is supersonic and information cannot travel upstream. In this case, the primitive variables at point 3 (figure D.13) are identical to the free-stream values. However if one eigenvalue has a different sign than the four others, the flow is subsonic and information can travel both upstream and downstream. In this case, one piece of information (pressure or density etc.) must be taken from downstream (points 4 or/and 2) and the four others from upstream (free-stream).

Consider the two points L and R located on the edge of the domain e (J = JN plane, figure D.13). The primitive variables at point R are identical to the primitive variables at the centre of cell 1 (zero order interpolation from point 1 to R). At point L, the primitive variables have the free-stream values. Therefore the velocity normal to the edge of the computational domain can be evaluated at points L and R (V_{NL} and V_{NR}). The Riemann invariants ψ are then calculated:

$$\psi_L = V_{NL} + \frac{2.a_L}{\gamma - 1} = V_{Ne} + \frac{2.a_e}{\gamma - 1} \tag{D.23}$$

$$\psi_R = V_{NR} - \frac{2.a_R}{\gamma - 1} = V_{Ne} - \frac{2.a_e}{\gamma - 1} \tag{D.24}$$

where a is the speed of sound. Note that only equation D.24 involves downstream information. Hence the velocity normal to the edge of the domain as well as the speed of sound can be obtained at point e.

$$V_{Ne} = \frac{1}{2}.(\psi_R + \psi_L) \tag{D.25}$$

$$a_e = \frac{\gamma - 1}{4} \tag{D.26}$$

From equations D.25 and D.26, the Mach number normal to the edge of the domain follows:

$$M_{Ne} = \frac{V_{Ne}}{a_e} \tag{D.27}$$

If $M_{Ne} > 1$ (supersonic inflow), the primitive variables at point 3 are identical to the free-stream values. However, if $M_{Ne} < 1$ (subsonic inflow), the tangential velocity components and the entropy at point e have the free-stream values and V_{Ne} and a_e are taken from equations D.26 and D.27. It should be noted that these five variables are independent of each other and are direct functions of the primitive variables. These variables are interpolated to point 3 also using information at points 1 and 2. Once the tangential velocity components, the entropy, V_N and a are obtained at point 3, the primitive variables are calculated at this same location. The inviscid and viscous fluxes through surface SF can be evaluated since ρ, u, v, w and P are known at points 1, 2, 3 and 4. The fluxes through the surface at the edge of the computational domain are calculated directly from the primitive variables at this location (point e).

D.7 Post-processor

A post-processor was created to extract the information needed for the present study.

D.7.1 T, V, P and Ho Profiles at the attachment-line location

Consider the first two cells next to the attachment-line (figure D.14). Points AL is located at the attachment- line itself (I=1 plane) and points 1 and 2 are positioned at the centre of cells 1 and 2 respectively. The temperature (for example) at points 1 and 2 is directly evaluated from the primitive variables supplied by the iteration process. To obtain T at the attachment-line, an interpolation is needed. Thus, a cubic expression linking temperature to surface position has been assumed to characterise its variation in the I direction (S increasing).

$$T = AS^3 + BS^2 + CS + D \tag{D.28}$$

where S is the distance around the cylinder (figure D.14). Since a symmetry boundary condition has been specified at the plane I=1 (attachment-line plane), it follows for the cells next to the attachment-line:

$$T_{S1} = T_1 = AS_1{}^3 + BS_1{}^2 + CS_1 + D \tag{D.29}$$

$$T_{S-1} = T_1 = AS_{-1}{}^3 + BS_{-1}{}^2 + CS_{-1} + D \tag{D.30}$$

From equations D.29 and D.30

$$\Longrightarrow T_{S1} - T_{S-1} = 2AS_1{}^3 + 2CS_1 \tag{D.31}$$

Now considering cell 2 and its symmetry:

$$T_{S2} = T_2 = AS_2{}^3 + BS_2{}^2 + CS_2 + D \tag{D.32}$$

$$T_{S-2} = T_2 = AS_{-2}{}^3 + BS_{-2}{}^2 + CS_{-2} + D \tag{D.33}$$

From equations D.32 and D.33

$$\Longrightarrow T_{S2} - T_{S-2} = 2AS_2{}^3 + 2CS_2 \tag{D.34}$$

From equations D.31 and D.34, the solution for the coefficients A and C is:

$$A = C = 0 \tag{D.35}$$

Hence equation D.28 of the temperature is reduced to:

$$T = BS^2 + D \tag{D.36}$$

At the attachment-line since S = 0, the temperature is represented by the coefficient D in equation D.36.

$$T_{S1} = T_{S-1} = T_1 = BS_1{}^2 + D \tag{D.37}$$

$$T_{S2} = T_{S-2} = T_2 = BS_2{}^2 + D \tag{D.38}$$

Rearranging equations D.37 and D.38 together leads to

$$T_{AL} = D = \frac{T_1 S_2{}^2 - T_2 S_1{}^2}{S_2{}^2 - S_1{}^2} \tag{D.39}$$

Applying equation D.39 to all the cells in the vicinity of the attachment-line (along the J and K axis), the temperature profiles at, and along, the attachment-line are obtained. In the same manner, the profiles of the static pressure and velocity components u, v and w are calculated. Using equations D.40 and D.41, the profiles of the velocity component in the spanwise direction V and of the total enthalpy are evaluated.

$$V_a = v_a \cos\Lambda + u_a \sin\Lambda \tag{D.40}$$

$$H_{0a} = CpT_a + \frac{{u_a}^2 + {v_a}^2 + {w_a}^2}{2} \tag{D.41}$$

The post-processor then outputs the profiles of the static pressure, static temperature, velocity and stagnation enthalpy along the attachment-line with the corresponding J values.

D.7.2 Heat transfer at the wall

The temperature distribution in the normal to the wall direction is assumed to be quadratic hence:

$$T = Aa^2 + Ba + C \tag{D.42}$$

with a being the distance as moving away from the cylinder surface (figure D.15). At the wall (a = 0), the temperature T is known to be Tw. Thus

$$C = Tw$$

and equation D.42 becomes:

$$T = Aa^2 + Ba + Tw \tag{D.43}$$

which can be used to estimate the heat transfer rate at the wall since:

$$\left(\frac{dT}{da}\right)_{a=0} = B \tag{D.44}$$

If T1 represents the temperature at the centre of cell 1 and T2 the temperature at the centre of cell 2 (see figure D.15) then:

$$T1 = A{a_1}^2 + Ba_1 + Tw \tag{D.45}$$

$$T2 = A{a_2}^2 + Ba_2 + Tw \tag{D.46}$$

$$\Longrightarrow Ba_1 = (T1 - Tw) - A{a_1}^2 \tag{D.47}$$

and

$$Ba_2 = (T2 - Tw) - A{a_2}^2 \tag{D.48}$$

Thus

$$\Longrightarrow {a_2}^2 Ba_1 = {a_2}^2(T1 - Tw) - A{a_1}^2{a_2}^2 \tag{D.49}$$

and

$${a_1}^2 Ba_2 = {a_1}^2(T2 - Tw) - A{a_1}^2{a_2}^2 \tag{D.50}$$

Subtracting equation D.50 to equation D.49, it follows:

$$a_1{}^2 B a_2 - a_2{}^2 B a_1 = a_1{}^2 (T2 - Tw) - a_2{}^2 (T1 - Tw) \tag{D.51}$$

$$B\left[a_1 a_2 (a_1 - a_2)\right] = a_1{}^2 (T2 - Tw) - a_2{}^2 (T1 - Tw) \tag{D.52}$$

Hence the heat transfer rate at the wall is:

$$\dot{q}_W = \left(\frac{dT}{da}\right)_{a=0} = B = \frac{a_1{}^2 (T2 - Tw) - a_2{}^2 (T1 - Tw)}{a_1 a_2 (a_1 - a_2)} \tag{D.53}$$

Taking T1 and T2 at the centres of the surfaces lying along the attachment-line as shown by figure D.16 and using equation D.53 for every spanwise station (K direction), the surface heat transfer rate variation along the attachment-line can be evaluated. It should be noted that T1 and T2 are interpolated to the attachment-line as described in section D.7.1.

From the grid file, the co-ordinates x, y and z of each grid points are known and the grid points are the points in each corners of the cells. Hence the co-ordinates of the points Pt1 and Pt2 (figure D.16) can be evaluated. For example for Pt1 the co-ordinates are:

$$X_{Pt1} = \frac{X_A + X_B + X_F + X_G}{4} \tag{D.54}$$

$$Y_{Pt1} = \frac{Y_A + Y_B + Y_F + Y_G}{4} \tag{D.55}$$

$$Z_{Pt1} = \frac{Z_A + Z_B + Z_F + Z_G}{4} \tag{D.56}$$

Therefore the evaluation of the distances a_1 and a_2 leading to the heat transfer rate (equation D.53) can be calculated. The post processor then gives the heat transfer rate along the attachment-line with its corresponding value of $\frac{L}{D}$.

D.7.3 The chordwise velocity

The velocity components u, v and w are known at the cells centres from the iteration process. An average of these values is used to calculate u, v and w at the surface centres in the I direction only (chordwise direction). Indeed, the values of u, v and w on the surface S2 (figure D.17) are evaluated from the velocity components at points C1 and C2 from:

$$u_{S2} = \frac{1}{2}(u_1 + u_2) \tag{D.57}$$

$$v_{S2} = \frac{1}{2}(v_1 + v_2) \tag{D.58}$$

$$w_{S2} = \frac{1}{2}(w_1 + w_2) \tag{D.59}$$

Where the velocity components at point S1 are interpolated in the way described for the temperature in section D.7.1.

By calculating the velocity vector $\vec{u}$ at each surface centre (equation D.60) and the surface unit vector $\vec{n}$ (equation D.61), the chordwise velocity is evaluated from equation D.62.

$$\vec{u} = u_{S2}\vec{x} + v_{S2}\vec{y} + w_{S2}\vec{z} \tag{D.60}$$

where $\vec{x}$, $\vec{y}$ and $\vec{z}$ are the unit vectors in the X, Y and Z directions respectively.

$$\vec{n} = n_x\vec{x} + n_y\vec{y} + n_z\vec{z} \tag{D.61}$$

Hence the chordwise velocity component at the surface 2 is:

$$U = \vec{u}_{S2}.\vec{n} \tag{D.62}$$

The co-ordinates of the points at the surface centres are calculated using equations D.54, D.55 and D.56 leading to the evaluation of their distances from the attachment-line plane measured along the I axis. From these calculations, the post-processor gives U calculated at the surface centres and their distances from the attachment-line along the I axis.

Knowing u, v, and w at the surface centres in the I direction e.g. surface S2 on figure D.17, the velocity magnitude Q can be evaluated at the same locations. Starting from the wall and moving away along the J axis, the ratio of the velocity magnitude at a certain cell to the velocity magnitude at the following cell is calculated for every K station along the attachment-line.

$$\frac{Q_{J-1,K}}{Q_{J,K}} \tag{D.63}$$

When this ratio reaches 0.999, the edge of the velocity boundary layer is said to be found. At this location (edge of the velocity boundary layer), the edge chordwise velocity U_e is determined for all stations I and K (around the cylinder and in the spanwise direction respectively).

D.8 Runs achieved by the Navier-Stokes code

Computations have been carried out for the cases listed in table B.2. Most of these runs correspond to experimental conditions (described in appendix G). Some others were

created in order to complete the present investigation (see chapter 3, section 3.2). All runs were carried out on smooth surfaces.

D.9 Figures

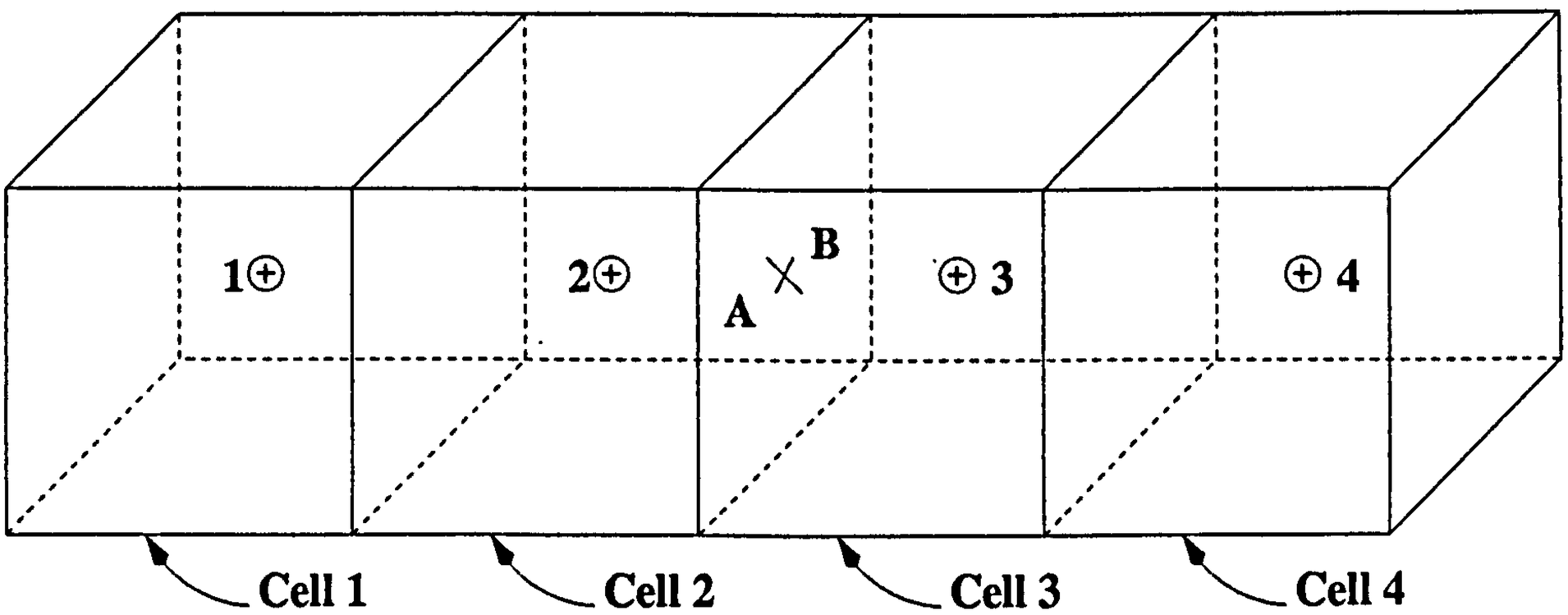

Figure D.1: Sketch of four computational cells aligned in only one direction.

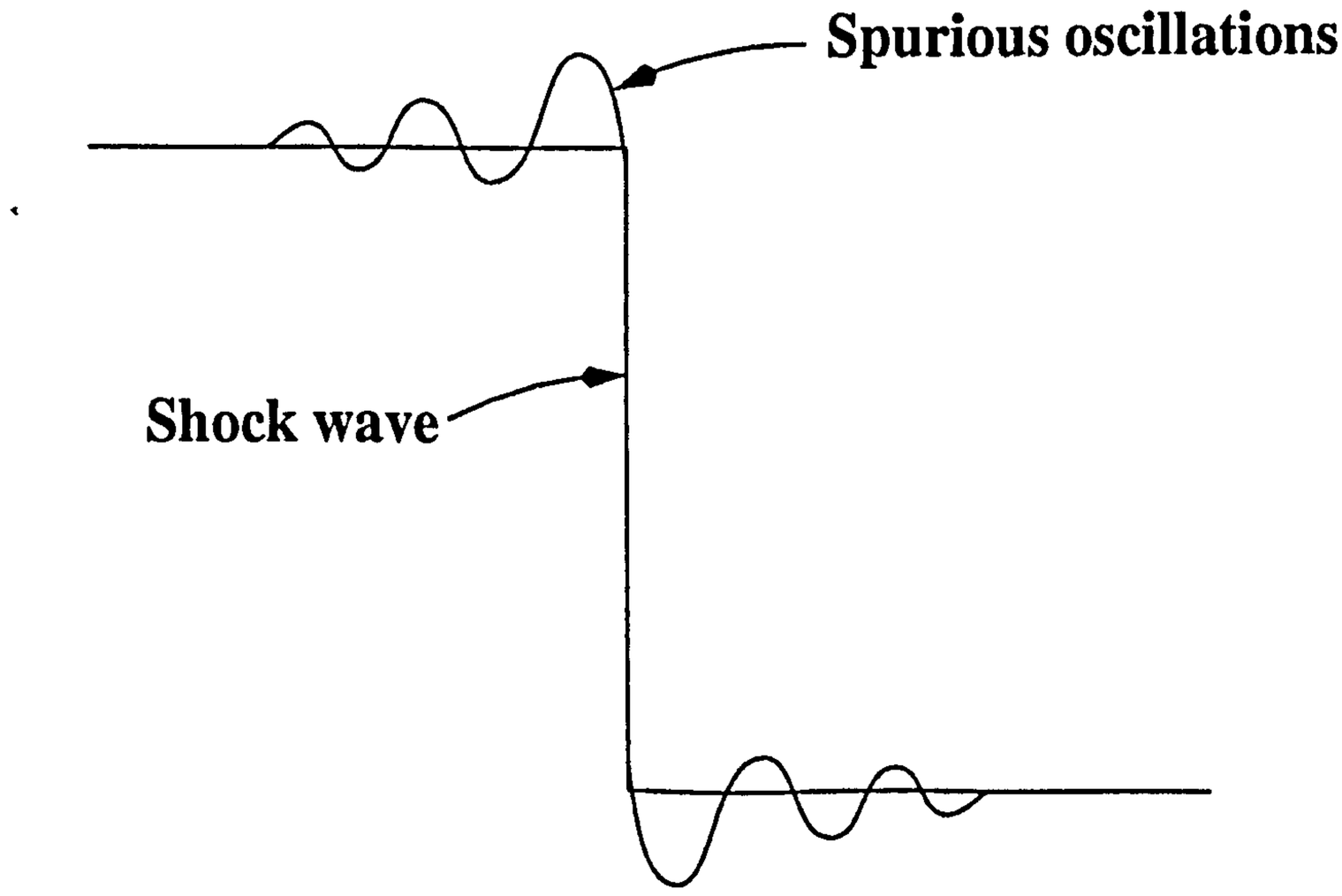

Figure D.2: Sketch of spurious oscillations.

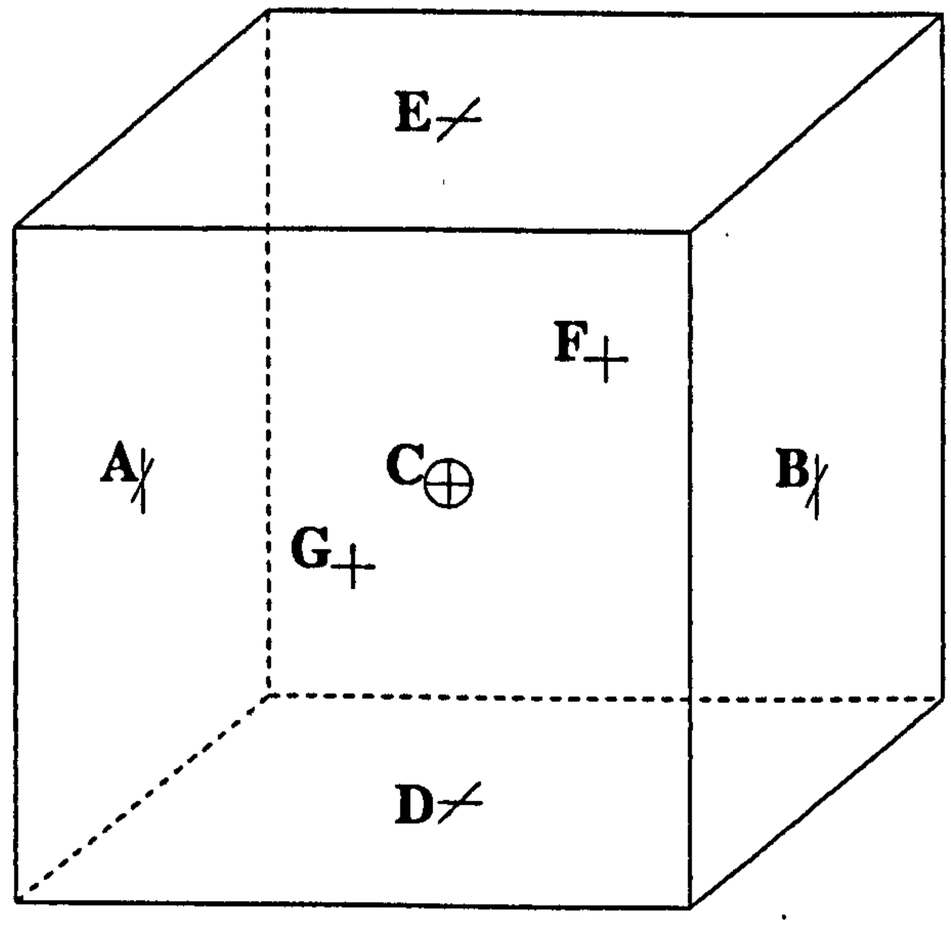

Figure D.3: Sketch of a single cell in the computational domain.

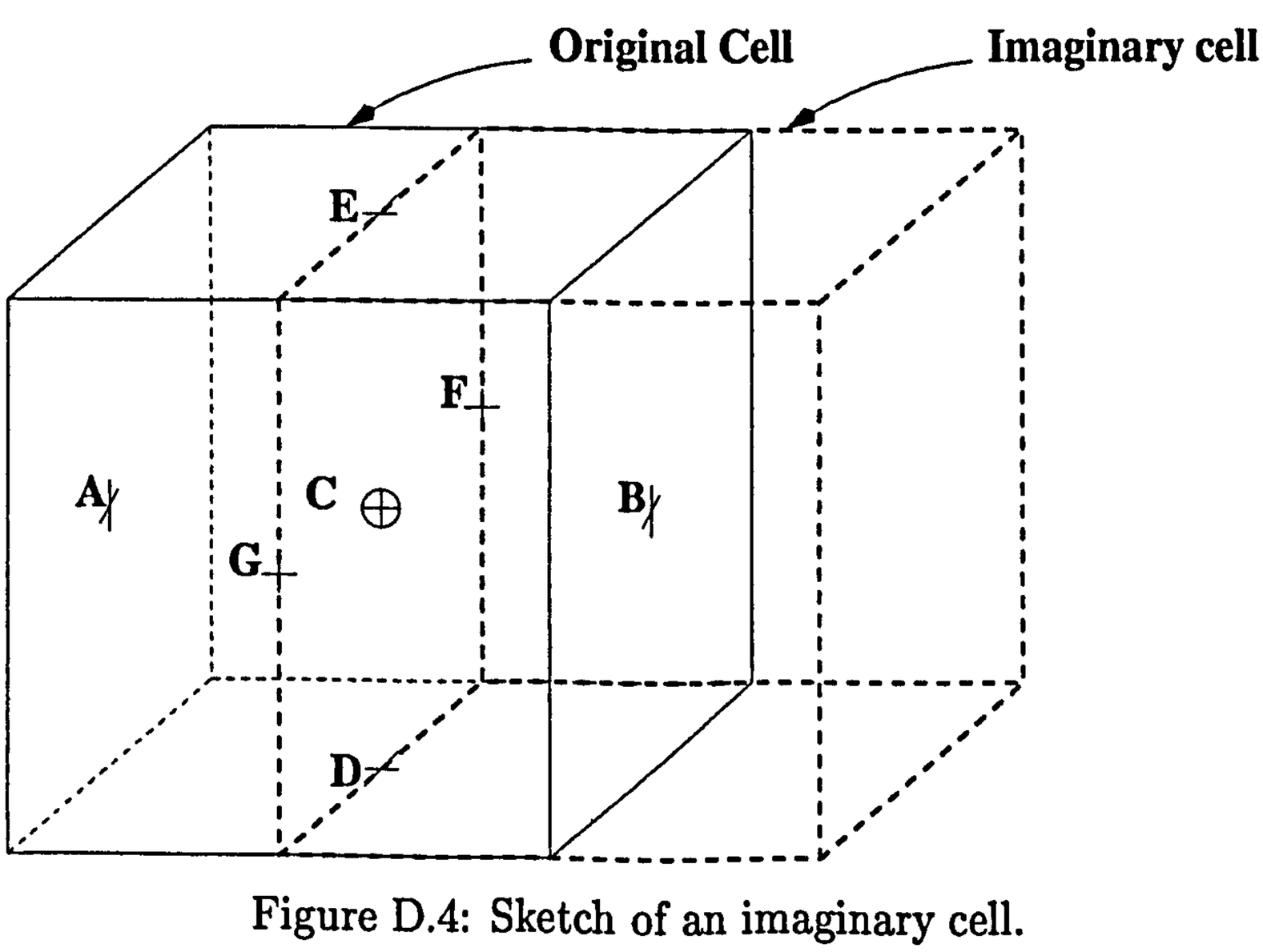

Figure D.4: Sketch of an imaginary cell.

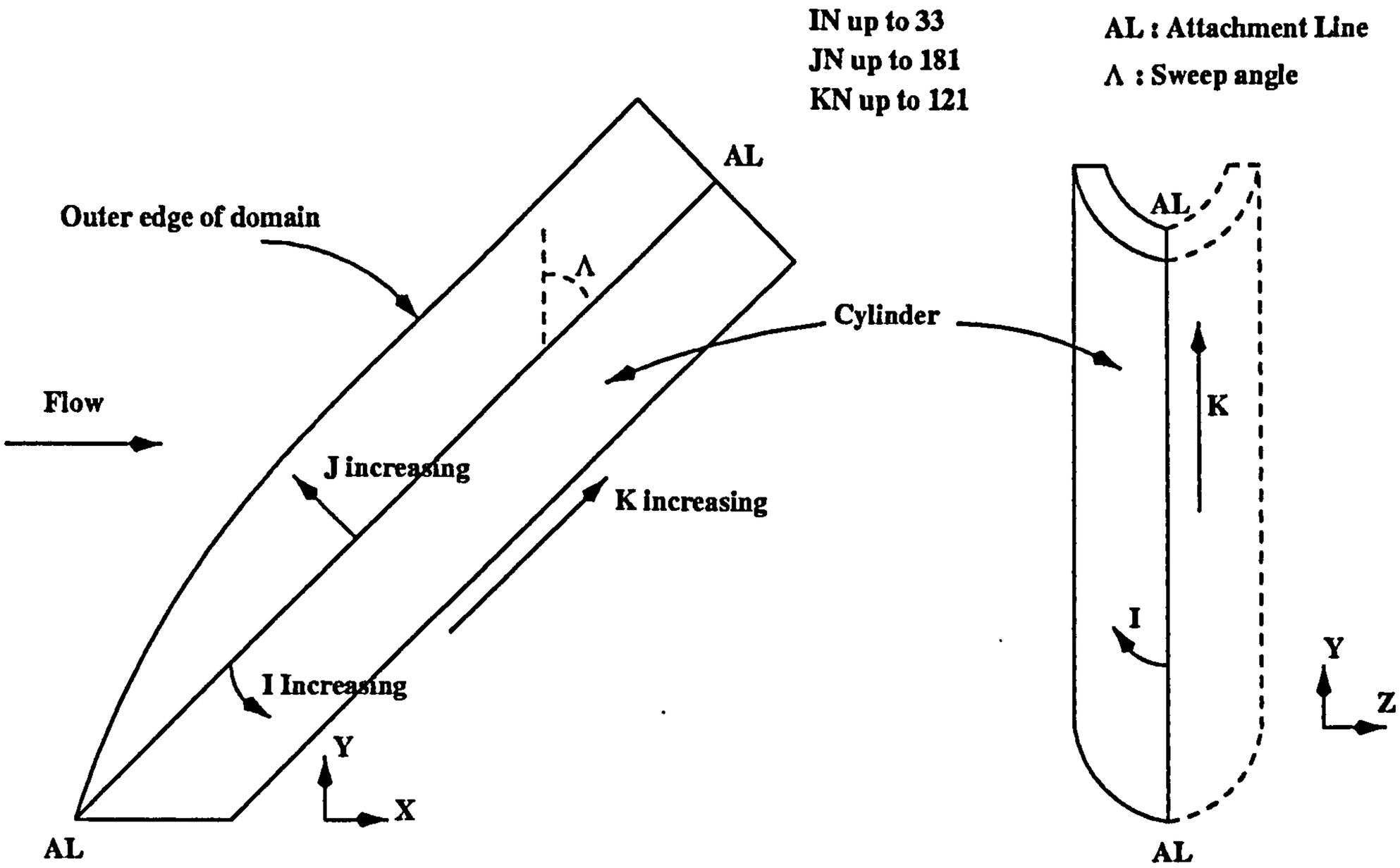

Figure D.5: Vector co-ordinates and axis orientation (Right hand orthogonal, cylindrical co-ordinate system).

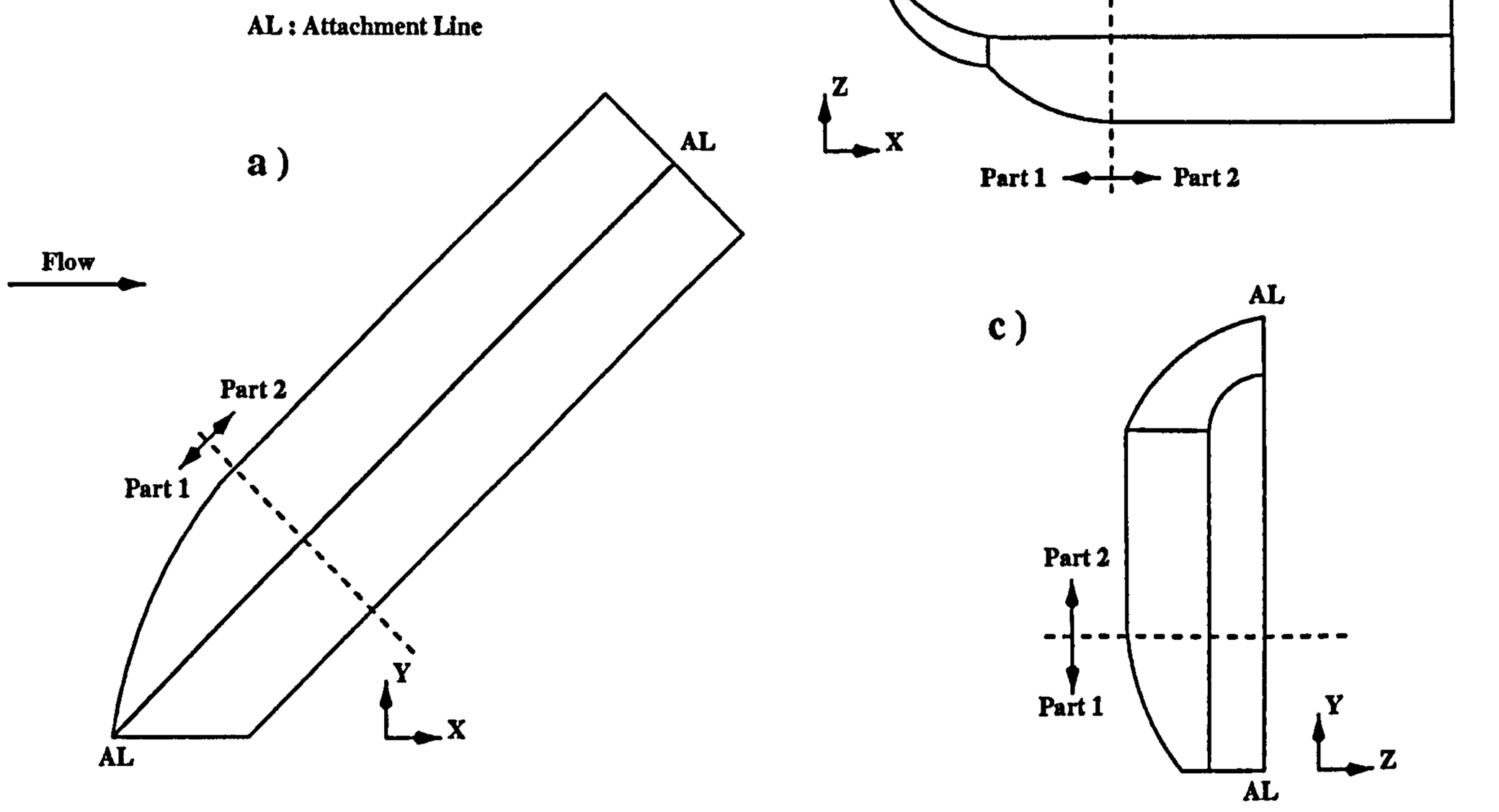

Figure D.6: Parts composing the grid.

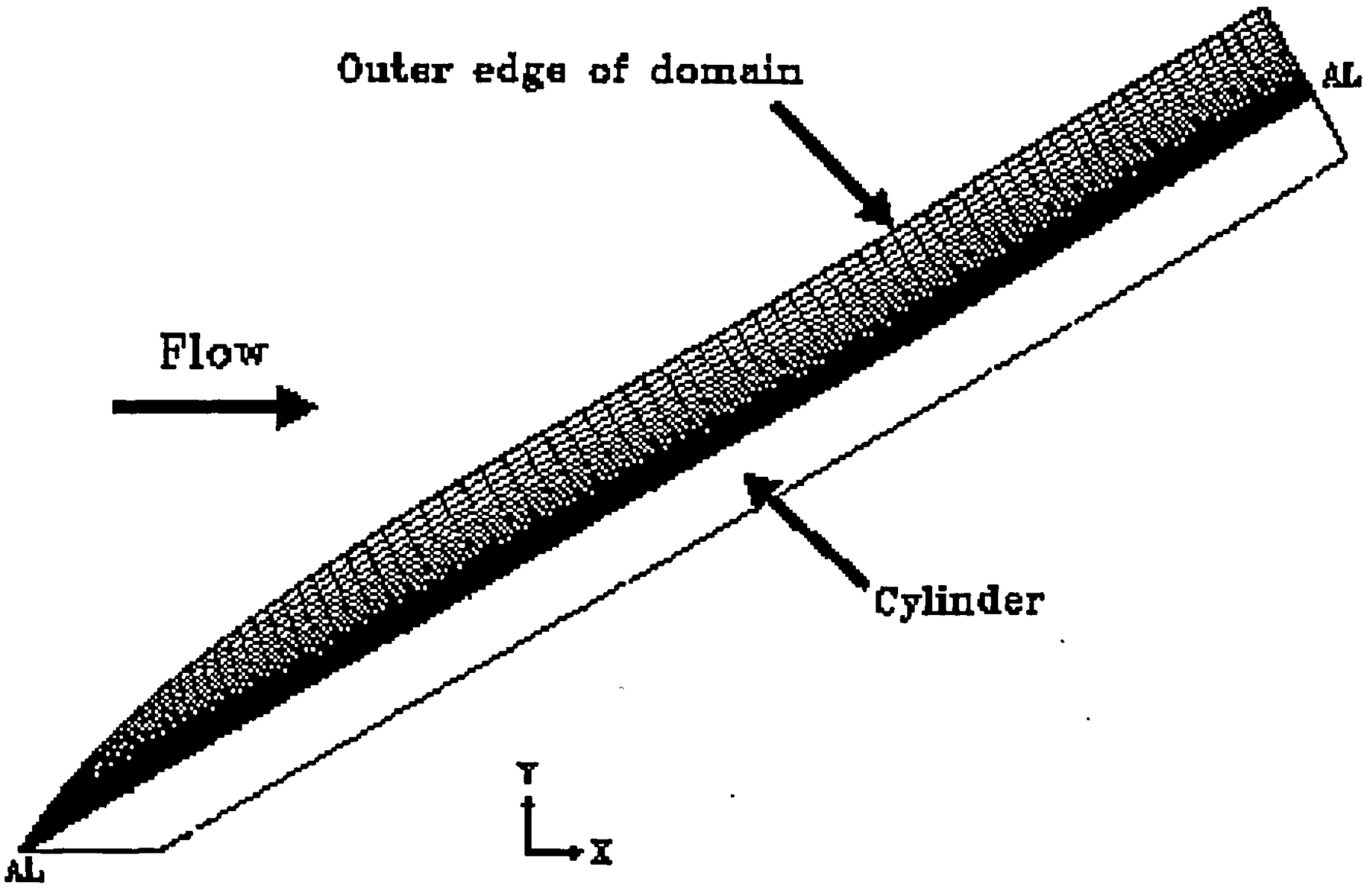

Figure D.7: Grid stretching in the normal to the wall direction (J). Every 3 cells centre shown.

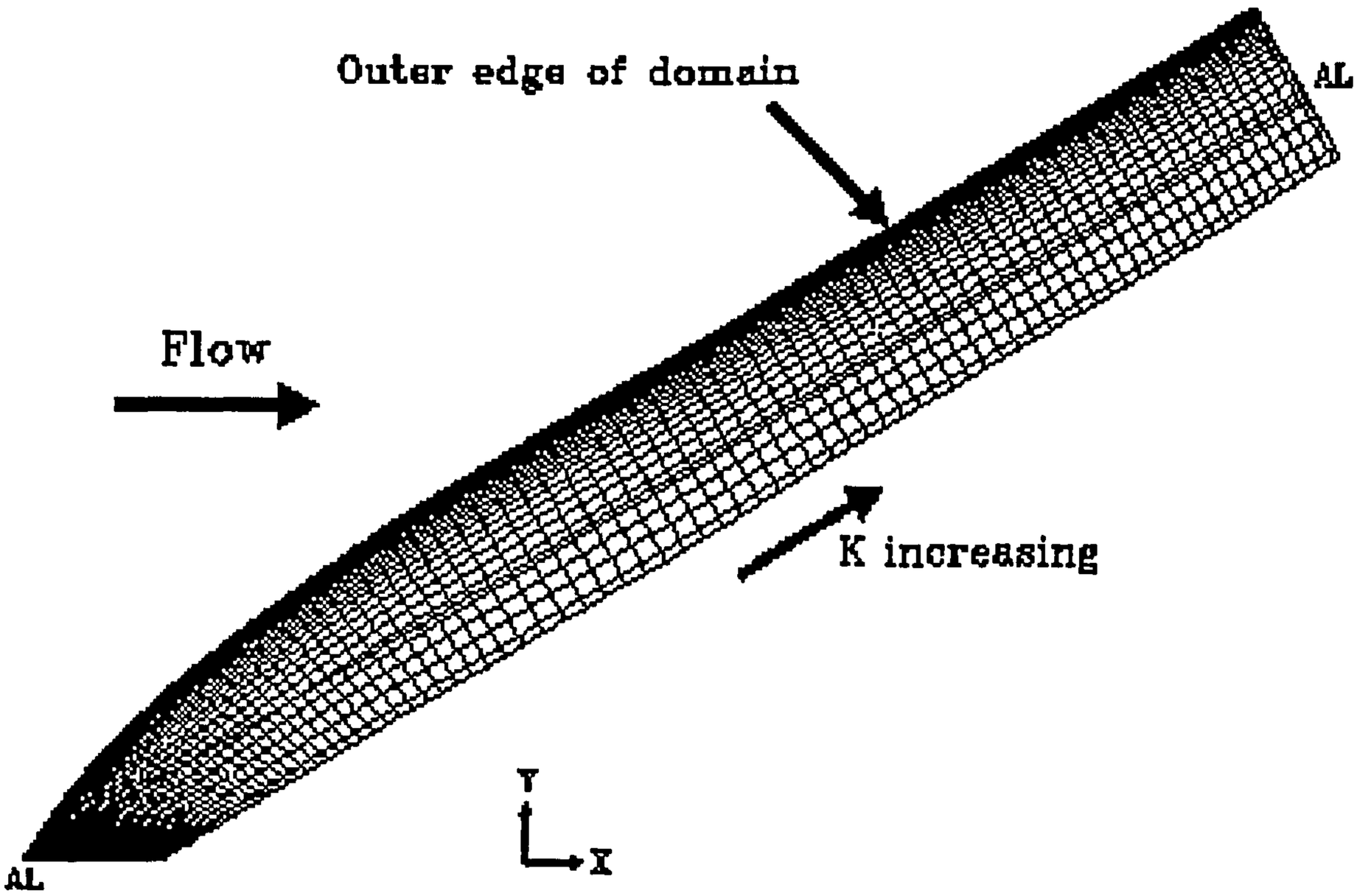

Figure D.8: Grid stretching along the cylinder (K direction).

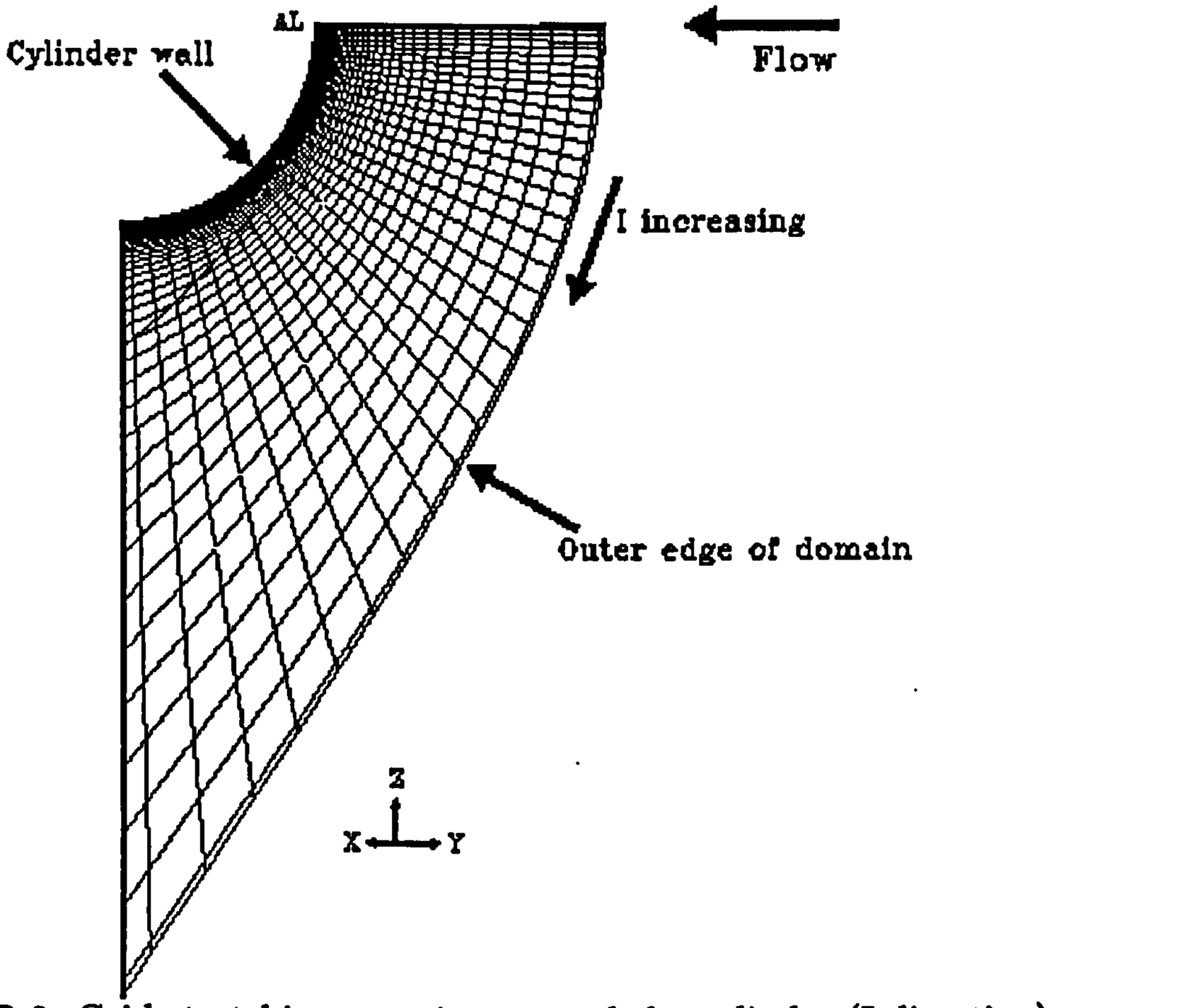

Figure D.9: Grid stretching as going around the cylinder (I direction).

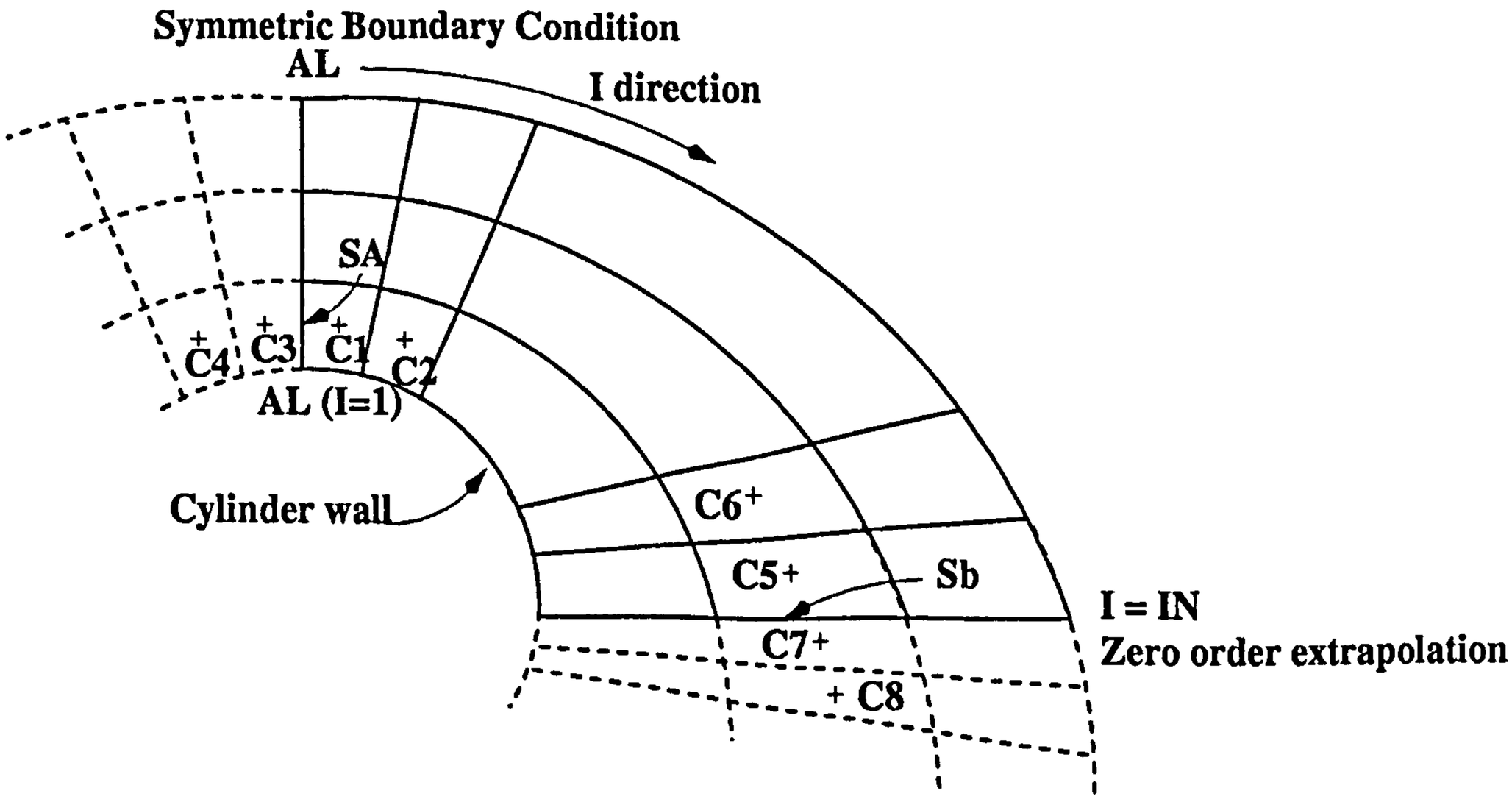

Figure D.10: Sketch showing the symmetric boundary condition at I=1 and the zero order extrapolation at I=IN.

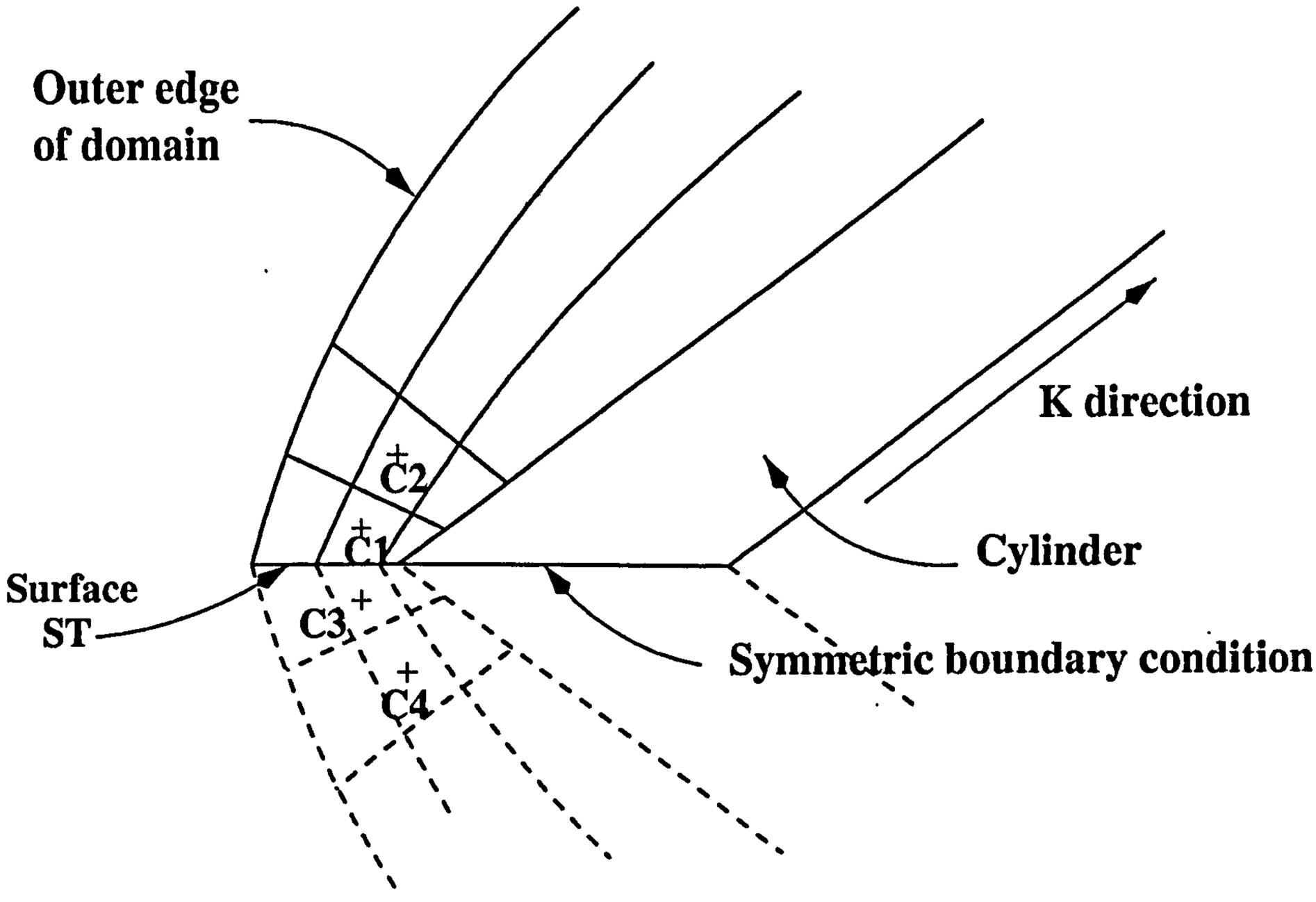

Figure D.11: Sketch of the symmetric boundary condition specified at the upstream tip of the cylinder (K=1 plane).

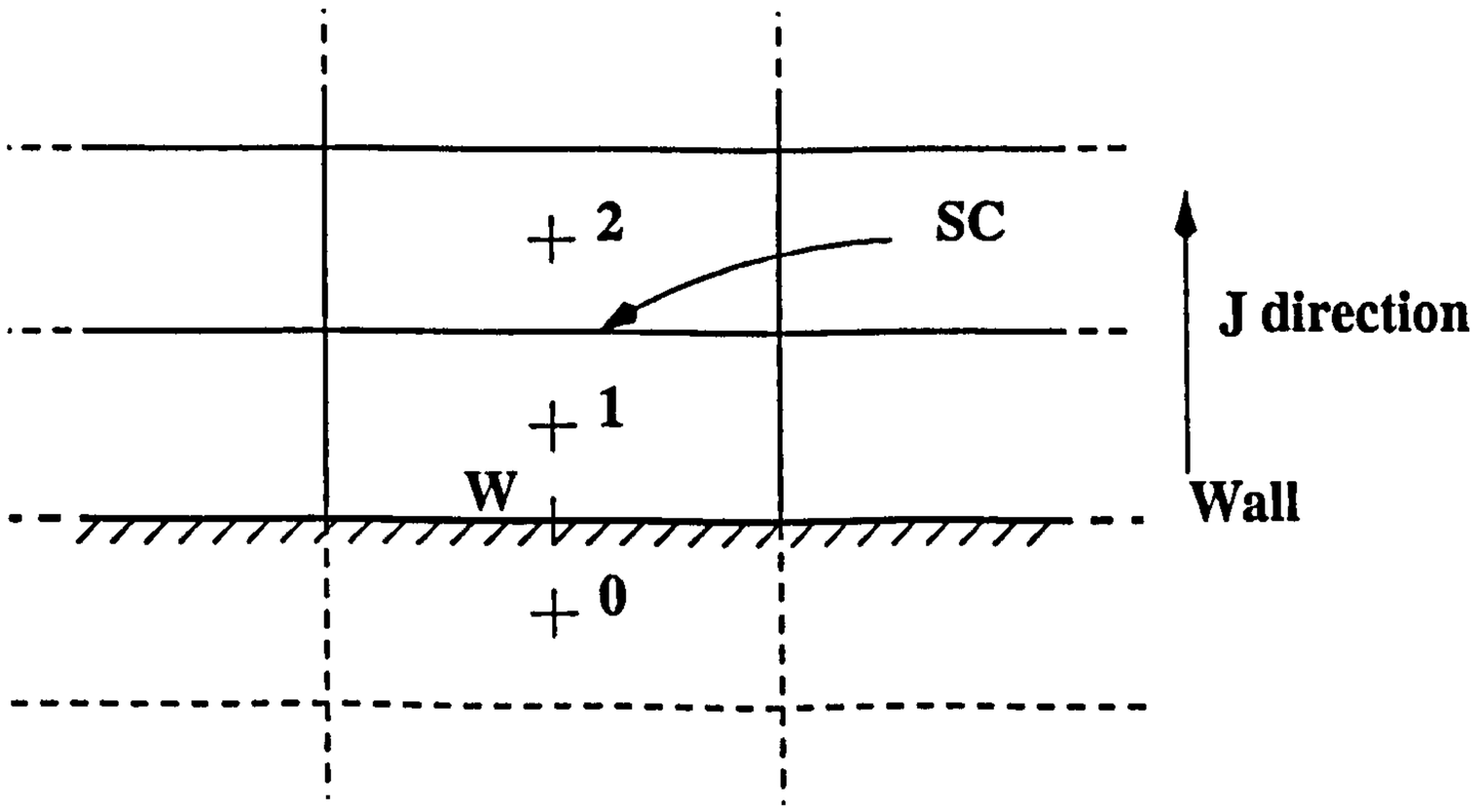

Figure D.12: Sketch of the computational cells next to the wall.

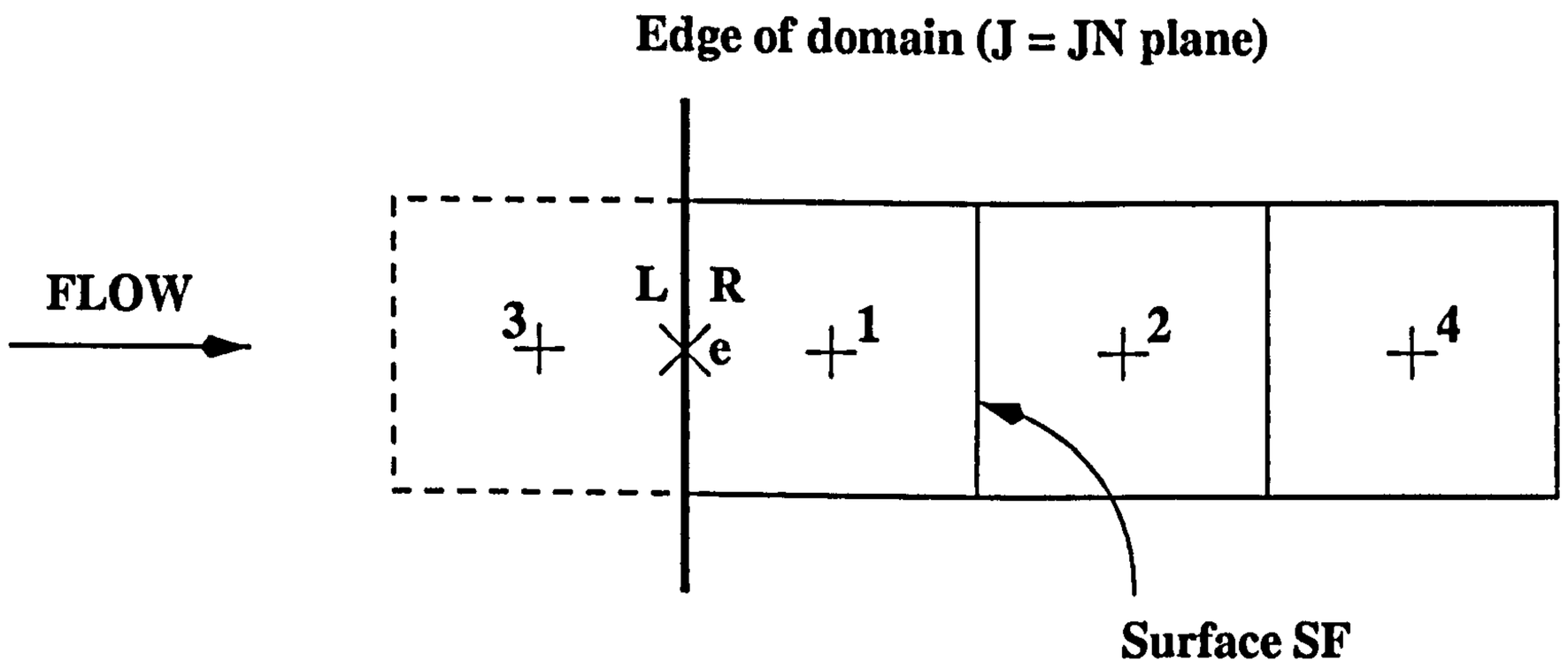

Figure D.13: Sketch of the cells next to edge of the computational domain (J = JN plane).

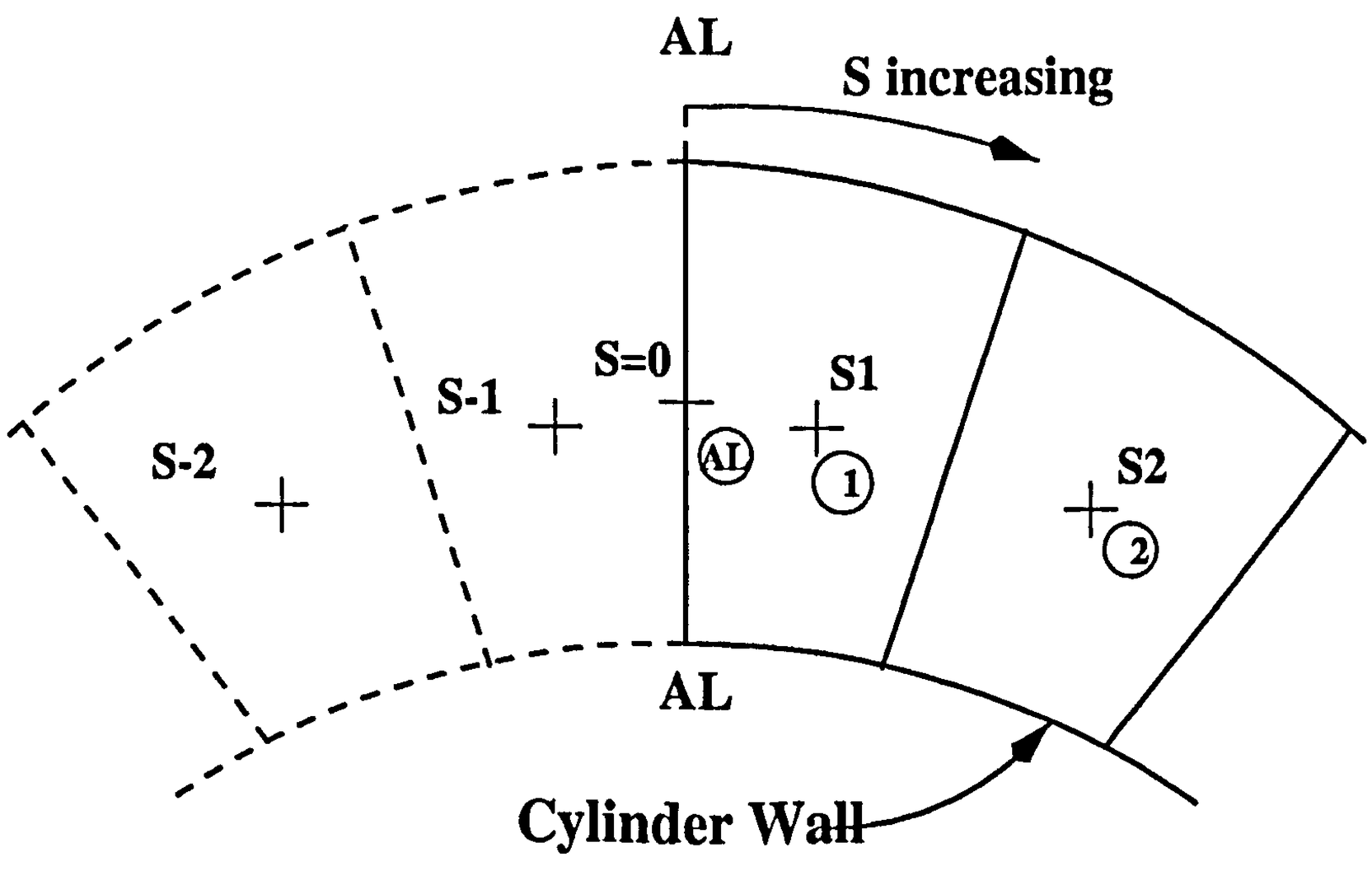

Figure D.14: Sketch of the 2 computational cells next to the attachment-line.

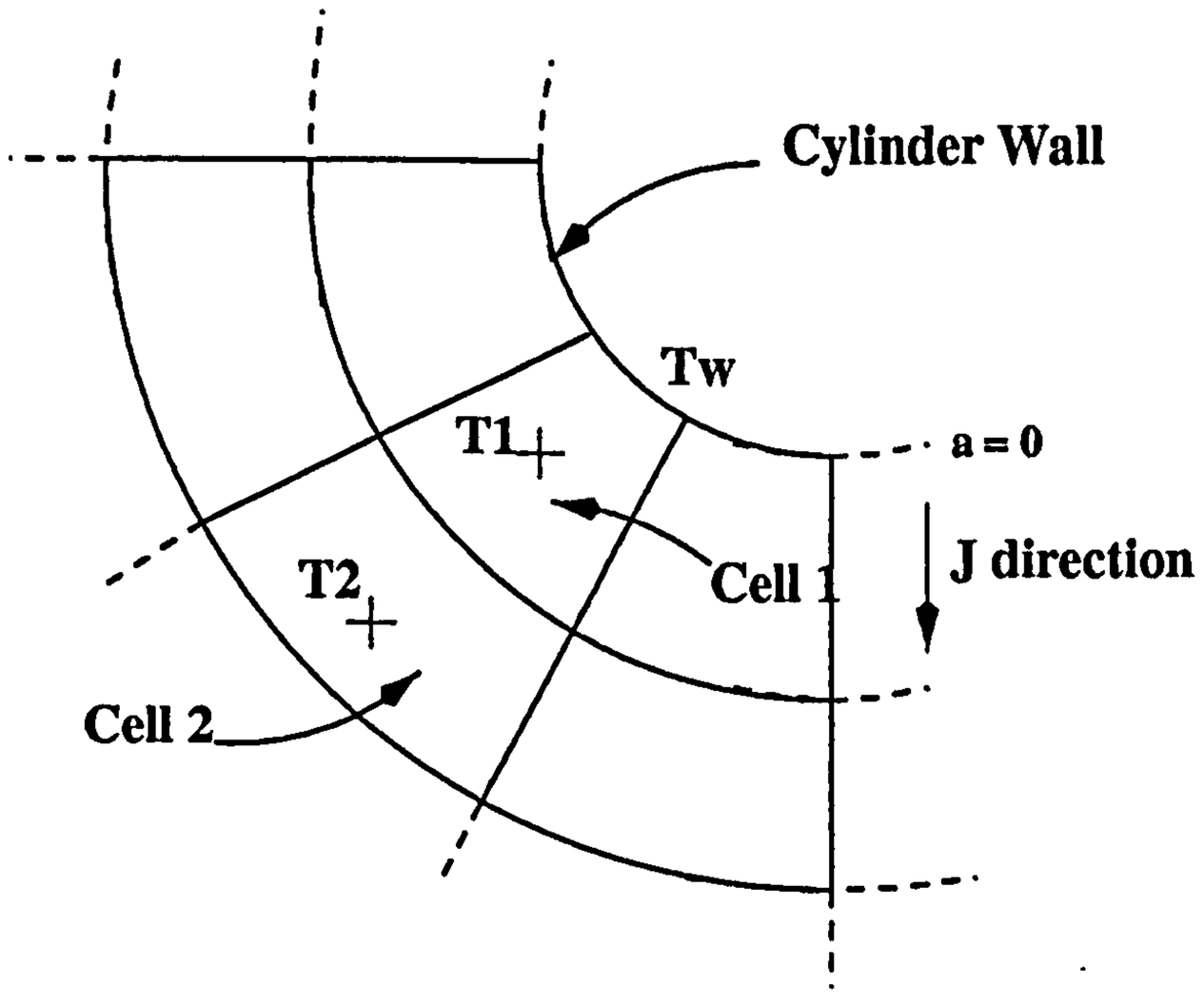

Figure D.15: Sketch of cells 1 and 2 allowing the heat transfer at the wall to be evaluated.

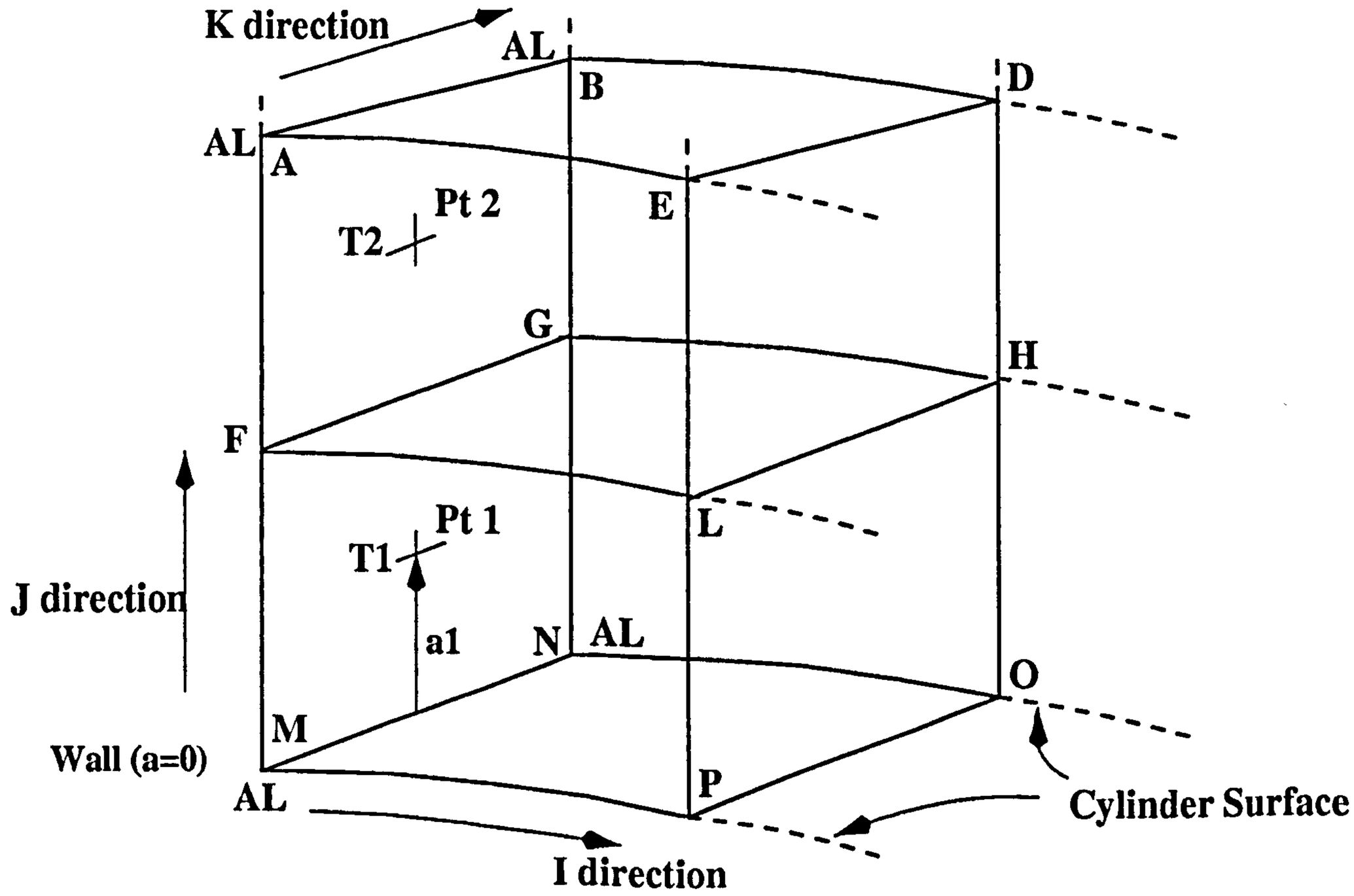

Figure D.16: Sketch showing the location of T1 and T2 allowing the heat transfer at the wall along the attachment- line to be evaluated.

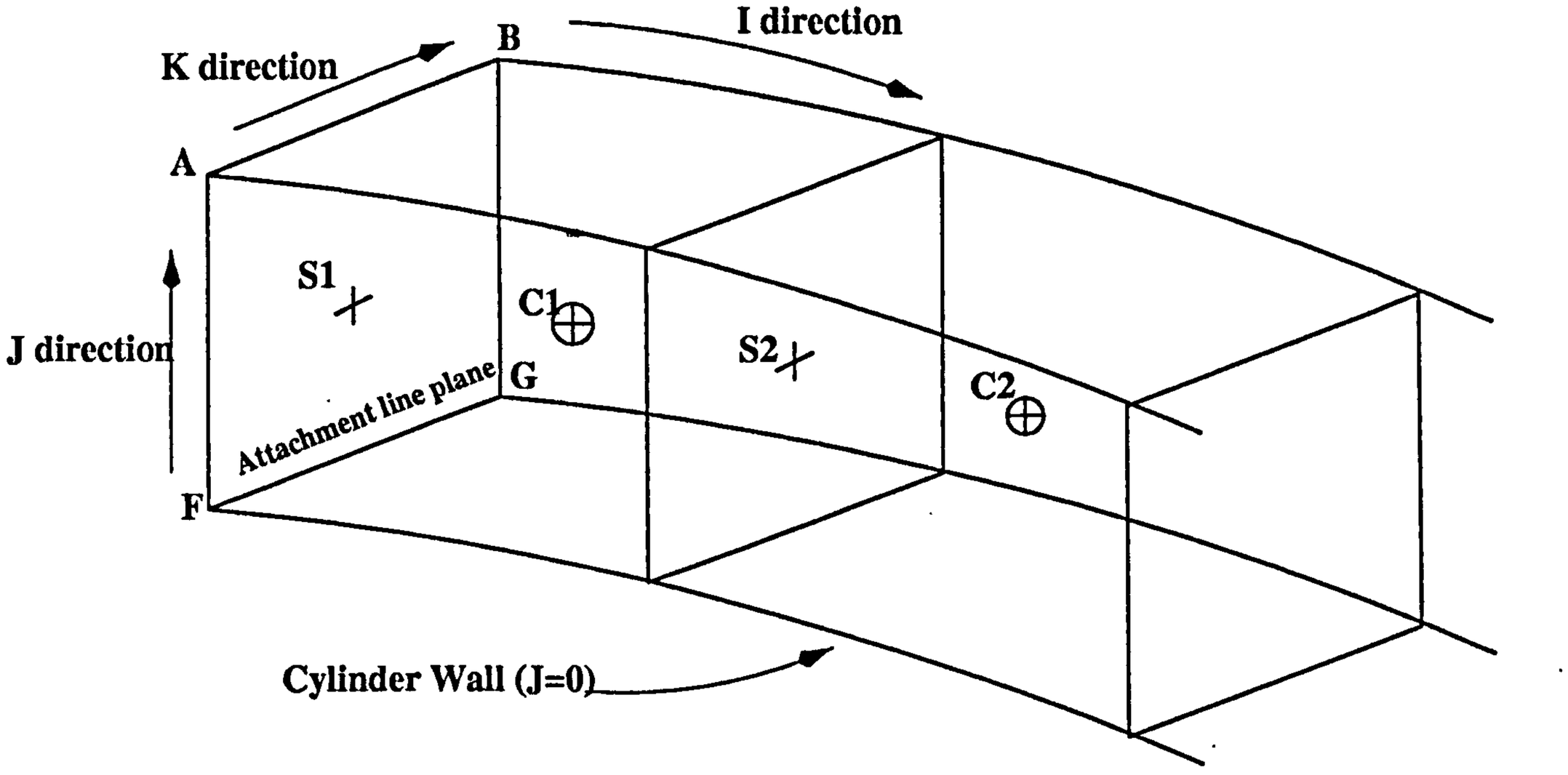

Figure D.17: Sketch of two computational cells aligned in the I direction allowing the chordwise velocity to be evaluated.

Appendix E

Boundary layer solution

E.1 Governing equations

A code developed by Adams [1] in 1973 and then later improved and extended by Poll was also used for the purpose of the present investigation. This solves the steady, compressible, turbulent boundary layer equations for flow over an infinite extent body. Using the orthogonal co-ordinate system X, Y, Z as shown by figure E.1, the governing equations for turbulent flow at the attachment-line are:

CONTINUITY EQUATION:

$$\frac{\partial \bar{\rho}\bar{u}}{\partial X} + \frac{\partial \bar{\rho}V}{\partial Y} + \frac{\partial \bar{\rho}\bar{w}}{\partial Z} = 0 \tag{E.1}$$

X - MOMENTUM EQUATION:

$$\bar{\rho}\bar{u}\frac{\partial \bar{u}}{\partial X} + \bar{\rho}V\frac{\partial \bar{u}}{\partial Y} + \bar{\rho}\bar{w}\frac{\partial \bar{u}}{\partial Z} = -\frac{\partial \bar{P}}{\partial X} + \frac{\partial}{\partial Y}\left[\mu\frac{\partial \bar{u}}{\partial Y} - \bar{\rho}\bar{u'v'}\right] \tag{E.2}$$

Y - MOMENTUM EQUATION:

$$\frac{\partial \bar{P}}{\partial Y} = 0 \tag{E.3}$$

Z - MOMENTUM EQUATION:

$$\bar{\rho}\bar{u}\frac{\partial \bar{w}}{\partial X} + \bar{\rho}V\frac{\partial \bar{w}}{\partial Y} + \bar{\rho}\bar{w}\frac{\partial \bar{w}}{\partial Z} = -\frac{\partial \bar{P}}{\partial Z} + \frac{\partial}{\partial Y}\left[\mu\frac{\partial \bar{w}}{\partial Y} - \bar{\rho}\overline{v'w'}\right] \tag{E.4}$$

ENERGY EQUATION:

$$\bar{\rho}\bar{u}\frac{\partial \bar{H}_0}{\partial X} + \bar{\rho}V\frac{\partial \bar{H}_0}{\partial Y} + \bar{\rho}\bar{w}\frac{\partial \bar{H}_0}{\partial Z} = \frac{\partial}{\partial Y}\left[\mu\left(\frac{\partial \bar{H}_0}{\partial Y} + \frac{1-Pr}{Pr}.\frac{\partial \bar{h}}{\partial Y}\right) - \bar{\rho}\overline{v'H_0'}\right] \tag{E.5}$$

where

$$V = \bar{v} + \frac{\overline{\rho' v'}}{\bar{\rho}} \tag{E.6}$$

$$\bar{H}_0 = \bar{H} + \frac{\bar{u}^2 + \bar{w}^2}{2} \tag{E.7}$$

with also the usual expression for the mean and fluctuating parts of the dependent variables e.g.,

$$\rho = \bar{\rho} + \rho' \tag{E.8}$$

Because the boundary layer code solves the governing equations for flow over an infinite extent body (in the Z direction), all $\partial/\partial Z$ derivatives in equations E.1 to E.5 are set to zero.

If the subscripts w and e denote the wall and the outer edge of the boundary layer respectively, the associated boundary conditions are

MOMENTUM:

for non-porous walls

$$Y = 0 : \bar{u} = \bar{v} = \bar{w} = 0$$

for porous walls

$$Y = 0 : \bar{u} = \bar{w} = 0 \qquad and \qquad \bar{v} = -\frac{f_w . \rho_e . w_e}{\rho_w . \bar{R}}$$

where f_w is the non-dimensional stream function at the wall. Note that $\bar{v}$ is positive for blowing and negative for suction.

$$Y \to \infty : \bar{u} \to U_e, \bar{w} \to W_e \tag{E.9}$$

ENERGY:

$$Y = 0 : \bar{H}_0 = H_{0W} = h_W$$

$$Y \to \infty : \bar{H}_0 \to H_{0e} \tag{E.10}$$

E.2 Co-ordinate transformation

Since equation E.2 is singular at the attachment-line (since the chordwise velocity component $\bar{u}$ is zero at this specific location), the equations can only be solved after the

introduction of a co-ordinate transformation that removes the singularity at x=0. To achieve this and to stretch the co-ordinate system, the Illingworth-Levy transformation has been used (reference [28], p.30). Thus the new independent variables are:

$$\xi_{(X)} = \int_0^X \rho_e \mu_e U_e dX \tag{E.11}$$

$$\eta_{(X,Y)} = \frac{\rho_e U_e}{\sqrt{2\xi}} \int_0^Y \frac{\bar{\rho}}{\rho_e} dY \tag{E.12}$$

By introducing a non-dimensional stream function $f(\xi, \eta)$ such that

$$\psi_{(\xi,\eta)} = \sqrt{2\xi}.f(\xi, \eta) \tag{E.13}$$

the governing boundary layer equations E.2, E.4 and E.5 become in the transformed co-ordinates (ξ, η) at the attachment-line where $\xi = 0$ since $x = 0$:

CROSSFLOW (X) MOMENTUM:

$$l^* f''' + \left[\frac{\partial l^*}{\partial \eta} + f\right] f'' + \beta \left[\theta - (f')^2\right] = 0 \tag{E.14}$$

STREAMWISE (Z) MOMENTUM:

$$l^* c'' + \left[\frac{\partial l^*}{\partial \eta} + f\right] c' = 0 \tag{E.15}$$

ENERGY:

$$\left(\frac{l^{**}}{Pr}\right) g'' + \left[\frac{\partial}{\partial \eta}\left(\frac{l^{**}}{Pr}\right) + f\right] g' + \Omega' = 0 \tag{E.16}$$

with the new dependent variables

$$f'_{(\xi,\eta)} = \frac{\bar{u}}{U_e} \tag{E.17}$$

$$c_{(\xi,\eta)} = \frac{\bar{w}}{W_e} \tag{E.18}$$

$$g_{(\xi,\eta)} = \frac{\bar{H}_0}{H_{0e}} \tag{E.19}$$

and the following definitions which apply to the above equations:

$$\theta = \frac{\rho_e}{\bar{\rho}} = \frac{\bar{T}}{T_e} \tag{E.20}$$

$$l = \frac{\bar{\rho}\mu}{\rho_e \mu_e} \tag{E.21}$$

$$l^* = l\left[1 + \frac{\varepsilon}{\mu}\right] \tag{E.22}$$

$$l^{**} = l\left[1 + \frac{\varepsilon}{\mu}\frac{Pr}{Pr_t}\right] \tag{E.23}$$

$$\beta = \frac{2\xi}{U_e}.\frac{dU_e}{d\xi} \tag{E.24}$$

$$\Omega = l\left[\frac{\varepsilon}{\mu}\left(1 - \frac{1}{Pr_t}\right) + \left(1 - \frac{1}{Pr}\right)\right].\left[\frac{U_e^2}{H_{0e}}f'f'' + \frac{W_e^2}{H_{0e}}cc'\right] \tag{E.25}$$

Note that $\beta = 1$ at $\xi = 0$ (attachment-line) under the restriction that near $x = 0$:

$$U_e = \left[\frac{dU_e}{dX}\right]_{X=0} X \tag{E.26}$$

In the transformed governing equations, primes denote partial differentiation with respect to the η co-ordinate, i.e.,

$$f' = \frac{\partial f}{\partial \eta} \tag{E.27}$$

$$f'' = \frac{\partial^2 f}{\partial \eta^2} \tag{E.28}$$

In the transformed co-ordinate system, the dependent variables $f'_{(\xi,\eta)}$, $c_{(\xi,\eta)}$ and $g_{(\xi,\eta)}$ at point (m+1,n) are evaluated from the solution of the dependent variables at point (m,n) but also at points (m,n+1) and (m,n-1)(see figure E.2). For the points close to the wall and the edge of the domain, boundary conditions are needed. These are:

MOMENTUM:

for non-porous walls

$$\eta = 0 : f' = f = c = 0$$

for porous walls

$$\eta = 0 : f' = c = 0 \qquad and \qquad f = -\frac{v_w.\rho_w.\bar{R}}{\rho_e.w_e}$$

$$\eta \to \infty : f' \to 1, c \to 1 \tag{E.29}$$

ENERGY:

$$\eta = 0 : g = \frac{H_{0W}}{H_{0e}} = \frac{h_W}{h_e} = g_W$$

$$\eta \to \infty : g = 1 \tag{E.30}$$

Following the approach by Blottner [8] and Davis [27] the momentum and energy equations (E.14, E.15 and E.16) are rewritten in "standard" form for a parabolic partial differential equation as

$$\frac{\partial^2 W}{\partial \eta^2} + \alpha_1 \frac{\partial W}{\partial \eta} + \alpha_2 W + \alpha_3 + \alpha_4 \frac{\partial W}{\partial \xi} = 0 \tag{E.31}$$

where $W = f'$ for the X-momentum equation, $W = c$ for the Z-momentum equation and $W = g$ for the energy equation. Using equations E.14, E.15 and E.16 one can find the coefficients α_1 through α_4 in linearised form:

X-MOMENTUM:

$$\alpha_1 = \frac{\frac{\partial l^*}{\partial \eta} + f}{l^*} \tag{E.32}$$

$$\alpha_2 = \frac{-\beta f'}{l^*} \tag{E.33}$$

$$\alpha_3 = \frac{\beta \theta}{l^*} \tag{E.34}$$

$$\alpha_4 = \frac{-2\xi f'}{l^*} = 0 \tag{E.35}$$

Z-MOMENTUM:

$$\alpha_1 = \frac{\frac{\partial l^*}{\partial \eta} + f}{l^*} \tag{E.36}$$

$$\alpha_2 = 0 \tag{E.37}$$

$$\alpha_3 = 0 \tag{E.38}$$

$$\alpha_4 = \frac{-2\xi f'}{l^*} = 0 \tag{E.39}$$

ENERGY:

$$\alpha_1 = \frac{\frac{\partial}{\partial\eta}\left(\frac{l^{**}}{Pr}\right) + f}{\left(\frac{l^{**}}{Pr}\right)} \tag{E.40}$$

$$\alpha_2 = 0 \tag{E.41}$$

$$\alpha_3 = \frac{\Omega'}{\left(\frac{l^{**}}{Pr}\right)} \tag{E.42}$$

$$\alpha_4 = \frac{-2\xi f'}{\left(\frac{l^{**}}{Pr}\right)} = 0 \tag{E.43}$$

The η derivatives in equation E.31 are replaced with finite difference quotients (equations E.44, E.45 and E.46) which allow variable grid spacing in the η direction in order to concentrate grid points in the region near the body surface where the dependent variables $f'_{(\xi,\eta)}$, $c_{(\xi,\eta)}$ and $g_{(\xi,\eta)}$ change the most (figure E.2).

$$\left[\frac{\partial^2 W}{\partial\eta^2}\right]_{m+1,n} = \frac{2[W_{n+1} + KW_{n-1} - (1+K)\,W_n]_{m+1}}{D_2} \tag{E.44}$$

$$\left[\frac{\partial W}{\partial\eta}\right]_{m+1,n} = \frac{[W_{n+1} - K^2 W_{n-1} - (1-K^2)\,W_n]_{m+1}}{D_1} \tag{E.45}$$

$$\left[\frac{\partial W}{\partial\xi}\right]_{m+1,n} = \frac{W_{m+1,n} - W_{m,n}}{\Delta\xi} \tag{E.46}$$

where

$$D_1 = (\eta_{n+1} - \eta_n) + K^2 (\eta_n - \eta_{n-1}) \tag{E.47}$$

$$D_2 = (\eta_{n+1} - \eta_n)^2 + K(\eta_n - \eta_{n-1})^2 \tag{E.48}$$

$$K = \frac{\eta_{n+1} - \eta_n}{\eta_n - \eta_{n-1}} \tag{E.49}$$

$$\xi = \eta_2 - \eta_1 \tag{E.50}$$

where K represents the normal grid step size multiplication factor and ξ the first $d\eta$ step size. Both of these terms are constants. For laminar flow, $K = 1.0$ whereas for turbulent flow $K = 1.03$ as suggested by Surah [59].

Note that since the solution is assumed to be known at point (m,n) (see next section) and unknown at point (m+1,n), the finite difference scheme used herein is of an implicit nature.

Considering equations E.44, E.45 and E.46 it is possible to change the differential equation E.31 into an approximate algebraic equation:

$$\bar{A}_n W_{m+1,n+1} + \bar{B}_n W_{m+1,n} + \bar{C}_n W_{m+1,n-1} = \bar{D}_n \tag{E.51}$$

where

$$\bar{A}_n = \frac{2}{D_2} + \frac{\alpha_1}{D_1} \tag{E.52}$$

$$\bar{B}_n = \frac{-2\,(1+K)}{D_2} - \frac{\alpha_1\,(1-K^2)}{D_1} + \alpha_2 + \frac{\alpha_4}{\Delta\xi} \tag{E.53}$$

$$\bar{C}_n = \frac{2K}{D_2} - \frac{K^2\alpha_1}{D_1} \tag{E.54}$$

$$\bar{D}_n = -\alpha_3 + \frac{\alpha_4 W_{m,n}}{\Delta\xi} \tag{E.55}$$

Since the coefficients $\bar{A}_n$, $\bar{B}_n$, $\bar{C}_n$ and $\bar{D}_n$ are known at point (m,n) from the iteration process (see next section), the expression E.51 forms a set of simultaneous linear algebraic equations depending on the number of points considered across the boundary layer thickness. The solution of this set of equations is determined using the tri-diagonal method of solution as recommended by Richtmyer and Morton (reference [55], pp198 - 201 and pp 274 - 282).

E.3 Iteration process

In order to perform iterations to solve equation E.51 at station m+1 (figure E.2), the dependent variables $f'_{(\xi,\eta)}$, $c_{(\xi,\eta)}$ and $g_{(\xi,\eta)}$ must be known at station m. Thus initial profiles of the dependent variables are input to the analysis.

$$f'_I = 1 - e^{-2\eta} \tag{E.56}$$

$$c_I = 1 - e^{-2\eta} \tag{E.57}$$

$$g_I = g_W + \left[(1-g_W)\,.\,\left(1-e^{-2\eta}\right)\right] \tag{E.58}$$

where the subscript I denotes the initial approximation. It has to be specified that η and g_W are directly evaluated from the input parameters using:

$$\bar{\eta} = \frac{\eta_{max}}{NPoints - 1} \tag{E.59}$$

where the two input parameters η_{max} and NPoints respectively represents the maximum value of η (i.e. from the wall to the edge of the domain) and the number of grid points across the domain. The η value starting from the wall for each cell is then evaluated.

$$\eta_I = (\bar{\eta}.K) + \eta_{(I-1)} \tag{E.60}$$

where K is the stretching factor defined by equation E.49 (K=1 in laminar i.e. no stretching applied and K=1.03 in turbulent) and I the vector co-ordinate in the normal to the wall direction (η direction).

$$g_W = \frac{T_W}{T_0} \tag{E.61}$$

where the input parameter T_W/T_0 is the wall to stagnation temperature ratio.

From the initial values of the dependent variables (equations E.56, E.57, E.58), the coefficients $\bar{A}_n$, $\bar{B}_n$, $\bar{C}_n$ and $\bar{D}_n$ can be evaluated (equations E.52 to E.55) at station m (figure E.2). Equation E.51 can hence be solved using the tri-diagonal method (reference [55], pp198 - 201 and pp 274 - 282). This leads directly to the evaluation of the dependent variables and the coefficients $\bar{A}_n$ to $\bar{D}_n$ at station m+1. Equation E.51 is then solved again using variables at station m+1 to get the dependent variables at the following station (so called iteration process). Iteration at a given station is continued until successive values of $f'_{(\xi,\eta)}$, $c_{(\xi,\eta)}$ and $g_{(\xi,\eta)}$ differ by less than 10^{-5}.

E.4 Heat transfer at the wall

Given the numerical solution to the governing equations of motion (equations E.14, E.15 and E.16), following the integration procedure described in the previous sections, the associated local heat transfer at the body surface (Y=0) is given by the Fourier law:

$$\dot{q}_W = -k_W \left(\frac{\partial \bar{T}}{\partial Y}\right)_W = \frac{-k_W}{Cp}\left(\frac{\partial \bar{h}}{\partial Y}\right)_W \tag{E.62}$$

which can be written in the equivalent form

$$\dot{q}_W = -\frac{\mu_W}{Pr}\left(\frac{\partial \bar{H}_0}{\partial Y}\right)_W \tag{E.63}$$

through use of equations E.7 and $Pr = \frac{Cp.\mu}{K}$ it follows:

$$\left(\frac{\partial \bar{H}_0}{\partial Y}\right)_W = \left(\frac{\partial \bar{h}}{\partial Y}\right)_W + \left[\underbrace{\bar{u}}_{=0}\frac{\partial \bar{u}}{\partial Y} + \underbrace{\bar{w}}_{=0}\frac{\partial \bar{w}}{\partial Y}\right]_W \tag{E.64}$$

At the wall, for non-porous walls, the velocity components $\bar{u}$, $\bar{v}$ and $\bar{w}$ are all zero (non-slip conditions), the heat transfer at the wall in terms of the transformed co-ordinates (ξ, η) is:

$$\dot{q}_W = \frac{-l_W \rho_e \mu_e U_e H_{0e}}{Pr\sqrt{2\xi}}.g'(\xi, \eta = 0) \tag{E.65}$$

where

$$l_W = \frac{\bar{\rho_W}\mu_W}{\rho_e \mu_e} \tag{E.66}$$

At the attachment-line itself equation E.65 is reduced to the following limiting forms (equation E.67) under the restriction that $Ue \approx \left[\frac{dUe}{dX}\right]_{X=0} X$ near $X = 0$ so that $\xi = \frac{1}{2}\rho_e\mu_e\left[\frac{dUe}{dX}\right]_{X=0} X^2$ near $X = 0$.

$$[\dot{q}w]_{X=0} = \frac{-l_W H_{0e}}{Pr}\sqrt{\rho_e\mu_e\left[\frac{dUe}{dX}\right]_{X=0}}.g'(\xi, \eta = 0) \tag{E.67}$$

It can be seen from equation E.65 that the evaluation of heat transfer rate at the surface requires numerical determination of the wall derivative $g'(\xi, \eta = 0)$. As a result of the grid stretching towards the body surface (η direction), the wall derivative is evaluated in the present code by application of the three- point Lagrangian interpolation formula (see reference [23], pp71 - 77) evaluated according to figure E.3 which yields at station m+1 to:

$$g'(\eta = 0) = \xi\left[B_1(2 + K)\, g_{\eta_1} + B_2(1 + K)\, g_{\eta_2} + B_3 g_{\eta_3}\right] \tag{E.68}$$

where

$$B_1 = \frac{-1}{\xi^2(1 + K)} \tag{E.69}$$

$$B_2 = \frac{1}{K\xi^2} \tag{E.70}$$

$$B_3 = \frac{-1}{\xi^2 K(1 + K)} \tag{E.71}$$

and

$$g_{\eta_I} = g(\eta = \eta_I) \tag{E.72}$$

with I = 1, 2, 3. The parameters K and ξ are the stretching factor and the first $d\eta$ step size of the grid from the wall (see previous sections).

Complete and detailed description of the boundary layer code can be found in reference [1] but also in chapter 3 of reference [59].

E.5 Input parameters

The solution of the governing equations is obtained following the specification of the attachment-line Reynolds number, $\bar{R}$, the spanwise Mach number at the edge of the velocity boundary layer, M_{ae}, the wall to total temperature ratio, $\frac{Tw}{To}$, and the ratio of the Sutherland's constant to the stagnation temperature $\frac{s}{To}$. In addition to the flow parameters, the number of grid points in the computational domain, Npoints, and the maximum height of the computational domain η_{max} need to be specified.

E.6 Effects of Npoints and η_{max} on the solution accuracy

A study was carried out to establish the optimum values (values giving the best accuracy and consistency of the results) of the grid parameters i.e. the total number of points across the domain, Npoints, and the maximum height of the computational domain, η_{max}, for both laminar and turbulent flows. A wide range of cases covering incompressible and compressible flows and wind tunnel to flight conditions was used i.e. $\bar{R}$ between 100 and 2000, M_{ae} from 0 to 8, T_w/T_o between 0.1 and unity and T_o up to 4000 K (see chapter 3, section 3.5 for the justification of the range of conditions). The stretching parameter K

(equation E.49) was kept constant to 1.03 for the turbulent code as suggested by Surah [59] ($K = 1.0$ in laminar).

The effect of the number of points across the viscous layer was investigated as follow. For a given case, a relatively high value of η_{max} was used initially and the thickness of the thermal boundary layer (taken at 100.5% of the inviscid value) was obtained, $\eta_{thermal}$. The value of η_{max} corresponding to a ratio $\frac{\eta_{max}}{\eta_{thermal}}$ of 1.6 was then calculated and the effects of the number of points across the domain investigated.

Once the optimum number of points have been obtained for a particular case, the effects of the ratio $\frac{\eta_{max}}{\eta_{thermal}}$ could be studied. Knowing the optimum ratio $\frac{\eta_{max}}{\eta_{thermal}}$ (ratio giving the best consistency of the results) a second iteration of this process was undertaken. The results of this procedure are discussed below.

Laminar flow

Typical plots of the skin friction coefficient Cfe, shape factor H, Reynolds number based on the momentum thickness R_θ and Stanton number $S\bar{t}_{ae}$ (definition of the later in the nomenclature) obtained with different values of Npoints and of the ratio $\frac{\eta_{max}}{\eta_{thermal}}$ are shown in figures E.4 to E.9. The results are given as percentage variation between the values for different grid parameter values.

By inspection of the results, the optimum values for laminar flows are

$$Npoints \geq 700 \qquad \text{and} \qquad \frac{\eta_{max}}{\eta_{thermal}} \geq 1.5$$

Turbulent flow

The results obtained for turbulent flow are shown in figures E.10 to E.15. Note that the turbulence model described in chapter 5 was used. For turbulent flow, the optimum grid parameters for a stretching factor K of 1.03 are

$$Npoints > 300 \qquad \text{and} \qquad \frac{\eta_{max}}{\eta_{thermal}} \geq 1.7$$

It is surprising that the turbulent boundary layer needs fewer points for a converged solution. This is a consequence of the numerical scheme used. In laminar grid independence is obtained at $Npoints \geq 700$ and $\frac{\eta_{max}}{\eta_{thermal}} \geq 1.5$ with no stretching whereas in turbulent grid independence is obtained for $Npoints > 300$ and $\frac{\eta_{max}}{\eta_{thermal}} \geq 1.7$ for a stretching factor K of 1.03.

The stretching factor K of 1.03 was suggested by Surah [59]. Since for boundary layer study, the grid is determined by the combination of the stretching factor K and the number of points (as well as the thickness of the domain as studied above), the optimum value of Npoints was obtained here for the fixed K value of 1.03. When K is increased to 1.05, the optimum Npoints and $\frac{\eta_{max}}{\eta_{thermal}}$ become 300 and 1.4 respectively. In this particular case, the skin friction Cfe, shape factor H, Reynolds number based on the momentum thickness R_θ and Stanton number differ by less than 0.01% from their respective values when a stretching factor of 1.03 was used (with the optimum Npoints and $\frac{\eta_{max}}{\eta_{thermal}}$ given above). Therefore it can be concluded that whatever stretching factor K is used, the optimum number of points and computational domain thickness corresponding to this particular K, lead to the same flow properties values.

In the present investigation K was kept to 1.03 for turbulent flow and to unity for laminar flow. The optimum number of points and computational domain thickness given above for both types of flow were used. For every case studied, the maximum domain thickness η_{max} was initially guessed. The thermal boundary layer thickness was then evaluated and η_{max} was thus re-adjusted so that the optimum ratio $\frac{\eta_{max}}{\eta_{thermal}}$ could be used.

E.7 Figures

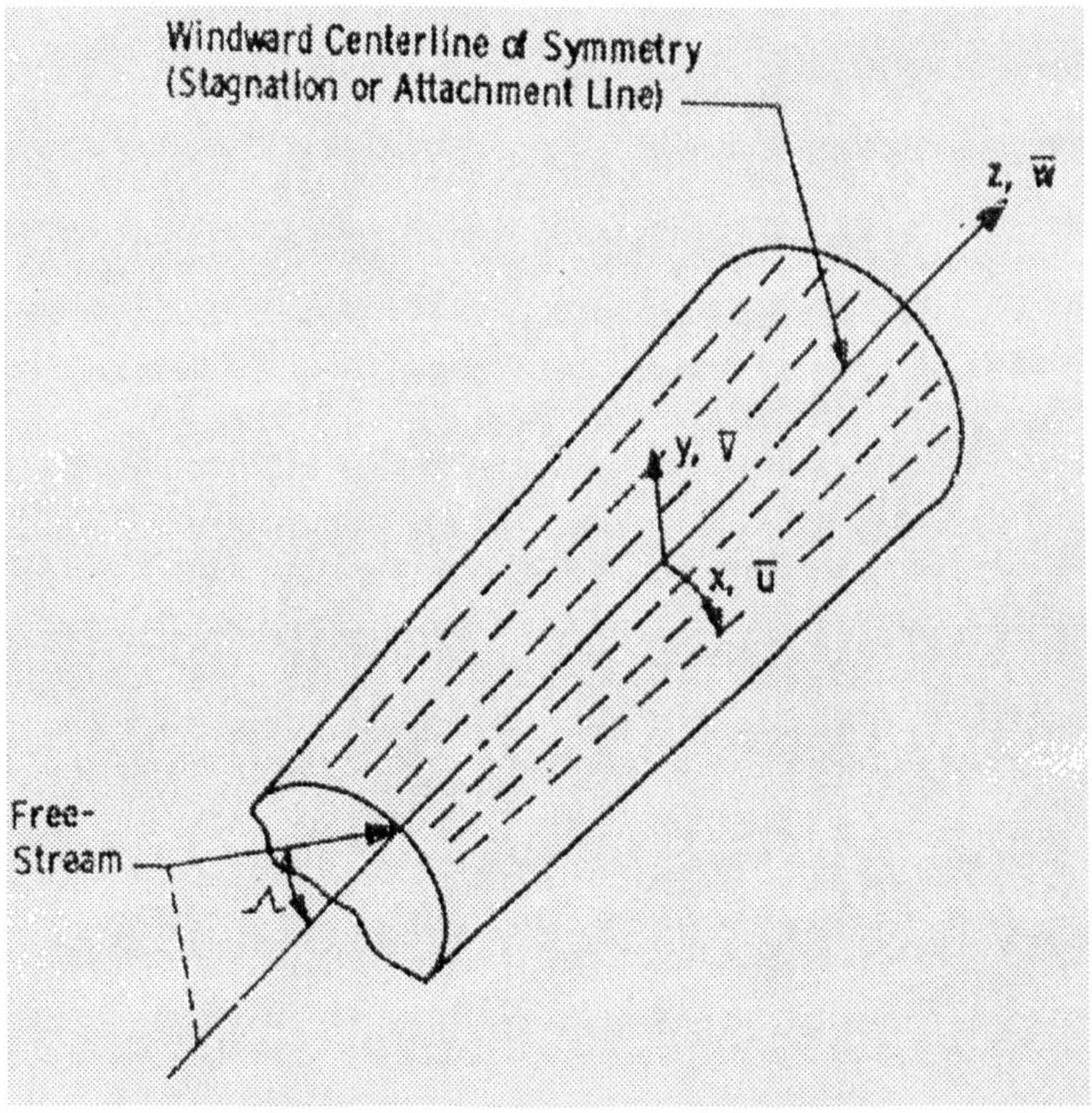

Figure E.1: Surface Orthogonal co-ordinate system as used in the boundary layer code [1].

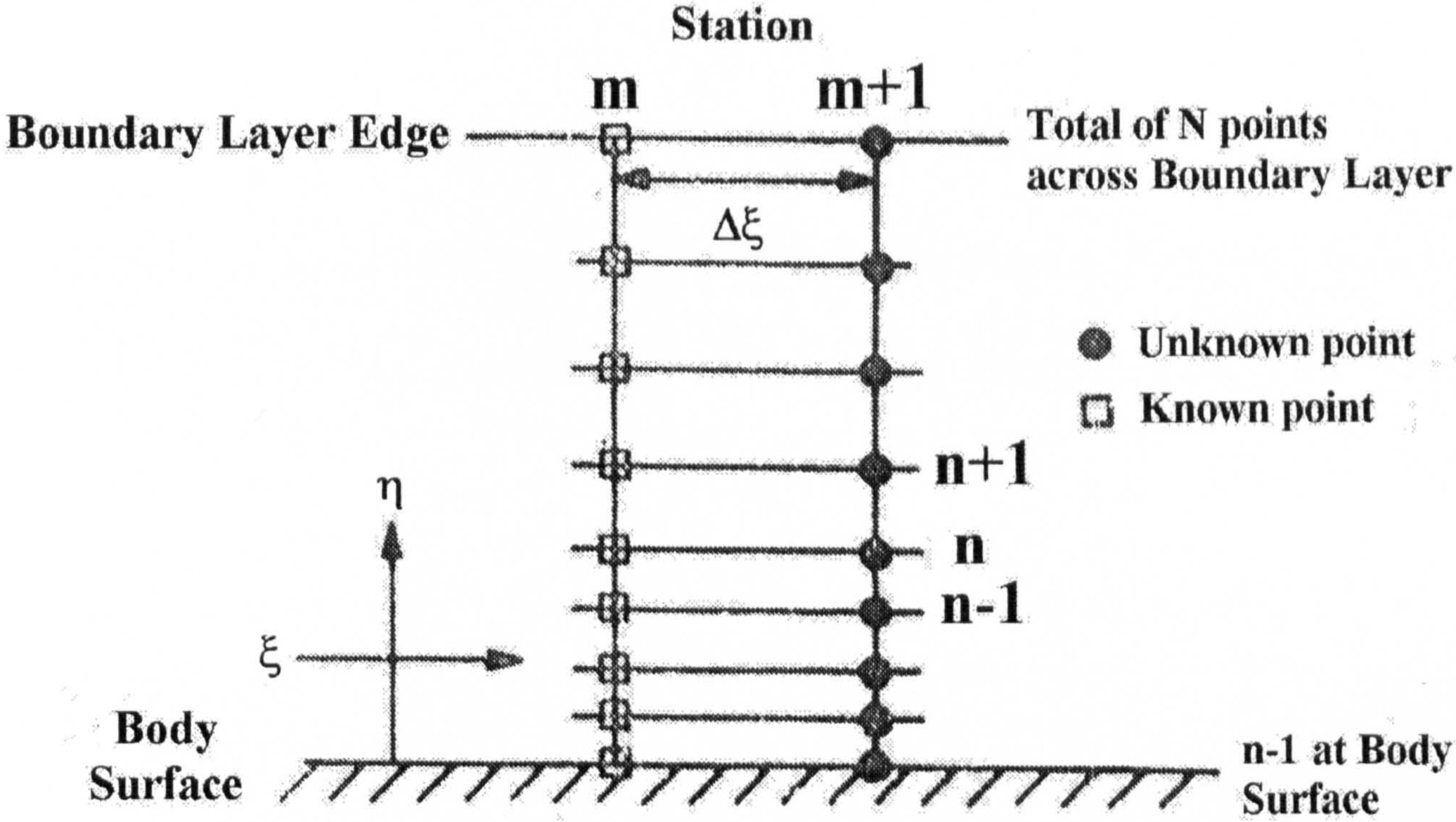

Figure E.2: Stations m and m+1 used by the boundary layer code [1].

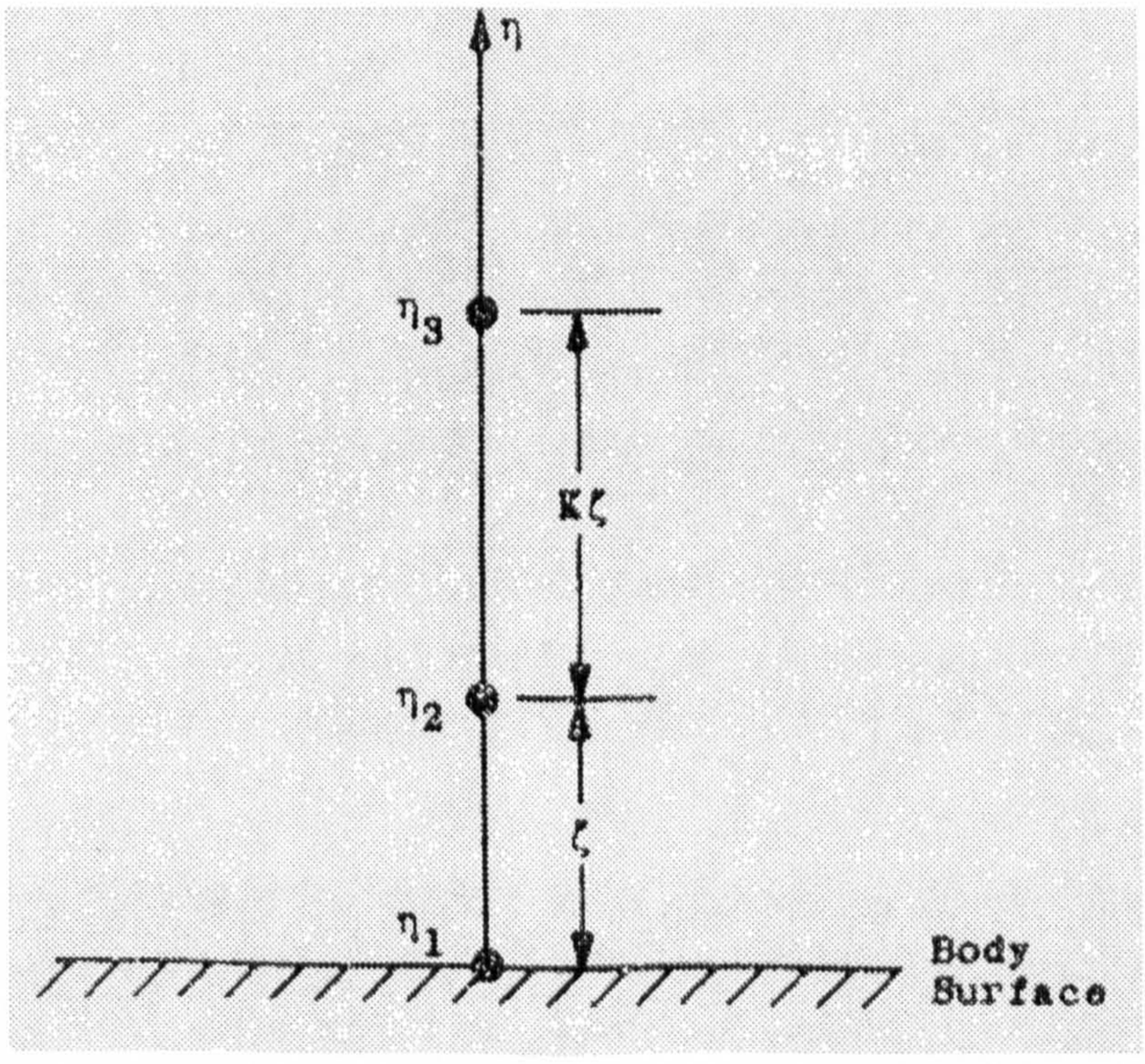

Figure E.3: Grid stretching at the wall as used by the boundary layer code [1].

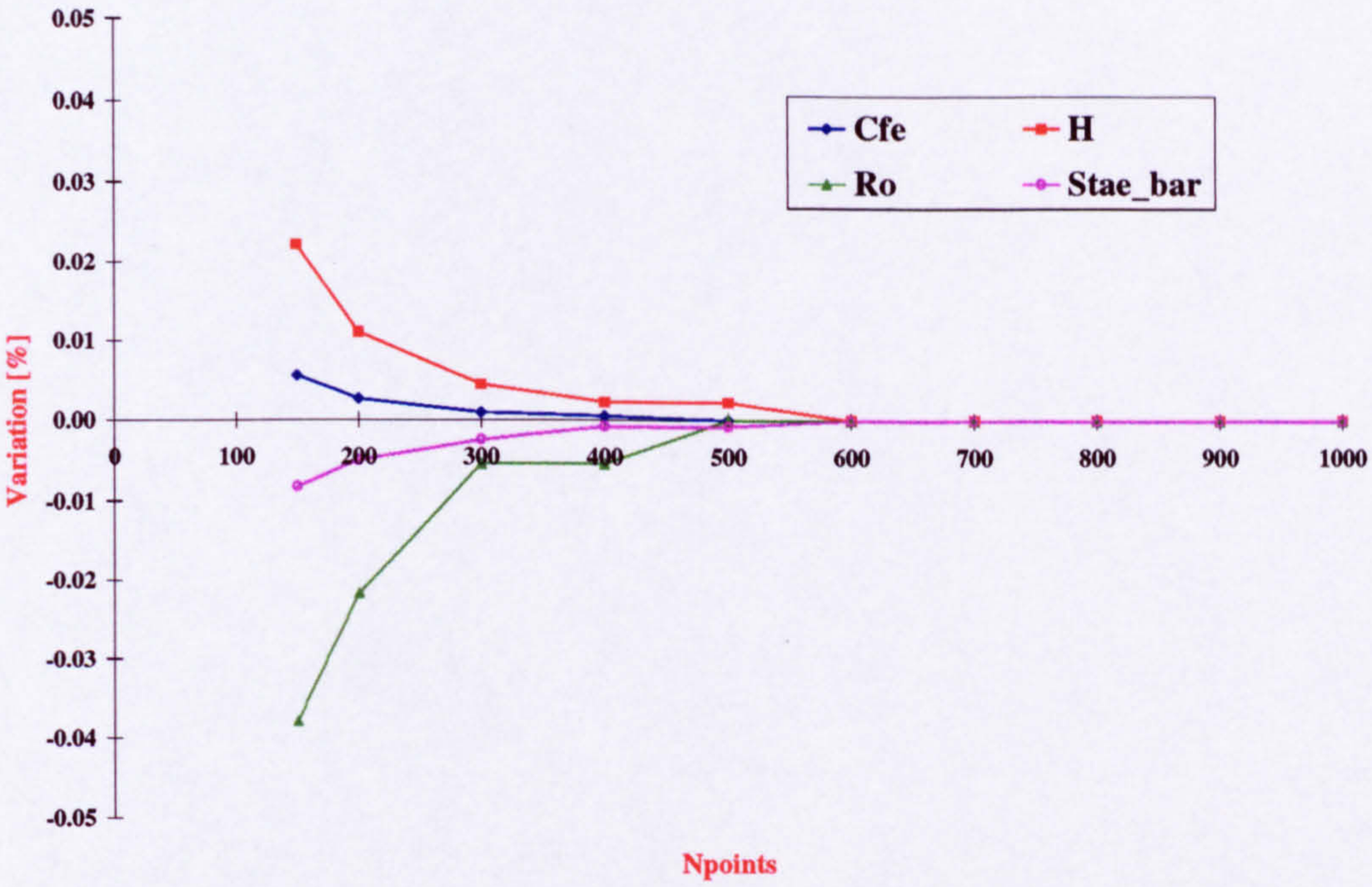

Figure E.4: Variation of Skin friction Cfe, Shape factor H, Reynolds number R_θ and Stanton number $S\bar{t}_{ae}$ with the number of points across the computational domain for laminar flow and $\bar{R} = 500$, $M_{ae} = 3$, $T_w/T_o = 0.4$, $T_o = 800K$ and $\frac{\eta_{max}}{\eta_{thermal}} = 1.6$.

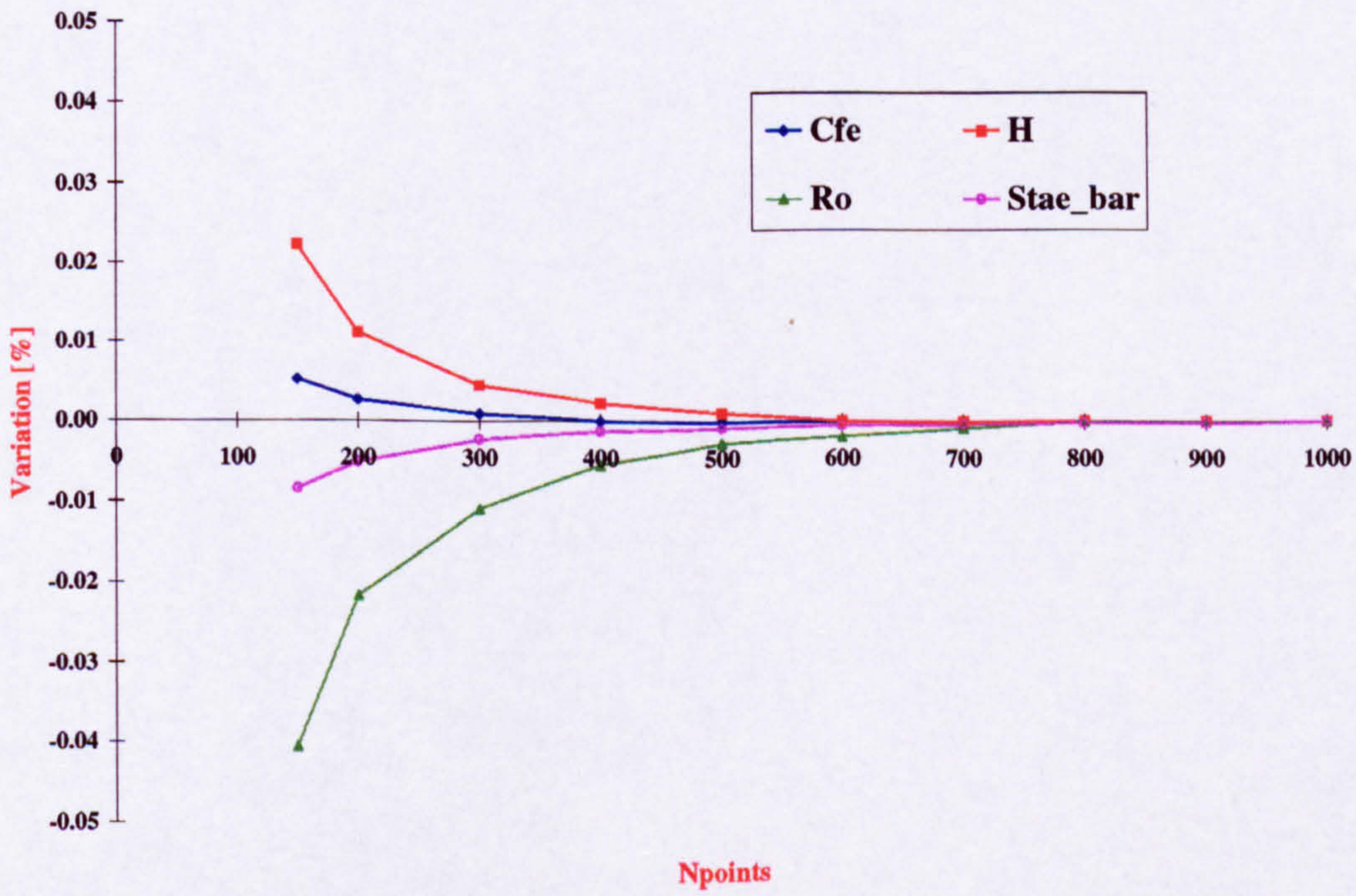

Figure E.5: Variation of Skin friction Cfe, Shape factor H, Reynolds number R_θ and Stanton number $S\bar{t}_{ae}$ with the number of points across the computational domain for laminar flow and $\bar{R} = 1000$, $M_{ae} = 3$, $T_w/T_o = 0.4$, $T_o = 800K$ and $\frac{\eta_{max}}{\eta_{thermal}} = 1.6$.

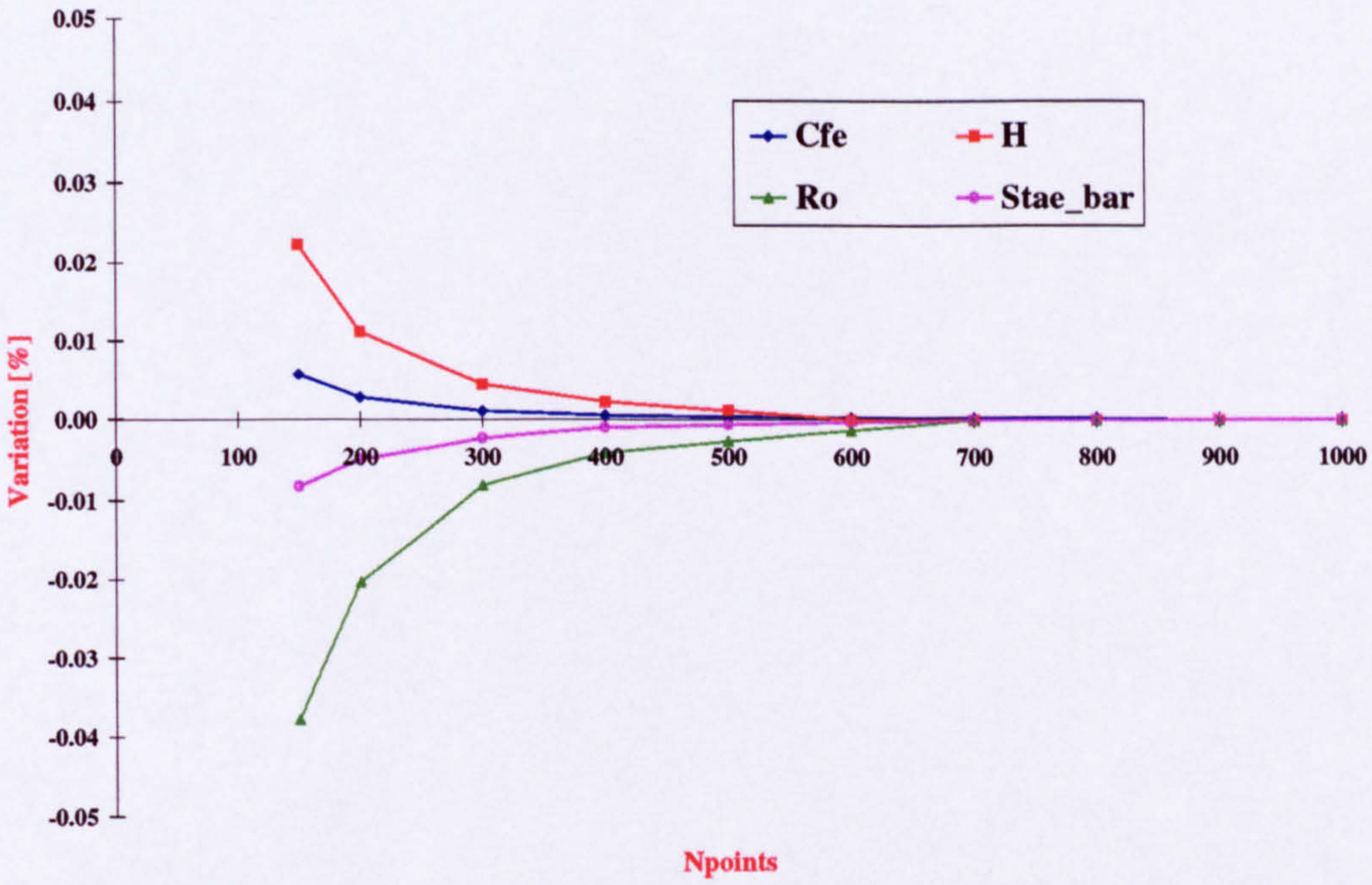

Figure E.6: Variation of Skin friction Cfe, Shape factor H, Reynolds number R_θ and Stanton number $\bar{St}_{ae}$ with the number of points across the computational domain for laminar flow and $\bar{R} = 2000$, $M_{ae} = 3$, $T_w/T_o = 0.4$, $T_o = 800K$ and $\frac{\eta_{max}}{\eta_{thermal}} = 1.6$.

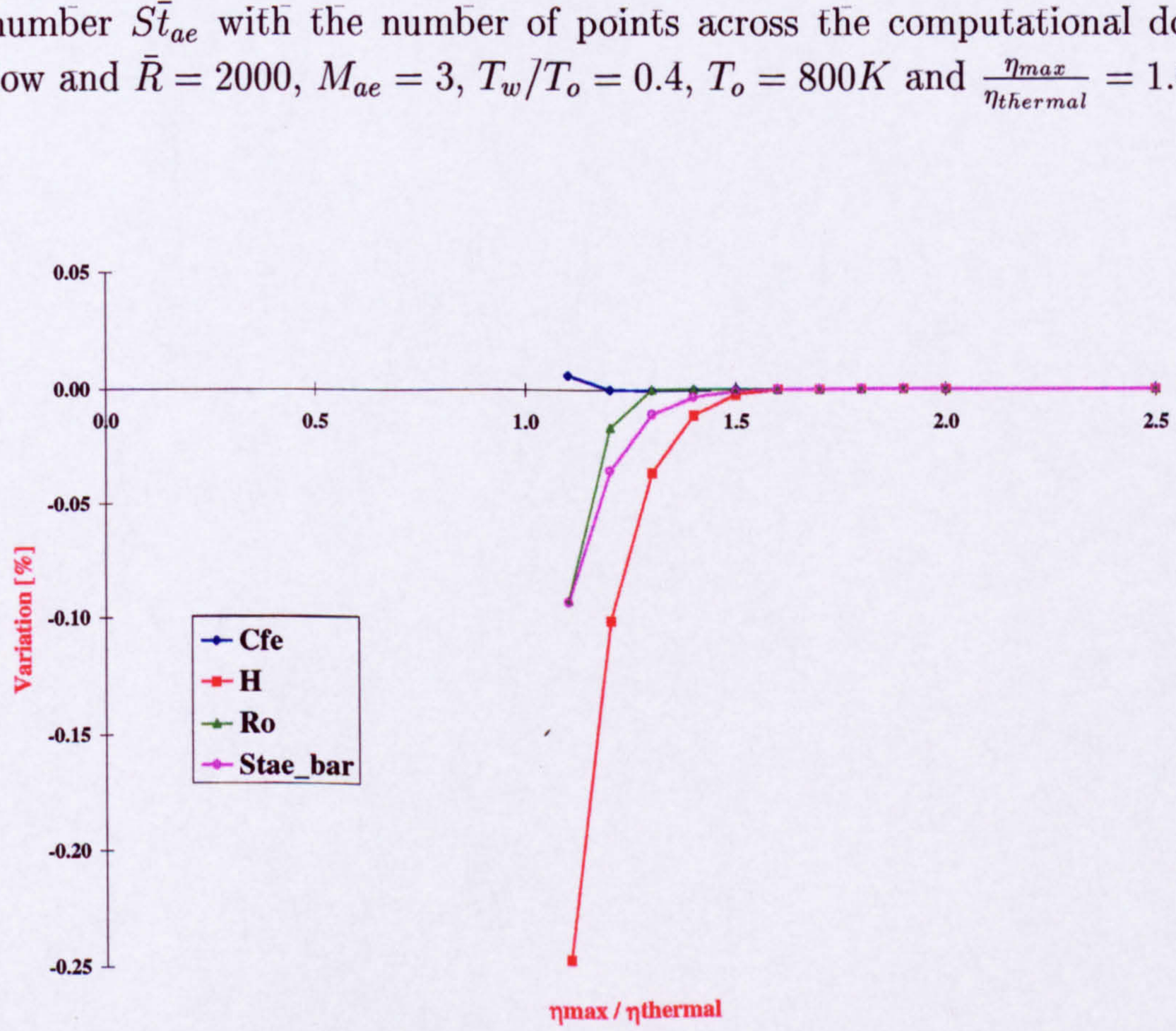

Figure E.7: Variation of Skin friction Cfe, Shape factor H, Reynolds number R_θ and Stanton number $\bar{St}_{ae}$ with the ratio $\frac{\eta_{max}}{\eta_{thermal}}$ for laminar flow and $\bar{R} = 500$, $M_{ae} = 3$, $T_w/T_o = 0.4$, $T_o = 800K$ and $Npoints = 1000$.

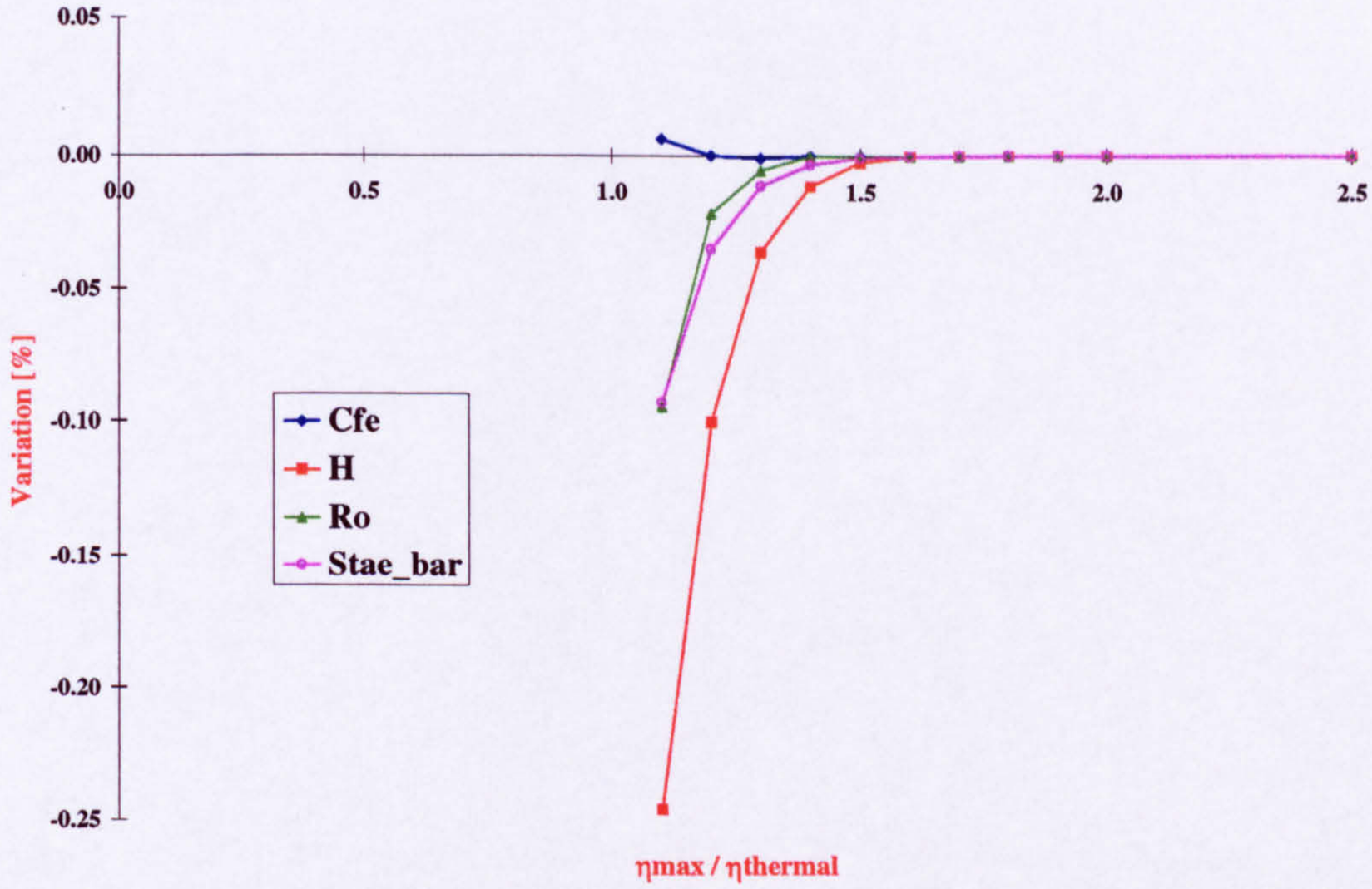

Figure E.8: Variation of Skin friction Cfe, Shape factor H, Reynolds number R_θ and Stanton number $S\bar{t}_{ae}$ with the ratio $\frac{\eta_{max}}{\eta_{thermal}}$ for laminar flow and $\bar{R} = 1000$, $M_{ae} = 3$, $T_w/T_o = 0.4$, $T_o = 800K$ and $Npoints = 1000$.

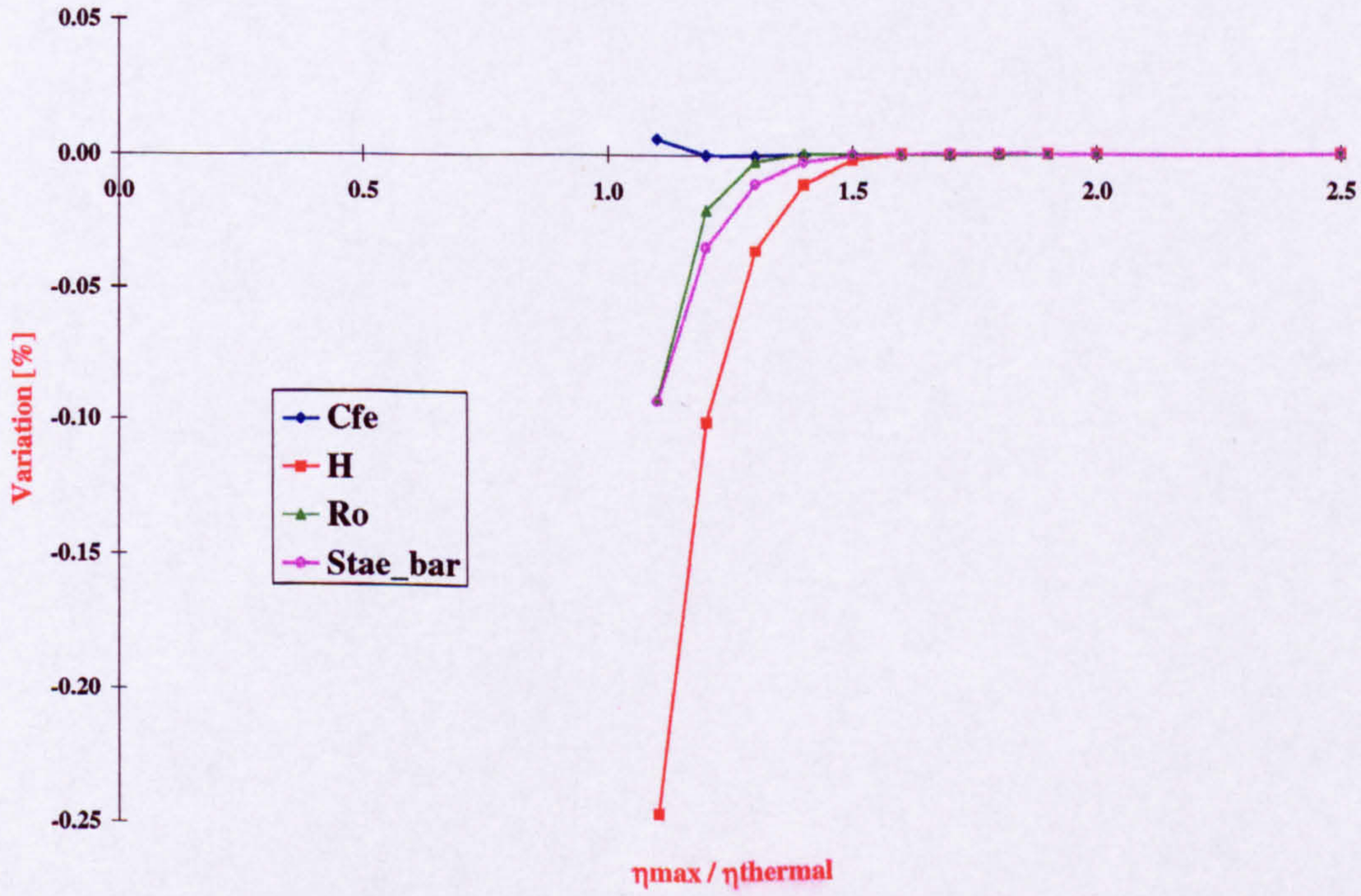

Figure E.9: Variation of Skin friction Cfe, Shape factor H, Reynolds number R_θ and Stanton number $S\bar{t}_{ae}$ with the ratio $\frac{\eta_{max}}{\eta_{thermal}}$ for laminar flow and $\bar{R} = 2000$, $M_{ae} = 3$, $T_w/T_o = 0.4$, $T_o = 800K$ and $Npoints = 1000$.

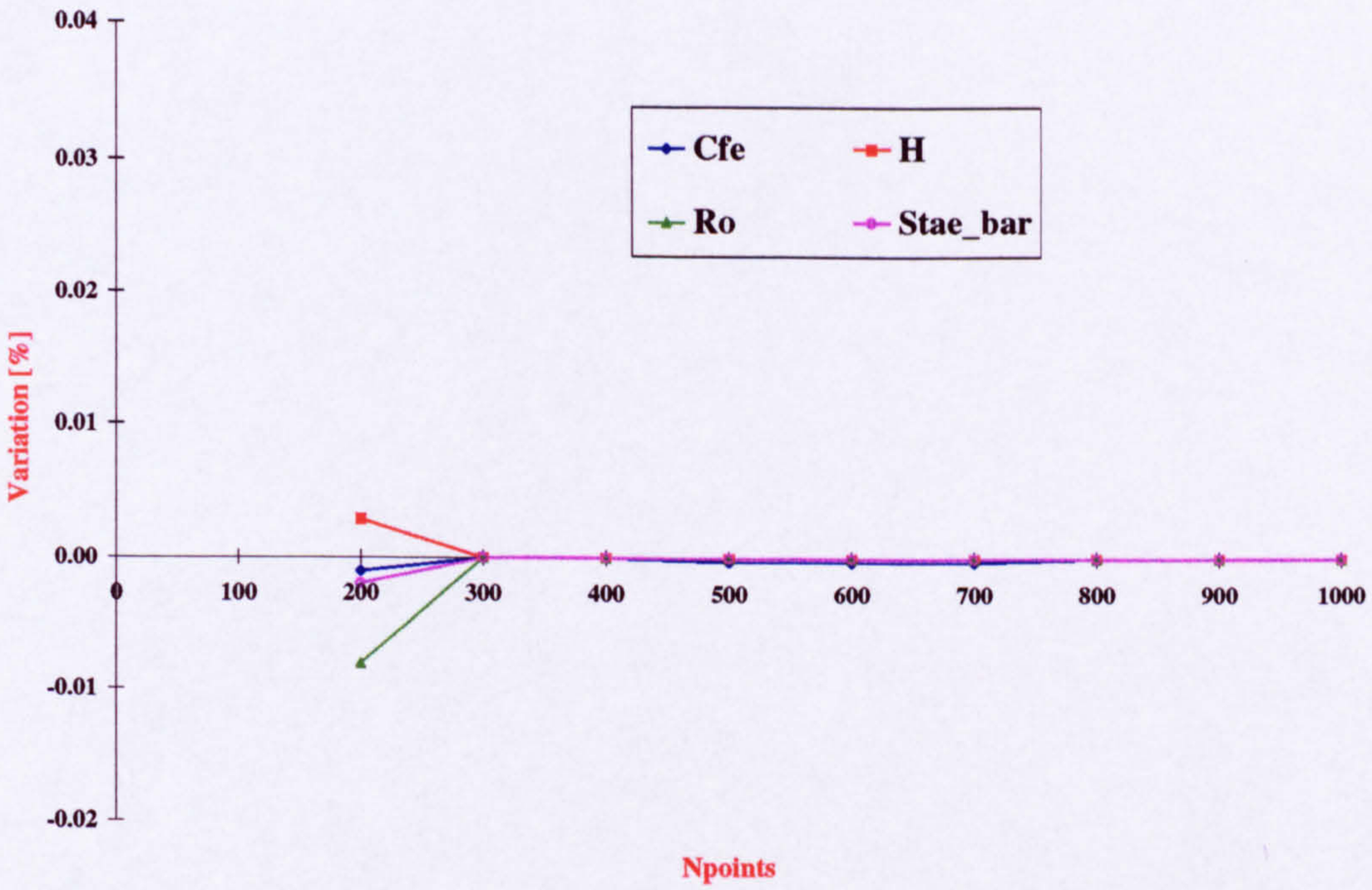

Figure E.10: Variation of Skin friction Cfe, Shape factor H, Reynolds number R_θ and Stanton number $\bar{St}_{ae}$ with the number of points across the computational domain for turbulent flow and $\bar{R} = 500$, $M_{ae} = 3$, $T_w/T_o = 0.4$, $T_o = 800K$ and $\frac{\eta_{max}}{\eta_{thermal}} = 1.7$.

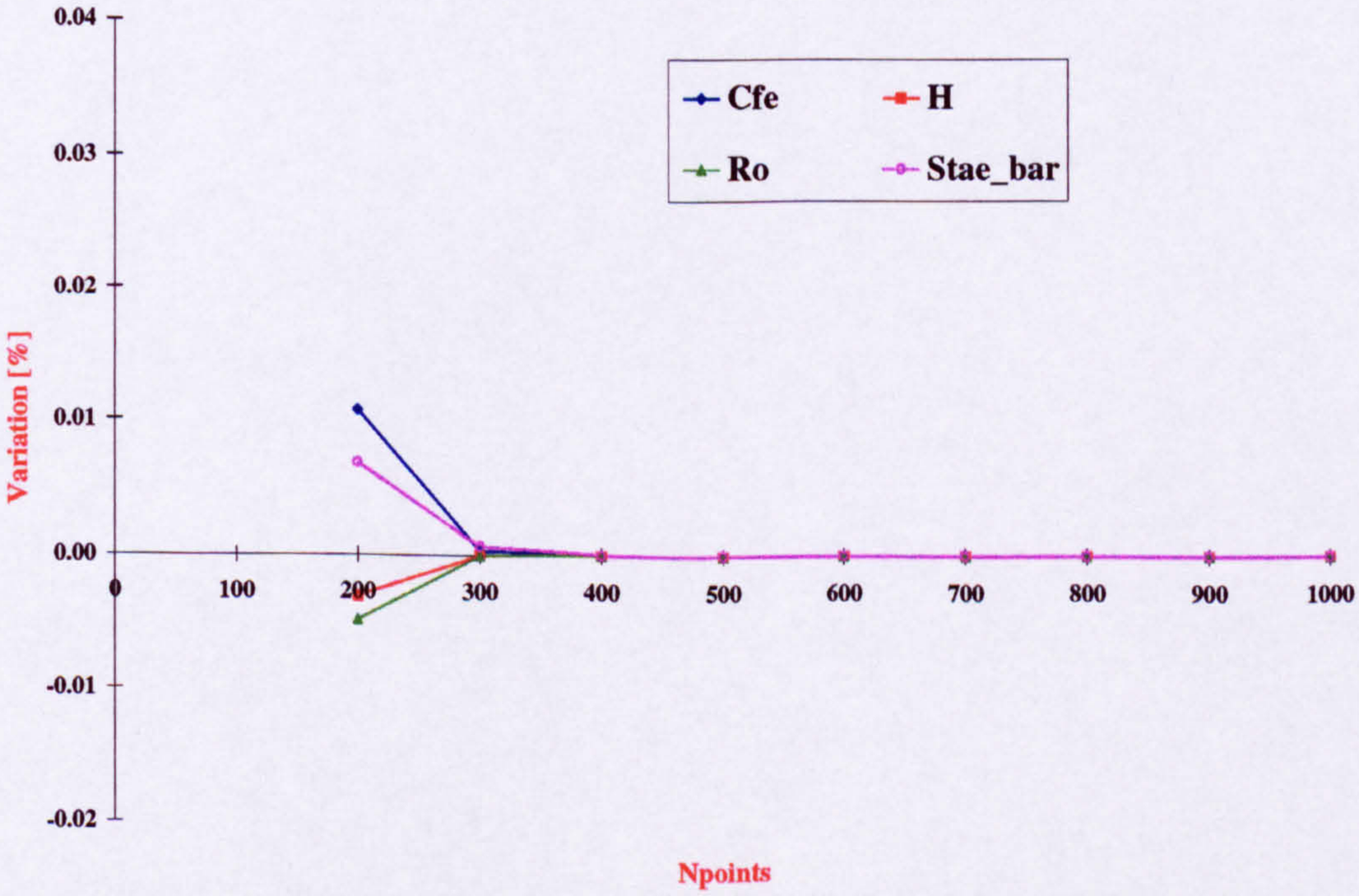

Figure E.11: Variation of Skin friction Cfe, Shape factor H, Reynolds number R_θ and Stanton number $\bar{St}_{ae}$ with the number of points across the computational domain for turbulent flow and $\bar{R} = 1000$, $M_{ae} = 3$, $T_w/T_o = 0.4$, $T_o = 800K$ and $\frac{\eta_{max}}{\eta_{thermal}} = 1.7$.

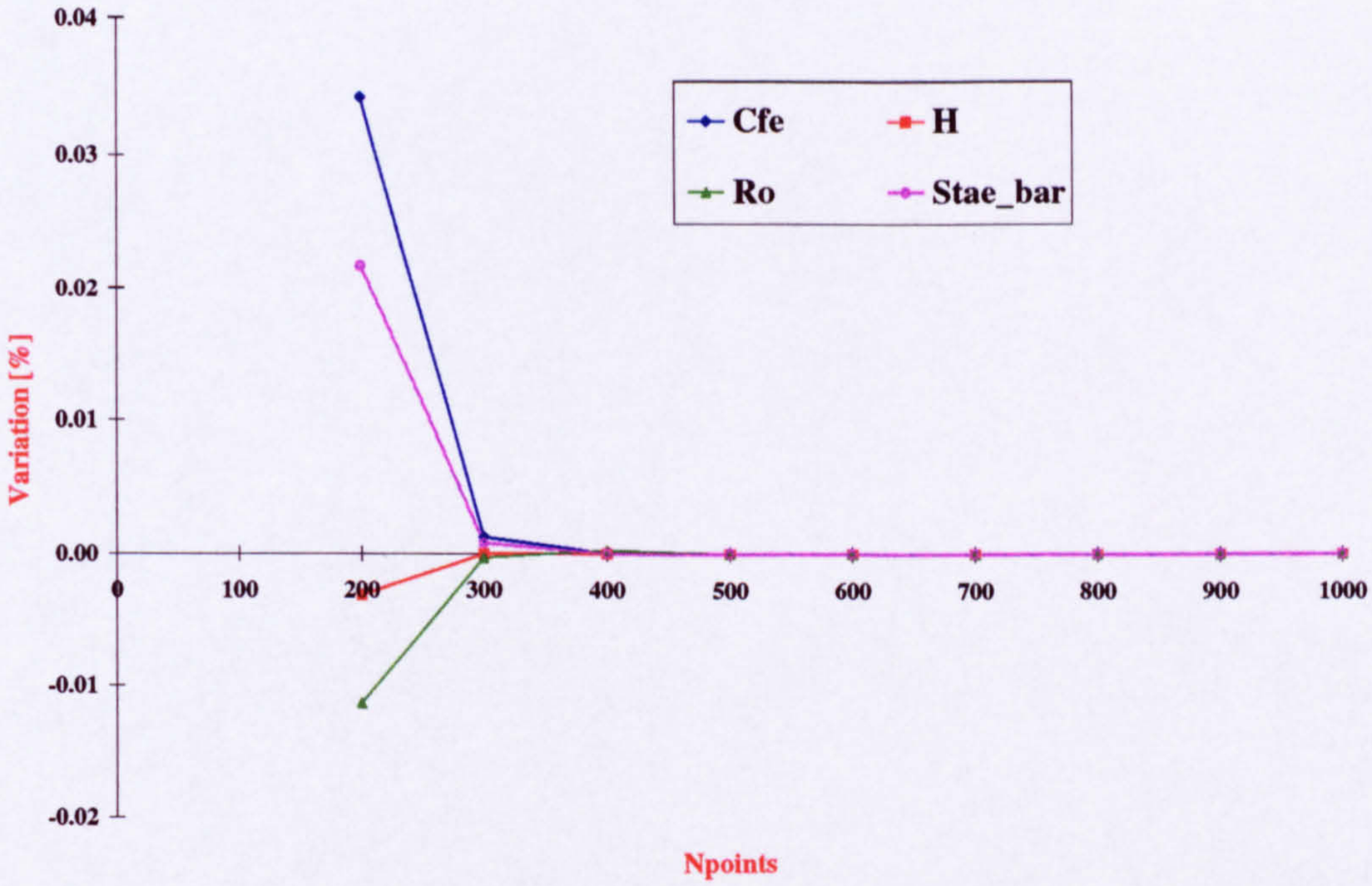

Figure E.12: Variation of Skin friction Cfe, Shape factor H, Reynolds number R_θ and Stanton number $\bar{St}_{ae}$ with the number of points across the computational domain for turbulent flow and $\bar{R} = 2000$, $M_{ae} = 3$, $T_w/T_o = 0.4$, $T_o = 800K$ and $\frac{\eta_{max}}{\eta_{thermal}} = 1.7$.

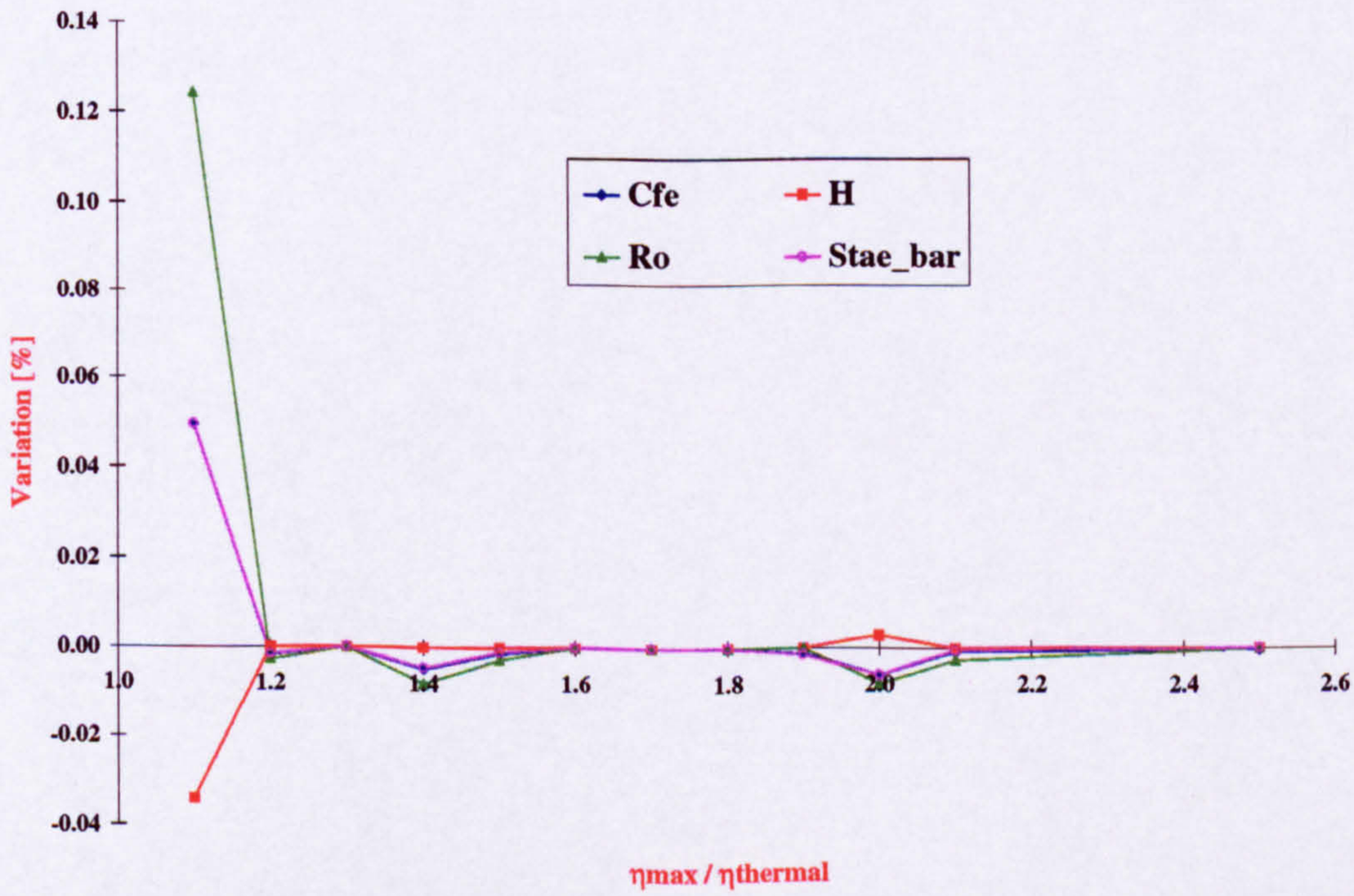

Figure E.13: Variation of Skin friction Cfe, Shape factor H, Reynolds number R_θ and Stanton number $\bar{St}_{ae}$ with the ratio $\frac{\eta_{max}}{\eta_{thermal}}$ for turbulent flow and $\bar{R} = 500$, $M_{ae} = 3$, $T_w/T_o = 0.4$, $T_o = 800K$ and $Npoints = 400$.

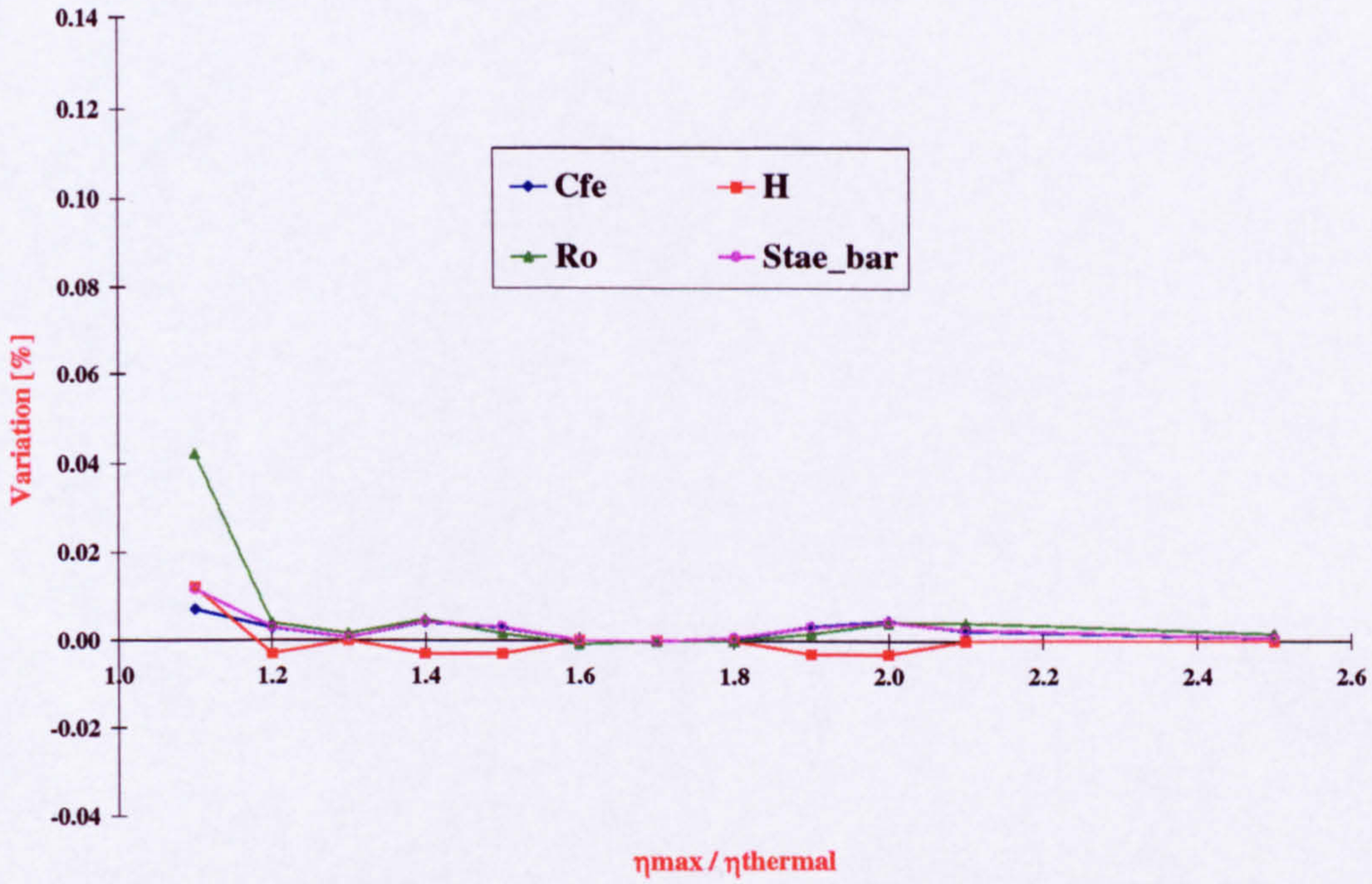

Figure E.14: Variation of Skin friction Cfe, Shape factor H, Reynolds number R_θ and Stanton number $\bar{St}_{ae}$ with the ratio $\frac{\eta_{max}}{\eta_{thermal}}$ for turbulent flow and $\bar{R} = 1000$, $M_{ae} = 3$, $T_w/T_o = 0.4$, $T_o = 800K$ and $Npoints = 400$.

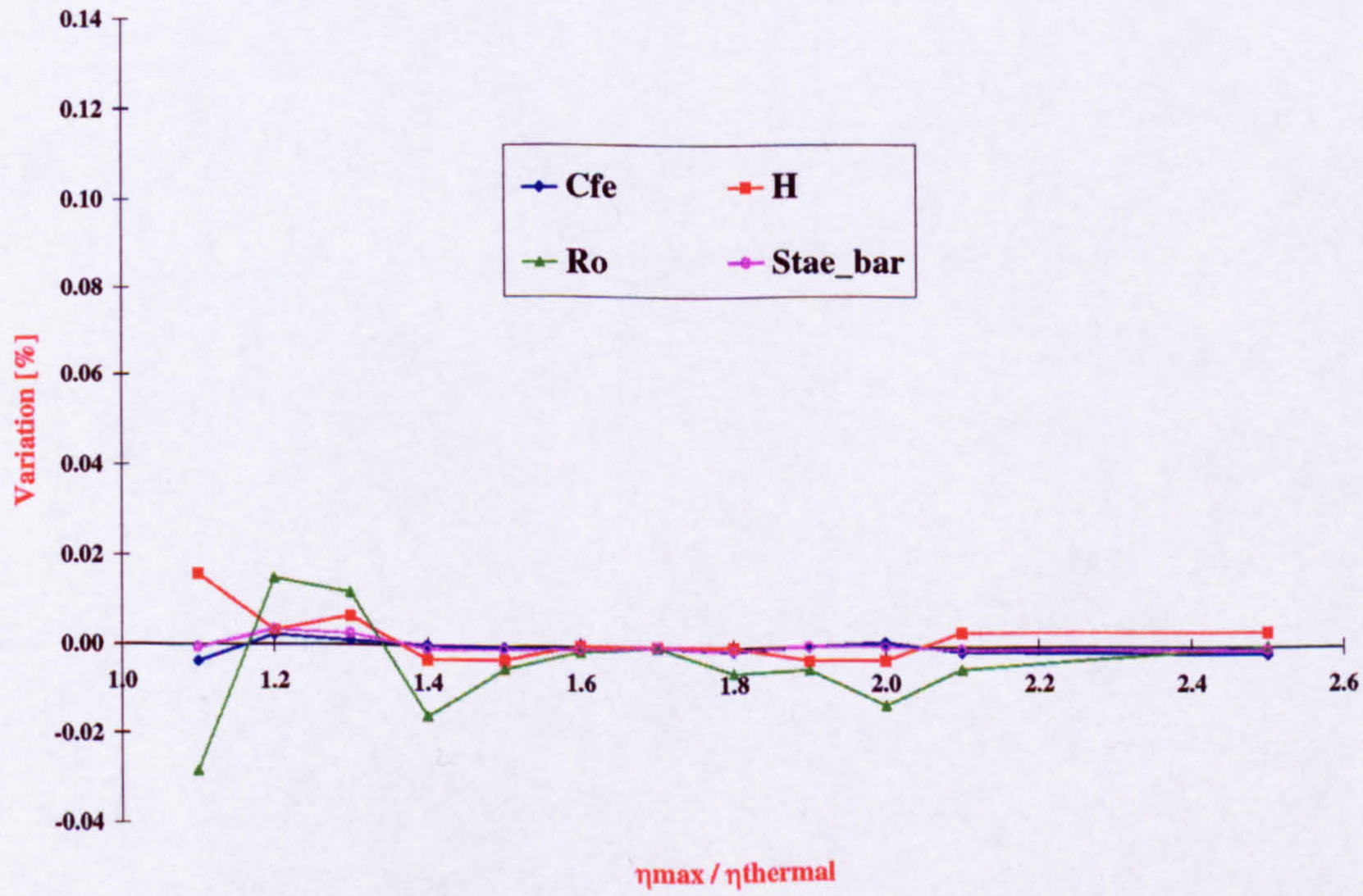

Figure E.15: Variation of Skin friction Cfe, Shape factor H, Reynolds number R_θ and Stanton number $\bar{St}_{ae}$ with the ratio $\frac{\eta_{max}}{\eta_{thermal}}$ for turbulent flow and $\bar{R} = 2000$, $M_{ae} = 3$, $T_w/T_o = 0.4$, $T_o = 800K$ and $Npoints = 400$.

Appendix F

Flow properties at the edge of the viscous layer

F.1 Local flow properties at the edge of the attachment-line boundary layer

F.1.1 Total enthalpy Ho

The total enthalpy *Ho* is a very useful variable since it involves the velocity and the temperature (two important variables in the case of the present study).

$$Ho = Cp.T + \frac{Q^2}{2} \tag{F.1}$$

where Cp is the specific heat at constant pressure, T is the static temperature and Q is the total velocity.

The total enthalpy also has the advantage that it is constant throughout the inviscid part of the flow including across shock waves. Hence, a typical Ho profile, at a particular

position along an attachment-line, can be split in two distinct parts i.e. viscous and inviscid (figure F.1). The "inviscid" part of the Ho profile is well defined by the plateau where Ho is constant. By selecting two points on this plateau, a line can be drawn (line P on figure F.1). Hence, starting from the wall, for a given Z/D, the difference (Ω) between the inviscid plateau value of Ho and the actual (viscous) value can be evaluated. The edge of the total enthalpy profile is defined at the location where Ω becomes less than 0.001 (viscous value then equals 99.9% of the inviscid value).

F.1.2 Velocity and static temperature

The method used to locate the edge of the total enthalpy boundary layer was also applied to the velocity and static temperature. However the resulting edge value distributions were found to be unsatisfactory. This was because oscillations appeared at stations close to the upstream tip i.e. low values of L/D as indicated in figures F.2 and F.3. This is due to the fact that, unlike the total enthalpy, the velocities and temperatures jump across a shock wave. Hence, there is no plateau as opposed to the total enthalpy. This feature is specially important at low values of $\frac{L}{D}$ where the shock layer is very thin.

To produce a smooth distribution of the edge conditions, the boundary layer code (MGNS3D) was used. For every Navier-Stokes run produced (see table B.2), the infinite swept values of $\bar{R}$ and M_{ae} were calculated using the equations derived in appendix C. These quantities, together with $\frac{Tw}{To}$ and To, were used as input to the boundary layer code. The computations (figure F.4) gave values for η_{Ho}, η_T and η_V at 99.9% of the inviscid value. Hence, the ratios $(\frac{\eta_T}{\eta_{Ho}})_{Inf-swept}$ and $(\frac{\eta_V}{\eta_{Ho}})_{Inf-swept}$ could be obtained. These correspond to the ratio of the thermal viscous layer thickness to the total enthalpy boundary layer

thickness and velocity viscous layer thickness to the total enthalpy boundary layer thickness.

With the distance from the wall, $\frac{Z}{D}$, corresponding to the edge of the total enthalpy boundary layer being estimated for every station $\frac{L}{D}$, the edge of the velocity V and temperature viscous layers can be calculated all along the attachment-line by using

$$(\frac{Z}{D})_T = (\frac{\eta_T}{\eta_{Ho}})_{Inf-swept} \cdot (\frac{Z}{D})_{Ho} \tag{F.2}$$

$$(\frac{Z}{D})_V = (\frac{\eta_V}{\eta_{Ho}})_{Inf-swept} \cdot (\frac{Z}{D})_{Ho} \tag{F.3}$$

where $(\frac{Z}{D})_T$, $(\frac{Z}{D})_V$ and $(\frac{Z}{D})_{Ho}$ are local values.

Using this method the smoothness of the distributions of the edge velocity and edge static temperature was found to be acceptable as shown for example by figure F.5.

F.1.3 Static pressure, density and Mach number

Using the Navier-Stokes results for the static pressure profiles at every station $\frac{L}{D}$ (e.g. figure F.6), the distribution of the edge static pressure along the attachment-line was obtained. The choice was made to take the static pressure values at the edge of the thermal boundary layer. However, since the static pressure gradient at the wall is close to zero (figure F.6), taking the static pressure at the edge of the velocity or thermal viscous layer give identical P_{ae} values. This also justifies the use of a boundary layer code.

Having obtained the velocity, static temperature and static pressure distributions along

the attachment-line, the density and Mach number distributions can be calculated using equations F.4 and F.5.

$$P_{ae} = \rho_{ae}.R.T_{ae} \tag{F.4}$$

$$M_{ae} = \frac{V_{ae}}{\sqrt{\gamma.R.T_{ae}}} \tag{F.5}$$

However, a different approach was needed for Beckwith et al. [5] results on cylinders swept at 20^o or less. As explained in appendix G, section G.4.4, Navier-Stokes calculations could not be performed for these particular runs since the code would not converge for detached bow shock situations. In these cases, the infinite swept assumption was made. This is justifiable since Beckwith et al. took their measurements at values of L/D high enough for the infinite swept conditions to be reached (see appendix G, figure G.20). For 20^o of sweep angle, for example, the first heat transfer gauge was located at a L/D value of 2.5. When the cylinder is swept at 40^o, the maximum difference between the local flow properties and the infinite swept values at this gauge is 7%. As the sweep angle decreases, the difference decreases. Therefore, for 20^o of sweep angle, the error introduced by the infinite swept assumption is well below 7%. Hence, it is safe to conclude that the infinite swept assumption can be made for runs carried out by Beckwith et al. [5] on cylinders swept at 20^o or less.

F.1.4 Accuracy of the results

The accuracy of the flow property distributions depends on the computational results and on the way the edges of the velocity and thermal profiles were found.

Ratios $(\frac{\eta_T}{\eta_{Ho}})_{Inf-swept}$ and $(\frac{\eta_V}{\eta_{Ho}})_{Inf-swept}$

It could be argued that the single values of $(\frac{\eta_T}{\eta_{Ho}})_{Inf-swept}$ and $(\frac{\eta_V}{\eta_{Ho}})_{Inf-swept}$ (equations F.2, F.3) used to estimate the edge of the velocity and thermal boundary layer cannot be applied to every station along the attachment-line, since they have been obtained on the basis of infinite swept conditions. To test the validity of these ratios, the Navier-Stokes run for Holden Run36 has been chosen, since it is the highest Mach number ($M_\infty = 10.62$) and sweep angle ($\Lambda = 80^o$) considered in this study. Therefore, it is the case in which the infinite swept conditions are the furthest away from the local values for a given spanwise station. Taking the local values of $\bar{R}$ and M_{ae} (see section F.2 for the evaluation of $\bar{R}$) at stations $\frac{L}{D} = 0.2$ and $\frac{L}{D} = 13.86$, the local values of the ratios $\frac{\eta_T}{\eta_{Ho}}$ and $\frac{\eta_V}{\eta_{Ho}}$ can be obtained from the boundary layer code (note that at station L/D of 0.2, the difference between the infinite swept conditions and the local values of $\bar{R}$ and M_{ae} is as high as 50% and F.7 and F.8 show that the velocity and temperature distributions obtained for η ratios calculated from the infinite swept conditions and from the actual local values of $\bar{R}$ and M_{ae} are almost identical. Hence, the pressure distribution (figure F.9) was not affected by the definition of the η ratio and the same is true for Mach number and density (see equations F.4 and F.5). This means that the ratios $(\frac{\eta_T}{\eta_{Ho}})_{Inf-swept}$ and $(\frac{\eta_V}{\eta_{Ho}})_{Inf-swept}$ evaluated from the infinite swept conditions can be applied in all cases without reducing the accuracy of the estimations.

Convergence of the computational solution

The convergence of the Navier-Stokes results was checked in every case. It was found that the flow properties along the attachment-line were unchanged (solution converged)

when the residuals (equation D.14) dropped below 5.10^{-4} (figures F.10 to F.12). However, converged heat transfer rates at the wall were achieved only after the residuals had dropped below 5.10^{-5} (figure F.13). Therefore, the solution file written by the Navier-Stokes code was compiled, using the post-processor (see appendix D, section D.7), once the residuals dropped below 5.10^{-5}. Strictly speaking, the value of the residuals at which the solution is converged varies from case to case. However, the solution convergence was checked for every case carried out before compiling the results.

Grid Independence

Results were obtained on a baseline grid with the following minimum dimensions: $I_{max} = 33$, $J_{max} = 97$ and $K_{max} = 97$ (figure D.5). In some cases, more grid points were needed in the normal to the wall direction and along the cylinder to better resolve the viscous layer. In these cases, J and K values were increased up to a maximum of 181 and 121 respectively.

To investigate the influence of the grid on the solution, two cases were considered. The first was Holden Run36, which involves the highest Mach number ($M_\infty = 10.6$), the highest sweep angle ($\Lambda = 80^o$) and the lowest wall to stagnation temperature ratio ($\frac{Tw}{To} = 0.26$) considered in the whole investigation. The second case was Beckwith Run15, involving the lowest Mach number ($M_\infty = 4.15$), the lowest sweep angle ($\Lambda = 40^o$) and highest wall-to-stagnation temperature ratio ($\frac{Tw}{To} = 0.92$) encountered.

For Holden Run36, three grids were created in addition to the "baseline" version. The first, Grid-H1, had more points than the "baseline" with $I_{max} = 65$, $J_{max} = 121$ and $K_{max} = 121$ and had the edge of the computational domain closer to the bow shock, with

all the other parameters e.g. stretching factor etc identical. The second, Grid-H2, differed from the baseline by being coarser, with $I_{max} = 33$, $J_{max} = 61$ and $K_{max} = 61$. Finally, the third, Grid-H3, had less stretching with the edge of the computational domain being closer to the bow shock, whilst the total number of grid points was the same. The velocity, temperature and pressure distributions shown in figures F.14 to F.16 show no significant grid effect. Hence, it is concluded that the solutions obtained with the "baseline" layout are grid independent.

For Beckwith Run15 only one grid (Grid-B1) was created to be compared with the baseline which had $I_{max} = 33$, $J_{max} = 181$ and $K_{max} = 121$. Grid-B1 had however fewer points i.e. $I_{max} = 33$, $J_{max} = 121$, $K_{max} = 97$ and a less severe stretching. The edges of the computational domain were also closer to the bow shock. Figures F.17 to F.19 demonstrate that the computed flow properties are effectively grid independent.

F.2 Local attachment-line Reynolds number

F.2.1 Attachment-line chordwise velocity gradient

The distribution of the chordwise edge velocity gradient along the attachment-line has been the subject of a long investigation. The major problem was to obtain an accurate value of the chordwise velocity at the edge of the viscous layer, U_{ae}. This requires not only all the data points in the I direction (around the cylinder) but also all the data points in the J direction since the velocity profile must be used to find the edge of the viscous layer. Calculations are also required for all stations along the cylinder. Essentially, all the grid points in the computational domain have to be considered for the evaluation

of the distribution of the chordwise edge velocity. Therefore, a method that could be included within the post-processor had to be used without a major loss in accuracy. This is described in appendix D, section D.7.3.

Once U_e field was provided by the post-processor, the attachment-line, chordwise velocity gradient could be obtained from a plot of $\frac{U_e}{a_e}$ vs $\frac{X}{D}$. The local speed of sound at the thermal boundary layer edge, a_{ae}, was calculated using

$$a_{ae} = \left(\gamma.R.T_\infty.\frac{T_{ae}}{T_\infty}\right)^{\frac{1}{2}} \tag{F.6}$$

where the temperature ratio is evaluated by the method described in section F.1.2.

By plotting $\frac{U_e}{a_e}$ vs $\frac{X}{D}$ and fitting the "best" straight line (least squares fitting) between the data points, the attachment-line chordwise velocity gradient could be estimated. However, the estimation of the chordwise velocity gradient does depend on the θ range of the data. This is shown by figure F.20 (Holden run36, $\frac{L}{D} = 0.2$) which demonstrates that θ up to 5^o brings the most accurate evaluation of the attachment- line chordwise velocity gradient.

Note that in the absence of Navier-Stokes solutions, the infinite swept value of the chordwise velocity gradient was used for Beckwith et al. [5] when the cylinder sweep angle was 20^o or less (see section F.1.3).

F.2.2 Attachment-line Reynolds number

Having obtained the local speed of sound at the edge of the attachment-line thermal boundary layer, a_{ae}, the chordwise velocity gradient is

$$\frac{dU_e}{dX} = \frac{d\left(\frac{U_e}{a_{ae}}\right)}{d\left(\frac{X}{D}\right)} . \frac{a_{ae}}{D} \tag{F.7}$$

Also, knowing T_{ae} (see section F.1.2), the dynamic viscosity follows from Sutherlands law

$$\frac{\mu_{ae}}{\mu_{ref}} = \left(\frac{T_{ae}}{T_{ref}}\right)^{\frac{3}{2}} . \left(\frac{T_{ref} + s}{T_{ae} + s}\right) \tag{F.8}$$

where for air $s = 110.4$ K, $T_{ref} = 288.16$ K, $\mu_{ref} = 1.79.10^{-5}$ kg/(m.s). For nitrogen the values become 105 K, 273.15 K and $1.67.10^{-5}$ kg/(m.s) respectively.

The density along the attachment-line can be evaluated from the equation of state. Hence, the kinematic viscosity is

$$\nu_{ae} = \frac{\mu_{ae}}{\rho_{ae}} \tag{F.9}$$

The evaluation of the attachment-line Reynolds number $\bar{R}$ is therefore possible since

$$\bar{R} = \left[\frac{V_{ae}^2}{\nu_{ae} . \frac{dU_e}{dX}}\right]^{\frac{1}{2}} \tag{F.10}$$

A Navier-Stokes solution was obtained for each combination of sweep angle, cylinder diameter and free-stream Mach number studied in the various experiments. From this, the local value of the attachment-line Reynolds number was estimated. Reynolds number

scaling was used to obtained $\bar{R}$ for the runs involving identical model geometry, sweep angle and free-stream conditions but different free-stream Reynolds number - see chapter 3, section 3.3.2.

F.3 Local Stanton number

Having extracted the local heat transfer rates from the experiments, obtained the local properties at the edge of the attachment-line boundary layer and obtained the local recovery temperature (see chapter 3 for the estimation of the recovery temperature), the local Stanton number can be calculated. For all the other experimental runs, equation 3.8 was used. In this equation, the ratios $\frac{\rho_{ae}}{\rho_\infty}$, $\frac{V_{ae}}{Q_\infty}$, $\frac{T_{ae}}{T_\infty}$ and $\frac{T_r}{T_o}$ (which leads to $\frac{T_r}{T_{ae}}$) come directly from the computation (MGNS3D and boundary layer code). They depend only on sweep angle and free-stream Mach number. The heat transfer rate, wall temperature, free-stream density, velocity and temperature correspond directly to the experimental run considered.

In wind tunnels, the free-stream Mach number does vary slightly with the free-stream Reynolds number (see appendix G, figures G.3, G.14 and G.23). Hence the bow shock strength varies and the flow properties across the bow shock change. Therefore, correction factors might be needed.

Runs carried out by Bushnell et al. [12][13] on a 60° swept cylinder have been considered to investigate this issue. CFD calculations have been performed on Run 17a ($M_\infty = 7.88$) giving the ratios $\frac{T_{ae}}{T_\infty}$, $\frac{P_{ae}}{P_\infty}$ and $\frac{V_{ae}}{Q_\infty}$. However, for the free-stream Reynolds number range covered by Bushnell, the free-stream Mach number varies from 7.8 to 8.0 (see table B.8). By calculating the infinite swept values of $\frac{T_{ae}}{T_\infty}$, $\frac{P_{ae}}{P_\infty}$ and $\frac{V_{ae}}{Q_\infty}$ for Run17a and comparing

them to the infinite swept values of these three ratios for Runs 12 to 20, a correction factor in the worst case ($M_\infty = 8$, Run 20) of 1.016 was found. Hence, it can be safely concluded that, for the free-stream Mach number variation with Reynolds number, the bow shock strength does not vary significantly. Hence, the local values of $\frac{T_{ae}}{T_\infty}$, $\frac{P_{ae}}{P_\infty}$ and $\frac{V_{ae}}{Q_\infty}$ can be assumed to be independent of Reynolds number.

F.4 Figures

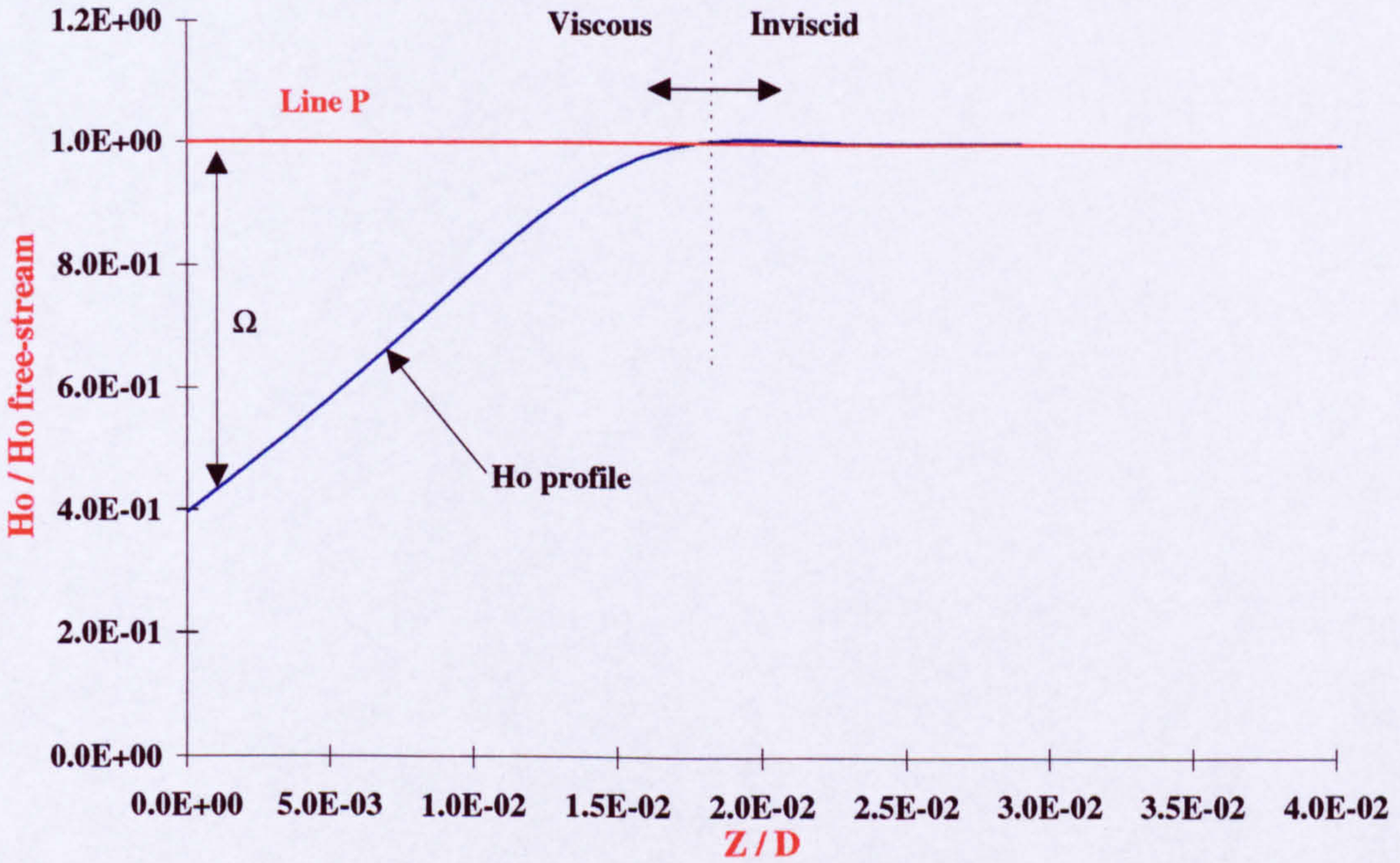

Figure F.1: Total enthalpy profile at station $\frac{L}{D} = 6.15$. Poitiers university, CFD run70, $M_\infty = 7.14$, $\Lambda = 80^o$.

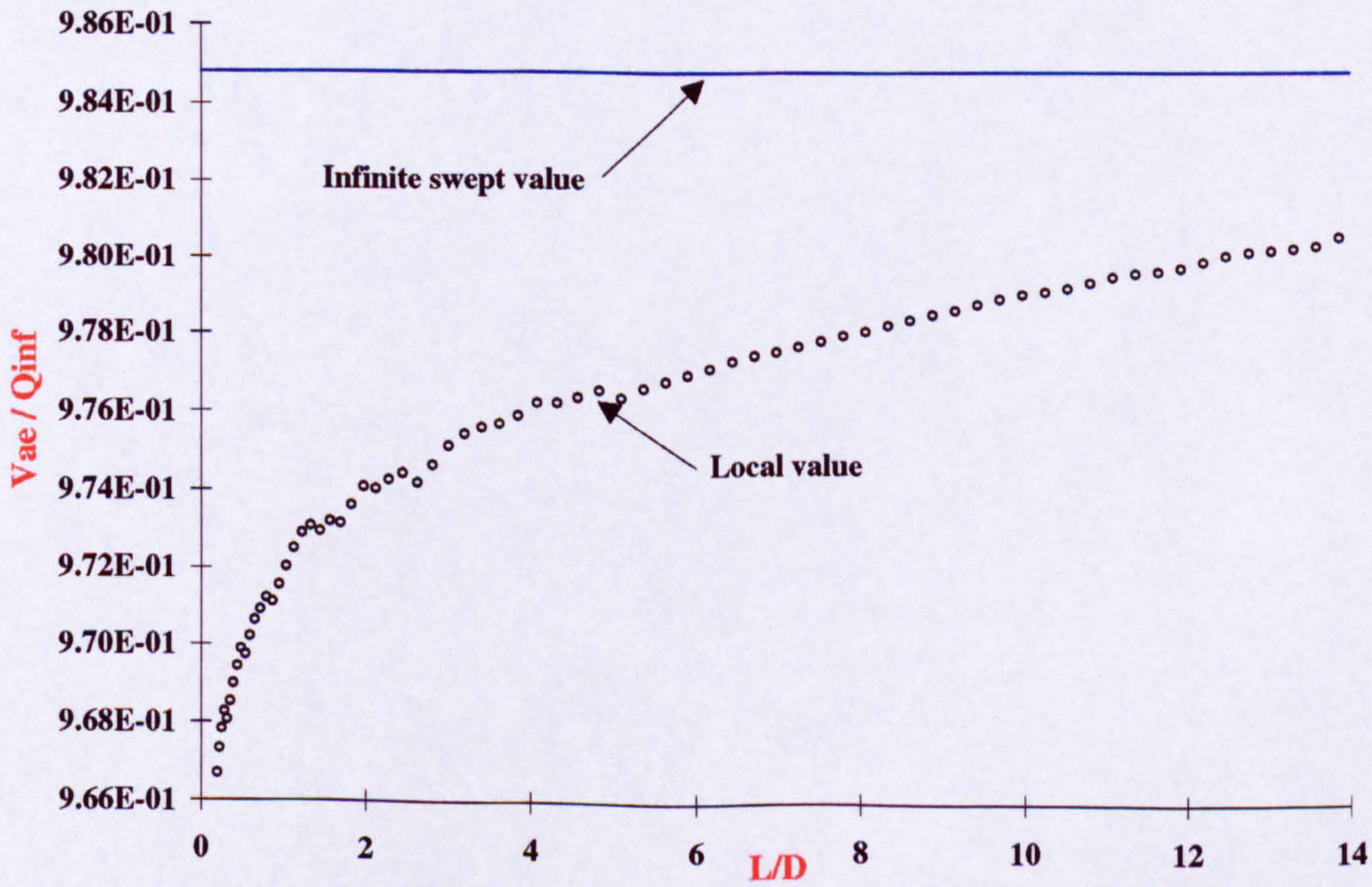

Figure F.2: Edge velocity distribution along the attachment-line of an 80^o swept cylinder (Holden Run 36, $M_\infty = 10.6$).

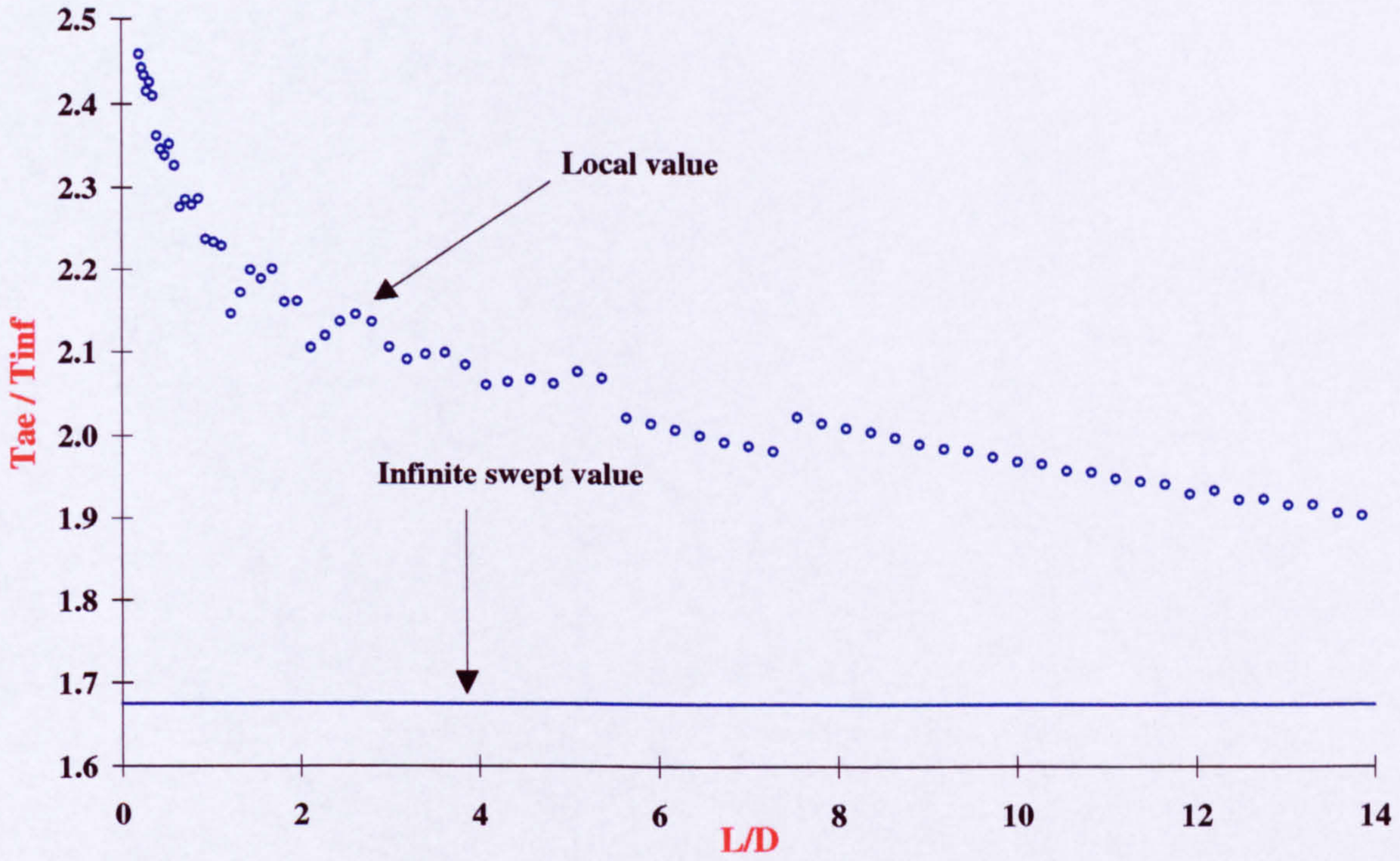

Figure F.3: Edge static temperature distribution along the attachment-line of an 80° swept cylinder (Holden Run 36, $M_\infty = 10.6$).

INFINITE YAWED ATTACHMENT-LINE COMPRESSIBLE LAMINAR BOUNDARY-LAYER ANALYSIS

BOUNDARY LAYER CHARACTERISTICS

PART OF THE INPUT PARAMETERS

RBAR=1481.0 EDGE MACH= 4.0966 TW/TO=0.4000 S/TO=0.14720 WBLOW=0.000000E+00

ITERATIONS = 21 FPP(0)=0.201456E+01 CP(0)=0.673590E+00 GP(0)=0.291736E+00

CFZ(EDGE)=0.826740E-03 ST(EDGE) =0.414429E-03 REYANFZ =1.0026

DELTA*/LREF =0.260289E+01 THETAMOM/LREF =0.341185E+00 H = 7.6290

EDGE REYTHETAMOM = 505.29Delta.995 =

ETA	W/WE	U/UE	T/TE	H/HE	ThetaInt
0.0000	0.00000	0.00000	1.74259	0.40000	0.00000
0.2202	0.15062	0.40150	1.97202	0.47014	0.41091
0.4404	0.30270	0.70889	2.09296	0.55102	0.86056
0.6607	0.44943	0.91966	2.10428	0.63865	1.32463
0.8809	0.58301	1.04519	2.02299	0.72624	1.78053
1.1011	0.69717	1.10527	1.88075	0.80619	2.21115
1.3213	0.78893	1.12162	1.71282	0.87271	2.60702
1.5415	0.85863	1.11303	1.54764	0.92327	2.96578
1.7618	0.90895	1.09320	1.40251	0.95848	3.29016
1.9820	0.94360	1.07078	1.28460	0.98088	3.58552
2.2022	0.96643	1.05039	1.19431	0.99374	3.85799
2.4224	0.98081	1.03395	1.12837	1.00018	4.11333
2.6426	0.98947	1.02178	1.08216	1.00272	4.35642
2.8629	0.99447	1.01335	1.05097	1.00320	4.59106
3.0831	0.99721	1.00784	1.03064	1.00275	4.82010
3.3033	0.99866	1.00442	1.01785	1.00203	5.04555
3.5235	0.99938	1.00239	1.01007	1.00136	5.26877
3.7437	0.99973	1.00125	1.00551	1.00084	5.49066
3.9640	0.99989	1.00063	1.00291	1.00049	5.71178
4.1842	0.99995	1.00030	1.00149	1.00027	5.93247
4.4044	0.99998	1.00014	1.00074	1.00014	6.15293
4.6246	0.99999	1.00006	1.00035	1.00007	6.37326
4.8448	1.00000	1.00003	1.00016	1.00003	6.59354
5.0651	1.00000	1.00001	1.00007	1.00002	6.81378
5.2853	1.00000	1.00000	1.00003	1.00001	7.03401
5.5055	1.00000	1.00000	1.00001	1.00000	7.25424
5.7257	1.00000	1.00000	1.00001	1.00000	7.47446
5.9459	1.00000	1.00000	1.00000	1.00000	7.69468
6.1662	1.00000	1.00000	1.00000	1.00000	7.91490
6.3864	1.00000	1.00000	1.00000	1.00000	8.13512
6.6066	1.00000	1.00000	1.00000	1.00000	8.35534
6.8268	1.00000	1.00000	1.00000	1.00000	8.57556
7.0470	1.00000	1.00000	1.00000	1.00000	8.79578
7.2673	1.00000	1.00000	1.00000	1.00000	9.01600
7.4875	1.00000	1.00000	1.00000	1.00000	9.23623
7.7077	1.00000	1.00000	1.00000	1.00000	9.45645
7.9279	1.00000	1.00000	1.00000	1.00000	9.67667
8.1481	1.00000	1.00000	1.00000	1.00000	9.89689
8.3684	1.00000	1.00000	1.00000	1.00000	10.11711
8.5886	1.00000	1.00000	1.00000	1.00000	10.33733

Figure F.4: Typical output from the boundary layer code. Variables in boxes were used in the present study.

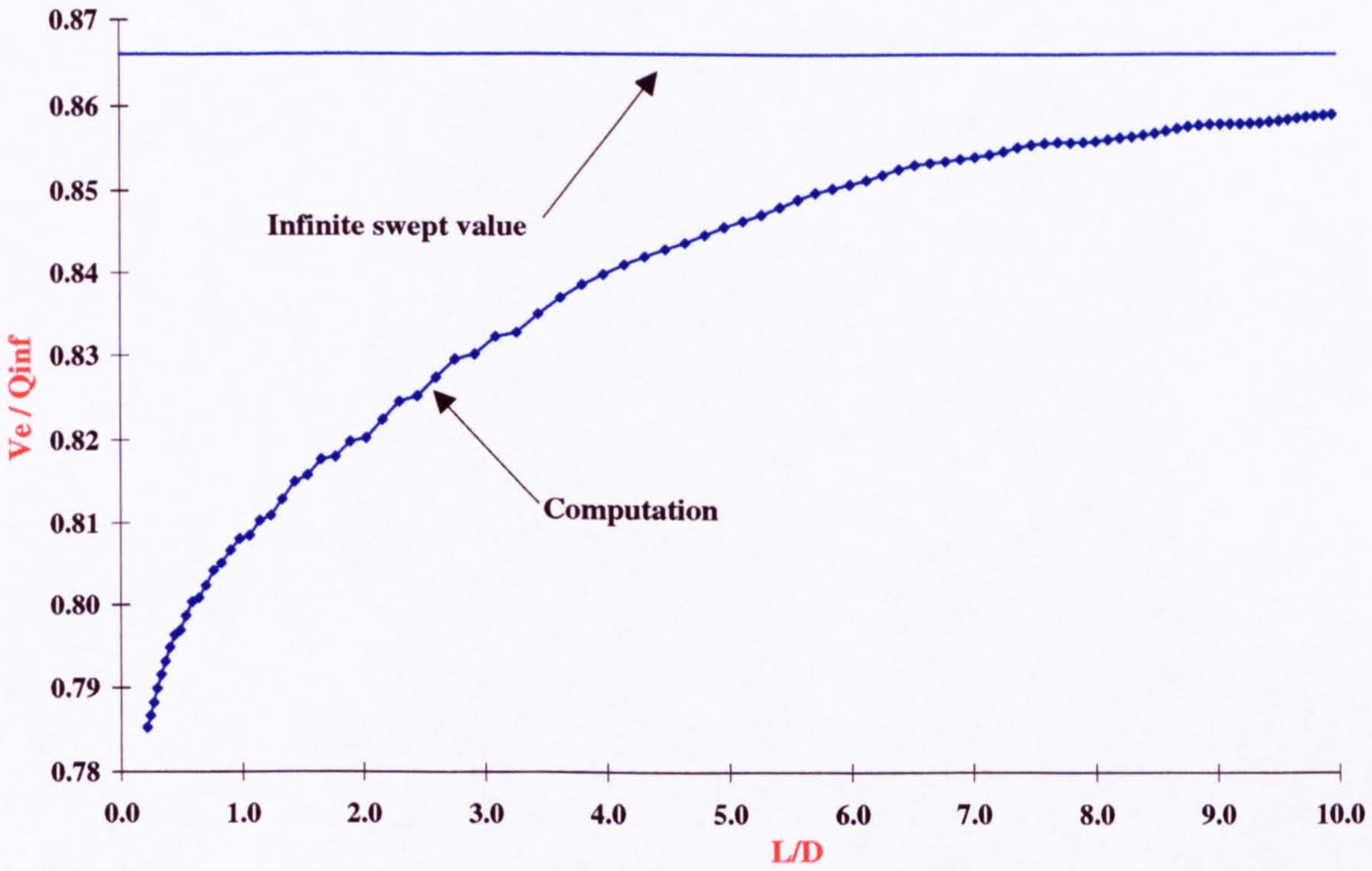

Figure F.5: Spanwise variation of the edge velocity. (CFD run on Bushnell run17a, $M_\infty = 7.88$, $\Lambda = 60^o$).

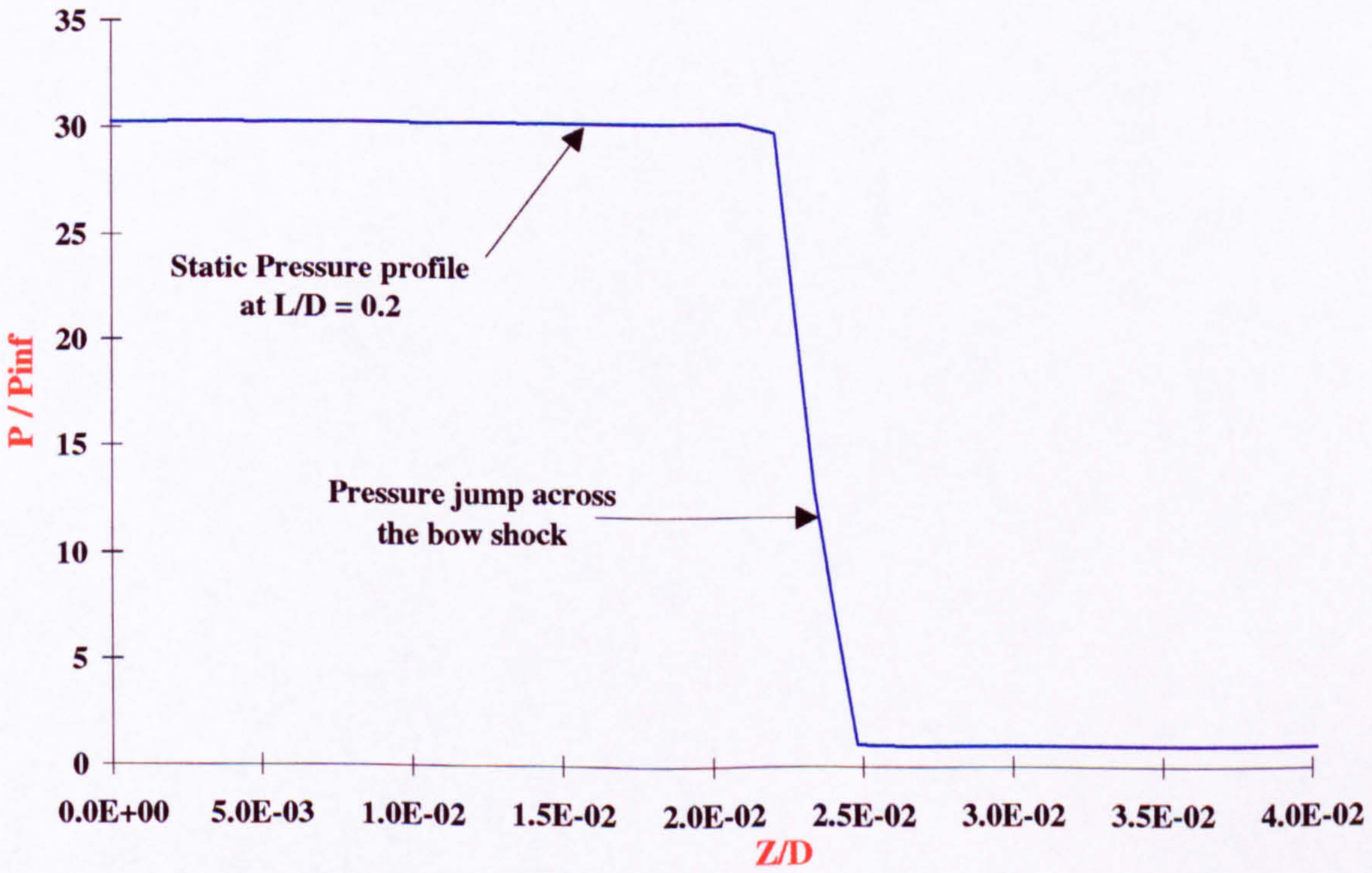

Figure F.6: Typical static pressure profile obtained from MGNS3D (CFD run on Holden run5, $M_\infty = 10.5$, $\Lambda = 66.5^o$).

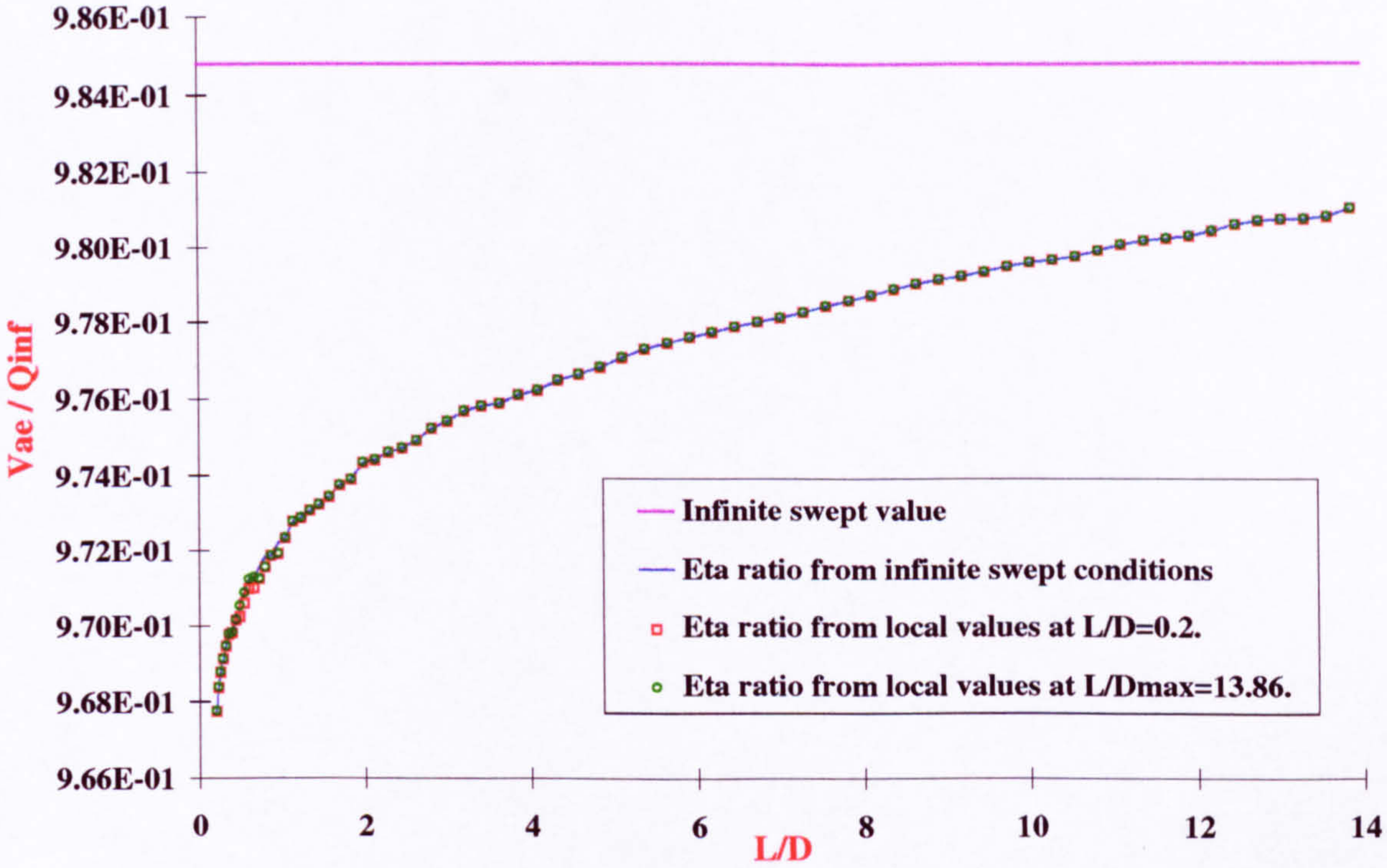

Figure F.7: Edge velocity distribution along the attachment-line of an 80° swept cylinder at Mach 10.6 (Holden Run36) for different $\frac{\eta_V}{\eta_{Ho}}$ ratio estimates.

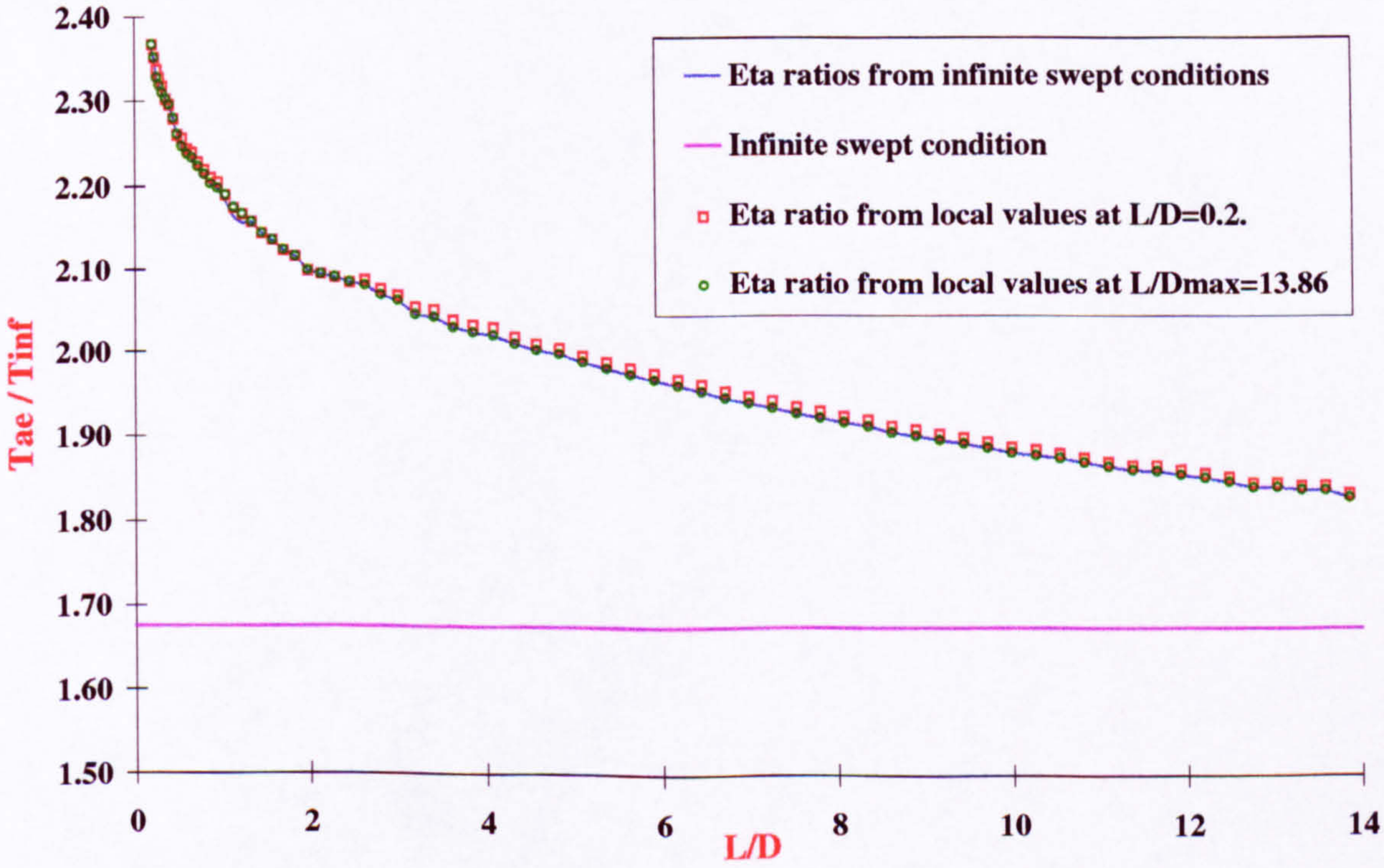

Figure F.8: Edge static temperature distribution along the attachment-line of an 80° swept cylinder at Mach 10.6 (Holden Run36) for different $\frac{\eta_T}{\eta_{Ho}}$ ratio estimates.

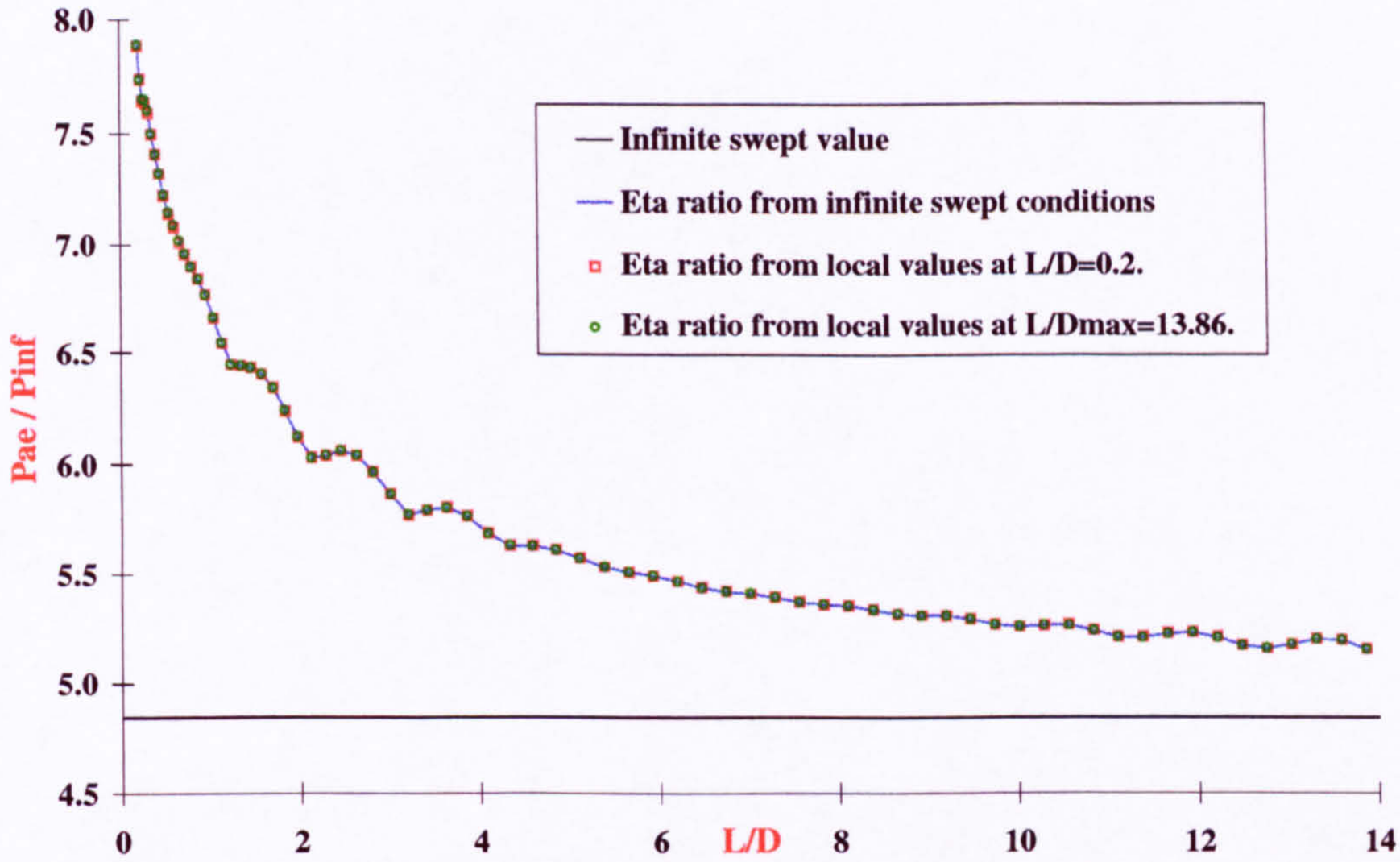

Figure F.9: Static edge pressure distribution along the attachment-line of an 80^o swept cylinder at Mach 10.6 (Holden Run36) for different $\frac{\eta_T}{\eta_{Ho}}$ ratio estimates.

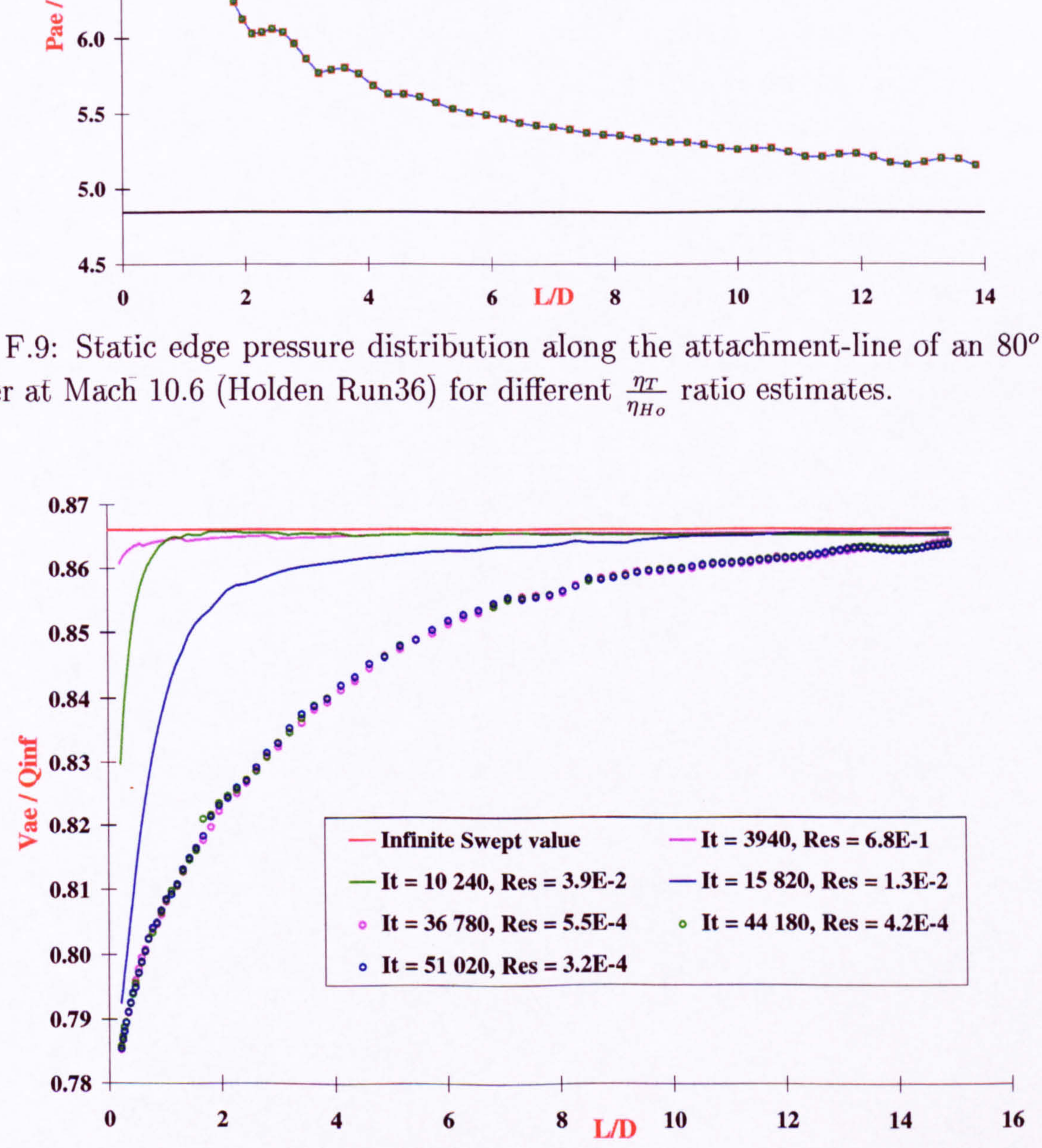

Figure F.10: Edge velocity distribution along the attachment-line for a range of computational residuals and iterations. (Poitiers run19, $M_\infty = 7.14$, $\Lambda = 60^o$).

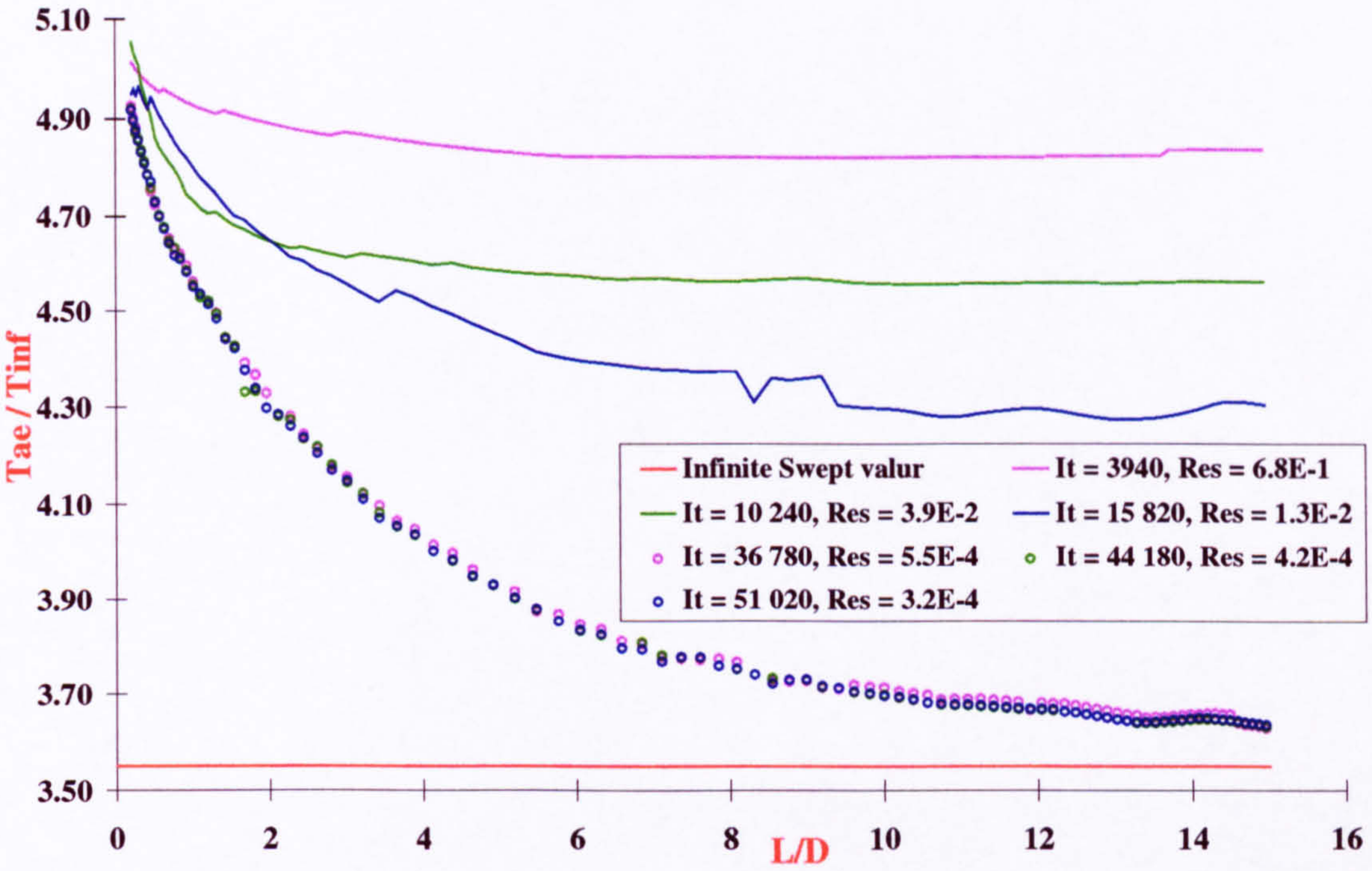

Figure F.11: Edge static temperature distribution along the attachment-line for a range of computational residuals and iterations. (Poitiers run19, $M_\infty = 7.14$, $\Lambda = 60^o$).

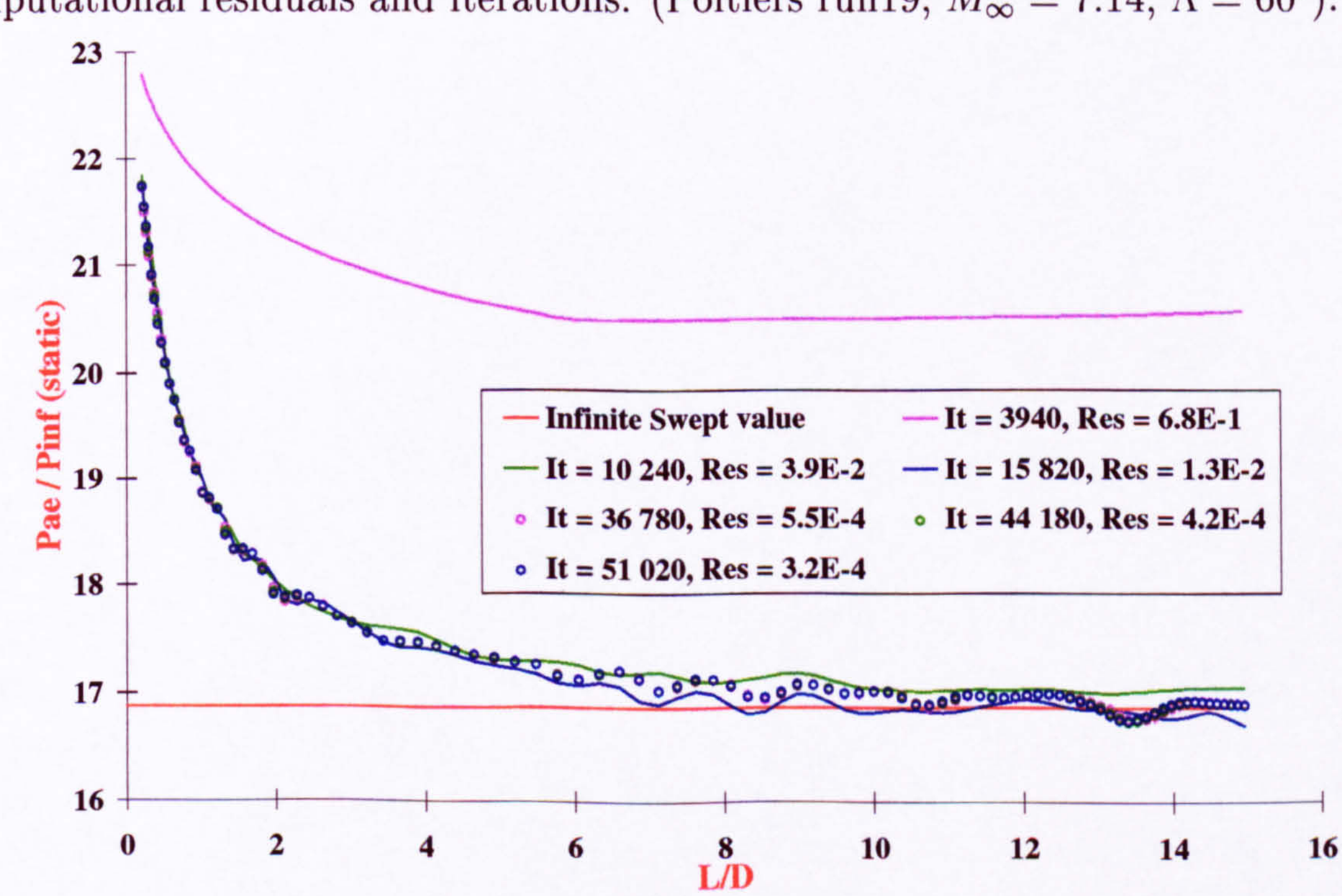

Figure F.12: Edge static pressure distribution along the attachment-line for a range of computational residuals and iterations. (Poitiers run19, $M_\infty = 7.14$, $\Lambda = 60^o$).

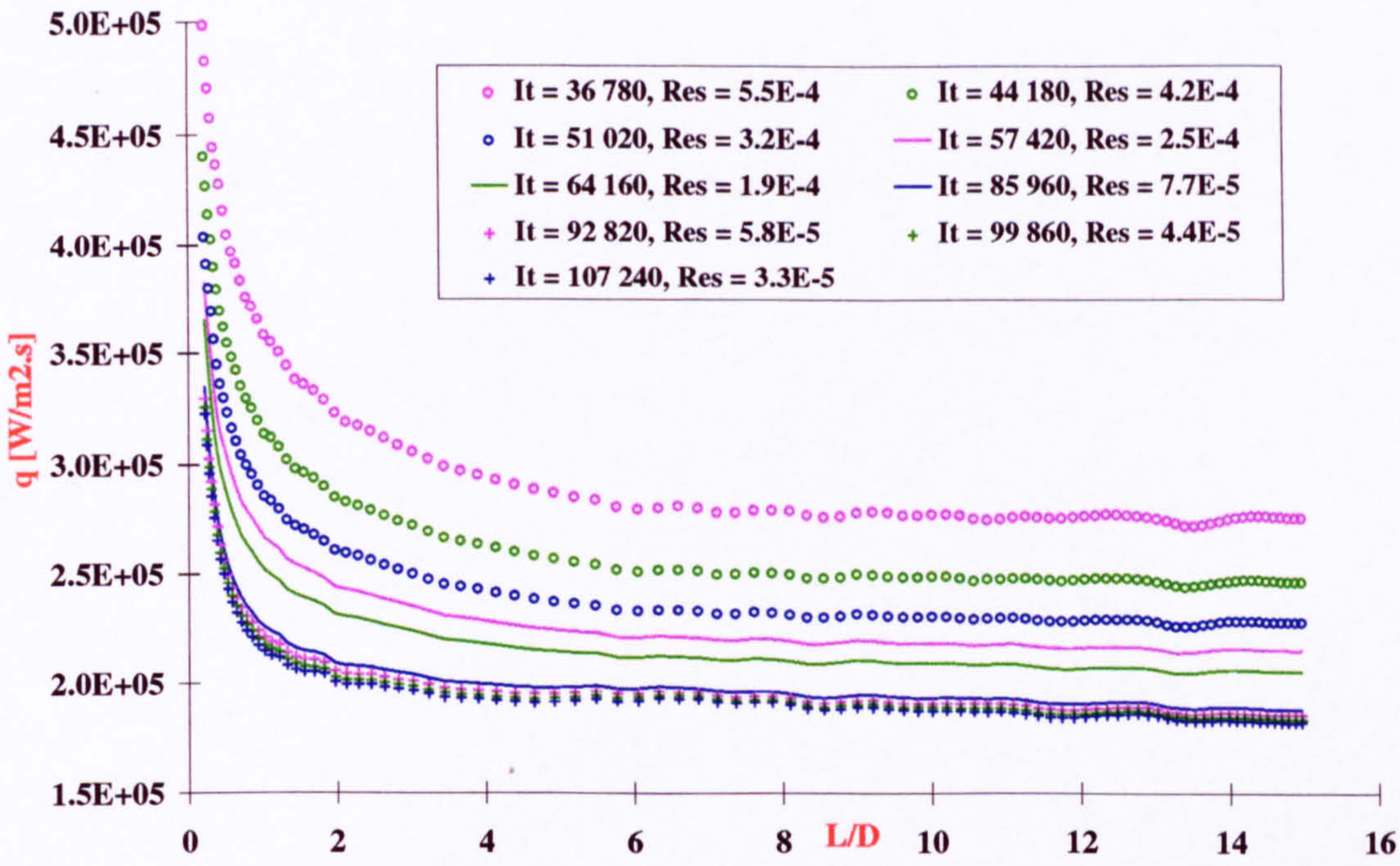

Figure F.13: Local heat transfer rate along the attachment-line for a range of computational residuals and iterations. (Poitiers run19, $M_\infty = 7.14$, $\Lambda = 60^o$).

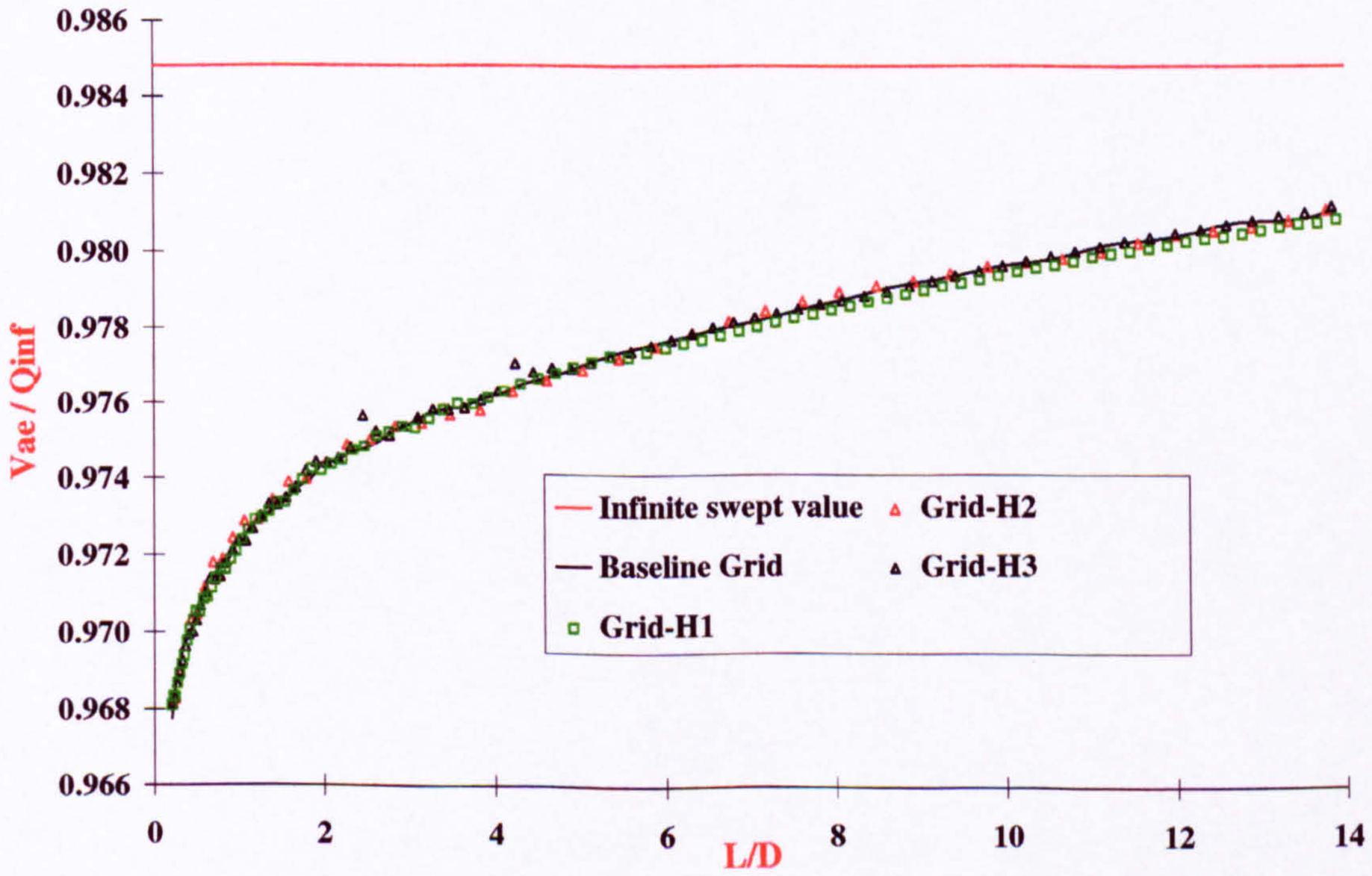

Figure F.14: Grid effects upon the edge velocity distribution along the attachment-line (Holden run36, $M_\infty = 10.6$, $\Lambda = 80^o$, $\frac{Tw}{To} = 0.26$).

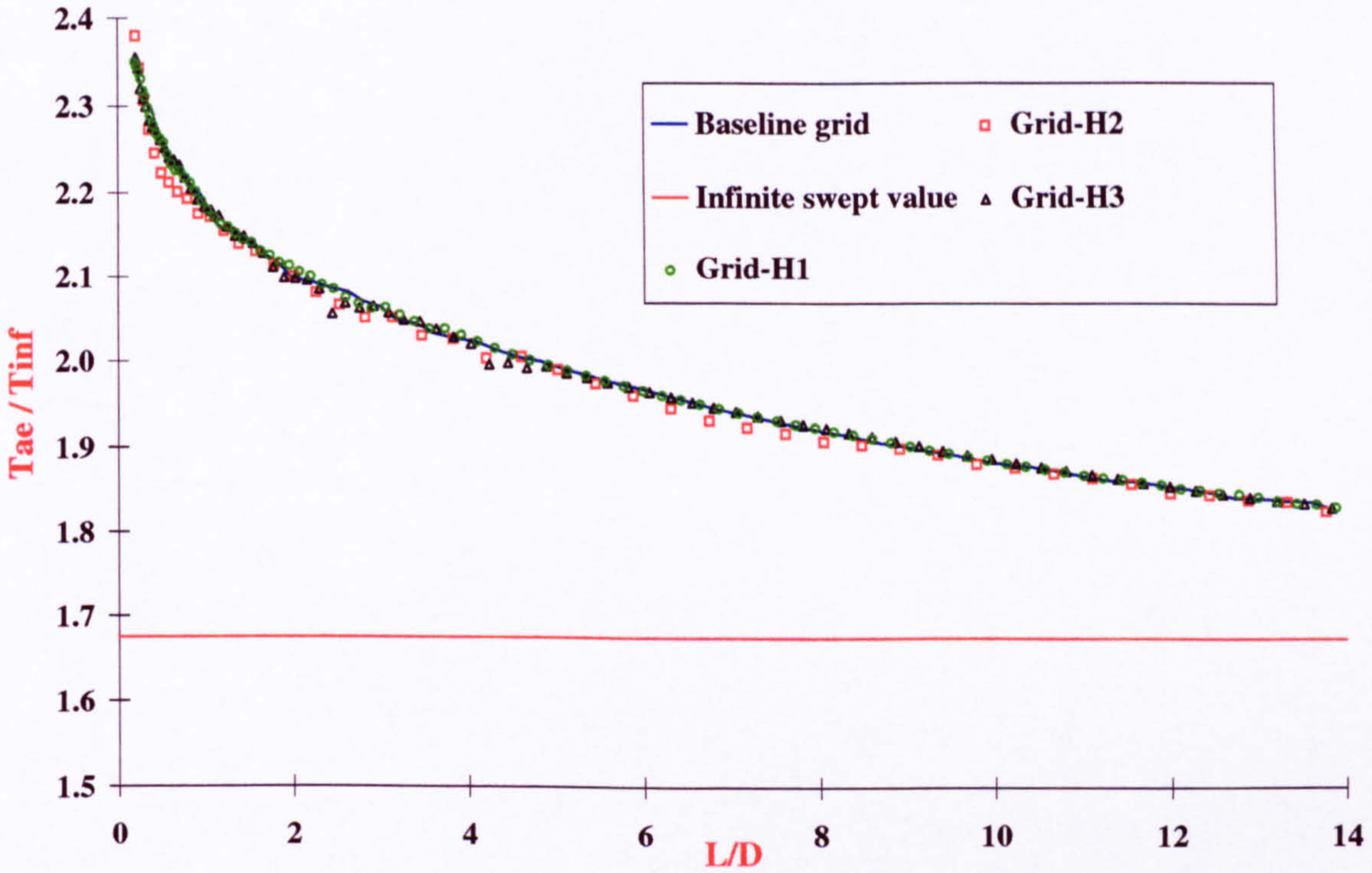

Figure F.15: Edge static temperature distribution along the attachment-line for different computation grid (Holden run36, $M_\infty = 10.6$, $\Lambda = 80^o$, $\frac{Tw}{To} = 0.26$).

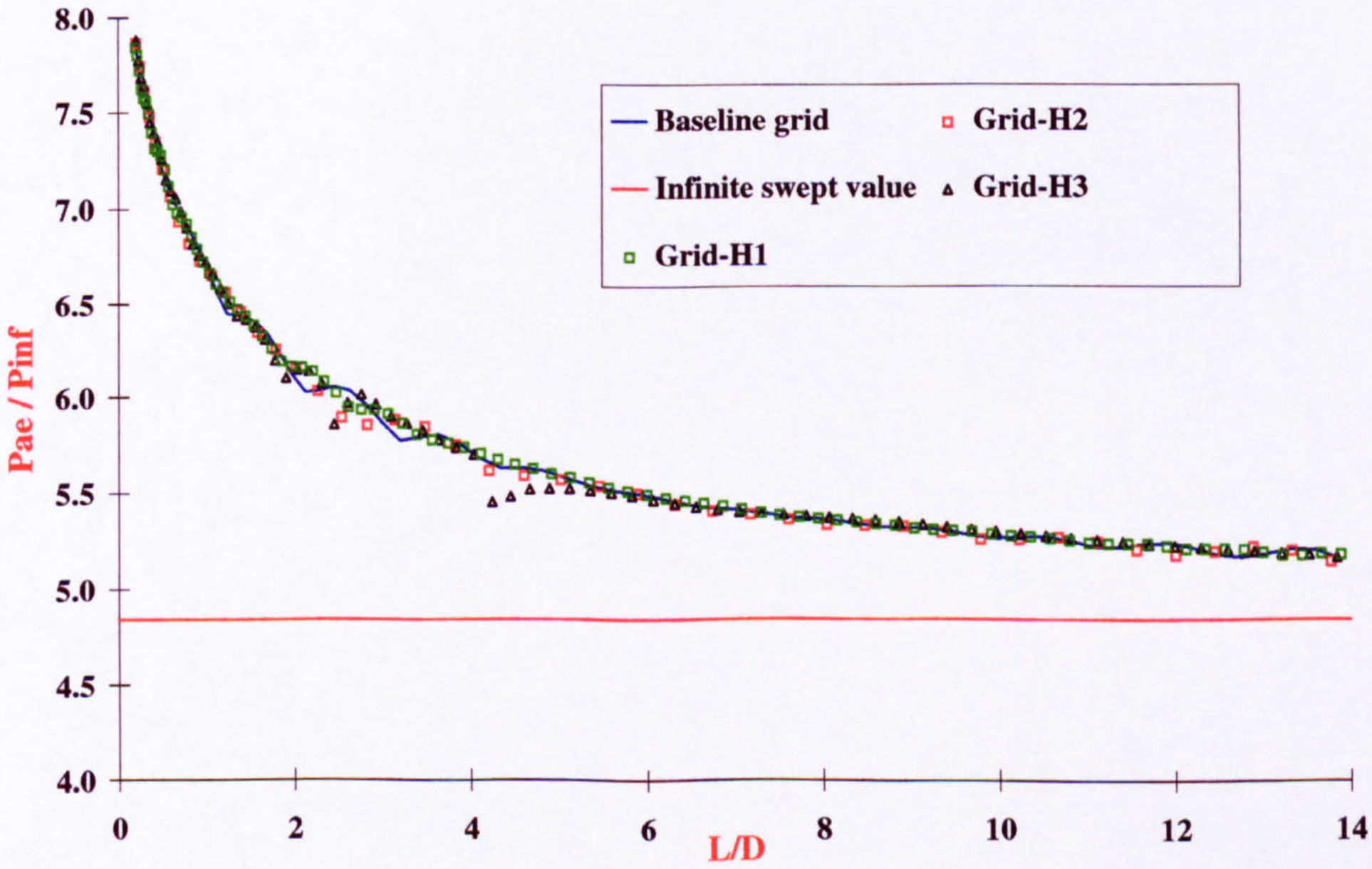

Figure F.16: Grid effects upon the edge static pressure distribution along the attachment-line for different computational grids (Holden run36, $M_\infty = 10.6$, $\Lambda = 80^o$, $\frac{Tw}{To} = 0.26$).

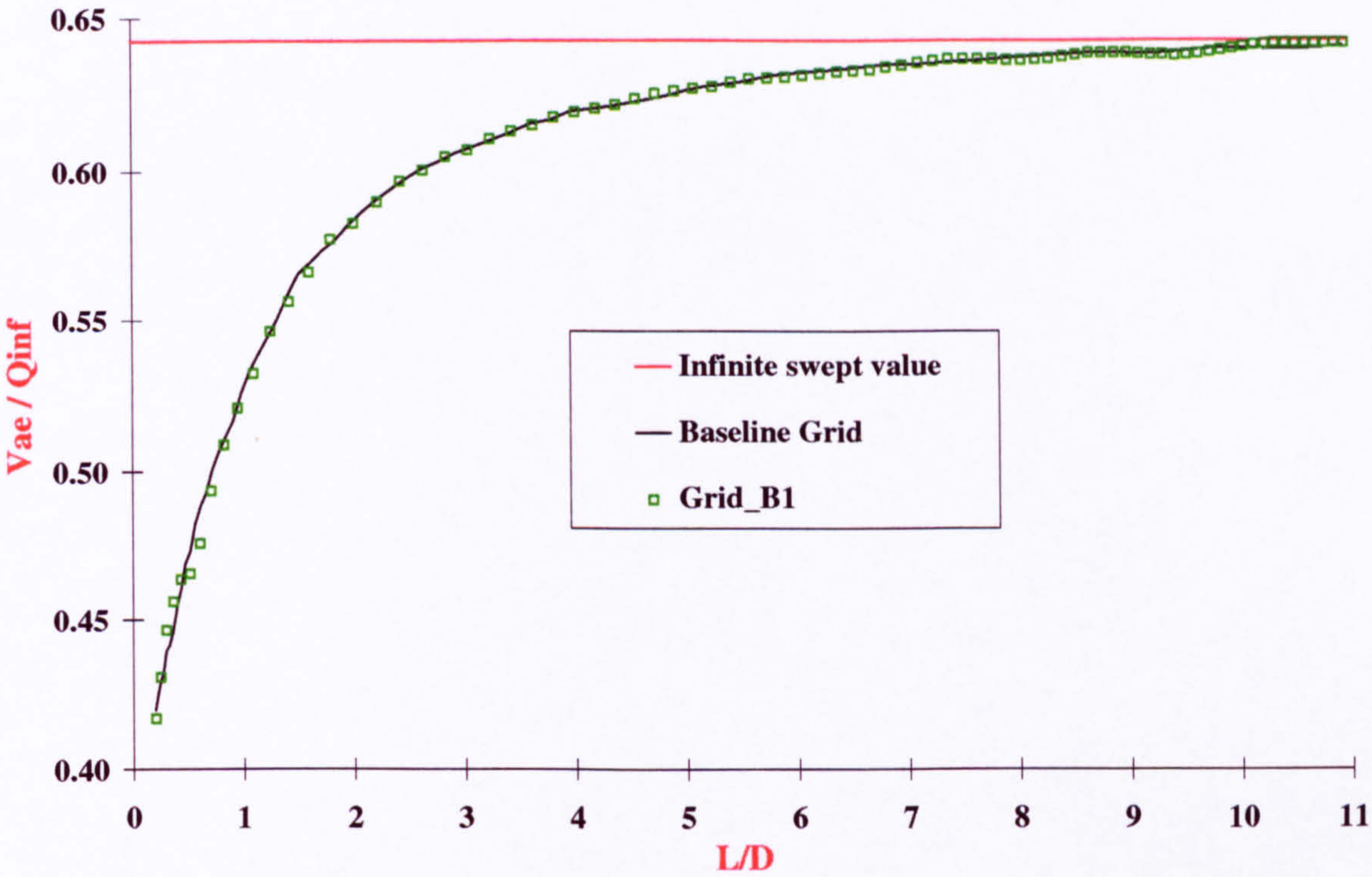

Figure F.17: Edge velocity distribution along the attachment-line for different computational grids (Beckwith run15, $M_\infty = 4.15$, $\Lambda = 40^o$, $\frac{Tw}{To} = 0.92$).

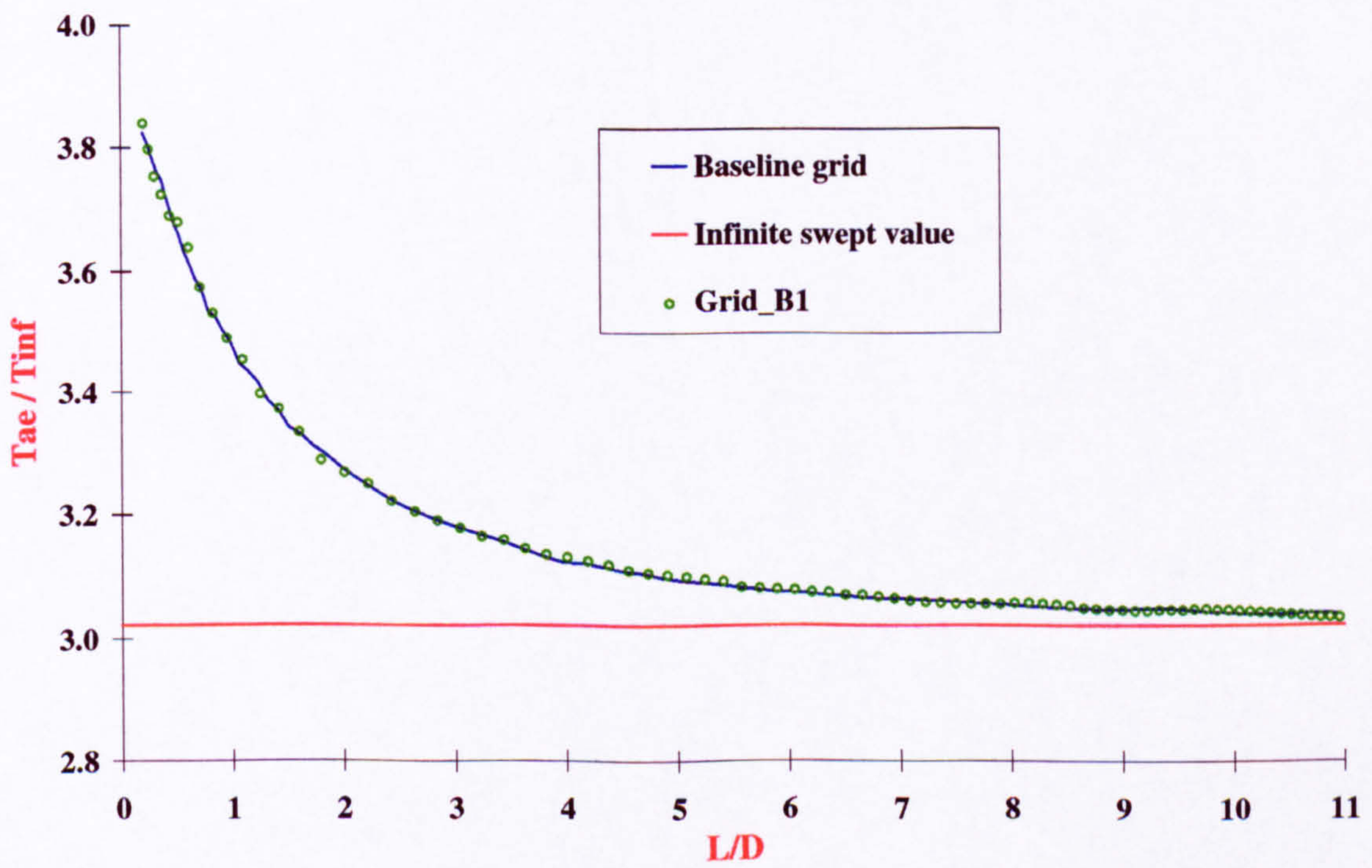

Figure F.18: Edge static temperature distribution along the attachment-line for different grids (Beckwith run15, $M_\infty = 4.15$, $\Lambda = 40^o$, $\frac{Tw}{To} = 0.92$).

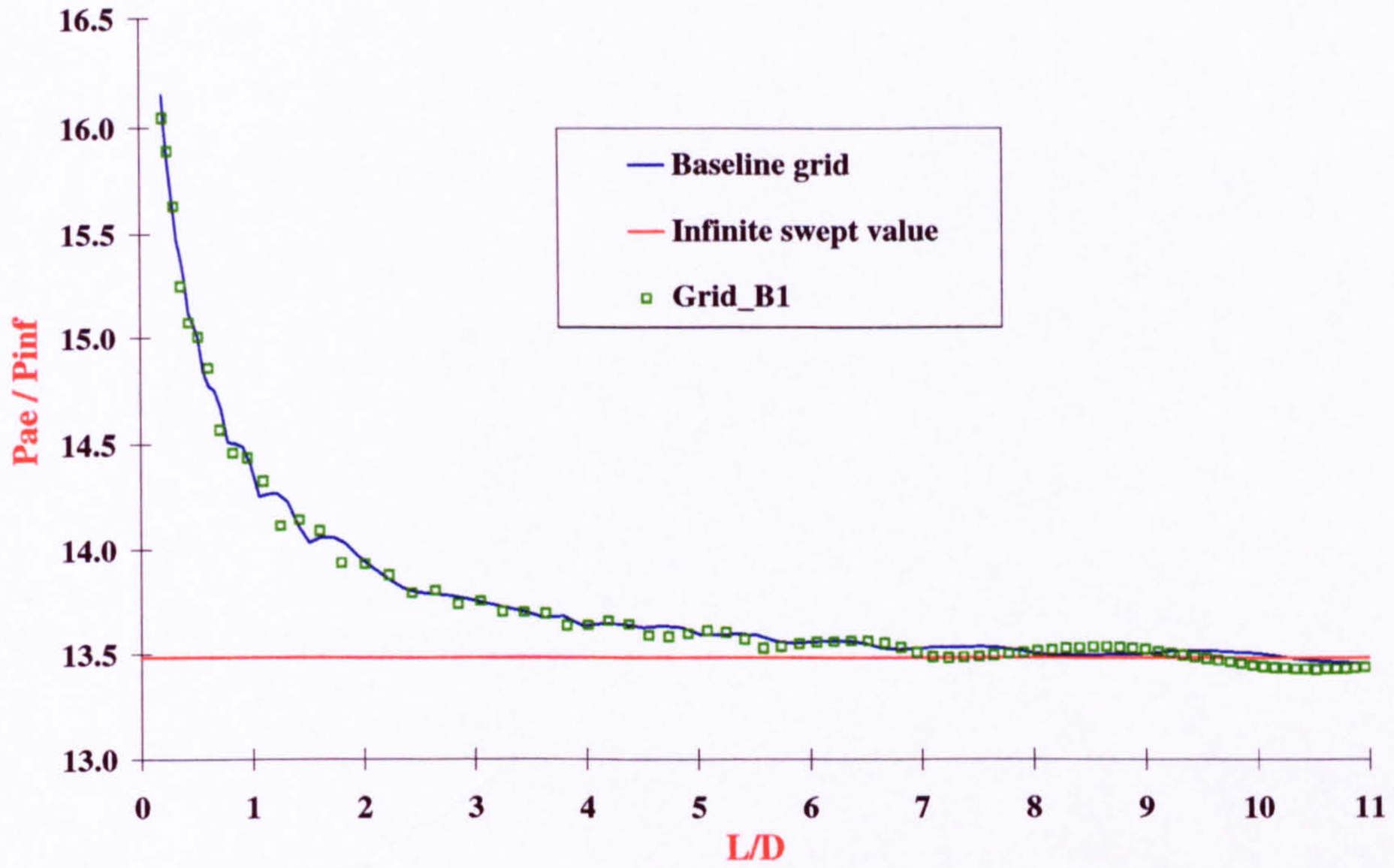

Figure F.19: Edge static pressure distribution along the attachment-line for two grid arrangements (Beckwith run15, $M_\infty = 4.15$, $\Lambda = 40^o$, $\frac{Tw}{To} = 0.92$).

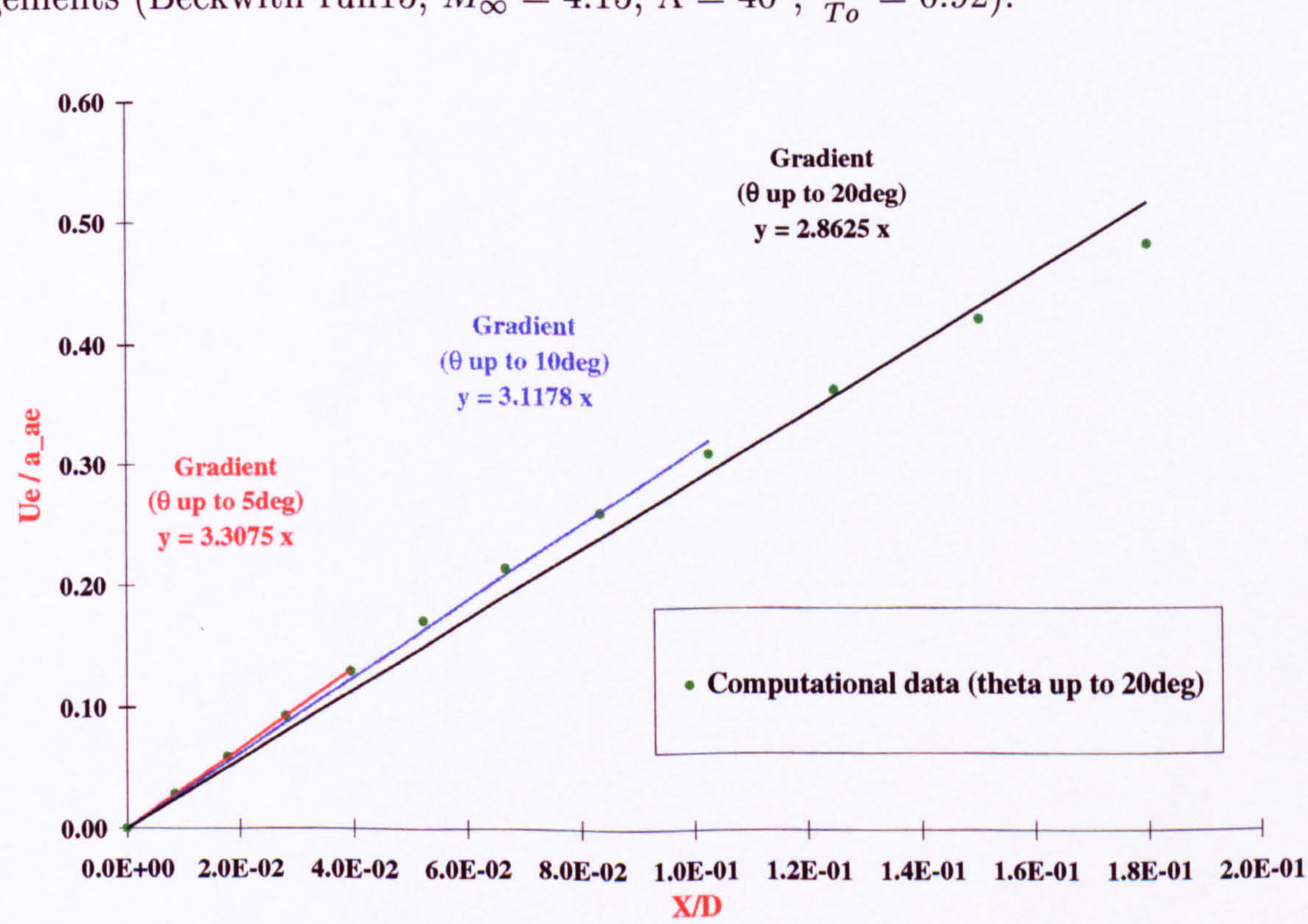

Figure F.20: Variation of the chordwise velocity, $\frac{U_e}{a_{ae}}$, with distance around the cylinder, $\frac{X}{D}$, at a $\frac{L}{D}$ of 0.2 (Holden run36, $M_\infty = 10.6$, $\Lambda = 80^o$). θ is the polar angle.

Appendix G

Description of the experiments

G.1 Holden et al.

G.1.1 Introduction

In 1994 Holden, Kolly and Bower [37] [38] carried out an experimental investigation of attachment-line heating on swept cylinders in high Mach number flow. The authors explained that since there were no published measurements for free-stream Mach numbers higher than 8, they undertook tests at Calspan-UB Research Centre with free-stream Mach numbers from 10 to 12. Although the primary objective of their study was to obtain data on attachment- line heating at high Mach numbers they also investigated the effects of attachment-line contamination by introducing roughness elements and adding end plates to try to trip the attachment-line flow to the turbulent state.

G.1.2 Experimental facilities

The Calspan 48 inch shock tunnel is a blow down facility using nitrogen as the test gas. Mach numbers ranging from 10 to 12 can be achieved with test times varying from 10 to 25 milliseconds. The unit free-stream Reynolds number ranged from $4.4.10^4$ to $3.8.10^6$ per foot ($1.44.10^5$ to $1.25.10^7$ per metre) as shown in figure G.1. This tunnel has the added advantage of giving low wall-to-free stream stagnation temperature ratios without having to cool the model below room temperature. In this investigation $\frac{Tw}{To}$ was typically 0.26. From the different runs conditions described in references [37] and [38], a calibration of the tunnel has been obtained (figures G.2 to G.4). A complete description of the tunnel can be found in reference [37].

G.1.3 Model and instrumentation

A 3 inch (0.0762m) diameter, swept circular cylinder was used (figure G.5). This had interchangeable leading edges in order to align the upstream tip of the model with the free-stream. The cylinder was instrumented with 28 thin-film, heat transfer gauges and 26 piezoelectric pressure gauges. Most of the heat transfer instrumentation was located along the attachment-line (table D.7.2) but some heat transfer gauges were placed on the -45^o and 45^o generators. Unfortunately the spanwise location at which the heat transfer and pressure gauges were positioned around the cylinder is not specified in either reference [37] or [38]. Holden et al. estimated the uncertainties associated with the gauge calibrations and the recording equipment to be $\pm 5\%$ and $\pm 3\%$ for the heat transfer and pressure measurements respectively. The data were obtained at sweep angles ranging from 60^o to 80^o.

The effects of trip wires and endplates on attachment-line transition were also investigated. In one case trip wires (k=0.015" and k=0.03") were wrapped around the model (see figure G.5) at an $\frac{L}{D}$ of approximately 0.75. In the other case, small streamwise endplates were added to the upstream tip of the cylinder.

The gauges used allowed both the mean and fluctuating components of the heat transfer to be obtained and this aided the identification of the beginning of transition by detecting bursts of turbulence travelling along the attachment-line.

G.1.4 Tests conditions and extraction of the heat transfer data

Table B.4 shows a listing of the model configurations and the respective tests conditions that have been considered in the present investigation. The runs carried out at Mach 11.3 and 12.5 were not considered here because of problems related to the CFD solutions. Local flow properties along the attachment-line e.g. $\frac{Tae}{T_\infty}$, $\frac{Mae}{M_\infty}$ etc. were obtained from the CFD for runs 5, 12, 25, 31, 34 and 36 (table B.2).

In references [37] and [38], the measured heat transfer rate at the wall, $\dot{q}_W$, is presented in both tables and graphs. Using equation G.1, $\dot{q}_W$ can be extracted in S.I. units by using the conversion factor

$$1\left[\frac{W}{m^2.sec}\right] = 11353\left[\frac{BTU}{ft^2.sec}\right] \tag{G.1}$$

G.2 Poitiers University

G.2.1 Introduction

An extensive experimental investigation on laminar and turbulent attachment-line heating and the transition between the two regimes was undertaken at Poitiers University between 1990 and 1998 (references [25], [35] and [6]). Tests were carried out in the CEAT H210 hypersonic tunnel using highly swept circular cylinders in free-stream flows with Mach numbers of 7.15 and 8.15. The model configurations used (see chapter G.2.4) gave values of M_{ae} from 3.3 to 6.8. Attachment-line transition was studied for smooth surfaces, with roughness elements of various shapes and with a range of streamwise endplates.

G.2.2 Experimental facilities

The CEAT H210 hypersonic tunnel is a blowdown facility in which the free-stream air flow lasts for approximately 20 seconds. The working section diameter is 210mm but, due to the presence of turbulent boundary layers on the walls, the "useful" diameter is reduced to 150mm. Two Mach numbers can be used (7.14 and 8.15), depending on the nozzle geometry. The free-stream Reynolds number per metre varies from $5.7.10^6$ to 34.10^6 with the Mach 7.14 nozzle and from $8.5.10^6$ to $18.5.10^6$ for the Mach 8.15 nozzle. The tunnel calibration, obtained from the tests conditions (see section G.2.4), can be seen in figures G.6 to G.8. The stagnation temperature is such that with the model at room temperature the $\frac{Tw}{To}$ ratio is approximately 0.38. The free-stream Mach number fluctuation is $\pm 0.5\%$ and $\pm 0.7\%$ at Mach 7.14 and 8.15 respectively. Moreover, Benard [6] reported that the free-stream pressure fluctuation $\frac{P'}{P}$ is approximately $\pm 3\%$.

Once the tunnel is started, the model is injected into the working section (see figure G.9) with a pneumatic jack. This takes only 0.1sec and has the advantage that it avoids tunnel start problems and, hence, allows larger models to be used. Further information on the CEAT H210 hypersonic tunnel can be found in references [25], [35] and [6].

G.2.3 Model and instrumentation

Circular cylinders with diameters of 13.5, 14, 19, 20 and 33mm were tested at sweep angles varying from 60° to 81°. The upstream tip of the models was sealed and cut off in a plane parallel to the free-stream flow direction. Natural surface finish of the cylinders was around 0.8μm and according to Benard [6] this is approximately 200 times smaller than the boundary layer thickness. Heat flux measurements were obtained using the thin wall technique. This involved the spot-welded of thermocouples onto the inner surface of the models thin skin along the attachment-line. Heat flux was determined by analysing the temperature/time history immediately after cold model injection. No pressure measurements were made. The accuracy of the heat flux data has been estimated by the authors (see [6], page 61) to be better than 15%.

Attachment-line heating was studied for smooth cylinder surface and then the effects of local 2D and 3D roughness elements, as well as endplates of various sizes, were considered. Trip wires, steps and cavities were also tested.

To study the effects of the wall temperature on transition the model was cooled by running liquid nitrogen along the inner surface of the model (figure G.9) before injecting. Once the wall temperature stabilised at the liquid nitrogen temperature, the cooling was

stopped and the tunnel started. Whilst the model was being cooled it was kept in an environment of gaseous nitrogen (outside the tunnel itself as the free-stream gas is air ; page 52 of reference [35]). If the model had been kept in contact with room air during the process, ice would be formed acting as roughness on the external surface of the models. With this technique the ratio $\frac{Tw}{To}$ could be decreased to approximately 0.24.

Tests carried out by Gaillard [35] on rectangular cylinders were not considered in the present investigation.

G.2.4 Tests conditions and extraction of the heat transfer data

Attachment-line results obtained at Poitiers university are presented in references [6] [35] by plots of St_{ae} against $\bar{R}^*$ (see appendix H for the definition of these two parameters). In the present investigation, only the heat transfer rate at the wall $\dot{q}_W$ is of an interest and it is shown how this was extracted from references [6] and [35] in appendix H.

Tables B.6 and B.7 contain the runs considered in this study. Although many others have been carried out at Poitiers only those exhibiting a repeatability better than ±5% have been used. CFD calculations were performed for runs 9, 19, 24 and 70 (note that all dimensions in those tables are in millimetres and that l, d and w stand for length (in spanwise direction), depth and width (in chordwise direction) respectively. Table B.7 is explained in more details in chapter 5.

G.3 Bushnell

G.3.1 Introduction

In 1965 Bushnell et al. [12] measured heat transfer and pressure distributions along a swept cylinder attached to a 12° half angle wedge (figure G.10). The aim was to study the effects of the interaction between the shock emanating from the tip of the wedge and the bow shock formed in front of the cylinder. Tests were conducted in the Langley Mach 8 variable density tunnel with the cylinder swept at 45° and 60° with respect to the free-stream direction. To eliminate the effects of contamination of the cylinder flow by the wedge boundary layer, the model was detached from the wedge as shown in figure G.11. In this separated configuration, the cylinder was equipped with a small elliptical end plate. The results obtained with the wedge attached and wedge detached were compared with those obtained on the swept cylinder alone. However, with the wedge absent the elliptical end plate was retained as shown in figure G.12.

Bushnell also made measurements on the isolated with the upstream tip (and end plate) aligned with the free-stream flow direction. In this case, the cylinder was swept at 72°. These data are given in reference [13].

G.3.2 Experimental facilities

The Langley Mach 8 variable density tunnel uses air as the test gas and is a blowdown type. It has an axially symmetric nozzle with contoured walls. The calibration of the tunnel was obtained from reference [58] (pages 12, 13) and is presented in figures G.13

to G.15. This shows that the free stream Mach number varies from 7.72 to 7.93 as the absolute stagnation pressure ranges from 2.52x10^5 to 5.0x10^6 N/m^2 whilst free-stream Reynolds number per meter increases from 7.55.10^5 to 1.03.10^7. The tunnel flow duration is approximately 4 seconds.

G.3.3 Model and instrumentation

The model consisted of a sharp flat plate inclined at a 12^o angle to the test section flow. A circular cylinder, 1 inch (0.0254m) in diameter, swept at 45^o and 60^o, was either attached to or just separated from the wedge. However, it is the results for the cylinder in isolation and swept at 60^o that have been considered in the present study (figure G.12). The measurements taken on the same cylinder at 72^o sweep with the upstream tip aligned to the free-stream flow (reference [13]) were also considered. In the latter case, the size of the end plate was reduced so that the protrusion which was originally 0.25 inch (0.635 cm) from the outside of the cylinder (figure G.11), became 0.12 inch (0.305 cm).

Heat transfer and pressure measurements were taken along the attachment-line and at azimuth angles θ of 30^o and 60^o as shown by figure G.16. Two models, identical in geometry were built. The first was equipped with 19 thermocouples and the second model had 19 pressure orifices.

The heat transfer measurements were made with the thin wall heating technique. Steady flow in the working section was established with the model held outside the tunnel. The cylinder was then injected into the test section. With the cylinder at ambient temperature the ratio T_w/T_o varied from 0.48 to 0.39 due to the variation in T_o (see next section).

Bushnell et al. recorded that the time required to move the model through the tunnel wall boundary layer was about 0.05 second and care was taken to remove this transient effect from the data. The heat transfer and pressure measurements which were taken at the same spanwise locations were estimated to be accurate to within ±15% and ±5% respectively.

All the tests were made with the little elliptical end plate fixed to the upstream tip. No roughness elements, such as trip wires, were attached to the cylinder.

G.3.4 Tests conditions and extraction of the heat transfer data

Table B.8 shows the tests conditions considered for the present investigation. For runs 15 to 20 only heat transfer measurements taken at the spanwise station of 5.35 diameters from the tip were used. These measurements are only used in chapter 5 and are called Bushnell60s.

In references [12] and [13], the data is reported in the form of a heat transfer coefficient, h, defined as

$$h = \frac{-\dot{q}_W}{T_{adia} - T_W} \tag{G.2}$$

where h has units of $\left[\frac{BTU}{ft^2.sec.R}\right]$ units. The adiabatic wall temperature, T_{adia} (in Rankine), is related to the recovery factor by

$$r = \frac{T_{adia} - T_{ae}}{T_o - T_{ae}} \tag{G.3}$$

For every run reported in references [12] and [13], the free-stream Reynolds number is specified. Hence, T_o can be found from the tunnel calibration. With T_{ae} evaluated from the infinite swept conditions (see appendix C) and r taken to be 0.85 for laminar flow and 0.89 for transitional, turbulent flow, T_{adia} can be calculated. In reference [58], the variation of $\frac{T_W}{T_o}$ is given for the range of T_o permitted by the tunnel and with the model at room temperature (see figure G.17). Since T_o is known from the tunnel calibration, the wall temperature T_W can be evaluated. This leads, with T_{adia}, to the heat transfer rate $\dot{q}_W$. Transformation of the units was achieved using equations G.4 and G.5.

$$1\,[^oR] = \frac{9}{5}\,[^oK] \tag{G.4}$$

$$1\left[\frac{W}{m^2.sec}\right] = 11353\left[\frac{BTU}{ft^2.sec}\right] \tag{G.5}$$

G.4 Beckwith and Gallagher

G.4.1 Introduction

In 1959 Beckwith and Gallagher [5] conducted a series of tests to determine the effects of sweep angle on the heat transfer and pressure distributions along the attachment-line of a circular cylinder. The investigation was carried in *"one of the blowdown tunnels of the Gas Dynamics Branch at the Langley Reserach Center"* at a fixed Mach number of 4.15. The model was swept from 0^o to 60^o and the free-stream Reynolds number per metre ranged from approximately $3.5x10^7$ to $14x10^7$. Internal cooling of the model was used to give $\frac{T_W}{T_O}$ ratios varying from 0.92 to 0.88.

G.4.2 Experimental facilities

The tunnel used air as the free-stream gas and had a conventional two dimensional nozzle with a test section of 12 inches in width (30.48cm) and 13 inches in height (33.02cm). The Mach number was fixed at 4.15 ($\pm$ 0.03) and the maximum running time varied from 20 to 40 minutes depending on the stagnation conditions. The tunnel calibration obtained from reference [5], page 42, is given in figures G.18 and G.19. Note that it is not specified in reference [5] which tunnel of the Gas Dynamics Branch at the Langley Research Center was used for the experiments.

G.4.3 Model and instrumentation

The model was a circular cylinder, 1.115 inches (2.8321cm) in diameter, made from stainless steel and equipped with three heat transfer gauges plus two pressure orifices. Figure G.20 shows the relevant model dimensions and their variation with sweep angle (0^o, 10^o, 20^o, 40^o and 60^o). The locations at which the heat transfer and static pressure measurements were made (designated as stations 1, 2 and 3 for the heat transfer) are shown in this figure and are summarised in table B.9. Heat transfer was obtained at stations 1, 2 and 3 by using chromel alumel thermocouples located along the inner surface of the model (with a known thermal conductivity of the steel).

The model was cooled by passing Varsol (hydrocarbon solvent, boiling point 340^oK to 370^oK) through the cylinder. The temperature of the coolant was adjusted by pumping it through a cooler (alcohol and dry-ice) or a heater (steam) or any combination of each. Hence, the Varsol temperature could be varied from approximately 230^oK to 340^oK. This

gave wall-to-stagnation temperature ratios between 0.88 and 0.92 (see figure 2 of reference [5]).

No roughness elements were applied along the attachment-line. However the cylinder was always equipped with a small streamwise end plate which extended ahead of the model. The extension distance is also given in figure G.20 for all sweep angles, whilst the width of the end plate was constant for all configurations.

G.4.4 Tests conditions and extraction of experimental data

Tests were conducted by first starting the tunnel with the desired stagnation conditions. The temperature of the coolant was then set. During the run the model was rotated by means of an actuator and pulley system so that a complete chordwise survey of the heat transfer and pressure could be obtained. Two sets of measurements were made at each sweep angle. The first was performed at approximately constant tunnel conditions whilst the model surface temperature was varied by changing the coolant temperature. The second involved constant wall temperature over a range of stagnation pressures to obtain the variation of the Nusselt number with Reynolds number.

Tables B.10 and B.11 show the runs undertaken and considered in the present investigation. CFD calculations were performed for run 1 ($\Lambda = 60°$) and run 15 ($\Lambda = 40°$) only. It was found that at sweep angles from 20° or less, the bow shock was detached from the upstream tip of the cylinder and this gave severe computational problems.

The heat transfer rate at the wall, $\dot{q}_W$, is of primary importance for the present in-

vestigation. However, the authors chose to present their results in terms of the Nusselt number as defined below.

$$Nu = \frac{-\dot{q}_W.D}{(T_r - T_W).k_\infty} \tag{G.6}$$

with k_∞ being the free-stream thermal conductivity. Since only a little information is provided in reference [5], the heat transfer rate itself cannot be evaluated from equation G.6. However, the Stanton number can be related to the Nusselt number as follows

$$Nu = \underbrace{\left[\frac{\dot{q}_W}{\rho_{ae}.V_{ae}.Cp.(T_r - T_W)}\right]}_{St_{ae}} \cdot \underbrace{\left[\frac{\rho_\infty.D.Q_\infty}{\mu_\infty}\right]}_{Re_D} \cdot \underbrace{\left[\frac{\mu_\infty.Cp}{k_\infty}\right]}_{Pr} \cdot \underbrace{\left[\frac{\rho_{ae}.V_{ae}}{\rho_\infty.Q_\infty}\right]}_{Correction} \tag{G.7}$$

hence

$$St_{ae} = \frac{Nu}{Re_D.Pr.\left(\frac{\rho_{ae}.V_{ae}}{\rho_\infty.Q_\infty}\right)} \tag{G.8}$$

Therefore using a Prandtl number of 0.7, the Nusselt number and Re_D given for every run in reference [5] and the CFD to provide $\frac{\rho_{ae}.V_{ae}}{\rho_\infty.Q_\infty}$, the Stanton number can be calculated.

G.5 Jones

G.5.1 Introduction

In 1964 Jones [40] was investigating the problem of interference effects on heat transfer to aerodynamic control surfaces of hypersonic vehicles. Specifically, he studied the problem of the impingement of the body shock wave onto the control surfaces and the corner interference between control surfaces and body surface. Jones carried out experimental

tests in the NASA Langley Mach 6, low-density tunnel on a swept fin with a cylindrical leading edge mounted on a streamwise flat plate with a sharp leading edge as shown by figure G.21.

G.5.2 Experimental facilities

The NASA Langley Mach 6, low-density tunnel is a blow down facility using air as the test gas. It has a test section of approximately 30.48cm (12 inches) by 35.56cm (14 inches). The stagnation pressure varies from 0 to approximately $4.14.10^6 N/m^2$ (600 psig), with stagnation temperatures ranging from $422^o K$ to about $610^o K$. Run time can vary from 1 minute to continuous operation depending on the total pressure. The tunnel calibration, extracted from references [40] and [41], is shown in figures G.22 and G.23. At a fixed stagnation pressure, the maximum variation of the free-stream Mach number throughout the working section was recorded to be only $\pm 1.2\%$

The tunnel is equipped with a model injection device mounted directly over the working section and the model was strut mounted to a plate which was moved up and down very rapidly by a pneumatic piston. When the model was in the tunnel, the plate is flush with the top wall of the working section. Since the entire injection device is enclosed in a sealed box kept at the working section static pressure, the tunnel can be run with the model in, or out of the test section.

G.5.3 Model and instrumentation

Three sets of models, identical in geometry (approximately 0.027m in diameter ; 1.06 inch) but with different instrumentation were manufactured. The first contained thermocouples, the second had pressure tappings and the last was only used for flow visualisation. Heat transfer and pressure measurements were made on the flat plate, along the fin attachment-line and around the fin leading edge. Figure G.24 shows the instrumentation location on the entire model and table G.5.4 gives the thermocouples and pressure orifices location along the fin attachment-line.

No roughness elements were added to the attachment-line and the flat plate was always aligned to the free-stream flow.

G.5.4 Tests conditions and extraction of the heat transfer data

Heat transfer data were obtained by the thin skin technique. The tunnel was started and brought to the desire testing conditions. The model was then injected and the temperature versus time signals recorded. Although the model was kept in the working section for about 5 seconds, measurements were only made during the first 0.1 to 1.1 seconds. It has been estimated in reference [40] that the time required for the free-stream flow to become steady after the model first entered the airstream was about 0.05 second.

Heat transfer data are reported in reference [40] in the form of a heat transfer coefficient h (see equation G.9) non-dimensionalised by the theoretical value of h at zero sweep

(equation G.10) i.e. $h/h_{\Lambda=0}$. The definitions of h and $h_{\Lambda=0}$ being

$$h = \frac{-\dot{q}_W}{T_r - T_W} \tag{G.9}$$

$$h_{\Lambda=0} = \frac{-\dot{q}_W}{(T_{adiaW} - T_W)} = 0.57.Pr^{-0.6}.(\rho_{ae}.\mu_{ae})^{\frac{1}{2}}.\left(\frac{dU_e}{dX}\right)^{\frac{1}{2}}.\frac{\gamma R}{\gamma - 1} \tag{G.10}$$

where $Pr = 0.72$. The chordwise velocity gradient $\frac{dU_e}{dX}$ in equation G.10 was evaluated from the equations shown in appendix C with $\Lambda = 0$. Using the ratios of the temperature and static pressure (using equations in appendix C with $\Lambda = 0$), the density ratio could be obtained:

$$\frac{\rho_{ae}}{\rho_\infty} = \frac{P_{ae}}{P_\infty}.\frac{T_\infty}{T_{ae}} \tag{G.11}$$

The free-stream Reynolds numbers are given for every run. Using the tunnel calibration, the stagnation conditions can be determined, leading to the free-stream conditions via equations G.12 and G.13.

$$\frac{T_o}{T_\infty} = 1 + \left(\frac{\gamma - 1}{2}\right) M_\infty^2 \tag{G.12}$$

$$\frac{P_{o\infty}}{P_\infty} = \left[1 + \left(\frac{\gamma - 1}{2}\right) M_\infty^2\right]^{\frac{\gamma}{\gamma - 1}} \tag{G.13}$$

The free-stream density was then evaluated from the equation of state. Using equation G.11 the density along the attachment-line at the boundary layer edge ρ_{ae} was obtained. Finally the viscosity term present in equation G.10 was calculated from Sutherland's law.

Having obtained $h_{\Lambda=0}$, the heat transfer coefficient h for each run and station was evaluated. Using equation G.9, the heat transfer rate at the wall, $\dot{q}_W$, was calculated by assuming a wall temperature of 300K. The recovery temperature was evaluated (equation G.14) by always assuming a laminar recovery factor i.e.

$$r = \left(\frac{T_r - T_{ae}}{T_o - T_{ae}}\right) = 0.85 \tag{G.14}$$

The stagnation temperature was taken from the tunnel calibration and T_{ae} from the infinite swept conditions (appendix C). Hence T_r could be calculated.

Table B.13 shows the conditions of the tests achieved by Jones and considered in the present study. Note that CFD was only performed on Run 2 (see table B.2).

G.6 Figures

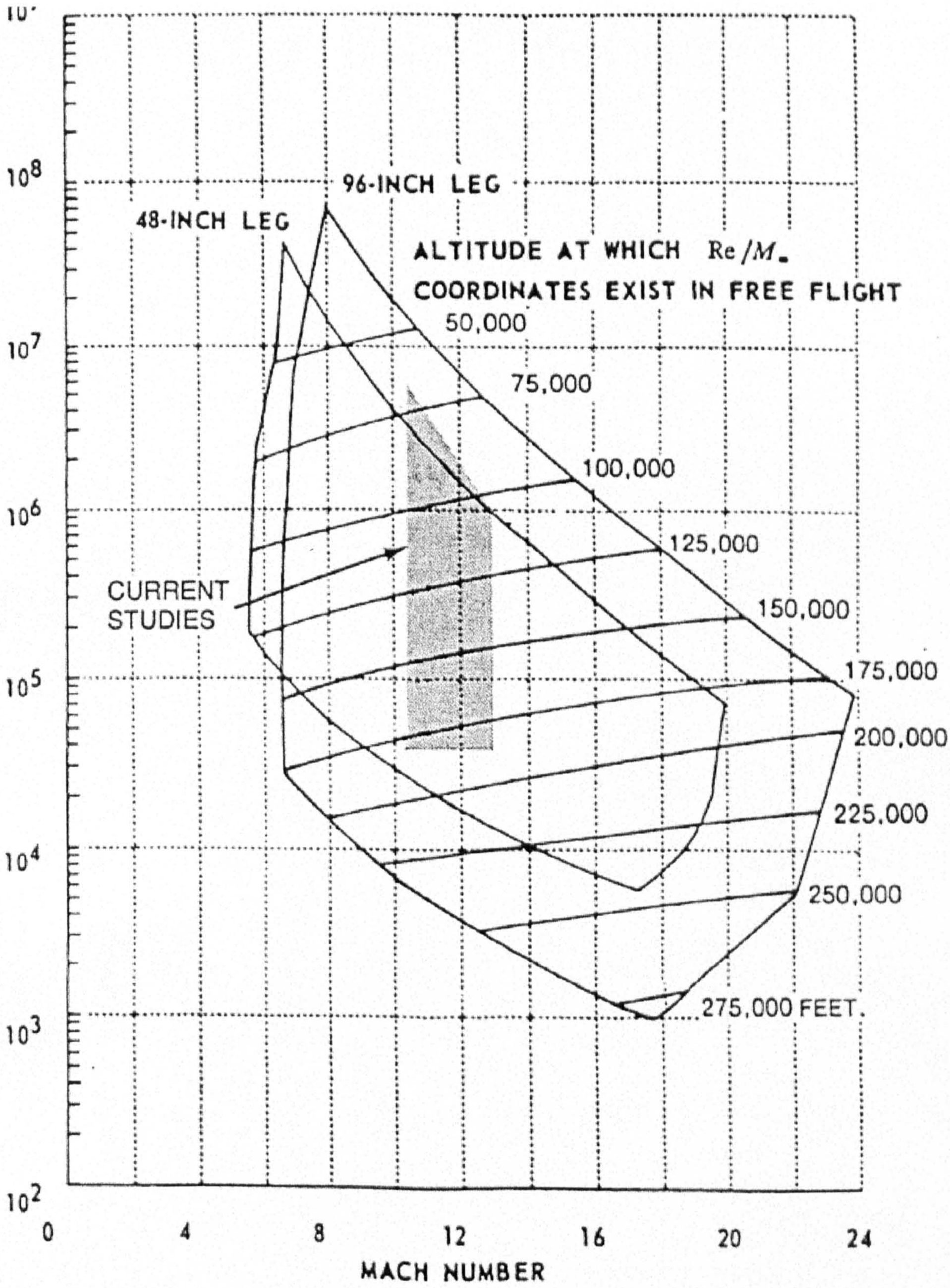

Figure G.1: Range of free-stream conditions in the Calspan shock tunnel [37] [38].

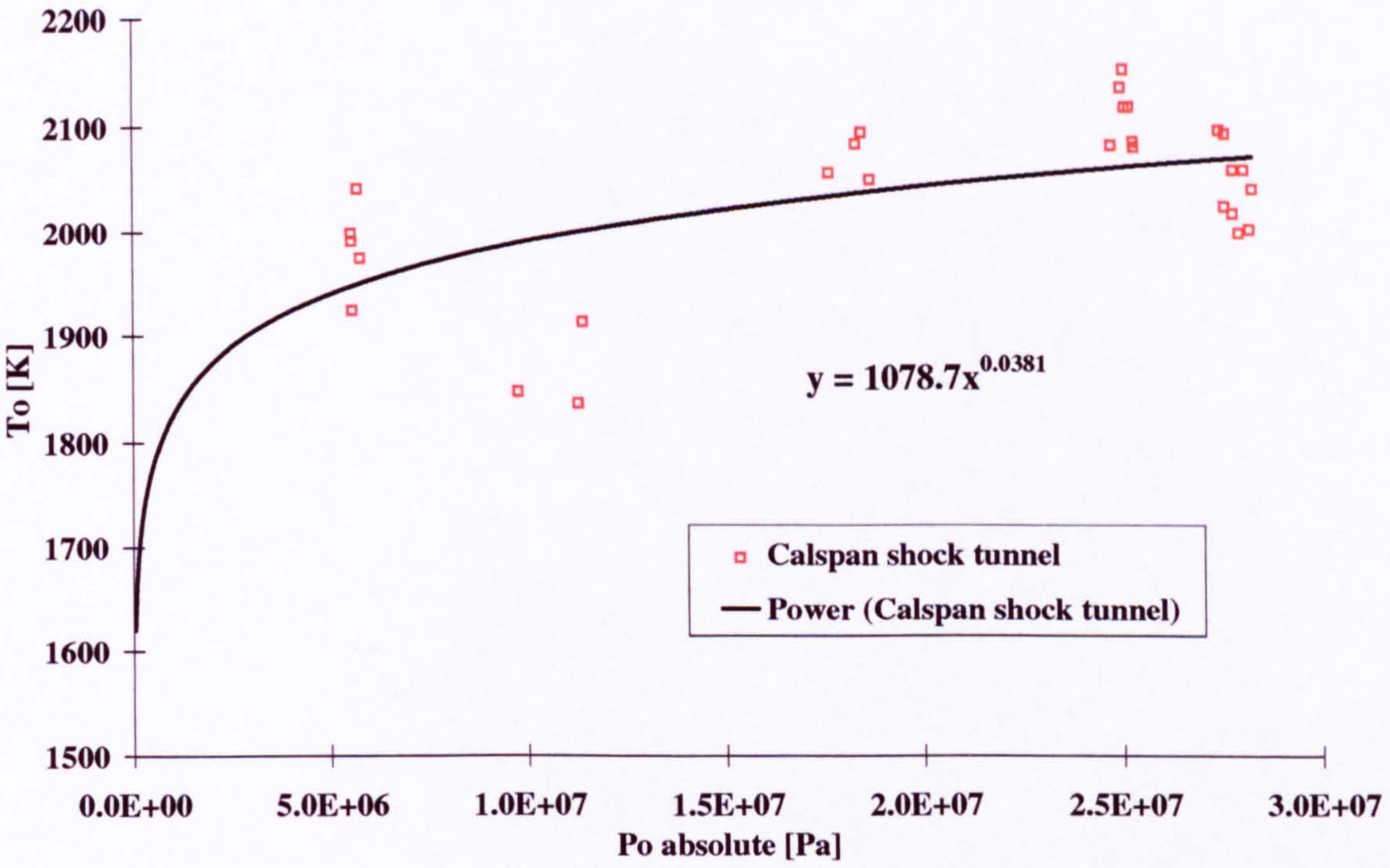

Figure G.2: Stagnation temperature variation with stagnation pressure (Calspan shock tunnel calibration after [37] [38]).

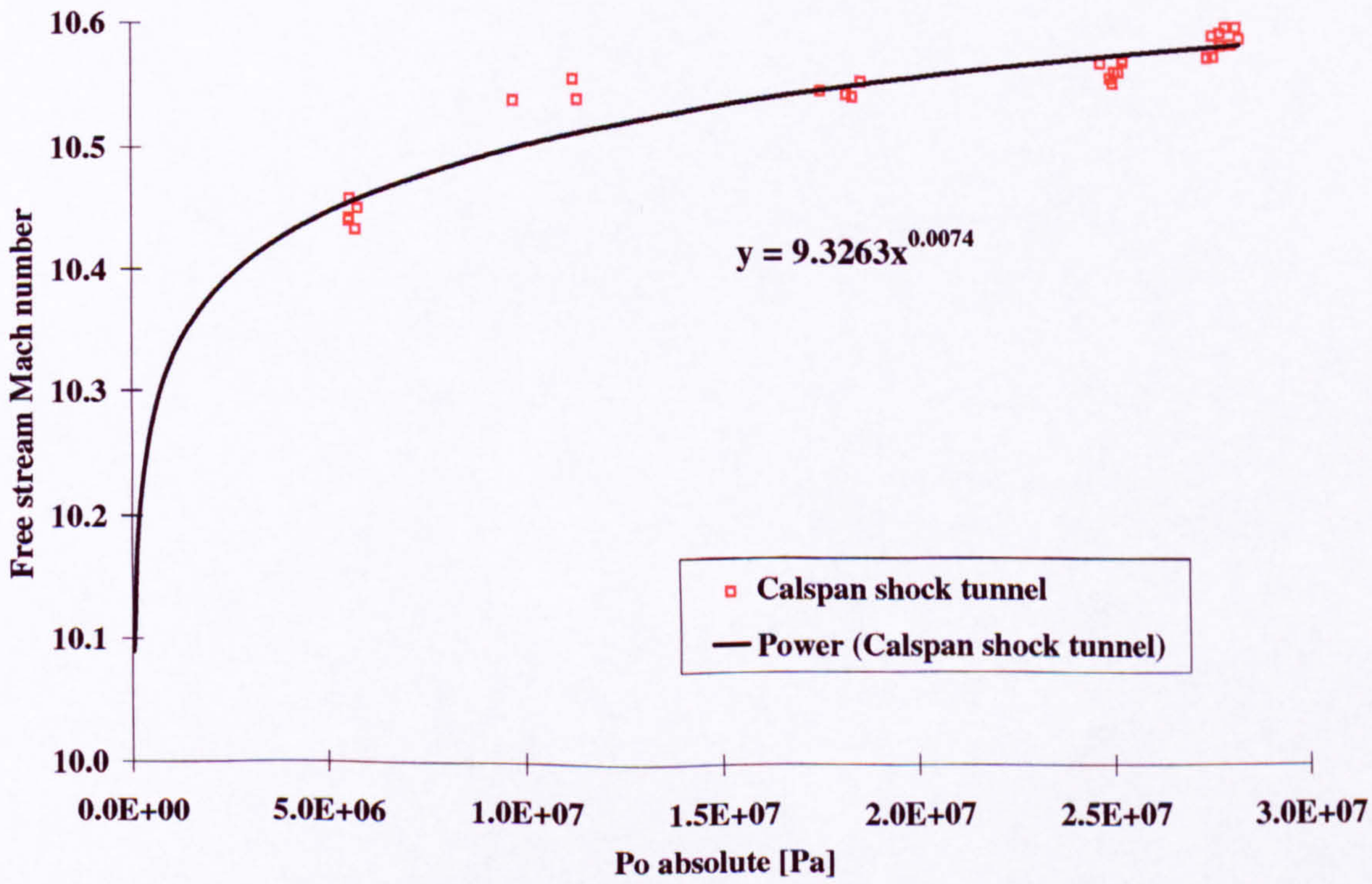

Figure G.3: Mach number variation with stagnation pressure in the Calspan shock tunnel [37] [38].

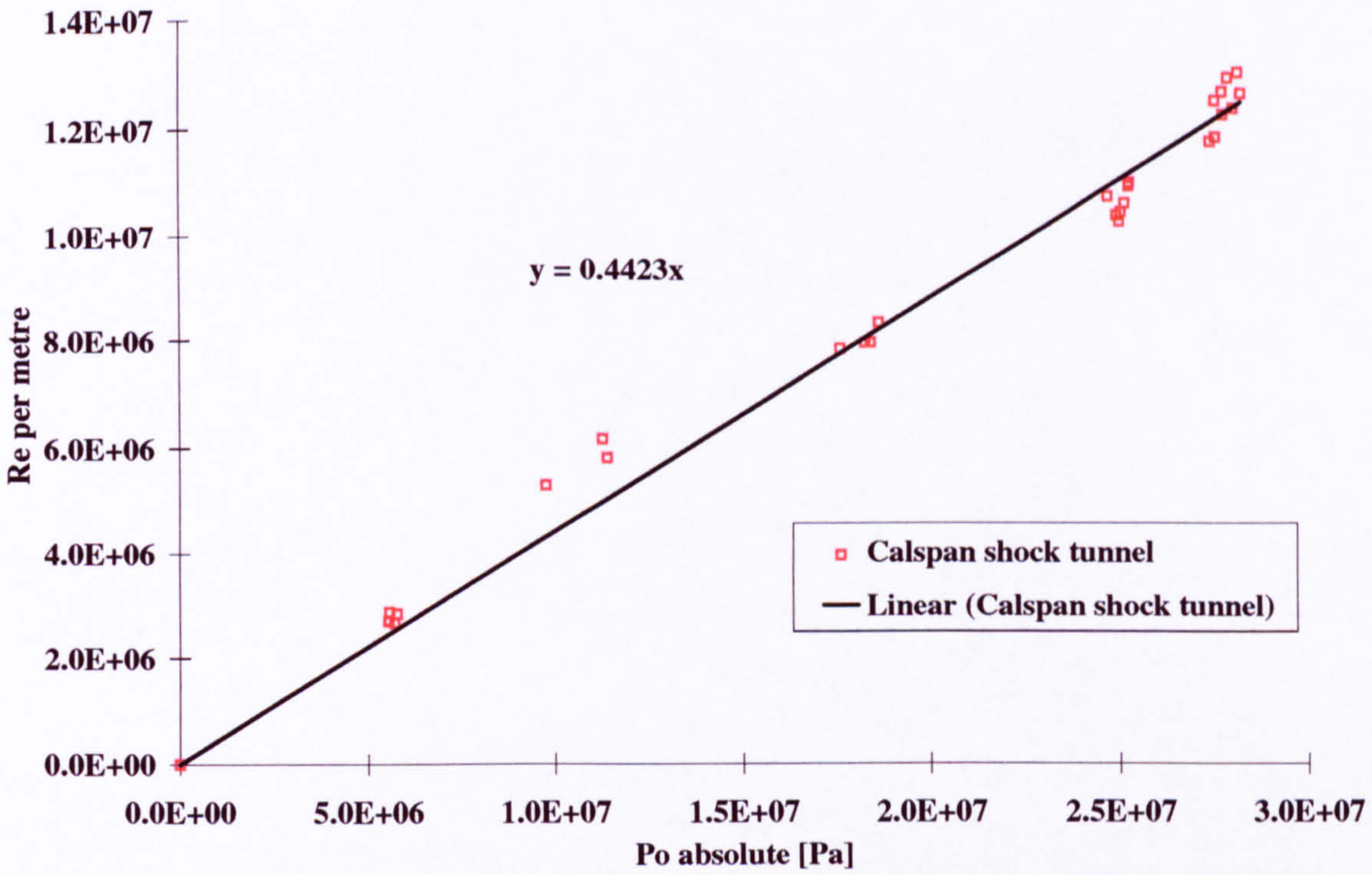

Figure G.4: Stagnation Pressure variation with Reynolds number (Calspan shock tunnel calibration after [37] [38]).

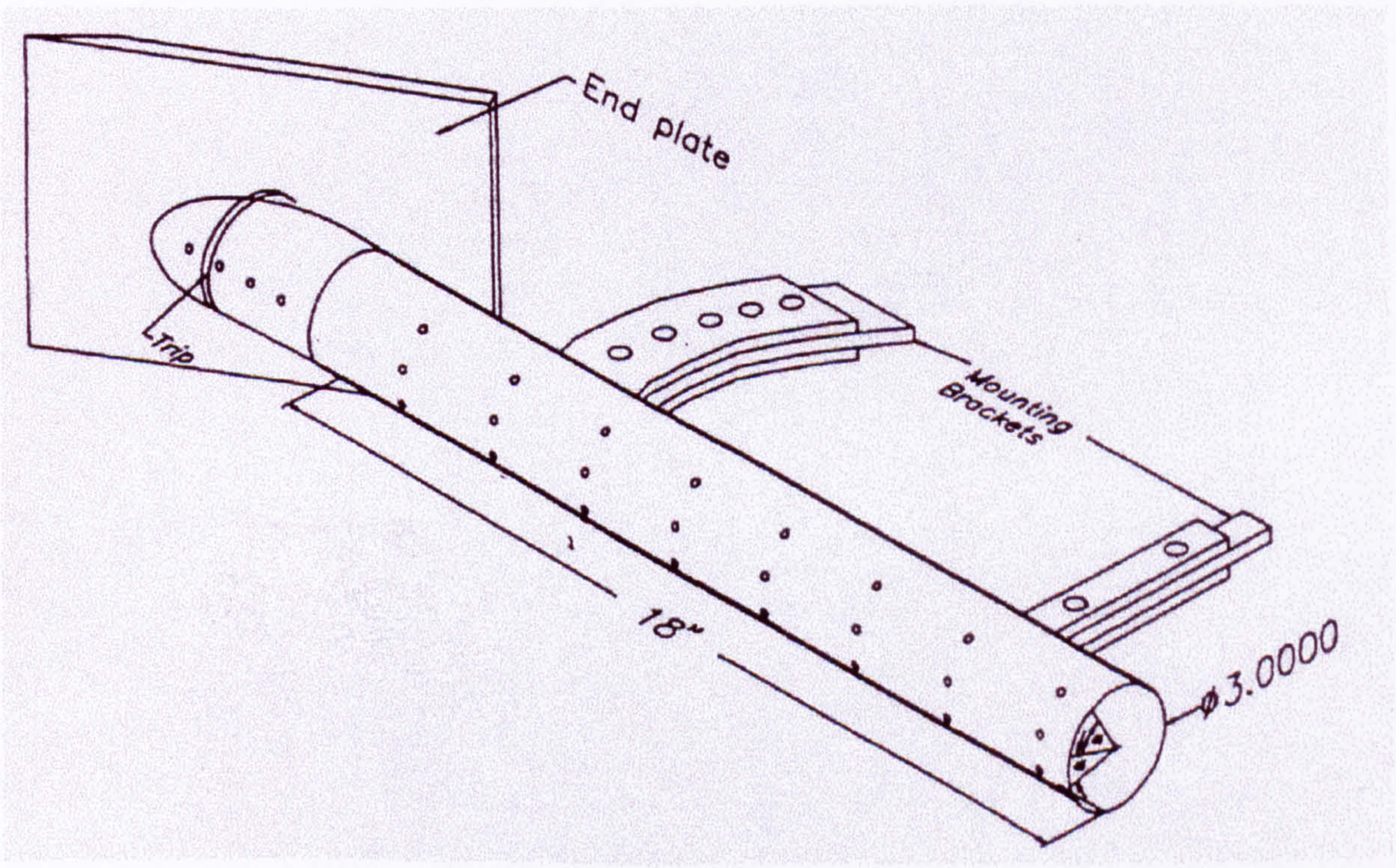

Figure G.5: Swept cylinder model used by Holden et al. [37] [38]. (All dimensions in inches).

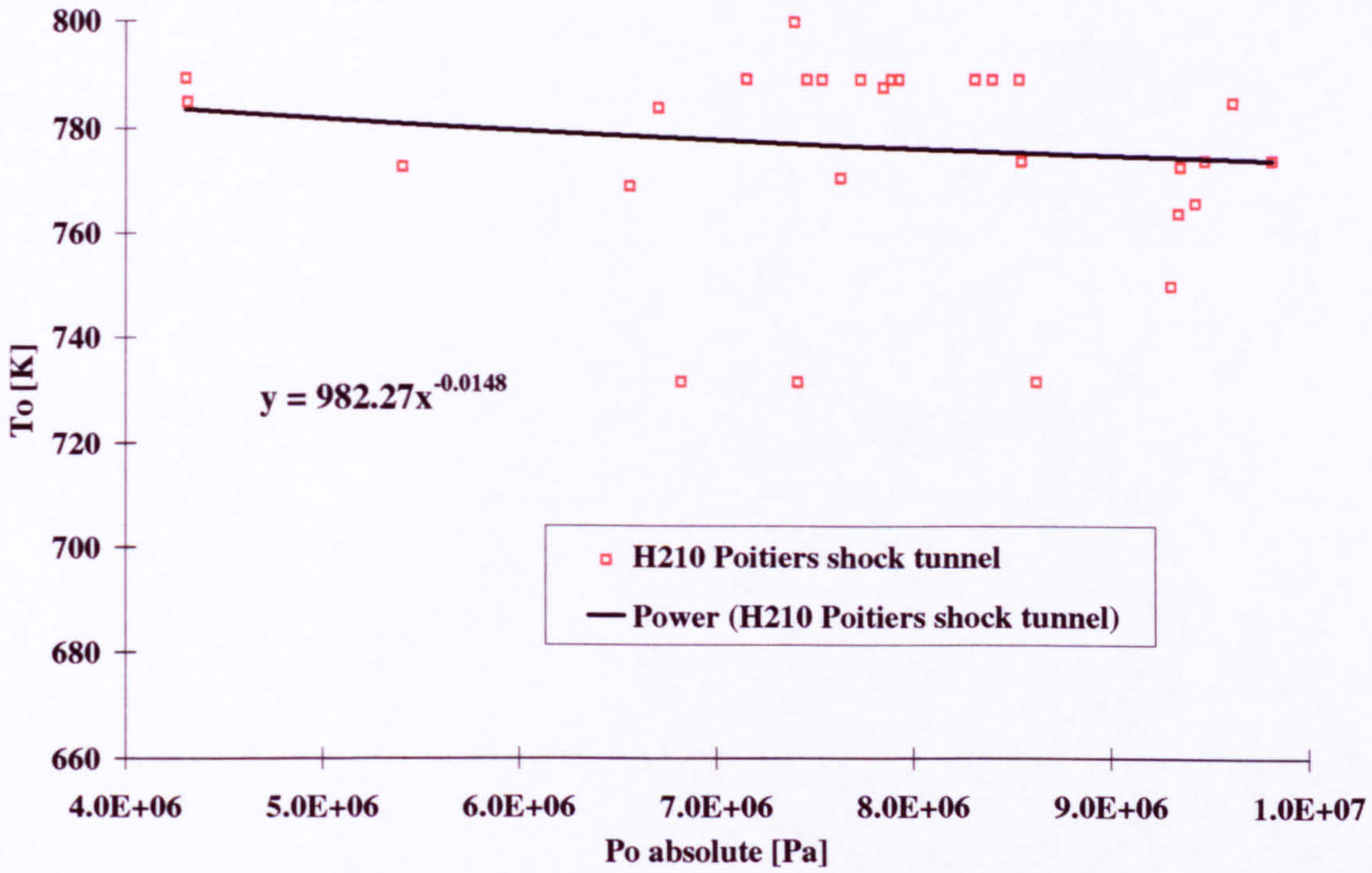

Figure G.6: Stagnation temperature variation with stagnation pressure in the Poitiers University H210 hypersonic tunnel after [6] [35]. (Mach 7.14 nozzle fitted).

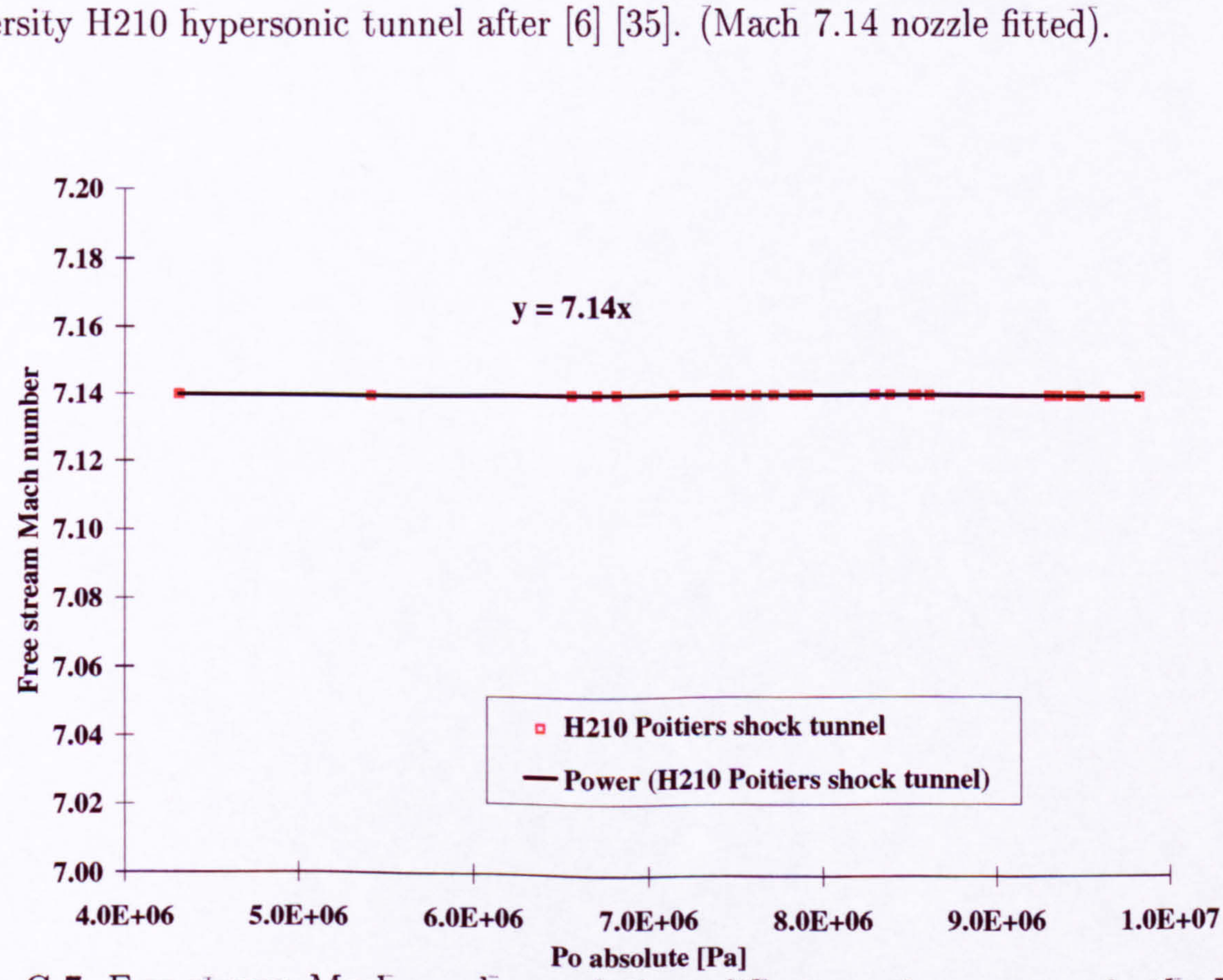

Figure G.7: Free-stream Mach number variation with stagnation pressure in the Poitiers University H210 hypersonic tunnel after [6] and [35]. (Mach 7.14 nozzle fitted).

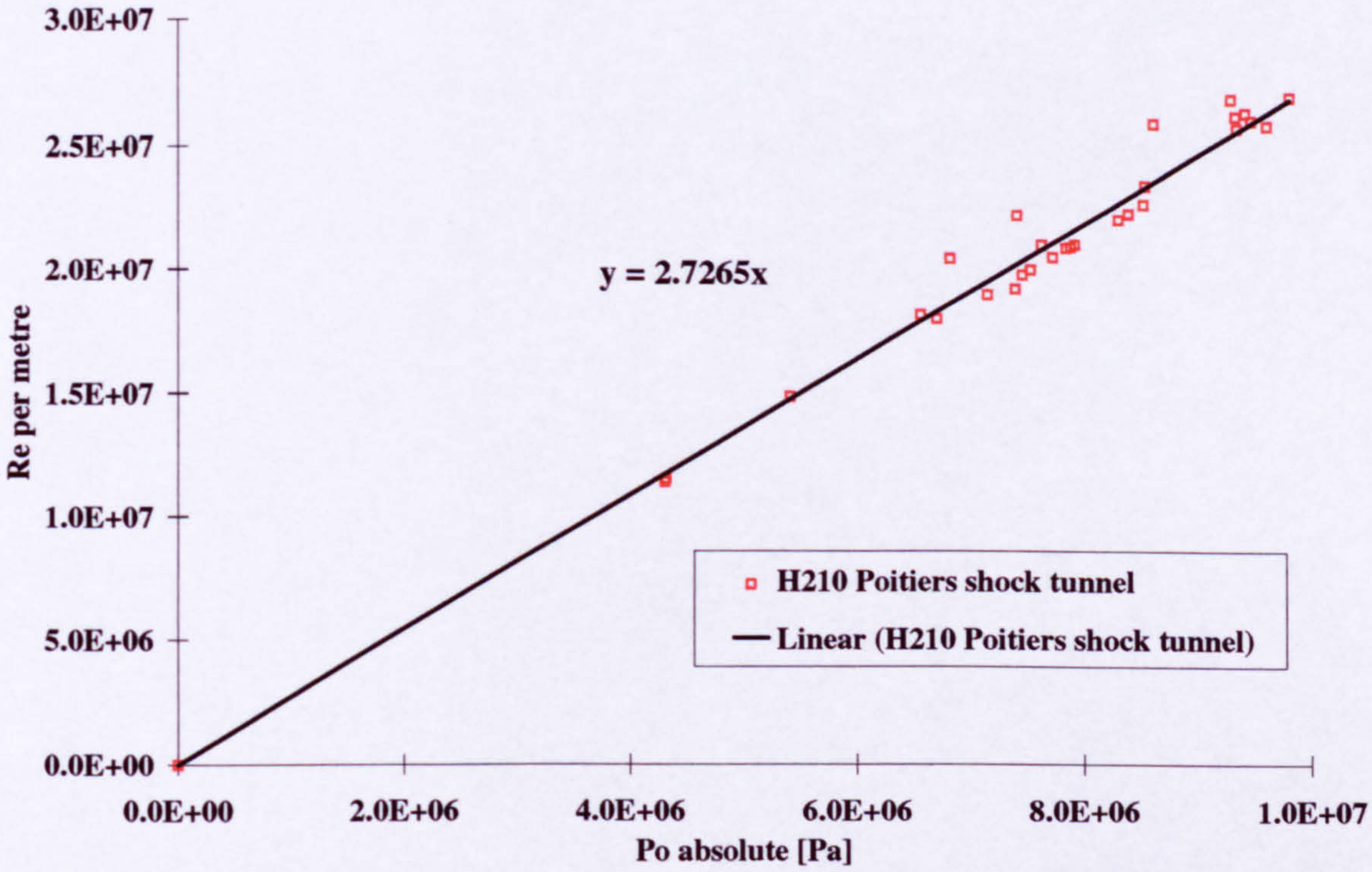

Figure G.8: Stagnation pressure variation with free-stream Reynolds number in the Poitiers University H210 hypersonic tunnel after [6] and [35]. (Mach 7.14 nozzle fitted).

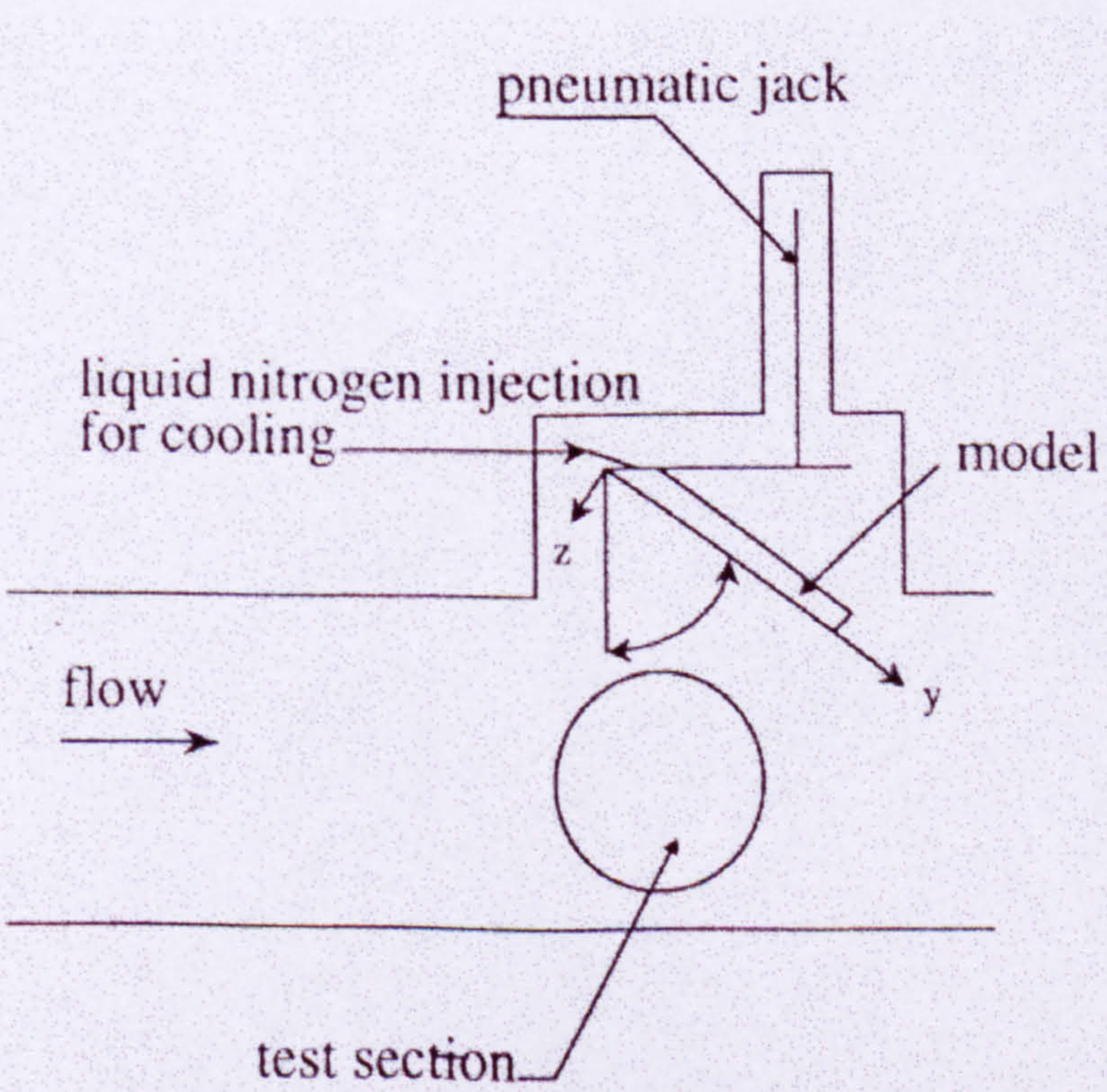

Figure G.9: Experimental set-up in the Poitiers H210 hypersonic tunnel [6], [25] and [35].

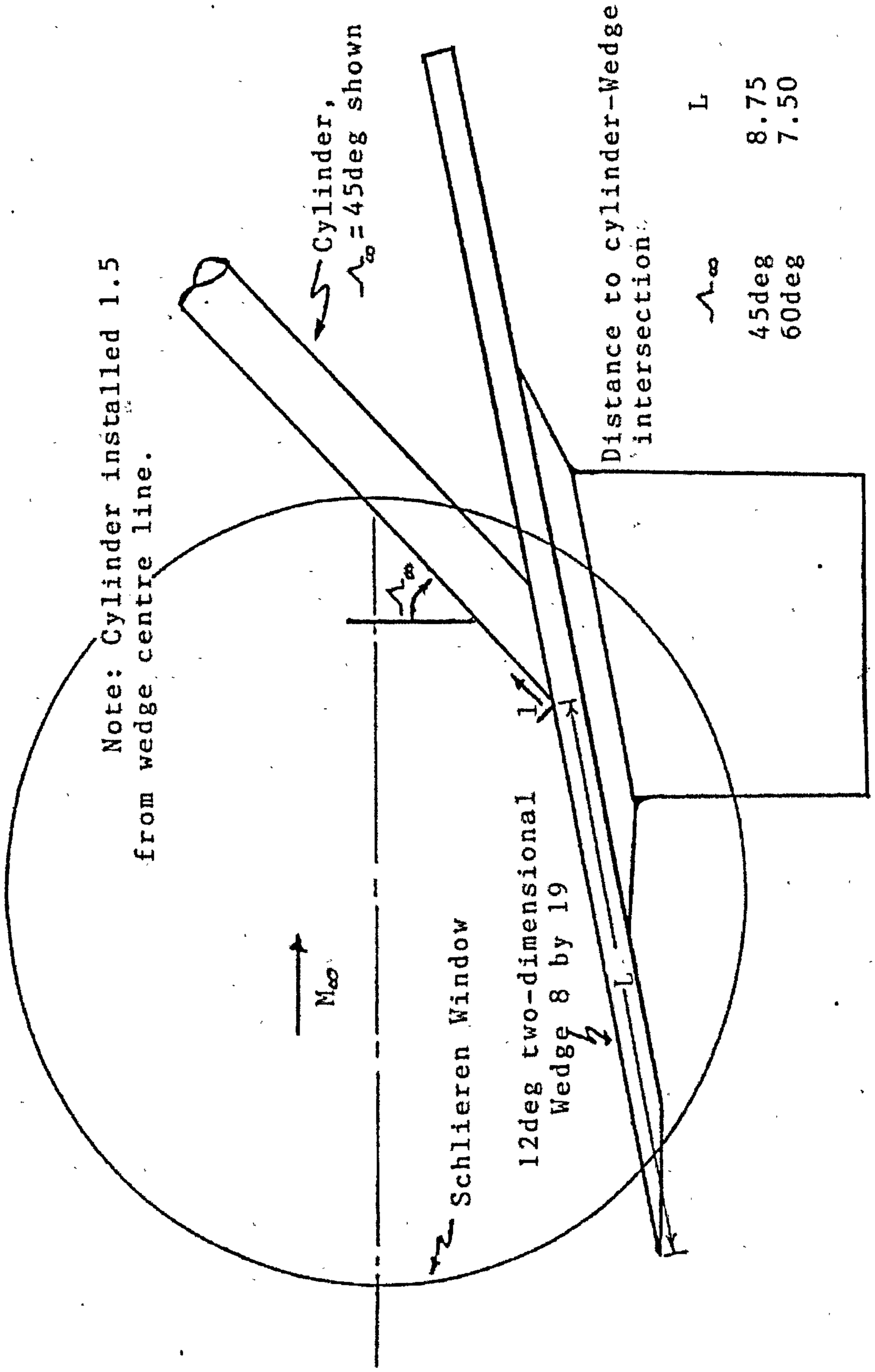

Figure G.10: Model configuration used by Bushnell [12]. Cylinder and wedge attached (all length made non-dimensional with the cylinder diameter).

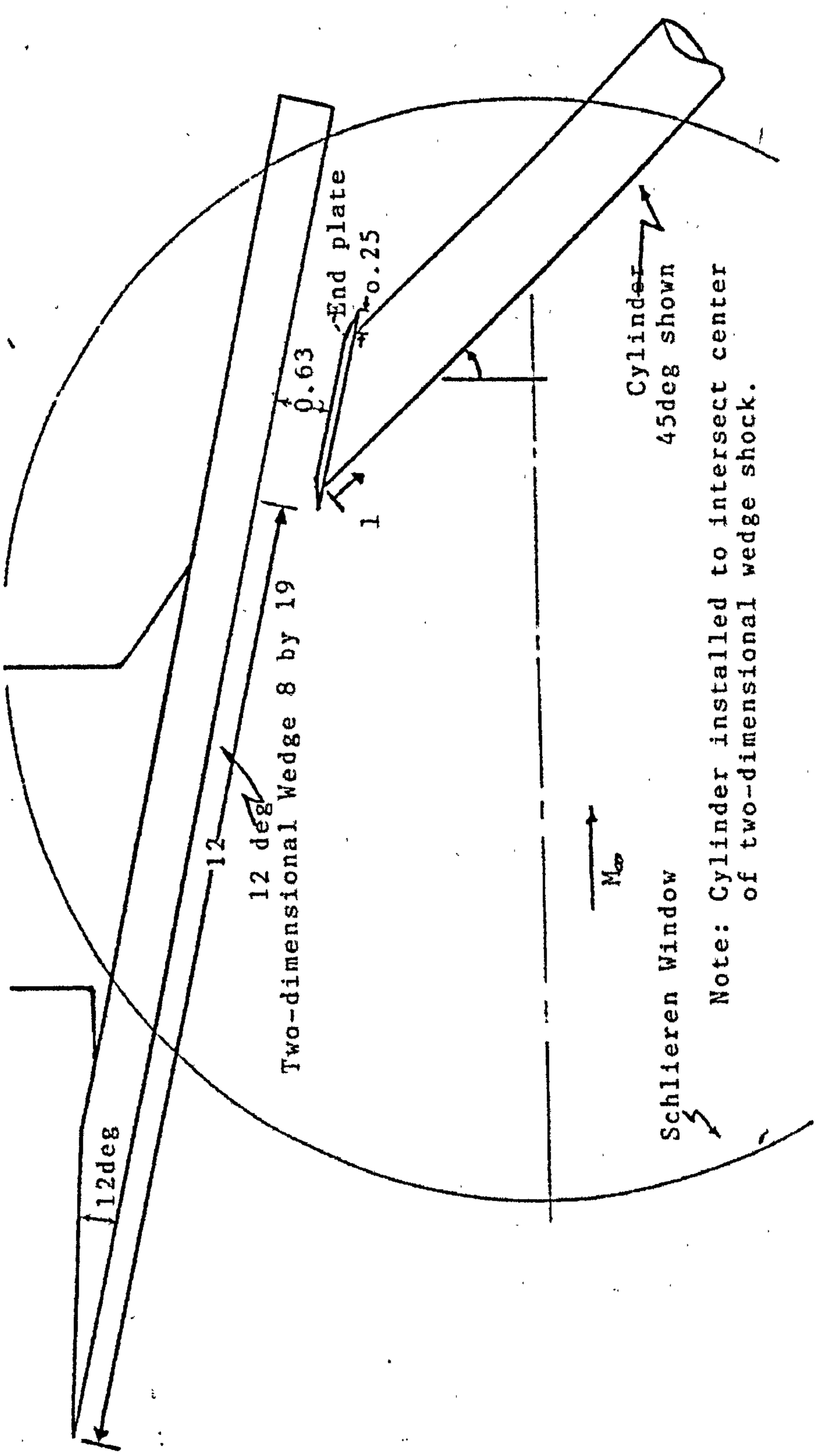

Figure G.11: Test configuration used by Bushnell [12]. Cylinder and wedge separated (all length made non-dimensional with the cylinder diameter).

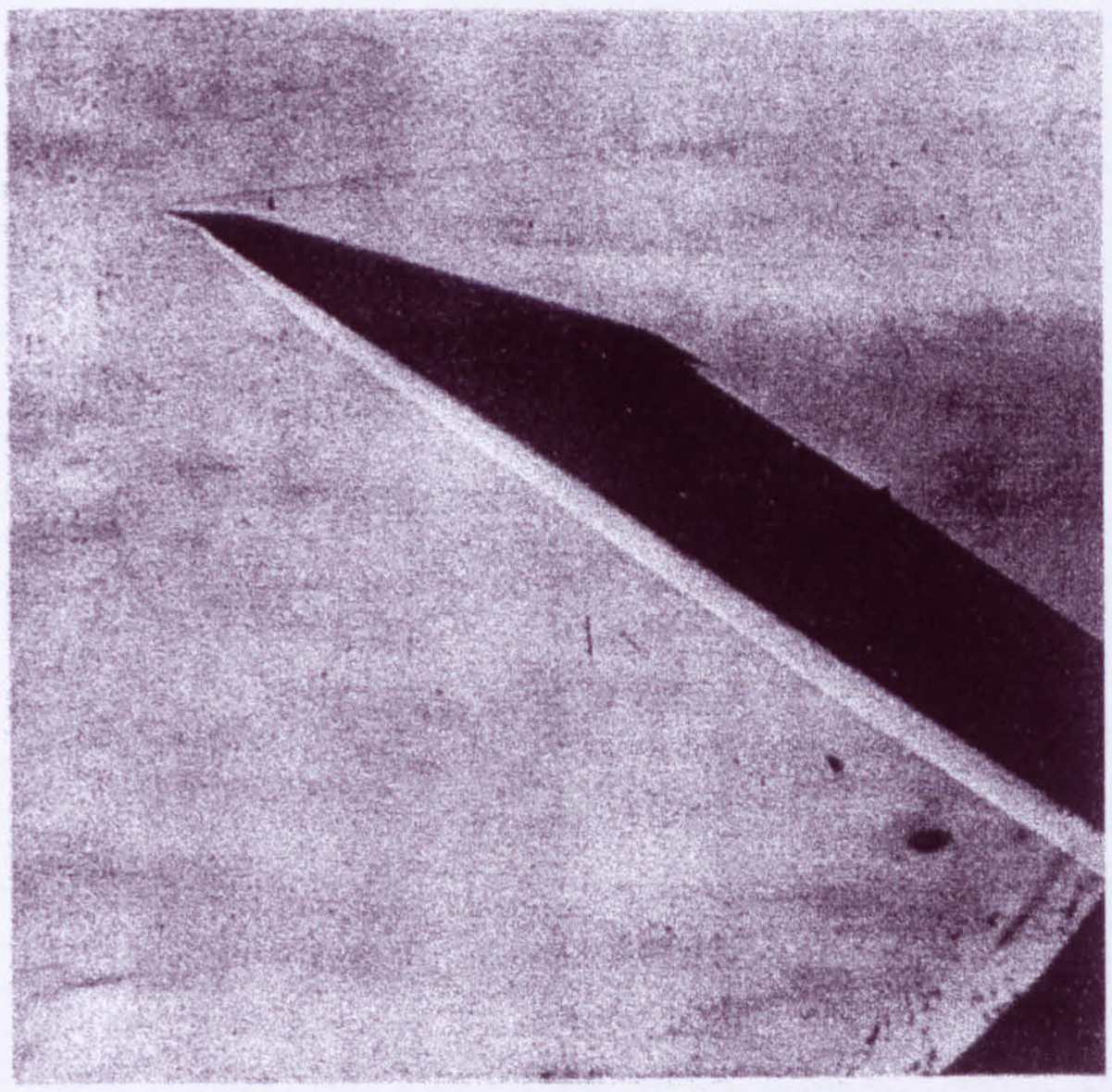

Figure G.12: Schlieren picture of the 60° swept cylinder used by Bushnell [12]. (Cylinder alone with little end plate).

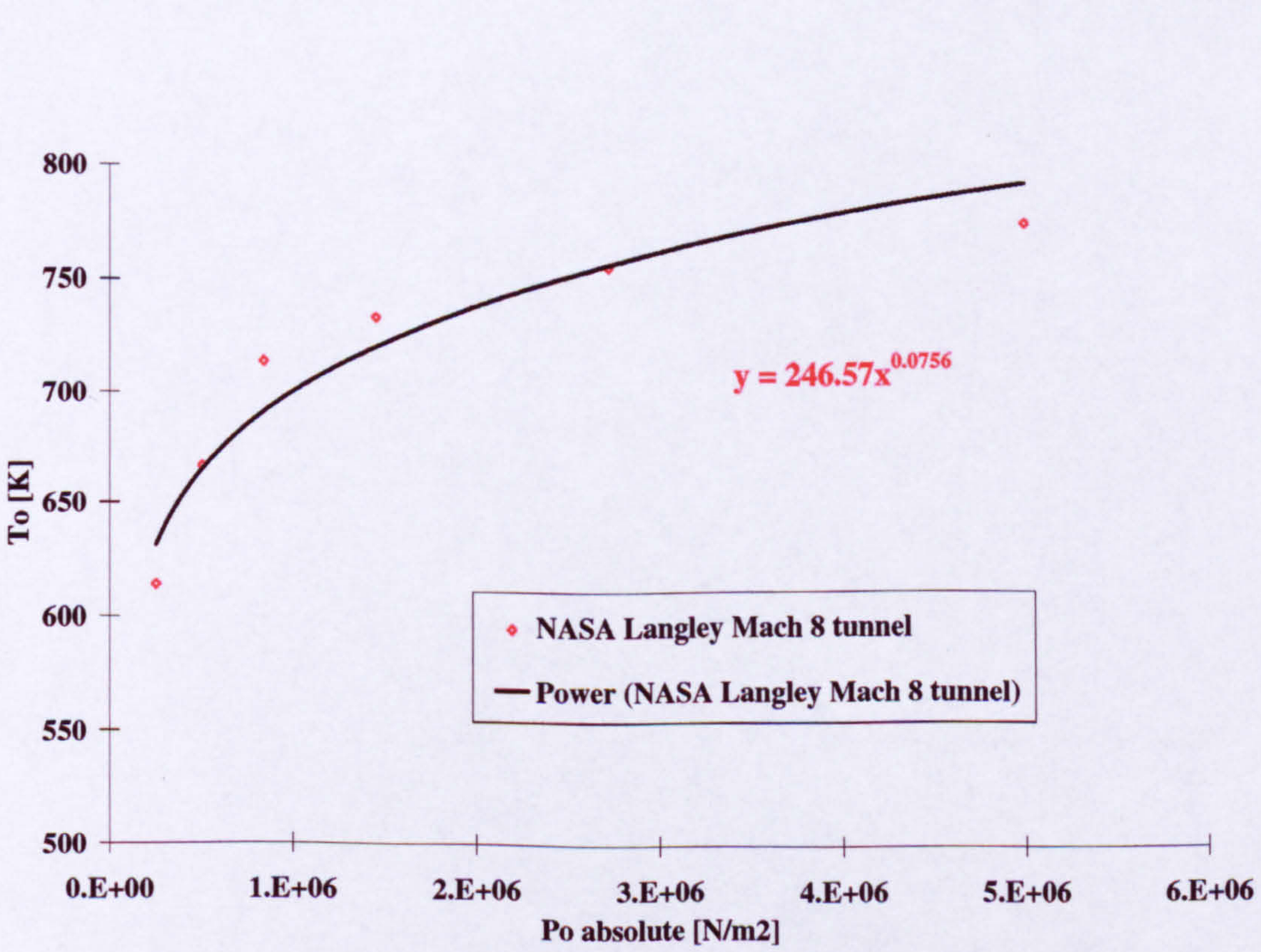

Figure G.13: Calibration of the Langley Mach 8 variable density tunnel. Stagnation temperature vs stagnation pressure after [58].

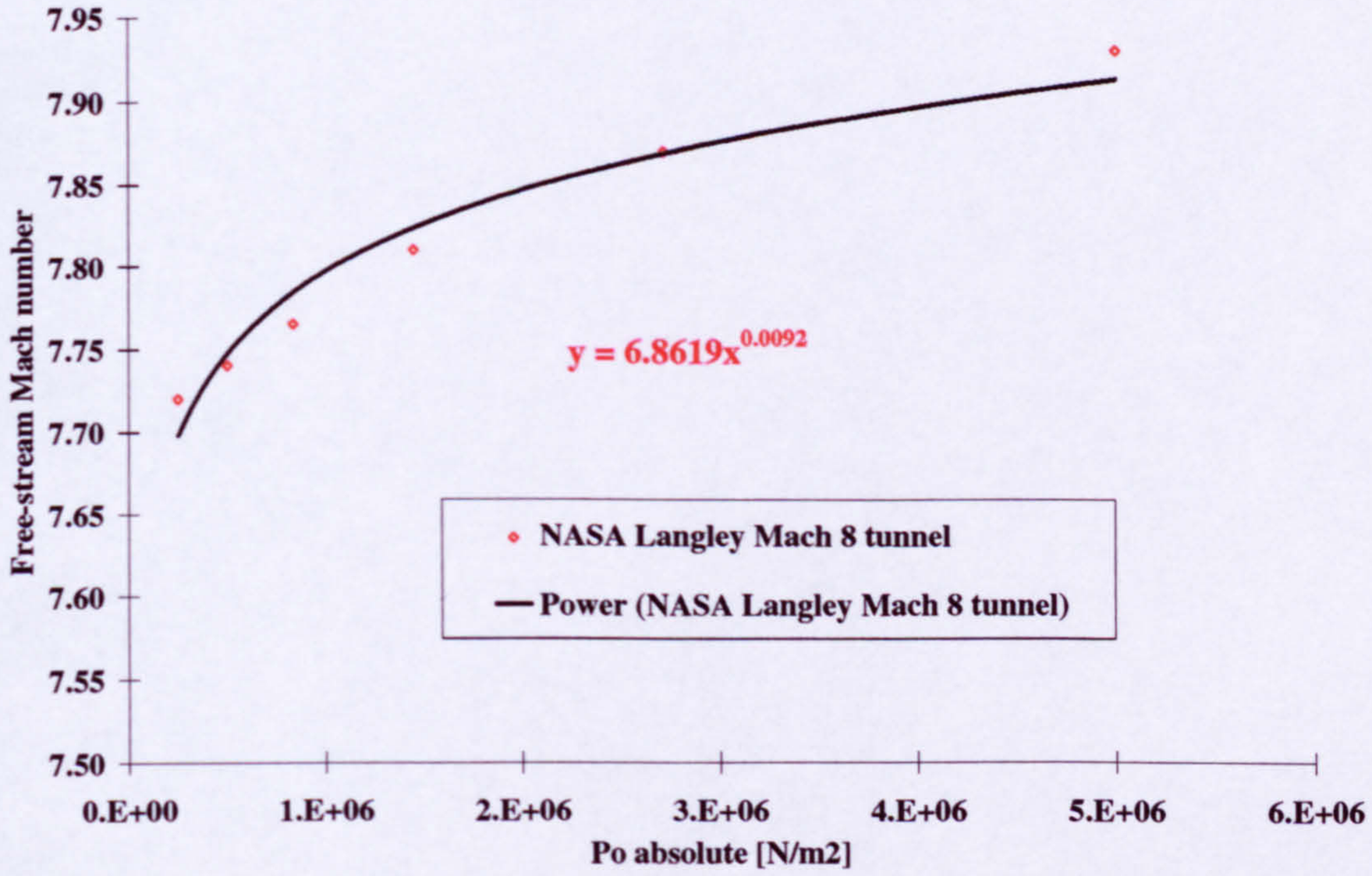

Figure G.14: Free-stream Mach number variation with stagnation pressure in the Langley Mach 8 variable density tunnel after [58].

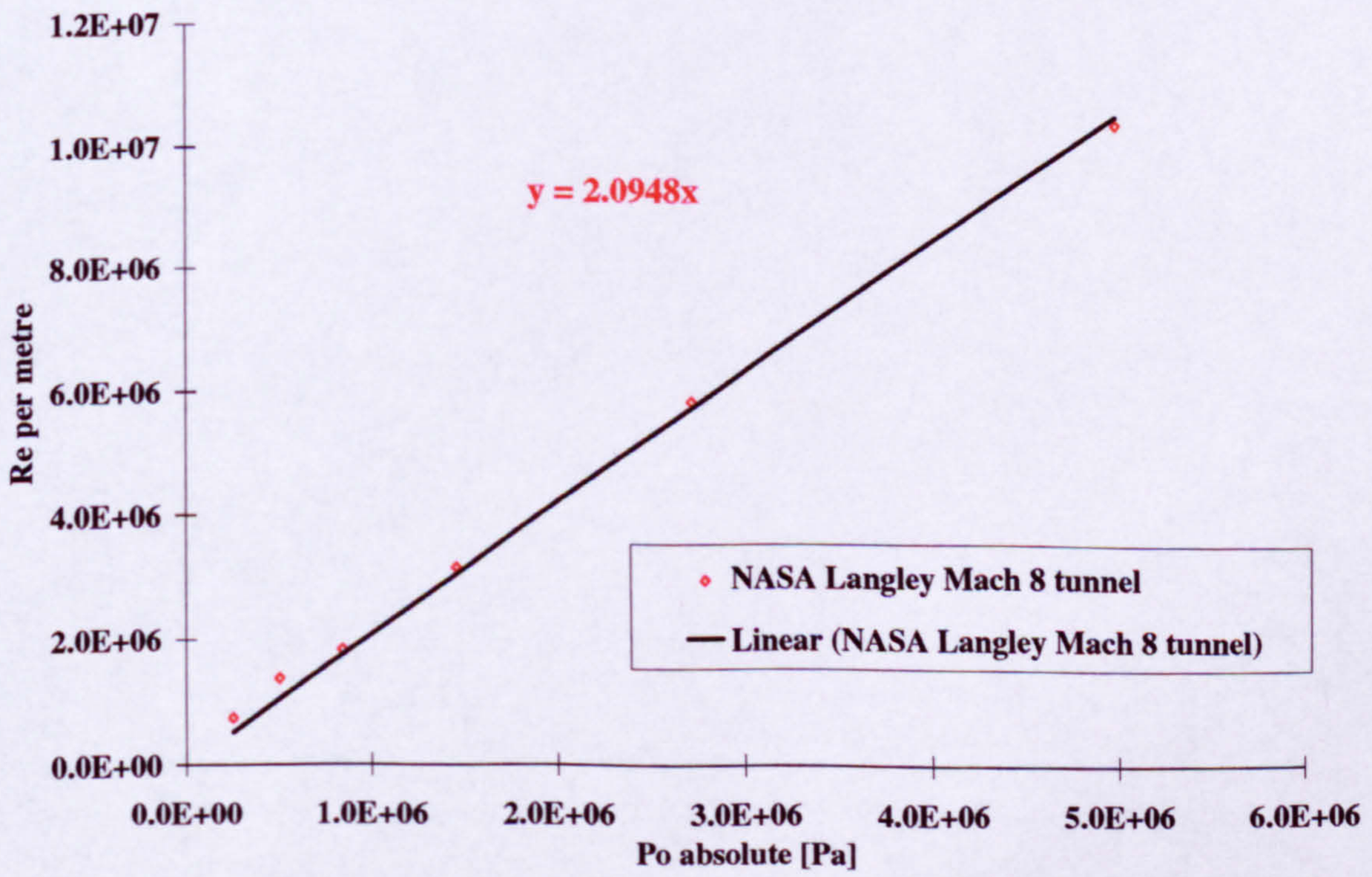

Figure G.15: Free-stream Reynolds number variation with stagnation pressure in the Langley Mach 8 variable density tunnel [58].

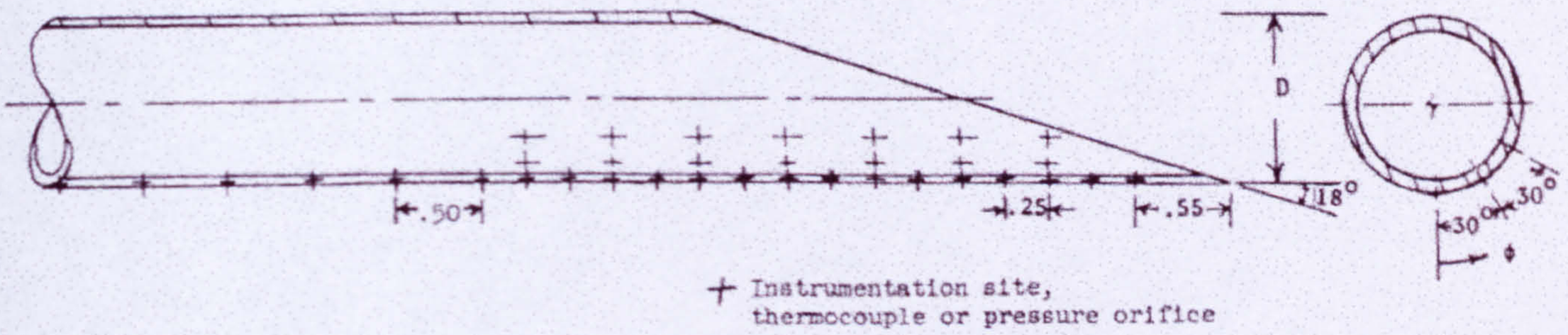

Figure G.16: Heat transfer and pressure instrumentation location on the 60° swept cylinder used by Bushnell [12] ; Cylinder alone ; length made non-dimensional with the cylinder diameter.

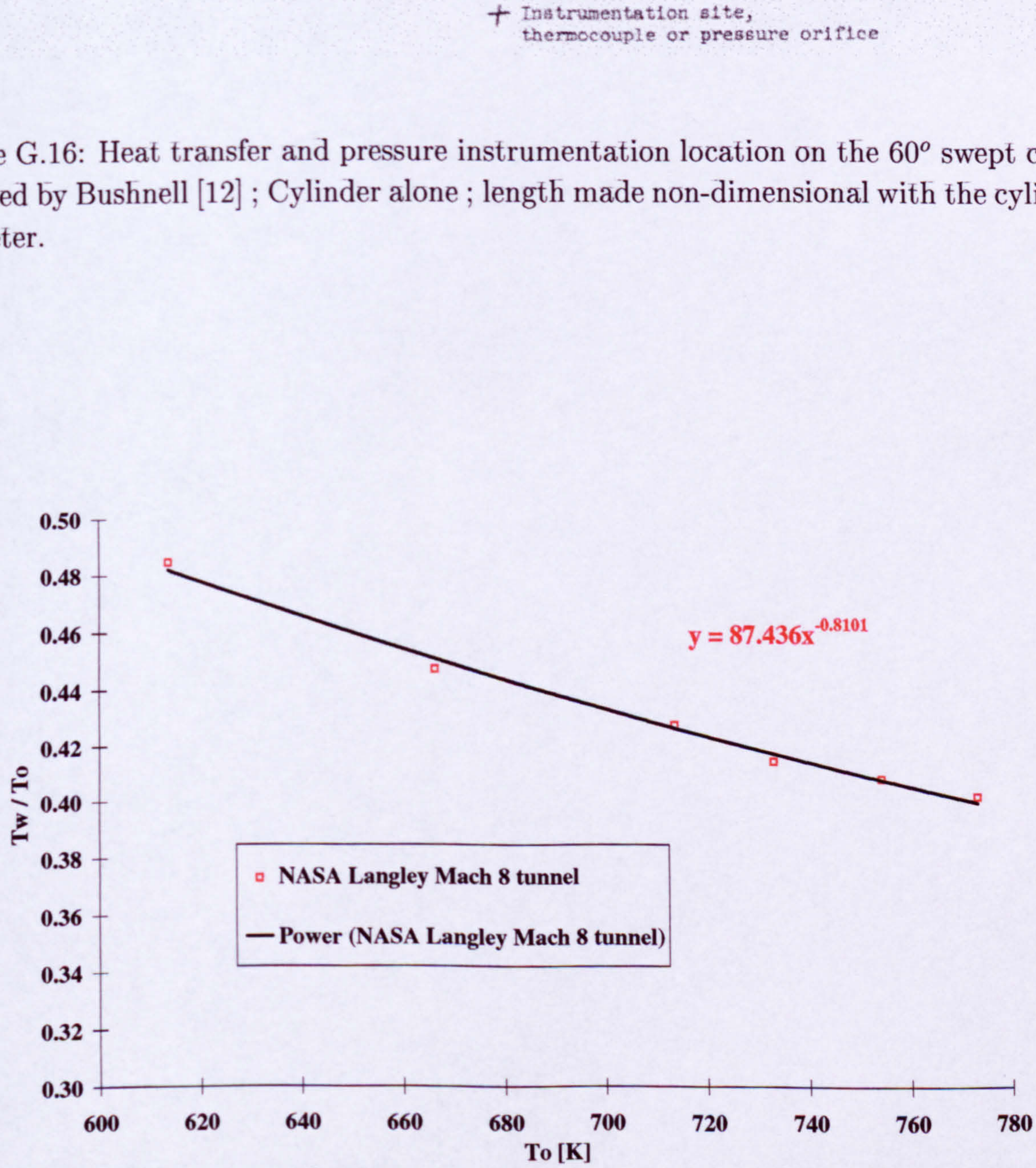

Figure G.17: Wall-to-stagnation temperature ratio variation with stagnation temperature in the Langley Mach 8 variable density tunnel after [58].

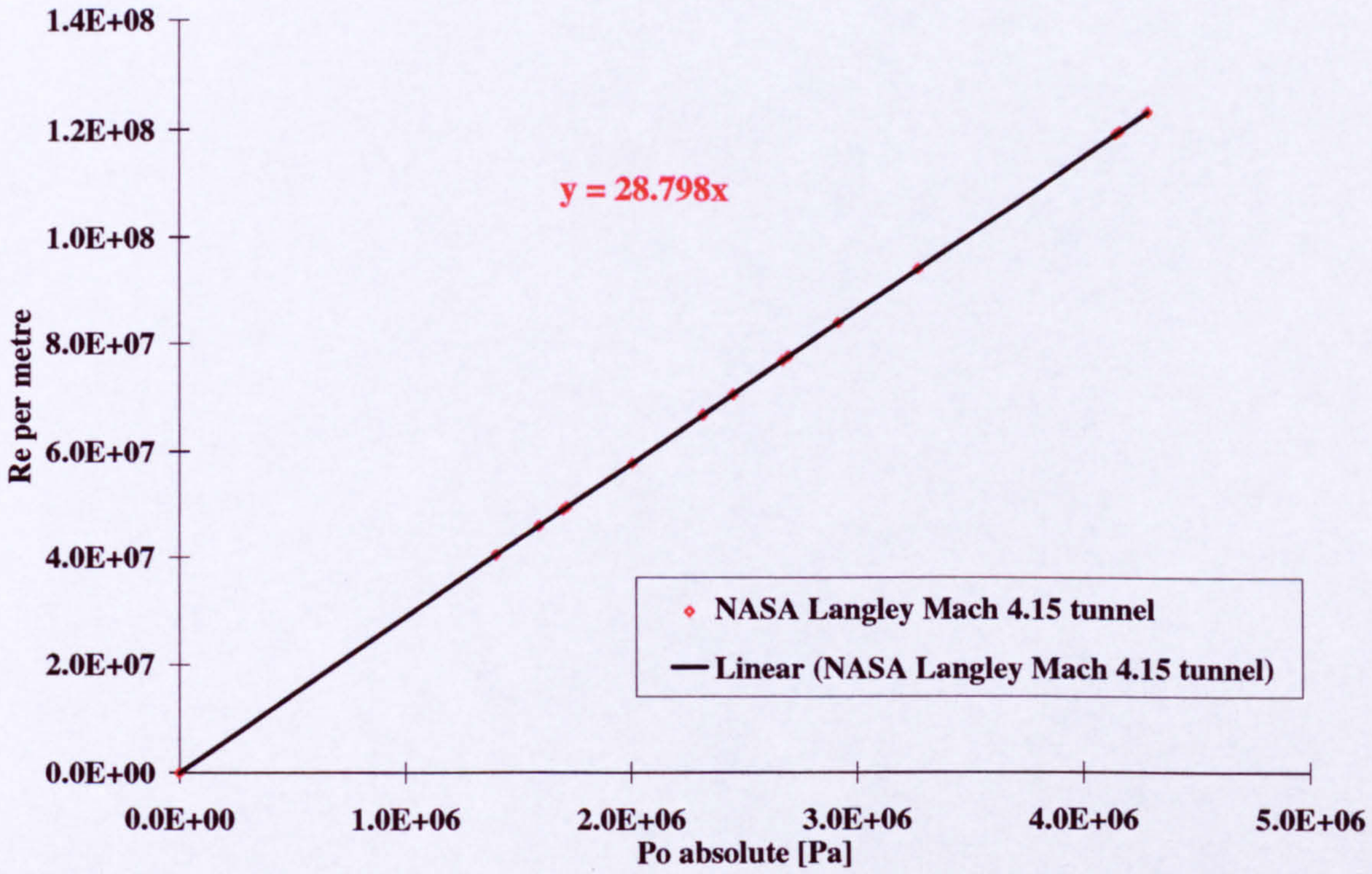

Figure G.18: Stagnation pressure variation with unit free-stream Reynolds number in the NASA Langley Mach 4.15 tunnel used by Beckwith and Gallagher [5].

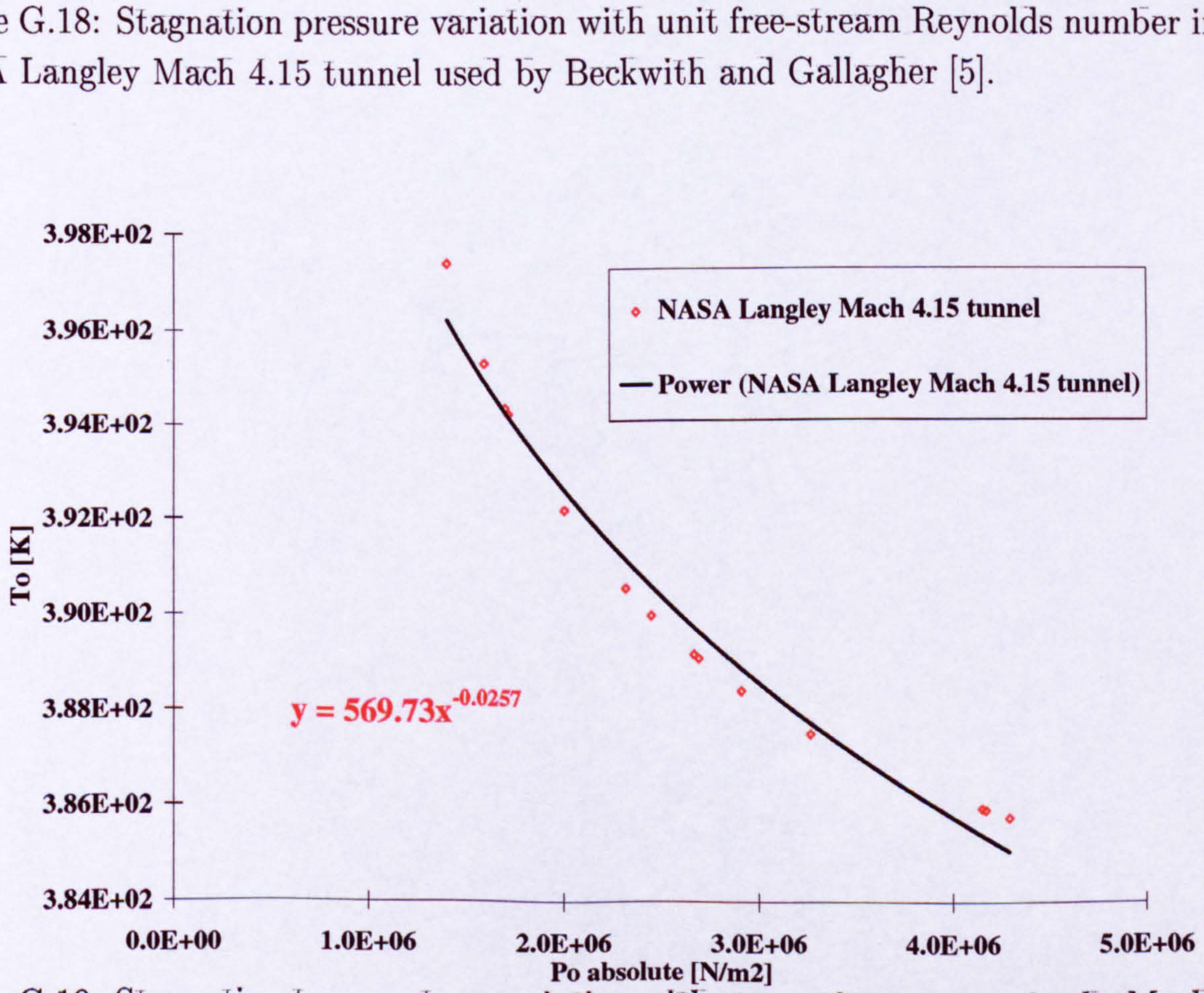

Figure G.19: Stagnation temperature variation with stagnation pressure in the Mach 4.15 tunnel used by Beckwith and Gallagher [5].

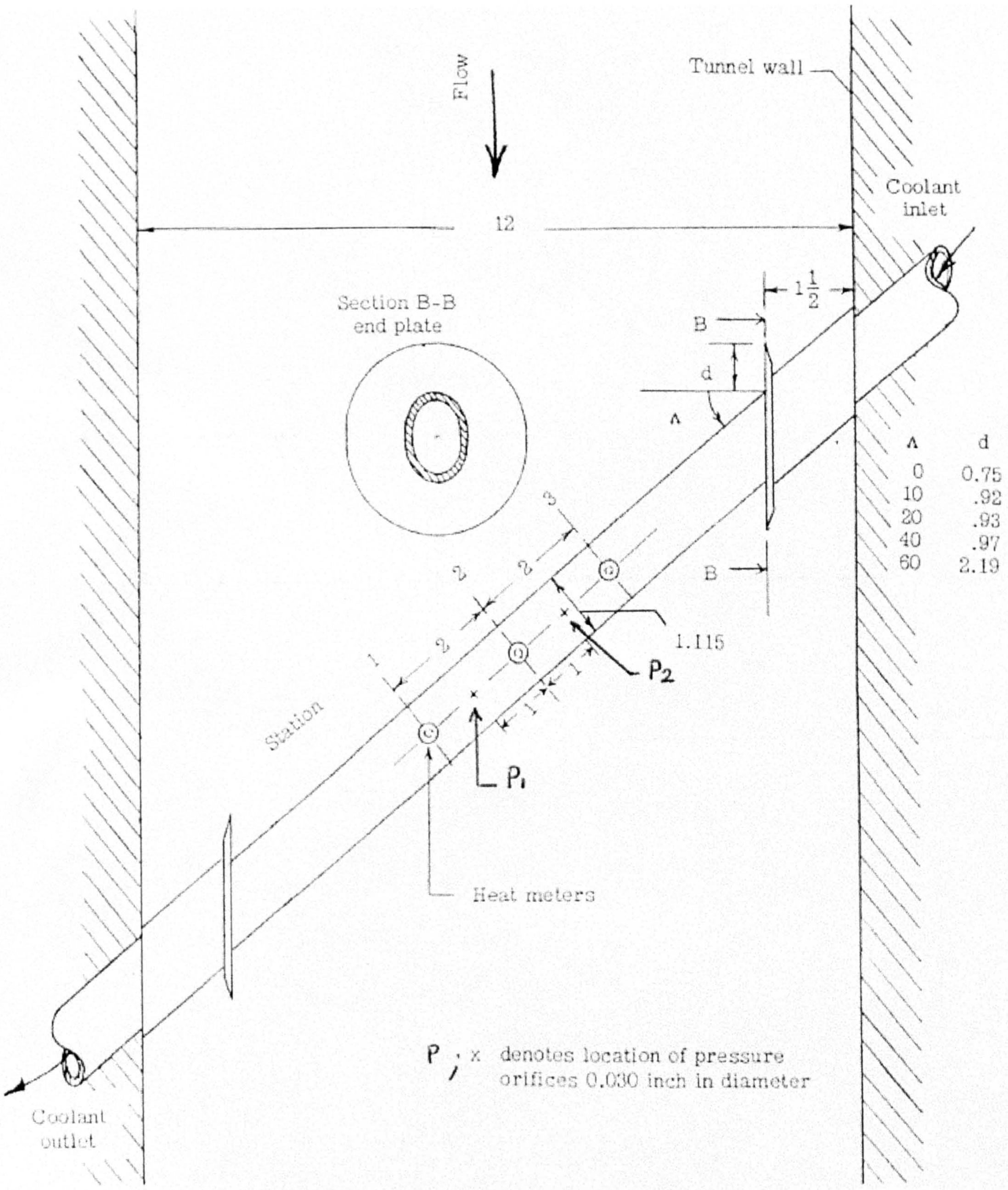

Figure G.20: Schematic of the model used by Beckwith et al. [5]. Cylinder shown is swept at 40°. (All dimensions in inches).

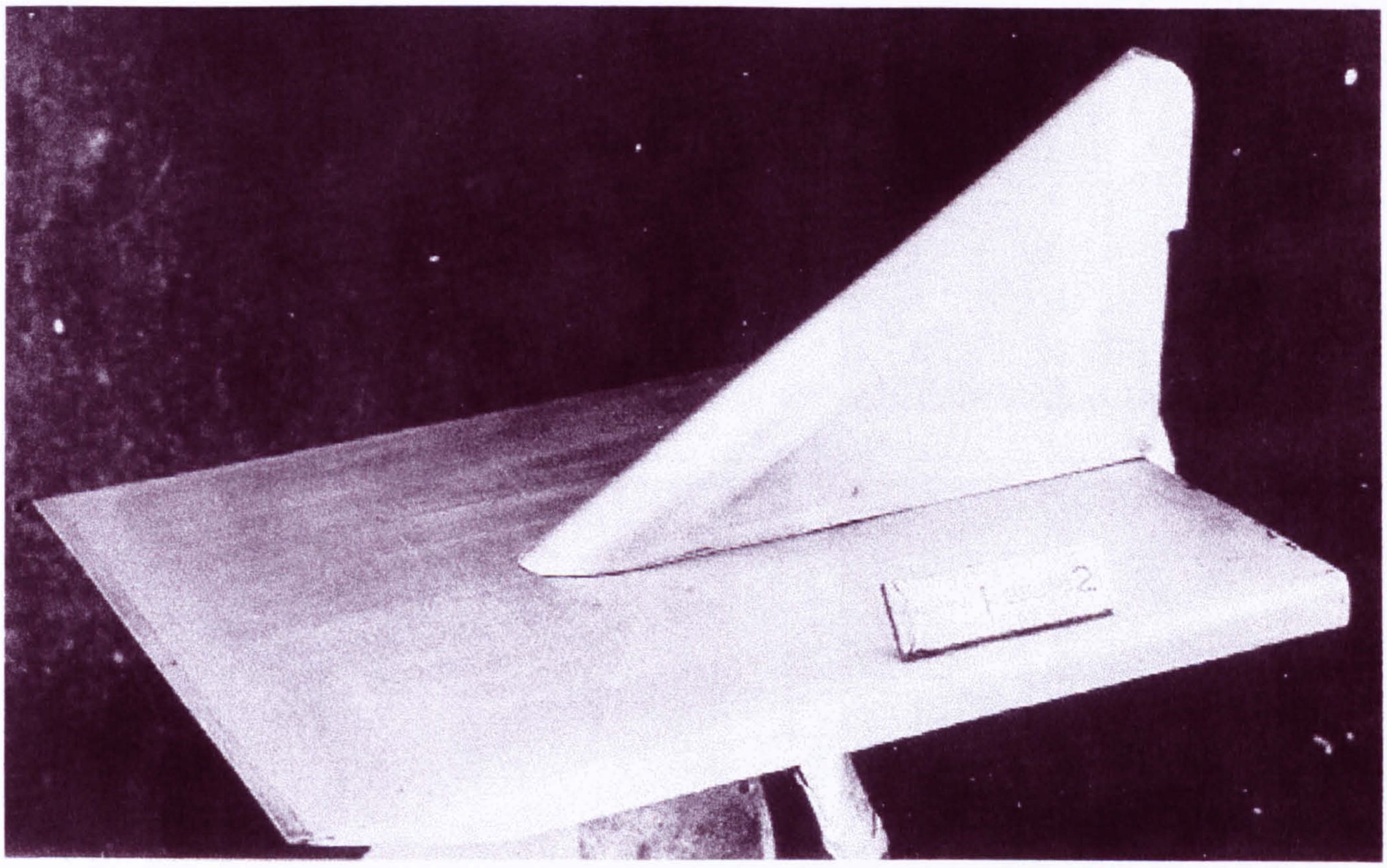

Figure G.21: Swept cylindrical leading edge fin mounted on a sharp plate as used by Jones [40].

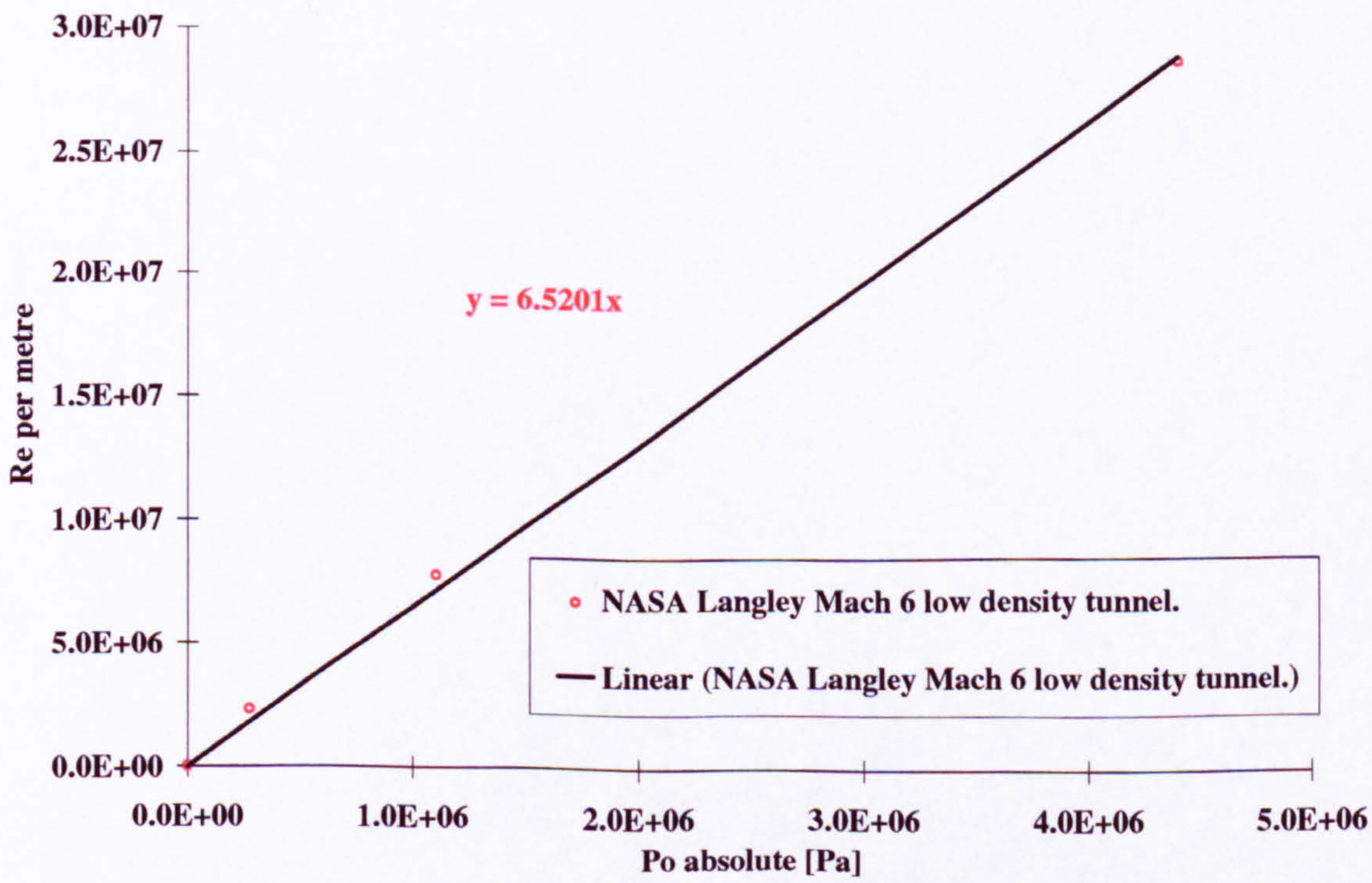

Figure G.22: Stagnation pressure variation with free-stream Reynolds number in the Langley Mach 6 low density tunnel after [40].

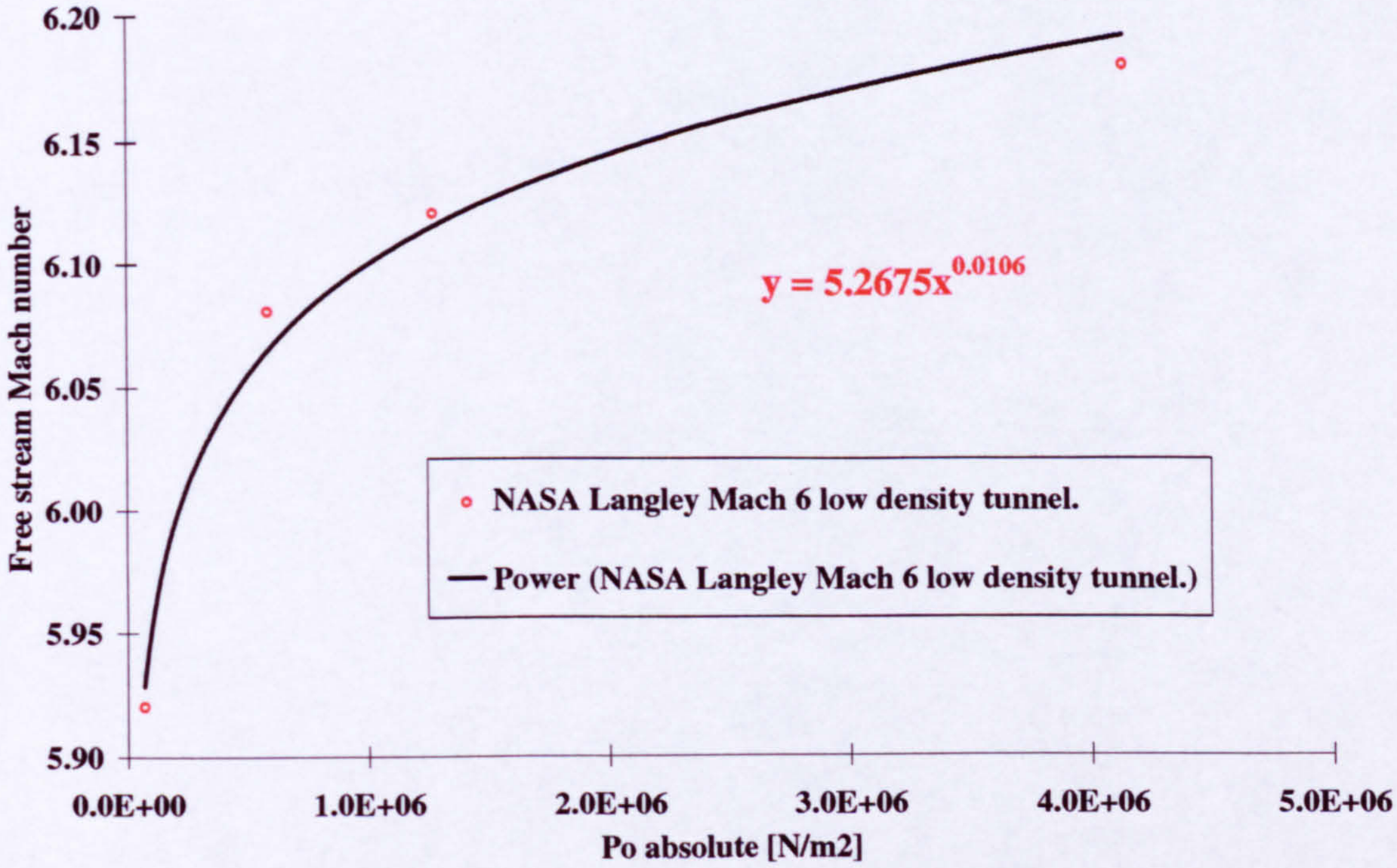

Figure G.23: Calibration of the Langley Mach 6 low density tunnel. Free-stream Mach number vs stagnation pressure [41].

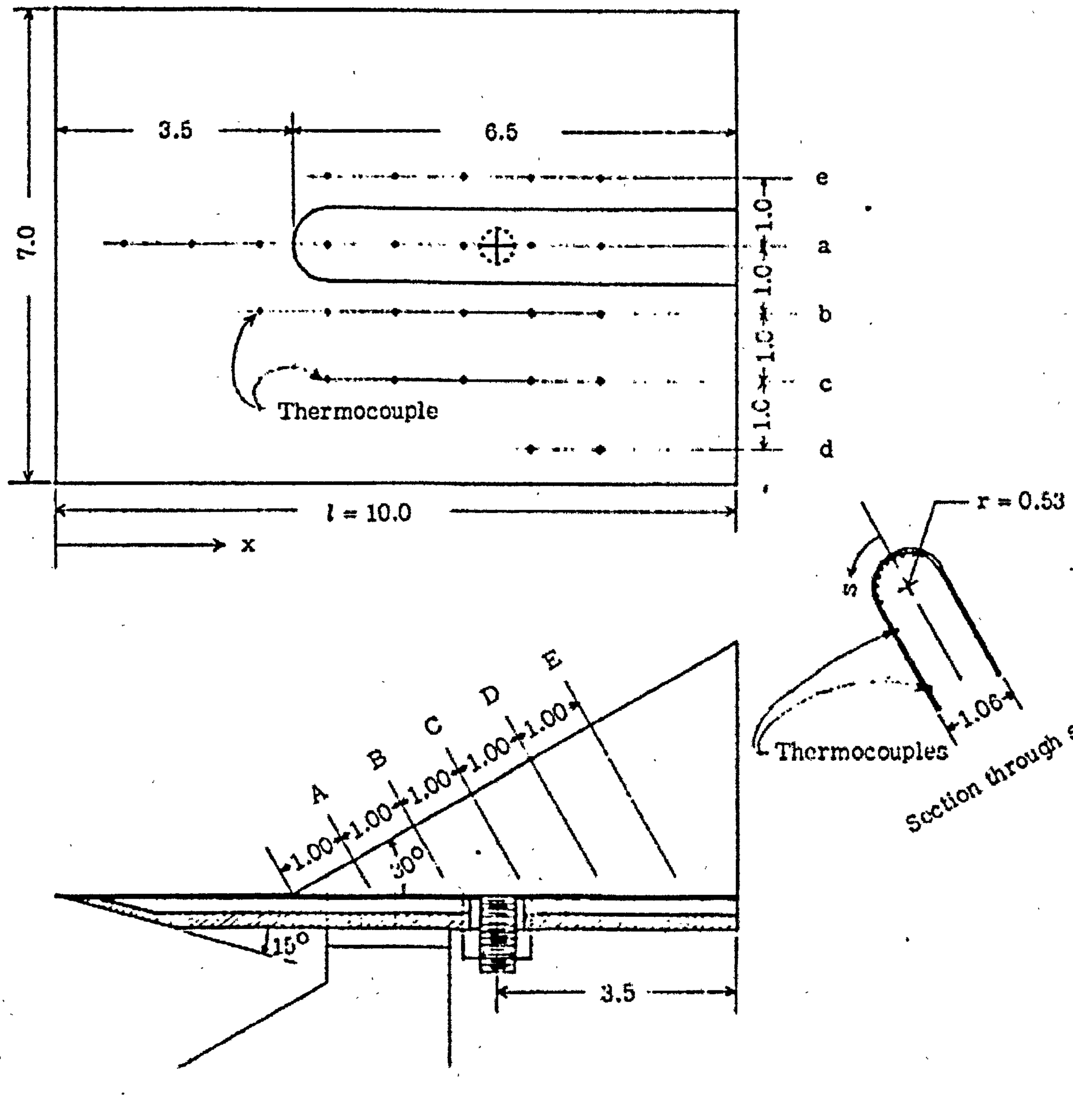

Figure G.24: Instrumentation location on the leading edge fin and plate as used by Jones [40]. (All dimensions in inches).

Appendix H

Heat transfer measurements obtained at Poitiers university

Attachment-line heat transfer data obtained at Poitiers University are presented in references [6] [25] and [35] in the form of St_{ae} plotted against $\bar{R}^*$.

$$St_{ae} = \frac{-\dot{q_w}}{\rho_{ae}.V_{ae}.Cp\,(T_r - T_w)} \tag{H.1}$$

$$\bar{R}^* = \left(\frac{{V_{ae}}^2}{\nu_{ae}{}^*.\frac{dUe}{dX}}\right)^{\frac{1}{2}} \tag{H.2}$$

with

$$T^* = T_{ae} + 0.10\,(T_W - T_{ae}) + 0.60\,(T_r - T_{ae}) \tag{H.3}$$

For the purpose of the present investigation, only the heat transfer rate at the wall, $\dot{q}_W$, is of an interest. This appendix lists the equations used to extract $\dot{q}_W$ from references [6] and [35].

H.1 Known variables

For each run the free-stream Mach number, cylinder sweep angle and diameter, wall-to-stagnation temperature ratio and wall temperature are known. The free-stream gas is air and, hence, the ratio of specific heat γ and the gas constant R are also known. Benard and Gaillard also used a recovery factor r of 0.85 for all cases, independent of the boundary layer state. The Prandtl number used by Gaillard was 0.72 whereas Benard used 0.725.

H.2 Equations leading to $\dot{q_W}$

$$T_o = \frac{T_W}{\frac{T_W}{T_o}} \qquad [K] \tag{H.4}$$

$$T_\infty = \frac{T_o}{1 + \left(\frac{\gamma-1}{2}\right).M_\infty^2} \qquad [K] \tag{H.5}$$

$$Q_\infty = M_\infty.(\gamma.R.T_\infty)^{\frac{1}{2}} \qquad [m/s] \tag{H.6}$$

$$T_{ae} = T_\infty \left[1 + \left(\frac{\gamma-1}{2}\right).M_\infty^2.cos^2\Lambda\right] \qquad [K] \tag{H.7}$$

$$V_{ae} = V_\infty = Q_\infty.sin\Lambda \qquad [m/s] \tag{H.8}$$

$$M_{ae} = \frac{V_{ae}}{(\gamma.R.T_{ae})^{\frac{1}{2}}} \tag{H.9}$$

$$T_r = T_{ae}\left[1 + r\left(\frac{\gamma-1}{2}\right)M_{ae}^2\right] \qquad [K] \tag{H.10}$$

$$T^* = T_{ae} + 0.1\,(T_W - T_{ae}) + 0.6\,(T_r - T_{ae}) \qquad [K] \tag{H.11}$$

$$\bar{R} = \frac{\bar{R^*}}{\left(\frac{T_{ae}}{T^*}\right)^{\frac{3}{4}} \left(\frac{1+\frac{110}{T^*}}{1+\frac{110}{T_{ae}}}\right)^{\frac{1}{2}}} \tag{H.12}$$

$$\frac{P_{ae}}{P_\infty} = \left[\left(\frac{\gamma+1}{2}\right) M_\infty^2 cos^2\Lambda\right]^{\frac{\gamma}{\gamma-1}} . \left[\frac{\gamma+1}{2.\gamma.M_\infty^2.cos^2\Lambda - (\gamma-1)}\right]^{\frac{1}{\gamma-1}} \tag{H.13}$$

$$M_{n\infty} = M_\infty . cos\Lambda \tag{H.14}$$

$$Kp_o = \frac{\frac{P_{ae}}{P_\infty} - 1}{\frac{\gamma}{2}.M_{n\infty}^2} \tag{H.15}$$

$$U_\infty = Q_\infty . cos\Lambda \qquad [m/s] \tag{H.16}$$

$$\frac{\rho_\infty}{\rho_{ae}} = \frac{P_\infty}{P_{ae}} . \frac{T_{ae}}{T_\infty} \tag{H.17}$$

$$\frac{dU_e}{dX} = \left(Kp_o . \frac{\rho_\infty}{\rho_{ae}}\right)^{\frac{1}{2}} . \frac{U_\infty}{\frac{D}{2}} \qquad \left[m^{-1}\right] \tag{H.18}$$

$$\nu_{ae} = \frac{V_{ae}^2}{\bar{R}^2 . \frac{dU_e}{dX}} \qquad \left[m^2/s\right] \tag{H.19}$$

$$\mu_{ae} = 1.711.10^{-5} . \left(\frac{T_{ae}}{273}\right)^{\frac{1}{2}} . \left[\frac{1+\frac{110.4}{273}}{1+\frac{110.4}{T_{ae}}}\right] \qquad [kg/m.s] \tag{H.20}$$

$$\rho_{ae} = \frac{\mu_{ae}}{\nu_{ae}} \qquad \left[kg/m^3\right] \tag{H.21}$$

$$P_{ae} = \rho_{ae} . R . T_{ae} \qquad [Pa] \tag{H.22}$$

$$P_\infty = \frac{P_\infty}{P_{ae}} . P_{ae} \qquad [Pa] \tag{H.23}$$

$$P_o = P_\infty \left[1 + \left(\frac{\gamma - 1}{2}\right) M_\infty^2\right]^{\frac{\gamma}{\gamma - 1}} \qquad [Pa] \tag{H.24}$$

$$\rho_\infty = \frac{\rho_\infty}{\rho_{ae}} . \rho_{ae} \qquad \left[kg/m^3\right] \tag{H.25}$$

$$\mu_\infty = 1.711.10^{-5} . \left(\frac{T_\infty}{273}\right)^{\frac{1}{2}} . \left[\frac{1 + \frac{110.4}{273}}{1 + \frac{110.4}{T_\infty}}\right] \qquad [kg/m.s] \tag{H.26}$$

$$\nu_\infty = \frac{\mu_\infty}{\rho_\infty} \qquad \left[m^2/s\right] \tag{H.27}$$

$$Re_\infty = \frac{Q_\infty}{\nu_\infty} \tag{H.28}$$

$$Cp = \frac{\gamma . R}{\gamma - 1} \qquad [J/kg.K] \tag{H.29}$$

$$\dot{q}_W = St_{ae} . \rho_{ae} . V_{ae} . Cp . (T_r - T_W) \qquad \left[W/m^2\right] \tag{H.30}$$

Appendix I

The law of the wall

As proposed by Prandtl and von Kármán, a turbulent boundary layer may be considered to consist of two regions. These are the inner region which is dominated by viscous shear and strongly influenced by the wall and the outer region which is mainly determined by turbulent stresses and is governed by conditions at the boundary layer edge. Between there is a blending region so called the "overlap" layer where both sources of shear stresses are important (figure I.1).

The traditional arguments for the determination of the velocity profile in the inner and outer regions are well documented (see for example Schlichting [56]). The functional dependence for each region can be deduced from dimensional analysis alone. The postulation of an overlap region gives rise to the well known semi-logarithmic law of the wall. However, a more convincing argument for the law of the wall has been proposed by Bradshaw [11].

For flow very close to a solid boundary, the properties depend only on the distance from

the wall, Y, the shear stress at the wall, τ_w and the local transport properties ρ and μ. The structure of the flow near the wall is essentially independent of the events taking place in the outer part of the viscous layer.

Near the wall, the mean velocity $\bar{u}$ is given by

$$\frac{\bar{u}}{u_\tau} = f_1\left(\frac{Y.u_\tau}{\nu}\right) \tag{I.1}$$

where u_τ is the friction velocity i.e.

$$u_\tau = \left(\frac{\tau_w}{\rho}\right)^{\frac{1}{2}} \tag{I.2}$$

Differentiation of equation I.1 yields

$$\frac{\partial \bar{u}}{\partial Y} = \frac{u_\tau}{Y}.f_1'\left(\frac{Y.u_\tau}{\nu}\right).\frac{Y.u_\tau}{\nu} = \frac{u_\tau}{Y}.f_2\left(\frac{Y.u_\tau}{\nu}\right) \tag{I.3}$$

which can be written as

$$\frac{Y}{u_\tau}.\frac{\partial \bar{u}}{\partial Y} = f_2\left(\frac{Y.u_\tau}{\nu}\right) \tag{I.4}$$

where the term $Y.u_\tau/\nu$ is usually referred as Y^+.

When Y^+ becomes large i.e. greater than 30, the effect of viscosity on the turbulence is assumed to be negligible i.e. Reynolds number independent. Expression I.4 reduces to

$$\frac{Y}{u_\tau}.\frac{\partial \bar{u}}{\partial Y} = k \tag{I.5}$$

where k is the von Kármán's constant.

Integration of equation I.5 leads to the logarithmic law

$$\frac{\bar{u}}{u_\tau} = \frac{1}{k} ln \left(\frac{Y.u_\tau}{\nu} \right) + C \tag{I.6}$$

in which C is the additive constant.

Coles [22] extended this model to include the wake portion of the boundary layer. By analysing the available mean-velocity profile measurements in incompressible flows with zero pressure gradient, he demonstrated that the mean velocity distribution, outside the sublayer, could be accurately represented by the following expression for Y^+ greater than

$$\frac{\bar{u}}{u_\tau} = \underbrace{\frac{1}{k} ln \left(\frac{Y.u_\tau}{\nu} \right) + C}_{law.of.the.wall} + \frac{\Pi}{k} w \left(\frac{Y}{\delta} \right) \tag{I.7}$$

In equation I.7, Π is the maximum deviation of the velocity profile from the extended log law (see figure I.2) and is usually called the wake strength. The term $w\,(Y/\delta)$ is Coles's wake function and is approximately $2sin^2\left(\frac{\pi}{2}.\frac{Y}{\delta}\right)$ such that $\int_0^1 (Y/\delta).dw$ and $w\,(1) = 2$.

Coles [22] specified that for low Reynolds number flows, the wake strength variation with R_θ is as shown by figure I.3 and could be approximated by the following relation

$$\Pi = 0.55 \left[1 - exp \left(-0.243 \sqrt{\frac{R_\theta}{425} - 1} - 0.298 \left(\frac{R_\theta}{425} - 1 \right) \right) \right] \tag{I.8}$$

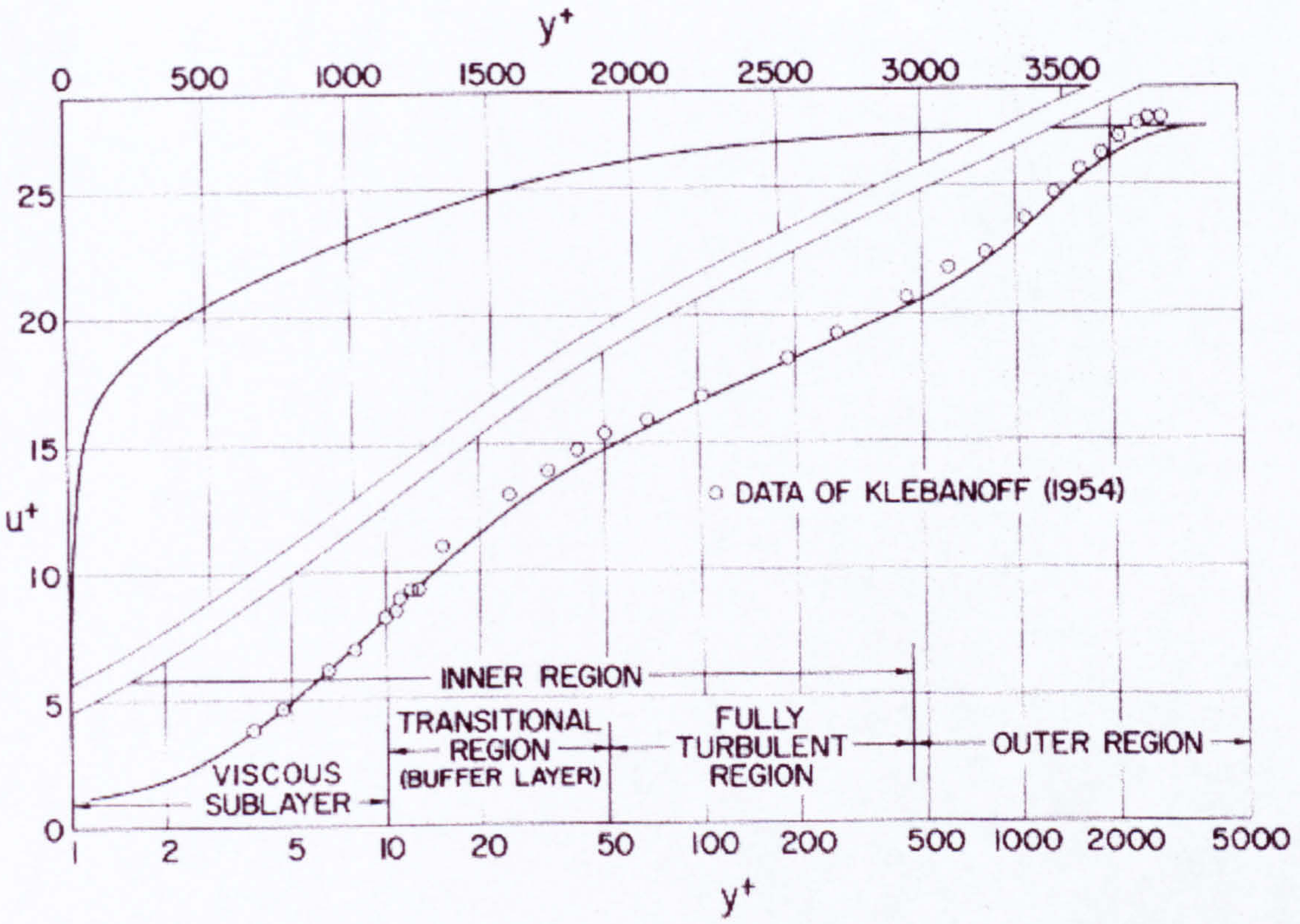

Figure I.1: Typical plots of the mean velocity distribution across a turbulent boundary layer with zero pressure gradient after Cebeci and Smith [21].

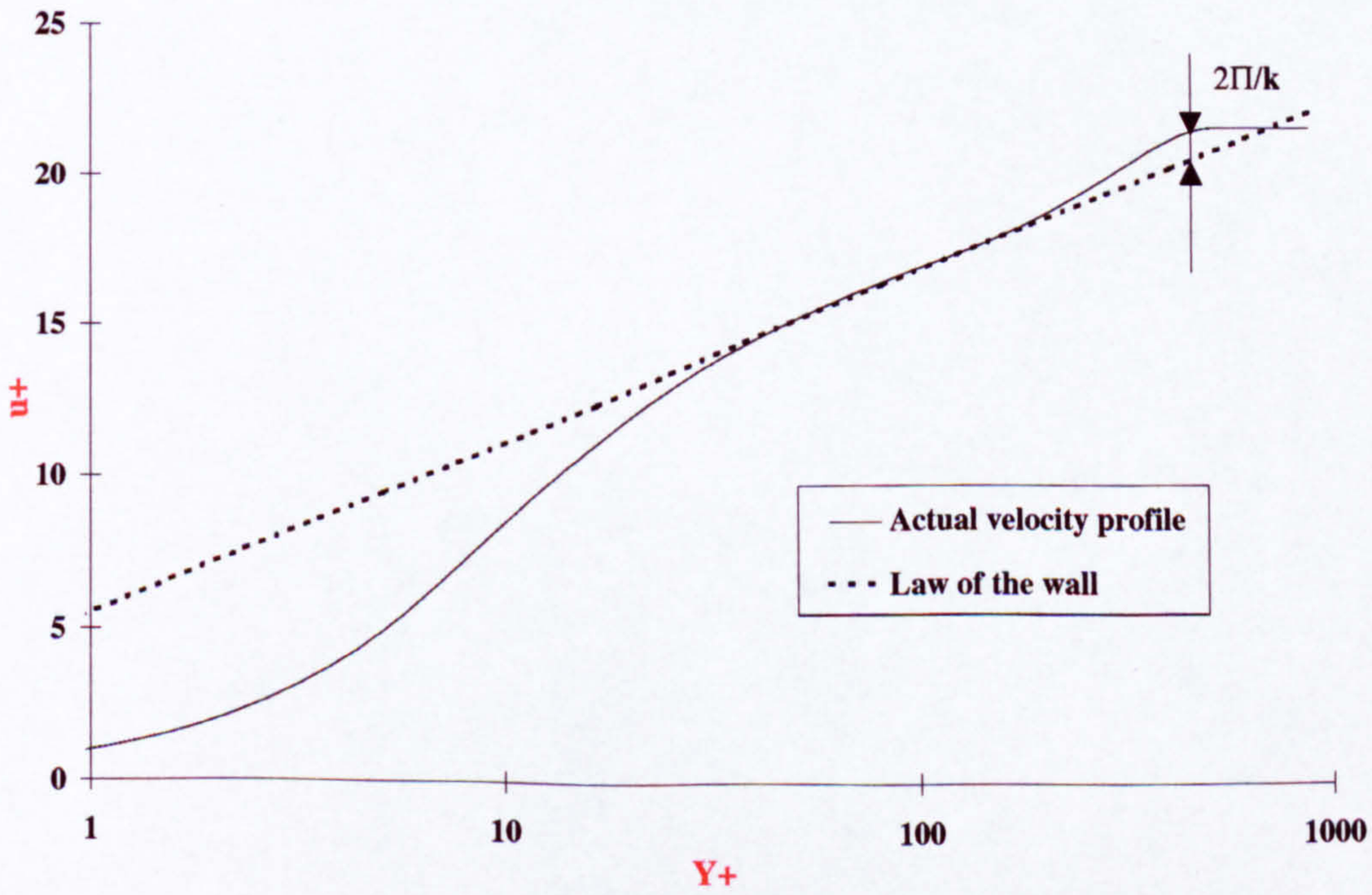

Figure I.2: Plot of the mean velocity distribution across a turbulent boundary layer with zero pressure gradient. Highlight of the wake strength Π.

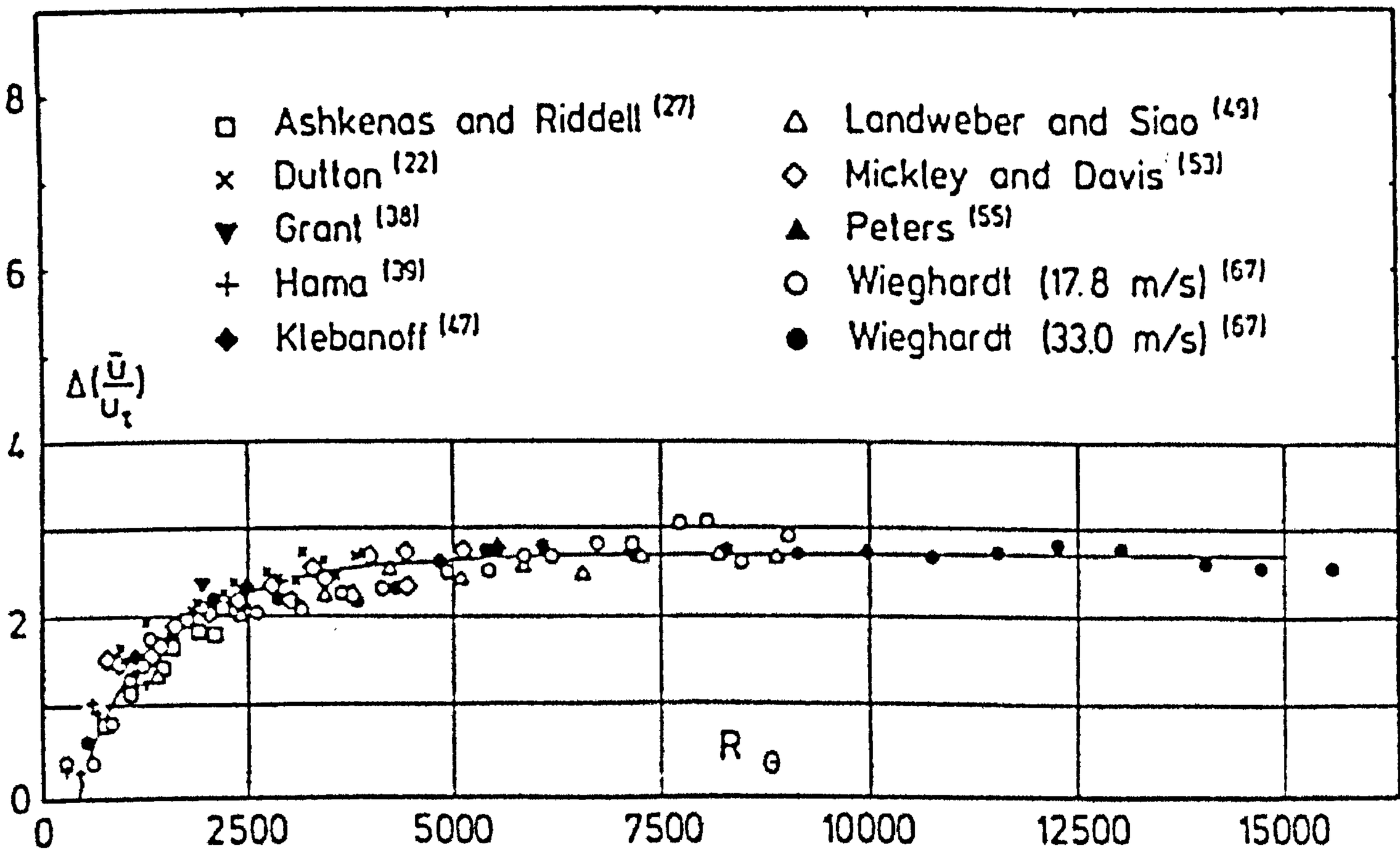

Figure I.3: Variation of the wake strength component in zero pressure gradient equilibrium incompressible turbulent flow. Here $\Delta(\bar{u}/u_\tau) = 2\Pi/k$. From Coles [22].

Appendix J

Morkovin's hypothesis

Morkovin's hypothesis can be found in many text book (e.g. [19][21]) or in reference [45]. However, for convenience, it is reported herein.

Using the equation of state and its logarithmically differentiated form it follows

$$\frac{\rho'}{\bar{\rho}} = \frac{P'}{\bar{P}} - \frac{T'}{\bar{T}} \tag{J.1}$$

Assuming that the ratio of the pressure fluctuation P' to the mean absolute pressure $\bar{P}$ is small leads to

$$\frac{\rho'}{\bar{\rho}} \simeq -\frac{T'}{\bar{T}} \tag{J.2}$$

Morkovin [45] observed that the total temperature fluctuations in supersonic boundary layers were much smaller than the static temperature fluctuations i.e.

$$T'_o \ll T' \tag{J.3}$$

Recalling the definition of the instantaneous total temperature i.e.

$$T_o + T'_o = T + T' + \frac{1}{2.Cp}\left[(u+u')^2 + (v+v')^2 + (w+w')^2\right] \tag{J.4}$$

Bearing in mind that all velocity fluctuations are small compared with w (see figure J.1 for the co-ordinate system) and that at the attachment-line where the flow is predominant in the Z direction it follows

$$u \ll w \tag{J.5}$$

and

$$v \ll w \tag{J.6}$$

By then expanding the squared terms and neglecting small quantities, equation J.4 becomes

$$T_o + T'_o \simeq T + T' + \frac{w^2}{2.Cp} + \frac{ww'}{Cp} \tag{J.7}$$

Considering Morkovin's work (equation J.3), then subtracting from the above equation its own time average $T_o = T + w^2/2Cp$, it follows

$$T' \simeq -\frac{ww'}{Cp} \tag{J.8}$$

This result is believed to be qualitatively plausible for high speed boundary layer since the mean temperature is high where the velocity is low (e.g. near the wall). Fluctuations of velocity and temperature are hence expected to have opposite signs.

Recalling now the definition of the speed of sound i.e.

$$a^2 = (\gamma - 1)\, Cp.T \tag{J.9}$$

and the local Mach number

$$M = \frac{w}{a} \tag{J.10}$$

it follows

$$\frac{T'}{T} \simeq -(\gamma - 1)\, M^2.\frac{w'}{w} \tag{J.11}$$

hence the key result for high speed flow follows

$$\boxed{\frac{\rho'}{\rho} \simeq (\gamma - 1)\, M^2.\frac{w'}{w} \qquad \text{(J.12)}}$$

Since w'/w is usually small, ρ'/ρ is small in the region close to the wall. This leads to the conclusion that the fluctuating component of the density is negligible compare to its mean value. The turbulent structure is therefore not affected by compressibility effects.

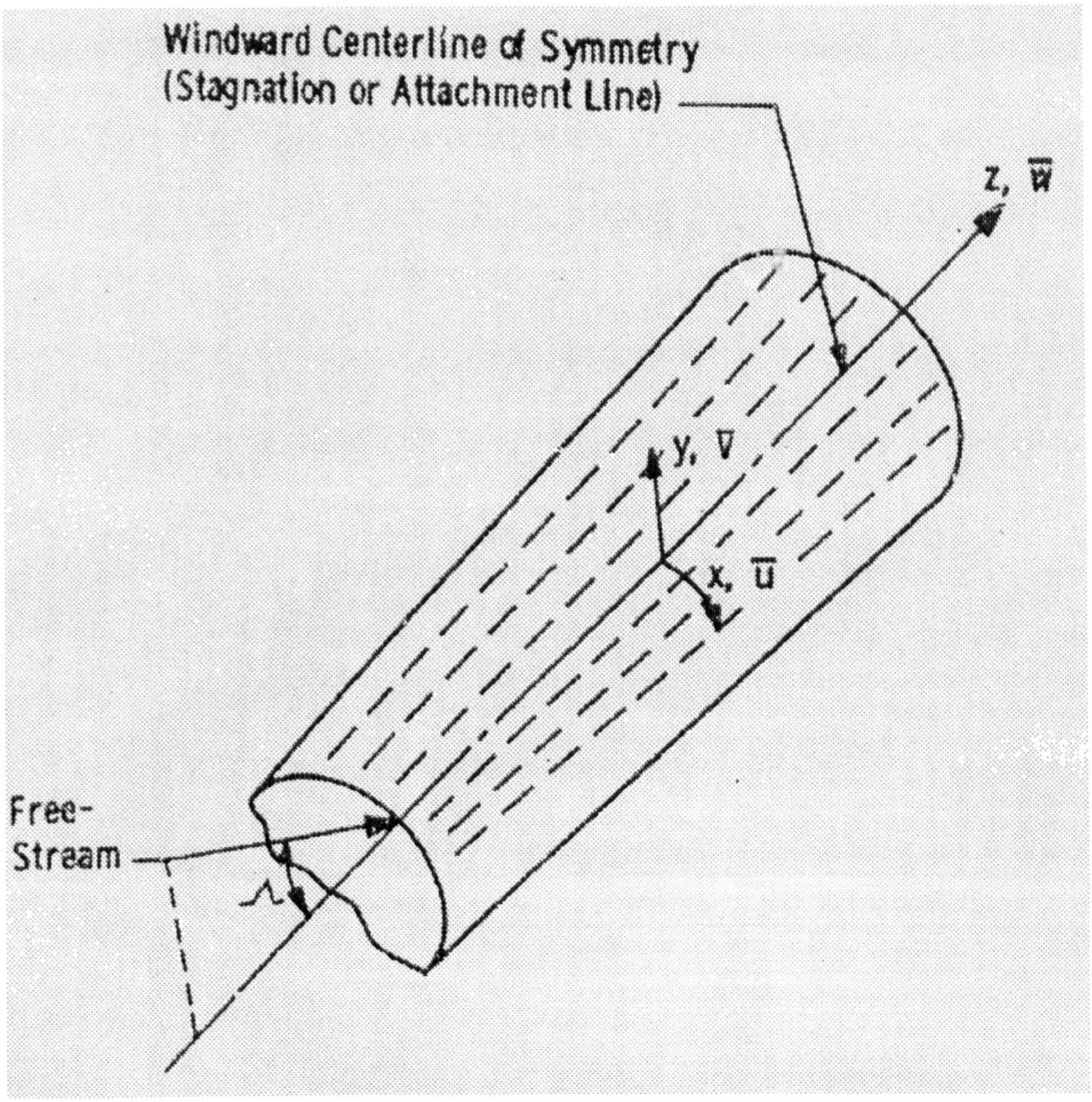

Figure J.1: Surface Orthogonal co-ordinate system as used in the boundary layer code [1].

Appendix K

Experimental data set from Beckwith et al.

Using the turbulence model developed in chapter 5, it was found that the experimental data of Beckwith et al. [5] obtained at 40° of sweep was well predicted as shown by figure K.1 (see appendix G for more information about the experiments). However, figure K.2 shows that the corresponding prediction for the data at 60° of sweep does not fall within the ±15% with the experimental data. Since the Reynolds number is higher than for 40° of sweep, this data set is believed to be fully turbulent. Moreover when compared to all the other data, the accuracy of the predictions was found to be within ±15% (see chapter 5). Hence, the 60° set is believed to contain a systematic error and therefore was discarded.

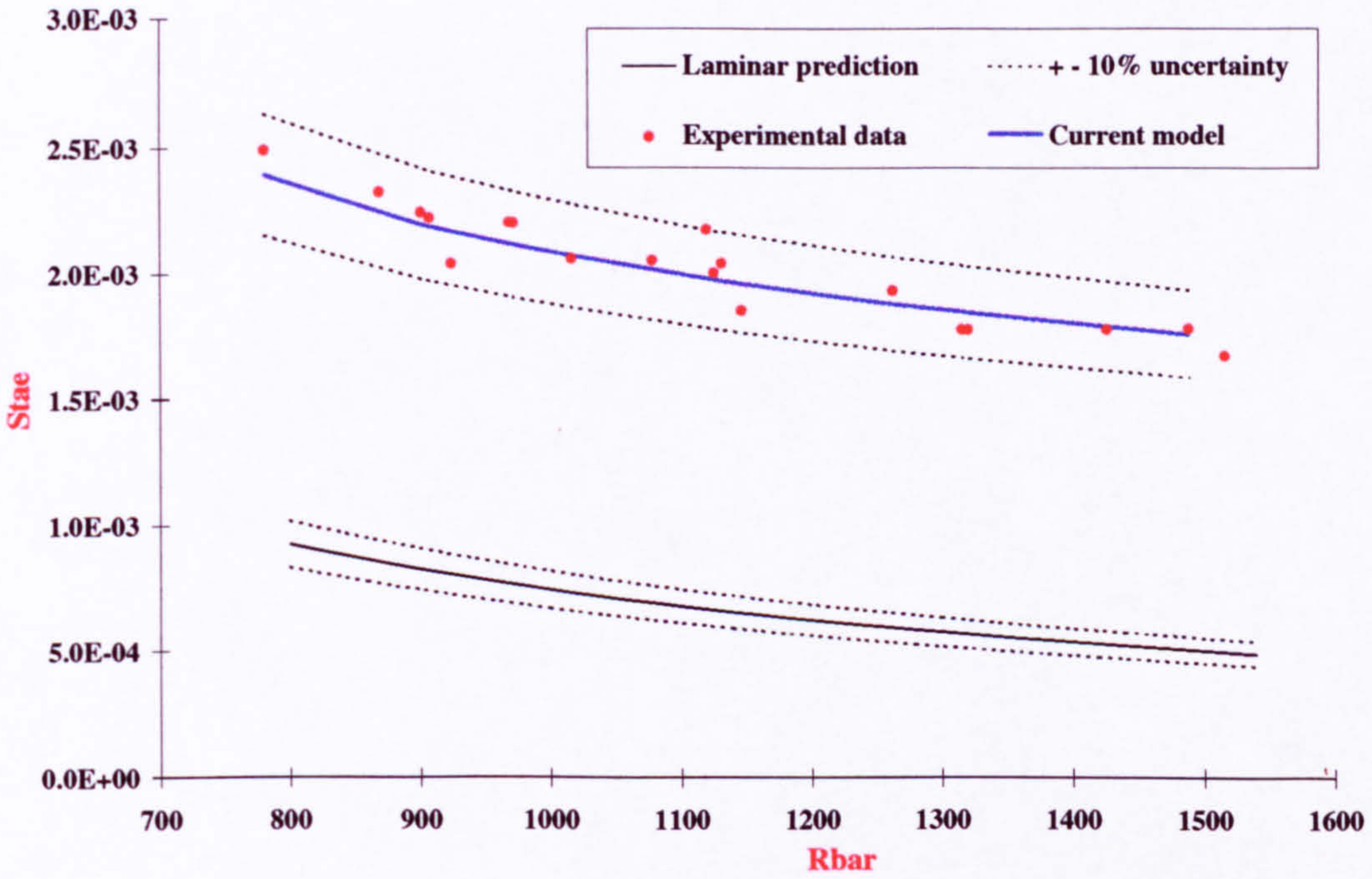

Figure K.1: Variation of the heat transfer rate along the 40^o swept cylinder used by Beckwith et al. [5] (Air, $Pr = 0.7$, $M_\infty = 4.15$ and $T_w/T_o = 0.92$).

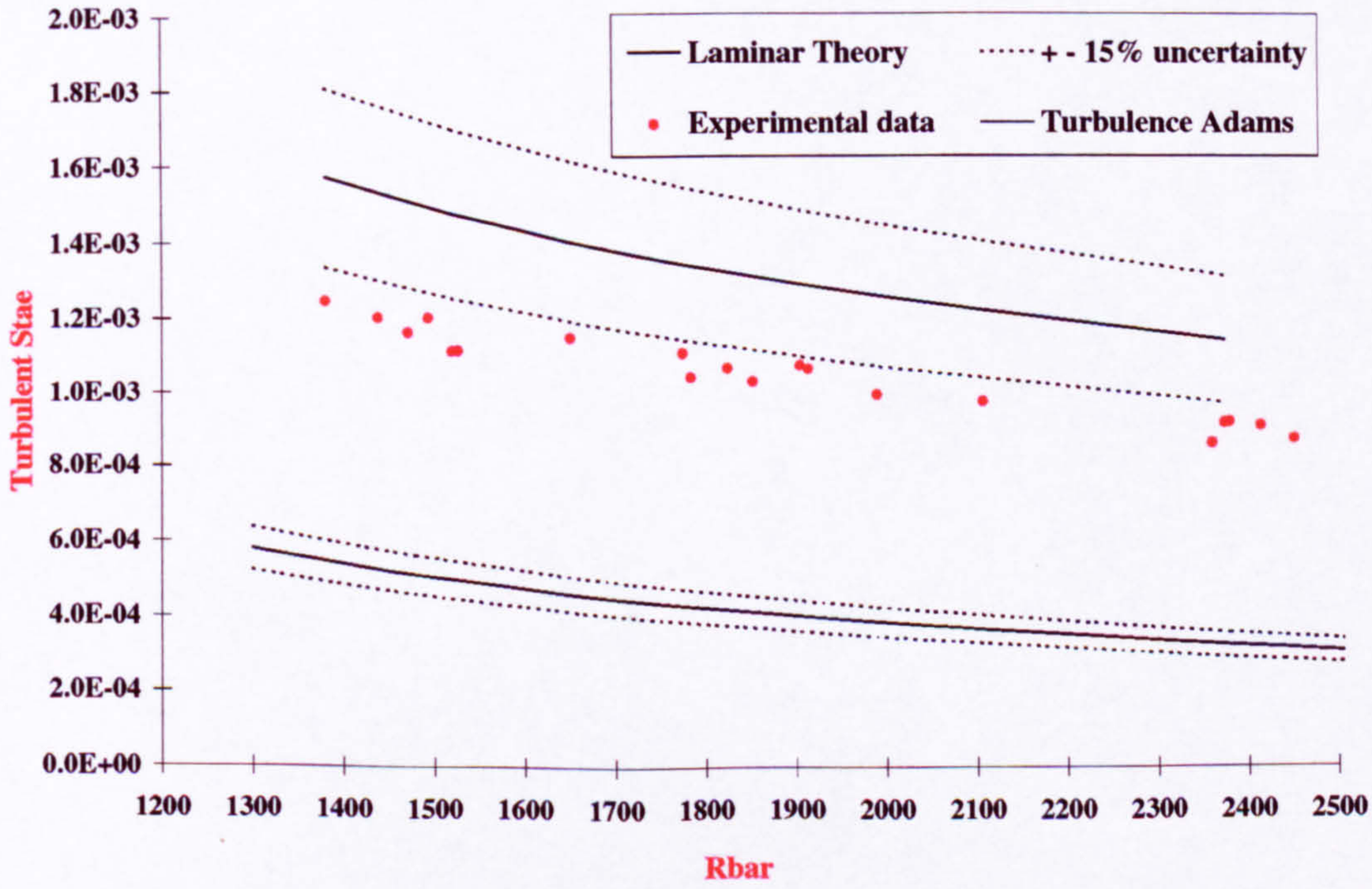

Figure K.2: Variation of the heat transfer rate along the 60^o swept cylinder used by Beckwith et al. [5] (Air, $Pr = 0.7$, $M_\infty = 4.15$ and $T_w/T_o = 0.92$).

Appendix L

The "perfect" reference temperature

L.1 Incompressible relation

The incompressible relation linking the Stanton number, St_{ae}, and attachment-line Reynolds number, $\bar{R}$, can be expressed in this form

$$St_{ae} = \frac{A}{\bar{R}^B} \tag{L.1}$$

L.2 Transformed Stanton number

Starting from the definition of the Stanton number i.e.

$$St_{ae} = \frac{-\dot{q}_w}{\rho_{ae}.V_{ae}.(H_r - H_w)} \tag{L.2}$$

where H is the enthalpy.

Using the reference temperature, T^*, the transformed Stanton number, $St_{ae}{}^*$, becomes

$$St_{ae}{}^* = \frac{-\dot{q}_w}{\rho^*.V_{ae}.(H_r - H_w)} \tag{L.3}$$

or

$$St_{ae}{}^* = St_{ae}.\left(\frac{\rho_{ae}}{\rho^*}\right) \tag{L.4}$$

From the equation of state

$$\frac{\rho_{ae}}{\rho^*} = \frac{P_{ae}}{P^*}.\frac{R}{R}.\frac{T^*}{T_{ae}} = \frac{T^*}{T_{ae}} \tag{L.5}$$

Therefore equation L.4 becomes

$$\boxed{St_{ae}{}^* = St_{ae}.\left(\frac{T^*}{T_{ae}}\right) \qquad \text{(L.6)}}$$

L.3 Transformed attachment-line Reynolds number

Recalling the definition of the attachment-line Reynolds number i.e.

$$\bar{R} = \left(\frac{V_{ae}{}^2}{\nu_{ae}.\frac{dU_e}{dX}}\right)^{\frac{1}{2}} \tag{L.7}$$

Using the reference temperature, $\bar{R}$, is transformed as follows

$$\bar{R}^* = \left(\frac{V_{ae}{}^2}{\nu^*.\frac{dU_e}{dX}}\right)^{\frac{1}{2}} \tag{L.8}$$

or

$$\bar{R}^* = \frac{\bar{R}}{\left(\frac{\nu^*}{\nu_{ae}}\right)^{\frac{1}{2}}} = \bar{R}.\left(\frac{\nu_{ae}}{\nu^*}\right)^{\frac{1}{2}} \tag{L.9}$$

From the definition of the kinematic viscosity

$$\frac{\nu_{ae}}{\nu^*} = \frac{\mu_{ae}}{\mu^*}.\frac{\rho^*}{\rho_{ae}} = \frac{\mu_{ae}}{\mu^*}.\frac{T_{ae}}{T^*} \tag{L.10}$$

Hence equation L.9 becomes

$$\boxed{\bar{R}^* = \bar{R}.\left(\frac{\mu_{ae}}{\mu^*}.\frac{T_{ae}}{T^*}\right)^{\frac{1}{2}}} \tag{L.11}$$

L.4 The "perfect" reference temperature

From equations L.1, L.6 and L.11 it follows that

$$St_{ae}{}^* = \frac{A}{\bar{R}^B.\left(\frac{\mu_{ae}}{\mu^*}.\frac{T_{ae}}{T^*}\right)^{\frac{B}{2}}} = St_{ae}.\frac{T^*}{T_{ae}} \tag{L.12}$$

and, hence

$$\frac{T^*}{T_{ae}}.\left(\frac{\mu_{ae}}{\mu^*}.\frac{T_{ae}}{T^*}\right)^{\frac{B}{2}} = \frac{A}{St_{ae}.\bar{R}^B} \tag{L.13}$$

Using Sutherland's law, this becomes

$$\frac{A}{St_{ae}.\bar{R}^B} = \left(\frac{T^*}{T_{ae}}\right)^{1-\frac{B}{2}}.\left[\left(\frac{T_{ae}}{T^*}\right)^{\frac{3}{2}}.\left(\frac{T^*+s}{T_{ae}+s}\right)\right]^{\frac{B}{2}} \tag{L.14}$$

where s is the Sutherland's law constant (s=110.4 K for air and s=105.0 K for nitrogen)

Therefore

$$\frac{A}{St_{ae}.\bar{R}^B} = \left(\frac{T^*}{T_{ae}}\right)^{\frac{2-B}{2}} \cdot \left[\left(\frac{T_{ae}}{T^*}\right)^{\frac{3}{2}} \cdot \frac{T^* \cdot \left(1+\frac{S}{T^*}\right)}{T_{ae} \cdot \left(1+\frac{S}{T_{ae}}\right)}\right]^{\frac{B}{2}} \tag{L.15}$$

$$\frac{A}{St_{ae}.\bar{R}^B} = \left(\frac{T^*}{T_{ae}}\right)^{\frac{2-B}{2}} \cdot \left[\left(\frac{T_{ae}}{T^*}\right)^{\frac{1}{2}} \cdot \frac{\left(1+\frac{S}{T^*}\right)}{\left(1+\frac{S}{T_{ae}}\right)}\right]^{\frac{B}{2}} \tag{L.16}$$

$$\frac{A}{St_{ae}.\bar{R}^B} = \left(\frac{T^*}{T_{ae}}\right)^{\frac{4-3B}{4}} \cdot \left(\frac{1+\frac{S}{T^*}}{1+\frac{S}{T_{ae}}}\right)^{\frac{B}{2}} \tag{L.17}$$

Finally

$$\boxed{\left(\frac{A}{St_{ae}.\bar{R}^B}\right)^{\frac{4}{4-3B}} = \left(\frac{T^*}{T_{ae}}\right) \cdot \left(\frac{1+\frac{S}{T^*}}{1+\frac{S}{T_{ae}}}\right)^{\frac{2B}{4-3B}}} \tag{L.18}$$

Note that A and B are functions of $\bar{R}^*$ only. Therefore iterations are needed in order to calculate the "perfect" value of T^* from equation L.18. As a first guess A and B were taken as functions of $\bar{R}$ instead of $\bar{R}^*$. In this case, it was found that only three iterations were needed.

Appendix M

Effects of roughness elements and end plates

M.1 Introduction

Navier-Stokes calculations were performed on smooth surface cylinders as explained in appendix D. Local edge flow properties such as the density, ρ_{ae}, the static temperature, T_{ae}, and the velocity, V_{ae}, were extracted from the CFD solution. However, these numerical results were coupled with some experimental data carried out on cylinders equipped with end plates or roughness elements (see appendix G for the description of the experiments). Hence, local edge flow properties would be suitable only for smooth surface cylinder since a trip wire for example, located on the cylinder, would generate a shock wave (figure M.1). Therefore, a given external stream line can cross two shock waves. If the shock emanating from the trip wire is not negligible, the flow properties along the attachment-line will suddenly vary and thus, the computational results will not be suitable for "non-smooth" surfaces. Note that for Jones experiments [40], the first three data points were discarded because of the strong shock emanating from the flat plate which

interacted with the swept leading edge shock (see chapter 3, section 3.7.1). It is here the same feature that is investigating.

M.2 Effects of roughness elements and end plates

A circular cylinder of diameter D, swept at an angle Λ, in a flow field at a free-stream Mach number M_∞ in which the ratio of the wall-to-stagnation temperature is $\frac{T_W}{T_o}$ is considered. If the heat transfer along the attachment-line is independent of the surface state (smooth or tripped with a roughness element) then it could be concluded that the shock system emanating from the roughness element has a negligible effect on the flow parameters.

Recalling the definition of the attachment-line Reynolds number evaluated from the temperature of reference i.e.

$$\bar{R}^* = \left(\frac{{V_{ae}}^2 . \rho^*}{\mu^* . \frac{dU_e}{dX}} \right)^{\frac{1}{2}} \tag{M.1}$$

then

$$\bar{R}^* = \left(\frac{{V_{ae}}^2 . \rho^*}{\mu^* . \frac{U_\infty}{D} . \frac{d\left(\frac{U_e}{U_\infty}\right)}{d\left(\frac{X}{D}\right)}} \right)^{\frac{1}{2}} \tag{M.2}$$

which becomes

$$\bar{R}^* = \left(\frac{V_{ae}^2}{U_\infty} . \frac{\rho^*}{\mu^*} . \frac{D}{U1} \right)^{\frac{1}{2}} \tag{M.3}$$

where U1 is the chordwise velocity gradient non-dimensionalised by U_∞ and D i.e.

$$U1 = \frac{\frac{dU_{ae}}{U_\infty}}{\frac{dX}{D}} \tag{M.4}$$

Introducing variables in order to bring the free-stream Reynolds number, it follows that

$$\bar{R}^* = \left(Q_\infty . \frac{V_{ae}}{Q_\infty} . \frac{V_{ae}}{U_\infty} . \frac{\rho_\infty}{\mu_\infty} . \frac{\rho^*}{\rho_\infty} . \frac{\mu_\infty}{\mu^*} . \frac{D}{U1}\right)^{\frac{1}{2}} \tag{M.5}$$

$$\Rightarrow \bar{R}^* = \left(\frac{Q_\infty . \rho_\infty . D}{\mu_\infty}\right)^{\frac{1}{2}} . \left(\frac{V_{ae}}{Q_\infty} . \frac{V_{ae}}{U_\infty} . \frac{\rho^*}{\rho_\infty} . \frac{\mu_\infty}{\mu^*} . \frac{1}{U1}\right)^{\frac{1}{2}} \tag{M.6}$$

Recalling the definition of the Stanton number evaluated from the temperature of reference i.e.

$$St_{ae}{}^* = \frac{-q_W}{\rho^* . V_{ae} . Cp . (T_r - T_W)} \tag{M.7}$$

Introducing T_o in order to recast the Stanton number in terms of the stagnation temperature, gives

$$St_{ae}{}^* = \left(\frac{-\dot{q}_W}{\rho^* . V_{ae} . Cp . (T_o - T_W)}\right) . \frac{(T_o - T_W)}{(T_r - T_W)} \tag{M.8}$$

and based on the free-stream conditions i.e.

$$\Rightarrow St_{ae}{}^* = \left(\frac{-\dot{q}_W}{\rho_\infty . Q_\infty . Cp . (T_o - T_W)}\right) . \left(\frac{\rho_\infty . Q_\infty}{\rho^* . V_{ae}}\right) . \left(\frac{T_o - T_W}{T_r - T_W}\right) \tag{M.9}$$

Since the Stanton number and $\bar{R}$ from the temperature of reference are related as follow (see Poll [49] or chapter 6).

$$St_{ae}{}^* = \frac{A}{\bar{R}^{*B}} \tag{M.10}$$

hence using equations M.6 and M.9

$$\left(\frac{-\dot{q}_W}{\rho_\infty.Q_\infty.Cp.(T_o - T_W)}\right) =$$

$$= \left(\frac{\rho^*.V_{ae}}{\rho_\infty.Q_\infty}\right).\left(\frac{T_r - T_W}{T_o - T_W}\right).\left[\frac{A}{\left(\frac{Q_\infty.\rho_\infty.D}{\mu_\infty}\right)^{\frac{B}{2}}}\right].\left(\frac{Q_\infty}{V_{ae}}.\frac{U_\infty}{V_{ae}}.\frac{\rho_\infty}{\rho^*}.\frac{\mu^*}{\mu_\infty}.U1\right)^{\frac{B}{2}} \qquad \text{(M.11)}$$

which becomes

$$\left[\frac{-\dot{q}_W}{\rho_\infty.Q_\infty.Cp.(T_o - T_W)}\right].\left[\frac{Q_\infty.\rho_\infty.D}{\mu_\infty}\right]^{\frac{B}{2}}$$

$$=$$

$$A.\left(\frac{\rho^*.V_{ae}}{\rho_\infty.Q_\infty}\right).\left(\frac{T_r - T_W}{T_o - T_W}\right).\left(\frac{Q_\infty}{V_{ae}}.\frac{U_\infty}{V_{ae}}.\frac{\rho_\infty}{\rho^*}.\frac{\mu^*}{\mu_\infty}.U1\right)^{\frac{B}{2}} \qquad \text{(M.12)}$$

Note that equation M.12 is identical to equation M.10 ; only non-dimensionalised variables have been added in equation M.12 in order to investigate the effect of roughness elements on the heat transfer distribution along the attachment-line. Note also that all the terms in the right hand side of equation M.12 might be affected by the trip flow field whereas on the left hand side only $\dot{q}_W$ could be flow field affected since every other term correspond to the free-stream conditions.

M.3 Results

Holden run 17 (smooth surface), runs 6 and 9 (2D trip wire, k=0.015 inch), run 13 (2D trip wire, k=0.030 inch) and run 24 (end plate) have been considered herein. These runs

have been carried out at approximately the same free-stream Mach number ($M_\infty \approx 10.5$), wall-to-stagnation ratio ($\frac{T_W}{T_o} \approx 0.26$) and identical sweep angle ($\Lambda = 66.5^o$) and cylinder diameter (D = 0.0762m). Note that the free-stream Reynolds number varies between these runs but equation M.12 does take into consideration this feature. Figure M.2 shows that these five runs lead to the same value of $St_\infty.Re_D{}^{\frac{B}{2}}$ (left hand side of equation M.12). Note that the right hand side of equation M.12 is also shown in figure M.2 (denoted f=(Minf, Tw/To, D and sweep). This means that for a fixed, given swept cylinder and free-stream conditions, the heat transfer along the attachment-line is independent of the cylinder surface state (i.e. smooth or with roughness elements). In other words, the shock wave emanating from the roughness element (trip wire or end plate) has no discernible effect on the flow field. It is therefore possible to use the computational results obtained on smooth surfaces to runs having non-smooth surface. This feature is obviously correct to a certain extent. If the roughness element is very large, the shock wave generated must have an impact. In Jones experiments, the flat plate shock wave does change the flow field in the vicinity of the fin attachment-line as stated in reference [40] and reported in section 3.7.1 of the present report.

Note that the reference temperature T^* is needed in equation M.12. The two coefficients K1 and K2 (0.09 and 0.28 respectively) allowing T^* to be calculated (equation 6.10) are investigated in the chapter 6.

Holden runs 28 to 31 have also been used to investigate the effect of shock waves emanating from roughness elements. These runs involve similar free-stream Mach number ($M_\infty \approx 10.5$), wall-to-stagnation ratio ($\frac{T_W}{T_o} \approx 0.26$) and identical sweep angle ($\Lambda = 75^o$) and cylinder diameter (D = 0.0762m). The only major feature that differentiates these

runs (apart from the free-stream Reynolds number) is their surface states. In run 28, a 2D trip wire (k=0.030 inches) was fitted to the cylinder whereas in runs 29, 30 and 31 the cylinder surface was kept smooth. Figure M.3 also reveals that the roughness element has no noticeable impact on the flow field.

Finally, Runs 29, 30 and 31 achieved at Poitiers University have been taken into account. These runs were carried out at a free-stream Mach number of 7.14, wall-to-stagnation temperature ratio of 0.38 over a cylinder (D=19mm) swept at 70°. In run 29, a 3D cavity (1mm in spanwise length, 2mm in depth and 4mm in chordwise width) was located at station $\frac{L}{D} = 9.5$. At the same location, a 2D groove of 5mm in spanwise length and 1mm in depth was tested in run 30 and a 2D groove of 5mm in spanwise length and 2mm in depth was tested in run 31. As shown by figure M.4, when the attachment-line boundary layer becomes fully turbulent under the effect of these roughness elements, the variable $St_\infty.Re_D{}^{\frac{B}{2}}$ which appears on the left hand side of equation M.12 collapse together. Note that runs 29 and 30 have fully turbulent boundary layers all along the cylinder attachment-line (hence they collapse together in figure M.4) and that for run 31, the boundary layer was found to be become fully turbulent from station 12.3. Again this demonstrates that the shock emanating from the roughness element is weak since the heat transfer along the attachment-line is independent of the state of the cylinder surface.

However, it could be argued that although the heat transfer rate at the wall does not vary, the edge flow properties might change in one way and another boundary layer property could change in the other way. The combination of the edge properties and another boundary layer property varying together in two different ways might result in a constant heat transfer rate at the wall.

To investigate the influence of the edge properties on the heat transfer at the wall, two cases were considered. The first was Holden Run36, which involves the highest Mach number ($M_\infty = 10.6$), the highest sweep angle ($\Lambda = 80°$) and the lowest wall-to-stagnation temperature ratio ($\frac{Tw}{To} = 0.26$) considered in the whole investigation. The second case was Beckwith Run15, involving the lowest Mach number ($M_\infty = 4.15$), the lowest sweep angle ($\Lambda = 40°$) and highest wall-to-stagnation temperature ratio ($\frac{Tw}{To} = 0.92$) encountered. Using the boundary layer code and the infinite swept conditions for both cases, it was found that a variation of 10% in M_{ae} resulted, in the worst case to a 16% change in heat transfer (other properties such as V_{ae}, ρ_{ae} led to smaller changes in heat transfer). This suggests that a small change in edge flow properties involves a more important variation of the wall heat transfer rate. Hence, as the heat transfer was found relatively unchanged when the cylinder was equipped with endplates or trip wires (see above), it is safe to conclude that the edge properties did not vary dramatically across the shock waves generated by the roughness elements. Therefore, the computational results obtained on smooth surface can be applied to the trip wire and end plate configurations examined in the present study.

M.4 Conclusions

It has been seen that, for the cases considered, the shock emanating from a roughness elements or end plates attached to the swept cylinder did not change the distribution of the heat transfer along the attachment-line. Moreover, it was found that a small change in edge flow properties resulted in a bigger change of the heat transfer at the wall. This means that the edge properties did not vary dramatically as a result of the shock waves produced by the roughness elements. Therefore, computational results obtained

from smooth surface cylinders can directly be used with experimental data obtained on "non-smooth surface".

M.5 Figures

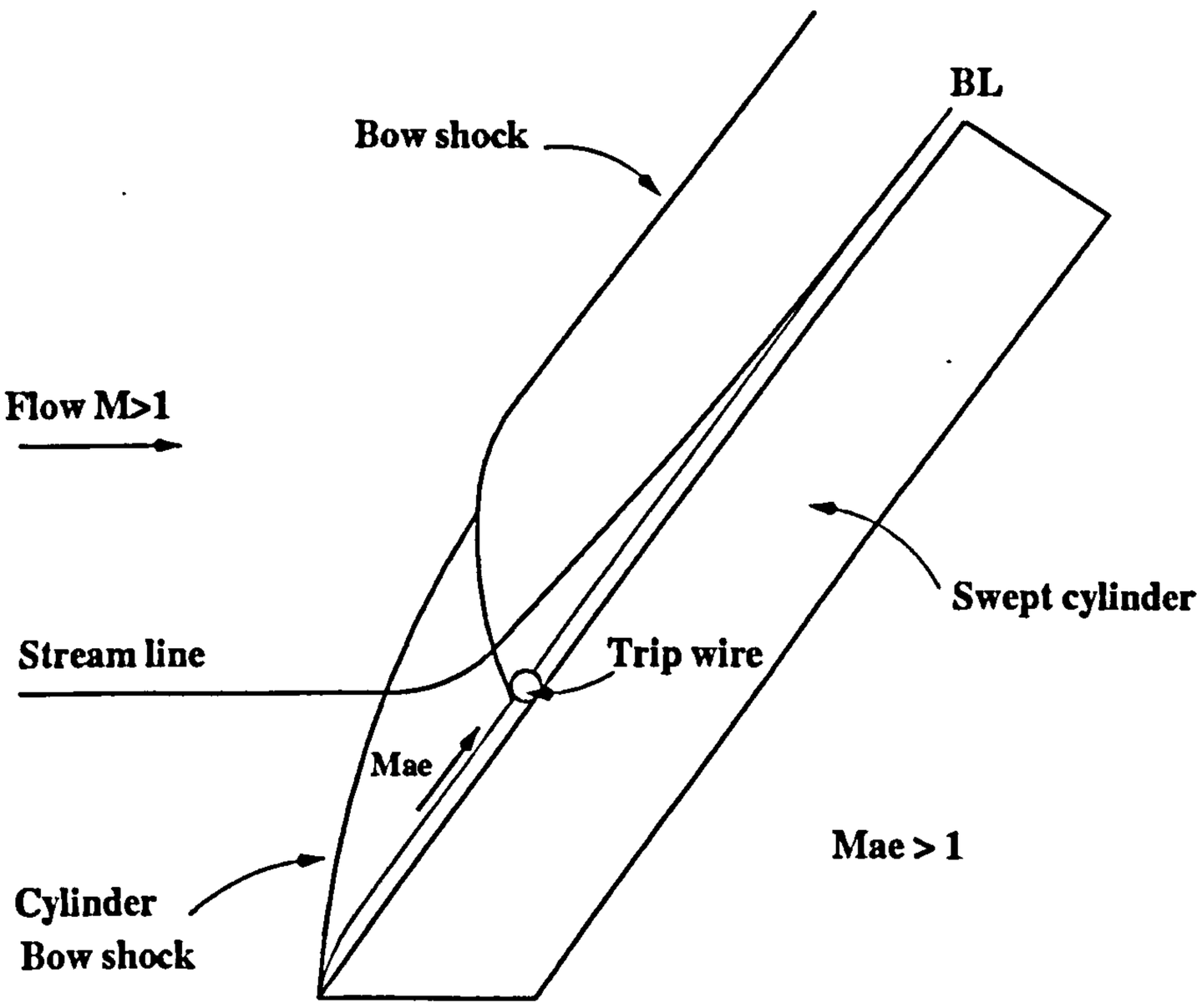

Figure M.1: Schematic of the bow shock and roughness element shock interaction.

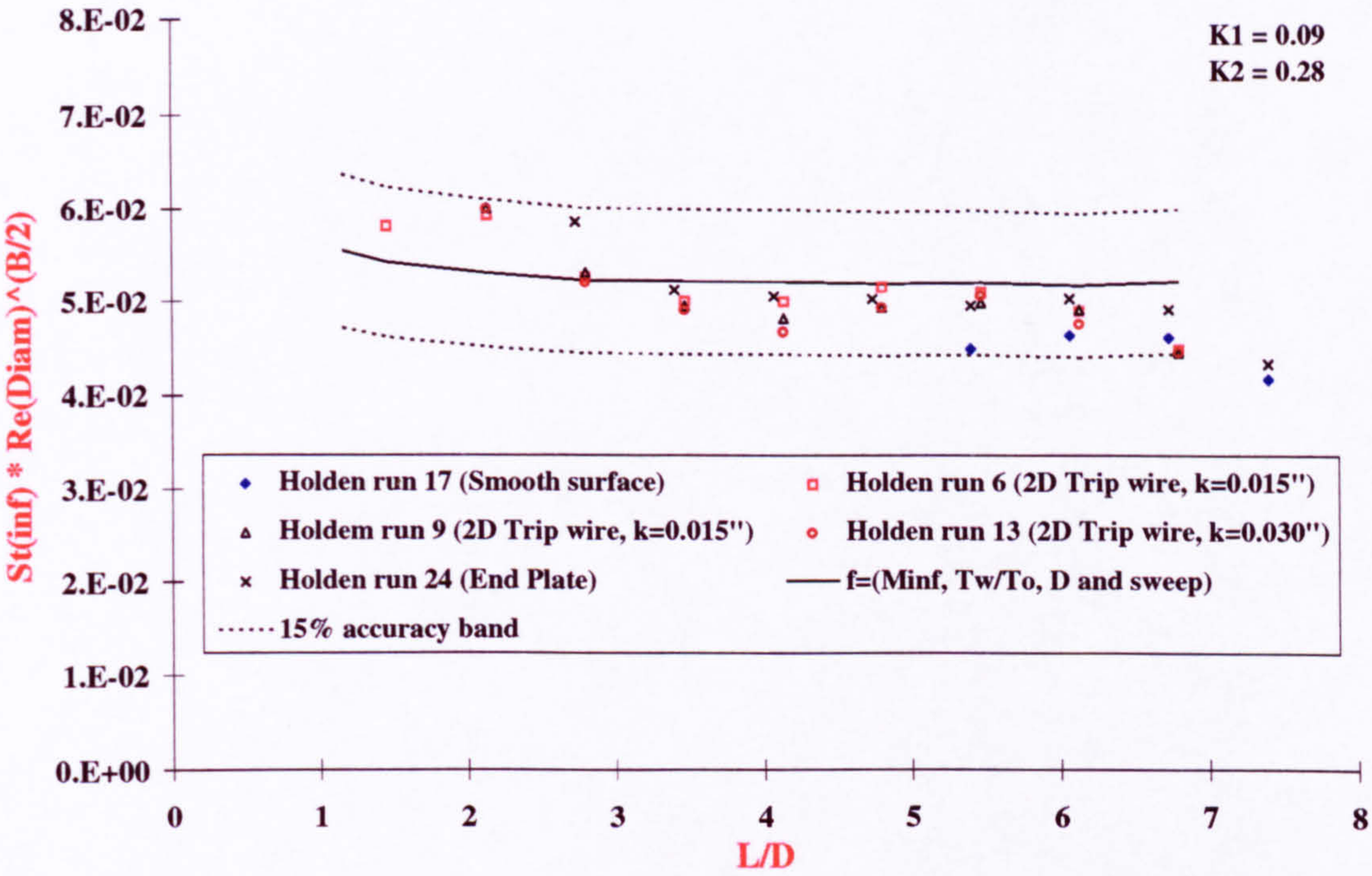

Figure M.2: Effect of roughness elements upon the flow field (Holden runs 6, 9, 13, 17 and 24). $M_\infty \approx 10.5$, $\frac{T_W}{T_o} \approx 0.26$, $\Lambda = 66.5^o$ and $D = 0.0762m$.

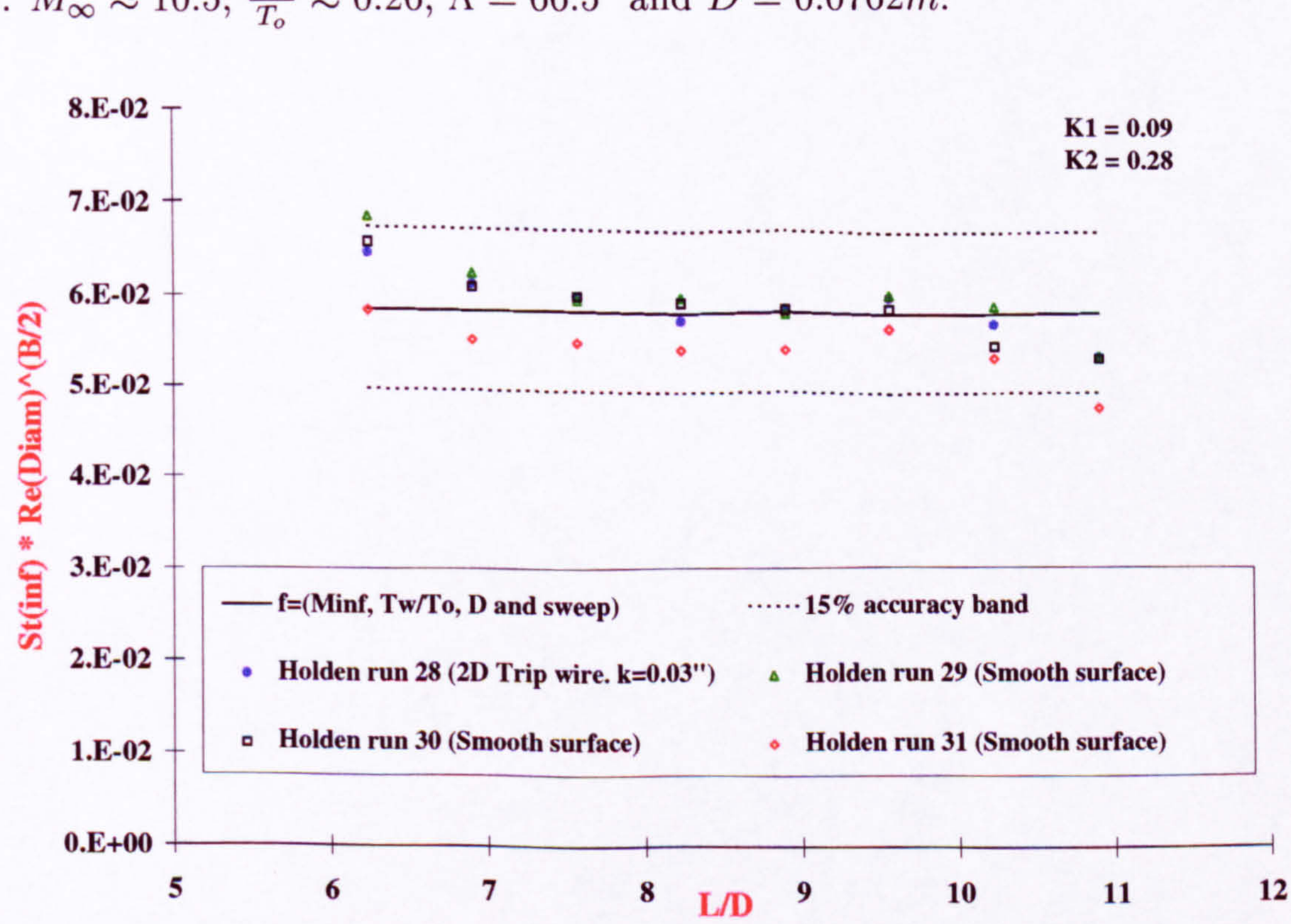

Figure M.3: Effect of roughness elements upon the flow field (Holden runs 28 to 31). $M_\infty \approx 10.6$, $\frac{T_W}{T_o} \approx 0.26$, $\Lambda = 75^o$ and $D = 0.0762m$.

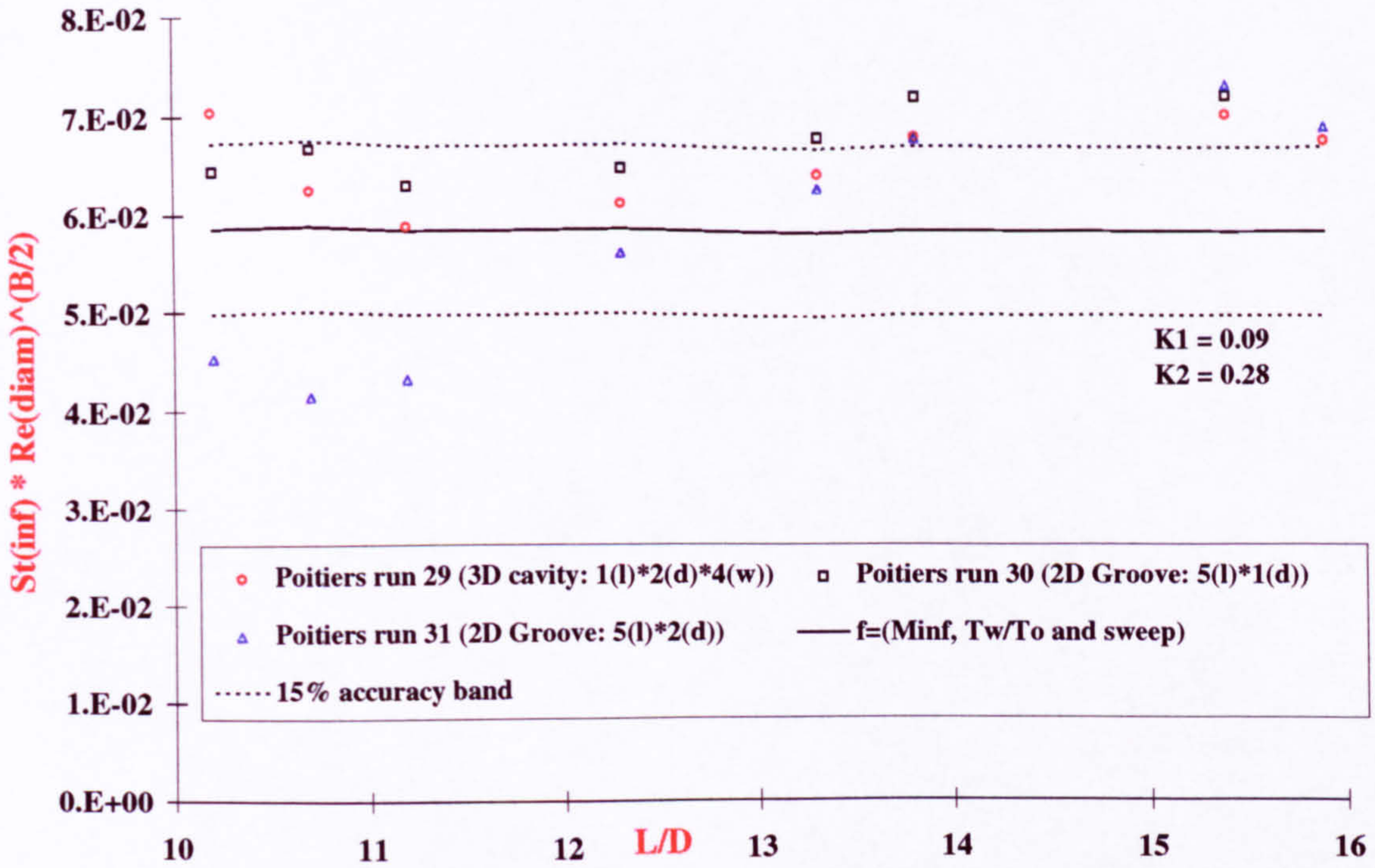

Figure M.4: Effect of the roughness elements upon the flow field (Poitiers runs 29, 30 and 31). $M_\infty = 7.14$, $\frac{T_W}{T_o} = 0.38$, $\Lambda = 70^o$ and $D = 19mm$.